Hydrothermal Synthesis of Inorganic Nanoparticles for Potential Technological Applications

A thesis presented in partial fulfilment of the requirements for the degree of

Doctor of Philosophy

in

Chemistry

at Massey University, Manawatū, New Zealand

Hossein Etemadi

2021

Dedicated to My Beloved Family

MASSEY UNIVERSITY
TE KUNENGA KI PŪREHUROA
UNIVERSITY OF NEW ZEALAND

GRADUATE RESEARCH SCHOOL

Note for Examiners
Explanation of COVID-19 Impacts

Thank you for taking the time to examine this thesis, which has been undertaken during the Covid-19 pandemic. The New Zealand Government's response to Covid-19 includes a system of Alert Levels which have impacted upon researchers. Our University's pandemic plan applied the Government's expectations to our research environment to ensure the health and safety of our researchers, however, research was impacted by restrictions and disruptions, as outlined below.

For a six-week period from March 26 to April 27 2020, New Zealand was placed under very strict lockdown conditions (Level 4 – Lockdown), with students and staff unable to physically access University facilities, unless they were involved in essential research related to Covid-19. All field work ceased and data collection with humans was restricted to online methods, if appropriate. The restrictions were partially lifted on April 27, but students and staff were not generally allowed back into University facilities until May 13.

Ongoing disruptions have also been encountered for some students due to uncertainties over the potential for future Covid-19-related restrictions on activities, and a Covid-19 cluster outbreak based in Auckland in New Zealand on 12 August 2020 led to the imposition of rolling Level 2 (Reduce) and Level 3 (Restrict) conditions until 23 September 2020. Auckland campus based students remained on Level 2 until 7 October 2020. This Alert Level system continues to be utilised throughout 2021.

These changing Alert Levels have meant that some research students had experimental, clinical, laboratory, field work, and/or data collection or analysis interrupted, and consequently may have had to adjust their research plans. For some students, the impacts of Covid-19 stretched far beyond the lockdown period in April/May 2020, as they may have had to significantly revise their research plans.

Overseas travel is not permitted by the University and restrictions have been placed on the New Zealand borders which are closed to non-New Zealand citizens and permanent residents. This meant that international students who were based offshore at the time of lockdown, were unable to return to New Zealand. A small number of offshore students were provided permission to return to New Zealand in early 2021. Many students have also suffered from anxiety and stress-related issues, and have had financial impacts, meaning their research progress has been significantly delayed.

This form, as completed by the supervisor and student, outlines the extent that the research has been affected by Covid-19 conditions.

Approved by DRC 10/Feb/2021
DRC 21/02/03

Please consider the factors listed below in your assessment of the work.

This statement has been prepared by the candidate's supervisor in consultation with the student and has been endorsed by the relevant Head of Academic Unit.

Student Name:	Hossein Etemadi	ID Number:	16277452
Supervisor Name:	Paul G. Plieger	Date:	04-Mar-21
Thesis title:	Hydrothermal Synthesis of Iron Oxide Nanoparticles for Potential Technological Applic		

Considerations to be taken into account. Note: This statement will remain in the final copy of the thesis which will be available from the Massey University Library following the examination process.
[*Enter key considerations here for the examiners. This can include but is not limited to change of scope, scale, topic, focus; limitations in relation to data collection, access to necessary literature or archival materials, laboratories, field sites; disruptions as a result of lockdown and various alert levels, medical or health considerations etc*]

For the chapter 7 of my thesis, I had to perform the following measurements in NZ and Japan, however due to the pandemic I just sent samples off for the measurements:

- Vibrating Sample Magnetometry (VSM) magnetization measurements with Dr. Simon Granville and Victoria University of Wellington, NZ

- X-ray photoelectron spectroscopy (XPS) measurements with Dr. Colin Doyle, University of Auckland, NZ

- Photocatalytic water splitting measurements with Prof, Yoshida, The University of Kyoto, Japan

I also planned to attend in a recognized international conference related to "Nanoparticles" however due to that fact that borders have been closed I could not take part in any conferences unfortunately.

Approved by DRC 10/Feb/2021
DRC 21/02/03

Confidential for Examiners Only: [*Please enter any other considerations which are confidential for examiners only and should not be placed in the final thesis version submitted to Library following the examination process]*

[redacted]

Signed, confirming this is a fair reflection of the impact of Covid-19 on this research.

Student Hossein Digitally signed by Hossein Date: 2021.03.04 14:05:08 +13'00'

Supervisor Paul Plieger Digitally signed by Paul Plieger DN: cn=Paul Plieger, c=NZ, o=Massey University, ou=School of Fundamental Sciences, email=p.g.plieger@massey.ac.nz Date: 2021.03.04 15:28:56 +13'00'

Head of Academic Unit (or nominee) E Sattlegger Digitally signed by E Sattlegger Date: 2021.03.05 08:33:48 +13'00'

Approved by DRC 10/Feb/2021
DRC 21/02/03

Abstract

Iron oxide nanoparticles (IONPs) are of interest in a diverse range of environmental and biomedical applications due to their intrinsic chemical, physical and thermal features such as superparamagnetism, high surface-to-volume ratios, high biocompatibility, low toxicity and easy magnetic separation. Many technological applications necessitate small (diameter < 20 nm) nanoparticles with narrow size distributions (< 5 %) and pronounced saturation magnetisation (M_s) for uniform physical and chemical effects. Historically, the synthesis of IONPs with controlled size and size distribution without particle agglomeration has proved challenging. In this thesis, we utilised an easy hydrothermal route and successfully synthesized two common phases of IONPs, namely Fe_3O_4 (magnetite) and α-Fe_2O_3 (hematite), using $Fe(acac)_3$ as iron source. By controlling the reaction conditions such as time, temperature, and the concentration of surfactants such as PVP and oleic acid, the different phases were selectively synthesized. The prepared nanoparticles were fully characterized with X-ray diffraction (XRD), transmission electron microscopy (TEM), dynamic light scattering (DLS), energy dispersive X-Ray spectroscopy (EDS), atomic absorption spectroscopy (AAS), X-ray photoelectron spectroscopy (XPS), Fourier transform infrared spectroscopy (FTIR), thermogravimetric analysis (TGA), vibrating-sample magnetometry (VSM), Brunauer-Emmett-Teller (BET) surface area measurements, photoluminescence (PL) and UV–Vis diffuse reflectance spectroscopy (UV–Vis/DRS). In Part I of this thesis, Fe_3O_4 and metal-doped spinel $M_xFe_{3-x}O_4$ (M = Fe, Mg, Mn, Zn) nanoferrites were synthesised as agents for cancer treatment via a method called magnetic fluid hyperthermia (MFH). In Part II, α-Fe_2O_3 nanoparticles were hybridized with tin (II) sulfide (SnS) to create p-n heterojunction photocatalysts for efficient H_2 production via ethanol photoreforming.

Acknowledgements

I would like to appreciate large number of people for their help during my PhD journey and thesis.

First of all, I would like to express my sincere gratitude to my supervisor Prof. Paul G Plieger for always supporting my ideas and research plans in a great extend and his great scientific input! Paul, I Appreciate the nice environment you provided during my PhD with you. Thank you! I would also like to thank my co-supervisor, A/ Professor Catherine Whitby, for her helpful advices. I would like to thank Mrs. Jenna Buchanan very much for proofreading of my thesis.

I would like to thank Dr. Colin Doyle, University of Auckland, NZ, for helping me in X-ray photoelectron spectroscopy (XPS) measurements. I would like to thank Dr. Simon Granville, Victoria University of Wellington, NZ, for Vibrating Sample Magnetometry (VSM) magnetization measurements. I would like to thank Dr. May Lim, The University of New South Wales, Australia, for magnetic fluid hyperthermia (MFH) measurements. I would like to thank Dr. Tayyebeh Soltani and Prof, Yoshida, The University of Kyoto, Japan, for photocatalysis measurements.

Thanks to my office colleagues, Becky, Tyson, Sidney, Marryllyn and Brodie for their assistance and very friendly atmosphere.

I also want to thank SFS administration and technical staff for their kind assistance during my PhD.

I would like to gratefully acknowledge the New Zealand International Doctoral Research Scholarships (*NZIDRS*) committee for funding my PhD, giving me this wonderful opportunity to come to lovely New Zealand.

I would like to thank Mohsen Bagheri on his friendship during my time in Palmy.

Lastly, but always first in my heart, I want to thank my family, my parents specifically, Gholam and Kobra, for your unconditional love throughout my life. I also thank my brothers, Ali and Mehdi and lovely sisters, Melika and Fatima, sister in law Fatima, brothers in law, Ali and Yaser and particularly, new family members, Mohamad Sadra and Ayhan for your great support.

Thesis Overview

The research conducted in this thesis aims to develop a simple hydrothermal method for the synthesis of two important phases of IONPs, Fe_3O_4 and α-Fe_2O_3, with a variety of sizes and shapes. The thesis is divided into two sections, where the focus is on Fe_3O_4 nanoparticles in section I, which includes Chapters 2 – 5. Section II focuses on the α-Fe_2O_3 phase and includes chapters 6 and 7. The thesis is organized into 8 chapters as follows:

Chapter 1: Introduction to Iron Oxide Nanoparticles (IONPs)

This chapter gives a brief introduction to IONPs, specifically the Fe_3O_4 and α-Fe_2O_3 phases. Their physicochemical properties, crystal structures and magnetic properties are discussed.

Section I: Magnetite (Fe_3O_4) Nanoparticles

Chapter 2: Iron Oxide Nanoparticles: Physicochemical Characteristics and Historical Developments to Commercialization for Potential Technological Applications

This chapter overviews the Fe_3O_4-based suspensions developed for potential biomedical applications including magnetic resonance imaging (MRI), magnetic drug targeting (MDT), magnetic fluid hyperthermia (MFH), immunomagnetic separation (IMS) and magnetic particle imaging (MPI), and also Fe_3O_4-based fluids for industrial applications including electronic and mechanical devices, from their historical evolution to preclinical investigations, clinical trials, FDA approval and commercialisation.

Chapter 3: Magnetic Fluid Hyperthermia (MFH) based on Magnetic Nanoparticles (MNPs): Physical Characteristics, Historical Perspective, Clinical Trials, Technological Challenges and Recent Advances

Following the screening of different topics in Chapter 2, MFH was selected as the focus of this Ph.D. study. In Chapter 3, a second literature review comprehensively examines MFH based on Fe_3O_4 NPs by considering the chemical, physical and biological perspectives of the technique. This chapter also presents the technical hurdles associated with the MFH technique. Finally, recent technological progress in the field towards the advancement of MFH is outlined.

Chapter 4: Improvements in the Organic Phase Hydrothermal Synthesis of Monodisperse $M_xFe_{3-x}O_4$ (M = Fe, Mg, Zn) Spinel Nanoferrites for Magnetic Fluid Hyperthermia Application

From the proposed strategies to address the low heating potential of clinical Fe_3O_4 fluid in MFH, I chose to focus on the metal doping of Fe_3O_4. In this chapter I investigated experimentally the metal dopant substitution of Fe^{2+} with an M^{2+} cation in the tetrahedral (T_d) or octahedral (O_h) interstitial sites of an Fe_3O_4 crystal lattice. Metal-doped spinel $M_xFe_{3-x}O_4$ (M = Fe, Mg, Zn) nanoferrites were successfully synthesised through a modified organic phase hydrothermal route. A maximum temperature (T_{max}) of 66 °C was achieved for an aqueous ferrofluid of Fe_3O_4 NPs after magnetic field activation for 12 min.

Chapter 5: Synthesis and Characterisation of $M_xFe_{3-x}O_4$ (M = Fe, Mn, Zn) Spinel Nanoferrites through a Solvothermal Route

In the previous chapter, we found that our particles exhibited decreased magnetisation after substituting Fe_3O_4 with diamagnetic Mg^{2+} ions. Additionally, they were only dispersible in an organic solvent (hexane). In this chapter, we attempted to increase the magnetisation by the substitution of paramagnetic Mn^{2+} ions into the Fe_3O_4 structure and subsequently explored the effect of this substitution on the crystallinity and magnetisation values of bare Fe_3O_4 NPs. In addition, considering that polyvinylpyrrolidone (PVP) is a water-soluble stabilising agent, we replaced oleic acid (OA) with PVP in an attempt to directly synthesise water-dispersible nanoferrites without additional phase exchange treatments.

Section 2: **Hematite (α-Fe_2O_3) Nanoparticles**

Chapter 6: An introduction to photocatalysis for Water splitting/ Ethanol Photoreforming

This chapter outlines the basic principles of water splitting and ethanol photoreforming reactions through UV-Vis photocatalysis to generate H_2 and O_2 as clean and environmentally - friendly green energy sources. The proposed photocatalysts, the challenges of using a single photocatalyst and proposed strategies to improve the efficiency of a single photocatalyst are for water splitting/ ethanol photoreforming also described.

Chapter 7: Synergistic Effect of Redox Dual PdO_x/MnO_x Cocatalysts on Enhanced H_2 Production Potential of SnS/α-Fe_2O_3 heterojunction via Ethanol Photoreforming

This chapter describes the aqueous phase hydrothermal synthesis of monodisperse α-Fe_2O_3 NPs by controlling the reaction parameters such as time and temperature. The as - synthesised α-Fe_2O_3 photocatalyst was fused with SnS to develop α-Fe_2O_3 /SnS hetrocatalyst. (FeOSnS). The optimum FeOSnS hetrocatalyst (FeOSnS2) was loaded with PdO_x and MnO_x redox cocatalysts (with different percentages) as a potential catalyst for H_2 fuel production through water splitting and ethanol photoreforming. The results revealed the success of the hybrid strategies, namely heterostructuring and cocatalyst loading, so that FeOSnS2- PdO_x 2 % / MnO_x1 % achieved the maximum H_2 evolution efficiency

Chapter 8: Conclusion and future directions

This chapter discusses the linkages between the earlier chapters and provides some directions for future research.

Preface

The structure of this thesis complies with the Massey University "Guidelines for Doctoral Thesis by Publications", 2020 issued by the graduate research school (GRS). Formatting changes have been conducted to ensure a consistent style throughout the thesis. The following chapters in this thesis have been published, submitted or are ready for submission to international peer-reviewed journals.

Chapter 2:

H Etemadi and Paul G. Plieger. Iron Oxide Nanoparticles: Physicochemical Characteristics and Historical Developments to Commercialization for Potential Technological Applications. (accepted for publication at *ACS Biomaterial Science& Engineering*)

Chapter 3:

H Etemadi and P. G. Plieger. Magnetic Fluid Hyperthermia (MFH) based on Superparamagnetic Iron Oxide Nanoparticles: Characteristics, Historical Perspective, Clinical Trials, Technological Challenges and Recent Advances. H Etemadi, PG Plieger, *Advanced Therapeutics*, 2000061, **2020.** https://doi.org/10.1002/adtp.202000061

Chapter 4:

H Etemadi and P. G. Plieger. Improvements in the Organic Phase Hydrothermal Synthesis of Monodisperse $M_xFe_{3-x}O_4$ (M = Fe, Mg, Zn) Spinel Nanoferrites for Magnetic Fluid Hyperthermia Application, *ACS omega,* 5 (29), 18091-18104, **2020.** https://doi.org/10.1021/acsomega.0c01641

Chapter 5:

H Etemadi, and P. G. Plieger. Synthesis and Characterisation of $M_xFe_{3-x}O_4$ (M = Fe, Mn, Zn) Spinel Nanoferrites through a Solvothermal Route (accepted for publication at *Journal of Materials Science*), **2021**

Chapter 7:

H Etemadi , Tayyebeh Soltani, Hisao Yoshida, Yiming Zhang, Shane G. Telfer and Paul G. Plieger. Synergistic Effect of Redox Dual PdO_x/MnO_x Cocatalysts on Enhanced H_2 Production Potential of SnS/α-Fe_2O_3 heterojunction via Ethanol Photoreforming (submitted to *Nano Research*), **2021**

Additional publications

H Etemadi, T. Soltani Kalat, H. Yoshida and P.G. Plieger. The role of (Pd; Pd +MnO_x; Ag and Ag + CuO_x) Co-Catalysts on Selective Solar-light Photocatalytic Reactions over Hierarchical SnS Semiconductor (under preparation for submission)

H Etemadi, T. Soltani Kalat, H. Yoshida and P.G. Plieger. Hydrothermal Synthesis of monodisperse MoS_2 nanoparticles for Photocatalysis (under Preparation for submission)

Contributions Hossein Etemadi made to the publications are as follows:

Chapter 2: This review was drafted by Hossein Etemadi (including text and images). The draft was then proofread by Jenna Buchanan and Paul Plieger. Final edits were then completed by Hossein Etemadi. Nadia provide some comments in the preparation of the manuscript.

Chapter 3: This review was drafted by Hossein Etemadi (including text and images). The draft was then proofread by Jenna Buchanan and Paul Plieger. Final edits were then completed by Hossein Etemadi.

Chapter 4: Hossein Etemadi did the experimental design and trials, data analysis and draft of the manuscript. Magnetic Fluid Hyperthermia (MFH) measurements were done by Dr. May Lim, The University of New South Wales, Australia. The draft was then proofread by Jenna Buchanan and Paul Plieger. Final edits were then completed by Hossein Etemadi.

Chapter 5: Hossein Etemadi did the experimental design and trials, data analysis and draft of the manuscript. The draft was then proofread by Jenna Buchanan and Paul Plieger. Final edits were then completed by Hossein Etemadi.

Chapter 7: Hossein Etemadi did experimental design and trials, data analysis and draft of the manuscript. Jenna Buchanan proofread the manuscript. Shane G Telfer and Yiming Zhang contributed to BET measurements. Tayyebeh Soltani and Yoshida from The University of Kyoto, Japan contributed to UV-Vis DRS and photocatalysis measurements. Tayyebeh Soltani provided some scientific advisory in photocatalysis section. Paul did proofreading and finalisation of the manuscript. Final edits were then completed by Hossein Etemadi.

X-ray photoelectron spectroscopy (XPS) measurements was done by Dr. Colin Doyle, University of Auckland, NZ.

Vibrating Sample Magnetometry (VSM) magnetization measurements was done under training of Dr. Simon Granville, Victoria University of Wellington, NZ.

This is to certify that above mentioned work was done by Hossein Etemadi.

Signature Date Signature Date

Table of Contents

Abstract iv

Acknowledgements v

Thesis Overview vi

Preface ix

Contributions Hossein Etemadi made to the publications are as follows: xi

Table of Contents xii

List of Figures xvii

List of Tables xxvi

Chapter 1. Introduction to iron oxide nanoparticles 1

1.1. References 4

Chapter 2. Iron Oxide Nanoparticles: Physicochemical Characteristics and Historical Developments to Commercialization for Potential Technological Applications 6

Abstract 6

2.1. Introduction 7

2.2. Physicochemical Characteristics involved in the success of IONPs 8

2.3. Commercial Applications of IONPs 11

2.3.1. Industrial applications 11

2.3.2. Biomedical Applications 14

2.3.2.1. Diagnostic applications 15

2.3.2.1.1 Magnetic Resonance Imaging: IONPs as Contrast Agents 15

2.3.2.1.2 Magnetic Particle Imaging: IONPs as *in vivo* Tracers 20

2.3.2.1.3 Immunomagnetic Separation: IONPs for Cell Separation Fluids 22

2.3.2.2. Therapeutic applications 27

2.3.2.2.1 Magnetic Fluid Hyperthermia: IONPs as Thermal Mediators for Cancer Treatment 27

2.3.2.2.2 Magnetic Drug Targeting: IONPs as Drug Delivery Vehicles in a Clinical Setting 30

2.3.3. Theragnostic applications: Preclinical Stage....36
2.4. Selected applications of IONPs in the research development phase....37
2.4.1. Applications of IONPs to environmental water remediation....37
2.4.2. Applications of IONPs in Tissue Engineering....40
2.5. Overall challenges associated with IONPs in the biomedical field and proposed strategies....42
2.6. Concluding Remarks....45
2.7. References....48
Chapter 3. Magnetic fluid hyperthermia (MFH) based on magnetic nanoparticles (MNPs): Physical characteristics, historical perspective, clinical trials, technological challenges, and recent advances....56
Abstract....56
3.1. Introduction....57
3.2. History of MFH and current clinical stage....59
3.3. Magnetism at nanoscale: Magnetic hysteresis and relaxation loss....64
3.4. Technological challenges associated with MFH....74
3.5. Proposed strategies to maximise the efficiency of MFH....76
3.5.1. Optimization of the intrinsic features of IONPs....77
3.5.1.1. Size sorted IONPs for MFH....77
3.5.1.2. Shape - controlled synthesis of IONPs for MFH....83
3.5.2. Biomineralised magnetotactic bacteria....89
3.5.3. Composition altering strategies....98
3.5.3.1. Metal-Doped IONPs....98
3.5.3.2. Exchange-coupled core@shell magnetic NPs for MFH....106
3.5.4. Near-infrared (NIR) light contribution to MFH....109
3.5.4.1. Near-infrared (NIR) light activation of IONPs....110

3.5.4.2. Magnetic-plasmonic multifunctional nanohybrids.....120
3.5.4.3. NIR/AMF biomodal mode for MFH.....125
3.5.5. Targeted nanoscale MFH.....132
3.5.6. Self-controlled MFH.....146
3.5.7. Magnetic particle imaging (MPI) for MFH.....147
3.5.8. Other proposed candidates for MFH.....148
3.6. Conclusion and outlook.....152
3.7. Acknowledgement.....153
3.8. References:.....153
Chapter 4. Improvements in the organic phase hydrothermal synthesis of monodisperse $M_xFe_{3-x}O_4$ (M = Fe, Mg, Zn) spinel nanoferrites for magnetic fluid hyperthermia application.....190
Abstract.....190
4.1. Introduction.....190
4.2. Results and Discussion.....192
4.2.1. Structural and Compositional Studies.....192
4.2.2. Magnetization Studies.....204
4.2.3. Magnetic hyperthermia studies:.....207
4.3. Conclusion.....212
4.4. Experimental Section.....212
4.4.1. Materials.....212
4.4.2. Synthesis of Monodisperse $M_xFe_{3-x}O_4$ (M = Fe, Mg, Zn) Spinel Nanoferrites.....212
4.4.3. Instrumentation and Measurements.....213
4.5. References.....215
4.6. Supporting Information Improvements in the Organic Phase Hydrothermal Synthesis of Monodisperse $M_xFe_{3-x}O_4$ (M = Fe, Mg, Zn) Spinel Nanoferrites for Magnetic Fluid Hyperthermia Application.....219

Chapter 5. Synthesis and characterisation of $M_xFe_{3-x}O_4$ (M = Fe, Mn, Zn) spinel nanoferrites through a solvothermal route.....234
Abstract:.....234
5.1. Introduction.....235
5.2. Experimental Section.....237
5.2.1. Materials.....237
5.2.2. Synthesis of $M_xFe_{3-x}O_4$ (M = Fe, Mn, Zn) Spinel Nanoferrites.....237
5.2.3. Characterisation.....238
5.3. Results And Discussion.....238
5.3.1. Structural and Compositional Studies.....238
5.3.2. Magnetometry.....249
5.4. Conclusion.....253
5.5. References.....254
5.6. Supporting Information for.....259
Chapter 6. An Introduction to H_2 production from water splitting / ethanol photoreforming.....270
6.1. H_2 production from water splitting.....270
6.2. H_2 production from alcohol (ROH) photoreforming.....272
6.2.1 Photocatalytic Reforming of Methanol.....272
6.2.2 Photocatalytic Reforming of Ethanol.....273
6.3. Photocatalysts for H_2 Production.....273
6.4. Challenges of a single photocatalyst.....274
6.5. Proposed strategies to improve the H_2 evolution efficiency.....274
6.5.1. Elemental doping.....274
6.5.2. Heterojunction engineering.....275
6.5.3. Decoration of photocatalyst surface with a cocatalyst.....275

6.5.4. Nanostructuring 276

6.6. References: 277

Chapter 7. Synergistic Effect of Redox Dual PdO_x/MnO_x Cocatalysts on Enhanced H_2 Production Potential of SnS/α-Fe_2O_3 heterojunction via Ethanol Photoreforming 280

Abstract: 280

7.1. Introduction 281

7.2. Experimental Section 282

7.2.1. Synthesis of the α-Fe_2O_3 Catalyst 282

7.2.2. Synthesis of the SnS Catalyst 283

7.2.3. Synthesis of α-Fe_2O_3 - SnS (FeOSnS) Heterocatalysts 283

7.2.4. Loading of PdO_x/MnO_x Cocatalysts onto FeOSnS2 283

7.2.5. Photocatalytic Water Splitting and Ethanol Reforming for Hydrogen Production 283

7.3. Results and Discussion 284

7.3.1. Photocatalytic water splitting 295

7.3.2. Photocatalytic Reforming of Ethanol 297

7.3.3. Proposed Mechanism for H_2 production 299

7.4. Conclusion 301

7.5. References 303

7.6. Synergistic Effect of Redox Dual PdO_x/MnO_x Cocatalysts on Enhanced H_2 Production Potential of SnS/α-Fe_2O_3 heterojunction via Ethanol Photoreforming 306

Chapter 8. Conclusion and future directions 321

List of Figures

Figure 1.1 Crystal structure of Fe_3O_4 (magnetite) and α-Fe_2O_3 (hematite) (the black ball is Fe^{2+}, the green ball is Fe^{3+} and the red ball is O^{2-}). (Reprinted with permission from Ref.4) ...4

Figure 2.1 The composition of a commercial ferrofluid. 12

Figure 2.2 Ferrofluid based on IONPs are utilized in industrial products such as (a) loudspeakers, (b) switches and (c) seals. Copyright 2021, Ferrotec Corporation (U.S.). 14

Figure 2.3 IONPs in preclinical and clinical settings 15

Figure 2.4 Schematic representation of commercialized Feraheme™ fluid for MRI and MDT applications. Feraheme™ image copyright 2020, AMAG Pharmaceuticals (U.S.). 17

Figure 2.5 Schematic representation of commercialized Resovist® ferrofluid for MPI applications. Resovist® image copyright 2020, Bruker BioSpin MRI GmbH (Germany). 21

Figure 2.6 Schematic representation of commercialised VivoTrax™ ferrofluid for MPI applications. VivoTrax™ image copyright 2020, Magnetic Insight, Inc (U.S.). 21

Figure 2.7 A picture of (a) the CELLSEARCH® System for enumeration of circulating tumor cells (CTCs) and (b) CliniMACS® CD34. CELLSEARCH® image copyright 2020, Janssen Diagnostic Inc. CliniMACS® image copyright 2020, Miltenyi Biotec. 26

Figure 2.8 Schematic representation of commercialized NanoTherm® – ferrofluid for MFH applications. Nanotherm® image copyright 2020, MagForce AG (Germany). 28

Figure 2.9 Magnetic separation of organic pollutant by functional IONPs. 39

Figure 2.10 Photocatalytic degradation of an organic pollutant by an IONP photocatalyst...40

Figure 2.11 Historical evolution of IONPs to their current state in commercial biomedical and industrial market. Included are milestones achieved by the community with regards to stepwise development of IONPs for potential biotechnological applications. The milestones can be found in the following papers: Freeman (1960),[101] Papell (1963),[36] Rosensweig (1968),[37] Application of ferrofluid in loudspeaker (1973), Copyright 2021, Sony (Japan)[38] Molday (1975),[76] Jordan (1993),[84] Lübbe (1996),[107] the first FDA-approved contrast agent based on IONPs for MRI (1996),[43] Gleich and Weizenecker (2001),[59] the first MFH clinical fluid (2003), copyright 2020, MagForce AG (Germany),[86] the first FDA-approved

IMS fluid (2004), copyright 2020, Janssen Diagnostic Inc[78] approval of Feraheme™ by the FDA (2009), copyright 2020, AMAG Pharmaceuticals (U.S.), [111] the first commercial fluid for MPI (2013), copyright 2020, Bruker BioSpin MRI GmbH (Germany), [60] the second FDA-approved IMS fluid (2014), copyright 2020, Miltenyi Biotec (Germany),[79] the second commercial MPI fluid (2017), copyright 2020, Magnetic Insight, Inc (U.S.),.[158] 45

Figure 3.1. Pictures of (a) NanoTherm® ferrofluid (b) NanoPlan® and (c) NanoActivator® (Copyright: MagForce AG (Germany). 60

Figure 3.2. (a)The behaviour of superparamagnetic and ferromagnetic particles in the presence and absence of a magnetic field. (Reprinted with permission from ref 89. Copyright 2012 MDPI Publishing Group.) (b) A typical hysteresis loop for different magnetic particles. (Reprinted with permission from ref 93. Copyright 2012 Elsevier Publishing Group.) (c) Size-dependence of coercivity for magnetic particles. (Reprinted with permission from ref 91. Copyright 2017 RSC Publishing Group.).....67

Figure 3.3.The two mechanisms responsible for cell death under an MFH protocol. (a) Hysteresis or relaxation loss (depending on the magnetic phase and size of MNPs) which results in temperature elevation of the tumor area and subsequent necrosis and or apoptosis. (b) Nanoscale thermal phenomenon which regulates the biochemical mechanisms that trigger cancer cell death pathways. 73

Figure 3.4. Proposed strategies to boost the efficiency of MFH for cancer treatment. 77

Figure 3.5. a) Transmission electron microscopy images of IONPs. Scale bars equal 100 nm. SAR of MIONs dispersed in b) deionized water and c) in water vs 50 % glycerol, under AMF (operating at f= 325 kHz H= 9.35 kA/m). d) Experiment set up of tumor-bearing mouse. e) *In vivo* tumor heating profiles. (Reprinted from ref 119. Copyright 2017 American Chemical Society).....81

Figure 3.6. a) SEM image of FVIOs. b) Comparison of SAR for FVIOs and Resovist at different fields at the frequency of 400 kHz. c) Dosage dependence of cell viability for MCF-7 cells treated with magnetic hyperthermia using FVIOs and Resovist. d) Immunofluorescence images of MCF-7 cells treated with different groups. Live and dead cells appear green and orange, respectively. e) Mice xenografted with breast cancer cells (MCF-7) before and 40

days after treatment with different tratement groups. (Reprinted with permission from ref 158. Copyright 2014 Wiley-V).....86

Figure 3.7. TEM micrograph of the chains of magnetosomes extracted from the bacteria a) Ch-Std and b) individual magnetosomes (IM). c) Percentage of inhibition of MDA-MB-231 cells incubated in the presence of Ch-Std, IM, SPION@Citrate, or SPION@PEG exposed to AMF = 0 and AMF of strength 40 mT. d) Photographs of the treated tumor in a mouse after 0 days (D0), 14 days (D14), and 30 days after the treatment (D30). Reprinted from ref 83. Copyright 2011 American Chemical Society).....91

Figure 3.8. a) Comparison of ILP value of $Mg_{0.13}Fe_2O_3$ nanofluids to other previously reported MNPs. b) A schematic diagram of spinel structure of $Mg_{0.13}Fe_2O_3$ NPs. c) Fluorescence microscopy images of U87MG cells treated with $Mg_{0.13}Fe_2O_3$ nanofluids: left) before and right) after MFH. d) Photographs of xenografted nude mice after MFH with $Mg_{0.13}Fe_2O_3$ nanofluids and Resovist. (Reprinted with permission from ref 188. Copyright 2014 Wiley-VCH.).....101

Figure 3.9. a) TEM (left) and overlay EELS mapped images (right) of $CoFe_2O_4$@$MnFe_2O_4$ core–shell NPs. b) M–H curve of synthesized NPs measured at 5 K using a SQUID magnetometer. c) SLP values of single-component (left) and various core–shell NPs (right). d) Nude mice xenografted with cancer cells (U87MG) before and 18 days after treatment with $CoFe_2O_4$@$MnFe_2O_4$, Feridex and doxorubicin respectively. e) Immunofluorescence histological images of the tumor region before and after MFH. (Reprinted with permission from ref 225. Copyright 2012 Nature Publishing Group.).....108

Figure 3.10. a) Schematic illustration of the synthesis and theranostic procedure of MSIOs for dual-modal photothermal tumor ablation b) Tumor growth curves of the four groups over a period of 15 days (left) and tumor weights after 15 days of the treatment (right). c) Representative photos of tumors in the four groups after 15 days treatment., Reprinted from ref 243. Copyright 2011 Ivyspring International Publisher).....111

Figure 3.11. Representative *in vivo* a) UCL and b) T2-weighted MR images of 4T1 tumor-bearing Balb/c mice taken 2 h after injection of MFNP-PEG NPs under magnetic field (MF) and without MF, c) The growth of 4T1 tumors in different groups of mice after treatment,

d) Representative photos of mice after various treatments indicated. (Reprinted from ref 255. Copyright 2011 Ivyspring International Publisher). 121

Figure 3.12. a) Live/Dead assay of MNP10 and AHP@MNP10 exposed to PDT and MHT, alone and in combination, in K1735 cells (live: green, dead: red). White scale bar is 50 µm. b) K1735 tumor volumes in the five treatment groups after treatment (n = 5). c) Images of mice bearing K1735 tumors before and after each treatment. Black circle indicates tumor (n = 5). (Reprinted with permission from ref 291. Copyright 2013 Wiley-VCH). 126

Figure 3.13.a) Thermal images and b) temperature change of the aqueous dispersion of Fe_3O_4/DOX/PPy-PEG-FA and Resovist NPs under AMF; (c) Change of tumor volume, non-treated mice (black), mice treated with chemotherapy (yellow), AMF (green), injected with Fe_3O_4/DOX/PPy-PEG-FA NPs intratumorally (purple), MHT (blue), and combined MHT and chemotherapy (red). The inset shows the magnified view for the first 12 days after treatment; (d) Photographs of mice treated with different protocols 45 days after treatment. (Reprinted with permission from ref 304. Copyright 2014 Ivyspring International Publisher.). 135

Figure 3.14.A historical perspective of MFH from the initial proposal of the idea to *in vivo* and clinical MFH application. Included are milestones achieved by the MFH community with regards to step - wise improvement in the heating potential of synthesized fluids as indicated by ILP values. MFH (magnetic fluid hyperthermia), MPI (magnetic particle imaging), LRT (linear response theory), ILP (intrinsic loss power), NIR (near-infrared (NIR) light, AMF (alternating magnetic field). The milestones information can be found in the following papers: Jordan 1993[31], Jordan 1997[32b], Bernhard 2001[428b], Sun 2002[120b], Rosensweig 2002[64],Hergt 2004[137],Hergt 2005[121a], Novosad 2009[370], Cheon 2012[250], Pellegrino2012[189], Rinaldi 2013[451], Yang 2015[276], Wilhelm 2015[327], Bae 2107[235], Zeisberger 2107[27a], Bao 2017[144] and Zeng 2018[252]. 151

Figure 4.1. TEM images of the synthesized Fe1 (a,b) and Fe2 (c,d) NPs at different magnifications of 100 nm and 25 nm. (TOPO 0.5 mmol, time 120 min at 240 ^{0}C). Inserts: Size distribution of Fe1 (e) and (f) Fe2 with mean size and standard deviation value (σ). 194

Figure 4.2. TEM images of the synthesized ZnFe1 (a,b) and ZnFe2 (c,d) NPs at different magnifications of 100 nm and 25 nm. (TOPO 0.5 mmol, time 120 min at 240 ^{0}C). Inserts: Size distribution of ZnFe1 (e) and (f) ZnFe2 with mean size and standard deviation value (σ). ..196

Figure 4.3. TEM images of the synthesized MgFe1 (a,b) and MgFe2 (c,d) NPs at different magnifications of 100 nm and 25 nm. (TOPO 0.5 mmol, time 120 min at 240 ^{0}C). Inserts: Size distribution of MgFe1 (e) and (f) MgFe2 with mean size and standard deviation value (σ).197

Figure 4.4. (a) Powder X-ray diffraction patterns and (b) the highlighted (311) diffraction peak of $M_xFe_{3-x}O_4$ (M = Fe, Mg, Zn) nanoferrites. 199

Figure 4.5. (a, b) TGA curves of $M_xFe_{3-x}O_4$ (M = Fe, Mg, Zn) nanoferrites. 200

Figure 4.6. XPS spectra of the Fe1 nanoferrite (a) survey scan (b) C1s (c) O 1s and (d) Fe 2p regional scans.....204

Figure 4.7. (a) Magnetic hysteresis loops of $M_xFe_{3-x}O_4$ (M = Fe, Mg, Zn) nanoferrites at room temperature (b) Magnified view of hysteresis loop of nanoferrites in low magnetic field, as indicated by red bracket in (a). (c) The inset shows the magnetic response of ZnFe2 to an external magnetic field. 206

Figure 4.8. FC/ZFC curves of the $M_xFe_{3-x}O_4$ (M = Fe, Mg, Zn) nanoferrites recorded at a constant magnetic field of 10 Oe.....207

Figure 4.9. (a) Heating curves of water-dispersed $M_xFe_{3-x}O_4$ (M = Fe, Mg, Zn) nanoferrites at field amplitude 114.01 mT. (b) SAR and (c) ILP values obtained from these curves.....211

Figure 4.10. TEM images of the synthesised Fe_3O_4 NPs with molar ratio of OA to OAm (a) 1:0 (b) 0:1 (c) 1:1; (d) 1:4 and (e) 1:5 mmol; 0.5 mmol of TOPO at 240 °C for 120 min.....223

Figure 4.11. TEM images of the synthesized Fe_3O_4 NPs with a 1:4 molar ratio of OA to OAm by different amounts of TOPO: (a) without TOPO; (b) 0.1 mmol; (c) 0.3 mmol; (d) 0.4 mmol; (e) 0.5 mmol of TOPO at 240 °C for 120 min. 224

Figure 4.12. TEM images of the synthesised Fe_3O_4 NPs with a 1:4 molar ratio of OA to OAm; TOPO 0.5 mmol at different reaction times of (a) 30 min; (b) 60 min (c) 90 min and (d) 120 min. 225

Figure 4.13. Volume particle size distribution (based on DLS data) of Fe1. PdI referrers to polydispersity index. 226

Figure 4.14. Volume particle size distribution of Fe2. 226

Figure 4.15. Volume particle size distribution of MgFe1. 227

Figure 4.16. Volume particle size distribution of ZnFe1. 227

Figure 4.17. Volume particle size distribution of MgFe2. 228

Figure 4.18. Volume particle size distribution of ZnFe2 228

Figure 4.19. EDX pattern of (a) the Fe1 and (b) the Fe2 NPs. 229

Figure 4.20. EDX pattern of (a) the MgFe1 and (b) the MgFe2 NPs. 229

Figure 4.21. EDX pattern of (a) the ZnFe1 and (b) the ZnFe2 NPs. 229

Figure 4.22. nanoferrite (a) survey scan (b) C1s (c) O1s and (d) Fe2p regional scans 230

Figure 4.23. XPS spectra of the MgFe1 nanoferrite (a) survey scan (b) C1s (c) O1s (d) Fe2p and (e) Mg1s regional scans 230

Figure 4.24. XPS spectra of the MgFe2 nanoferrite (a) survey scan (b) C1s (c) O1s (d) Fe2p and (e) Mg1s regional scans. 231

Figure 4.25. XPS spectra of the ZnFe1 nanoferrite (a) survey scan (b) C1s (c) O1s (d) Fe2p and (e) Zn2p regional scans. 231

Figure 4.26. XPS spectra of the ZnFe2 nanoferrite (a) survey scan (b) C1s (c) O1s (d) Fe2p and (e) Zn2p regional scans. 232

Figure 5.1 TEM images of the synthesised Fe1 (a, b) and Fe2 (c, d) NPs at different magnifications. Inserts: Size distribution of Fe1 (e) and Fe2 (f) with mean size (Dh)and standard deviation (σ) 240

Figure 5.2 TEM images of the synthesised MnFe1 (a, b) and MnFe2 (c, d) NPs at different magnifications Inserts: Size distribution of MnFe1 (e) and MnFe2 (f) with mean size (Dh) and standard deviation (σ) 241

Figure 5.3 TEM images of the synthesised ZnFe1 (a, b) and ZnFe2 (c, d) NPs at different magnifications. Inserts: Size distribution of ZnFe1 (e) and ZnFe2 (f) with mean size (Dh) and standard deviation (σ) 242

Figure 5.4(a) Powder X-ray diffraction patterns and (b) the highlighted (311) diffraction peaks of $M_xFe_{3-x}O_4$ (M = Fe, Mg, Zn) nanoferrites. 244

Figure 5.5 TGA curves of $M_xFe_{3-x}O_4$ (M = Fe, Mn, Zn) nanoferrites. 246

Figure 5.6 XPS spectra of the Fe1 nanoferrite (a) survey scan (b) C*1s* (c) O*1s* and (d) Fe*2p* regional scans..... 249

Figure 5.7(a) Magnetic hysteresis loops of $M_xFe_{3-x}O_4$ (M = Fe, Mn, Zn) nanoferrites at room temperature and (b) the magnetic response of MnFe2 to an external magnetic field. 251

Figure 5.8 FC/ZFC curves of the $M_xFe_{3-x}O_4$ (M = Fe, Mn, Zn) nanoferrites recorded at a constant magnetic field of 10 Oe..... 252

Figure 5.9 Powder X-ray diffraction (XRD) patterns of $M_xFe_{3-x}O_4$ (M = Fe, Mg, Zn) nanoferrites. 263

Figure 5.10 EDS pattern of (a) the Fe1 and (b) the Fe2 NPs. 263

Figure 5.11 EDS pattern of (a) the MnFe1 and (b) the MnFe2 NPs. 264

Figure 5.12 EDS pattern of (a) the ZnFe1 and (b) the ZnFe2 NPs. 264

Figure 5.13 Calibration results obtained for the determination of Fe by atomic absorption spectrometry..... 265

Figure 5.14 Calibration results obtained for the determination of Mn by atomic absorption spectrometry..... 265

Figure 5.15 Calibration results obtained for the determination of Zn by atomic absorption spectrometry..... 266

Figure 5.16 XPS spectra of the Fe2 nanoferrite (a) survey scan (b) C *1s* (c) O *1s* and (d) Fe *2p* regional scans..... 266

Figure 5.17 XPS spectra of the MnFe1 nanoferrite (a) survey scan (b) C *1s* (c) O *1s* (d) Mn *2p* and (e) Fe *2p* regional scans. 267

Figure 5.18 XPS spectra of the MnFe2 nanoferrite (a) survey scan (b) C *1s* (c) O *1s* (d) Mn *2p* and (e) Fe *2p* regional scans. 267

Figure 5.19 XPS spectra of the ZnFe1 nanoferrite (a) survey scan (b) C*1s* (c) O*1s* (d) Fe*2p* and (e) Zn*2p* regional scans. 268

Figure 5.20 XPS spectra of the ZnFe2 nanoferrite (a) survey scan (b) C*1s* (c) O*1s* (d) Fe*2p* and (e) Zn*2p* regional scans. 268

Figure 5.21(a) Magnetic hysteresis loops of $M_xFe_{3-x}O_4$ (M = Fe, Mn, Zn) nanoferrites at room temperature (sample masses used are recorded on each spectra). 269

Figure 6.1 Basic principle of overall water splitting on a semiconductor particle. Reprinted with permission from Ref. [8]. Copyright 2007 ACS group. 271

Figure 6.2 Band edge positions of representative semiconductors on the basis of redox potentials. Reprinted with permission from Ref. [7]. Copyright 2015 MPDI group. 272

Figure 6.3 a) Proposed band diagram for the as-grown and bismuth-doped crystals. Reprinted with permission from Ref. [17]. Copyright 2017 RSC group. b) Charge transfer in a heterojunction-type photocatalytic system. Reprinted with permission from Ref. [20]. Copyright 2014 Wiley group. c) Schematic of solar-driven WS process in the presence of cocatalysts. Reprinted with permission from Ref. [17]. Copyright 2019 Science Direct group. 276

Figure 7.1 PXRD patterns of as-synthesized α-Fe_2O_3 and SnS, FeOSnS1-3 and (c) FeOSnS2-PdO_x/MnO_x catalysts. 285

Figure 7.2 TEM images (a, b), HRTEM image (c) and PXRD pattern (d) of α-Fe_2O_3 catalyst. Patterns for α-Fe_2O_3 (AMCSD card no. 0000143) is shown for comparison. 286

Figure 7.3 TEM images (a, b), HRTEM image (c) and a typical XRD pattern (d) of SnS catalyst. Patterns for SnS (AMCSD 0018115) is shown for comparison 287

Figure 7.4 TEM images FeOSnS2 (a), FeOSnS2- PdO_x 2 % (b), and FeOSnS2-PdO_x 2 % / MnO_x 1 % (c), catalysts. HRTEM images (d, f) and the corresponding particle size distributions (e, g) of PdO_x in FeOSnS2- PdO_x 2 % (b), and FeOSnS2- PdO_x 2 % / MnO_x 1 % (c), catalysts.....289

Figure 7.5 HAADF-STEM, and EDX elemental mapping images of FeOSnS2-PdO_x 2 % / MnO_x 1 % catalyst. 290

Figure 7.6 N_2 adsorption-desorption isotherm of as-synthesized α-Fe_2O_3, SnS, FeOSnS1-3 (a) and FeOSnS2 / PdO_x / MnO_x catalysts (b) measured at 77 K. Filled circles = adsorption points; empty circles = desorption points. 291

Figure 7.7 XPS survey spectra (a), and high-resolution XPS spectra of (b) C 1s, (c) O 1s, (d) S 2p, (e) Sn 3d, (f) 2p, (g) Pd 3d and (h) Mn 2p for FeOSnS2-PdO_x 2 % / MnO_x 1 % catalyst...295

Figure 7.8 a) Time course and b) accumulated H_2 evolution amount from water splitting over 0.2 g α-Fe_2O_3, SnS, and FeOSnS catalysts after a 3 h illumination. 297

Figure 7.9 a) Time course and b) accumulated H_2 evolution amount from water splitting over 1 g α-Fe_2O_3, SnS and FeOSnS catalysts after a 3 h illumination. 299

Figure 7.10 Band bending and carrier transport at the surface or interface for FeOSnS2/PdO_x/MnOx catalysts. 300

Figure 7.11 (a) ATR-FTIR spectra of as-synthesized α-Fe_2O_3, SnS, and FeOSnS1-3 catalysts, (b) magnified view of the ATR-FTIR spectra showing the chemical shift of -C=O functional group after heterostructure formation, (c) ATR-FTIR spectra of FeOSnS2/ PdO_x/MnO_x catalysts..309

Figure 7.12 UV-VIS diffuse reflectance spectra represented as Kubelka-Munk Function of as-synthesized (a) α-Fe_2O_3, SnS, FeOSnS1-3 and (b) FeOSnS2/ PdO_x/MnO_x catalysts. 311

Figure 7.13**.** Tauc plots for calculation of the direct optical band gaps of as-synthesized α-Fe_2O_3, SnS, FeOSnS1-3 and FeOSnS2/PdO_x/MnO_x catalysts. 312

Figure 7.14 EDS patterns of (a) *α*-Fe_2O_3 (b) SnS, (c) FeOSnS1, (d) FeOSnS2, (e) FeOSnS3, (f) FeOSnS2-PdO_x 1 % (g) FeOSnS2-PdO_x 2 % and (c) FeOSnS2-PdO_x 2 % / MnO_x 1 % catalysts. 314

Figure 7.15 PL spectra of as-synthesized α-Fe_2O_3, SnS, FeOSnS1-3 (a) and FeOSnS2/PdO_x/MnO_x catalysts (b) under 325 nm excitation.....316

Figure 7.16 (a) Hysteresis loops of α-Fe2O3 and FeOSnS2 catalysts measured at RT. (b) Magnified view of hysteresis loop in low magnetic field, as indicated by blue circle in (a). (c) Inset shows the magnetic response of FeOSnS2 catalysts to an external magnetic field. ...317

List of Tables

Table 1.1. Chemical properties of α-Fe_2O_3 and Fe_3O_4 nanoparticles. 3

Table 2.1 Commercially available IONP-based contrast agents for MRI. 18

Table 2.2 Companies that manufacture IMS platforms. 24

Table 2.3 Companies that manufacture MFH devices. 29

Table 2.4 A summary of clinical trials of MDT. 33

Table 2.5 Commercial fluids used in Nanodrug applications. 35

Table 3.1.The clinical trials of NanoTherm® therapy (f = 100 kHz with a variable field strength H = 0 - 18 kA/m, and fluid concentration = 112 mg/mL). 62

Table 3.2. Overview of shape - controlled IONPs for *in vitro* MFH on mice. 87

Table 3.3. Overview of shape - controlled IONPs for *in vivo* MFH on mice. 88

Table 3.4. Overview of biomineralised MTB for *in vitro* MFH. 93

Table 3.5. Overview of biomineralised MTB for *in vivo* MFH on mice. 95

Table 3.6. Overview of the metal - doped IONPs for *in vitro* MFH. 102

Table 3.7. Overview of the metal - doped IONPs for *in vivo* MFH on mice. 104

Table 3.8. Overview of NIR activated IONPs for *in vitro* MFH. 112

Table 3.9. Overview of NIR activated IONPs for *in vivo* MFH on mice. 114

Table 3.10. Overview of magnetic-plasmonic multifunctional nanohybrids for *in vitro* MFH. 122

Table 3.11. An overview of magnetic-plasmonic multifunctional nanohybbrides for *in vivo* MFH on mice. 123

Table 3.12. An overview of NIR/AMF Biomodal Mode for *in vitro* MFH. 127

Table 3.13. An overview of NIR/AMF Biomodal Mode for *in vivo* MFH on mice. 128

Table 3.14. An overview of biofunctionalized magnetic NPs for tumor specific *in vitro* MFH. 136

Table 3.15. An overview of biofunctionalized magnetic NPs for tumor specific *in vivo* MFH on mice. 140

Table 4.1. Calculated values of size and lattice parameters for $M_xFe_{3-x}O_4$ (M = Fe, Mg, Zn) spinel nanoferrites 201

Table 4.2. Molar ratios and chemical formula for $M_xFe_{3-x}O_4$ (M = Mg, Zn) nanoferrites found by AAS. 202

Table 4.3. Parameters of ZFC/FC and M-H hysteresis loops for $M_xFe_{3-x}O_4$ (M = Fe, Mg, Zn) nanoferrites 207

Table 4.4. Relaxation times and heating parameters for $M_xFe_{3-x}O_4$ (M = Fe, Mg, Zn) nanoferrites 211

Table 4.5. Synthesis conditions of $M_xFe_{3-x}O_4$ (M = Fe, Mg, Zn) spinel nanoferrites 213

Table 5.1 Synthesis conditions for $M_xFe_{3-x}O_4$ (M = Fe, Mn, Zn) nanoferrites. 238

Table 5.2 Calculated values of size and lattice parameters for MxFe3−xO4 (M = Fe, Mn, Zn) nanoferrites 243

Table 5.3 Theoretical and experimental (AAS) molar ratios and chemical formula of $M_xFe_{3-x}O_4$ (M = Mn, Zn) nanoferrites. 247

Table 5.4 Parameters of ZFC/FC and M-H hysteresis loops for $M_xFe_{3-x}O_4$ (M = Fe, Mg, Zn) nanoferrites 252

Table 7.1 Products yields for the photocatalytic reforming by photocatalyst. 299

Table 7.2 Physicochemical properties of as-synthesized α-Fe_2O_3, SnS, FeOSnS1-3 and FeOSnS2/PdO_x/MnO_x catalysts. 310

Table 7.3 Quantification of PdO_x and MnO_x cocatalyst in FeOSnS2 heterocatalysts. 315

Chapter 1. Introduction to iron oxide nanoparticles

Iron oxide exists in several crystalline polymorphic forms including FeO (wüstite), Fe_3O_4 (magnetite), γ-Fe_2O_3 (maghemite), α-Fe_2O_3 (hematite), β-Fe_2O_3 and ε-Fe_2O_3.[1] In comparison to bulk iron oxide particles with an average diameter greater than 100 nm, iron oxide nanoparticles (IONPs) with diameters of 1 – 100 nm present unique magnetic, optical, electrical and thermal properties resulting from the size reduction effect.[1] As the size of the particle decreases, more atoms appear at the surface, such that a particle of 30 nm has 5 % of its atoms at its surface compared to 50 % surface atoms for a 3 nm particle. Therefore, smaller nanoparticles have a greater specific surface area per unit mass. As chemical reactions take place at the surface, smaller NPs would be much more reactive with extra surface energy. Therefore, nanoscale particles show significant potential for various technological applications.[2] Of all the available IONPs, Fe_3O_4 and α-Fe_2O_3 are the most widely studied. Fe_3O_4 is a black magnetic compound which possesses the strongest magnetism of all the transition metal oxides.[3] The compound α-Fe_2O_3 is reddish-brown in colour and the most stable iron oxide in air under environmental conditions.[3] The iron oxide Fe_3O_4 ($Fe^{2+}Fe^{3+}{}_2O_4$) presents an inverse spinel_crystallographic configuration with a unit cell consisting of 32 O^{2-} anions in a face centred cubic (f.c.c.) close-packed arrangement, 16 Fe^{3+} ions occupying octahedral (B) and tetrahedral (A) sites equally and 8 Fe^{2+} ions residing in B sites.[3] α-Fe_2O_3 crystallises in the rhombohedral lattice system with O^{2-} in a hexagonal close-packed (h.c.p.) arrangement and Fe^{3+} cations occupying octahedral sites.[3] (Figure 1.1) The iron atom has four unpaired electrons in its 3d orbitals. Fe^{3+} and Fe^{2+} ions have 5 and 4 unpaired electrons in their 3d orbitals respectively. The motion of electrons in an orbital around the nucleus (orbital angular momentum) for iron (+2) and the rotation of electrons around their axes (spin angular momentum), for both iron oxidation states, causes iron to have a strong magnetic moment. Crystals containing Fe^{2+} and Fe^{3+} ions can be in the ferromagnetic, ferrimagnetic or antiferromagnetic state.[4] In paramagnetic materials, unpaired electrons produce magnetic dipoles (due to spin and orbital angular momentum) which are randomly oriented, resulting in zero net magnetisation. Under an external applied magnetic field (AMF) these magnetic dipoles align in the direction of the applied field, resulting in a net small positive magnetisation and susceptibility (γ). These materials are weakly attracted to an applied field and do not retain their magnetic

properties upon the removal of the AMF.[4] For ferromagnetic materials, unpaired electrons in partially filled orbitals of atoms or ions produce magnetic moments (due to spin and orbital angular momentum) which are aligned parallel resulting in large net magnetisation. These materials are strongly attracted to an external magnetic field and retain their magnetic properties even after the removal of the applied field, therefore exhibit large positive magnetisation and susceptibility ($\gamma >> 1$).[4] In ferrimagnetic materials, the magnetic moments are unequal in magnitude and order in an antiparallel arrangement resulting in small magnetisation and susceptibility ($\gamma > 1$).[4] In antiferromagnetic materials the magnetic moments are equal in magnitude but in completely an antiparallel array resulting in zero net magnetisation ($\gamma = 0$).[4] Bulk Fe_3O_4 exhibits ferrimagnetic properties at room temperature, but when the size of Fe_3O_4 decreases below a critical value (< 30 nm) it becomes superparamagnetic at room temperature. As a result of this superparamagnetism, Fe_3O_4 nanoparticles have been highly utilised in various biomedical applications,[4] as will be discussed in the Chapter 2 and 3 of this thesis. Bulk α-Fe_2O_3 is weakly ferromagnetic or antiferromagnetic at room temperature. As the size decreases to the nanometer scale, α-Fe_2O_3 can exhibit ferromagnetic and even superparamagnetic features as observed in some literatures.[5] α-Fe_2O_3 has been utilised for several for environmental applications such as CO_2 remediation, H_2O splitting, photocatalytic dye degradation and Li ion batteries.[6] A summary of psychochemical properties of Fe_3O_4 and α-Fe_2O_3 is provided in Table 1.1.

Table 1.1. Chemical properties of α-Fe_2O_3 and Fe_3O_4 nanoparticles.

Iron Oxide	**Molecular formula**	**Density (g/cm^3)**	**Melting point (°C)**	**Hardens**	**Crystallographic system**	**Structural type**	**Space group**	**Lattice constants (nm)**	**Type of magnetism**	***M*$_S$ at 300 K ($A.m^2/kg$)**
Hematite	α-Fe_2O_3	5.26	1350	6.5	Rhombohedral, hexagonal	Corundum	R3c (hexagonal)	a = b = 0.5034, c = 1.375	Weakly ferromagnetic or antiferromagnetic	0.3
Magnetite	Fe_3O_4	5.18	1583– 1597	5.5	Cubic	Inverse spinel	Fd3m	a = 0.8396	Ferrimagnetic	92 – 100

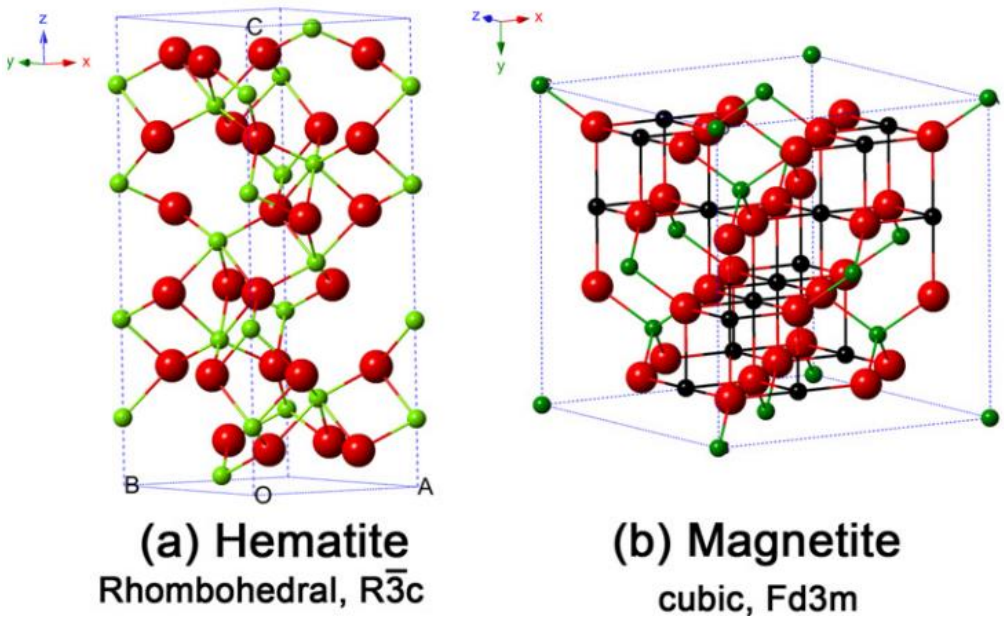

Figure 1.1 Crystal structure of Fe_3O_4 (magnetite) and α-Fe_2O_3 (hematite) (the black ball is Fe^{2+}, the green ball is Fe^{3+} and the red ball is O^{2-}). (Reprinted with permission from Ref.4)

1.1. References

[1] N. Ajinkya, X. Yu, P. Kaithal, H. Luo, P. Somani, S. Ramakrishna, *Materials (Basel)* **2020**, 13.

[2] S. Chaturvedi, P. N. Dave, N. K. Shah, *J. Saudi Chem. Soc* **2012**, 16, 307.

[3] J. Wallyn, N. Anton, T. F. Vandamme, *Pharmaceutics* **2019**, 11.

[4] A. S. Teja, P.-Y. Koh, Prog. Cryst. *Growth Charact. Mater* **2009**, 55, 22.

[5] L. De Los Santos Valladares, A. Bustamante Domínguez, L. León Félix, J. B. Kargin, D. G. Mukhambetov, A. L. Kozlovskiy, N. O. Moreno, J. Flores Santibañez, R. Castellanos Cabrera, C. H. W. Barnes, *J. Sci: Adv Mat and Dev* **2019**, 4, 483.

[6] M. Mishra, D.-M. Chun, *Appl Catal A-Gen* **2015**, 498, 126.

MASSEY UNIVERSITY
GRADUATE RESEARCH SCHOOL

STATEMENT OF CONTRIBUTION
DOCTORATE WITH PUBLICATIONS/MANUSCRIPTS

We, the candidate and the candidate's Primary Supervisor, certify that all co-authors have consented to their work being included in the thesis and they have accepted the candidate's contribution as indicated below in the *Statement of Originality*.

Name of candidate:	Hossein Etemadi
Name/title of Primary Supervisor:	Paul G. Plieger
Name of Research Output and full reference:	
Iron Oxide Nanoparticles: Physicochemical Characteristics and Historical Developments to Commercialization for Potential Technological Applications	
In which Chapter is the Manuscript /Published work:	2
Please indicate:	
• The percentage of the manuscript/Published Work that was contributed by the candidate:	90%
and	
• Describe the contribution that the candidate has made to the Manuscript/Published Work:	
This review was drafted by Hossein Etemadi (including text and images). The draft was then proofread by Jenna Buchanan and Paul Plieger. Final edits were then completed by Hossein Etemadi. Nadia provide some comments in the preparation	
For manuscripts intended for publication please indicate target journal:	
Accepted for publication at : ACS Biomaterials Science&Engineering	
Candidate's Signature:	Hossein Digitally signed by Hossein Date: 2021.08.28 11:29:47 +12'00'
Date:	28/08/21
Primary Supervisor's Signature:	Paul Plieger Digitally signed by Paul Plieger DN: cn=Paul Plieger, c=NZ, o=Massey University, ou=School of Fundamental Sciences, email=p.g.plieger@massey.ac.nz Date: 2021.08.30 15:05:17 +12'00'
Date:	30/08/21

(This form should appear at the end of each thesis chapter/section/appendix submitted as a manuscript/ publication or collected as an appendix at the end of the thesis)

Chapter 2. Iron Oxide Nanoparticles: Physicochemical Characteristics and Historical Developments to Commercialization for Potential Technological Applications

Hossein Etemadi,[a] Jenna K. Buchanan,[a] Nadia G. Kandile[b] and Paul G. Plieger*[a]

[a] School of Fundamental Sciences, Massey University, Private Bag 11 222, Palmerston North 4410, New Zealand

[b] Department of Chemistry, Faculty of Women, Ain Shams University, Heliopolis 11757, Cairo, Egypt

Keywords: nanoparticles, magnetic properties, imaging agents, antitumor agents, drug delivery

Abstract

Iron oxide nanoparticles (IONPs) have gained increasing attention in various biomedical and industrial sectors due to their physicochemical and magnetic properties. In the biomedical field, IONPs are being developed for enzyme/protein immobilization, magnetofection, cell labelling, DNA detection and tissue engineering. However, in some established areas, such as magnetic resonance imaging (MRI), magnetic drug targeting (MDT), magnetic fluid hyperthermia (MFH), immunomagnetic separation (IMS) and magnetic particle imaging (MPI), IONPs have crossed from the research bench, received clinical approval and have been commercialized. Additionally, in industrial sectors, IONP-based fluids (ferrofluids) have been marketed in electronic and mechanical devices for some time. This review explores the historical evolution of IONPs to their current state in biomedical and industrial applications.

2.1. Introduction

Iron oxide nanoparticles (IONPs) are a class of inorganic biomaterials which have been applied as multifunctional tools for advanced theranostic (medical diagnostic and therapeutic) and industrial applications.[1] IONPs include Fe_3O_4 (magnetite), γ-Fe_2O_3 (maghemite) and α-Fe_2O_3 (hematite). IONPs exhibit a range of intrinsic and unique chemical, physical and thermal features due to their composition and crystallographic structure. Firstly, they exhibit controllable sizes at the nanometer scale, an advantage when interacting with sub-micron biological components. This enables them to function on a molecular and cellular level, crossing the physiological barriers to reach biological entities of interest.[2] Importantly, IONPs can be activated on demand by an externally applied magnetic field (MF) due to their magnetic properties.[3] As a result of the size-dependent magnetic features and safety profile, IONPs have garnered success in industrial and biomedical fields. IONPs were first commercialized for use in industrial applications around 50 years ago. For these applications the physical form is called a ferrofluid in which IONPs-coated surfactants are statistically distributed in a carrier liquid in the absence of magnetic field. In this form the whole system responds to an external magnetic field as a homogenous system. The fact that the properties of ferrofluid such as magnetisation and viscosity can be controlled by external magnetic fields, created various applications with resulted in commercial success as use in seals, loudspeakers, dampers and electric motors, which are all now widely used.[4] In biomedical fields, IONPs are used in the form of colloidal suspensions where they can be separated out from a dispersion media by subjecting them to an externally applied magnetic field. IONPs are (*i*) at preclinical or clinical stages in their development, or (*ii*) have been validated by either the U.S. Food and Drug Administration (FDA) or the European Union (EU) for a number of diagnostic and therapeutic applications such as such as magnetic resonance imaging (MRI),[5, 6] magnetic drug targeting (MDT),[7] immunomagnetic separation (IMS),[8, 9] magnetic fluid hyperthermia (MFH),[10, 11] and magnetic particle imaging (MPI).[12] In MRI, a suspension of IONPs is injected into the tissue of interest and acts as a negative contrast agent, creating darker images of the tissue and thereby improving the imaging resolution.[13] In MDT, an IONP suspension is injected into the blood and guided to the site of action using an external static MF gradient. The use of *in vivo* magnetic particles and magnetic field penetration from outside the human body

permits the localization of a high concentration of NPs at the desired site. This enables site-specific drug distribution and the reduction of unwanted side-effects.[14] In IMS, IONPs are used as magnetic separation fluids to provide a potent, rapid and inexpensive systematic separation and analysis of the biomarkers in blood such as DNA, RNA and many low abundant proteins.[15] In MFH, a suspension of IONPs is injected into the cancer site and the remote actuation of the NPs under an alternating MF results in a temperature increase of the targeted area to 42 – 46 °C, followed by heat radiation to necrotize/apoptosize the cancer cells.[16] In MPI, an IONP suspension is injected into the blood stream intravenously and a high resolution three-dimensional (3D) image is created from their localized area. MPI creates images with high contrast and zero-tissue background signal, in contrast to MRI with poor contrast and slow image collection times.[17] Several publications reviewing IONPs have addressed the advances in the synthesis, physicochemical characterization techniques and technological applications of IONPs.[15, 18]To the best of our knowledge, a review discussing the existing market applications of IONPs in industrial and biomedical environments has not been comprehensively undertaken. Accordingly, in this review we examine the current landscape of IONPs which have been commercialized or gained FDA or EU approval. Conjointly, comprehensive lists of technological companies involved in the commercialization of IONPs are provided.

2.2. Physicochemical Characteristics involved in the success of IONPs

IONPs present a combination of favorable physicochemical properties such as biodegradability, biocompatibility, minimal toxicity, high magnetic susceptibility, superparamagnetism, high coercivity and low Curie temperature.[19] These have led to their successful commercialization as innovative industrial and biomedical products. Bulk Fe_3O_4 is ferromagnetic in nature and is composed of small magnetic regions called domains. In each domain, the individual magnetic moments are aligned in the same direction. However, the moments of different domains are randomly oriented, resulting in net zero magnetization in the absence of an applied magnetic field. After exposure to an applied MF, these magnetic domains align in parallel to the direction of the applied field and maximum magnetization (M_s) is achieved. When the MF is switched off, the magnetite is still magnetized to some extent, as some of the magnetic moments remain aligned, which results in a residual magnetization called remanence (M_r). Accordingly, a magnetic field of opposite sign, called

the coercive field or coercivity (H_c), is applied to bring the M_r to zero. Therefore, for bulk Fe_3O_4 the magnetization (M) as a function of applied MF *(H)* is described by a hysteresis loop.[20, 21]

When Fe_3O_4 is formed as crystals with diameters of 20 nm or less, its permanent magnetism is lost and it becomes superparamagnetic. Under an applied MF, superparamagnetic Fe_3O_4 nanocrystals become strongly magnetized because each nanocrystal behaves as a single magnetic moment. However, in contrast to larger ferromagnetic particles, the net magnetization is zero in the absence of an MF. This is because thermal fluctuations of superparamagnetic Fe_3O_4 dominate the magnetocrystalline anisotropy at room temperature. In this situation, a magnetic moment can rotate freely, so there is no hysteresis loop in its M-H plot*, the* magnetic remanence and coercivity are very close to zero and the magnetic interactions between particles are cancelled.[22] The Fe_3O_4 particles can rotate freely inside the solution through a mechanism called Brownian motion. Even when the applied MF is off, the Brownian torques (molecular collisions) lead to particle rotation. For superparamagnetic Fe_3O_4 particles, the Brownian motion is stronger than the gravitational forces, leading to their colloidal stability.[23, 24] Superparamagnetism is also IONPs present a combination of favorable physicochemical properties such as biodegradability, biocompatibility, minimal toxicity, high magnetic susceptibility, superparamagnetism, high coercivity and low Curie temperature.[19] These have led to their successful commercialization as innovative industrial and biomedical products. Bulk Fe_3O_4 is ferromagnetic in nature and is composed of small magnetic regions called domains. In each domain, the individual magnetic moments are aligned in the same direction. However, the moments of different domains are randomly oriented, resulting in net zero magnetization in the absence of an applied magnetic field. After exposure to an applied MF, these magnetic domains align in parallel to the direction of the applied field and maximum magnetization (M_s) is achieved. When the MF is switched off, the magnetite is still magnetized to some extent, as some of the magnetic moments remain aligned, which results in a residual magnetization called remanence (M_r). Accordingly, a magnetic field of opposite sign, called the coercive field or coercivity (H_c), is applied to bring the M_r to zero. Therefore, for bulk Fe_3O_4 the magnetization (M) as a function of applied MF *(H)* is described by a hysteresis loop.[20, 21]

When Fe_3O_4 is formed as crystals with diameters of 20 nm or less, its permanent magnetism is lost and it becomes superparamagnetic. Under an applied MF, superparamagnetic Fe_3O_4 nanocrystals become strongly magnetized because each nanocrystal behaves as a single magnetic moment. However, in contrast to larger ferromagnetic particles, the net magnetization is zero in the absence of an MF. This is because thermal fluctuations of superparamagnetic Fe_3O_4 dominate the magnetocrystalline anisotropy at room temperature. In this situation, a magnetic moment can rotate freely, so there is no hysteresis loop in its M-H plot*, the* magnetic remanence and coercivity are very close to zero and the magnetic interactions between particles are cancelled.[22] The Fe_3O_4 particles can rotate freely inside the solution through a mechanism called Brownian motion. Even when the applied MF is off, the Brownian torques (molecular collisions) lead to particle rotation. For superparamagnetic Fe_3O_4 particles, the Brownian motion is stronger than the gravitational forces, leading to their colloidal stability.[23, 24] Superparamagnetism is also crucial in biomedical applications because there is no interaction between particles after removal of MF, and potential embolization of the capillary vessels is minimized.[24] Another factor involved in the successful commercialization of IONPs in biomedicine is their low toxicity for living cells. The toxicity of any particles on the biological environment depends on the physiochemical properties of the particles and the administered dose.[25] For example, metals such as nickel, zinc, cobalt, silver, and cadmium are toxic to biological entities. Titanium and iron oxide-based particles are considered less toxic to the cells.[26] Naked Fe_3O_4 nanoparticles (if not sufficiently small) have low solubility and a high rate of aggregation under physiological conditions. In available commercial ferrofluids, Fe_3O_4 nanoparticles are coated with surface agent molecules in order to improve their biocompatibility and biodistribution, negate the oxidation of Fe_3O_4 core, enhance the stability and protect Fe_3O_4 against agglomeration, and increase the blood circulation half-life of the Fe_3O_4 core. Iron-containing nanoparticles are biocompatible. After the degradation of Fe_3O_4 in organs such as the liver, the released iron binds to apoferritin and apotransferrin to form ferritin and transferrin, protein complexes responsible for iron storage and transportation. The iron can then be incorporated in red blood cells or expelled from the body after being filtered through the kidneys.[27] Several clinical trials have reported minor side effects in patients upon the intravenous administration of clinically approved IONP-based fluids. In a study using Ferumoxtran-10, a commercial dextran-coated Fe_3O_4

developed for magnetic resonance lymphography, only 6 % of patients experienced mild side effects such as back pain, headache, nausea, diarrhea, and urticaria.[28] Resovist®, a commercial dextran-coated Fe_3O_4 ferrofluid developed for contrast-enhanced MRI of the liver, revealed side effects such as headache and irritation at the site of injection in only a small number of patients. In another study assessing the toxicity profile of ferumoxytol and ferumoxtran, commercial polyglucose sorbitol carboxymethylether-coated IONPs developed for angiography, less than 1 % of patients exhibited serious side effects (such as chest pain, hypotension and dyspnea) whilst 10 – 20 % of patients exhibited moderate adverse events (such as headache back pain, and urticaria).[29] Vadhan-Raj *et al*. studied the safety profile of ferumoxytol VR for the treatment of iron deficiency anemia (IDA). The revealed side effects were headaches (detected in 7 % of patients), urinary tract infection (5.6 % of patients), and any combination of nausea, diarrhea, vomiting, back pain, and dizziness (2 – 5 % of patients).[30] FeridexVR, a commercial dextran-coated Fe_3O_4 developed for MRI, was recognized as a safe agent with back pain observed in only 4 % of patients.[31]

2.3. Commercial Applications of IONPs

The applications of IONPs are dependent on the type of applied magnetic field. Industrial products such as seals, loudspeakers, dampers and electric motors utilize a steady magnetic field (ranging from 0.05 mT to 2 T). Biomedical applications such as MFH and MRI use relaxation time characteristics of particle moment in an AC magnetic field.[32] In this section the existing market applications of IONPs in industrial and biomedical environments are discussed.

2.3.1. Industrial applications

In the industrial sector, IONPs are beings used in the form of fluids called ferrofluids. A ferrofluid is a stable colloidal suspension which responds to an external magnetic field as a single homogeneous system. It is composed of superparamagnetic IONPs, functionalized with a surface-active agent and dispersed in a carrier fluid.[32] The commercial ferrofluids are typically magnetite (Fe_3O_4) or maghemite (γ-Fe_2O_3) with diameters in the order of 20 nm.[32] This ensures their colloidal stability, as the Brownian motion and thermal fluctuation is strong enough to oppose the gravitational force when the particles are very small in size. Additionally, the steric repulsive forces provided by the surfactant are stronger than the

magnetic dipole and Van der Waals forces for very small nanoparticles. Steric stabilization is achieved by surfactant molecules where the polar head is attached to the particle surface and the non-polar side chain extends into the carrier medium. This leads to the suppression of particle agglomeration and the formation of a homogeneous colloidal suspension.[33] Typical surfactants for the preparation of commercial ferrofluids are oleic acid and sodium bis(2-ethylhexyl) sulfosuccinate. The carrier fluids utilized are organic solvents (kerosene, freon, heptane, toluene), mineral oils or high-molecular weight synthetic oils (hydrocarbons, synthetic esters, glycols, silicones, polyphenyl ethers. The volume composition of a typical ferrofluid is about 85 % solvent, 10 % surfactant and 5 % magnetic particles.[4, 34] The composition of a commercial ferrofluid is shown schematically in Figure 2.1.

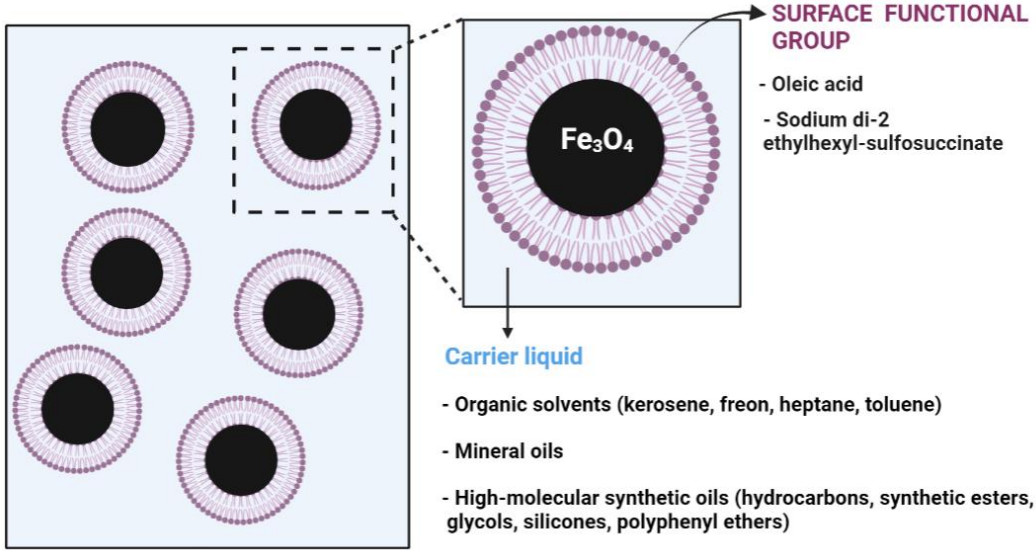

Figure 2.1 The composition of a commercial ferrofluid.

Commercial ferrofluids are prepared by size reduction and chemical precipitation methods.[32] The size reduction method requires the mechano-chemical grinding of micron sized Fe_3O_4 powder in the presence of surfactants (such as oleic acid) and solvent (such as kerosene) in a vibrating ball mill for a period of several weeks. After the grinding, centrifugation is applied to separate aggregated large particles from the suspension, and a stable Fe_3O_4-based ferrofluid is formed. The problems associated with this technique are the long grinding times (> 40 days) and the polydispersity of synthesized nanoparticles.[34]

The chemical coprecipitation method involves the addition of NH_3 solution to a mixture of $FeCl_2$ and $FeCl_3$ in water at 40 – 50 °C under intensive stirring. This results in the precipitation of Fe_3O_4 in a basic medium as described by equation (1):

$$Fe^{2+} + 2Fe^{3+} + 8OH^- \rightarrow Fe_3O_4 + 4H_2O$$

The first stable ferrofluid was invented by Steve Papell at the National Aeronautics and Space Administration (NASA) Glenn Research Center in 1963.[36] The task was to direct liquid rocket fuel into the engine in the absence of gravity. Papell proposed the idea to make a magnetic fluid and direct it to the engine under an applied MF. The fluid consisted of finely grinded particles of Fe_3O_4 coated with oleic acid and suspended in kerosene. This set the foundation for research development into ferrofluid technology. Ronald Rosensweig was the pioneer in the elucidation of the physicochemical principles of ferrofluids. With his colleagues, he licensed the technology from NASA, founded the Ferrofluidic Corporation (later Ferrotec Corporation) in 1969 and formulated ferrofluids with improved magnetization for a variety of applications.[37] The first commercial device based on ferrofluid was a pressure seal for a rotating shaft in which a ferrofluid was utilized to prevent leakage allowing the shaft to rotate with minimal friction.[38] In 1972, Dana Hathaway discovered the cooling effect of ferrofluids while working on damping the resonance of a tweeter.[39] In loudspeakers the presence of large currents can lead to the melting of the voice coil of the speaker. Covering the voice coil with a few drops of ferrofluid results in heat dissipation and reduces the friction between the diaphragm and the coil in the loudspeaker. The physical consequence of incorporating ferrofluids is a much clearer sound.[39] Today, ferrofluids have been integrated into some 300 million speakers, in different electronic products such as computers, laptops, headphones, earbuds, phones, and tablets. The advantage of using ferrofluids in loudspeakers is that they possess a Curie temperature of ~ 575 °C, which is higher than the operational temperature within loudspeaker. Accordingly, there is no loss of magnetization during operation.[40]

Ferrofluids have also been used as viscous dampers in automotive devices. New industrial applications of ferrofluids which are currently in the research and development stages include power and distribution transformers, quiet solenoids, material recycling, sensors and switches (Figure 2.2).

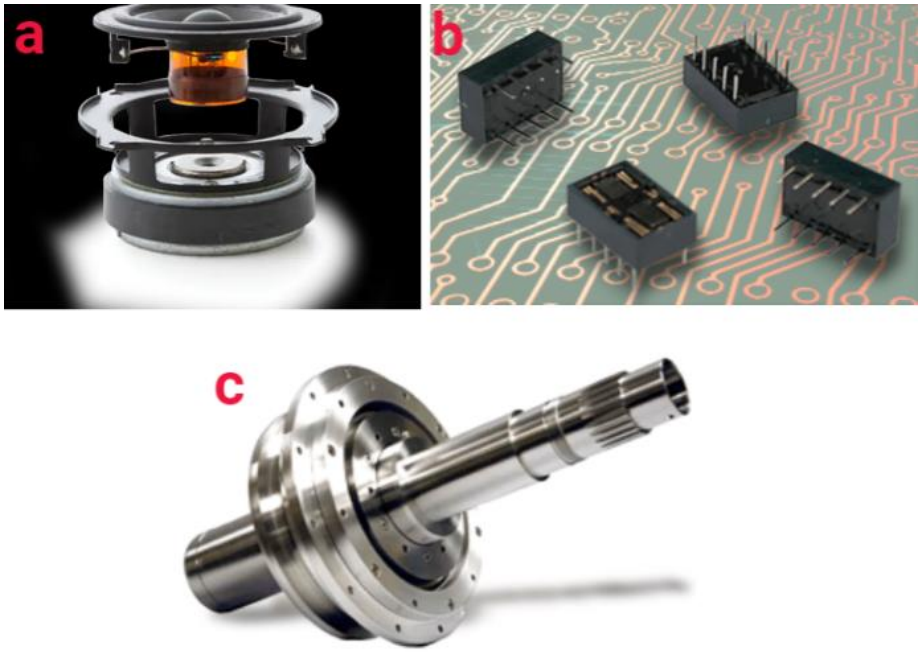

Figure 2.2 Ferrofluid based on IONPs are utilized in industrial products such as (a) loudspeakers, (b) switches and (c) seals. Copyright 2021, Ferrotec Corporation (U.S.), Copyright 2021, Sony Group Corporation (U.S.).

2.3.2. Biomedical Applications

As a result of the size-dependent magnetic features and safety profile, IONPs have garnered success in fields such as magnetic resonance imaging,[6] magnetic drug targeting,[7] immunomagnetic separation,[9] magnetic fluid hyperthermia,[10, 11] and magnetic particle imaging.[12] These include the realization of several fluids that (*i*) are at preclinical or clinical stages in their development, or (*ii*) have been validated by either the U.S. Food and Drug Administration (FDA) or the European Union (EU) for a number of diagnostic and therapeutic biotechnological applications (Figure 2.3).

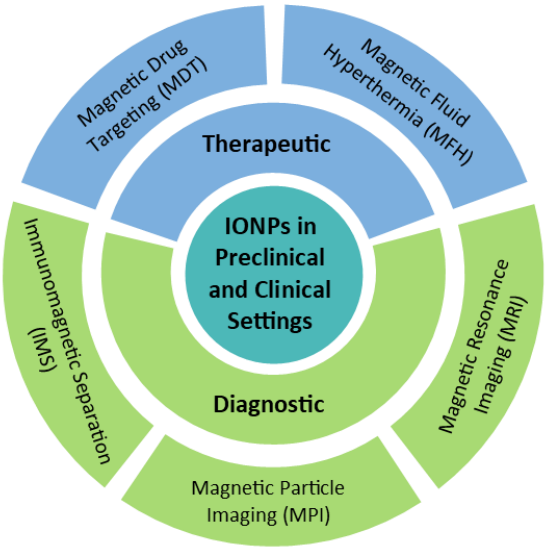

Figure 2.3 IONPs in preclinical and clinical settings

2.3.2.1. Diagnostic applications

2.3.2.1.1 Magnetic Resonance Imaging: IONPs as Contrast Agents

Magnetic resonance imaging is one of the most sophisticated imaging modalities in clinical diagnosis owing to its excellent spatial resolution, non-radioactive and non-invasive nature, strong soft tissue contrast and real-time monitoring characteristics.[5] MRI utilizes a strong magnetic field that aligns the magnetic moments of the protons of water and fat in tissues and organs. A beamed radio frequency (RF) pulse into the magnetic field then disorders the proton alignment. When the radiofrequency is off, excited protons return back to their aligned position with energy emitted as nuclear magnetic resonance (NMR) signals that can be detected by MRI, leading to an image of the soft tissues of the human body. The time it takes for protons to return to their aligned position is referred as the T_1 relaxation time, and the time for excited protons to rotate after being disturbed is referred as the T_2 relaxation time.[6] In most tissues, variations in T_1 and T_2 are intrinsically small, hence contrast agents are employed to bestow better imaging resolution between the tissue of interest and the surrounding tissue. The contrast agents fall into two categories. Positive contrast agents are based on gadolinium complexes that shorten the T_1 relaxation times, increasing signal intensity of the protons and resulting in brighter areas in MRI pictures. Negative contrast agents are based on superparamagnetic IONPs that shorten the T_2 relaxation times,

decreasing signal intensity of the protons and resulting in darker areas in MRI pictures.[6] In 1988 the first MRI contrast agent based on a paramagnetic gadolinium complex, Gd-DTPA (Magnevist, Schering AG), was introduced for clinical use in order to improve the imaging resolution by shortening the T_1 relaxation times of water protons.[41] In general, paramagnetic gadolinium complexes are preferred clinically as contrast agents as their inclusion results in brighter images with better resolution. Nevertheless, their short blood circulation times and the possibility of nephrotoxicity has aroused concern in their continued use due to the higher risk of kidney and liver disease.[42] This has led to the introduction of superparamagnetic IONPs for MRI as T_2 contrast agents, due to their biocompatibility and reduced toxicity. As such, Feridex IV® was the first FDA-approved contrast agent based on IONPs for liver and spleen imaging in 1996, however it was removed from the U.S market in November 2008 due to a lack of sales.[43] It is still available in Europe under the name Endorem®. Several formulations of IONPs have now been commercialized as MRI contrast agents by various companies and are listed in Table 1. IONP-based contrast agents have exhibited limited clinical success in liver, spleen, and lymph node imaging, as they passively accumulate in these regions. The lack of active specificity has prevented their widespread adaptation in the U.S. market. Additionally, these early examples suffered from signal loss in low signal body regions, low resolution and background interference, large particle size and low monodispersity.[42] Of all the previously commercialised FDA-approved contrast agents based on IONPs, Feraheme® (Ferumoxytol) is the only MRI angiography agent currently in use and is used to characterize and map the metastatic lymph nodes.[44] Feraheme® consists of superparamagnetic IONPs coated with polyglucose sorbitol carboxymethylether, with an overall colloidal particle diameter of 17 – 31 nm (Figure 2.4).

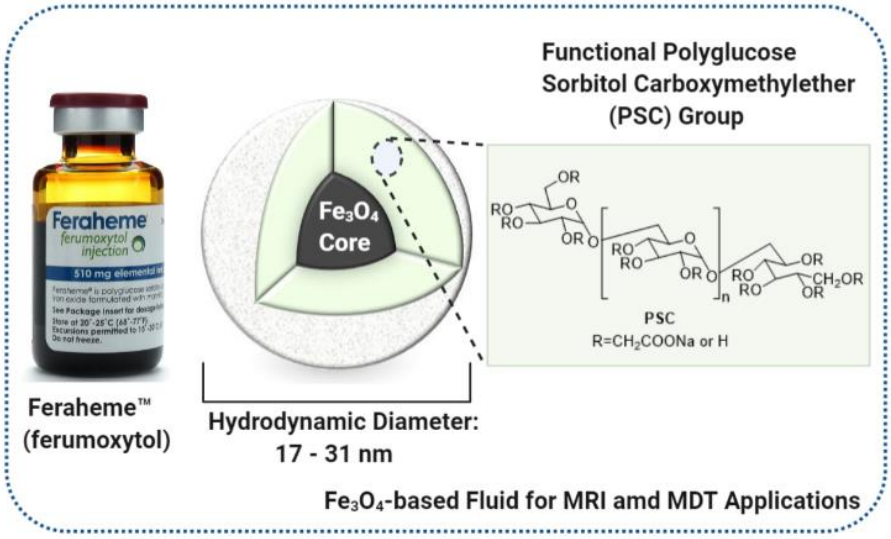

Figure 2.4 Schematic representation of commercialized Feraheme™ fluid for MRI and MDT applications. Feraheme™ image copyright 2020, AMAG Pharmaceuticals (U.S.).

Ultrasmall IONPs such as ultrathin nanowires (diameter ~ 3 nm) and ultrasmall nanospheres (diameter ~ 4 nm) have recently been proposed as T_1 contrast agents for MRI in an effort to address the disadvantages of the gadolinium-based T_1 contrast agents.[45] This together with a significant improvement in the synthesis of high quality IONPs with great monodispersity,[46] raises hopes to critically address the shortcomings of current contrast agents. Zhang *et al.*[47] and Frantellizzi *et al.*[48] have critically reviewed the fundamental principles, diagnostic aspects, possible toxicity and recent developments in the design of T_1 and T_2 contrast agents based on IONPs for MRI applications.

Table 2.1 Commercially available IONP-based contrast agents for MRI.

Brand name (Company)	**Structure / Hydrodynamic size (nm)**	**Mode of administration / Classification**	**Clinical dose**	**Target**	**Status**
Ferumoxides (Feridex IV®, Endorem™) (Advanced Magnetics (U.S.A))	Dextran-coated IONPs 80 – 150	Intravenous T_2 agent	0.56 mg Fe/kg	Reticuloendothelial system, Liver	FDA approved (1996) Discontinued (2008)
Gastromark™; Lumirem® (Guerbet (France))	Silicon-coated IONPs 300	Oral T_2 agent	0.9 – 1.4 mmol Fe/mL solution	Bowel imaging	FDA approved (1996) Discontinued (2012)
Ferumoxsil® (Advanced Magnetics (U.S.A), Guerbet (France))	Silicon-coated IONPs 300	Oral T_2 agent	0.175 mg Fe/mL	Liver	EU approved (1996) Discontinued (2006)
Resovist®, Cliavist®, Ferucarbotran (Bayer Schering (Germany))	Carboxydextran-coated IONPs 45 – 60	Bolus T_2 agent	0.45 – 0.7 mmol Fe/mL solution	Blood pool Stem cell labelling	EU approved (2001) Discontinued (2009)
Feruglose NC100150 (GE-Healthcare (U.S.A))	PEGylated starch-coated IONPs 11 – 20	Intravascular T_1 agent	0.1 mmol Fe/kg	Blood pool	The product was never commercially launched. Discontinued (2006)
Ferumoxtran-10, Sinerem®, Combidex® (Guerbet (France))	Dextran-coated IONPs 15 – 30	Intravenous T_2 agent	3 – 7 mg Fe/kg body	Lymph node metastases imaging	The application for approval was submitted to EU in 2006. Withdrawn from EU (2007).
VSOP-C184 (Ferropharm (Germany))	Citrate 4 – 8	Intravenous T_1 agent	0.52 mol Fe/L	Liver	Phase I
Ferumoxytol (Feraheme® (USA), Rienso® (EU)) (Advanced Magnetics (U.S.A)	Polyglucose sorbitol carboxymethylether-coated IONPs 17 – 30	Intravenous T_2 agent	30 mg Fe/mL	Angiography	FDA approved (2009)

2.3.2.1.2 Magnetic Particle Imaging: IONPs as *in vivo* Tracers

Introduced at the beginning of the 21st century, magnetic particle imaging is a non-invasive tomographic method which generates high resolution three-dimensional images of the concentration and location of IONP tracers after they have been injected into the blood stream intravenously.[49] The efficacy of MPI signal generation can be affected by IONP physicochemical properties, such as size, size distribution, crystallographic structure, colloidal stability, surface conjugation, systematic blood circulation time, magnetization and localization in the tumor site.[50] MPI has garnered significant interest as it features high sensitivity, high contrast and faster collection times in comparison to MRI. While MRI is based on changes in the nuclear magnetization of surrounding water molecules, MPI has higher sensitivity as it relies on the change in the direct magnetization of the IONPs. This also causes MPI to have zero tissue background signal and high contrast images, while collection times for MPI are much faster than that of MRI.[49] MPI is able to quantitatively image tracers at any depth in the body as the tissue does not cause depth attenuation.[51] In contrast to other techniques such as positron emission tomography (PET), computed tomography (CT) and single photon emission computed tomography (SPECT), MPI does not utilize ionizing radiation such as X-rays, positrons and γ-rays.[52] Due to these features, MPI has been utilized for imaging brain[53] and cancerous tissue,[54] angiography,[55] monitoring cardiovascular diseases,[56] tracking stem cells,[57] and magnetic fluid hyperthermia.[58] The concept of MPI was initially proposed by Gleich and Weizenecker in 2001 at Philips in Hamburg, Germany. They published the principles of the first MPI scanner in *Nature* in 2005.[59] From its conception in 2001, MPI has risen to become a growing technology in biological imaging. The augmentation of hardware and new image reconstruction approaches, in conjunction with the smart design of IONP tracers, has resulted in viable commercial preclinical MPI scanners. In 2013, Bruker BioSpin MRI GmbH (Germany) developed the world's first commercial MPI device. The company utilizes the clinically approved concentration of the FDA-approved IONP-based contrast agent Resovist® (formerly developed by Bayer Schering Company for MRI application) as a tracer (Figure 2.5).[60] Resovist® consists of superparamagnetic IONPs coated with carboxydextran, with a hydrodynamic diameter ranging between 45 and 60 nm.

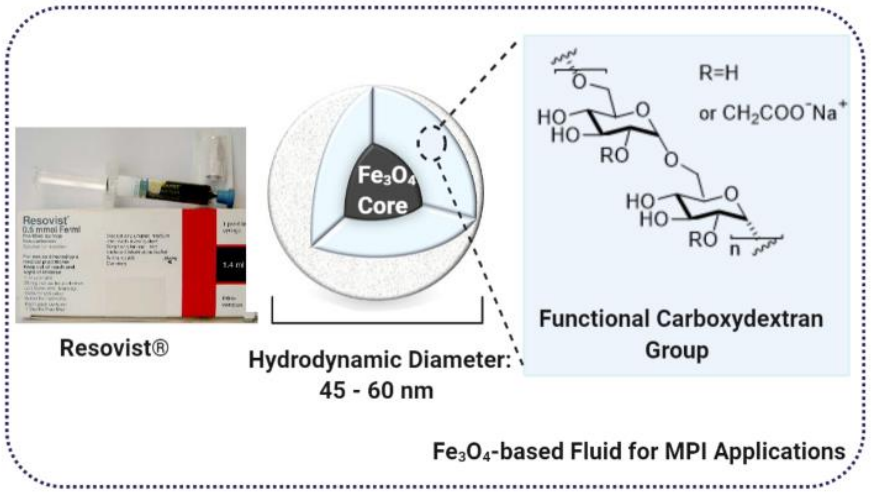

Figure 2.5 Schematic representation of commercialized Resovist® ferrofluid by (Bayer Schering Company) for MPI applications. Resovist® image copyright 2020, Bruker BioSpin MRI GmbH (Germany).

The second commercial MPI scanner was unveiled by Magnetic Insight, Inc (U.S) in 2017. They have also developed preclinical assessments with Resovist® under the new brand name of VivoTrax™ as IONP tracers (Figure 2.6).

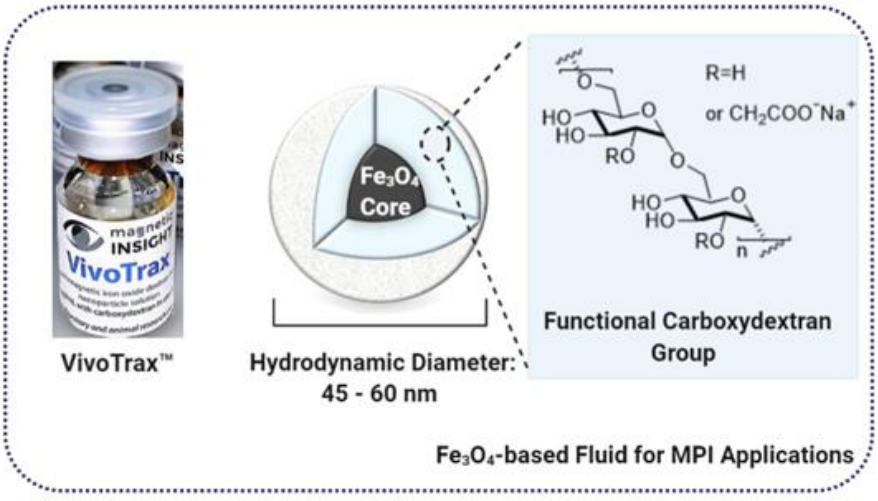

Figure 2.6 Schematic representation of commercialised VivoTrax™ ferrofluid (re-branded version of resovist) for MPI applications. VivoTraxTM image copyright 2020, Magnetic Insight, Inc (U.S.).

In parallel with hardware improvement, the optimization of IONP tracers has been of much interest, aiming to design innovatively engineered IONP tracers with strong responses toward an externally applied MF leading to precise signals for real-time *in vivo* monitoring.[61] For instance, Weizenecker *et al.* (2009) were the first group to implement *in*

vivo 3D real-time MPI scans on a mouse with a commercial tracer, Resovist®, at a clinically allowed dosage of 40 µmol (Fe) kg^{-1}.[56] In 2016, Krishnan and co-workers reported longer blood circulation times and improved MPI signals for polyethylene glycol coated IONPs compared to the commercially available Resovist®.[62] The research is ongoing, with the goal to develop tailored IONP tracers with longer half-lives for optimal MPI with strong precise signals. Additionally, multi-modal approaches have been adopted by combining MPI with MRI to augment the tracer distribution information with morphological information of the subject.[63] MPI is still considered a preclinical technology and is yet to receive EU or FDA approval.

2.3.2.1.3 Immunomagnetic Separation: IONPs for Cell Separation Fluids

Understanding the precise mechanism of cell behavior demands that firstly cells need to be grouped into subpopulations of high purity or homogeneity. The enrichment of a cell of interest from a large initial pool of cells is therefore the first critical step to unravelling specific molecular characteristics of, for example, blood and cancer cells. Immunomagnetic separation, also referred to as magnetic-activated cell sorting (MACS), is a crucial diagnostic separation tool based on IONPs (50 nm – 10 µm in diameter) for bioanalysis and immunoassays in benchtop and clinical settings.[64] It utilizes IONPs linked to specific cell-recognition moieties such as antibodies to selectively bind to a target cell and isolate it from a complex biological heterogeneous mixture. Binding of a ligand to the surface of IONPs improves the recognition of particular antigens expressed/overexpressed at the cell surface. Eventually, the magnetically tagged cells are separated under the activation of an externally applied MF.[65] IMS has gained increasing interest in a variety of biomedical areas such as oncology,[66] hematology,[67] immunology,[68] and proteomics for the purification of cells,[69] viruses,[70] bacteria,[71] proteins,[72] and nucleic acids.[73] IMS has been extensively utilized for the purification of biomarkers from blood, such as DNA, RNA and many low abundance proteins.[15] The technique can provide preliminary medical information about a gene expression profile, hematological characteristics, early diagnosis and progression, and prediction of different diseases such as cancer and infectious diseases. The current IMS automated systems offer substantial cell purities (> 96 %) at high throughput (~ 1010 cells/hr).[74] The first magnetic intrinsic cell separation was reported by Melville *et al.* in 1975 for the purification of red blood cells from whole blood.[75] IMS was initiated in 1977

by Molday *et al.* by application of magnetic microspheres functionalized with lectins or antibodies to separate lymphoid cells and red blood cells.[76] In 1989, Miltenyi *et al.* further developed the technique with antibody conjugated IONPs of about 100 nm diameter for the separation of various cells on HGM columns.[77] The company published a U.S. patent on this technology in 1990. Since then, the company has established a range of manual and automated reagents and tools for cell separation. In addition to Miltenyi Biotec, there are numerous companies (Table 2.2) that exclusively offer a portfolio of separation technologies and reagents based on magnetically-enabled cell separation for diverse biotechnological applications.

Table 2.2 Companies that manufacture IMS platforms.

Company	Country	Area of interest	Foundation Year	Website
Invitrogen and Dynal Biotech	Norway	Development of magnetic beads for life sciences, biotech and healthcare.	1986	www.dynabead.net
Miltenyi Biotec	Germany	Cell separation, flow cytometry and immunology, bioinformatics, and stem cell technologies	1989	www.miltenyibiotec.com
STEMCELL Technologies Inc	Canada	Biomagnetic separation of nucleic acid and protein	1993	www.stemcell.com
Micromod Partikeltechnologie GmbH	Germany	Separation of nucleic acids	1994	www.micromod.de
Aviva Bioscience	USA	Purification of nucleated cells from whole blood, Electrophysiology, Ion channel screening, flow cytometry	1999	www.avivabio.com
Magsense	USA	Immunoassays, protein purification	2003	www.magsenselifesci.com
MAGNISENSE SE	France	Bioassays for human and animal diagnostics	2003	www.magnisense.com
Chemicell	Germany	Bioseparation- gene transfection	2004	www.chemicell.com
Ocean Nanotech	USA	Biomagnetic isolation of nucleic acids and proteins	2004	www.oceannanotech.com
Diagnostic Biosensors, LLC	USA	Magnetic diagnostics sensors for immunoassays	2004	www.diagnosticbiosensors.com
Magnabeat Inc.	Japan	Magnetic purification of various bio-substances	2005	www.bloomberg.com
BioCep	Israel	Immunomagnetic isolation of rare cells	2006	www.biocep.com
SEPMAG technologies	Spain	Development of homogenous biomagnetic separation platforms for nucleic acid, protein purification	2007	www.sepmag.eu
TurboBeads	Switzerland	Biomagnetic isolation of proteins, peptides and DNA	2007	www.turbobeads.com

Cynvenio Biosystems	USA	Molecular analysis of cancer biomarkers in blood	2008	www.cynvenio.com
CellCap Technologies Ltd	UK	Purification of stem cells from blood or adipose lipoaspirate	2012	www.cell-capture.com
Quad Technologies	USA	Immunotherapy, stem cell, T Cell and circulating tumor cell (CTC) separation	2012	www.quadtechnologies.com

So far, the FDA has approved two cell separation systems both of which are based on IMS techniques. The first is the CELLSEARCH® system from Janssen Diagnostics Inc. This system is a semi-automated *in vitro* diagnostic device to identify, isolate and enumerate circulating tumor cells (CTCs) from a simple blood test utilizing an IONP ferrofluid. In this technology, IONPs decorated with anti-epithelial cell adhesion molecular antibodies (EpCAM) with an overall hydrodynamic size of 50 nm, separate the cancer cells expressing EpCAM immunomagnetically from the blood (Figure 2.7a). The CELLSEARCH® system was submitted by Janssen Diagnostics (formerly Veridex) in 2003 and granted the first FDA approval in 2004 for clinical diagnoses and enumeration of CTCs in patients bearing metastatic breast cancer.[78] The system was approved by the FDA for clinical monitoring of CTCs in patients bearing metastatic colorectal and prostate cancer in 2007 and 2008, respectively. Menarini Silicon Biosystems acquired CELLSEARCH® in 2017 and currently commercialize the technology. Miltenyi Biotec introduced the CliniMACS CD34 Reagent System in 1998 as the first semi-automated immunomagnetic cell separation system. In 2014 this system received FDA approval for clinical allogeneic stem cell transplantation in patients bearing acute myeloid leukemia. The CliniMACS® CD34 technology utilizes the anti-CD34 monoclonal antibody bound to IONPs to enrich cells expressing CD34 ($CD34^+$ cells) from hematopoietic stem cells (Figure 2.7b).[79] Notably, both FDA-approved separation systems have EU approval.

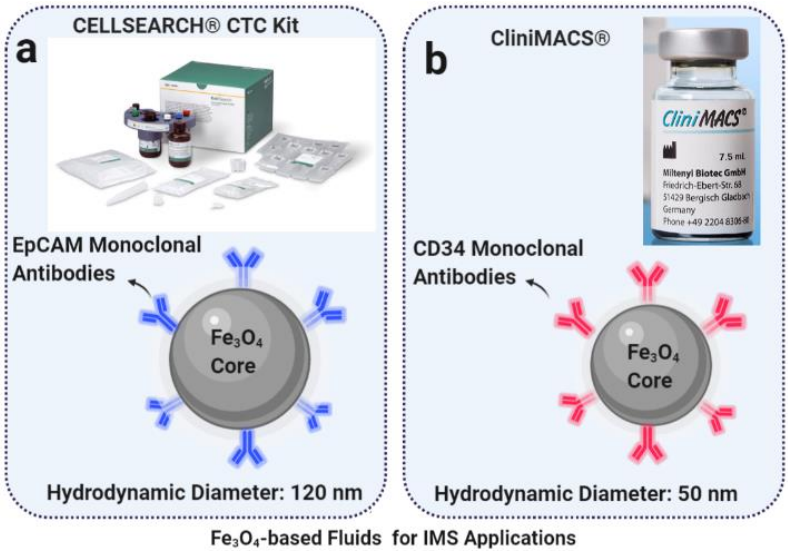

Figure 2.7 A picture of (a) the CELLSEARCH® System for enumeration of circulating tumor cells (CTCs) and (b) CliniMACS® CD34. CELLSEARCH® image copyright 2020, Janssen Diagnostic Inc. CliniMACS® image copyright 2020, Miltenyi Biotec.

2.3.2.2. Therapeutic applications

2.3.2.2.1 Magnetic Fluid Hyperthermia: IONPs as Thermal Mediators for Cancer Treatment

Magnetic fluid hyperthermia is a non-invasive therapeutic strategy based on IONPs for cancer treatment. [80],[81] The technique requires the injection of a ferrofluid into the tumor either directly or intravenously under the activation of an applied MF. When the magnetic forces provided by the MF overcome the linear blood flow rates in capillaries or arteries, the IONPs accumulate at the target site. The applied MF, operated within biologically safe frequencies (*f*) and amplitudes (*H*), switches the magnetic moments of IONPs rapidly. This results in heat dissipation and increases the temperature of the targeted area to 42 – 46 °C due to the mechanism of relaxation losses, denoted as Néel or Brown relaxation. Depending on the applied temperature and the duration of heating, this modality either results in direct tumor cell death or sensitises the cells to be more susceptible to concomitant radio or chemotherapy.[82] In 1957, Gilchrist *et al.* examined for the first time the potential of IONPs for the heating of tumor tissue under an alternating MF.[83] Subsequent pre-clinical studies evaluated the potential of MFH for the treatment of tumors, utilizing various field strengths and frequencies, magnetic materials, and a range of methods of encapsulation and delivery.[84, 85, 86] In 2001, Jordan *et al.* introduced a new MFH therapy system which featured an AC magnetic field applicator at a frequency of 100 kHz with a field strength of 0 – 15 kA m^{-1}. The ferrofluid utilized for the study is patented as NanoTherm® (Figure 2.8), which consists of IONPs with an aminosilane-type shell, approximately 15 nm in diameter, dispersed in water with an iron concentration of 112 mg/mL. In a review of MFH based on magnetic NPs, we summarised the clinical trials of MFH utilizing NanoTherm® as the ferrofluid.[11] These phase I/II trials were conducted on patients with primarily glioblastoma or prostate carcinomas and showed a reduction in side effects in comparison to other conventional hyperthermia techniques.[87, 88]

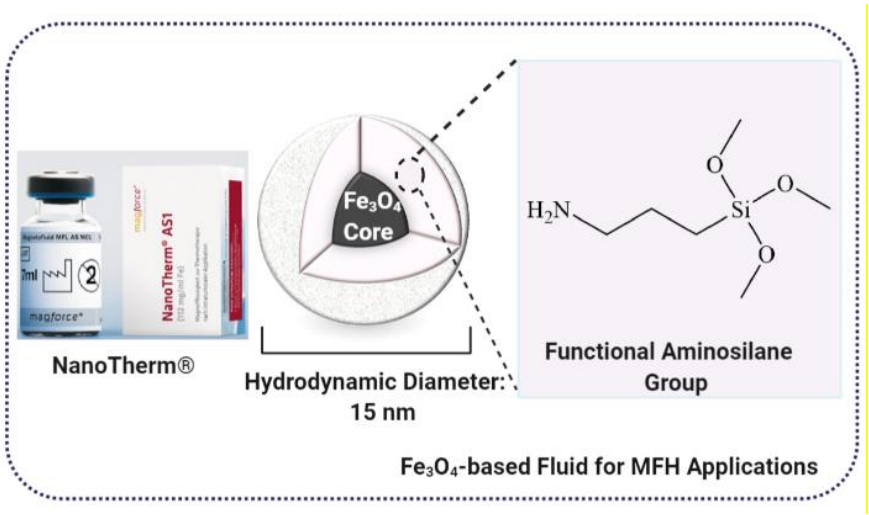

Figure 2.8 Schematic representation of commercialized NanoTherm® – ferrofluid for MFH applications. Nanotherm® image copyright 2020, MagForce AG (Germany).

The ethical guidelines on MFH treatment of glioblastoma were published in 2009,[89] and the efficiency and safety of NanoTherm® on recurrent glioblastoma was reported in 2011.[88] The European Medicines Agency (EMA) and the German Federal Institute for drug and medical devices (BfArm) gave MagForce the approval to start treating glioblastoma using NanoTherm® therapy in 2013.[90] An affiliate of MagForce was founded in U.S. in March 2014 to launch NanoTherm® therapy for the treatment of glioblastoma and prostate cancer in the U.S.[90] In May 2015, a Pre-Investigational Device Exemption (IDE) meeting was held at the FDA to consider NanoTherm® therapy in the U.S.[90] In 2017, MagForce signed a financial agreement with the European Investment Bank (EIB) to ease the access of glioblastoma patients to MFH therapy.[91] MagForce received FDA (IDE) approval in 2018 for a clinical trial of NanoTherm® therapy in the U.S. for patients with prostate cancer.[90] Nanotherm™ has also been extended to 27 European countries, as well as Japan and China. In line with the MagForce company, several companies have developed and manufactured devices for MFH purposes as summarized in Table 2.3.

Table 2.3 Companies that manufacture MFH devices.

Company	Country	Area of interest	Foundation Year	Website
Quantum Design Inc	USA	Manufacture temperature and magnetic field testing devices for materials characterisation	1982	www.qdusa.com
Magnetfabrik Bonn GmbH	Germany	*Develops* magnetic devices for high temperature application	1988	www.magnetfabrik.de
Nanoprobes, Inc	USA	Develops the most sensitive reagents for biological purposes	1990	www.nanoprobes.com
NanoTherics Ltd	United Kingdom	Produces magnet assisted transfection devices for various biomedical applications	2007	www.nanotherics.com
^{n}B nanoScale Biomagnetics	Spain	Develop biomedical instruments for MFH application and nanoheating	2008	www.nbnanoscale.com
Nanobacterie	France	Develops magnetosomes from magnetotactic bacteria for MFH application	2008	www.nanobacterie.com
Aspen Medisys, LLC	USA	Develops medical equipment & devices for MFH therapy of cancer	2009	www.aspenmedisys.com
Kaio Therapy, LLC	USA	Develops novel active immunotherapy fluids to treat solid tumors	2012	www.kaiotherapy.com
Pyrexar Medical	USA	Manufactures innovative and highly effective devices for MFH therapy of cancer	2015	www.pyrexar.com

While MFH has shown potential in clinical trials, there are drawbacks which have hindered the clinical application of this technique. The heat dissipation potency is insufficient to completely eradicate tumors, while cellular uptake of NanoTherm® prevents sufficient doses of the fluid accumulating in the tumor region. Temperature fluctuations can also result from an inability to regulate the temperature elevation in the tumor tissue, as well as the inhomogeneous fluid distribution of in the tumor. In addition, once IONPs are at the lesion site, the ability to monitor tumor growth by MRI, after application of MFH, is severely hindered due to the magnetic artifacts caused by the IONPs.[88] This encourages the application of other techniques such as CT, however the use of CT to visualize the distribution of Nanotherm® fluid also exposes patients to X-ray radiation. Several strategies have been proposed to mitigate these issues, such as the optimisation of the geometry,[92] crystallinity,[93] size and size distribution of the IONPs.[94] Additional methods such as self-controlled MFH,[95] metal-doped spinel ferrite NPs,[96] and exchange-coupled core-shell magnetic NPs[97] have also been proposed. The suggested strategies are discussed in detail in our comprehensive review of IONP-based MFH.[11]

2.3.2.2.2 Magnetic Drug Targeting: IONPs as Drug Delivery Vehicles in a Clinical Setting

Magnetic drug targeting, also called magnetophoresis, is a targeting strategy which promotes the accumulation of IONPs in the desired site in the body. Using an external magnetic field, MFH guides the therapeutic entity (drug, radionuclide, or gene loaded IONPs) previously injected or delivered locally via catheter toward the area of interest. Once the NPs have accumulated at the desired site, they are held there, and the encapsulated drug is released using an applied external magnetic gradient. This approach can limit nonspecific distribution and possible unwanted adverse drug effects.[98] However, magnetic targeting suffers from some challenges, such as a difficulty in bypassing the tissue and cellular barriers, as well as the nonspecific uptake of therapeutic IONPs by the reticuloendothelial system (spleen, liver and kidneys). As a result, a strategy of combined active targeting together with magnetic targeting is utilized in which therapeutic IONPs functionalized with cell-specific targeting recognition moieties (i.e. antibodies, proteins), alongside an applied MF with higher magnetic susceptibility and stronger force, accelerate the intracellular accumulation of the particles and the subsequent theragnostic efficacy. Additionally, the whole process can be visualized by MRI.[99] The efficiency of MDT depends

upon various parameters such as the applied magnetic field configuration (strength and gradient), the hydrodynamic size of the IONPs, physiological parameters such as the infusion route, the reversibility/strength of the drug/carrier bond, blood half-life and tumor volume.[100] The concept of magnetic targeting was proposed by Freeman *et al.* in 1960 where they successfully accumulated magnetic NPs in the body by virtue of applied MF.[101] In 1963, Meyers *et al.* accumulated small metallic iron particles in the leg veins of dogs through intravenous injection under an applied MF.[102] Zimmerman *et al.* in 1976 loaded red blood cells with paramagnetic tritium-labelled methotrexate for anti-cancer purposes. The results demonstrated that more than 50 % of the drug could be accumulated in the liver under the applied magnetic field compared to 25 % accumulation of methotrexate in the liver injected in the usual manner.[103] In 1978, Senyei *et al.* developed albumin microspheres with entrapped magnetite NPs bearing the chemotherapeutic agent Adriamycin and injected this into the capillary beds of tumors either intravenously or intraarterially. The magnetic albumin microspheres presented potential therapeutic benefit in the animal experiments, however it was not successful in clinical trials due to the insufficient magnetic susceptibility of microspheres.[104] In 1990 Ito *et al.* targeted oesophageal cancer in rabbits using magnetic granules under the activation of a magnetic field.[105] All of these initial strategies utilized particles that were on the micron size scale. Lübbe *et al.* initiated, for the first time, the application of IONPs in a preclinical animal model in 1996 followed by the first phase I clinical experience of MDT on 14 patients bearing breast, chondrosarcoma, squamous cell carcinoma, Ewing sarcoma and malignant histiocytoma cancers.[106] A ferrofluid, which contained IONPs (average size 100 nm) stabilized by anhydroglucose polymers and functionalized with the anticancer drug epirubicin, was administered to patients intravenously under an applied magnetic field of 0.8 T. The ferrofluid was effectively targeted to the tumors of 6 out of 14 patients, with some non-specific accumulation in the liver.[107] Koda *et al.*[108] and Wilson *et al.*[109] performed the second and third clinical trials on 32 and 4 patients respectively with hepatocellular carcinoma in 2002 and 2004. However, clinical development was terminated in phase II/III as the tumor response to the treatment was ineffective. The difficulty associated with MDT is the inability to precisely locate magnetic nanocarriers in targets deep within the body. There is a lack of real-time monitoring of nanocarriers *in vivo* in order to direct therapy to the disease target using an external MF. Another challenge is the short

lifetime of nanocarriers circulating in the blood. Additionally, the setup of magnetic fields for successful application in humans is costly. Along with the need to design optimized external magnets (with stronger and deeper forces), mathematical models need to be developed to predict the motion of carriers within living cells under the influence of an external MF. In the past few decades, multifunctional nanocarriers with higher magnetization and theragnostic features have been designed with promising outputs, however this research is still in the development stage. A summary of the trial conditions and outcomes is given in Table 2.4. Notably none of these trials presented clear clinical successes.

Table 2.4 A summary of clinical trials of MDT.

NPs type	Size (nm)	Cancer type	Trial Phase	Number of Patients	Injection route	MF strength (T)	Therapeutic Outcome	Year /Ref
Fe_3O_4 / anhydroglucose epirubicin	100	Breast, chondrosarcoma, carcinoma, sarcoma and histiocytoma	I	14	Intra-venous	0.8	Accumulation of 50 % of the IONPs in the liver.	1996 [107]
Metallic iron-activated carbon–doxorubicin (MTC-DOX)	500-5000	Hepatocellular carcinoma	I/II	32	Intra-arterial	0.5	Localization of MTC-DOX in 30 out of 32 patients. Minimal presence of DOX in systematic circulation.	2002 [108]
Metallic iron-activated carbon–doxorubicin	500-5000	Hepatocellular carcinoma	I/II	4	Intra-arterial	0.5	The dual MR imaging/conventional angiography assists magnetically targeted tumor therapy.	2004 [109]

In light of the versatility of IONPs for surface functionalization and stabilization, magnetic nanocarriers have been designed with nano-size dimensions, biocompatibility and prolonged circulation lifespan that raises hopes for this technology to find its way into the clinician's toolbox and become a commercial success.[98, 110] Several companies are active in the commercialization of magnetic fluids for drug delivery purposes such as Chemicell GmbH, Magnamedics GmbH, Biophan Technologies, Inc., Alnis Biosciences, Inc, Polymicrospheres (division of Vasmo, Inc.) and Micromod Partikeltechnologie GmbH. Whilst MDT was tested in a clinical setting, different forms of IONP-based drugs with various formulations and brand names have been granted FDA and EU approval for the treatment of iron deficiency anemia (IDA). Anaemia is a disease in which the number of healthy red blood cells decreases in the body. This can be due to the impaired kidney function which results in inadequate production of erythropoietin responsible for red blood cell production in the body. Additionally, inadequate daily intake of iron, folate or vitamin B-12 could also lead to iron deficiency. Intravenous injection of ferumoxytol increases the iron levels in the blood and in macrophages in the spleen and liver so that the total amount of body iron is normalized. CosmoFer®, a colloid of an IONP-coated dextran, was approved by the FDA in 1992 and commercialized by Pharmacosmos for the treatment of IDA. Several formulations later received FDA approval as illustrated in Table 2.5. Of all the FDA approved NPs for iron-replacement, ferumoxytol (Feraheme™) is the only nanodrug currently in use and was approved by the FDA in 2009 for the treatment of chronic kidney disease.[111]

Table 2.5 Commercial fluids used in Nanodrug applications.

Brand name	Structure	Target	Company	Website	Approval (year)
CosmoFer®	Iron dextran colloid	Iron deficient anaemia	Pharmacosmos	www.pharmacosmos.com	FDA (1992), EU (2001)
DexFerrum	Iron dextran colloid	Iron deficient anaemia	American Regent	www.americanregent.com	FDA (1996)
Ferrlecit	Iron gluconate colloid	Iron replacement for anaemia treatment in patients with chronic kidney disease	Sanofi	www.sanofi.com	FDA (1999)
Venofer	Iron sucrose colloid	Iron replacement for anaemia treatment in patients with chronic kidney disease	American Regent	www.americanregent.com	FDA (2000)
Ferumoxytol/ Feraheme	Iron polyglucose Sorbitol carboxymethyl-ether colloid	Iron deficiency in patients with chronic kidney disease	AMAG Pharmaceuticals	www.amagpharma.com	FDA (2009)
Monofer®	10 % Iron isomaltoside 1000^{1} colloid	Iron deficiency and anaemia	Pharmacosmos	www.pharmacosmos.com	EU (2009)
Injectafter/ Ferinject	Iron carboxymaltose colloid	Iron deficient anaemia	Vifor	www.viforpharma.com	FDA (2013)
Diafer®	5 % Iron isomaltoside 1000^{1} colloid	Iron deficient anaemia	Pharmacosmos	www.pharmacosmos.com	EU (2013)

2.3.3. Theragnostic applications: Preclinical Stage

Theragnostic is the integration of therapeutic and diagnostic entities into a single delivery vehicle for efficient image-guided therapy and early-stage detection of disease.[112] Superparamagnetic IONPs are ideal candidates for theragnostic purposes because of their visibility with MRI or MPI and surface functionalization with targeting moieties.[113] One theragnostic application has been to use IONPs as a diagnostic tool to monitor the target site localization rate and based on that, predict a treatment strategy. For example, Miller *et al.* labeled FDA-approved ferumoxytol with fluorescent dye. Using MRI, they investigated the *in vivo* intratumoral localization of the fluid in HT1080 human fibrosarcoma xenografts tumors in nude mice. The accumulation rate of the fluid enabled a strategy that deployed an efficient application of an anticancer paclitaxel-loaded PLGA-PEG fluid.[114] Ramanathan *et al.* determined the deposition characteristics of ferumoxytol in different cancer lesions within patients using MRI in a pilot clinical study. Based on the cellular uptake of ferumoxytol fluid, they studied the tumor lesion response tumor size reduction to nanoliposomal irinotecan via CT scans. There was a statistical relation between the degree of uptake of FMX fluid and changes in lesion size.[115] Another theragnostic application of IONPs has been to surface functionalize IONPs with imaging agents (quantum dots, near-infrared dye, fluorescent dyes) and pharmacologically active compounds such as siRNA or anticancer agents via chemical conjugation or physical interactions, such as π-π stacking and specific targeting ligands. For example, in a preclinical study, Medarova *et al.* conjugated IONPs with siRNA, a near-infrared dye and a membrane translocation peptide as a multimodal image-guided delivery nanoplatform. They monitored the accumulation of the nanodevice with MRI and near-infrared in vivo optical imaging. Significant silencing output for this theragnostic nanodevice was achieved in mice bearing 9L or LS174T tumors.[116] Large numbers of theragnostic IONP-based nanovectors have been designed and examined in the field, but all are in the research development phase and have not yet been introduced in a clinic setting. Microbubbles (MB) are clinically approved microvesicles with a lipidic, polymeric or protein-based shell employed for contrast-enhanced ultrasound (US) imaging. Theragnostic MB have been functionalized with IONPs for US-guided drug delivery to the brain in preclinical studies. The process includes the release of IONPs from the MB shell upon exposure to US pulses, crossing the blood brain barrier (BBB), localizing in brain tissue

and monitoring the extent of the BBB opening using MRI.[117] To translate this phenomenon to the clinical settings, further studies are in demand to optimize the size, concentration and composition of MB plus the power and frequency ultrasound.[118] IONPs have received great attention in regenerative medicine as a tracer to track cells. In this context, stem cells are being labeled with IONPs and their *in vivo* delivery to the site of interest is noninvasively monitored with MRI (and recently also MPI). For example Zheng *et al.* reported that the injected ferucarbotran-labeled neuronal progenitor cells (NPC) in the forebrain of rats could be sensitively visualized with MPI for up to 87 days post- injection.[119] Few clinical tests have been trialed with IONP-loaded cells, such as IONP-labeled neuronal stem cells for brain injury and IONP -labeled pancreatic islet cells for diabetes. However, none of these are currently utilized in clinical settings.[120] Overall, IONP-based fluids as theragnostic agents are still undergoing research development and have not yet been translated to the clinical phase.

2.4. Selected applications of IONPs in the research development phase

Whilst the focus of this review is on industrial and biomedical commercialized technologies based on IONPs, there have been some promising applications that could translate into the market in the near future. These include in the areas of water remediation and tissue engineering applications.

2.4.1. Applications of IONPs to environmental water remediation

Ground water can be contaminated with chemical and biological pollutants such as heavy metals (Pb(II), Hg(II), Cd(II), Cr(VI) and Co(II)), toxic textile and paper industrial dyes (congo red, methylene blue, basic fuchsin and acid black), chlorinated and non-chlorinated aliphatic and aromatic compounds, perfluorocarbons, detergents, pesticides, and pathogens (bacteria, fungi and viruses).[121] Current ongoing industrial water remediation techniques include adsorption, ion-exchange, chemical precipitation, bio-precipitation, solvent extraction and electrochemical separation techniques.[122] Despite extensive use, there are some challenges associated with these techniques, such as low performance, complexity of the operational aspects, long operation times required, dangers of bacterial growth, high-energy consumption, high solvent costs, and resin fouling and degradation.[122] In recent years there

has been increased interest in the application of nanoparticles in water remediation technology. Nanoparticles offer attractive alternatives to conventional techniques in view of their higher adsorption capacity, enhanced reactivity and potential of treating multiple contaminants at the same time.[123] However, the safe disposal and complete recovery of nanoparticles is a concerning issue, so much that there is an area of research dedicated to it known as nanotoxicology.[123] To overcome the safety issue of nanoparticles in water purification, magnetic separation based on magnetic nanoparticles has been proposed as a promising solution. Magnetic metallic nanoparticles containing Fe, Ni, and Co possess high saturation magnetization, nevertheless, their high toxicity and susceptibility to oxidation hamper their application. Magnetic alloy nanoparticles, such as FeCo, FePt, and FePd, possess good resistance towards oxidation, however their chemical stability is poor. [20] In contrast, iron oxide nanoparticles (IONPs) are less susceptible to oxidation and less toxic. IONPs are utilized for water remediation in two general ways including magnetic solid-phase extraction and photocatalysis. [122] Magnetic solid-phase extraction technology utilizes functionalized IONPs as the adsorbent. The particles contain magnetic IONPs at the core, and due to the nanoscale size provide more surface sites for contaminant capture. The particles can be easily recovered with an applied magnetic field due to the inherent magnetic properties and are also able to be modified on the shell surface, improving the stability and negating the oxidation of the IONP core. Further modification that incorporates tailored ligand groups can facilitate selective separation of the target contaminant from aqueous effluents.[124] The mechanism of operation includes injecting the functionalized IONPs into the wastewater stream, sequestration of the contaminant by the IONP, separation of the functional IONP + contaminant by applying high magnetic field gradients, and finally, stripping the contaminant to recycle the IONP for further treatment cycles (Figure 2.9). The advantages of this technology are numerous: it can be operated in a continuous manner and is simple to operate, high adsorption capacity is possible due to the high surface to volume ratio of the IONP adsorbent, it is contaminant-target specific and the IONP adsorbent can be completely recovered.[125] Currently, research on magnetic pollutant separation is carried out at a laboratory scale with handheld magnets. To successfully commercialize this technology, some improvements need to be made: IONP adsorbents must be colloidally stable and capable of operating on a large scale, be able to be separated from high- throughput water volumes using low field gradients, be completely recyclable

and they must be economically comparable with existing technologies.[122] Recently, Powel *et al.*[126] and Baresel *et al.*[127] have both reported high gradient magnetic separation (HGMS) technologies for larger-scale separation of IONP absorbents from flowing water.

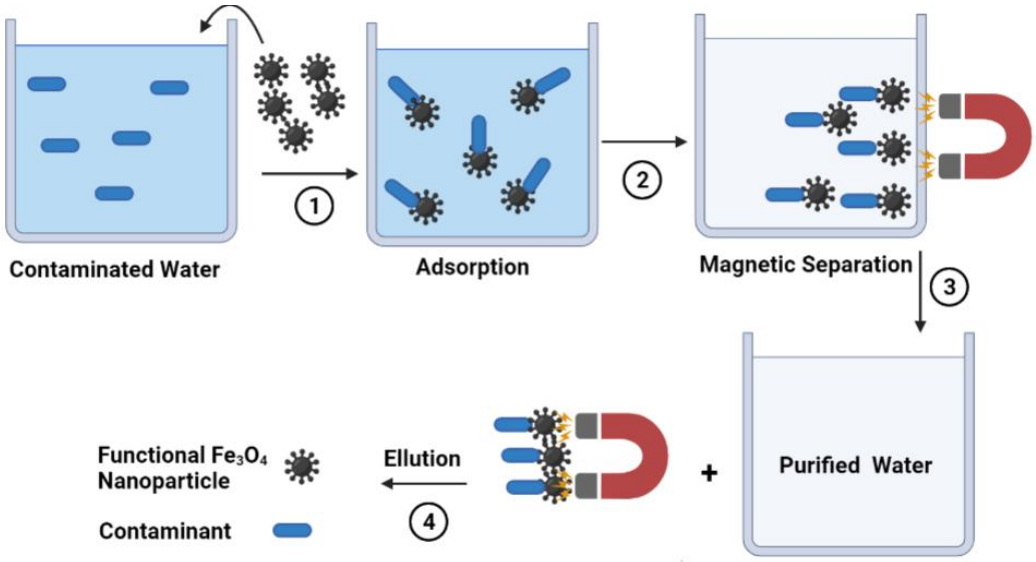

Figure 2.9 Magnetic separation of organic pollutant by functional IONPs.

A second method by which IONPs can contribute to water remediation is through photocatalysis. Degradation of organic or inorganic pollutants by IONPs (utilized as semiconducting catalysts) in water under UV-Vis light, ambient temperature and atmospheric pressure can result in non-toxic products. The reaction involves four main steps (Figure 2.10): (1) the absorption of light in the ultraviolet (400 nm > λ > 290 nm) or the visible region (700 nm > λ > 400 nm) by the semiconductor IONP, (2) the excitation of electrons (e^-) from the valence band (VB) to the conduction band (CB) of the semiconductor, leaving holes (h^+) in the VB, (3) the photoexcited electrons are transported to the reduction site on the semiconductor surface and react with the adsorbed O_2 molecules generating superoxide radicals ($\cdot O_2^-$), at the same time the holes are transported to the oxidation site to oxidize the pollutants directly or react with hydroxide ions (OH^-) or H_2O to yield hydroxyl radicals (·OH), and (4) the generated radicals react with the organic pollutants, forming H_2O and CO_2 as by-products.[128]

Magnetite (Fe_3O_4) is not considered to be a potential catalyst for photocatalysis as the material aggregates and is unstable.[129] In contrast, hematite (α-Fe_2O_3) has attracted great attention for use as a photocatalysis due to its abundance, non-toxicity, good corrosion resistance, low cost and high photo/thermostability.[130] It is not the focus of this review to discuss the potential of α-Fe_2O_3 for photocatalysis applications and previous reviews have covered the subject in sufficient detail.[131] Photocatalysis using IONPs is a technology that has not yet reached its commercial potential.

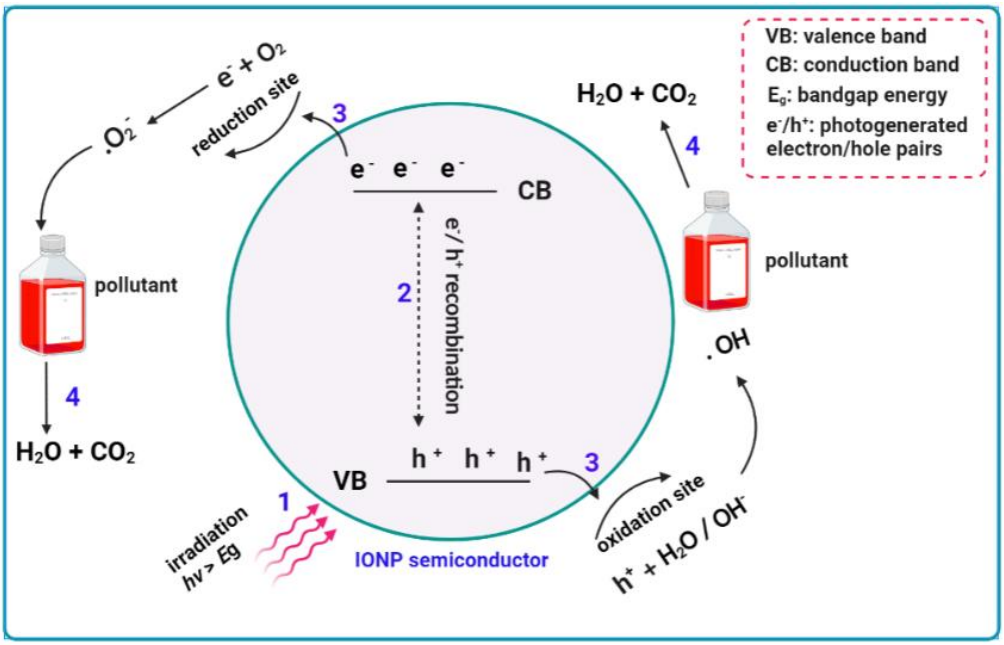

Figure 2.10 Photocatalytic degradation of an organic pollutant by an IONP photocatalyst.

2.4.2. Applications of IONPs in Tissue Engineering

Bone is a natural self-healing composite material composed of 60 % inorganic crystalline hydroxyapatite, 30 % organic fibrous collagen and 10 % water.[132] In certain cases, such as bone tumor excision or external damage such as fracture, the self-repairing ability of the bone alone is not sufficient enough to achieve complete healing.[133] Tissue engineering (TE) is a strategy whereby construction of functional artificial tissue is stimulated thus mimicking the function of the native tissue.[134] The current predominant TE technology requires the use of seeding cells and growth factors into a 3D biocompatible and degradable structure

called a scaffold. The scaffold is prepared from complexes of components including inorganic materials (e.g. bioactive glass / glass ceramic, hydroxyapatite), synthetic polymers (e.g. PLA, PLGA-PEG), biopolymers, silk, chitosan and collagen.[135] There are a number of problems with the current TE technology, such as limited cell migration into the scaffold, the inability to create organized tissue with a precise arrangement of cells, inaccurate localization of stem cells in the complex tissue structure and the risk of inflammation after the degradation of the scaffold.[133] IONPs, together with magnetic stimulation, have contributed to bone regeneration by way of stem cell therapy. This have been achieved through stem cell patterning, adhesion, proliferation, differentiation and the ability of *in vivo* delivery and monitoring.. [134] The ability to manipulate the stem cell migration, distribution and differentiation, and determine their fate post-injection into the area of interest are crucial for successful bone regeneration utilizing stem cell therapy. Applying a magnetic field to stem cells attached to IONPs can lead to the cells assembling in a variety of geometries. Wen *et al*. demonstrated that magnetically labeled endothelial cells could successfully align and maintain their geometrical patterns in the designed template under an applied magnetic field.[136] Current techniques are unable to selectively direct stem cells to the targeted sites.[135] IONPs as delivery vehicles can drive cells to the center of the 3D scaffold, localize cells or support the scaffold complex at the desired site, all under the application of a magnetic field in a process known as magnetic homing. In addition, the real-time *in vivo* cell delivery can be monitored by MRI.[135] Yun *et al*.,[137] Díaz *et al*.,[138] and Xia *et al*.[139] reported significant improvements in the adhesion and proliferation of stem cells loaded on a hydroxyapatite/IONP scaffold. Fernandes *et al*. achieved better cell adhesion and gene expression for a polycaprolactone/IONP scaffold compared to the polycaprolactone scaffold alone.[140] The magnetic field itself has been found to improve the fusion of bone, enhance the bone density and calcium content, and boost the healing of damaged bone.[141] Even though, the potential of IONPs in bone regeneration has been proven, some challenges such as the non-uniform distribution of IONPs in the scaffold and the exact mechanism behind the enhanced cell performance in the presence of IONPs need to be understood in order to transfer the technique into the clinical phase.[133, 135]

2.5. Overall challenges associated with IONPs in the biomedical field and proposed strategies

Poor understanding of the interactions at a cellular level, *in vivo* fate and toxicity are the main challenges in the clinical success of Fe_3O_4 NPs-based fluids.[142] The biological uptake of Fe_3O_4 is dependent upon their physicochemical characteristics and on the biological environment.[142] Although clinical trials have evidenced the biocompatibility and low toxicity of IONP-based fluids, the injection of high doses of Fe_3O_4 can lead to toxicity in humans. As

discussed earlier, many fluids have been withdrawn from the market due to low efficacy and safety concerns after their initial approval by the FDA.[142] Therefore, the biocompatibility and safety profiles of Fe_3O_4 need to be addressed for successful clinical adoption. The toxicity of Fe_3O_4 NPs has been studied in several *in vivo* preclinical studies with inconsistent results. Some studies revealed that Fe_3O_4 at doses of 100 µg/mL or higher may cause some toxicity. Hong *et al.* examined the toxicity profile of IONP-based fluids with different surface charge, surface functional groups and size. All fluids exhibited zero cytotoxicity at concentrations below 200 µg/mL and were found to be relatively safe up to 500 µg/mL.[143] Patil *et al.* reported no toxicity of fluids at concentrations below 100 µg/mL whilst a concentration of 250 µg/mL resulted in considerable cell viability in some cases.[144] The main cause of toxicity by Fe_3O_4 NPs is oxidative stress resulting from reactive oxygen species (ROS) such as superoxide anions, hydrogen peroxide and hydroxyl radicals. The enzymatic degradation of Fe_3O_4 core-coated surface functional groups results in the release of ferrous ion (Fe^{2+}). This then reacts with hydrogen peroxide and oxygen generated by the mitochondria to form highly reactive hydroxyl radicals through the Fenton reaction. Hydroxyl radicals can damage DNA, lipids and proteins in the cellular structure.[142] Additionally, iron overload results in an imbalance in homeostasis and increased risk of cancer, especially liver cancer.[145] Another challenge associated with Fe_3O_4 NPs is the insufficient dose of fluid in the targeted area. Irrespective of the method of injection, administered NPs reside in off-target excretory organs such as liver, spleen or kidneys as evidenced in clinical MRI and MFH trials. Additionally, particles are taken in by phagocytes. This is worst when particles aggregate and form large clusters which eases their recognition by macrophages.[146] In the MFH clinical trial on GBM patients, the CT scan revealed the

minor accumulation of aggregated particles in targeted glioblastoma cells and major uptake by macrophages. Therefore, the addition of targeting properties to current clinical fluids has been proposed to increase their cellular uptake. The process, called active targeting, involves the functionalization of Fe_3O_4 NPs with specific targeting moieties such as cell-penetrating peptides, antibodies, aptamers, carbohydrates, folic acid and drugs. Binding of these specific moieties to the membrane receptors overexpressed on targeted cells selectively, would improve their localization in the tissue of interest.[147] Functionalized IONPs are currently not used in clinical trials, however a great number of scientific publications have been examining their potential in *in vitro* and *in vivo* preclinical examinations. The clinical spherical-shaped IONPs used for MRI and MFH applications are usually prepared with the coprecipitation method. It results in the preparation of NPs with low saturation magnetization values (≈ 50 – 60 emu/g for nanosized Fe_3O_4 lower than that of bulk Fe_3O_4 ≈ 85 – 100 emu/g), large surface spin disorder, nonuniformity in size and shape and high degree of aggregation.[35] For successful biomedical adoption, IONPs should present superparamagnetism with high magnetization, zero remanence and coercivity, higher monodispersity (smaller than 20 nm in diameter), and narrow size distribution (< 10 %).[148] Numerous chemical (90 %), physical (8 %), and biological (2 %) synthetic routes have been proposed for the synthesis of IONPs with controlled size, shape and high monodispersity. In particular, great attention has been drawn to the thermal decomposition of iron precursors in organic solvents in the presence of oleic acid or oleylamine surfactant. This method results in creation of highly monodisperse NPs with high crystallinity, high magnetization, great size uniformity, and well-shaped configurations. The prepared NPs are soluble in organic solvents and applicable for industrial applications, but are transferred to the aqueous phase for biomedical applications.[149] Upon the injection of NPs into blood, plasma proteins and lipids tend to associate with NPs forming a new surface layer on their surfaces called the protein corona (PC). Accordingly, what biological entities, such as cells, organs and tissues actually encounter are NPs-PC complexes rather than pristine NPs.[150] Protein coronas are not fixed layers because the proteins adsorbed to a nanoparticle surface are in an ongoing state of dynamic exchange. The interaction between NPs and the protein corona could have some consequences. The adsorption of proteins on NP surfaces gives them a new biological identity and changes their physicochemical properties such as size, surface composition, surface charge and functionality.[151] The ungoverned protein

attachment onto NPs may have detrimental effects such as rapid clearance from the bloodstream (opsonization), hindrance of targeting capacity, reduced bioavailability and induction of toxicity.[152] Additionally, after adsorption to the NP surface, proteins can experience conformational changes, which are normally irreversible after desorption. Since proteins interact with other biomolecules and substances to activate or express their biological functions, a tiny perturbation in protein structure may induce a huge impact on their pharmacological activity, cellular function and cause toxicity *in vitro* and *in vivo.*[153] For example, conformational changes in transferrin have been reported to be irreversible after desorption from superparamagnetic IONPs .[154] The affinity of proteins to NPs has been shown to increase with the enhancement of charge density and hydrophobicity. Different strategies have been implemented to minimize PC formation on the surfaces of NPs. One strategy is to coat the surface of bare colloidally unstable NPs with long chain hydrophilic polymers to reduce nonspecific binding and undesirable biorecognition of NPs. This is commonly known as the enhanced permeability and retention (EPR) effect.[155] Polyethylene glycol, an FDA-approved polymer, has been considered extensively for Fe_3O_4 coating in order to minimize the uptake through the stealth effect. PEG has excellent anti-fouling properties (preventing opsonization) and high steric hindrance to stabilize IONPs.[155] Nonetheless, limitations such as low cellular uptake efficiency and the formation of circulating anti-PEG antibodies have led in the development of alternative biocompatible and biodegradable stealth-inducing polymers such as poly(ethylenimine) (PEI), poly-phosphoesthers and zwitterionic polymers. Red blood cells (RBCs), leukocytes, platelets, and cell-derived exosomes and viruses have also been examined.[156] The overall sizes of injected surface-functionalized IONPs are important in order to maximise the EPR effect. Several studies validated that NPs of ~ 50 nm in size have optimal cellular uptake and slower opsonization. NPs larger than 100 nm are cleared by reticuloendothelial system (RES) such as liver and spleen whilst NPs smaller than 10 nm are removed from blood through renal clearance.[157]

The timeline of milestones (Figure 2.11) highlights the important dates and efforts over the last few decades that have established the foundation for the evolution of IONPs from basic research to clinical practice and commercialization. These advancements include the synthesis and surface modification and functionalization of IONPs cumulating in the

invention of IONP fluids. These functional fluids have since found utility by the scientific community for biomedical applications, preclinical examinations, clinical trials and ultimately, commercialization of several IONP-based fluids.

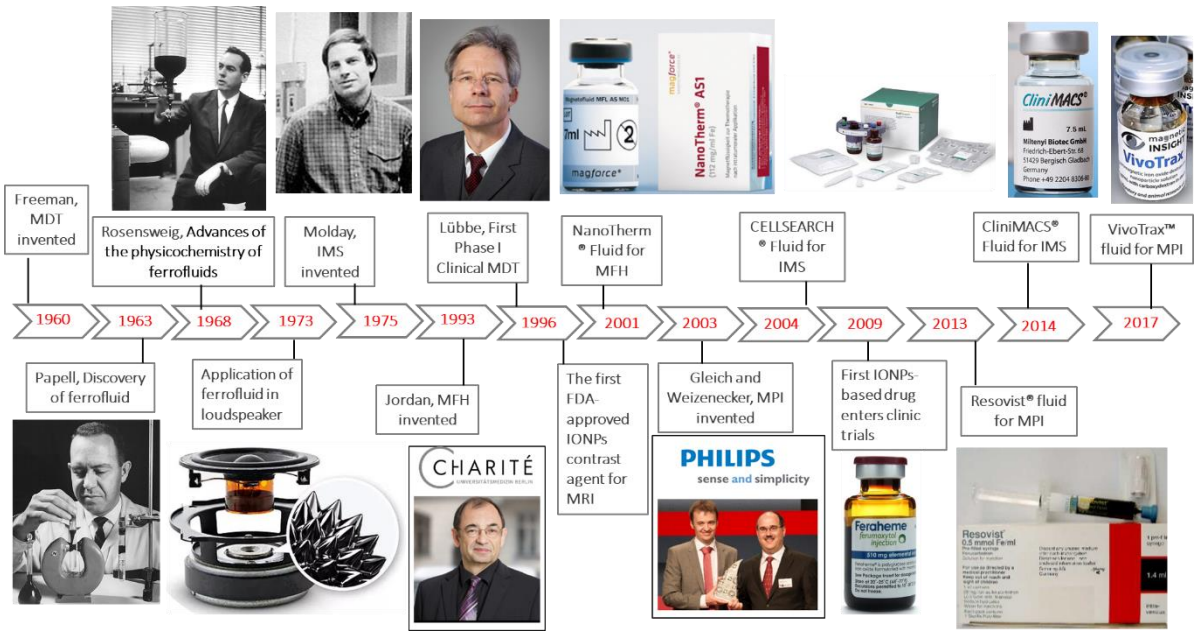

Figure 2.11 Historical evolution of IONPs to their current state in commercial biomedical and industrial market. Included are milestones achieved by the community with regards to stepwise development of IONPs for potential biotechnological applications. The milestones can be found in the following papers: Freeman (1960),[101] Papell (1963),[36] Rosensweig (1968),[37] Application of ferrofluid in loudspeaker (1973), copyright 2021, Sony (Japan) [38] Molday (1975),[76] Jordan (1993),[84] Lübbe (1996),[107] the first FDA-approved contrast agent based on IONPs for MRI (1996),[43] Gleich and Weizenecker (2001),[59] the first MFH clinical fluid (2003), copyright 2020, MagForce AG (Germany),[86] the first FDA-approved IMS fluid (2004), copyright 2020, Janssen Diagnostic Inc [78] approval of Feraheme™ by the FDA (2009), copyright 2020, AMAG Pharmaceuticals (U.S.), [111] the first commercial fluid for MPI (2013), copyright 2020, Bruker BioSpin MRI GmbH (Germany), [60] the second FDA-approved IMS fluid (2014), copyright 2020, Miltenyi Biotec (Germany),[79] the second commercial MPI fluid (2017), copyright 2020, Magnetic Insight, Inc (U.S.),.[158]

2.6. Concluding Remarks

In this review, we have outlined the physicochemical properties of commercial IONP-based ferrofluids and their synthetic methods. Due to properties such as superparamagnetism,

high Curie temperature and low toxicity, IONP-based ferrofluids have been translated from laboratory research to industrial commercialization and clinical success. This includes their utility in diverse industry sectors such as electronics devices and biomedical fields such as MRI, MFH and IMS. There are still some challenges to be addressed for their broader entry to the market, including low saturation magnetization as well as the difficulty in synthesizing single-domain particles with minimal aggregation, which has not been achieved with the current coprecipitation method. The thermal decomposition method has addressed these problems to some extent, however methods which are relatively simple, rapid, environmentally acceptable, economical, and scalable are yet to be identified. Although the marketed or clinical IONPs are surface coated with dextran or its derivatives, other hydrophilic polymers such as FDA-approved polyethylene glycol, or poly-phosphoesthers and zwitterionic polymers could also be considered. Further advances are also expected in the surface functionalization of IONPs with specific cell targeting moieties to improve their residence time in the blood and their ability to prevent opsonization with plasma proteins. Although there is significant research into the biodistribution, biodegradation, clearance and toxicity of IONPs, the results are not conclusive. This is because of the variation in physicochemical characteristics of utilized IONPs such as size, shape, surface charge and coating and different undertaken experimental set up such as cell types, administration dose and route and quantification techniques. Therefore, more consistency is required, especially in terms of experimental conditions to help the advancement in understanding NP-cell interactions. Considering the advances in the field of ferrofluids, it is expected that in the following decades the challenges of the current commercial IONP-based fluids will be addressed. Meanwhile, multifunctional IONP-based fluids are expected to be routinely available for future industrial and biomedical commercial markets.

Author Information

Corresponding Author

* Email: P.G.Plieger@massey.ac.nz

Author Contributions

The manuscript was written through contributions of all authors. HE drafted the initial manuscript. JKB, NGK and PGP contributed to the final preparation of the manuscript. All authors have given approval to the final version of the manuscript.

Funding Sources

The authors gratefully acknowledge New Zealand International Doctoral Research Scholarships (NZIDRS) committee for their financial support.

Abbreviations

3D, three-dimensional; CT, computed tomography; CTC, circulating tumor cell; FDA, U.S. Food and Drug Administration; EMA, European Medicines Agency; EpCAM, epithelial cell adhesion molecule; EU, European Union; IDE, investigational device exemption; IMS, immunomagnetic separation; IONP, iron oxide nanoparticle; MACS, magnetic activated cell sorting; MDT, magnetic drug targeting; MF, magnetic field; MFH, magnetic fluid hyperthermia; MPI, magnetic particle imaging; MRI, magnetic resonance imaging; NMR, nuclear magnetic resonance; NP, nanoparticle; PEG, polyethylene glycol; PET, positron emission tomography; PLA, polylactic acid; PLGA, poly lactic-co-glycolic acid; RF, radio frequency; SPECT, single photon emission computed tomography.

2.7. References

[1] W. C. Elmore, Phys. Rev. A. 1938, 54, 1092; G. Kandasamy, D. Maity, Int. J. Pharm. 2015, 496, 191.

[2] M. Mahmoudi, S. Sant, B. Wang, S. Laurent, T. Sen, Advanced Drug Delivery Reviews 2011, 63, 24; H. Arami, A. Khandhar, D. Liggitt, K. M. Krishnan, Chem. Soc. Rev. 2015, 44, 8576.

[3] Q. A. Pankhurst, J. Connolly, S. K. Jones, J. Dobson, J. Phys. D: Appl. Phys. 2003, 36, R167; A. Hervault, N. T. K. Thanh, Nanoscale 2014, 6, 11553.

[4] K. Raj, R. Moskowitz, J. Magn. Magn. Mater. 1990, 85, 233.

[5] Z. R. Stephen, F. M. Kievit, M. Zhang, Mater. Today 2011, 14, 330.

[6] Z. Shen, A. Wu, X. Chen, Mol. Pharm. 2017, 14, 1352.

[7] G. R. Mahdavinia, H. Etemadi, Mater. Sci. Eng. C 2014, 45, 250; G. R. Mahdavinia, H. Etemadi, F. Soleymani, Carbohydr. Polym. 2015, 128, 112.

[8] S. S. Leong, S. P. Yeap, J. Lim, Interface Focus 2016, 6, 20160048.

[9] J. A. Thomas, F. Schnell, Y. Kaveh-Baghbaderani, S. Berensmeier, S. P. Schwaminger, Chemosensors 2020, 8, 17.

[10] H. Etemadi, P. G. Plieger, ACS Omega 2020, 5, 18091.

[11] P. G. P. Hossein Etemadi, Adv. Therap 2020.

[12] L. M. Bauer, S. F. Situ, M. A. Griswold, A. C. S. Samia, The Journal of Physical Chemistry Letters 2015, 6, 2509.

[13] J. Huang, X. Zhong, L. Wang, L. Yang, H. Mao, Theranostics 2012, 2, 86.

[14] H. Kempe, S. A. Kates, M. Kempe, Expert Rev. Med. Devices 2011, 8, 291.

[15] M. K. Masud, J. Na, M. Younus, M. S. A. Hossain, Y. Bando, M. J. A. Shiddiky, Y. Yamauchi, Chem. Soc. Rev. 2019, 48, 5717.

[16] A. J. Giustini, A. A. Petryk, S. M. Cassim, J. A. Tate, I. Baker, P. J. Hoopes, Nano Life 2010, 1, 10.1142/S1793984410000067; M. Bañobre-López, A. Teijeiro, J. Rivas, Reports of Practical Oncology & Radiotherapy 2013, 18, 397.

[17] J. Salamon, M. Hofmann, C. Jung, M. G. Kaul, F. Werner, K. Them, R. Reimer, P. Nielsen, A. Vom Scheidt, G. Adam, T. Knopp, H. Ittrich, PLoS One 2016, 11, e0156899.

[18] S. Laurent, A. A. Saei, S. Behzadi, A. Panahifar, M. Mahmoudi, Expert Opinion on Drug Delivery 2014, 11, 1449; S. Laurent, J.-L. Bridot, L. V. Elst, R. N. Muller, Future Med. Chem. 2010, 2, 427; K. Wu, D. Su, J. Liu, R. Saha, J.-P. Wang, Nanotechnology 2019, 30, 502003; M. Mahmoudi, M. A. Sahraian, M. A. Shokrgozar, S. Laurent, ACS Chem. Neurosci. 2011, 2, 118; N. V. S. Vallabani, S. Singh, 3 Biotech 2018, 8, 279; S. Tong, H. Zhu, G. Bao, Mater. Today 2019, 31, 86.

[19] W. Wu, Z. Wu, T. Yu, C. Jiang, W.-S. Kim, Sci Technol Adv Mat 2015, 16, 023501.

[20] H. Etemadi, P. G. Plieger, Advanced Therapeutics 2020, 3, 2000061.

[21] L. Lopez-Diaz, L. Torres, "Transition from ferromagnetism to superparamagnetism in uniaxial nanoparticles. The role on non-uniformities in the magnetization", presented at *2002 IEEE International Magnetics Conference (INTERMAG)*, 28 April-2 May 2002, 2002.

[22] V. Singh, V. Banerjee, Indian Journal of Physics 2014, 88, 939.

[23] B. I. Kharisov, H. V. R. Dias, O. V. Kharissova, A. Vázquez, Y. Peña, I. Gómez, RSC Adv. 2014, 4, 45354.

[24] B. Issa, I. M. Obaidat, B. A. Albiss, Y. Haik, Int. J. Mol. Sci. 2013, 14, 21266.

[25] R. Vakili-Ghartavol, A. A. Momtazi-Borojeni, Z. Vakili-Ghartavol, H. T. Aiyelabegan, M. R. Jaafari, S. M. Rezayat, S. Arbabi Bidgoli, Artif Cells Nanomed Biotechnol 2020, 48, 443.

[26] H. Markides, M. Rotherham, A. J. El Haj, J. Nanomater. 2012, 2012, 614094.
[27] S. Wang, J. Luo, Z. Zhang, D. Dong, Y. Shen, Y. Fang, L. Hu, M. Liu, C. Dai, S. Peng, Z. Fang, P. Shang, Am. J. Cancer Res. 2018, 8, 1933.
[28] Y. Anzai, C. W. Piccoli, E. K. Outwater, W. Stanford, D. A. Bluemke, P. Nurenberg, S. Saini, K. R. Maravilla, D. E. Feldman, U. P. Schmiedl, J. A. Brunberg, I. R. Francis, S. E. Harms, P. M. Som, C. M. Tempany, Radiology 2003, 228, 777.
[29] H. Elhalawani, M. J. Awan, Y. Ding, A. S. R. Mohamed, A. K. Elsayes, I. Abu-Gheida, J. Wang, J. Hazle, G. B. Gunn, S. Y. Lai, S. J. Frank, L. E. Ginsberg, D. I. Rosenthal, C. D. Fuller, Scientific Data 2020, 7, 63.
[30] S. Vadhan-Raj, D. C. Ford, N. V. Dahl, K. Bernard, Z. Li, L. F. Allen, W. E. Strauss, Am. J. Hematol. 2016, 91, E3.
[31] B. Fubini, M. Ghiazza, I. Fenoglio, Nanotoxicology 2010, 4, 347.
[32] C. Scherer, A. M. Figueiredo Neto, Brazilian Journal of Physics 2005, 35, 718.
[33] S. W. Charles, J. Popplewell, in *Handbook of Ferromagnetic Materials*, Vol. 2, Elsevier, 1980, 509.
[34] K. Raj, R. J. Boulton, Materials & Design 1987, 8, 233.
[35] W. Wu, Q. He, C. Jiang, Nanoscale Res Lett 2008, 3, 397.
[36] P. S. Stephen, Patent 1965, 3, 215, 572
[37] R. E. Rosensweig, *Ferrohydrodynamics*, Cambridge University Press, New York 1985.
[38] H. Urreta, G. Aguirre, P. Kuzhir, L. N. López De Lacalle, International Journal of Precision Engineering and Manufacturing 2018, 19, 495.
[39] R. E. Rosensweig, Annual Reviews 1987, 247 (4), 136.
[40] K. Raj, B. Moskowitz, S. Tsuda, Indian Journal of Engineering and Materials Sciences 2004, 11, 241.
[41] A. De Roos, D. Baleriaux, in *Essentials of Clinical MRI*, (Ed: T. H. M. Falke), Springer Netherlands, Dordrecht 1988, 41.
[42] Y. Bao, J. A. Sherwood, Z. Sun, J. Mater. Chem C. 2018, 6, 1280.
[43] B. Hamm, T. Staks, M. Taupitz, R. Maibauer, A. Speidel, A. Huppertz, T. Frenzel, R. Lawaczeck, K. J. Wolf, L. Lange, J. Magn. Reson. Imaging 1994, 4, 659.
[44] A. Neuwelt, N. Sidhu, C.-A. A. Hu, G. Mlady, S. C. Eberhardt, L. O. Sillerud, AJR Am J Roentgenol. 2015, 204, W302.
[45] L. M. Bauer, S. F. Situ, M. A. Griswold, A. C. S. Samia, Nanoscale 2016, 8, 12162; J. J. Yang, J. Yang, L. Wei, O. Zurkiya, W. Yang, S. Li, J. Zou, Y. Zhou, A. L. W. Maniccia, H. Mao, F. Zhao, R. Malchow, S. Zhao, J. Johnson, X. Hu, E. Krogstad, Z.-R. Liu, J. Am. Chem. Soc. 2008, 130, 9260.
[46] S. Sun, H. Zeng, J. Am. Chem. Soc. 2002, 124, 8204; T. Hyeon, S. S. Lee, J. Park, Y. Chung, H. B. Na, J. Am. Chem. Soc. 2001, 123, 12798.
[47] M. Jeon, M. V. Halbert, Z. R. Stephen, M. Zhang, Adv. Mater. 2020, n/a, 1906539.
[48] V. Frantellizzi, M. Conte, M. Pontico, A. Pani, R. Pani, G. De Vincentis, Nucl. Med. Mol. Imaging (2010) 2020, 54, 65.
[49] X. Y. Zhou, Z. W. Tay, P. Chandrasekharan, E. Y. Yu, D. W. Hensley, R. Orendorff, K. E. Jeffris, D. Mai, B. Zheng, P. W. Goodwill, S. M. Conolly, Curr. Opin. Chem. Biol. 2018, 45, 131.
[50] G. K. Michael, S. Johannes, K. Tobias, I. Harald, A. Gerhard, W. Horst, J. Caroline, Phys. Med. Biol. 2018, 63, 064001.
[51] O. Kosch, H. Paysen, J. Wells, F. Ptach, J. Franke, L. Wöckel, S. Dutz, F. Wiekhorst, J. Magn. Magn. Mater. 2019, 471, 444; H. Paysen, J. Wells, O. Kosch, U. Steinhoff, J. Franke, L. Trahms, T. Schaeffter, F. Wiekhorst, Phys. Med. Biol. 2018, 63, 13NT02.

[52] L. Fass, Mol. Oncol. 2008, 2, 115; J. V. Frangioni, Am. J. Clin. Oncol. 2008, 26, 4012.
[53] P. Ludewig, N. Gdaniec, J. Sedlacik, N. D. Forkert, P. Szwargulski, M. Graeser, G. Adam, M. G. Kaul, K. M. Krishnan, R. M. Ferguson, A. P. Khandhar, P. Walczak, J. Fiehler, G. Thomalla, C. Gerloff, T. Knopp, T. Magnus, ACS Nano 2017, 11, 10480.
[54] E. Y. Yu, M. Bishop, B. Zheng, R. M. Ferguson, A. P. Khandhar, S. J. Kemp, K. M. Krishnan, P. W. Goodwill, S. M. Conolly, Nano Lett. 2017, 17, 1648.
[55] Y. Takeuchi, H. Suzuki, H. Sasahara, J. Ueda, I. Yabata, K. Itagaki, S. Saito, K. Murase, Adv. Biomed. Eng. 2014, 3, 37.
[56] J. Weizenecker, B. Gleich, J. Rahmer, H. Dahnke, J. Borgert, Phys. Med. Biol. 2009, 54, L1.
[57] B. Zheng, M. P. von See, E. Yu, B. Gunel, K. Lu, T. Vazin, D. V. Schaffer, P. W. Goodwill, S. M. Conolly, Theranostics 2016, 6, 291.
[58] Z. W. Tay, P. Chandrasekharan, A. Chiu-Lam, D. W. Hensley, R. Dhavalikar, X. Y. Zhou, E. Y. Yu, P. W. Goodwill, B. Zheng, C. Rinaldi, S. M. Conolly, ACS Nano 2018, 12, 3699.
[59] B. Gleich, J. Weizenecker, Nature 2005, 435, 1214.
[60] J. Franke, U. Heinen, H. Lehr, A. Weber, F. Jaspard, W. Ruhm, M. Heidenreich, V. Schulz, IEEE Trans. Med. Imaging 2016, 35, 1993.
[61] R. M. Ferguson, K. R. Minard, A. P. Khandhar, K. M. Krishnan, Med. Phys. 2011, 38, 1619; G. Song, M. Chen, Y. Zhang, L. Cui, H. Qu, X. Zheng, M. Wintermark, Z. Liu, J. Rao, Nano Lett. 2018, 18, 182.
[62] A. P. Khandhar, P. Keselman, S. J. Kemp, R. M. Ferguson, P. W. Goodwill, S. M. Conolly, K. M. Krishnan, Nanoscale 2017, 9, 1299.
[63] J. Franke, U. Heinen, H. Lehr, A. Weber, F. Jaspard, W. Ruhm, M. Heidenreich, V. Schulz, IEEE Trans. Med. Imaging 2016, 35, 1993.
[64] M. Zborowski, J. J. Chalmers, Anal. Chem. 2011, 83, 8050.
[65] H. Xu, Z. P. Aguilar, L. Yang, M. Kuang, H. Duan, Y. Xiong, H. Wei, A. Wang, Biomaterials 2011, 32, 9758.
[66] C.-H. Wu, Y.-Y. Huang, P. Chen, K. Hoshino, H. Liu, E. P. Frenkel, J. X. J. Zhang, K. V. Sokolov, ACS nano 2013, 7, 8816.
[67] R. T. van Beem, E. Nur, J. J. Zwaginga, P. P. Landburg, E. J. van Beers, A. J. Duits, D. P. Brandjes, I. Lommerse, H. C. de Boer, C. E. van der Schoot, J.-J. B. Schnog, B. J. Biemond, Exp. Hematol. 2009, 37, 1054.
[68] M. Takahashi, T. Yoshino, H. Takeyama, T. Matsunaga, Biotechnol. Progr. 2009, 25, 219.
[69] A. Pramanik, A. Vangara, B. P. Viraka Nellore, S. S. Sinha, S. R. Chavva, S. Jones, P. C. Ray, ACS Appl. Mater. Interfaces 2016, 8, 15076.
[70] Y. Chen, Y. Xianyu, Y. Wang, X. Zhang, R. Cha, J. Sun, X. Jiang, ACS Nano 2015, 9, 3184.
[71] D. Cheng, M. Yu, F. Fu, W. Han, G. Li, J. Xie, Y. Song, M. T. Swihart, E. Song, Anal. Chem. 2016, 88, 820.
[72] Y. Wang, G. Wang, Y. Xiao, Y. Yang, R. Tang, ACS Appl. Mater. Interfaces 2014, 6, 19092.
[73] H. Fang, N. Xie, M. Ou, J. Huang, W. Li, Q. Wang, J. Liu, X. Yang, K. Wang, Anal. Chem. 2018, 90, 7164.
[74] B. D. Plouffe, S. K. Murthy, L. H. Lewis, Rep Prog Phys. 2015, 78, 016601.
[75] D. Melville, F. Paul, S. Roath, Nature 1975, 255, 706.
[76] R. S. Molday, S. P. S. Yen, A. Rembaum, Nature 1977, 268, 437.

[77] S. Miltenyi, W. Müller, W. Weichel, A. Radbruch, Cytometry 2005, 11, 231.
[78] L. Wang, P. Balasubramanian, A. P. Chen, S. Kummar, Y. A. Evrard, R. J. Kinders, Semin. Oncol. 2016, 43, 464.
[79] T. A. P. Staff, 2014.
[80] H. Etemadi, P. G. Plieger, Adv. Ther. 2020, 3, 2000061.
[81] D. Chang, M. Lim, J. A. C. M. Goos, R. Qiao, Y. Y. Ng, F. M. Mansfeld, M. Jackson, T. P. Davis, M. Kavallaris, Front. Pharmacol. 2018, 9.
[82] E. Guisasola, L. Asín, L. Beola, J. M. de la Fuente, A. Baeza, M. Vallet-Regí, ACS Appl. Mater. Interfaces 2018, 10, 12518.
[83] R. K. Gilchrist, R. Medal, W. D. Shorey, R. C. Hanselman, J. C. Parrott, C. B. Taylor, Ann. Surg. 1957, 146, 596.
[84] A. Jordan, P. Wust, H. Fähling, W. John, A. Hinz, R. Felix, Int. J. Hyperthermia 1993, 9, 51.
[85] A. Jordan, R. Scholz, P. Wust, H. Schirra, S. Thomas, H. Schmidt, R. Felix, J. Magn. Magn. Mater. 1999, 194, 185; A. Jordan, R. Scholz, K. Maier-Hauff, F. K. H. van Landeghem, N. Waldoefner, U. Teichgraeber, J. Pinkernelle, H. Bruhn, F. Neumann, B. Thiesen, A. von Deimling, R. Felix, J. Neurooncol. 2006, 78, 7; M. Johannsen, A. Jordan, R. Scholz, M. Koch, M. Lein, S. Deger, J. Roigas, K. Jung, S. Loening, J. Endourol. 2004, 18, 495; M. Johannsen, B. Thiesen, U. Gneveckow, K. Taymoorian, N. Waldöfner, R. Scholz, S. Deger, K. Jung, S. A. Loening, A. Jordan, The Prostate 2005, 66, 97; M. Johannsen, B. Thiesen, A. Jordan, K. Taymoorian, U. Gneveckow, N. Waldöfner, R. Scholz, M. Koch, M. Lein, K. Jung, S. A. Loening, The Prostate 2005, 64, 283.
[86] A. Jordan, R. Scholz, K. Maier-Hauff, M. Johannsen, P. Wust, J. Nadobny, H. Schirra, H. Schmidt, S. Deger, S. Loening, W. Lanksch, R. Felix, J. Magn. Magn. Mater. 2001, 225, 118.
[87] M. Johannsen, U. Gneveckow, L. Eckelt, A. Feussner, N. WaldÖFner, R. Scholz, S. Deger, P. Wust, S. A. Loening, A. Jordan, Int. J. Hyperthermia 2005, 21, 637; M. Johannsen, U. Gneveckow, K. Taymoorian, B. Thiesen, N. Waldöfner, R. Scholz, K. Jung, A. Jordan, P. Wust, S. A. Loening, Int. J. Hyperthermia 2007, 23, 315; K. Maier-Hauff, R. Rothe, R. Scholz, U. Gneveckow, P. Wust, B. Thiesen, A. Feussner, A. von Deimling, N. Waldoefner, R. Felix, A. Jordan, J. Neurooncol. 2007, 81, 53; F. K. H. van Landeghem, K. Maier-Hauff, A. Jordan, K.-T. Hoffmann, U. Gneveckow, R. Scholz, B. Thiesen, W. Brück, A. von Deimling, Biomaterials 2009, 30, 52; Wust, gt, Peter, U. Gneveckow, Wust, gt, Peter, U. Gneveckow, M. Johannsen, D. Böhmer, T. Henkel, F. Kahmann, J. Sehouli, R. Felix, J. Ricke, A. Jordan, Int. J. Hyperthermia 2006, 22, 673.
[88] K. Maier-Hauff, F. Ulrich, D. Nestler, H. Niehoff, P. Wust, B. Thiesen, H. Orawa, V. Budach, A. Jordan, J. Neurooncol. 2011, 103, 317.
[89] R. Gupta, D. Sharma, ACS Chem. Neurosci. 2019, 10, 1157.
[90] F. (IDE), 2018.
[91] European Investment Bank, 2017.
[92] P. Bender, J. Fock, C. Frandsen, M. F. Hansen, C. Balceris, F. Ludwig, O. Posth, E. Wetterskog, L. K. Bogart, P. Southern, W. Szczerba, L. Zeng, K. Witte, C. Grüttner, F. Westphal, D. Honecker, D. González-Alonso, L. Fernández Barquín, C. Johansson, J. Phys.. Chem. C 2018, 122, 3068.
[93] E. C. Abenojar, S. Wickramasinghe, J. Bas-Concepcion, A. C. S. Samia, Progress in Natural Science: Materials International 2016, 26, 440.
[94] B. Luigjes, S. M. C. Woudenberg, R. de Groot, J. D. Meeldijk, H. M. Torres Galvis, K. P. de Jong, A. P. Philipse, B. H. Erné, J. Phys.. Chem. C 2011, 115, 14598.

[95] A. Ereath Beeran, F. B. Fernandez, P. R. H. Varma, ACS Biomaterials Science & Engineering 2018.
[96] G. S. Ningombam, R. S. Ningthoujam, S. N. Kalkura, N. R. Singh, The Journal of Physical Chemistry B 2018, 122, 6862.
[97] V. Pilati, R. Cabreira Gomes, G. Gomide, P. Coppola, F. G. Silva, F. L. O. Paula, R. Perzynski, G. F. Goya, R. Aquino, J. Depeyrot, J. Phys.. Chem. C 2018, 122, 3028.
[98] K. T. Al-Jamal, J. Bai, J. T.-W. Wang, A. Protti, P. Southern, L. Bogart, H. Heidari, X. Li, A. Cakebread, D. Asker, W. T. Al-Jamal, A. Shah, S. Bals, J. Sosabowski, Q. A. Pankhurst, Nano Lett. 2016, 16, 5652.
[99] N. Schleich, C. Po, D. Jacobs, B. Ucakar, B. Gallez, F. Danhier, V. Préat, J. Control. Release. 2014, 194, 82.
[100] M. Arruebo, R. Fernández-Pacheco, M. R. Ibarra, J. Santamaría, Nano Today 2007, 2, 22.
[101] M. W. Freeman, A. Arrott, J. H. L. Watson, J. Appl. Phys. 1960, 31, S404.
[102] P. H. Meyers, C. M. Nice, G. R. Meckstroth, H. C. Becker, P. J. Moser, M. Goldstein, AJR Am J Roentgenol. 1966, 96, 913.
[103] U. Zimmermann, P. Scheurich, G. Pilwat, R. Benz, Angewandte Chemie International Edition in English 1981, 20, 325.
[104] A. Senyei, K. Widder, G. Czerlinski, J. Appl. Phys. 1978, 49, 3578.
[105] R. Ito, Y. Machida, T. Sannan, T. Nagai, Int. J. Pharm. 1990, 61, 109.
[106] A. S. Lübbe, C. Bergemann, W. Huhnt, T. Fricke, H. Riess, J. W. Brock, D. Huhn, Cancer Res. 1996, 56, 4694.
[107] A. S. Lübbe, C. Bergemann, H. Riess, F. Schriever, P. Reichardt, K. Possinger, M. Matthias, B. Dörken, F. Herrmann, R. Gürtler, P. Hohenberger, N. Haas, R. Sohr, B. Sander, A.-J. Lemke, D. Ohlendorf, W. Huhnt, D. Huhn, Cancer Res. 1996, 56, 4686.
[108] Eur. J. Cancer 2002, 38, S18.
[109] M. W. Wilson, R. K. Kerlan, N. A. Fidelman, A. P. Venook, J. M. LaBerge, J. Koda, R. L. Gordon, Radiology 2004, 230, 287.
[110] P. Kheirkhah, S. Denyer, A. D. Bhimani, G. D. Arnone, D. R. Esfahani, T. Aguilar, J. Zakrzewski, I. Venugopal, N. Habib, G. L. Gallia, A. Linninger, F. T. Charbel, A. I. Mehta, Sci. Rep. 2018, 8, 11417; E. Allard-Vannier, S. Cohen-Jonathan, J. Gautier, K. Hervé-Aubert, E. Munnier, M. Soucé, P. Legras, C. Passirani, I. Chourpa, Eur. J. Pharm. Biopharm. 2012, 81, 498.
[111] M. Lu, M. H. Cohen, D. Rieves, R. Pazdur, Am. J. Hematol. 2010, 85, 315.
[112] M. E. Caldorera-Moore, W. B. Liechty, N. A. Peppas, Acc. Chem. Res. 2011, 44, 1061.
[113] S. M. Dadfar, K. Roemhild, N. I. Drude, S. von Stillfried, R. Knüchel, F. Kiessling, T. Lammers, Advanced Drug Delivery Reviews 2019, 138, 302.
[114] M. A. Miller, S. Gadde, C. Pfirschke, C. Engblom, M. M. Sprachman, R. H. Kohler, K. S. Yang, A. M. Laughney, G. Wojtkiewicz, N. Kamaly, S. Bhonagiri, M. J. Pittet, O. C. Farokhzad, R. Weissleder, Sci. Transl. Med. 2015, 7, 314ra183.
[115] R. K. Ramanathan, R. L. Korn, N. Raghunand, J. C. Sachdev, R. G. Newbold, G. Jameson, G. J. Fetterly, J. Prey, S. G. Klinz, J. Kim, J. Cain, B. S. Hendriks, D. C. Drummond, E. Bayever, J. B. Fitzgerald, Clin. Cancer Res. 2017, 23, 3638.
[116] Z. Medarova, W. Pham, C. Farrar, V. Petkova, A. Moore, Nat. Med. 2007, 13, 372.
[117] P. Koczera, L. Appold, Y. Shi, M. Liu, A. Dasgupta, V. Pathak, T. Ojha, S. Fokong, Z. Wu, M. van Zandvoort, O. Iranzo, A. J. C. Kuehne, A. Pich, F. Kiessling, T. Lammers, J. Controlled Release 2017, 259, 128.

[118] T. Lammers, P. Koczera, S. Fokong, F. Gremse, J. Ehling, M. Vogt, A. Pich, G. Storm, M. van Zandvoort, F. Kiessling, Adv. Funct. Mater. 2015, 25, 36.
[119] B. Zheng, T. Vazin, P. W. Goodwill, A. Conway, A. Verma, E. Ulku Saritas, D. Schaffer, S. M. Conolly, Sci. Rep. 2015, 5, 14055.
[120] M. E. Mertens, S. Koch, P. Schuster, J. Wehner, Z. Wu, F. Gremse, V. Schulz, L. Rongen, F. Wolf, J. Frese, V. N. Gesché, M. van Zandvoort, P. Mela, S. Jockenhoevel, F. Kiessling, T. Lammers, Biomaterials 2015, 39, 155; M. E. Mertens, A. Hermann, A. Bühren, L. Olde-Damink, D. Möckel, F. Gremse, J. Ehling, F. Kiessling, T. Lammers, Adv. Funct. Mater. 2014, 24, 754.
[121] C. Martinez-Boubeta, K. Simeonidis, in *Nanoscale Materials in Water Purification*, (Eds: S. Thomas, D. Pasquini, S.-Y. Leu, D. A. Gopakumar), Elsevier, 2019, 521.
[122] A. G. Leonel, A. A. P. Mansur, H. S. Mansur, Water Res. 2021, 190, 116693.
[123] P. T.C, S. K. Sharma, M. Kennedy, Sep. Purif. Technol. 2018, 199, 260.
[124] R. K. Sharma, K. Solanki, R. Dixit, S. Sharma, S. Dutta, Environmental Science: Water Research & Technology 2021, 7, 818.
[125] P. Xu, G. M. Zeng, D. L. Huang, C. L. Feng, S. Hu, M. H. Zhao, C. Lai, Z. Wei, C. Huang, G. X. Xie, Z. F. Liu, Sci. Total Environ. 2012, 424, 1.
[126] C. D. Powell, A. J. Atkinson, Y. Ma, M. Marcos-Hernandez, D. Villagran, P. Westerhoff, M. S. Wong, J. Nanopart. Res. 2020, 22, 48.
[127] C. Baresel, V. Schaller, C. Jonasson, C. Johansson, R. Bordes, V. Chauhan, A. Sugunan, J. Sommertune, S. Welling, Heliyon 2019, 5, e02325.
[128] D. Huang, S. Chen, G. Zeng, X. Gong, C. Zhou, M. Cheng, W. Xue, X. Yan, J. Li, Coord. Chem. Rev. 2019, 385, 44.
[129] R. Wang, X. Wang, X. Xi, R. Hu, G. Jiang, Advances in Materials Science and Engineering 2012, 2012, 409379.
[130] M. Mishra, D.-M. Chun, Applied Catalysis A: General 2015, 498, 126.
[131] S. Kment, F. Riboni, S. Pausova, L. Wang, L. Wang, H. Han, Z. Hubicka, J. Krysa, P. Schmuki, R. Zboril, Chem. Soc. Rev. 2017, 46, 3716.
[132] X. Feng, Curr. Chem. Biol. 2009, 3, 189.
[133] D. Fan, Q. Wang, T. Zhu, H. Wang, B. Liu, Y. Wang, Z. Liu, X. Liu, D. Fan, X. Wang, Frontiers in Chemistry 2020, 8.
[134] E. A. Lee, H. Yim, J. Heo, H. Kim, G. Jung, N. S. Hwang, Arch. Pharmacal Res. 2014, 37, 120.
[135] Y. Li, D. Ye, M. Li, M. Ma, N. Gu, Chemphyschem 2018, 19, 1965.
[136] B. R. Whatley, X. Li, N. Zhang, X. Wen, Journal of Biomedical Materials Research Part A 2014, 102, 1537.
[137] H.-M. Yun, S.-J. Ahn, K.-R. Park, M.-J. Kim, J.-J. Kim, G.-Z. Jin, H.-W. Kim, E.-C. Kim, Biomaterials 2016, 85, 88.
[138] E. Díaz, M. B. Valle, S. Ribeiro, S. Lanceros-Mendez, J. M. Barandiarán, Nanomaterials 2018, 8, 678.
[139] Y. Xia, J. Sun, L. Zhao, F. Zhang, X.-J. Liang, Y. Guo, M. D. Weir, M. A. Reynolds, N. Gu, H. H. K. Xu, Biomaterials 2018, 183, 151.
[140] M. M. Fernandes, D. M. Correia, C. Ribeiro, N. Castro, V. Correia, S. Lanceros-Mendez, ACS Appl. Mater. Interfaces 2019, 11, 45265.
[141] M. Filippi, B. Dasen, J. Guerrero, F. Garello, G. Isu, G. Born, M. Ehrbar, I. Martin, A. Scherberich, Biomaterials 2019, 223, 119468.

[142] J. Dulińska-Litewka, A. Łazarczyk, P. Hałubiec, O. Szafrański, K. Karnas, A. Karewicz, Materials (Basel) 2019, 12.
[143] S. C. Hong, J. H. Lee, J. Lee, H. Y. Kim, J. Y. Park, J. Cho, J. Lee, D. W. Han, Int J Nanomedicine 2011, 6, 3219.
[144] R. M. Patil, N. D. Thorat, P. B. Shete, P. A. Bedge, S. Gavde, M. G. Joshi, S. A. M. Tofail, R. A. Bohara, Biochem Biophys Rep 2018, 13, 63.
[145] L. Li, L.-L. Jiang, Y. Zeng, G. Liu, Chinese Physics B 2013, 22.
[146] M. K. D. Manshadi, M. Saadat, M. Mohammadi, M. Shamsi, M. Dejam, R. Kamali, A. Sanati-Nezhad, Drug Delivery 2018, 25, 1963.
[147] F. Salahpour Anarjan, Nano-Structures & Nano-Objects 2019, 19, 100370.
[148] M. Gonzales-Weimuller, M. Zeisberger, K. M. Krishnan, J. Magn. Magn. Mater. 2009, 321, 1947.
[149] S. Gul, S. B. Khan, I. U. Rehman, M. A. Khan, M. I. Khan, Frontiers in Materials 2019, 6.
[150] M. De, C.-C. You, S. Srivastava, V. M. Rotello, J. Am. Chem. Soc. 2007, 129, 10747.
[151] C. C. Fleischer, C. K. Payne, Acc. Chem. Res. 2014, 47, 2651.
[152] S. R. Saptarshi, A. Duschl, A. L. Lopata, Journal of Nanobiotechnology 2013, 11, 26.
[153] R. Rampado, S. Crotti, P. Caliceti, S. Pucciarelli, M. Agostini, Frontiers in Bioengineering and Biotechnology 2020, 8.
[154] M. Mahmoudi, M. A. Shokrgozar, S. Sardari, M. K. Moghadam, H. Vali, S. Laurent, P. Stroeve, Nanoscale 2011, 3, 1127.
[155] H. Maeda, J. Wu, T. Sawa, Y. Matsumura, K. Hori, J. Control. Release 2000, 65, 271.
[156] Z. Amoozgar, Y. Yeo, Wiley Interdiscip Rev Nanomed Nanobiotechnol 2012, 4, 219.
[157] P. Mishra, B. Nayak, R. K. Dey, Asian Journal of Pharmaceutical Sciences 2016, 11, 337.
[158] 2017.

MASSEY UNIVERSITY
GRADUATE RESEARCH SCHOOL

STATEMENT OF CONTRIBUTION
DOCTORATE WITH PUBLICATIONS/MANUSCRIPTS

We, the candidate and the candidate's Primary Supervisor, certify that all co-authors have consented to their work being included in the thesis and they have accepted the candidate's contribution as indicated below in the *Statement of Originality*.

Name of candidate:	Hossein Etemadi
Name/title of Primary Supervisor:	Paul G. Plieger
Name of Research Output and full reference:	
Magnetic Fluid Hyperthermia Based on Magnetic Nanoparticles: Physical Characteristics, Historical Perspective, Clinical Trials, Technological Challenges, and Recent Advances	
In which Chapter is the Manuscript /Published work:	3
Please indicate:	
• The percentage of the manuscript/Published Work that was contributed by the candidate:	90%
and	
• Describe the contribution that the candidate has made to the Manuscript/Published Work:	
This review was drafted by Hossein Etemadi (including text and images). The draft was then proof read by Jenna Buchanan and Paul Plieger. Final edits were then completed by Hossein Etemadi	
For manuscripts intended for publication please indicate target journal:	
Advanced Therapeutics, 2000061, 2020. https://doi.org/10.1002/adtp.202000061	
Candidate's Signature:	Hossein Digitally signed by Hossein Date: 2021.02.11 14:09:16 +13'00'
Date:	11/02/2021
Primary Supervisor's Signature:	Paul Plieger Digitally signed by Paul Plieger DN: cn=Paul Plieger, c=NZ, o=Massey University, ou=School of Fundamental Sciences, email=p.g.plieger@massey.ac.nz Date: 2021.02.26 12:09:46 +13'00'
Date:	26/02/2021

(This form should appear at the end of each thesis chapter/section/appendix submitted as a manuscript/ publication or collected as an appendix at the end of the thesis)

Chapter 3. Magnetic fluid hyperthermia (MFH) based on magnetic nanoparticles (MNPs): Physical characteristics, historical perspective, clinical trials, technological challenges, and recent advances

Hossein Etemadi and Paul G. Plieger*

School of Fundamental Sciences, Massey University, Private Bag 11 222, Palmerston North, New Zealand

E-mail: p.g.plieger@massey.ac.nz, h.etemadi@massey.ac.nz

Fax: + 64 6 350 5682, Tel: + 64 6 356 9099

Keywords: magnetic fluid hyperthermia; cancer; iron oxide nanoparticles; biofunctionalization; tumor

Abstract

Advances in nanotechnology have resulted in the introduction of magnetic fluid hyperthermia (MFH), a promising non-invasive therapeutic localized cancer treatment. Exposure of a fluid of superparamagnetic iron oxide nanoparticles (IONPs) to an alternating magnetic field (AMF) operating at biologically benign conditions, leads to heat dissipation within the tumor and ultimate apoptosis and/or necrosis. Despite use in a clinical setting, there are still impediments preventing widespread use of MFH. These include insufficient heat dissipation potency of IONP fluid, inadequate dose or concentration of deposited fluid to the tumor, inhomogeneous distribution of fluid inside the tumor, the lack of control of real-time monitoring of temperature rises during treatment and exposure of the patients to X-ray radiation produced by computed tomography (CT) scans. Accordingly, massive efforts have been put forth to promote the successful clinical adoption of MFH. In this contribution, the technique of MFH is describe, including the present state of clinical MFH. The physical mechanisms behind heat dissipation by MNPs that instigate cell death pathways are discussed, as is recent technological progress in the field towards the advancement of MFH. Finally, an outlook on the future considerations required to accelerate the clinical adoption of MFH is presented.

3.1. Introduction

Cancer is the second cause of global mortality according to the World Health Organization (WHO).[1] On account of the complexity in cancer biology, the current classical therapeutic regimes such as chemotherapy, radiation doses or surgery have failed to achieve resounding success for the complete elimination of cancer cells.[2] Another clinical technique of interest is hyperthermia in which the tumor temperature is elevated from normal physiological temperature of 37 °C to temperatures up to 42-46 °C.[3] This range of temperature has been developed from cell culture and animal studies.[4] The rationale behind this treatment is that cancer cells are less resistant to thermal shock due to hypoxicicity, insufficient nutrients, disorganized vascular network, low blood flow, low tissue conduction and normal acid concentrations.[5]. If the achieved temperature is in the range of 42-46 ˚C, hyperthermia is combined with concomitant radio/chemotherapy to mediate cell death through nucleus condensation, membrane blebbing, DNA damage, protein folding, protein denaturation, signalling interruption, anti-cancer immune response induction and inducing apoptosis.[6] Higher temperatures > 46°C (up to 55 °C), also called 'thermoablation', are capable of killing the cancer cells directly with coagulation, carbonisation or necrosis.[7] The temperature elevation in standard hyperthermia can be achieved from different external sources such as hot water, microwaves, ultrasonic waves and radio waves.[8] In spite of advancements in clinical routines, there still exist some challenges associated with these conventional hyperthermia techniques. These include burns, blisters, unregulated tissue growth, poor penetration ability of the heat waves, imprecise localization of thermal energy and poor tumor targeting.[9] The advance of nanotechnology has introduced magnetic fluid hyperthermia (MFH) as a novel potential solution to this challenge. MFH provides a path to tissue - specific localization of heat in deep tissues with high intensity in a non-invasive manner thanks to the presence of MNPs accompanied by high penetration capability of applied magnetic field to the human body. [10] Of all the studied MNPs, superparamagnetic IONPs have been the cornerstone of various theranostic (therapeutic and diagnostic) applications.[11]

Superparamagnetic IONPs (Fe_3O_4, γ-Fe_2O_3 or intermediate phases) exhibit a range of interesting properties such as biocompatibility, biodegradability, superparamagnetism, low toxicity, chemical functionality, remote actuatinability and nanometer size arising from a

combination of their atomic composition and crystal configuration.[12] From one side, utilizing the fact that biological tissue is weakly diamagnetic (negligible absorption and scattering of the AMF), allows the penetration of low frequency magnetic fields to the target tissue deep inside the body.[10a, 13] With a sufficient concentration of IONPs accumulated at the site of interest, the remote actuation of these particles under external alternating magnetic field (AMF) results in heat dissipation and temperature elevation of the targeted area through a number of different mechanisms depending on their magnetic profile and size regimes.[14] For an ideal *in vivo* MFH treatment, IONPs should present pure superparamagnetism, small particle size, d < 7 - 9 nm, and a narrow size distribution (< 10 %). This would allow easy transportation and circulation in the blood vessel without agglomeration.[15] In particular, they should raise the temperature of the tumor tissue at a low particle dose for complete necrosis/apoptosis with minimized side effects under safe AMF field geometries.[16] This safe threshold is limited to $H \times f < 4.8 \times 10^9$ A m^{-1} s^{-1} value where f is the applied frequency and H is amplitude of the applied AMF.[17] Unfortunately, the heat diffusion potential of IONPs is insufficient at this field configuration attributed to their intrinsic low saturation magnetization (M_s), large surface spin disorder and degraded magnetic susceptibility ((χm = χ'm (in-phase) + χ''m (out-of-phase))[18]

On this account, significant research efforts have been directed toward optimization of the intrinsic features of IONPs by modulating their geometry,[19] size and size distribution[20] and crystallinity[21]. Even after this optimization, there is an eventual limit to the temperature increase obtainable with IONPs due to their intrinsic non-resonance absorption nature under an AMF.[22] To circumvent this limitation, other inorganic nanoparticles (NPs) such as gold,[23] perovskite,[24] spinel ferrites,[25] Fe[26] and Co metallic NPs[27] have been proposed as candidate heating hubs instead of IONPs. The activation of IONPs with other stimuli such as near-infrared (NIR) light has also been proposed for optically - induced *in vitro* and *in vivo* ablation of tumors.[28] Despite achieving promising results these proposed strategies still suffer from a number of drawbacks (see discussion below). Therefore, further work is needed to realize the full potential of MFH as a new frontier in cancer medicine.

In this review article, we have comprehensively surveyed the literature over the last 27 years (1993 – 2020) with consideration of the chemical, physical and biological perspectives of MFH. We begin with a historical overview of the MFH technique and its clinical status

(Section 2). Following that, a description of magnetism at the nanoscale and the magnetic phase and domain structure of MNPs are provided (Section 3). The physical modeling of magnetic heating, techniques to estimate the heat diffusion characteristics of magnetic fluid and pathways that trigger cancer cell death are discussed in Section 4. In Section 5, the technical limitations of commercial fluid and clinical settings are outlined. The recent proposed experimental and theoretical solutions to improve the efficiency of MFH are critically reviewed in Section 6. The review is concluded with a discussion on the areas of future developments required for the worldwide adoption of MFH (Section 7).

3.2. History of MFH and current clinical stage

Gilchrist *et al*. initially conceptualized magnetic hyperthermia with exposure of various dog tissues to an AMF operating at 1.2 MHz with magnetic particles relatively large multidomain particles (>100 nm) in 1957.[29] In 1979, Gordon *et al.* utilized Fe_3O_4-coated dextran for cancer treatment on rats bearing mammary carcinomas in an *in vivo* study.[30] Applying nanotechnology to cancer medicine, Jordan *et al.* developed the initial idea of the potential of MFH for cancer treatment in 1993.[31] Thereafter, several preclinical examinations of human mammary carcinoma,[32] rat glioma[33] and rat prostate carcinoma[34] validated the efficacy and feasibility of this therapeutic anti-cancer concept. Motivated by preclinical outputs, Jordan *et al.* outlined the scheme of the first whole body magnetic field applicator for clinical MFH applications in 2001.[35] It consists of (i) the magnetofluid MFLAS called NanoTherm® composed of an aqueous solution of 15 nm IONPs coated aminosilane shells with an iron concentration of 112 mg/mL Fe (Figure 3.1a) (ii) NanoPlan® software package that uses the bioheat transfer equation to favors the temperature simulation in the site of interest (Figure 3.1b) and (iii) an alternating magnetic field applicator 300F called the NanoActivator® operating at fixed frequency (*f)* of 100 kHz with a magnetic field range (*H*) of 0 - 15 kA/m. (Figure 3.1c). The MFH therapy plan, NanoTherm® therapy, is initiated by measuring the tumor using computed tomography (CT) so that the injection dose and position for the injection of the NanoTherm® is optimally planned. The patient is immersed inside the NanoActivator® device and exposed to a rapidly AMF focused on the tumor site. Thereafter, NanoTherm® fluid is injected into the patient either directly into the tumor or into the resection cavity wall. A catheter is also installed in the targeted area to promote the monitoring of the tumor temperature. The applied AMF provided by the NanoActivator®,

field generator activates the remote actuation of IONPs inside the ferrofluid and leads to temperature elevation of the targeted area. The physician monitors the therapy utilizing the NanoPlan® software that shows the fluid distribution using a CT scan. Depending on the rate of fluid distribution, the physician then tunes the treatment temperature with appropriate magnetic field range (*H*) and frequency (*f)* modifications. The treatment plan typically follows six one-hour sessions over a period of three weeks.

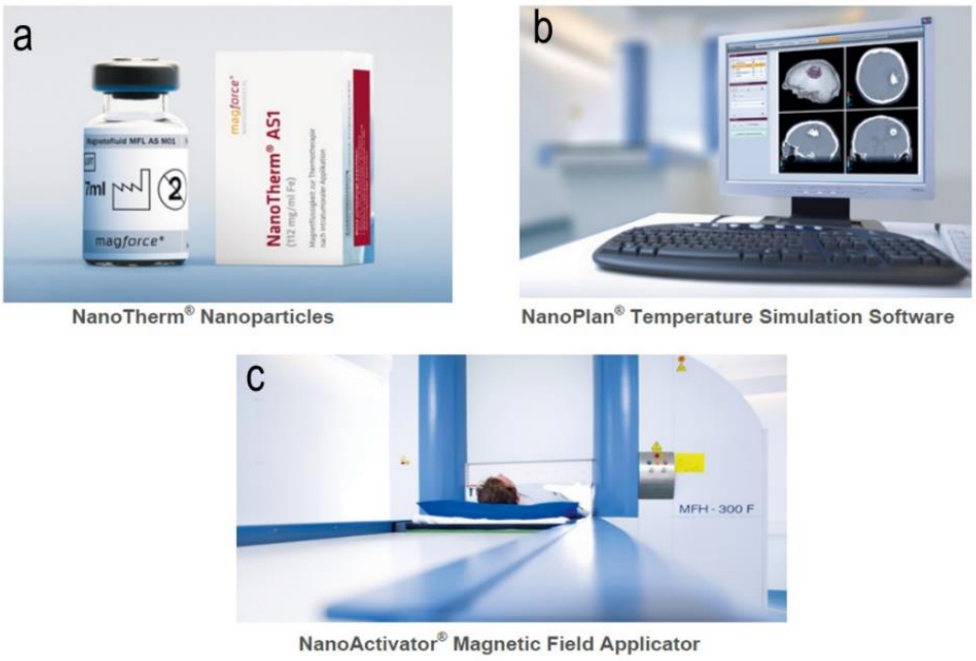

Figure 3.1. Pictures of (a) NanoTherm® ferrofluid (b) NanoPlan® and (c) NanoActivator® (Copyright: MagForce AG (Germany).

Regarding the oncological outcome, the potential of this therapeutic technique has been documented clinically on Glioblastoma multiforme *(*GBM*)* and on prostate carcinoma either synergistically with external radiotherapy/brachytherapy or chemotherapy (with temozolomide)radio/chemotherapy or in a monotherapy mode.[36] For instance, the first clinical trial of MFH was performed on patients with prostate carcinoma at Charité Hospital in Berlin, Germany, jointly with MagForce in 2006. The maximum intra-prostate temperature and specific absorption rate (SAR) at a field strength of 4.0 – 5.0 kA/m were 48.5°C and 288 W/Kg respectively. The distribution of fluid (120 mg/ml, injected transperineally, six hyperthermia sessions of 60 min duration at weekly intervals) and the

position of the thermometry probes inside the tumor were monitored by computerised tomography (CT). According to CT scans, NPs could be visualised six weeks after treatment, which eliminates the need for further injection of fluid. The field strength > 5 kA/m was intolerable to patients due to pain in the perineum. Notably, MRI is not being used as a diagnostic tool in MFH to monitor the progress of therapy because of the loss of signal in the areas of interest.[36e] In another clinical trial on patents with prostate carcinoma with the same fashion, the applicability of CT was examined to quantify the content of fluid. The detection rate of iron mass in the tissue was 89.5 %. Additionally, the maximum intra-prostate temperature and SAR at a field strength of 5.0 kA/m were 51.3 °C and 120 W/Kg respectively.[37] The feasibility of MFH was also assessed on patents with GBM. For instance, in the first MFH clinical trial on patents with GBM, the median maximum intratumoral temperature at a field strength of 8 kA/m was 44.6 °C. All patients received radiotherapy (irradiation doses of less than 60 Gy) and chemotherapy with temozolomide (200 mg per m^2 of body-surface area). A median survival rate of 14.5 months was achieved in this synergistic fashion.[36c] In another clinical study, a maximum intratumoral temperature of 82 °C and survival rate of 13.9 months was achieved for MFH therapy with radiotherapy (irradiation doses of 30 J/K)[36d] in comparison to 11.2 months for MFH therapy on its own.[36b] In 2013, MagForce received approval from the European Medicines Agency (EMA) and the German Federal Institute for drug and medical devices (BfArm) to begin the utilization of NanoTherm® for treatment of glioblastoma. In 2018, MagForce was granted FDA (IDE) approval to initiate a clinical trial with NanoTherm® therapy on patients bearing prostate cancer in U.S. However, the technique currently does not have FDA approval[10b, 38] The result of the clinical trials on patients with MFH are summarised in Table 3.1.

Table 3.1.The clinical trials of NanoTherm® therapy (f = 100 kHz with a variable field strength H = 0 - 18 kA/m, and fluid concentration = 112 mg/mL).

Cancer type	**Trial phase**	**Patient (number)**	**Injection route**	**Concomitant treatment (s)**	**Therapeutic outcome**	**Year/Ref**
Prostate carcinoma	I	1	Transperineal	-	The maximum intraprostate temperature was 48.5 °C. NPs were retained in tumor tissue for several weeks. The SAR value was 288 W/Kg at *H* = 100 kHz, *f* = 4 kA/m	2005 [36e]
Chondrosarcoma, sarcinoma, Cervical carcinoma, Prostate carcinoma, Ovarian carcinoma, Rectal carcinoma	I	22	Transperineal	Radio/chemotherapy	The median SAR value and maximum temperature of the tumor area were 130 W/kg and 39.5 °C respectively	2006 [36a]
Glioblastoma multiforme	I	14	Intratumoral	Radio/chemotherapy	The median maximum intratumoral temperature was 44.6 °C. Thermotherapy was tolerated well at MF strengths of 3.8 – 13.5 kA/m	2006[36c]
Prostate carcinoma	I	10	Transperineal	-	89.5 % of NPs were detected in tissue using CT. The median SAR value and maximum temperature of the tumor area were 115 W/kg and 42.7 °C respectively	2007 [37]

Prostate carcinoma	II	10	Transperineal	-	NPs deposits in the prostates one year after MFH. 89.5 % of NPs were detected in tissue using CT. The maximum temperature in the prostates was 55 °C	2007 [36f]
Glioblastoma multiforme	II	3	Intratumoral	Radio/chemotherapy	Low uptake of aggregated particles in glioblastoma cells. High uptake of particles by macrophages. No clinically adverse effects. Maximum intratumoral temperature was 65.6 °C	2009[36d]
Glioblastoma multiforme	II	66	Intratumoral	Radio/chemotherapy	The median overall survival was 13.4 months. The maximum intraprostate temperature was 82.0 °C	2011[36b]

3.3. Magnetism at nanoscale: Magnetic hysteresis and relaxation loss

In a ferromagnetic substance (such as iron, cobalt and others), a magnetic field is created due to the magnetic pole density at its surface. This magnetic field results in creation of an internal energy called magnetostatic energy. In order to minimize this potential internal energy, ferromagnetic particle divides into several small magnetic regions called domains situated in their structure.[39] In each domain, the individual magnetic moments align in the same direction, however, the direction of magnetization of different domains might vary from domain to domain. These domains are randomly aligned inside the substance so that the net resultant magnetization is zero in normal condition (no magnetic field applied).[40]

Large ferri- or ferromagnetic particles are in a multi-domain (MD) state. When exposed to a uniform magnetic field, these randomly orientated magnetic domains get aligned in parallel to the direction of the applied field. In this case, the maximum magnetization (M_s) is achieved. This is called saturation magnetization and the required field to reach M_s is called saturation field (H_k).[41] The direction and degree of a magnetic moment`s alignment depends on the particle features such as shape, atomic composition, volume and also on the magnitude of the applied magnetic field.[42] When the field is removed, domains return to their original positions however some of them remain aligned resulting in a residual magnetization called remanence (M_r). As a result, the ferromagnetic particle becomes slightly magnetized. To neutralise this magnetism, a magnetic field of opposite sign called a coercive field or simply coercivity (H_c) is applied in order to bring the remaining magnetization (M_r) to zero. In fact, for every cycle of domain reversal (magnetization in forward and demagnetization in reverse directions) there is a transformation of magnetic energy into thermal energy known as the hysteresis loss. This hysteretic behaviour created in a ferromagnetic particle is used as the source of heat in MFH.[43]

When the size of the ferromagnetic MD particle is decreased below a critical value, known as single domain limit, the necessary energy for the creation of the domain wall becomes prohibitively costly so that the particle prefers to form a stable single domain (SD).[44] In a SD ferromagnetic particle, the orientation of the magnetic moment to an easy axis is dictated by the magnetocrystalline anisotropy (if the particle is sphere) or by shape anisotropy (for non-spherical particles) in the absence of a field. Magnetocrystalline anisotropy is a way through which magnetic moments are aligned spontaneously to an easy direction in order to

further decrease the internal magnetostatic energy. [45] Magnetocrystalline anisotropy can be created by contribution of crystalline lattice (e.g. shape, structure, defects, volume,) and the collective magnetic interactions (e.g. exchange, self-field generation, interparticle).[46]

Therefore, for a SD ferromagnetic particle state, the largest possible magnetization is realized as all the internal magnetic moments are aligned. The magnitude of this moment is where saturation magnetization and is the volume of the particle.[47] The mechanisms leading to the hysteresis behaviour for MD ferromagnetic particle is quite different to that of SD. As stated, in a MD ferromagnetic particle, the motion or reorganisation of the domain wall leads to the reversal of the magnetization direction and subsequent hysteretic behaviour. For a SD particle, the coherent rotation of all the magnetic moments within the sample leads to magnetization reversal according to the Stoner–Wohlfarth theory.[48] Importantly, other incoherent magnetization reversal modes such as fanning or curling might occur for the magnetic moment within the SD particle which are not included in the Stoner-Wohlfarth model.[49] Whether the ferromagnetic particle will exhibit MD or SD behaviour depends upon its specific characteristics such as size, chemical and structural composition and on the magnitude of the applied field.[45b] The essential energy for the motion or reorganisation of the domain wall within the MD ferromagnetic particle is relatively small compared to the energy required for the complete reversal of the magnetic moment within the SD particle dictated mostly by crystalline or shape anisotropy. As a result, SD ferromagnetic particles are magnetically harder than MD ones and present the highest coercivity (H_c) and hysteresis loss.[42] As the size of SD ferromagnetic particle is scaled down further, coercive field and remanance reaches zero, the hysteresis loop gradually shrinks, and a transition to a SD superparamagnetic state occurs.[50] The temperature at which the crossover from ferromagnetic to superparamagnetism occurs is called the blocking temperature and is defined as $T_B = K_{eff}V_m/25k_B$.[51] (T_B: blocking temperature, K_{eff}: magnetic anisotropy constant, k_B is Boltzmann's constant (1.3807 x 10^{-23} J/K) and V_m is the volume of a single nanocrystal assuming sphere as $V_m = \pi D_m^3/6$ (D_m is the magnetic core diameter from transmission electron microscopy, TEM). The superparamagnetic nanoparticle now behaves as a paramagnetic particle however magnetic susceptibility is huge compared to a paramagnet with typical susceptibility values in the order of 10^{-5}).[50a]

When the particle size drops below the superparamagnetic limit, thermal fluctuations start to appear so that thermal energy dominates the magnetocrystalline anisotropy. In such situation, a magnetic moment can rotate freely, relax and reverse its direction rapidly. This magnetic fluctuation leads to a net magnetization of zero when the magnetic field is switched off.[52]

When subjected to an AMF, a superparamagnetic SD particle will dissipate heat through a series of relaxation losses by way of Néel and Brown relaxation mechanisms. In the case of Néel relaxation, magnetic energy is converted to heat while applied magnetic field overcomes the magnetocrystalline anisotropy energy which hinders the reorientation of magnetic moment. In the case of Brown relaxation, magnetic energy is converted to heat when the applied magnetic field overcomes the viscosity of the fluid in which particles are suspended.[53]

Despite M_s and M_r, H_c is size dependant. In Figure 3.2, the size dependence of coercivity (H_c) is shown for the non-interacting magnetic particles moving from a MD ferromagnetic region to SD ferromagnetic and then SD superparamagnetic state. Typically, the coercivity (H_c) value is zero for superparamagnetic NPs beyond the blocking temperature. The maximum H_c appears as the size moves from superparamagnetic to SD ferromagnetic region, then gradually decreases when approaching to the MD region.[54]

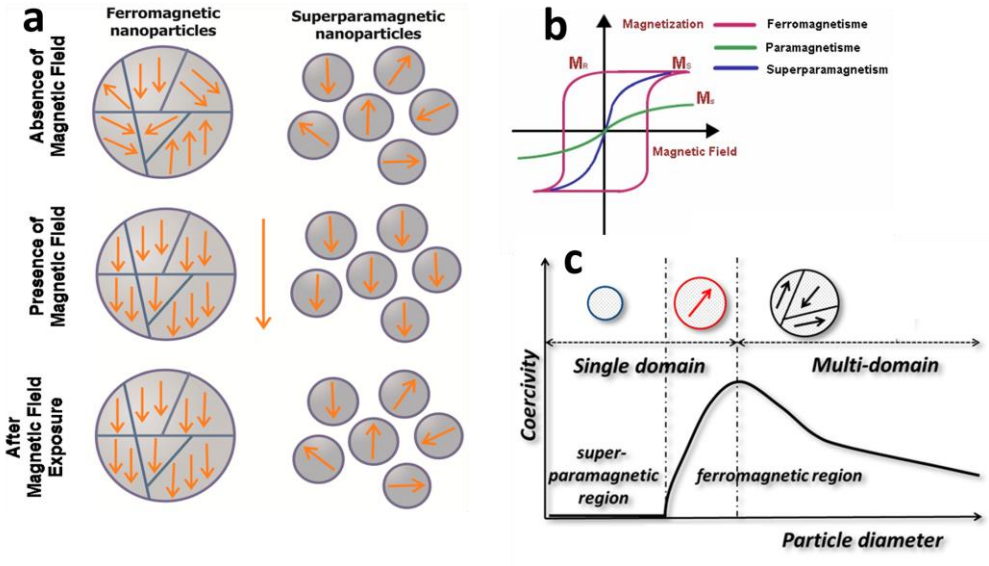

Figure 3.2. (a)The behaviour of superparamagnetic and ferromagnetic particles in the presence and absence of a magnetic field. (Reprinted with permission from ref 89. Copyright 2012 MDPI Publishing Group.) (b) A typical hysteresis loop for different magnetic particles. (Reprinted with permission from ref 93. Copyright 2012 Elsevier Publishing Group.) (c) Size-dependence of coercivity for magnetic particles. (Reprinted with permission from ref 91. Copyright 2017 RSC Publishing Group.)

The dimensional limit value for the transition from a MD to SD ferromagnetic state and further to a SD superparamagnetic state, is reported to be in the range from 2 nm to about 800 nm. However, there is not an exact defined size range for occurrence of theses transitions in any material, as theses crossovers could be influenced by for example, the physical properties of the material such as crystal structure (which can have spherical, cubic, or multiple phases), shape, strain, presence of the crystal defects (number and type) and surface/interface effects.[43, 47] In 1975, Butler and Banerjee estimated the particle size of about 80 nm and 10 nm for IONPs as upper limits for SD to MD crossover and for superparamagnetic state respectively.[55] The necessary particle size to achieve superparamagnetism for IONPs have latterly been reported somewhere between 20 and 30 nm.[55b, 56] SD ferrimagnetic behaviour has been reported for IONPs up to 40 nm.[57] Furthermore, the critical size to transit from a SD to MD ferromagnetic state, have been theoretically determined to be 128 nm for spherical[58] and 76 nm for cubic[55a] IONPs. The critical sizes of 30 – 46 nm have also been reported for cubic IONPs.[59] In a recent study, Li *et al*. studied the critical size for the MD/SD transition in the cubic IONPs with sizes of 10 – 300 nm synthesized under well-controlled crystal growth conditions. The critical value for

the transition was found to be 76 ± 4 nm which was in consistent with the theoretically estimated value.[60]

Superparamagnetic IONPs (< 30 nm) are preferred over ferromagnetic SD or MD ones for biomedical applications. Firstly, they exhibit zero remanence (M_r) and coercivity (H_c), zero net magnetization at room temperature (RT) and therefore no magnetic interaction between particles, which enables their easily stabilisation in solution.[61] Furthermore, because of the lack of interaction between particles in the absence of an applied magnetics field, agglomeration and the potential embolization of the capillary vessels can be aborted.[62] In addition, there are nearly no synthetic methods available to prepare stable aqueous suspensions of ferromagnetic NPs larger than 30 nm.[63] Magnetosomes extracted from magnetotatctic bacteria with size in the range of 30 - 100 nm have been developed in the recent years with ferromagnetic features, however their biomedical application is hindered as will be discussed in the next sections.

4. Physical Modeling of Magnetic Heating and Cell Death Pathways

The amount of heat produced by MNPs under AMF is termed as specific absorption rate (SAR) or specific loss power (SLP). This created heat approximately equals to the area of the hysteresis loop (A) during one cycle of the magnetic field and expressed as:

$$A = \int_{-H_{max}}^{+H_{max}} \mu_0 M(H) dH \qquad (1)$$

Where μ_0 is the permeability of free space (4 π ×10 $^{-7}$ m kg s^{-2} A^{-2}), M(H) is the magnetization of nanoparticle.

Two theoretical models have been developed to assess the hysteresis loop behaviour of a system of MNPs under applied magnetic field. This include linear response theory (LRT) model introduced by Rosensweig[64] and Stoner–Wohlfarth (SW) model.[65]

LRT also called Néel – Brown relaxation model consider the magnetic behavior of an assembly of single domain non-interacting superparamagnetic NPs with a linear response of their magnetization to the applied magnetic field at low field amplitudes.[64, 66] In this linear approximation, the hysteresis loop area is given by:

$$A = \frac{\pi \mu_0 H_{ac}^2 V_m M_S^2}{3 k_B T} \frac{2\pi f \tau}{[1+(2\pi f \tau)^2]} \quad (2)$$

Where μ_0 is the permeability of free space ($4\pi \times 10^{-7}$ m kg s^{-2} A^{-2}), M_s is the saturation magnetization, V_m is the volume of the particles, k_B = Boltzmann constant (1.38×10^{-23}J/K), T the absolute temperature (in Kelvin) and τ is t is the Néel–Brown relaxation time.[67] The Brownian (τ_B) and Néel (τ_N) relaxation times of a single superparamagnetic nanoparticle assuming as sphere can be calculated utilizing the following formulas:

$$\tau_N = \tau_0 \exp\left[\frac{K_{eff}\pi D_m^3}{6k_B T}\right] \quad (3)$$

$$\tau_B = \left[\frac{\pi \eta D_h^3}{2k_B T}\right] \quad (4)$$

Where τ_N = Néel relaxation time, τ_0 = effective relaxation time (~ 10^{-9} s), K_{eff} = magnetic anisotropy constant, D_m is the magnetic core diameter from TEM, k_B = Boltzmann constant (1.38×10^{-23} J/K), T = the absolute temperature in Kelvin, τ_B = Brownian relaxation time, η = dynamic viscosity of the surrounding medium (η = 0.7978×10^{-3} kg m^{-1} s^{-1} for water) and D_h is the hydrodynamic diameter (the diameter of the particle plus adsorbed surfactant , derived from dynamic light scattering (DLS)).[19f] Considering that these two mechanisms take place in parallel independently, the effective relaxation time τ_{eff} is given by

$$\tau = \frac{\tau_N \tau_B}{\tau_N + \tau_B} \quad (5)$$

When $\tau_N \gg \tau_B$ or $\tau_N \ll \tau_B$, τ_{eff} is the shorter (faster or smaller) one.

Hypothetically, for less viscous fluids and larger size particles, Brownian mechanism is dominant, whereas for small size regime and viscous fluids, the Néel mechanism is dominant. As a result, it is deduced that the heat loss by Brownian relaxation is negligible in biological tissue (tumor etc.) because of the high viscosity of the extracellular matrix of tissue. Therefore, Néel relaxation is the primary mechanism by which the temperature of the tumor tissue is increased under AMF.[68]

LRT models is only valid for small magnetic field amplitude and loses the linearity over a wide range of amplitudes at fixed frequency. Besides, it assumes the NPs as non-interacting however in real solutions there are some degree of interactions between particles.[69]

LRT is not applicable for magnetic NPs in the ferromagnetic regime and SW model is considered instead assuming the particles as non-interacting single domain. SW model does

not take into consideration any thermal activation (as LRT does). It is therefore proportional to the coercivity field and hysteresis loss happens only if the external field supress the coercivity field.[70] The area of hysteresis loop can be analytically estimated in the limit of *T = 0* and infinite field frequency (*f* → ∞*)* as:

$$A = 2\mu_0 H_c M_s \quad (6)$$

Where H_c is the coercive field. At $T \neq 0$ and finite frequency, the hysteresis loop area can be expressed as:

$$A(T, f) = 2\mu_0 H_c(T, f) M_s \quad (7)$$

SAR is given by *SAR = Af* where *f* is the frequency per second.[71]

To exclude the dependence of SAR/SLP value on amplitude of the applied AMF, Kallumadil *et al*. [72] proposed intrinsic loss power (ILP) defined as:

$$ILP = \frac{SLP}{f\ H^2} \quad (8)$$

A more detailed description of the implicit assumptions and limitations underlying LRT and SW models are presented in Hergt[73] and Carrey *et al*.[74] works. Overall, if the synthesized nanoparticle is in superparamagnetic regime ($H_c \sim 0$, $M_r \sim 0$), the LRT should be considered as an optimal model to unravel the dominant mechanism (Nèel or Brown relaxation), nevertheless for ferromagnetic NPs SW model would be the contributor. The heating potential of an ensemble of MNPs, is influenced by intrinsic physical and magnetic properties of the particles such as the size, size distribution, magnetization, magnetic anisotropy, polydispersity, concentration and injection volume of magnetic nanofluid. Additional extrinsic properties such as the applied magnetic field amplitudes, the viscosity of the tissue, the blood perfusion in the tumor tissue and tumor size are also important.[53, 75]

As shown by equation 2, the heating loss is proportional to the frequency and square of magnetic field strength and increases with both the *f* and *H* of the AMF. Having said that, one could think of increasing these parameters to achieve the maximum possible SAR value.[76] However, it should be noted that the applied AMF in MFH, in addition to selective heating of cancer tissue using MNPs, could also lead to undesirable nonspecific heating of healthy tissues via Joule heating through induced eddy currents.[77] Therefore, an upper limit of *f* and *H* known as Brezovich limit ($Hf < 4.85 \times 10^8$ A m^{-1} s^{-1}) , corresponding to *H* = 4.85

kA/m (60 Oe) and f = 100 kHz, is considered to favour the safe MFH treatment.[78] A less rigid upper limit of 5×10^9 A m^{-1} s^{-1} corresponding to H = 50 kA/m (625 Oe) and f = 100 kHz has also been considered.[73] In some studies the utilization of H higher than 80 kA/m (1000 Oe) at150 kHz resulted in serious side effects in animal body.[79] Therefore, the selection of an appropriate f and H of the AMF is crucial to reach effective safe treatment.

As discussed in Section 3, the magnetic energy provided by AMF is transferred into thermal energy (heat) through different mechanisms within the crystal lattice of the nanoparticle. Later on, this stored thermal energy is delivered to the cancerous tissue via heat conduction as the most possible mechanism.[80] The transferred heat to the tissue is however lost to some extent due to blood perfusion and cooling effect of water-based materials surrounding the tissue.[81] Therefore, a large concentration of particles should be localized in tumor area to favour effective MFH therapy. The concentration required to attain hyperthermia in a tumor tissue can be evaluated using the bioheat transfer equation proposed by Pennes *et al*.[82] Using this equation, it has been estimated that for MNPs with SAR/SLP value of the order of 1000 W/g, an approximate concentration of 650 mg/cm^3 would be necessary to treat a tumor tissue with diameter of 5 mm.[83] Importantly, the necessary concentration of particles to elevate the temperature of the tumor area to the hyperthermia range increases with a decrease in the tumor radius.[73, 80]

Different theoretical and experimental methods including magnetic or calorimetric methods have been proposed in the field to assess the SAR/SLP values of the synthesized NPs. Magnetic approaches are categorized into “AC magnetic susceptibility”[84] and “hysteresis loops”[85] whereas, calorimetric approaches include “initial slope method“,[86] “ΔT_{max} method“ [26b, 87] and “pulse heating method“. Very recently, infrared thermography (IRT),[88] and lock-in thermography[89] were also proposed for precise quantification of heat dissipation. Generally, calorimetric methods resemble the measurements in the clinical regime of MFH at 100 kHz and 2-15 kA/m.[90] Nevertheless, difficulty in standardization and matching experimental set-ups with precise thermal models, results in some degree of uncertainties.[91] Magnetic methods, on the other hand provide an accurate measurement of SAR/SLP values, however they do not function in the clinical MFH regime. For more details regarding the SAR/SLP measurement techniques, readers are recommended to study the review articles by petri-Fink *et al.* [92] and Natividad *et al*.[93]

In addition to hysteresis or relaxation loss mechanisms, the idea of magnetically mediated energy delivery (MagMED) also called nanoscale thermal phenomenon, was proposed by Rinaldi *et al.* as another potential way to destroy cancer cells under AMF. The idea was developed from a research where they functionalized IONPs with epidermal growth factor receptor (EGFR) for targeted intracellular hyperthermia. They concluded that the actuation of AMF might lead to the abrupt reduction (up to 99 %) in tumor cell viability due to the lysosomal membrane permeabilisation (LMP) without a perceptible temperature rise of the cell suspension.[94] Although promising, this idea confronted controversy with theoretical evaluations. For example, Rabin argued that since rate of heat lost due to conduction to the surroundings far surpass the rate of heat dissipation with MNPs, therefore nanoscale heating should have negligible influence on cells.[95] Keblinsky *et al.* did also reach the same conclusions based on the similar theoretical calculations.[96] In contradict to theoretical assumptions, a number of experimental studies evidenced the existence of local nanoscale heating effects in the vicinity of energy-dissipating MNPs in AMF.[97] For example, Huang *et al*. targeted superparamagnetic $MnFe_2O_4$ NPs to specific proteins on the plasma membrane of cells expressing TRPV1. They grafted one fluorophore on the surface of the NPs to monitor the temperature of the surface under the activation of AMF. Another fluorophore was suspended in solution to check the environment temperature as a control. Immediately upon activation of the AMF, a temperature rise of 20 °C was observed for surface bound fluorophore nevertheless, no temperature change was reported for fluorophore suspended in solution.[98] This nanoscale thermal effect was further supported by experimental research to regulate the biochemical mechanisms that trigger cell death pathways for killing cancer cells.[99]. This includes mechanical actuation exploited in various pathways with direct physical damage to the cell membrane[100] contained within the targeted tumor, induced lysosomal membrane permeabilisation,[94] signal transduction,[101] cytoskeletal disruption,[102] stress-induced gene expression[103] and the influx of calcium ions[104] to induce cell death.

Overall, further work is needed to understand the biological mechanisms by which nanoscale thermal phenomenon can lead to cell death.[105] An overview of the mechanism of cell death through MFH is provided in pictorial form (Figure 3.3).

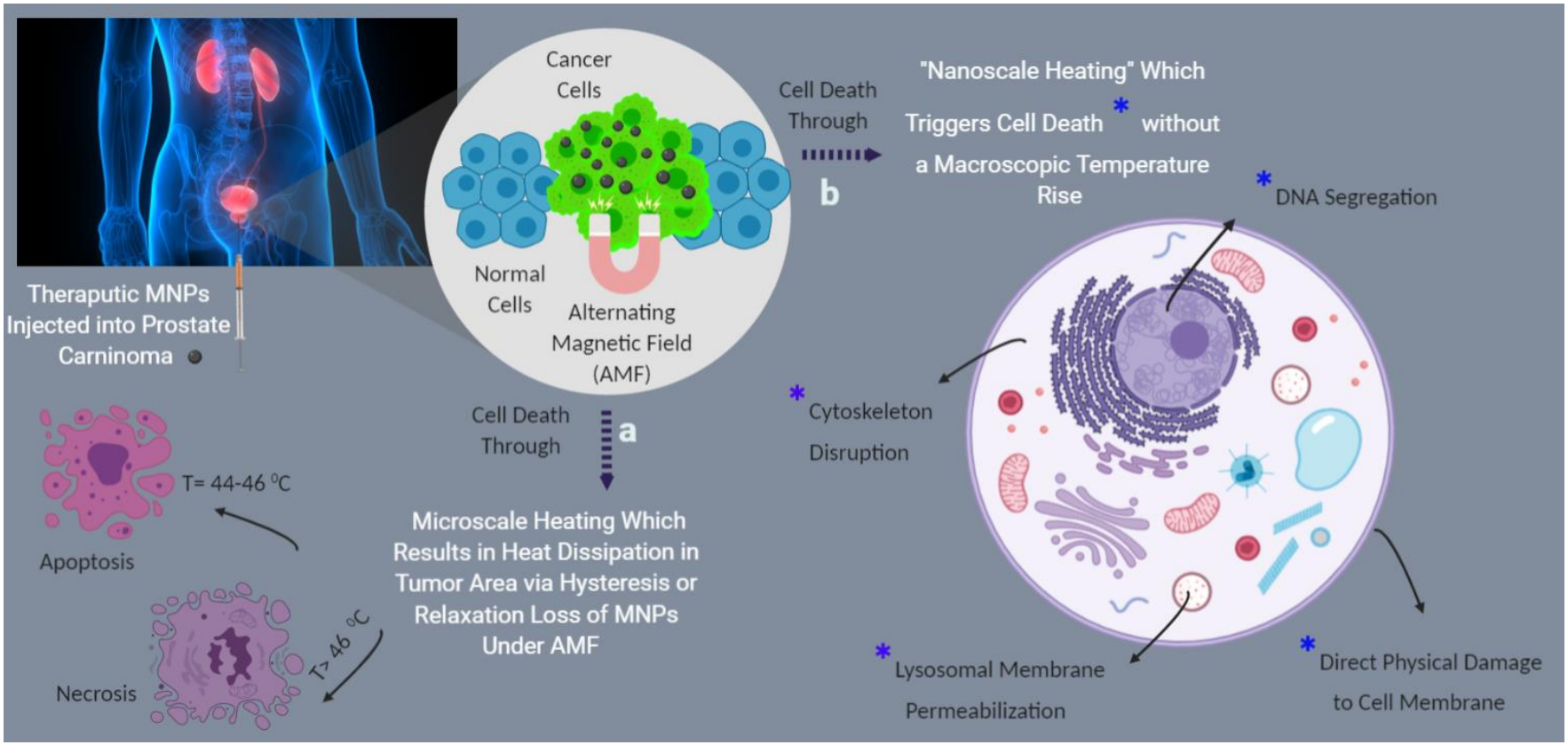

Figure 3.3.The two mechanisms responsible for cell death under an MFH protocol. (a) Hysteresis or relaxation loss (depending on the magnetic phase and size of MNPs) which results in temperature elevation of the tumor area and subsequent necrosis and or apoptosis. (b) Nanoscale thermal phenomenon which regulates the biochemical mechanisms that trigger cancer cell death pathways.

3.4. Technological challenges associated with MFH

In spite of the clinical establishment for cancer therapy, there are some impediments for successful clinical realization of MFH. Firstly, the heat dissipation potency of commercial magnetic NanoTherm® fluid, at quantities of ~ 112 mg Fe/mL within a physiologically safe range of alternating MF (f =100 kHz, H ~ 2-18 kA/m) is insufficient for the complete eradication of tumors.[106] Hergt *et al.* hypothesized that an SAR/SLP value of 1000 W/g at a fluid concentration of 5 mg/mL should be sufficient to realize effective treatment of cancer with MFH.[107] However, the currently available commercial IONPs including NanoTherm® fluid have exhibited the SAR/SLP values below this threshold.[36a, 36e] For example, commercial aqueous ferrofluid of Fe_3O_4 (Iron (III) oxide, gamma, 99 %, Alfa Aesar) presented the SAR value of 60 W/g compared to synthetic Fe_3O_4 ferrofluid with SAR of 332 W/g at H_0 = 10 kA/m and f = 400 kHz.[108] In another study, Parkin *et al*. compared the heating potential of their synthetic Fe_3O_4 NPs (formed in the presence of tiopronin using a co-precipitation method at 70 °C) with commercial Resovist (Bayer Schering Company) and Nanomag 100 nm (Micromods Company). The achieved values (at H_0 = 12 kA/m and f = 1.05 MHz) were SAR = 1179 W/g, 279 W/g and 263 W/g respectively. This low thermal feedback of spherical-shaped IONPs currently used for MRI and MFH applications is supposed to be due to intrinsic low saturation magnetization (M_s) value ~ 50 - 60 A m^2 $kg^{-1}$for nano-sized Fe_3O_4 lower than that of bulk Fe_3O_4 ~ 85-100 A m^2 kg^{-1}), large surface spin disorder and degraded magnetic susceptibility ((χm = χ'm (in-phase) +χ"m (out-of-phase)).[18] As a result, MFH is preferentially integrated with radiotherapy/chemotherapy in the current clinical settings in several sessions for 30 min each, rather than single MFH.[36a-c, 36e]

The second limitation is the insufficient dose of deposited fluid in tumor area due to the cellular uptake of NanoTherm® fluid by macrophages. Importantly, the aggregation of NPs encourages the formation of clusters, which facilitate the easy recognition of particles by phagocytes. In the clinical trial on GBM patients, the CT scan revealed the minor accumulation of aggregated particles in glioblastoma cells and major uptake by macrophages.[36d] This treatment is currently being performed clinically on anatomically reachable solid tumors (prostate carcinoma and GBM) through the direct intratumoral injection of fluid to achieve the higher therapeutic outcome. However, the success of such a strategy depends on the (i) delivery of large doses of NPs and (ii) homogenous deposition of

NPs into the tumor tissue. In a clinical trial on patient bearing prostate carcinoma, the mechanical resistance of prostate tissue inhibited the injection of the optimal amount of the magnetic fluid into the target region. This low availability of NPs together with the diffusion of fluid into the surrounding tissue necessitates the multiple injection of fluid rather than single MFH in the clinical routine.[109] Ideally, a high concentration of MNP's (and subsequent high heating effect) should be localized at the tumor and not accumulate in healthy tissues, in reality this is almost never the case.[110] Irrespective of the injection technique, introduced MNPs evenly decorated with cell-specific recognition moieties (i.e. antibodies, proteins) somehow find their way somehow to off-target excretory organs (spleen, liver, or kidneys). This subsequently results in side effects such as collateral heat damage to healthy tissues as validated in preclinical animal studies and MFH clinical settings on patients with GBM. Another major technical hurdle is the lack of control on the real-time monitoring of temperature rise during the treatment.[41b, 111] The maximum temperature of 82 °C was recorded in clinical trials on patients with GBM.[36b] This temperature uncontrollability is due to the thermal conductivity of human tissues, blood perfusion and the movement of organs.[41b, 111b] Furthermore, the inhomogeneous distribution of fluid inside the tumor results in relatively large temperature fluctuations during the application of MFH as calculated by thermometry utilizing invasive thermal sensors. This is because MNPs are being heated non-uniformly depending on their location in the tumor.[112] Lower magnetic field strengths, (H = 4 and 5 kA/m), are being tolerated by patients throughout the treatment nonetheless, higher H values have been reported to cause pain in the perineal region or groin, burning sensations and increased discomfort temperature in the skin due to the formation of the hot spots.[36e, 37] As a result, in the current clinical routine, temperature is being controlled externally in order to circumvent the overheating of surrounding healthy cells. Additionally, published data on the actual achieved clinical temperature of tumor cells measured by invasive thermometry reflects differences of several degrees Celsius as compared to temperature predicted with the bioheat transfer equation.[111b] Another drawback is the utilization of AC field amplitudes (f, H) that differs from that of the clinical settings provided by the product NanoActivator® operating at a fixed frequency of f = 100 kHz with a field strength (H) of 0-15 kA/m. Moreover, non-identical conditions such as concentration of fluid, various applied amplitude (f, H) and exposure time under AMF, has led to an increase in the variation of the SAR/SLP values reported in the

literature which makes the comparison difficult. Lastly, computed tomography (CT) is being utilized in the clinical settings to quantitatively visualise the distribution of magnetic fluid NanoTherm® in the tumor tissue which exposes the patients to X-ray radiation.[36a, 36b] The threshold (*f* and *H*) value should be below the Belzwerj limit < 4.85×10^9 A m^{-1} s^{-1} in order to safely apply MFH.[73] Nevertheless, many of the SAR/SLP values reported for MNPs are measured at *f* between 500 and 700 kHz and *H* between 10 and 20 kA/m which obviously supress this limit. Furthermore, the lack of standard measurement protocols, fluid concentration and injection volume lead to an increase in the variation of reported SAR/SLP values.[113]

3.5. Proposed strategies to maximise the efficiency of MFH

The injected ferrofluid should meet certain criteria in order to qualify as ideal optimal heating mediators for MFH. In the first place, they should generate maximum temperature and SAR/SLP values with low quantity of fluid at biologically benign field (*f*, *H*) values in order to minimize the potential side effects.[114] Secondly, NPs should possess high size uniformity to favour homogeneous heat dissipation inside the tumor.[115] The other influential factors include high magnetic susceptibility,[116] high M_s,[117] high magnetic anisotropy constant (k_{eff}),[74] superparamagnetism and biocompatability.[118] The current clinical commercial magnetic fluid, NanoTherm®, does not meet all of these specifications as discussed in the previous section. On account of this, alternative strategies have been proposed for laboratory-scale studies with suitable preclinical SAR/SLP values (Figure 3.4). This include the optimization of intrinsic features of IONPs by modulating their geometry,[19] size and size distribution [20a] and crystallinity. These advances are largely due to the outstanding research work by Hyeon *et al.*[119] and Sun *et al.* [120] on the creation of an arsenal of highly crystalline monodisperse single domain MNPs using a thermal decomposition route. Additionally, biologically extracted IONPs from magnetotactic bacteria,[121] metal-doped spinel ferrite NPs,[25a, 122] exchange-coupled core-shell magnetic NPs[123] magnetic-plasmonic multifunctional nanohybrids optically active in the NIR region,[124] self-controlled MFH[125] and targeted nanoscale MFH [126] have also been studied with outstanding outcomes. A great deal of research has focused on MFH studies in solution however, some studies have examined the heating features of the fluids in cellular

environments on various cancer cell lines *in vitro* and preclinical examinations on mice *in vivo*. In the following sections, all of these proposed strategies will be highlighted in detail.

Figure 3.4. Proposed strategies to boost the efficiency of MFH for cancer treatment.

3.5.1. Optimization of the intrinsic features of IONPs

3.5.1.1. Size sorted IONPs for MFH

For successful biomedical realization, IONPs should present superparamagnetism with higher monodispersity (smaller than 20 nm in diameter),[127] narrow size distribution (< 10 %), zero remanence (M_r) and coercivity (H_c) that negates the particle aggregation.[19a] Numerous synthetic routes have been proposed to synthesis IONPs with controlled shape and size with low polydispersity. The batch production of IONPs can be performed by chemical (90 %), physical (8 %) and biological techniques (2 %).[128] A more detailed description of the synthetic methods utilized for the preparation of IONPs, their toxicity concerns and biomedical applications could be found in some excellent review articles published in the field in the past few years.[129]

Of all these methodologies, chemical-based routes such as co-precipitation, sol–gel and polyol method, laser pyrolysis, sonochemistry and solvothermal/hydrothermal method have been adopted due to the high yield and low production cost. Nevertheless, synthesized IONPs suffer from some difficulties, such as hydrolysis, aggregation and agglomeration, condensation, and non-uniformity in size and shape.[129b, 129d] In the quest for a synthesis of highly crystalline monodisperse MNPs, Hyeon *et al.*[119a] and Sun *et al.*[120a] reported individually pioneering research work on an organic-phase synthesis of highly crystalline MNPs with thermal decomposition of iron precursors in the presence of oleic acid/oleylamine surfactants in early 2000.[120b] This method provides a versatile platform to synthesis oxide-based NPs with a great control over the size, size distribution and shape. Accordingly, an arsenal of monodisperse NPs have been synthesized in parametric studies through varying the reaction conditions such as time, temperature, precursor ratio/concentrations and capping agent concentration. This initiated promising perspectives for synthesis of high-quality NPs for various biotechnological applications including MFH. A plethora of research has therefore been directed towards the synthesis of NPs with great size uniformity, crystallinity and well-shaped configurations alongside excellent performances in the application of MFH.

Size-controlled synthesis of highly monodisperse NPs is believed to maximise heating rate through optimizing (i) the saturation magnetization (M_s), (ii) magnetocrystalline anisotropy (K_s), and (iii) the high size uniformity of NPs. Over the past decades, theoretical and experimental investigations have probed the size dependence of SAR values. Tailoring the size of IONPs is one strategy to enhance the SAR value through increasing Ms value. Typically, for particles in the superparamagnetic region (< 20 nm), M_s increases with the increased grain size. For instance, Xuan *et al.* synthesized IONPs using the hydrothermal method and controlled the size of particles from 5.9 to 21.5 nm by varying the sodium acrylate/sodium acetate weight ratios. The M_s values increased with the grain size of NPs.[130] Demortiere *et al.* synthesized monodisperse IONPs with size range from 2.5 to 14 nm through the thermal decomposition of an iron-oleate precursor. The 2.5 nm sized particle exhibited a M_s value of 29 A m^2 kg^{-1} however the largest nanocrystals (14 nm) showed a M_s value of 77 A m^2 kg^{-1}.[131] Hong *et al.* reported 5 nm sized IONPs with a low magnetization value of 27 A m^2 kg^{-1} [132] Ge *et al.* reported a large magnetization value of

53.3 A m^2 kg^{-1} for 15 nm sized spherical superparamagnetic IONPs.[133] The M_s reduction of IONPs with decreased size in the superparamagnetic region has been recognised to be due to the decrease in magnetic moments of NPs at the surface.[134] In addition, the spin disorder increases as the of size of NPs decrease. Spin disorder or spin canting effect is a phenomenon through which the surface atomic spins of NPs are inclined to a particular angle rather than being exactly parallel which results in reduced M_s values correspondingly.[135] This reduced M_s, might decrease heating potential (SAR/SLP) values. On account of the Rosensweig theory, the maximum SAR value for superparamagnetic IONPs lies in small sizes around (< 20 nm) and small field *f* (300 kHz).[64] A substantial number of experimental studies have now validated this theory. For example, the highest SAR was reported for IONPs of ∼15 nm in diameter and any increase from this size decreased the SAR value.[127] Gazeau *et al.* reported one of the highest SAR values so far corresponding to 16 nm γ-Fe_2O_3[136] (SLP = 1650 W/g at *f* = 700 kHz and *H* = 24.8 kA/m). Other studies include, 15.3 nm Fe_3O_4 coated –PEG [137] (SLP = 600 W/g at *f* = 400 kHz, *H* = 11 kA/m), 13.7 nm Fe_3O_4[138] (SAR = 3066 W/g at *f* = 274 kHz, *H* = 73 mT), 14 nm Fe_3O_4[127] (SAR = 447 W/g at *f* = 400 kHz, *H* = 24.5 kA/m), 16 nm γ-Fe_2O_3[139] (SAR = 950 W/g at *f* = 700 kHz, *H* = 27 KA/m), 22 nm Fe_3O_4 (SLP = 716 W/g at *f* = 500 kHz, *H* = 15 kA/m), 7 nm γ-Fe_2O_3[140] (SAR = 626 W/g at *f* = 500 kHz, *H* = 12.5 KA/m), 15.2 nm Fe_3O_4[75c] (SLP = 702 W/g at *f* = 210 kHz, *H* = 30 kA/m) and 18 nm Fe_3O_4 (SAR = 400 W/g at *f* = 410 kHz, *H* = 11 kA/m) respectively.

In sharp contrast to these results, some of the highest SAR values for Fe_3O_4 NPs have been recorded with sizes > 20 nm alongside an enhanced amplitude of the AMF signal. For instance, Nemati *et al.* successfully synthesized iron oxide nano-octopods with sizes in the range of 17 − 47 nm. The systematic study of size-dependent SAR, demonstrated an increased heating output with increased size with SAR = 400 W/g for 47 nm compared to 240 W/g for 17 nm at *f* = 310 kHz and *H* = 64 kA/m.[141] Additionally, 47 nm Fe_3O_4 (SAR = 415 W/g at *f* = 310 kHz, *H* = 64 kA/m), 50 nm Fe_3O_4[142] (SAR = 1075 W/g at *f* = 150 kHz, *H* = 86 kA/m) and 35 nm magnetosomes[121a] (SAR = 1000 W/g at *f* = 410 kHz, *H* = 10 kA/m), 28 nm Fe_3O_4[84b] (SAR = 801 W/g at *f* = 265 kHz, *H* = 50 kA/m), 22.5 nm Fe_3O_4[15] (SAR = 322 W/g at *f* = 110 kHz, *H* = 11 kA/m) underscored the potential of ferromagnetic rather than superparamagnetic NPs as effective heating mediators for MFH. Furthermore, Mehdaoui *et al.* proposed a phenomenological model through supplemental theoretical and

experimental reasoning for SAR measurement in clinically related AMF regime. According to this theory, (i) the Brownian motion is not considered a contributing element in MFH, (ii) the relevance of the hysteresis loss on the magnetic field strength (*H*) and frequency (*f*) is not linear and (iii) monodisperse MNPs > 20 nm are supposed to be more potent in heat induction.[138] Confirming this theory, very recently Bao *et al.* investigated the *in vivo* size-dependent heating of IONPs synthesized through seed-mediated growth for application of MFH on a mouse bearing GBM tumor. IONPs (6, 8, 11, and 15 nm) and ferromagnetic size regimes (19, 25, 33, and 40 nm) were synthesized by varying the ratio between oleic acid and oleylamine as surfactants. (Figure 3.5a). Contradictory to LRT model predictions, the measured SAR values of IONPs increased with nanocrystal size. Interestingly, 40 nm ferromagnetic nanocrystals, presented the maximum aqueous SAR value of 2560 W/g (at f = 325 kHz, H = 20.7 kA/m), one of the highest SAR values reported to date. While, the SAR value of 6 nm and 19 nm nanocrystals were 8.35 and 1233 W/g respectively. (Figure 3.5b). Additionally, the SAR values of nanocrystals were assessed in a high-viscosity solution of glycerol in order to determine the role of rotational Brownian relaxation in heat dissipation (Figure 3.5c). For IONPs of superparamagnetic regime from 6 to 25 nm, SAR values did not change in the glycerol solution, whereas for ferromagnetic size nanocrystals, SAR increased. This cast doubt on the accuracy of the LRT model and 15 nm IONPs as an optimal size for MFH application.[143] To evaluate size-dependent heating potential, nanocrystals of 6, 19, 40 nm in diameter (50 µg of Fe) were injected into mice intratumorally under AMF (operating at f = 325 kHz, H = 9.35 kA/m) for 60 min (Figure 3.5d). The tumors injected with the 6 nm IONPs did not present any remarkable temperature rise compared to PBS (phosphate buffer) solution as the control, whilst temperature rise of ~ 35.5 °C and ~ 43.4 °C were achieved for 19 nm and 40 nm size nanocrystals respectively (Figure 3.5e).[144]

The reason for higher SAR values of ferromagnetic NPs over superparamagnetic ones is the mechanism by which the heat is created. Ferromagnetic NPs exhibit higher reversal losses through hysteresis as compared to superparamagnetic NPs where heat loss is due to Néel-Brownian relaxation mechanisms.[145] Hergt *et al*. proposed that the highest heating output could be achieved when transiting from a superparamagnetic to a ferromagnetic region.[69b, 84b, 146] Despite presenting higher heating potentials, ferromagnetic NPs are not considered for biomedical *in vivo* applications. As discussed in Section 3, they present residual

magnetization when the magnetic field is switched off which can leads to agglomeration of NPs and potential embolism in blood vessels.[147] Overall, the optimal size range for effective MFH applications is still a matter of scientific debate and more research is required to explore the size-dependence of SAR/SLP values.

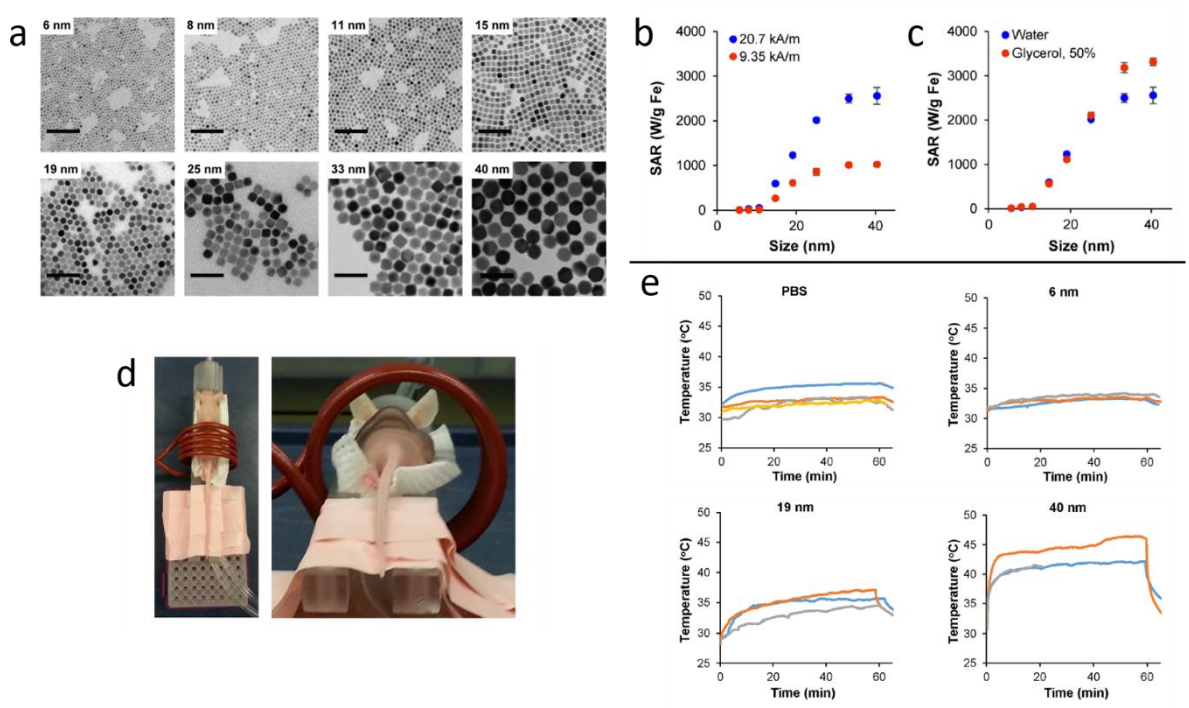

Figure 3.5. a) Transmission electron microscopy images of IONPs. Scale bars equal 100 nm. SAR of MIONs dispersed in b) deionized water and c) in water vs 50 % glycerol, under AMF (operating at f= 325 kHz H= 9.35 kA/m). d) Experiment set up of tumor-bearing mouse. e) *In vivo* tumor heating profiles. (Reprinted from ref 119. Copyright 2017 American Chemical Society).

The correlation between the aggregation state and the heating features of the NPs has also been probed via experimental[148] and computational work.[149] In a magnetic particle system of higher concentrations, aggregation of the single cores occur due to van-der-Waals forces or magnetic dipole-dipole attraction.[150] Using a Monte-Carlo simulation, Castro *et al.* confirmed the creation of dimers, trimers and larger aggregated clusters in a stable ferrofluid of MNPs. Based on their computation, at about 1 % volume fraction, there was a relatively small amount of aggregation caused by dimers. Nevertheless, above about 10 % volume fraction, more than half of the particles were merged together and created larger trimers.[151]

It has been shown that the dipolar interactions significantly impair the heat dissipation process because of the disturbed magnetization relaxation time.[152] For instance, Urtizberea *et al*. reported an increase in SAR value of about 100 % when the concentration was reduced by a factor of 4.[153] To further confirm, Fresnais *et al.* demonstrated that the dense aggregated IONPs clusters present very small SLP values compared to loose clusters because of a relatively little distance between NPs.[154] Additionally, increased fluid concentration, larger core sizes and isotropic shape of particles might favour the strong dipolar interactions and subsequent lower SLP values.[155] Notably, recent studies have revealed further aggregation in intracellular milieus compared to extracellular aggregates in aqueous suspensions.[156] It was found that intracellular super aggregates of 10^3 primary IONPs dramatically diminish the SAR values to 50 W/g compared to small clusters of fewer than 50 primary particles with a SAR value of 200 W/g.[157] This pronounced reduction in heating performance has been correlated with the influence of media viscosity, protein corona formation on NPs surface[158] inhibition of Brownian relaxation processes[159] and relatively high ionic strength of the media, which decrease the electrostatic repulsion between particles.[160]

In an opposing trend to Fresnais`s work, Dennis *et al*. achieved a SLP value of 1075 W/g for tightly associated IONPs compared to 150 W/g for the loosely associated ones.[161] Furthermore, performing a simulation study based on the Monte Carlo framework, Serantes *et al.* reported the superior heating performance (5 times in magnitude) for IONPs clusters in a chain-like arrangement compared to randomly distributed NPs. [162] Additionally Mehdaoui *et al.* reported an increase in heating efficiency of anisotropic cylinder-shape IONPs because of improved magnetic shape and additional uniaxial anisotropy.[163]

This trend for achieving higher SAR/SLP values with tightly associated NPs, has been further confirmed in a proposed configuration termed superferrimagnetic multicore NPs.[147, 164] It has been shown that very close packing of small SD superparamagnetic NPs (~ 10 nm) with very small interparticle distance, might result in the creation of a ferrimagnetic cluster in the size range of 20 – 80 nm. The exchange interactions between the single cores endow the multicore cluster with a ferrimagnetic feature so that it present hysteresis when exposed to an applied magnetic field (similar to that of SD ferromagnetic particle). However, despite SD ferromagnetic particle, this multicore cluster exhibit a very weak remanence in a zero field

due to special orientation of easy axes of the cores.[147, 164] The result of such an organisation manifests as a higher heating potential similar to SD ferromagnetic NPs (due do hysteresis behaviour) but a very low tendency to form agglomerates in contrast to SD ferromagnetic NPs. This interesting behavior, where superferrimagnetic multicore NPs exhibit higher heating, has been observed before.[108, 165] For instance, Thanh *et al*. synthesized a stable citric acid coated multi-core IONPs via microwave-based method. The resulting multi-core IONPs achieved the ILP value of 4.1 x 10^{-9} m^4 s^{-2} A^{-2} which was higher than that of commercial IONPs fluids, (Ferucarbotran ILP = 3.1 x 10-9, FluidMag-D ILP = 2.7 x 10-9, FluidMag-CT ILP = 1 x 10-9, and Nanomag-D-spio ILP = 3.1 x 10-9 m^4 s^{-2} A^{-2}) respectively.[166] Similar to the debate on the size effect, there is currently no full consensus on the influence of dipolar interactions on the heating efficiency of fluids in the literature due to a series of conflicting accounts.[153, 167]

3.5.1.2. Shape - controlled synthesis of IONPs for MFH

Different shapes minimise their internal energy by adopting different magnetic domain structures leading to different magnetic properties. By taking advantage of this approach, NPs of different shapes could enhance their heating potential (SAR/SLP values) by the optimization of shape anisotropy.[141, 168]

Shape-controlled synthetic strategies have therefore been pursued to develop IONPs with improved heating characteristics. As a result, various nanostructural frameworks such as nanospheres,[169] nanocubes,[170] nanotubes,[171] nanowires,[172] nanorods,[173] nanooctahedrons,[174] nanotetrahedrons[175] nanohexagons,[176] nanosheets,[177] nanoctapods,[178] nanoplates,[179] nanoflowers,[19f] nanodiscs,[19a] and nanorings[180] with unique crystal and magnetic features and heating potentials, have been designed in the field under varied synthetic protocols over the past few years. Tailoring the shape is believed to maximize the heating efficiency via either increased magnetocrystalline anisotropy or the coercive field value of the hysteresis loop.[181] Accordingly, to realize this, many endeavors have been directed in the field to design IONPs of various configurations. It has been shown that nanorings and nanodiscs have been realized that possess a stable unique magnetic vortex-domain structure that endows them with negligible remanence (M_r) and coercivity (H_c) but with much higher saturation magnetization (M_s), larger hysteresis loops and higher SAR/SLP values than spherical IONPs.[182] For instance, nanoring IONPs [180] with SAR = 426

W/g (at *f* = 300 kHz, *H* = 16 kA/m) has been reported. Ding *et al.* reported the extraordinary SAR value of ~5000 W/g (at *f* = 700 kHz, *H* = 47.8 kA/m) for the aqueous suspension of Fe_3O_4 nanodiscs (225 nm diameter; 26 nm thickness).[19a] Furthermore, Ma *et al.* achieved the SLP max of 253 W/g (at *f* = 180 kHz, *H* = 950 A/m) for the Fe_3O_4 nanodiscs (200 nm diameter; 15 nm thickness).[183] The reason is the parallel alignment of nanodiscs with respect to applied field together with enhanced shape anisotropy. Nevertheless, their larger size is believed to be a critical impediment for biomedical applications due to low average blood lifetime and potential aggregation. [184] Addressing this challenge, Srikanth *et al.* synthesized Fe_3O_4 nanodiscs of ~12 nm diameter and ~3 nm thickness, however the SLP max was 125 W/g (at *f* = 300 kHz, *H* = 64 kA/m).[18b]

Similarly, cubic shaped IONPs have presented higher heating values relative to spherical ones.[19c, 185] This higher MFH potency is mainly related to their lower spin disorder, lower surface anisotropy, small numbers of disordered spins as a result of the flat surface, chainlike arrangement and possessing low energy < 100 > facets.[186] The Monte Carlo computational model by Baldomir *et al.*, further corroborated the better heating performance for nanocubes ascribed to enhanced hysteresis loop for increased chain length.[187] Conjointly with the theoretical assumptions, experimental outcomes exhibited about two-fold increase in SLP of cubic IONPs (356.2 W/g) versus spherical analogs with SLP of 189.6 W/g at identical volume.[188] Some excellent results have been achieved by cubes IONPs for MFH application with some highest aqueous values of SAR = 2452 W/g (at *f* = 520 kHz , *H* = 29 kA/m),[189] SAR = 2000 W/g (at *f* = 520 kHz, *H* = 24 kA/m),[19d] SAR = 800 W/g (at *f* = 300 kHz, *H* = 64 kA/m),[190] SAR = 3000 W/g (at *f* = 274 kHz, *H* = 58 kA/m),[138] SAR = 450 W/g (at *f* = 700 kHz, *H* = 22 kA/m),[19b] SAR = 382 W/g (at *f* = 300 kHz, *H* = 24 kA/m),[191] SAR = 253 W/g (at *f* = 302 kHz, *H* = 23.8 kA/m),[19c] and SAR = 390 W/g (at *f* = 165 kHz, *H* = 29 kA/m).[192]

Besides, rod-shape IONPs have exhibited a much higher SAR value of 862 W/g in comparison to spherical (SAR = 140 W/g) or cubic SAR = 314 W/g counterparts at similar magnetic volumes under *f* = 310 kHz and *H* = 16 kA/m due to improved shape anisotropy.[173]

Other geometries such as Fe_3O_4 nanoflowers with SAR = 1944 W/g (at *f* = 700 kHz, *H* = 21.5 kA/m),[193] were also tested for MFH application. These results highlight the significance of shape anisotropy for improving the heating potential of IONPs.[194] In order to further reveal

the importance of geometry on heating potential, Several *in vitro* and *in vivo* MFH studies have been performed with promising results as listed (Table 3.2 and 3.3).

A representative preclinical example of a shape - tailored MFH study is the work by Ding *et al.* where they have synthesized Fe_3O_4 nanorings (FVIO) with an average outer diameter of 70 nm (scanning electron microscopy (SEM) images) (Figure 3.6a). The prepared particles presented the high SAR value of 3050 W/g (at f = 400 kHz, H = 59 kA/m), which was much higher than that of Resovist (106 W/g). This was ascribed to their unusual peculiar magnetic moment configuration (Figure 3.6b). The *in vitro* MFH efficacy was conducted on MCF-7 breast cancer cells incubating with prepared FVIO nanorings or Resovist at a concentration of 150 µg/mL Fe under the activation of AMF (f = 400 kHz, H = 40 kA/m) for 10 min. Interestingly, a cell viability of 13 % was achieved for FVIO nanorings compared to 85 % cell viability for Resovist. (Figure 3.6c). The fluorescence images of the MCF-7 breast cancer cells stained with acridine orange/ethidium bromide, presented strong red fluorescence for the FVIO that had been incubated for 10 min under alternating MF. This was in contrast to the green fluorescence for control group and Resovist (commercial IONPs) indicating the potential efficiency of FVIO for the thermal destruction of cancer cells. (Figure 3.6d). To further complement the cellular hyperthermia efficiency, the *in vivo* studies were performed on mice bearing MCF-7 breast cancer cells. FVIO nanorings and Resovist at a concentration of 150 µg/mL Fe were then injected to mice subcutaneously. The AC magnetic field of same configuration was applied on mice and tumor volume was monitored for up to 40 days. In validation of *in vitro* results, a significant reduction in tumor volume was achieved for the FVIO treated mice, however, the control mice and mice treated with Resovist presented enhanced tumor growth indicating the much higher heating efficiency and significant cytotoxicity of FVIO (Figure 3.6e).[195] The issue is these vortex-domain nanorings exhibited ferromagnetism with negligible remanence and coercivity that might encourage magnetic dipole–dipole interactions and undesired agglomeration.[182b, 196]

It should be noted that any conclusion drawn on an optimal geometry is difficult to make as the reported SAR/SLP values have been obtained in non-identical conditions in terms of fluid concentration, and AMF parameters (f and H_0). Additionally, different architectures confer unique shape anisotropy which results in different hysteresis loops and SAR values. However, progress in the shape-controlled synthesis of IONPs has resulted in the creation of

IONPs with different morphologies with promising higher magnetization and heating output values than are available with commercial spherical INOPs currently used for MFH applications.

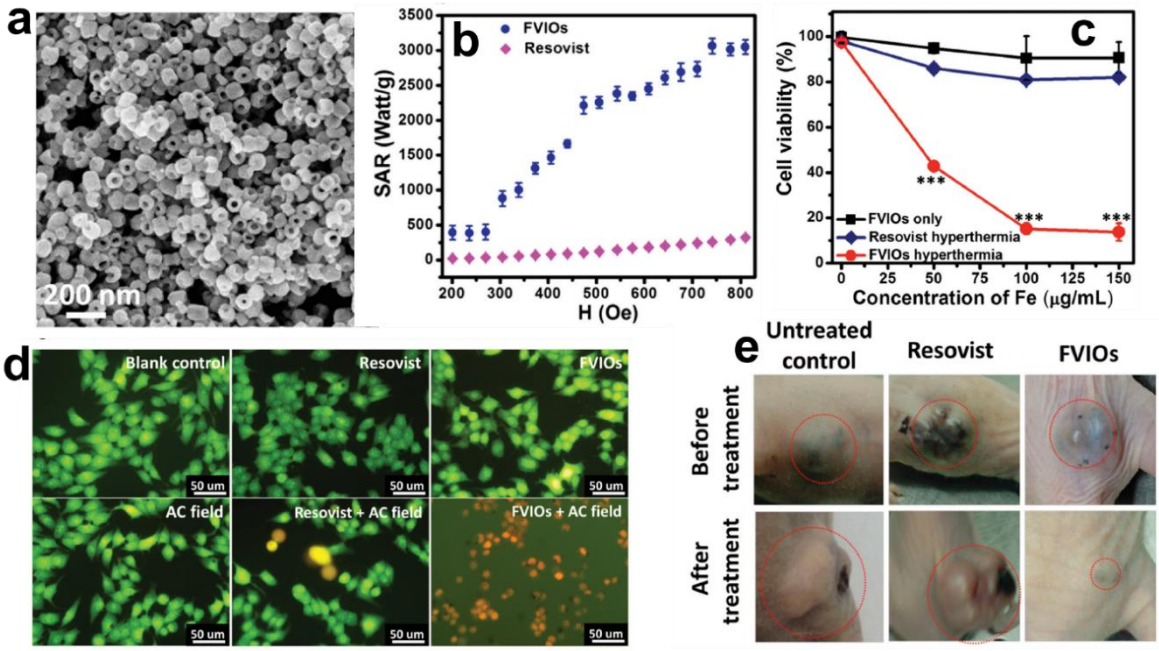

Figure 3.6. a) SEM image of FVIOs. b) Comparison of SAR for FVIOs and Resovist at different fields at the frequency of 400 kHz. c) Dosage dependence of cell viability for MCF-7 cells treated with magnetic hyperthermia using FVIOs and Resovist. d) Immunofluorescence images of MCF-7 cells treated with different groups. Live and dead cells appear green and orange, respectively. e) Mice xenografted with breast cancer cells (MCF-7) before and 40 days after treatment with different tratement groups. (Reprinted with permission from ref 158. Copyright 2014 Wiley-V).

Table 3.2. Overview of shape - controlled IONPs for *in vitro* MFH on mice.

NPs type	**Synthetic method**	**Shape**	**Concentration of fluid [Fe]**	**Cell death (%)**	**Size (nm)**	**Cancer cell line**	**Exposure condition [f^1: H^2: time]**	**T_{max} °C (Suspension)**	**Ref/ Year**
(α-Fe_2O_3) /(Fe_3O_4)	Hydrothermal	Nanoring	100 µg/mL	~ 65	100	HEK293	300 kHz[3]: 16 kA/m[4]: 10 min	NI[5]	2017[180]
γ- Fe_2O_3	Coprecipitation	Nanosphere	50 mM	NI[5]	10	SKOV-3	700 kHz[3]: 20 kA/m: 90 min	52 °C	2014[197]
γ- Fe_2O_3	Thermal decomposition	Nanocube	25 mM	NI[5]	18			56° C	
IONCs[7]	Thermal decomposition	Nanocube	1 g/L	50	19	KB	110 kHz: 20 kA/m: 60 min	43°C- cell medium	2012[189]

f^1: Applied frequency, H^2: Applied magnetic field strength, KHz[3]: Kilohertz, kA/m[4]: Kiloampere/meter, NI[5]: Not Informed, IONCs[7]: Iron oxide nanocrystals

Table 3.3. Overview of shape - controlled IONPs for *in vivo* MFH on mice.

NPs type	Synthetic method/shape	Injection dose (mg/kg) [Fe]	Injection route	Size (nm)	Cancer cell line	Exposure condition [*f*: *H*: time]	Tumor T_{max} °C	Therapeutic outcome	Ref/ Year
Fe_3O_4-Phosphorylated mPEG[1]	Hydrothermal/ Nanoring	150	Subcutaneous	133	MCF-7	740 kHz: 32 kA/m:10 min	44	Tumors treated with nanorings were completely eradicated 6 day after treatment nevertheless, Resovist presented tumor growth	2015[195]
Fe_3O_4- PEG	Thermal decomposition/ Nanocubes	700	Intratumoral	19	A431	111 kHz:23.8 kA/m:30 min	~ 41	Histological and TEM examinations revealed the penetration of nanocubes deeply in tumor core and large necrotic areas	2014[198]
Fe_3O_4-@Ag	Thermal decomposition/ Nanosphere	15	Intratumoral	10.4	SMMC-7721	390 kHz :18 A:20 min	43	Synergistic combination effect of Fe_3O_4 and silver hybrid resulted in tumor inhibition rate of 67 %	2017[199]

3.5.2. Biomineralised magnetotactic bacteria

Magnetotactic bacteria (MTB) are a distinctive group of largely aquatic bacteria that naturally biomineralise magnetosomes. Magnetosomes are specialized organelles composed of nanometer-sized (with typical size range of 35 - 120 nm), single-domain crystals of either Fe_3O_4 (magnetite), and/or less common Fe_3S_4 (greigite) in the core bound to a protein-containing phospholipid bilayer membrane.[200] The magnetosomes of most MTB have appeared in several various morphologies, size, shapes, different numbers and patterns depending on the species of MTB. MTB can produce Fe_3O_4 and Fe_3S_4 individually, however, some species are capable of producing both simultaneously. Furthermore, magnetosomes are most often arranged in a chain or chains within the cell that are believed to be utilized by MTB as a compass to navigate along geomagnetic field lines and locate most ideal conditions for their survival and growth.[121d] MTB was originally described by Salvatore Bellini in 1963 at the University of Pavia.[201] Twelve years later in 1975, Richard Blakemore reintroduced MTB when he observed magnetosome chains using an electron microscope.[202] There has been a surge of interest for a broad range of bio-applications of MTB particularly MFH which has been used to kill cancer and bacteria cells.[203] Biologically extracted magnetosomes are hypothesized to be more competent versus chemical Fe_3O_4 counterparts for MFH purposes. This is due to a series of merits such as high degree of crystallinity, high magnetism, monodispersity and bioengineerablity. Moreover, they are not prone to aggregation thanks to their chain-like arrangement which yields high rate of cellular internalization and a pronounced uniform *in vivo* heating efficiency presumably as a result of their close assembly. Additionally, the lipid bilayer present in the magnetosome membrane may favour the linkage of bioactive molecules, anticancerous agents or antibodies.[121c]

Hergt *et al.* initiated the application of suspensions of MTB for MFH application for the first time in 2005. They extracted the nano-sized crystals of Fe_3O_4 from Magnetospirillum gryphiswaldense species with an average size of 39 ± 5 nm. The prepared particles exhibited an exceptionally large SAR value of 960 W/g (at f = 410 kHz, H = 10 kA/m).[121a]

The potential of various MTB species have also been tested in the field. This include magnetosome chains extracted from Magnetospirillum magneticum strain AMB-1@RGD with SAR = 600 W/g (at f = 471 kHz, H = 14 kA/m),[204] Co and Zn doped Fe_3O_4 extracted

from Geobacter sulfurreducens including $Co_{0.4}Fe_{2.6}O_4$ with SAR = 253 W/g (at *f* = 87 kHz, *H* = 16 kA/m), and $Zn_{0.2}Fe_{2.8}O_4$ with SAR = 255 W/g (at *f* = 87 kHz, *H* = 16 kA/m),[121b] magnetosomes from Magnetospirillum magneticum strain AMB-1 with SAR = 1242 W/g (at *f* = 108 kHz, *H* = 70 kA/m),[205] magnetosome from Magnetospirillum magneticum strain AMB-1 with SAR = 400 W/g (at *f* =183 kHz, *H* = 64 kA/m),[206] magnetosome from Magnetospirillum magneticum strain AMB-1 with SAR = 723 W/g (at *f* = 198 kHz, *H* = 16 kA/m),[207] magnetosomes from M. gryphiswaldense strain MSR-1[236] with SAR = 880 W/g (at *f* = 200 kHz, *H* = 25 kA/m),[17] magnetosomes from AMB-1 with SAR = 390 W/g (at *f* = 183 kHz, *H* = 32 kA/m),[208] and Magnetospirillum gryphiswaldense MSR-1 with SAR = 482 W/g (at *f* = 183 kHz, *H* = 17 kA/m)[209] respectively.

Encouraged by promising solution SAR/SALP values, some *in vitro* and *in vivo* studies were performed in the field to further corroborate the potential of magnetotactic bacteria for MFH applications (Table 3.4 and 3.5). Specifically, Alphandéry *et al.* has been the pioneer group in the application of MTB for MFH and stablished an innovative cancer treatment center called Nanobacterie in France in 2008. Nanobacterie has already conducted two proof of concept preclinical studies using MFH for the treatment of glioblastoma and breast cancer on mouse models.[207, 210] In an *in vivo* survey, Alphandéry *et al.* investigated the feasibility of MTB on mice infected by MDA-MB-231 breast cancer cells using the MFH procedure. Heating mediators included ferromagnetic chains of magnetosomes extracted from MTB (designated as Ch-Std), individual magnetosomes (~ 45 nm in diameter) detached from magnetosomes (designated as IM), water stable superparamagnetic IONPs (SPION) (less than 20 nm in diameter) surface modified with either PEG molecules (SPION@PEG) or citrate ions (SPION@Citrate). TEM images revealed the homogeneous distribution of Ch-Std compared to individual IM, which presented the aggregation (Figure 3.7a, b). The *in vitro* antitumoral performance of mediators under AMF operating at *f* = 183 kHz and *H* = 32 kA/m for 20 min, revealed an inhibition rate of 38 % for 1 mg of Ch-Std when AMF was off (Figure 3.7c). This high output was ascribed to effective internalization of Ch-std within the cells. The same set of results were observed for Ch-Std compared to other tested NPs when AMF was on. The higher potency of magnetosomes was explained by their higher intrinsic SAR values. For *in vivo* MFH, mice developed with Xenografted breast cells, were exposed to AMF at *f* = 183 kHz and *H* = 32 kA/m for 20 min. Injection of 100 µL (10

mg/mL) of a suspension of Ch-Std increased the temperature of the tumor to 43 °C compared to 35 °C for IM. The progress of therapy was monitored at the day of the treatment (D0), 14 days post- treatment (D14), or 30 days post-treatment (D30) for Ch-Std and IM injected mice. Interestingly, 30 days after treatment the mice treated with Ch-Std presented a black spot at the position of initial tumor, whereas the tumor size increased for IM group treated at the same fashion (Figure 3.7d).[121c]

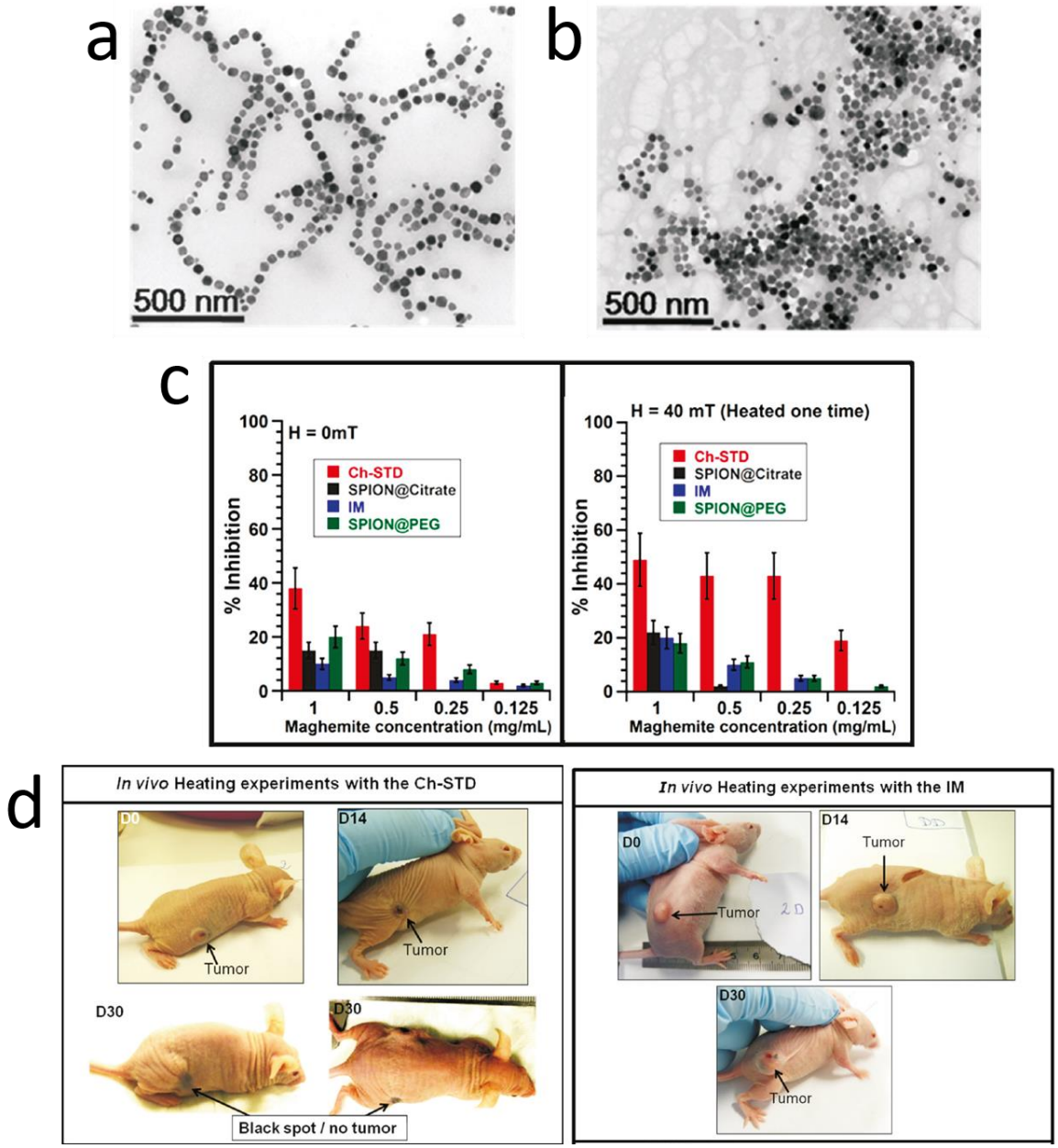

Figure 3.7. TEM micrograph of the chains of magnetosomes extracted from the bacteria a) Ch-Std and b) individual magnetosomes (IM). c) Percentage of inhibition of MDA-MB-231 cells incubated in the presence of Ch-Std, IM, SPION@Citrate, or SPION@PEG exposed to AMF = 0 and AMF of strength

40 mT. d) Photographs of the treated tumor in a mouse after 0 days (D0), 14 days (D14), and 30 days after the treatment (D30). Reprinted from ref 83. Copyright 2011 American Chemical Society).

Table 3.4. Overview of biomineralised MTB for *in vitro* MFH.

MTB species	**Magnetosome type**	**Surface coating**	**Size (nm)**	**Cancer cell lines**	**Concentration of fluid (mg/mL) [Fe]**	**Cell death (%)**	**Exposure condition [*f*: *H*: time]**	**T_{max} °C (Suspension)**	**Ref/ Year**
Mariprofundus ferrooxydans	M[1]	Doxorubicin	674	MD-MBA231 TXSA	0.25	44	230 kHz: 2 A/m : 10 min	50	2016[211]
M. gryphiswaldense strain MSR-1	M[1]	-	45	ANA-1 murine macrophage	200	40	149 kHz:24 kA/m:30 min	NI	2016[17]
Magnetospirillum magneticum strain AMB-1	M[1]	-	100	MDA-MB-231	1	NI	198 kHz: 16 kA/m:20 min	NI	2012[210c]
NI	M[1]	DNA-AuNPs	NI	THP-1	4.8×10^{8}	16.52	470 kHz:NI:45 min	NI	2016[212]
Magnetospirillum	M[1]-CR400[2]	-	22-40	MDA-MB-	20	NI	200 kHz:25	~ 30	2018[210d]

magneticum AMB-1		-	30-52	231			kA/m:30 min		
Magnetospirillum gryphiswaldense strain MSR-1	M[1]	Uncoated	10 -65	GL-261 glioma / RG-2	1	14/13	198 kHz: 27 kA/m: 30 min	5	2017[213]
		Chitosan	10 -65			11/17		37	
		Neridronate	10 -65			10/10		32	
		polyethyleneimine	10 -65			27/11		36	

M[1]: Magnetosome, CR400[2]: Magnetosomes cultivated in the presence of Rhodamine.

Table 3.5. Overview of biomineralised MTB for *in vivo* MFH on mice.

MTB species	**Magnetosome type/ Coating agent**	**Size (nm)**	**Cancer cell lines**	**Injection dose [Fe]**	**Injection route**	**Exposure condition [*f*: *H*: time]**	**Tumor T_{max} °C**	**Therapeutic Outcome**	**Ref/ Year**
Magnetospirillum gryphiswaldense	M[1]	42	U87MG	10 mg/mL	Intratumoral	110 kHz :23 A/m:20 min	32.6	Magnetosomes were clustered closer to the injection's site and distributed inhomogeneously within tumor tissue.	2018[214]
AMB-1	M[1]	300	MDA-MB-231	10 mg/mL	Subcutaneous	183 kHz:40 kA/m:20 min	43	Magnetosomes were distributed homogeneously. Low mitoses indicating tumor proliferation was observed.	2011[208]
Magnetospirillum magneticum AMB-1	M[1]	45	U87-Luc glioma	40 µg/mL	Intraperitoneal	198 kHz: 30:30 min	32.5	Administration of 40 µg of magnetosome leads to full tumor eradication of 40 % of treated mices.	2017[210a]

M. gryphiswaldense MSR-1	M^1-Co60 Fe_3O_4-aminosilane Co60	40 10	MCF-7	480 mg/kg 240 mg/kg	Intravenous	300 kHz: 8.8 kA/m :2 min	47 NI	The heating efficiency of magnetosomes were better than chemical counterparts under identical MF condition.	2012[215]
MSR-1 Gryphiswaldense	M^1 – PLL^2 $IONP^4$		U87-Luc glioblastoma	500 µg/mL	Intravenous	202 kHz:27 kA/m:30 min	42	The full tumor disappearance was achieved in 100 % of treated mice with M- PLL compared to 20 % with IONP	2017[216]
Magnetospirillum gryphiswaldense strain MSR-1	M^1-PLL IONPs	40.5 20	GL-261	25 µg/mL	Intratumoral	198 kHz: 15 kA/m:20 min	46	M-PLL presented larger SAR value and better antitumor efficiency with full tumor eradication in 50 % of treated mice compared to 20 % for IONPs.	2017[121c]
Magnetospirillum gryphiswaldense	M^1	42	HT-29	1	Intratumoral	187 KHz:23 kA/m:20	NI	Incomplete tumor elimination was obtained in	2014[217]

strain MSR-1	mg/mL	min	the treated mice, however necrosis was evidenced by both histology and MRI.

M[1]: Magnetosome, PLL[2]: poly-L-lysin, IONP[3]: iron oxide nanoparticles

Although, MTB species have presented the community with some of the highest SAR/SLP values, there are still some major hurdles restricting their utility for MFH applications. The first logistical challenge to overcome is that of the large-scale production of magnetosomes. Another challenge is a lack of certainty around the pharmacokinetics and biocompatibility. Having originated from a biological source, magnetosomes present slight acute toxicity at high concentrations (62.7 mg/kg) which has been attributed to (i) the deposition of nanoscale sized magnetosome and (ii) non-human proteins present in their membrane. Nonetheless, highly purified and sterilized magnetosomes did not present any toxicity on mouse fibroblasts cells *in vitro*.[218]

3.5.3. Composition altering strategies

3.5.3.1. Metal-Doped IONPs

The Fe_3O_4 naonparticle (also represented as $Fe^{3+\cdot}$ Fe^{3+} / $Fe^{2+}O^{2-}{}_4$) is an inverse spinel ferrite AB_2O_4 type. It contains 32 oxygen ions (O^{2-}), 8 Fe^{2+} ions at octahedral (O_h) site and 16 Fe^{3+} ions equally distributed among tetrahedral (T_d) (8 Fe^{3+} ions) and octahedral sites (8 Fe^{3+} ions).[219] The magnetic moment for each Fe^{2+} ion is 4 Bohr magnetons (having 4 unpaired electrons in the 3d orbital) compared to 5 Bohr magnetons for Fe^{3+} ion with 5 unpaired electrons in its 3d orbital. The magnetic moments of Fe^{3+} ions at the T_d and O_h sites are aligned in opposite directions and cancel each other. Accordingly, the magnetic moment of Fe^{2+} ions (4 μB) on O_h sites determines the net magnetization of Fe_3O_4 nanoparticle. Considering that in the overall unit cell of Fe_3O_4, there are 8 subcells (with Fe2+ ions in each subcell), therefore the overall magnetic moment of Fe_3O_4 is 32 Bohr magnetons. Compositional tuning through a metal dopant substitution of Fe^{2+} with doped M^{2+} in the T_d or O_h holes of Fe_3O_4 crystal lattice has been proposed as an effective tactic to improve magnetism and heating efficiency.[220] Such substitution aims to increase the saturation magnetization (Ms), magnetocrystalline anisotropy (Ks), magnetic susceptibility (χ) and render NPs with wider hysteresis areas on the magnetization loops and eventual higher heat dissipation. The achieved metal-doped spinel nanoferrites have the structural formula of $M_xFe_{3-x}O_4$ (M = Fe, Mn, Zn) with tunable nanomagnetism with magneto-thermal, magneto-optical and magnetoresistive features.[219a, 220a, 221] When doped with M^{2+}, T_d and O_h sites of Fe_3O_4 can be occupied by doped M^{2+} cations and the magnetization and antiferromagnetic coupling interactions of Fe^{3+} ions (in the Fe_3O_4 cell unit) can therefore be modulated by the

relative distribution and concentration of M2+ between the O_h and T_d sites. For instance, Deng *et al.* synthesized MFe_2O_4 (M=Fe, Co, Mn, Zn) microspheres by co-precipitation of M^{2+} and Fe^{3+} chlorides (M^{2+}/Fe^{3+} = 0.5). The magnetic properties of the resultant NPs were investigated with a vibrating sample magnetometer (VSM) where Fe_3O_4 exhibited the highest M_s value of 81.9 A m^2 kg^{-1}. The M_s values were 53.2 A m^2 kg^{-1} for $MnFe_2O_4$, 60.0 A m^2 kg^{-1} for $ZnFe_2O_4$ and 61.6 A m^2 kg^{-1} for $CuFe_2O_4$.[222] In another example, Lee *et al.* synthesized 12 nm MFe_2O_4 (M=Fe, Mn, Ni and Co) by thermal decomposition of divalent metal chloride (MCl_2) and iron tris-2,4- pentadionate in the presence of oleylamine and oleic acid as surfactants and investigated the corresponding magnetic properties with a superconducting quantum interference device (SQUID) magnetometer. The $MnFe_2O_4$ NPs presented the highest M_s value of 110 A m^2 kg^{-1} compared to 101, 99 and 85 A m^2 kg^{-1} for $FeFe_2O_4$, $CuFe_2O_4$and $NiFe_2O_4$ respectively. The authors attributed the result to the distribution of M^{2+} cations into different sites of the crystal lattice. Whereas $MnFe_2O_4$ ferrite had a mixed spinel structure, all other metal ferrites had an inverse spinel structure. Under the applied AMF, the magnetic moments at the O_h site aligned in parallel towards the field compared to magnetic spins at the T_d site which aligned antiparallel which resulting in the highest magnetic susceptibility for $MnFe_2O_4$.[223] Prasad *et al.* fabricated 15 nm $Ce_xFe_{3-x}O_4$ NPs (x = 0.01, 0.05, 0.1, 0.3 and 0.5) by a microwave refluxing method. Room temperature magnetization measurements revealed a continuous decrease in the M_s value with enhanced Ce^{4+} concentration. They ascribed this reduction to the replacement of Fe^{3+} ions at the O_h sites in the host lattice.[224] Hu *et al.* examined the effect of doping Co^{2+} ions on the magnetic properties of IONPs prepared by the co-precipitation method with a stoichiometric formula of $Co_xFe_{3-x}O_4$ where (x= 0, 0.05, 0.1 and 0.15). A decrease in M_s was observed with enhanced cobalt content. This effect was ascribed to the replacement of small magnetic moment Co^{2+} ions (3 Bohr magnetons) with Fe^{2+} (4 Bohr magnetons) ions in the O_h site.[225]

In line with magnetic studies, great deal of research has also been focused on utilization of the $M_xFe_{3-x}O_4$ nanoferrites with improved magnetic characteristics for MFH *in vitro* and *in vivo*. The idea is the proper positioning of M^{2+} dopants in T_d sites in crystal lattice of Fe_3O_4 for ultimate maximised heating. Several studies have validated the efficacy of the

substitution strategy with high SAR/SLP values reported in the literatures. This include Mg 0.285 Mn 0.715 Fe_2O_4@lipid144 (SLP = 2170 W/g at f = 100 kHz, H = 11 kA/m),[122a] $MnFe_2O_4$-PAA (SAR = 390 W/g at f = 300 kHz, H = 32 kA/m),[226] $Zn_{0.2}Mn_{0.8}Fe_2O_4$ (SAR = 385 W/g at f = 300 kHz, H = 5 kA/m),[227] $Zn_{0.468}Fe_{2.532}O_4$ P-mPEG (SAR = 595 W/g at f = 240 kHz, H = 24.2 kA/m),[228] $Co_{0.7}Fe_{2.3}O_4$ (SAR = 915 W/g at f = 105 kHz, H = 32 kA/m),[18d] $Mn_{0.8}Zn_{0.2}Fe_2O_4$ (SAR = 1037.8 W/g at f = 114 kHz, H = 114.9 kA/m) and $Mn_{0.6}Zn_{0.4}Fe_2O_4$ (SAR = 1102.4 W/g at f = 114 kHz, H = 114.9 kA/m)[229] Zn0.4 $Mn_{0.6}Fe_2O_4$ (SAR = 432 W/g at f = 500 kHz, H = 3.7 kA/m),[230] $Gd_{0.06}Fe_{2.94}O_4$ (SAR = 450 W/g at f = 267 kHz, H = 40 kA/m),[231] Gd - Fe_3O_4 (SAR = 300.2 W/g at f = 370 kHz, H = 40 kA/m)[232] $CoFe_2O_4$ (SAR = 404 W/g at f = 325 kHz, H = 43 kA/m),[233] $CoFe_2O_4$ (SAR = 420 W/g at f= 117 kHz, H = 51 kA/m),[234] $Ni_{0.31}Fe_{2.69}O_4$ (SAR = 929 W/g at f = 872 kHz, H = 20 kA/m),[219b] and $Mn_{0.5}Zn_{0.5}Fe_2O_4$@SiO_2 (SAR = 256 W/g at f = 110 kHz, H = 11 kA/m)[122c], respectively. $M_xFe_{3-x}O_4$ nanoferrites that have also been examined in a series of preclinical *in vitro* and *in vivo* studies for MFH applications are presented in Tables 3.6 and 3.7. The best-in class example of a compositional tuning strategy through a metal dopant substitution is the preclinical study by Bae *et al*. They developed a series of $Mg_xFe_2O_3$ NPs (x = 0, 0.05, 0.10, 0.13, and 0.15) with the average size of ~ 7 nm via thermal decomposition method by mixing $Mg(acetate)_2$ and $Fe(acac)_3$ metal precursors in the presence of oleic acid as stabilizer. According to the results, $Mg_{0.13}Fe_2O_3$ exhibited the highly exceptional intrinsic loss power (ILP) value of 14.0 x 10^{-9} m^4 s^{-2} A^{-2} which was 100 times higher than that of Feridex (Commercial Fe_3O_4) (Figure 3.8a). It was ascribed to the improved χ"m and occupation of ≈ 50 % Fe vacancies (mostly O_h site Fe^{3+} vacancies) with Mg^{2+} ions calculated with the atomic structure model (Figure 3.8b). Accordingly, $Mg_{0.13}Fe_2O_3$ was considered as the optimized Mg-doped $_{Fe2O3}$ for MFH application. The *in vitro* exposure of U87MG cell lines with 700 µg/mL of $Mg_{0.13}Fe_2O_3$ nanofluid and Resovist under the activation of AMF (operating at f = 99 kHz, H =12.33 kA/m) for 1500 s resulted in T_{max} of 63.5 °C for $Mg_{0.13}Fe_2O_3$ compared to that of 37.5 °C for Resovist. The fluorescence microscopy images exhibited the drastic deformation and shrinkage of the U87MG cells after treatment with $Mg_{0.13}Fe_2O_3$ nanofluid. (Figure 3.8c). For *in vivo* MFH, Resovist and $Mg_{0.13}Fe_2O_3$ nanofluid (100 µL, 1.15 mg/mL) was introduced intratumorally into the mice developed Hep3B cells. After the activation of the AMF for 15 min, the temperature of the tumor injected with Resovist had slightly increased from 34 to

37.14 °C. In contrast, temperature of Hep3B injected with $Mg_{0.13}Fe_2O_3$ nanofluid had increased quickly to a thermoablation temperature of about ≈ 50.2 °C (Figure 3.8d).[235]

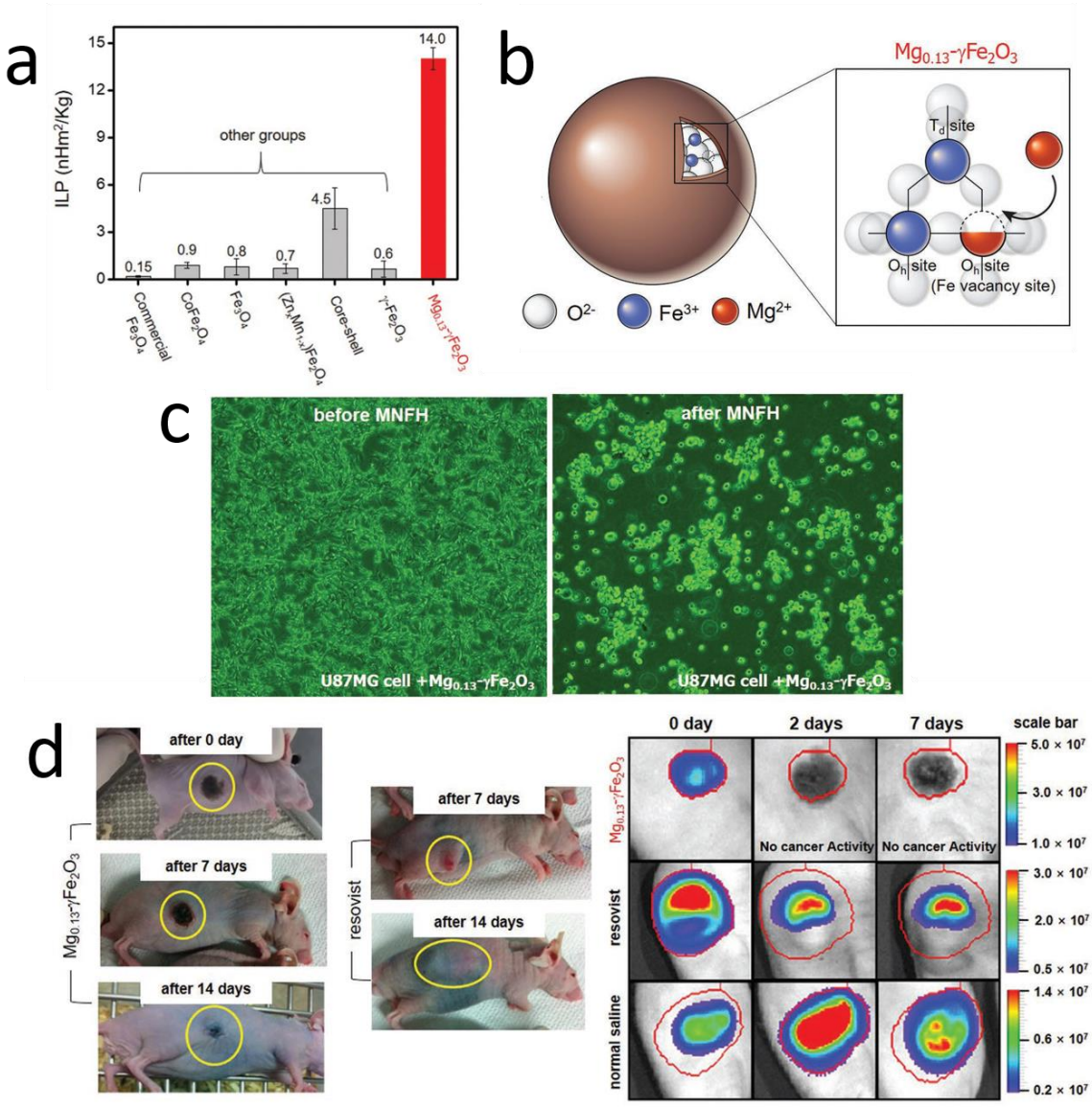

Figure 3.8. a) Comparison of ILP value of $Mg_{0.13}Fe_2O_3$ nanofluids to other previously reported MNPs. b) A schematic diagram of spinel structure of $Mg_{0.13}Fe_2O_3$ NPs. c) Fluorescence microscopy images of U87MG cells treated with $Mg_{0.13}Fe_2O_3$ nanofluids: left) before and right) after MFH. d) Photographs of xenografted nude mice after MFH with $Mg_{0.13}Fe_2O_3$ nanofluids and Resovist. (Reprinted with permission from ref 188. Copyright 2014 Wiley-VCH.).

Table 3.6. Overview of the metal - doped IONPs for *in vitro* MFH.

NPs type	**Overall size (nm)**	**Concentration of fluid (mg/mL) [Fe]**	**Cancer cell lines**	**Exposure condition [*f: H*: time]**	**T_{max} °C (Suspension)**	**Cell death (%)**	**Year /Ref**
γ-$Mn_xFe_{2-x}O_{3-}$ Acrypol 934	28	3.75	HeLa	425 kHz:50 kA/m :30 min	50	89	2007[236]
$Mn_{0.6}Zn_{0.4}Fe_2O_4$ (MNCs)[1]	100	0.2	MCF-7 and MCF-7/ADR	114 kHz:15 kA/m:15 min	57	90	2014[229]
$MnFe_2O_4$-CTAB[2]	13.3	0.5	Saos-2	765 kHz: 24 kA/m:10 min	45	75	2016[237]
$Zn_{0.4}Mn_{0.6}Fe_2O_4$	15	0.5	HeLa	500 kHz: 3.7 kA/m: 10	NI	84.4	2009[231]
$CoFe_2O_4$ - citric acid	5.4	1	Glial	329 kHz: 95.6 kA/m:60 min	NI	83.5	2108[238]
$CoFe_2O_4$ – HFt[3]	6.8	4.5 mM	B16	183 kHz, 12.4 kA/m:60 min	27	70	2014[239]
DOX[4]-loaded GdIO[5]	10	1	MCF7	267 kHz :40.1 kA/m :10 min	70	97	2016[231]
$CoFe_2O_4$	10	0.5	MCF-7	325 kHz: 40 kA/m :20 min	56	53	2015[233]

$Mn_{0.5}Fe_{2.5}O_4$@YVO4: Eu^{3+}	499	20	MCF-7	50 kHz:300 A: 10 min	~ 55	85	2018[122d]
MnZn ferrite nanoparticles	17	1	SMMC-7721	50 kHz:34 kA/m:40 min	35.1- agarose gel	46.4	2015[240]
MTX[6] loaded poly@Gd-MNPs[7]	15	0.05	MCF-7	70 kHz:7.2 kA/m:10 min	60	80	2016[241]

(MNCs)[1]: magnetic nanoclusters, CTAB[2]: cetyltrimethylammonium bromide. HFt[3]: human ferritin protein cage. DOX[4:] doxorubicin. GdIO[5]: gadolinium-doped iron oxide nanoparticles. MTX[6]: methotrexate. MNPs[7]: magnetic nanoparticles.

Table 3.7. Overview of the metal - doped IONPs for *in vivo* MFH on mice.

NPs type	**Size (nm)**	**Cancer cell lines**	**Injection dose [Fe]**	**Injection route**	**Exposure condition [*f*: $H_:$ time]**	**Tumor T_{max} °C**	**Therapeutic Outcome**	**Year /Ref**
MNCs[1]@PEG MNCs@RGD[2]	42.3 54.6	4T1	30 mg/kg	Intravenous	390 kHz:2.58 kA/m:30 min	42.5 44.1	MNCs@RGD provided higher *in vivo* MR imaging than MNCs@PEG thanks to its active targeting feature nevertheless its antitumor efficiency was not significantly improved compared with MNCs@PEG in the MFH treatments.	2016[242]
$Gd_{0.02}Fe_{2.98}O_4$	13	CT-26	16 mg/mL	Subcutaneous	52 kHz: 246 kA/m:30 min	NI	MFH treatment with $Gd_{0.02}Fe_{2.98}O_4$ NPs resulted in tumor size reduction of ~ 20 %.	2007[243]
$Mg_{0.13}\gamma Fe_2O_3$ - PEG	22.8	Hep3B	1.15 mg/mL	Subcutaneous	99 kHz: 12.33 kA/m:15 min	50.2	$Mg_{0.13}$-γFe_2O_3 nanofluids presented exceptionally high T_{max} of 180 °C at the physiologically benign range. Tumor was completely killed with nanofluids 2 days after MFH.	2018[18a]

PEI[3]$Mn_{0.5}Zn_{0.5}Fe_2O_4$	15-20	HepG2	5 mg/kg	Subcutaneous	230 kHz:4 kW[4]:30 min	45	The tumor mass inhibition rate of the combined treatment group was 93.38 %, significantly higher than that of 33.58 % for the radiation-alone group and 77.40 % for MFH-alone group.	2013[244]
$Zn_{0.4}Fe_{2.6}O_4$-amine-GM[5]	15	MDA-MB-231	1.42 µg/mL	Intratumoral	500 kHz: 37.4 kA/m:30 min	43	The tumors of mice treated with $Zn_{0.4}Fe_{2.6}O_4$-amine-GM[5] were eradicated by day 8 after MFH.	2013[245]
$ZnFe_2O_4$PEI/ miRNA	22.9	SUM159	50 mg/kg	Subcutaneous	225 kHz:5 kA/m: 45 min	44.1	A significant apoptotic output was achieved for combined mRNA/MFH (~ 34 % cell viability) compared to either mRNA treatment 69.8 % or MFH alone (63.14 % cell viability).	2014[246]

MNCs[1]: magnetic nanocrystals, RGD[2]: arginine-glycineaspartic acid, PEI[3]: Polyethylenimine, KW[4]: Kilowatt, GM[5]: geldanamycin

Looking at the $M_xFe_{3-x}O_4$ nanoferrites-related literature, it is obvious that this substitution strategy does not necessarily result in enhanced M_s and SAR/SLP values. The magnetization and heating potential of $M_xFe_{3-x}O_4$ nanoferrites have been changed in different ways (either increased or decreased) after doping. The diverse results are ascribed to the variable precursor concentration, the different distribution rate of the M^{2+} cations over T_d and O_h lattice sites and different synthetic methods.[54a] Therefore, careful control of the distribution of the dopant into the Fe_3O_4 cell unit to achieve maximum magnetization and heating outputs is crucial.

3.5.3.2. Exchange-coupled core@shell magnetic NPs for MFH

In 1989, Coehoorn conceptualised the phenomenon of exchange coupling effect between hard and soft magnetic phases in $Nd_2Fe_{14}B$–Fe_3B composite magnets.[247] Thereafter, immense attention was given to these configurations for energy-based and biomedical applications. This hybridisation of a hard magnetic (high anisotropy) and soft magnetic (low anisotropy and high M_s) components into a ferromagnetic core−shell structure, have been proposed as potential strategy to achieve maximum heating efficiency by modulating the magnetocrystalline anisotropy (K_{eff}) values.[248] Core/shell ferromagnetic NPs present the most effective exchange coupling due to a high contrast of anisotropy and magnetic susceptibility between soft and hard magnetic phases compared to the single phase constituents. In this core−shell configuration, the ferromagnetic (FM) coupling between nanoscale grains, the parallel alignment of the spins of the core and the shell to each other, or antiferromagnetic (AFM) antiparallel alignment of layers to each other induce a cooperative magnetization effect. The coherent rotation of spins of soft and hard magnetic phases transcribes therefore into a rich scenario of significantly optimized features such as higher coercivity, M_s and extra anisotropy.[249] Importantly, the improved magnetization does not solely depend on the exchange coupling but also on the size of the particles. Hence, the 8 nm $CoFe_2O_4$ core NPs exhibit distinct physical properties as compared to that of 12 nm $CoFe_2O_4$/$MnFe_2O_4$ core/shell NPs.[123b]

Cheon *et al.* have critically examined the phenomenon of exchange coupling for MFH applications. In a study, they synthesized core-shell $ZnFe_2O_4$@$CoFe_2O_4$ nanocubes of 60 nm via seed-mediated growth method. Under AMF operating at f = 500 kHz and H = 37.4 kA/m, the prepared core-shell nanocubes presented the extraordinary SLP value of 10600 W/g in

contrast to 4060 W/g for the single $ZnFe_2O_4$ ferrimagnetic nanocubes of the same size.[250] Furthermore, other studies have demonstrated the capability of this configuration for efficient MFH applications. This include $Zn_{0.2}Mn_{0.8}Fe_2O_4$@$MnFe_2O_4$ (SAR = 748 W/g at f = 300 kHz, H = 5 kA/m)[123b], $Zn_{0.17}Mn_{0.68}Fe_{1.9}O_4$@γ-$Fe_2O_3$ (SAR = 799 W/g at f = 831 kHz, H = 24 kA/m),[123c] $CoFe_2O_4$@$MnFe_2O_4$ (SAR = 553 W/g at f = 412.5 kHz, H = 22.4 kA/m),[251] $Co_{0.03}Mn_{0.28}Fe_{2.7}O_4$@$SiO_2$ (SAR = 3417 W/g at f = 380 kHz, H = 33 kA/m),[252] $MnFe_2O_4$@Co Fe_2O_4 (SAR = 160 W/g at f = 765 kHz, H = 28 kA/m),[253] $MnFe_2O_4$@$CoFe_2O_4$ (SLP = 428 W/g at f = 500 kHz, H = 37.30 kA/m),[254] Fe_3O_4@$CoFe_2O_4$ (SLP = 450 W/g at f = 765 kHz and H = 24 kA/m)[255] and Fe@Fe_3O_4 (SAR = 696 W/g at f = 303 kHz, H = 24.5 kA/m),[256] respectively. Recently, Zeng *et al.* achieved the SLP value of 500 W/g (at f = 380 kHz, H = 7 kA/m) which account for an ILP value of 26.8 x 10^{-9} m^4 s^{-2} A^{-2} (higher than that of ILP = 23.4 x 10^{-9} m^4 s^{-2} A^{-2} for bacteria magnetosomes) for their biocompatible $Zn_{0.3}Fe_{2.7}O_4$/SiO_2 NPs.[252]

A very significant result was obtained by Cheon *et al.* in which hard $CoFe_2O_4$ cores were coupled to $MnFe_2O_4$ soft shells to construct highly uniform size ferrite magnetic core@shell $CoFe_2O_4$@$MnFe_2O_4$ NPs for MFH applications. The TEM image exhibited the core-shell configuration of these NPs with homogeneous 3 nm $MnFe_2O_4$ shell layers on the initial 9 nm $CoFe_2O_4$ core (Figure 3.9a). Electron energy-loss spectrum (EELS) mapping confirmed the core-shell structure with Co at the core, Mn only on the shell and Fe distributed throughout the structure (Figure 3.9a). The magnetic hysteresis (M-H) curve presented a smooth hysteresis M–H loop in which the coercivity value (H_c) of $CoFe_2O_4$@Mn Fe_2O_4 = 201 kA/m at 5 K falls between the values for $MnFe_2O_4$ ($H_{c\ MnFe2O4}$ = 0 kA/m) and $CoFe_2O_4$ ($H_{c\ CoFe2O4}$ = 923 kA/m). This confirms the magnetically exchange coupled nature of core@shell NPs (Figure 3.9b). The SLP values of single-component NPs fall between 100 to 450 W/g, however, core–shell nanomagnets exhibited much higher values for various core and shell components ranging between 1000 - 3000 W/g (Figure 3.9c). The *in vivo* antitumor hyperthermia efficiency of core@shell NPs was tested in mice bearing U87MG human brain tumor. $CoFe_2O_4$@$MnFe_2O_4$ NPs (75 mg) were injected into the tumor subcutaneously under an AMF operating at 500 kHz and 37.3 kA/m for 10 min. For an identical injected dosage, core@shell NPs exhibited a significant eradication in tumor volume by day 18 after treatment, nevertheless Feridex (commercial IONPs) and chemotherapeutic drug doxorubicin (75 mg) resulted in tumor growth after treatment (Figure 3.9d). To achieve the same result of tumor

elimination with NPs (75 mg), (Feridex) of dose > 1200 mg did not result in significant reduction in tumor size. The immunofluorescence histology displayed the bright fluorescence for the untreated mouse tissue, nevertheless, absence of fluorescence after exposure to MFH confirmed the elimination of the tumor with core@shell NPs (Figure 3.9e).[257]

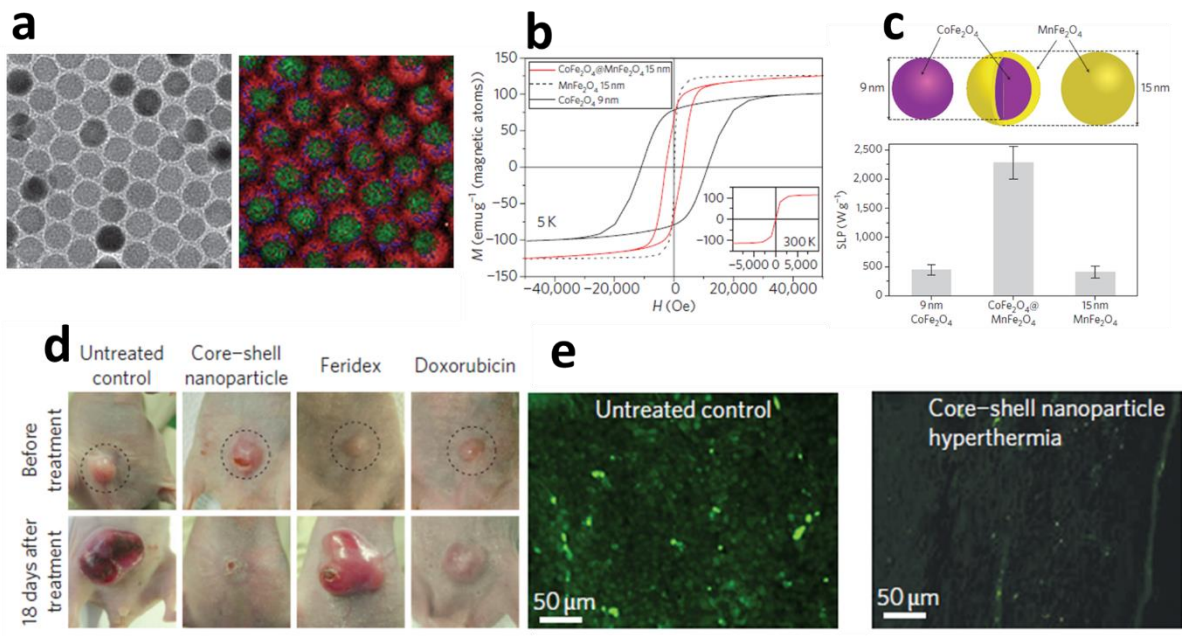

Figure 3.9. a) TEM (left) and overlay EELS mapped images (right) of $CoFe_2O_4$@$MnFe_2O_4$ core–shell NPs. b) M–H curve of synthesized NPs measured at 5 K using a SQUID magnetometer. c) SLP values of single-component (left) and various core–shell NPs (right). d) Nude mice xenografted with cancer cells (U87MG) before and 18 days after treatment with $CoFe_2O_4$@$MnFe_2O_4$, Feridex and doxorubicin respectively. e) Immunofluorescence histological images of the tumor region before and after MFH. (Reprinted with permission from ref 225. Copyright 2012 Nature Publishing Group.).

Exchange-coupled core/shell ferromagnetic NPs have been synthesized through different conventional physical techniques such as mechanical milling, sputtering and melt-spinning.[258] One issue associated with these techniques has been the difficulty in controlling the soft and hard phases at the nanoscale and also achieving a uniform phase distribution. Chemical methods have also been considered as a way to synthesise these NPs with controlled sizes, shapes, and compositions. However, it has been difficult to control the size of the hard phase. Additionally, impurities are often observed in these chemically-synthesized NPs.[259] Another challenge of this configuration is their ferromagnetic properties. As discussed in Section 3, ferromagnetic NPs possess residual magnetization

even when the applied magnetic field is removed which can encourage aggregation and increase the chances of an embolism in blood vessels.[260]

3.5.4. Near-infrared (NIR) light contribution to MFH

Light has been explored for therapeutic purposes since ancient times to treat diseases such as psoriasis, vitiligo and skin cancer.[261] The light in the near-infrared (NIR) region discovered by William Herschel in 1800, spans the wavelength range of 780 – 2500 nm in the electromagnetic radiation spectrum. The non-invasive nature of the NIR light (safe for irradiation dose under 50 mW/cm^2) together with unique penetration feature (few centimetres into the body), has rendered it with a toolbox of diagnostic and therapeutic applications such as monitoring of blood oxygenation, neuronal activity and light-activated phototherapy.[262] Phototherapy is classified into photothermal therapy (PTT) and photodynamic therapy (PDT) which rely on the interaction of NIR light photons with NPs or photosensitizers, respectively, for the ablation of cancer cells. In photothermal therapy (PTT) a minimally invasive localized phototherapy technique, photothermal agents absorb the optical vibrational energy from NIR light ($\lambda = 650 - 1350$ nm) and convert it to toxic heat resulting in light-triggered tumor ablation of cancer cells with a high penetration depth while sparing normal cells.[263] PDT is a clinically approved light-induced therapeutic concept that has been successfully applied for the treatment of dermatological diseases such as skin and esophageal cancer. The mechanism of action to induce tumor regression and apoptosis is distinct from that of PTT. In PDT, the excitation of photosensitizer by a designated wavelength of light (UV-Vis region, $\lambda \approx 400 - 700$ nm), or (NIR light, $\lambda \approx 800$ nm) can encourage the production of cytotoxic reactive oxygen species (ROS) and singlet oxygen to trigger cancer cell death. Additionally, PDT is also believed to damage tumor vasculature and actuate potential immune responses against cancer cells.[264]

NIR light has coupled MFH in three fashions: (*i*) the activation of IONPs under NIR light (*ii*) the activation of IONPs /PTT or IONPs /PDT agents under NIR light and (*iii*) the dual activation of IONPs /PTT or IONPs /PDT agents under NIR light + AMF simultaneously. All of these concepts have been thoroughly investigated with significant outcomes which will be discussed in the following sections.

3.5.4.1. Near-infrared (NIR) light activation of IONPs

Magnetophotothermal therapy is one strategy based on NIR light that has been proposed to maximise the heating efficiency of MFH. The process encompasses both guiding IONPs into the tumor area with an external static magnetic field (SMF) and subsequent irradiation of NPs with near NIR laser light to localize heat in the tumor region through electron–phonon and phonon–phonon processes. A wide variety of photothermal agents with strong localized surface plasmon resonance (SPR) and optical absorbance in the NIR region, have been assessed for the photothermal ablation of cancer cells. These include gold NPs,[265] carbon nanotube [266] graphene,[267] or graphene oxide, [268] semiconductor Ge nanocrystals,[269] CuSe nanodots,[270] and CuS microstructures[271] melanin[272] and tungsten nanocrystals.[273] Even so, the non-biodegradability, non-specific distribution in normal tissues and low tumor targeting efficiency of current photothermal agents, result in long-term toxicity, inflammatory cytokine production and cell death.[274] This has ultimately hindered their further clinical applications. IONPs have recently been demonstrated as potential photothermal agents due to low toxicity, good biocompatibility and biodegradability, targeting and magnetic resonance imaging capabilities.[129a] Moreover, iron is a nutrient and readily metabolised by cellular regulation using the transferrin pathway.[275] The integration of NIR photothermal potency with the strong magnetic component, renders IONPs with double functionality to be employed as dual attack non-invasive magneto/optical hyperthermia. Manipulation of IONPs by an externally applied magnetic field allow the NPs to be guided to the tumor area and irradiated with NIR light for potential cancer eradication. The potential of NIR activation of IONPs for MFH application have been explored in several preclinical *in vitro* and *in vivo* studies (Table 3.8 and 3.9).

Shen *et al*. were the first to report the optically-induced heat generation capability of IONPs under the irradiation of NIR light for the photothermal ablation of tumors both *in vitro* and *in vivo*. They synthesized cluster IONPs with the average size of about 5-10 nm via hydrothermal method. Thereafter, they injected a 50 mg/mL solution into the mice intratumorally 24 hours before NIR irradiation. The A549 tumor models developed in mice were then irradiated with an 808 nm NIR laser (5 W/cm2; spot size, 5 mm) for 60, 120 s and 180 s respectively. This resulted in exhibited cytotoxic effects and a cell killing rate of about 8.9 %, 33.5 % and 72.8 % for different illumination times of 60, 120 and 180 s,

respectively.[276] Notably, the mechanism of photothermal action of IONPs on the structure of the tumor tissue is unclear at present.

In another study, Zhao *et al.* designed MoS_2/Fe_3O_4 composite (MSIOs) by the integration of MoS_2 (MS) flakes as a NIR light to- heat converter and Fe_3O_4 NPs served as targeting moiety for *in vivo* magnetophothothermal therapy (Figure 3.10a). The differences in tumor volumes for group (I) (PBS injection) and (II) (PBS + 808 nm NIR) were negligible indicating the ineffective potential of NIR laser irradiation alone. By contrast, treatment in group (III) (MSIOs injection + NIR laser) resulted in an obvious decrease in tumor volume because of enhanced permeability and retention effect of the prepared MSIOs (Figure 3.10b). Expectedly, the tumors in group (IV) (MSIOs + NIR laser + MF) gradually disappeared 9 days post-treatment with only black scars left at the original sites (Figure 3.10c).[277]

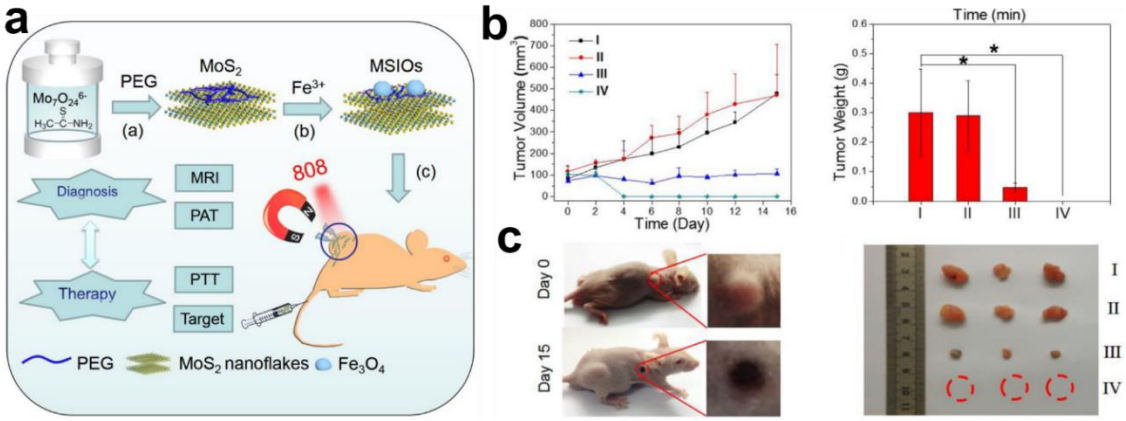

Figure 3.10. a) Schematic illustration of the synthesis and theranostic procedure of MSIOs for dual-modal photothermal tumor ablation b) Tumor growth curves of the four groups over a period of 15 days (left) and tumor weights after 15 days of the treatment (right). c) Representative photos of tumors in the four groups after 15 days treatment., Reprinted from ref 243. Copyright 2011 Ivyspring International Publisher).

Table 3.8. Overview of NIR activated IONPs for *in vitro* MFH.

NPs type	**Size (nm)**	**Concentration of fluid (µg/mL) [Fe]**	**Cancer cell lines**	**Exposure condition laser wavelength (nm): power (W/cm^2): exposure time (min)**	**T_{max} (°C) suspension**	**Cell death (%)**	**Year /Ref**
IR820[1]-CSQ[2]-Fe	11.9	0.8 2 4	MDA-MB-231	808:8:5	NI	25.3 30.9 66.5	2016[278]
Fe_3O_4	127	50	human primary astrocytes SKNMC neuronal CHME-5 glia	808:1.5:2	37-cell medium	101.58 96.90 98.45	2016[279]
Glu[3]- Fe_3O_4	20	1000	MCF-10A Hep G2	808:0.4:1	55	5 30	2015[280]
Fe_3O_4@SiO_2-APTES[4]-FITC[5]	125	150	HeLa cells, HUVEC, L929 cells	808:2:3	55	NI	2016[281]
Pt@Fe_2O_3	4	50	4T1 murine	808: 0.75:10	73.4	90	2015[282]

Mn-Fe_3O_4@MoS2[6]@CS[7]	50	100	LO2 Hep3B	808:1.5: 8	54	0 50	2018[283]

IR820[1]: Indocyanine Green, CSQ[2]: Chitosan quaternary ammonium salt. Glu[3]: glucose-6-phosphate. APTES[4]:(3-aminopropyl) triethoxysilane. FITC[5]: fluorescein isothiocyanate. MoS2[6]: Molybdenum disulfidechitosan. CS[7]: Chitosan

Table 3.9. Overview of NIR activated IONPs for *in vivo* MFH on mice.

NPs type	**Size (nm)**	**Cancer cell lines**	**Injection dose [Fe]**	**Injection route**	**Exposure condition laser wavelength (nm): power (W/cm^2): exposure time (min)**	**Tumor T_{max} (°C)**	**Therapeutic outcome**	**Year /Ref**
Fe_3O_4@$Cu_{2-x}S$	10	HeLa	50 mg/L	Intratumoral	980:0.6:10	42-Water	NPs presented the necrosis rate of 38 % compared to ~27 % for control group	2013[284]
$CoFe_2O_4$@PDA[1] @ZIF-8[2]	150	HepG2	3 mg/L	Inravenous	808:1.3:10	50	NPs + NIR + MF resulted in 97 % apoptotic and necrotic of tumor cells.	2017[285]
BMPs[3]	50	H22	16 mg/kg	Intratumoral	808:1.5:3	57	Cell necrosis was achieved with NPs + NIR group with the T_{max} of 57 °C in contrast to the control group with T_{max} of 45 °C under identical conditions.	2016[286]
Fe@γ-Fe_2O_3@H-TiO_2	NI	HeLa	2 mg/L	Inravenous	808:1.5:5	84.6	Activation of MF resulted in T_{max} of 84.6 °C compared to 53.9 °C when MF was off.	2018[287]

Fe_3O_4@$mSiO_2$	12	KB	0.5 mg/kg	Intratumoral	808:2:10	38	MR images revealed the effective localization of NPs in tumor site.	2012[288]
MFNP[4]-PEG	220	4T1	50 mg/kg	Inravenous	808:1:5	50	NPs + NIR + MF achieved the T_{max} of 50 °C compared to 38 °C for MF + laser group without NPs injection.	2012[289]
CNTs-IONP[5]/DOX- PEG	198	4T1	15 mg/kg	Inravenous	808:2:6	49.1	NIR irradiation of the tumor site under MF increased the temperature of tumor to 49.1°C compared to 40.5°C when MF was off.	2017[290]
Fe_3O_4 nanoclusters	225	A549	2 mg/L	Intratumoral	808:5:3	55.9	The tumor volume was decreased from 955.3 mm^3 to 222.8 mm^3 after 19 days of treatment for NPs+ MF+ NIR irradiation	2015[276]
PEG-Fe_3O_4@PDA@$mSiO_2$-Tf[6]	275	A549	5 mg/kg	Inravenous	785:0.5:5	38	The temperature of the tumor injected with NPs + MF + NIR laser was 38 °C, which was still enough to lead to cell death.	2016[291]
Fe_3O_4@Ag/Au	34.2	U87MG-luc2	20 mg/kg	Inravenous	1064:3:20	45.4	The tumor temperature for NPs + NIR + MF increased to 45.4 °C	2018[292]

							compared to 38.3 °C when MF was off.	
DOX - Fe_3O_4-PNIPAM[7]	140	S180	10 mg/L	Inravenous	808:1.5:5	50	The tumor inhibition rate was 91.5 % for mice treated with NPs + NIR + MF group compared to 40.3 % for nanoparticles without laser radiation.	2017[293]
PFH[8]@PLGA[9]/ Fe_3O_4	347	SKOV3	0.32 mg/mL	Percutaneou	780:1.5: 12	59	Tumor cells treated with NPs + NIR + MF presented severe coagulative necrosis.	2015[294]
^{125}I-RGD[10]-PEG-Fe@ Fe_3O_4	40	U87MG	10 mg/kg	Inravenous	808: 0.5: 5	45.2	Compared to re-growth of tumor for about ~8.0 times for control group, PTT resulted in completely destruction of tumor after 16 days.	2016[295]
MHI[11]-DSPE[12]-SPION[13]	74	SCC7	10 mg/kg	Intratumoral	808:1:10	50	The temperature of tumors increased to 50 °C after NIR irradiation for 10 min. Histological analysis also revealed coagulative necrosis in tumors.	2017[296]
Fe_3O_4@CMCTS[14]	228	S180	10	Inravenous	808:1.5:5	52	Histological examination revealed	2013[297]

			mg/L				degenerative changes of karyorrhexis and karyolysis for NPs + MF + NIR. Tumors on mice also disappeared within 10 days post-irradiation.	
Fe_3O_4/(DSPE-PEG-COOH	NI	Eca-109	8 mg/mL	Intratumoral	808:0.25: 20	50-Water	The tumor growth was markedly inhibited for NPs + NIR + MF group. Tumor had completely disappeared on one mouse on day 9 of irradiation.	2013[298]
Fe_3O_4-C^{15}-ICG^{16}-BSA^{17}	10	4T1	5 mg/kg	Intratumoral	808:2:5	47.3	NPs + NIR group resulted in complete ablation of tumor within 18 days post-treatment. Histological analysis revealed cell shrinkage and nuclear damage.	2017[299]
Fe_3O_4@ PDA	370	A549	2 mg/mL	Intratumoral	808:6.6:3	59.7	The tumor temperature for NPs + NIR increased to 59.7 °C compared to 42.9 °C for control group.	2015[300]
Cu_9S_5@$mSiO_2$@ Fe_3O_4-PEG	NI	H22	4 mg/kg	Inravenous	980:0.76:10	NI	The tumor inhibition rate was 89 % for NPs+ NIR + DOX + MF compared	2016[301]

							to 75.2 % when MF was off.	
MnIO-dBSA[18]	5	4T1	40 mg/kg	Intratumoral	808:1.5:5	70	The tumors in NPs + NIR + MF group were eradicated completely one day post-treatment.	2015[302]
Fe_3O_4@CuS-PEG	120	HeLa	20 mg/kg	Inravenous	808:3:10	35-cellular medium	The tumors in NPs + NIR laser + MF were eradicated completely on the 12th day post-treatment.	2015[303]
PPY[19]@Fe_3O_4	50	SW-1990	0.16 mg/kg	Intratumoral	808:0.25:5	48.8	Histological analysis presented coagulative necrosis and many regions of karyolysis.	2014[304]
Fe_3O_4@PB[20]@PEI[21]@BQDs[22]-HA[23]	139	HeLa	4 mg/mL	Inravenous	808:2:10	49	NPs + NIR + MF group presented the tumor growth inhibition of 89.95 %.	2017[305]

PDA[1]: Polydopamine, ZIF-8[2:] a kind of metal−organic framework, BMPs[3]: bacterial magnetic nanoparticles, MFNP[4]: multifunctional nanoparticles, CNTs-IONP[5]: carbon nanotubes- iron oxide nanoparticle, Tf[6]: transferrin, PNIPAM[7]: poly (N-isopropylacrylamide), PFH[8]: perfluorohexane, PLGA[9]: poly(lactic-co-glycolic acid), ^{125}I-RGD[10]: 125 I-c(RGDyK) peptide, MHI-148[11]: Heptamethine cyanine dye, DSPE[12]:1,2-distearoyl-sn-glycero-3-phosphoethanolamine, SPION[13]: superparamagnetic IONPs, CMCTS[14]: carboxymethyl chitosan, C[15]: carbon nanoparticles, ICG[16]: indocyanine green, BSA[17]: bovine serum albumin, MnIO-dBSA[18]: manganese doped iron oxide modified with denatured bovine serum albumin, PPY[19]: polypyrrole, PB[20]: Prussian blue. PEI[21]: polyethyleneimine, BQDs[22]: BSA coated ZCIS QDs, HA[23]: hyaluronic acid

3.5.4.2. Magnetic-plasmonic multifunctional nanohybrids

As discussed in Section 6.4.1, IONPs can generate heat under NIR light activation. In this strategy, IONPs are directed to the tumor area by the aid of applied magnetic field followed by irradiation with NIR light to generate heat through an unknown mechanism.

It is thought that the IONPs function in a dual role, both as a magnetic director and as a heating agent. In order to provide higher heating potentials under NIR light, plasmonic NPs have been introduced which results in the creation of an interesting class of NPs termed as magnetic-plasmonic nanohybrids. In this nanohybrid structure, IONPs are considered as an MRI or magnetic targeting agent at the core, surrounded by a thin plasmonic metal as a powerful NIR absorber at the shell.[306] Gold NPs are the most explored plasmonic materials due to several merits such as high biocompatibility, chemical stability and strong optical properties.[307] Gold NPs are active photothermally and generate heat by a localized SPR mechanism. The illumination of light at the resonance wavelength of 800 nm, induces collective oscillations of conductive gold electrons at the nanoshell surface which convert light energy to heat.[308] In addition, the gold nanoshell protects the MNP core from oxidation and provides for the possibility of further surface functionalization.[309] The potential of this magneto-plasmonic nanoplatform has been explored in some preclinical *in vitro* and *in vivo* studies for MFH applications (Table 3.10 and 3.11)**.** For instance, Liu *et al.* has developed multifunctional nanoparticles (MFNPs) with integrated functionalities. The particle design includes an upconversion component as the optical probes in the core, a layer of MNPs as a targeting probe in the intermediate shell, and a thin layer of gold as an strong NIR light-to-thermal energy conversion agent in the outer shell for potent in *vivo* magnetically targeted PTT under the guidance of dual upconversion luminescence/MR imaging. The upconversion luminescence and MRI image presented obvious bright luminescence emission and darker areas respectively for 4T1 tumor-bearing mice injected with MFNP-PEG indicating the higher uptake of NPs with cancer cells under the activation of MF (Figure 3.11a, b). Considering the *in vivo* photothermal study, the mice injected with MFNP-PEG and irradiated with an 808-nm laser at a power density of 1 W/cm^2 for 5 min under MF were tumor-free and survived for over 40 days post treatment. (Figure 3.11c). In sharp contrast, tumors in all control groups (no MFNP injection and no laser (Untreated); laser only without MFNP injection (Laser); injected with MFNP under the MF but without

laser irradiation (MFNP þ MF); injected with MFNP and exposed to the laser but without MF (MFNP + Laser) presented tumor growth without significant therapeutic output (Figure 3.11d).[289]

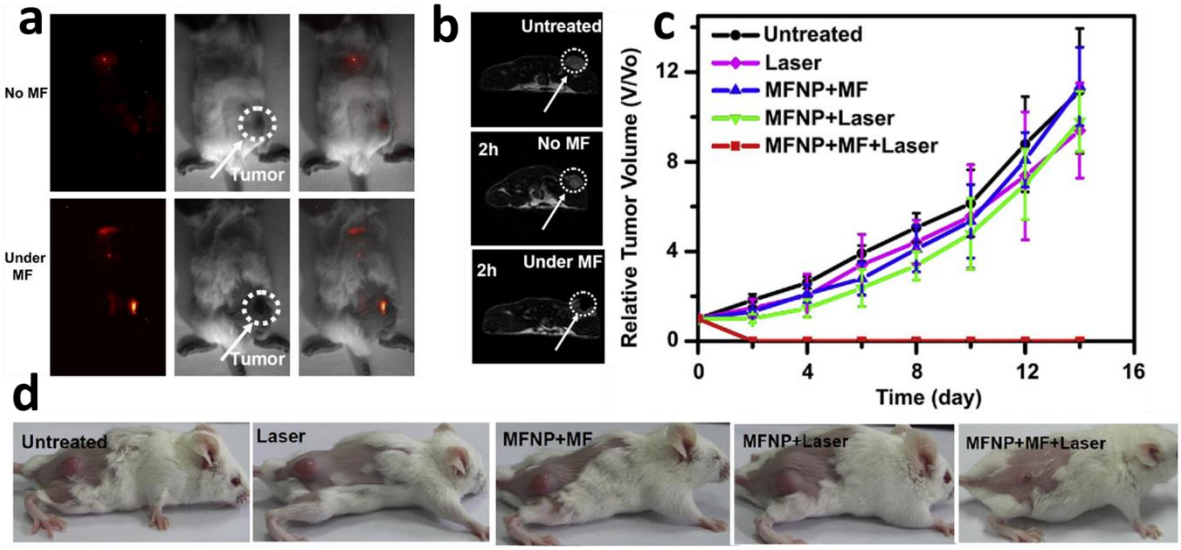

Figure 3.11. Representative *in vivo* a) UCL and b) T2-weighted MR images of 4T1 tumor-bearing Balb/c mice taken 2 h after injection of MFNP-PEG NPs under magnetic field (MF) and without MF, c) The growth of 4T1 tumors in different groups of mice after treatment, d) Representative photos of mice after various treatments indicated. (Reprinted from ref 255. Copyright 2011 Ivyspring International Publisher).

The problem with gold based magnetoplasmonic materials is that their application is only confined to NIR-I window (650–950 nm) where scattering is strong in biological media. To address that, semiconductor plasmonic NPs such as substoichiometric copper sulfide compounds ($Cu_{2-x}S$) have been proposed with the potential production cost (1 mol = US $330) being much cheaper than that of gold NPs (1 mol = US $52,200).[310]

Table 3.10. Overview of magnetic-plasmonic multifunctional nanohybrids for *in vitro* MFH.

NPs type	**Size (nm)**	**Cancer cell lines**	**Concentration of fluid (μg/ml) [Fe]**	**Cell death (%)**	**Laser exposure condition wavelength (nm): power (W/cm²): time (min)**	**T_{max} (° C) suspension**	**Year/Ref**
PS[1]/ IOC[2]–Au	190.2	KB-3-1 SK-BR-3	1	NI 98.8	808: 0.55:10	62, cell medium 45, cell medium	2015[311]
Au@ IONPs	33	KB	50	70	808:6.3:5	39.7, cell medium	2017[312]
Apt[3]-Au-Fe_3O_4	46	SKOV-3	1	65	605:2:10	NI	2017[313]
Au/PPY[4]@ Fe_3O_4	200	HeLa	1000	60	808:2:5	62.7	2014[314]
Fe_3O_4 @PZS[5]@Au	253	HeLa	50	79	808:1.6:15	66.5	2013[315]
Fe_3O_4@P(St[6]/MAA[7]) @CHI[8]@Au	305.3	Hep G2	100	82.4	808:1:3	59.05	2013[316]
Silica-coated Au/Fe_2O_3	100	MDA-MB-231	20000	NI	785:4.9:4	71.8- cell medium	2014[317]

PS[1]: photosensitizer, IOC[2]: iron oxide cluster, Apt[3]: aptamer, PPY[4]: polypyrrole, PZS[5]: Poly (cyclotriphosphazene-co-4, 4'-sulfonyldiphenol), St[6]: styrene, MAA[7]: methacrylic acid, CHI[8]: chitosan

Table 3.11. An overview of magnetic-plasmonic multifunctional nanohybbrides for *in vivo* MFH on mice.

NPs type	**Size (nm)**	**Cancer cell lines**	**Injection dose [Fe]**	**Injection route**	**Exposure condition** **Laser wavelength (nm): power (W/cm^2): time (min)**	**Tumor** **T_{max} (°C)**	**Therapeutic outcome**	**Year /Ref**
MMGNCs[1]	202	4T1	25 mg/kg	Intravenous	808:2.5:1	49.3	In the 7th day after treatment, tumor cells disappeared due to apoptosis and necroptosis.	2014[318]
γ-Fe_2O_3 @Au	179	4T1	10 mg/kg	Intravenous	808:1.5:5	72 - water	NPs induced severe necrosis and hemorrhagic without any re-growth during the 12th day after treatment.	2015[319]
Fe_3O_4@Au-HA[2]	119.4	Hela	32mM	Intratumoral	915:1.2:10	58.9	After 90 s of laser irradiation, the temperature of tumor increased abruptly from 32.8 to 58.9 °C. The tumor tissue almost completely eradicated on day 19 after laser irradiation.	2015[320]
DOX-	206	HT-29	150	Intravenous	808:.001:10	55 - water	Tumor growth was	2017[321]

Au/carboxylate-coated Fe_3O_4		colorectal	ppm				significantly inhibited down to 61.61 % after 600 s of laser irradiation.	
GNR[3]@IOs[4]-DOX[5]	241	4T1	1 mg/mL	Intravenous	808:1:7	57	The combined chemotherapy/PTT + MF with GNR@IOs-DOX resulted in prominent tissue necrosis.	2016[322]
Fe_3O_4/Au/Ag	34.2	U87MG-luc2	20 mg/kg	Intravenous	1064:3:20	45	The tumor temperature increased from 35.4 °C to 45.4 °C for NIR + MF and 36.6 to 38.3 °C without MF.	2018[292]
Fe_3O_4@SiO_2@Au- DOX[e]	161.9	Hela	0.55 mg/kg	Intravenous	808:30:10	47 - water	NIR illumination + MF lead to complete elimination of tumor 14 days post-treatment.	2014[323]
yolk–shell IONP[6]-C[7]	113	Hela	10 mg/kg	Intravenous	808:0.8:10	60 - water	NIR illumination + MF result in complete eradication of tumor 20 days post-treatment.	2016 [324]

MMGNCs[1]: magnetic gold "nanoclusters. HA[2]: Hyaluronic acid. GNR[3]: gold nanorod. IOs[4]: iron oxide nanoparticles. DOX[5:] doxorubicin. IONP[6]: iron oxide nanoparticles. C[7]: carbon

3.5.4.3. NIR/AMF biomodal mode for MFH

PTT has shown promising potential as a non-invasive technique in the battle against cancer thanks to its high light-to-thermal energy conversion efficiency and efficient bioconjugation chemistry of PTT agents. The prerequisite of high doses of laser irradiation (range 0.5 − 5 W/cm^2), shallow penetration range and low tumor targeting capability, have impeded the translation of the technique into clinics.[325] As discussed in Section 3, MFH requires a high dose of magnetic fluid for an effective result.[37] This ineffective outcome, gives rise to design of PTT/MFH for effective cancer therapy. Magnetically and optically active IONPs are merged with optically active PTT agents to form MFH/PTT biomodal therapy tool. Under the stimulation of an alternating MF, multifunctional NPs are guided to the target area. Subsequently, an NIR laser irradiation together with MF are applied simultaneously. IONPs and optical absorbing nanoagents convert NIR/MF and NIR light into localized heat energy conjointly. This combination of non-ionizing light and attenuated IONPs concentration results in the elevation of tumor tissue remotely. Wilhelm *et al.* have been actively utilizing this hybrid strategy for dual mode MFH/PTT.[204, 326] For instance, they studied the heating potency of IONPs at compatible clinical doses of laser (0.33 W/cm^2 for an 808 nm) and alternating MF (at *f* 110 - 900 kHz and *H* of 9.6 – 20 kA/m) with a low iron concentration [Fe] = 250 mM). This dual magneto/photothermal therapeutic approach was evaluated in tumor cells *in vitro* and *in vivo* on mice with A431 human epidermoid carcinoma cells. The heating power (SAR) in suspension increased from 700 to 900 W/g for MFH alone to 4850 W/g for dual mode MFH/PTT. Additionally, the cell viability significantly decreased to 14 ± 7 % for dual MFH/PTT compared to 74 ± 15 % and 36 ± 3 % for individual MFH and PTT respectively.[327]

As a supplementary technique for MFH, Na *et al.* developed pheophorbide (a photosensitizer) conjugated acetylated hyaluronic acid (AHP) coated Fe_3O_4 magnetic nanoparticles (AHP@MNPs) for dual PDT/MHT therapy. The *in vitro* Live/Dead cytotoxicity assay of MNP10 and AHP@MNP10 with alternating MF stimulation (*f* = 112 kHz, *H* = 19.9 kA/m) and 671 nm laser irradiation on K1735 cells presented extremely significant red cells for dual PDT/MHT combination therapy (Figure 3.12a). Additionally, mice with a K1735 tumor that were injected with AHP@MNP10 under dual PDT/MHT protocol, exhibited

markedly tumor growth inhibition 14 days post-treatment compared to mice with PDT or MHT alone (Figure 3.12b, c). [328]

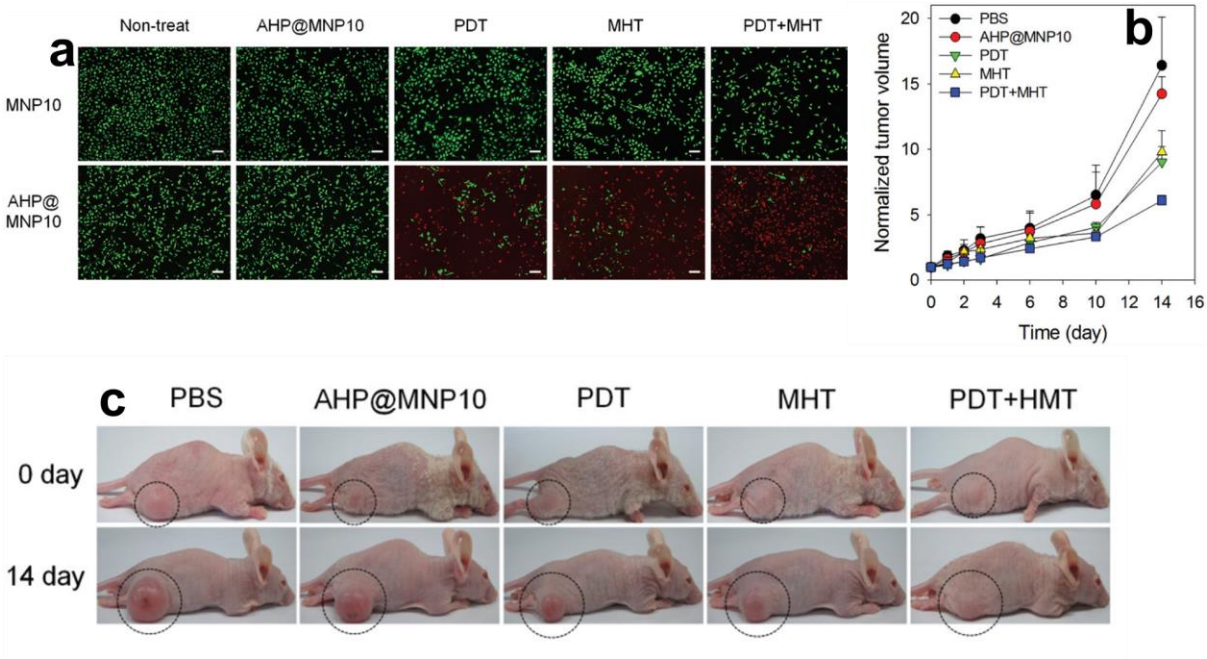

Figure 3.12. a) Live/Dead assay of MNP10 and AHP@MNP10 exposed to PDT and MHT, alone and in combination, in K1735 cells (live: green, dead: red). White scale bar is 50 µm. b) K1735 tumor volumes in the five treatment groups after treatment (n = 5). c) Images of mice bearing K1735 tumors before and after each treatment. Black circle indicates tumor (n = 5). (Reprinted with permission from ref 291. Copyright 2013 Wiley-VCH).

The potential synergistic effect of this biomodal mode, have been further confirmed in a set of *in vitro* and *in vivo* preclinical examinations given in Table 3.12 and 3.13**.**

Table 3.12. An overview of NIR/AMF Biomodal Mode for *in vitro* MFH.

NPs Type	Size (nm)	Cancer cell lines	Concentration of fluid (μg/ml) [Fe]	External stimuli	Exposure condition [*f: H:* time] Laser wavelength (nm): laser power (W/cm^2): exposure	T_{max} °C Suspension	Cell death (%)	Year/Ref

					time (min)			
CB[1]:ZnPc[2]-MLs[3]	209	B16-F10	0.25	MFH + PDT	1000 kHz: 3.2 kA/m :3 min 670:0.84:NI	NI	13	2012[329]
MNPs[4]	50	A431	5000	MFH + PTT	3 Hz, 300 mW:5 min 532:0.05:5	42- cell medium	41	2016[321]
LP[5]-HMNSs[6]	391	Eca-109	500	MFH + PTT	NI:36 kA/m :20 671: 0.2:20	44	76.4	2016[330]

CB[1]: cucurbituril, ZnPc[2]: zinc phthalocyanine, MLs[3]: magnetoliposomes, MNPs[4]: magnetic nanoparticles, HMNS[5]: Hollow magnetic nanospheres, GQDs[6]: quantum dots, DOX[7]: doxorubicin, HMNSs[6]: Hollow magnetic nanospheres, LP[5]: liposomes

Table 3.13. An overview of NIR/AMF Biomodal Mode for *in vivo* MFH on mice.

NPs Type	**Size (nm)**	**Cancer cell line**	**External stimuli**	**Exposure condition [*f: H*: time] Laser wavelength (nm): laser power (W/cm²):**	**Injection dose [Fe]**	**Injection route**	**Tumor T_{max} (°C)**	**Therapeutic outcome**	**Year/Ref**

				exposure time (min)					
UMPL[1]	150	SKOV-3	MFH+ PDT	111 kHz:23.9 kA/m :30 min 650:1:1.4	2.8 mg/kg	Intratumoral	40	Complete tumor regression was achieved under synergistic PDT/MHT mode compared to large necrosis under either PDT or MHT protocol individually	2015[106a]
Fe_3O_4/Au/ PVP[2]	53	PC3	MFH + PTT	110 kHz:20 kA/m :5 min 680:0.3:5	150 mM [Fe]	Intratumoral	48	MFH and PTT presented a temperature rise of 9 – 10 °C in a separate fashion, compared to almost 20 °C within 2 min for dual MFH /PTT stimulations	2015[326a]
MNP[3]@P ES[4]-Cy7[5]/ -DG[8]	94	MCF-7	MFH + PTT	200 kHz:38 kA/m:10 min 808:0.75: 10	20 mg/kg	Intravenous	52	At the day 35 post-treatment the tumors in the dual MFH/PTT group were entirely burnt, however tumors treated with individual treatments	2018[328]

								re-grew to some degree.	
MTX-MagTSLs[9]	107	Hella	MFH + PTT	500 kHz:20 kA/m:5 min 808:0.8:5	2 mg/kg	Intravenous	45 - water	The cellular uptake and tumor inhibition efficiency of MTX-MagTSLs in cancer cells were markedly higher in dual mode.	2018[331]
Fe_3O_4@Au-cetuximab (C225)	46	U251	MFH + PTT	230 kHz:30 A:30 min 635:0.3:3	0.5 mg/mL	Peritumorall	43-water	Dual MFH/PTT led to diffusion of fluid within the tumors, and subsequent necrosis compared to invisible necrosis for sole MFH or PTT.	2018[332]
Fe_3O_4@GO[10]	191	HeLa	MFH + PTT	425 kHz: NI:30 min 808:2:3	0.25 mg/kg	Intratumoral	43-water	Considering the histological result, MFH and PTT associated chemotherapy presented higher cell death and tissue necrosis than individual therapies.	2016[333]

UMPL[1]: Photosensitive Liposomes, PVP[2]: polyvinylpyrrolidone, MNP[3]: magnetic nanoparticles, [d]PES: poly (3,4-ethylenedioxythiophene): poly(4-styrenesulfonate), Cy7[5]: Cyanine7, DG[8]: 2-deoxyglucose (2-DG)-polyethylene glycol, MTX-MagTSLs[9]: methotrexate (MTX) modified thermo-sensitive magnetoliposomes, GO[12]: graphene oxide

3.5.5. Targeted nanoscale MFH

Two general approaches are used to introduce MNPs to cancer tissues. These are direct local delivery and systemic delivery. Direct local delivery has been the most utilized approach in many *in vivo* MFH and clinical studies for treating accessible glioblastoma, prostate and pancreatic tumors through direct intratumoral injection of the NanoTherm® fluid.[36b, 334] Direct delivery is appropriate for easily accessible tumors of known location and volume.[335] However, there are practical difficulties to achieve sufficient amounts of particles localized in the tumor region through direct injection. The aqueous suspension of NPs is not homogeneously distributed in organic tissue.[336] In addition, the suspension would spread out to some extent into the softer normal tissue than tighter tumor tissue resulting in an inhomogeneous distribution pattern and creation of hot spots.[337] The problems increase if the injection rate is too fast, which can result in uncontrollable leakage of the suspension away from the tumor region. Accordingly, in clinical MFH trials, the suspension is injected slowly at different sites of the tumor through multipoint Injection.[338] In contrast to non-targeted clinical MFH, targeted intracellular hyperthermia allows treatment of inaccessible and metastatic tumors inside the body with an intravenous injection of a minimum dose of magnetic multifunctional NPs.[126g, 339] This approach integrates diagnostic and therapeutic agents into a single multifunctional theranostic nanaoplatform to effectively advance the destruction of deep-seated tumors. Targeted MNPs can reach tumor site passively through the enhanced permeation and retention (EPR) effect aided by leaky vasculature surrounding the tumors[340],or actively by the aid of targeting ligands decorated on the surface of NPs[341] or magnetic directional manipulation of an external AMF.[342] Passive targeting is the preferential accumulation of NPs inside the tumor by a process called endocytosis in which NPs fully internalize the cancerous tissue.[343] Passive targeting is directly related to the circulation time and the defective architecture of the tumor vasculature. The tumor vasculature is very different from normal tissue anatomically and functionally. Unlike the tight endothelium of normal blood vessels, the tumor vasculature is more permeable and leaky, greatly heterogeneous in distribution, larger in size and high in vascular density.[343] To work in harmony with this mechanism of passive targeting, NPs should possess some features that endow them with a high residential time in the blood. Firstly, the hydrodynamic size of the NPs should be above 10

nm to escape leaking out of blood vessels and renal clearance.[344] NPs in a diameter range of 10 – 50 nm exhibit the longest prolonged intravascular circulation time.[345] Larger size particles (in the range of 50 – 150 nm), are eliminated by phagocytizing.[346] Several studies have validated that NPs of ≈ 50 nm in size have optimal cellular uptake and highest internalization whereas NPs with hydrodynamic sizes bigger than 60 nm are weakly taken up by cancer cells.[347] Secondly, they should have high ionic strength or the zeta potential (+ or −) values in order to negate the potential aggregation in the complex biological milieu.[348] It has been demonstrated that positively charged NPs have better interactions with the cell membranes because of its anionic nature.[349] Another important factor that affects the biodistribution, blood circulation and residence times of NPs is the hydrophobicity. Hydrophobic NPs possess short circulation half-lives due to the adsorption of plasma proteins to their surface, which can lead opsonization (elimination of foreign objectives by the phagocytes*)* and consequent removal from blood.[350] Surface modification with molecules like the hydrophilic polymers with long chains such as polyethylene glycol (PEG) have been shown to diminish opsonization through steric repulsion. [351] Once inhibiting in the blood, they can enter the leaky vasculature of a cancer tumor through the so-called 'enhanced permeation and retention' (EPR) effect. Active targeting strategy takes advantage of the principle of ligand-receptor recognition and the difference between receptor and antigen expression of the normal and cancer cells. Active targeting commonly employs NPs equipped with surface conjugated targeting moieties such as diagnostic agents and ligand to selectively or preferentially attach the surface receptor or antigen on specific cells in the body to stablish their full potential benefit latterly.[352] Accessibility of the particular receptor on targeted cells is of utmost importance for an effective binding of ligand-decorated NPs during this approach where abundant receptor and antigen presented on the surface of the cancer cells promotes the optimum delivery of drugs. Therefore, an important step is to recognize the nature of the receptor on the cell for which the nanocarrier will be targeted to.[353] The diagnostic agents with unique optical and fluorescent features ease the early diagnosis of the disease and visualisation of the tumor by MRI[354] or fluorescence imaging.[355] Additionally, it might help to monitor the progress of treatment.[356] One important point is that recognition of injected NPs does happen unless they are close to their target antigens. Therefore, the blood circulation time should be optimized at the first step by relying on the EPR effect to favour subsequent efficient attachment of ligand-

decorated NPs to target cells.[357] To further increase targeting efficiency and boost the accumulation of NPs into the destined site, a magnetic targeting strategy can be considered.[358] Magnetic targeting utilizes an external magnetic field gradient placed near the tumor outside of the body to magnetically guide the therapeutic MNPs toward this area.[359] In recent years, various organic dyes or inorganic semiconductor quantum dots have been conjugated with MNPs for minimally-invasive recognition of tumors. Thanks to several types of functionalization and coupling chemistry, various tumor-specific ligands such as antibodies, proteins, peptides, aptamers, small molecules and anticancer drugs have also been coupled to MNPs for MFH synergistically with chemotherapy.[126b, 126d, 360] Magnetic intracellular hyperthermia has been investigated in a number of *in vitro* and *in vivo* preclinical experiments. (Table 3.14 and 3.15).

The group of Hayashi *et al.* designed MF-responsive smart platform by combining doxorubicin (DOX), and clustered Fe_3O_4 NPs in polypyrrole (PPy). They achieved remarkable heating results and complete eradication of the tumor.[361] The NPs were modified with polyethylene glycol (PEG) and folic acid (FA) to improve their retention in the tumor. The prepared Fe_3O_4/DOX/PPy-PEG-FA NPs with the mean size of 70 nm were investigated for *in vivo* destruction of myeloma through the combined magnetic hyperthermia (MHT) and chemotherapy. The temperature rise of the aqueous solution of prepared NPs was 29 °C under the same alternating MF (operating at f = 230 kHz and H = 8 kA/m for 20 min) as compared to ~ 22°C for Resovist. The SAR value of NPs was 487 W/g compared to 360 W/g for Resovist® (Figure 3.13a). For *in vivo* studies, the mice bearing myeloma was injected intratumorally with NPs (5 mg/kg) and placed in alternating MF operating at the same magnitude. After 7 min of exposure, the tumor temperature of mice injected with NPs reached to the therapeutic temperature of 44°C (Figure 3.13b). However, the non-injected mice did not show temperature rise which puts the emphasize on the stand-alone incapability of MF for the elevation of body temperature. Additionally, the tumor volume of the mice after intratumoral injection of Fe_3O_4/DOX/PPy-PEG-FA NPs was compared with those of the control groups 45 days after treatment. The tumor were completely disappeared for the NPs however, the control groups presented tumor re-growth (Figure 3.13c, d).[361]

As discussed in Section 2, the internalized tumor-targeted MNPs have the potential to kill cancer cells through magneto-mechanical actuation.[362] To achieve this, the torque on the magnetization can be translated to a force applied to the cell and deliver direct mechanical damage to the cell membrane[100, 363] or even organelles if the MNPs are internalized by the cell.[99d, 364] In recent years, some MNPs has been proposed and studied for magneto-mechanical cell destruction such as Py vortex particles,[365] magnetic-vortex NiFe microdiscs, synthetic antiferromagnetic and ferrimagnetic microdiscs,[366] superferromagnetic Fe-Cr-Nb-B glassy alloys,[367] nanowires with various compositions,[368] and ultrathin perpendicularly magnetized magnetic particles.[369] In an *in vivo* study, Novosad *et al*. synthesized magnetic-vortex microdiscs (MDs) of 60-nm-thickness and ~ 1 µm diameter using an optical lithography technique. Under an applied AMF, the MDs were shown to oscillate with the subsequent mechanical force then activating calcium signaling, triggering the programmed cell-death pathway.[370]

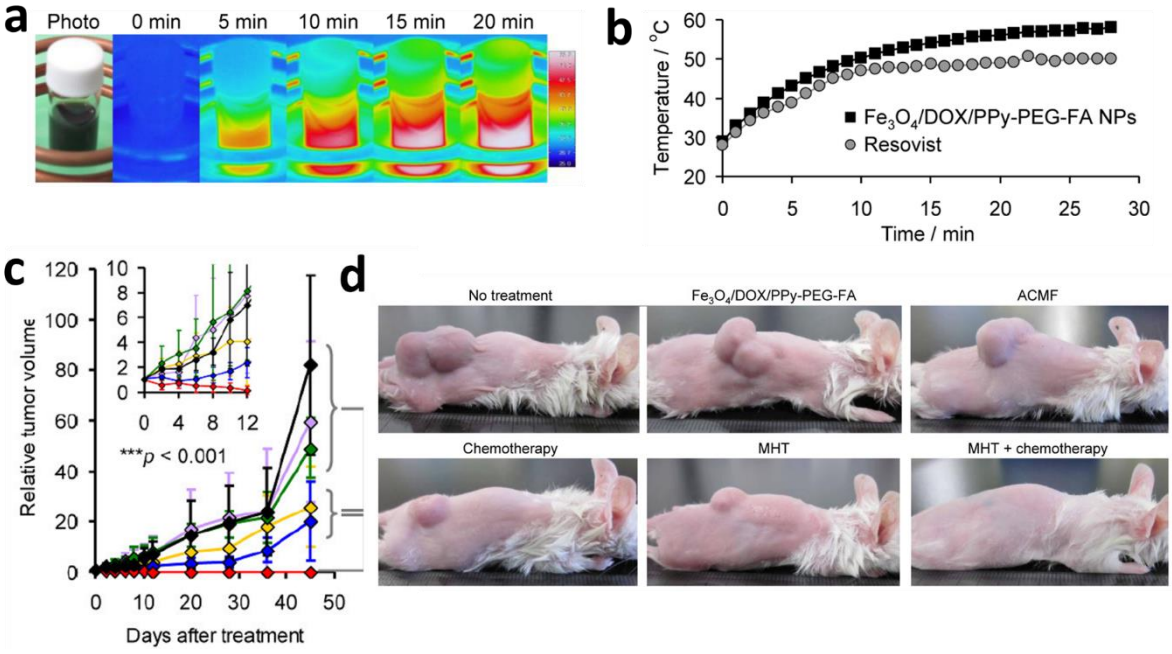

Figure 3.13.a) Thermal images and b) temperature change of the aqueous dispersion of Fe_3O_4/DOX/PPy-PEG-FA and Resovist NPs under AMF; (c) Change of tumor volume, non-treated mice (black), mice treated with chemotherapy (yellow), AMF (green), injected with Fe_3O_4/DOX/PPy-PEG-FA NPs intratumorally (purple), MHT (blue), and combined MHT and chemotherapy (red). The inset shows the magnified view for the first 12 days after treatment; (d) Photographs of mice treated with different protocols 45 days after treatment. (Reprinted with permission from ref 304. Copyright 2014 Ivyspring International Publisher.).

Table 3.14. An overview of biofunctionalized magnetic NPs for tumor specific *in vitro* MFH.

NPs Type	**Size (nm)**	**Cancer cell lines**	**Fluid concentration (mg/mL) [Fe]**	**Exposure condition [*f*: *H*: time]**	**T_{max} °C Suspension**	**Cell death (%)**	**Ref/ Year**
γ-Fe_2O_3 OEGMA[1] doxorubicin	328	PC-3	2.94	335 kHz:12 kA/m :30 min	65 -Water	68	2017[371]
Fe_3O_4 34DABA[2]	193.5	HepG2	1	751.51 kHz: 10.9 kA/m :60 min	42-water	88	2018[372]
Fe_3O_4 vitamin E /TPGS[3] micelles	145.5	MCF-7	1	240 kHz:89 kA/m :60 min	42-water	NI	2011[373]
DSPE-PEG 2000[4] Doxorubicin	28.12	HeLa	0.1	355 kHz: 23.77 kA/m: 60min	43-water	32	2015[5b]
Fe_3O_4 CMDx[5] EGF[6]	78	MCF-7	5	233 kHz:37.5 kA/m :120 min	43-water	20	2011[99a]
Fe_3O_4 CMDx[5] EGF[6]	61	MDA-MB-231	0.3	233 kHz:42 kA/m:60 min	NI	NI	2013[94]
Fe_3O_4 + γ-Fe_2O_3 poly (NIPAAm[7]- *co* – HMAAm[8])	350	COLO 679)	83	166 kHz:480 A:5 min	45-cell medium	70	2013[374]

doxorubicin							
Fe_3O_4 PLGA[9] Folate + transferrin curcumin + 5- fluorouracil	150	MCF7 G1	1	305 kHz:18.03 kA/m:120 min	NI NI	28 26	2014[375]
Fe_3O_4 MG[10]+ DY647[11]	40	R1G9-CCK2R	0.016	275 kHz: 41 kA/m:120 min	NI	67.1	2014[99b]
Fe_3O_4 PEI [12]	-	SH-SY5Y	0.1	570 kHz:23.9 kA/m:30 min	42.5 – cell medium	77.2	2017[5c]
$Mn_{0.6}Zn_{0.4}$ Fe_2O_4 [PLA-b-poly(N-co-D)][13] HSP70[14] Camptothecin	100	SK-OV-3 HepG2	0.1	114 kHz:89.9 kA/m:5 min	42.5-water	NI	2014[376]
γ-Fe_2O_3 citric acid	25	MCF-7	2 mM	520 kHz:29 kA/m:30 min	49 –cell medium	60	2012[377]
Fe_3O_4 carboxyl terephthalic acid	11	MCF-7	1	751.5 kHz: 10.9 kA/m:60 min	43.2-water	NI	2018[378]
Fe_3O_4 carboxymethyl	150	MCF7 G1	4	305 kHz:18.03 kA/m:60 min	NI	25 23	2013[379]

cellulose Folate – FITC[15]5-fluorouracil							
$MnFe_2O_4$ SiO_2@SiO_2	60–80	HeLa	0.5	250 kHz:13.3 kA/m:30 min	42-45 cell medium	85	2015[380]
Fe_3O_4	9.4	A549	4.8	128 kHz:20.3 kA/m:135min	NI	NI	2016[103a]
Fe_3O_4 citric acid	9.9		8.3				
HSP70B[16]	12.3		22.5				
Fe_3O_4 SiO_2 HSP70B[16]							
Fe_3O_4 chitosan-DOPA[17]	158	A 549	0.15	1 MHz: 208 A/m:20 min	42-water	78	2012[381]
Fe_3O_4 alginate doxorubicin	NI	MCF-7	100	700 kHz: 8.0 kA/m:120 min	53-water	95	2011[326b]
Fe_3O_4 graphene oxide	21	A549	0.2	325 kHz:16.72 kA/m:60 min	45-water	80	2018[382]
Fe_3O_4 YVO4:10Eu	22	WEHI-164	0.2	265 kHz:30 A:10 min	NI	20	2015[383]
Fe_3O_4 PEI [18] – PEG[19]	46.8	U87	0.02	300 kHz:5 kA/m:45 min	NI	38.3	2014[384]

ATAP[20]/ RGD[21]

OEGMA[1]: Oligo (ethylene glycol) methyl ether methacrylate. 34DABA[2]: 3,4-diaminobenzoic acid. TPGS[3]: D-a-Tocopheryl-co-poly (ethylene glycol) 1000 succinate. DSPE-PEG 2000[4]:1,2-distearoyl-sn-glycero-3-phosphoethanolamine-N-[methoxy(polyethylene glycol)-2000]. CMDx[5]: Carboxymethyldextran. EGF[6]: Epidermal growth factor. NIPAAm[7]: *N* –isopropylacrylamide. HMAAm[8]: *N* –hydroxymethylacrylamide. PLGA[9]: Poly (D, L-lactic-co-glycolic acid. MG[10]: synthetic replicate of gastrin. DY647[11]: Fluorescent dye. PEI[12]: Polyethylenimine. [PLA-b-poly(N-co-D)][13]: polylactide-b-poly (N-isopropyl- acrylamide-co-N, N-dimethylacrylamide. HSP70[14]: Heat Shock Protein 70. FITC[15]: Fluorescein isothiocyanate. HSP70B[16]: Heat Shock Protein 70B. DOPA[17]: L-3,4-dihydroxyphenylalanine. PEI[18]: polyethylenimine. PEG[19]: polyethylene glycol. ATAP[20]: amphipathic tail-anchoring peptide. RGD[21]: Arginylglycylaspartic acid.

Table 3.15. An overview of biofunctionalized magnetic NPs for tumor specific *in vivo* MFH on mice.

NPs Type	**Size (nm)**	**Cancer cell line**	**Injection dose [Fe]**	**Injection route**	**Exposure condition [*f: H*: time]**	**Tumor T_{max} (°C)**	**Therapeutic outcome**	**Ref/ Year**
Fe_3O_4 PEG[1] Folic acid	98.9	myeloma	48 µmol Fe/kg	Intravenous	230 kHz:8 kA/m:20min	38	The tumor volume of treated mice reduced to one-tenth of the original volume, 35 days post-treatment.	2013[385]
$Zn_{0.4}7Mn_{0.53}Fe_2O_4$ PEG[1]PPZ[2]-HSP70[3]	153	U-87 MG	8.7 µg Fe/mL	Intratumoral	389kHz:19.5 kA/m:25min	53	Obvious apoptosis and cell shrinkage were observed in the tumors treated by two cycles of MFH.	2016[386]
Fe_3O_4 MMSN@TRP[4] rhodamine B-fluorescent dye-doxorubicin	160	EL4	182 µg Fe/tumor	Intratumoral	105 kHz: 18:30 min	NI	The tumor growth was inhibited for NPs whereas the tumor volume for control group was doubled from day 3.	2018[387]
Fe_3O_4 DMSA[5] N6L[6] doxorubicin	175	MDA-MB-231	0.25 mg Fe/100 mm^3	Intratumoral	435 kHz:15.4 kA/m:NI	41.7	The tumor volume was decreased to ~ 40 % of the initial volume within 28 days, whereas it increased to a	2015[388]

			tumor				mean of 251 % for the control group.	
Fe_3O_4 HAP[7]	50	CT-26	(0.8 g/5 ml)	Subcutaneous	60 Hz:110 V:20 min	46	NPs + MF resulted in significant shrinkage of tumor whereas tumors without MF still grew post-treatment.	2009[389]
Fe_3O_4	15	Tu212	0.30 g/mL	Intratumoral	130 kHz:7kA/m:20 min	40	Severe inflammation and coagulative necrosis were revealed in the treated tumors under MFH protocol.	2012[390]
Fe_3O_4 pluronic f127 EGFR[8]	369	A549	270 ± 70 µg/min	Inhalation	386 kHz:6 kA/m:30min	NI	EGFR targeting enhances NPs accumulation in tumor zone.	2013[391]
Fe_3O_4 p(HEMA-co-DMA)[9] bortezomib	18	SCC7	40 mg/kg	Intratumoral	293kHz:12.57 kA/m:10min	43-Water	Synergistic MFH and drug delivery resulted in a marked reduction in the volume and weight of the tumor compared to control group.	2015[392]
Fe_3O_4 PS[10]	165	HepG2	0.42	Intratumoral	200 kHz:300 A:30min	45	In contrast to single therapy	2015[393]

doxorubicin				mg/kg				combined MFH/chemotherapy therapy result in nearly complete eradication of liver tumors after 16 days.	
Fe_3O_4 Doxorubicin +Docetaxel	**PEG[1]**	210	MDA-MB-231	18.7 mg/kg	Intratumoral	282kHz:19.99 kA/m:10min	48	MFH with codelivery of two anticancer drug presented marked antitumor activity compared with single drug.	2017[394]
Fe_3O_4 Doxorubicin +Docetaxel	**PEG[1]**	159	A2780	50 mg/kg	Intratumoral	250kHz:376 kA/m:20min	41	The viability of A2780-CisR cells remarkably decreased from 87 ± 3.2 (when AMF was off) to 50 ± 3.4 % in the presence of AMF.	2016[395]
Fe_3O_4 TNF-α[11]	**liposome**	NI	A549	NI	Intratumoral	118kHz:30.6 kA/m:20min	43.3	The tumor volume at the day 30 post-MFH with transfection was significantly repressed to 1.8 ± 0.2 cm^3 compared to 3.6 ± 0.3 cm^3 for transfection alone.	2013[396]
Fe_3O_4 PLGA[12]		NI	MCF-7	40 %	Intratumoral	626 kHz:28.6 A:2 min	60	After MFH tumors shrank up to 70 % in 2 days and almost	2014[397]

							disappeared after three days.	
Fe_3O_4 HPMC[13]	10-50	MB-231	90 %	Intratumoral	626 kHz:28.6 A:5 min	60	The tumor shrank remarkably on day 5 post-MFH and disappeared on the day 15.	2017[398]
Fe_3O_4 gold DNA aptamer- AS-14	50	carcinoma	1.6 µg/kg	Intravenous	50 Hz:8.0 kA/m :10 min	NI	On day 8, the tumor formed a crust with a remarkable reduction in size of the crust on day 13.	2017[399]
Fe_3O_4 PLGA[12]-Fe doxorubicin	NI	MMC-7721	20 %	Intratumoral	626 kHz:28.6 A:2 min	52	Tumors of mice in DOX/PLGA-20 % Fe + AMF group were eliminated 5 days post0-MFH.	2016[400]
Fe_3O_4 Alginate-cysteine doxorubicin	87	HGC-27	4 mg/mL	Intratumoral	217 kHz:8 kA/m:10 min	38	Chemotherapy or MFH alone presented little therapeutic outcome nevertheless MFH + chemotherapy significantly inhibited tumor growth.	2016[401]
Fe_3O_4 PLGA[12] doxorubicin	172	CT26	25 mg/Kg	Intratumoral	293 kHz:12.57 kA/m:20 min	44	MFH + chemotherapy presented marked tumor growth suppression compared to MFH and chemotherapy	2018[402]

							alone.	
Fe_3O_4 PEG2000-DSPE[14]- liposomes CD90	130	Huh7	5 mg/Kg	Intravenous	200 kHz:20 A:60 min	44	Hematoxylin-eosin staining revealed visible Fe_3O_4 sediment surrounded by necrotic tumor cells on day 7 post-MFH.	2016[403]
Fe-Fe_3O_4 PEG[1] c(RGDyK) peptide	33	U87MG glioblastoma	40 mg/kg	Intravenous	242.5 kHz:21.7 kA/m :40 min	38-water	On the day 15 post-MFH the relative tumor size volume reduced by a half in size. Hematoxylin-eosin staining revealed nuclear fragmentation and shrinkage.	2018[404]
Fe_3O_4 PLGA[12] doxorubicin	240	4T1	3 mg/kg	Intratumoral	390 kHz:NI:30min	42-water	7 days post-MFH, severe necrotic tissue happened with a dark gray color on tumor site. The tumor inhibition rate for MFH group was 3.4 folds than control group.	2015[405]
Fe_3O_4 PAA[15]-Ag	10	SMMC-7721	15 mg/kg	Intratumoral	390 kHz:18 A:20 min	43	Histopathology results revealed a massive complete necrosis and fibrosis	2017[199]

							symptoms for MFH group with a tumor inhibition rate of 67 %.	
Fe_3O_4 PEG[1] Trastuzumab (TRA)	100	SK-BR-3	10 mg/kg	Intravenous	230 kHz:NI:20 min	43-medium	MFH therapy extended the survival rate of mice to 33 % in a 30 days course of treatment.	2017[406]
Fe_3O_4 NGO[16]-PLGA[12] IUdR	36.8	C6 glioma	2 mg/kg	Intravenous	13.56 MHz:40 kA/m:10 min	65-medium	MRI and Prussian blue staining reveled the higher localization of NPs in tumor under AMF.	2018[407]

PEG[1]: polyethylene glycol. PPZ[2]: Poly (organophosphazene). HSP70[3]: heat shock protein 70. MMSN@TRP[4]: magnetic mesoporous silica nanoparticles@ thermoresponsive polymer. DMSA[5:] dimercaptosuccinic acid (DMSA. N6L[6]: Nucant multivalent pseudopeptide. HAP[7]: hydroxyapatite. EGFR[8]: epidermal growth factor receptor p(HEMA-co-DMA)[9]: poly (2-hydroxyethyl methacrylateco-dopamine methacrylamide). PS[10]: polystyrene. TNF-α[11]: Tumor necrosis factor. PLGA[12]: polylactic-co-glycolic acid. HPMC[13]: hydroxypropyl methylcellulose. PEG2000-DSPE[14]: 1,2-Distearoyl-sn-Glycero-3-Phosphoethanolamine-N-[Methoxy(Polyethylene glycol)-2000. PAA[15]: Poly (acrylic acid). Nano-graphene oxide. NGO[16]: Nano-graphene oxide.

3.5.6. Self-controlled MFH

When subjected to alternating MF, the temperature of IONPs would increase until their Curie temperature (T_C). T_C is the temperature above which IONPs experience a phase transition from feromagnetic to paramagnetic phase. Consequently, the coercivity (H_c) and remanence (M_r) become zero and magnetic moments are randomly oriented so that heat dissipation is stopped automatically.[111b] Unfortunately, IONPs possess very high intrinsic T_C, $T_{C,Fe3O4}$ ~ 585 °C (858 K) and $T_{C,\gamma\text{-}Fe2O3}$ ~ 447 °C (720 K), which is far higher than that of the therapeutically threshold temperature of 42 – 47 °C (315-320 K).[408] The inhomogeneous distribution of the NanoTherm® fluid together with an uncontrollable temperature rise within the fluid result in an inhomogeneity in temperature distribution throughout the targeted tumor area and non-specific necrosis of surrounding healthy tissues. As a result, the temperature of the treatment area is controlled externally in the current clinical setting by adjusting *f* and *H* in order to circumvent the overheating of cancer cells and the surrounding normal cells.[112] An intelligent strategy that has been proposed to bypass this challenge is self-controlled MFH. It utilizes T_C as an intrinsic thermo-regulating feature to control the temperature of tissue in a smart fashion by means of thermal seeds with T_C close to therapeutic range.[111b] A plethora of NPs have been proposed in recent years as potential candidates with ideal T_C for self-controlled MFH.

As instance, Brusentsova *et al.* achieved the T_C of 107.4 °C for 9 nm $Mn_{0.36}Zn_{0.64}Fe_2O_4$ NPs.[409] Hejase *et al.* reported the T_C of 56.33°C for 35 nm $Mn_{0.2}Zn_{0.8}Fe_2O_4$ NPs.[410] Li *et al.* achieved the T_C of 42.9 °C for 7 nm $Mn_{0.2}Zn_{0.8}Fe_2O_4$ NPs.[411] Apostolov *et al.* achieved the T_C of 42°C for spherical 20 nm $Me_{1-x}Zn_xFe_2O_4$ NPs (Me = Ni, Cu, Co, Mn) for x: 0.4 – 0.5.[412] Shimizu *et al.* synthesized 20 nm $Mg_{1.37}Fe_{1.26}Ti_{0.37}O_4$ thermal seeds with a T_C of 46°C.[413] Hanini *et al.* reported 11 nm spherical $Zn_{0.9}Fe_{2.1}O_4$ NPs with a T_C of 93°C.[414] Zhang *et al.* reported the tetragonal $Zn_{0.54}Co_{0.46}Cr_{0.6}Fe_{1.4O4}$ NPs (the edge length around 30 nm) with a T_C of 45.7°C.[415] Other studies include , T_C of 39 °C for $Ni_{1-x}Cr_x$ alloy,[416] T_C of 54 °C for 27 nm $La_{1-x}Sr_xMnO_3$ NPs, [112] T_C of ~ 40 °C for 13 nm $ZnGd_{0.02}Fe_{1.98}O_4$ NPs,[417] T_C of 42 °C for 50 nm $Zr_{0.5}Fe_{2.5}O_4$,[418] T_C of 70°C for 17 nm $La_{0.7}Sr_{0.3}Mn_{0.95}Ti_{0.05}O_3$,[419] T_C of 93 °C for 11 nm $Zn_{0.9}Fe_{2.1}O_4$,[414] T_C of 44 °C for 26.9 nm $La_{0.77}S_{0.23}MnO_3$,[420] T_C of 82 °C for 12 nm $Mn_{0.2}Zn_{0.8}Fe_2O_4$,[421] T_C of 39 °C for 24 nm $Co_{0.4}Zn_{0.6}Fe_2O_4$,[422] T_C of 42 °C for 44 nm $La_{0.85}Sr_{0.15}MnO_3$,[423] and T_C of 89 °C for 20.9 nm $La_{0.75}Sr_{0.25}MnO_3$ NPs[424] respectively. The

major drawbacks associated with the proposed systems is poor biocompatibility and lower Ms values. In few studies, stable TC below 50 °C was successfully achieved during MFH with a lower concentration (0.5 to 10 mg/mL).[425] Nevertheless, such a low concentration may does not meet the clinical threshold of therapeutic temperature.[418] Additionally, very little research has been conducted on *in vitro* and *in vivo* examination of self-controlled MFH. In an *in vivo* study, Soleymani *et al*. synthesized silica coated La0.73Sr0.27MnO3 NPs for self-controlled MFH with close TC of 59 °C to the therapeutic temperature.[408]

3.5.7. Magnetic particle imaging (MPI) for MFH

Precise prior knowledge of the targeting and spatial localization of magnetic fluid in the targeted tumor zone is an important prerequisite to delineate an optimal treatment plan for a successful MFH. Currently, computed tomography (CT) is the anatomic imaging technique for clinical visualisation of fluid in MFH. It provided the high median detection rate of 89.5 % for injected fluid,[37] nevertheless it exposes patients to X-ray ionizing radiation. Since the treatment is been performed repeatedly, this could causes some health risks specifically for patients with chronic kidney disease.[426] Notably, MRI is not being used as a diagnostic tool in MFH to monitor the progress of therapy because of the signal loss in the areas of interest due to relatively high fluid doses.[427] These impediments necessitate the establishment of technology that empower spatial selective localization of fluid in the tumor region.

Magnetic particle imaging (MPI) has been proposed as an alternative tomographic diagnostic tool that utilizes the direct quantitative measurement of intense non-linear magnetization of Fe_3O_4 tracers in a non-invasive manner.[428] This relatively new technology results in high resolution three dimensional (3D) imaging of the spatial distribution and concentration of IONPs after their intravenous administration into the blood stream. MPI presents some significant advantages over other routinely used diagnostic clinical imaging modalities such as computed tomography (CT), magnetic resonance imaging (MRI), single photon emission computed tomography (SPECT) and positron emission tomography (PET). MPI uses a different magnetism recording mechanism as compared with MRI to detect IONPs traces.

By probing the electronic magnetization of IONPs directly, it gains advantages such as the zero tissue background signal, exquisite sensitivity (200 nM Fe) and fast image resolving times. In contrast, MRI indirectly visualises the nuclear magnetization of surrounding water

molecules with poor contrast and slow image collection times. For MPI, the ability to operate at low frequency of MF (20 kHz, 16 kA/m), favors the quantitative imaging of tissue at any depth even in the lungs and bones with zero signal depth attenuation.[429] MPI is a safe, radiation-free scanning probe, in contrast to CT scanning and nuclear imaging platforms such as PET and SPECT that utilize ionizing radiation of X-ray, positrons and γ rays. This distinctive assemblage of features has rendered MPI with a plethora of applications such as angiography,[430] brain perfusion,[431] cancer detection,[426a] gut bleed detection,[432] stem cell tracking,[433] cardiovascular and disease monitoring.[434]

Tasci *et al.* initiated the possibility of the integration of MPI and MFH into one unified image-guided theranostic framework for simultaneous diagnostic and therapeutic MPI/MFH modes. The central idea is that the same injected nanomagnetic fluid could be excited with alternating MF to generate signal and heat for visualisation of tumor position and destruction of tumor latterly.[435] This initial concept were further developed in other research works.[188, 436] For instance, Murase *et al.* probed the efficacy of the idea under various AMF and SMF condition for MPI-based temperature control in MFH. They also proposed an empirical equation to measure SAR values in the presence of both AMF and SMF. The results revealed a reduction in SAR values on increased strength of SMF.[437]

Zhi *et al.* demonstrated the viability of the idea in humans thanks to their *in vivo* studies on mice through the theoretical foundation and technical construction of MPI/MFH theranostic platform. Whilst, MPI scan (at 20 kHz, 16 kA/m) clearly visualised the biodistribution of Fe_3O_4 NPs tracers in tumor and liver (healthy clearance organs) with high contrast, the temperature rise was negligible. However, when the frequency increased to 354 kHz, tumor temperature increased to 43°C in only 12 min. Furthermore, histological assessment, confirmed the localization of heat to the target tumor with sparing the liver. The issue with this idea is that typical employed excitation *f* (20 kHz) and *H* (16 kA/m) in MPI are insufficient to actuate potential heating by IONPs. A next important direction therefore, might be optimizing Fe_3O_4 tracers to explore as potential candidates to deposit enough heat in MPI relevant conditions for simultaneous MPI/MFH applications.[110a]

3.5.8. Other proposed candidates for MFH

Among the various magnetic particles that have presented promising magnetic features such as high saturation magnetization, initial susceptibility and anisotropy constant (K_{eff}),

IONPs are the only clinically established fluids used for MFH applications thus far. The advantage of IONPs over other inorganic nanostructures is their proven biocompatability, low toxicity, excellent chemical stability and *in vivo* metabolization-ability even though they possess lower M_s and heating potentials.[438] In an attempt to achieve higher SAR/SLP values, several other inorganic nanostructures have been proposed in the field in recent years as alternative candidates instead of IONPs.[439] Nanoscale metallic magnetic such as NPs iron (Fe), nickel (Ni) and cobalt (Co) exhibits interesting properties such as narrow size distribution, large magnetic anisotropy, high coercivity, high magnetic moment, and saturation magnetization compared to their oxide counterparts.[440] For instance, Fe presents a M_s of about 218 A m^2 kg^{-1} higher than that of Fe_3O_4 with an M_s of 93 A m^2 kg^{-1} at 300 K.[441] Considering their potency for MFH, Zeisberger *et al.* synthesized metallic Co NPs by thermolysis of $Co_2(CO)_8$ with size of 6 nm and M_s of 77.5 A m^2 kg^{-1} for MFH applications. The achieved SLP through calorimetrical measurements varied from 500 to 1300 W/g at f = 410 kHz and H_0 = 13–25 kA/m.[27a] Mehdaoui *et al.* synthesized cubic shape ferromagnetic Fe(0) NPs with size of 16 nm and M_s of 200 ± 10 Am^2/kg. The NPs presented a high SAR value of 1690 ± 160 W/g at f = 300 kHz and H_0 = 53 kA/m.[76a] The challenges with metallic NPs is their poor biocompatibility and chemical stability, high oxidation ability, and pyrophoricity at room temperature.[442] To address these deficiencies, two or more metallic particles have been merged to form metallic alloy NPs such as Cu-Ni,[443] Fe-Co,[444] Ni–Cr[416], Fe–Co–Au[445] and Fe–Cr–Nb–B[446] in an effort to improve resistance towards oxidation.[443, 447] Cart *et al*. synthesized Fe – Co magnetic alloy coated SiO_2 utilizing a novel urea-assisted sol-gel route with size ranging between 3 to 8 nm. The alloy exhibited significant magnetization (M_s = 245 A m^2 kg^{-1}) but the ferromagnetic behaviour was disadvantageous for MFH applications.[448]

Finally, Gold NPs have been studied as a new possible candidate for MFH applications.[449] Opposed to bulk gold with diamagnetic feature, it has unrevealed that gold NPs in the range of 1.4 – 5 nm display permanent magnetism in zero field at room temperature. This magnetization were more pronounced when gold was capped with dodecanethiol as a strong binding agent.[450] Similar magnetization behavior was observed for Ag and Cu-capped-dodecanethiol synthesized using the same method.[450c] Additionally, Ackerson *et al*.

reported that $Au_{102}(p\text{MBA})_{44}$ nanocluster exhibited paramagnetic characteristics and could create heat through Néel and Brownian relaxations similar to that of IONPs.[450a]

Milestones in the history of MFH has been shown in pictorial form (Figure 3.14). As discussed in Section 2, MFH was initiated by Jordan *et al.* at 1993 followed by the first preclinical *in vivo* MFH in 1997. The first clinical phase I MFH was conducted on patients bearing prostate carcinoma at Charité Hospital jointly with MagForce in 2006. In order to address the phycological and technological hurdles of the commercial fluid and treatment set up, a large amount of research has been undertaken by the MFH community. The result has been the introduction of various magnetic fluids with much higher ILP values than current commercial ones including magnetosomes, cube and disc shape IONPs, metallic Fe and Co NPs, doped Fe_3O_4 NPs and exchange-coupled core-shell MNPs. Additionally, near infrared (NIR) light has been proposed as another source of activating Fe_3O_4 for MFH.

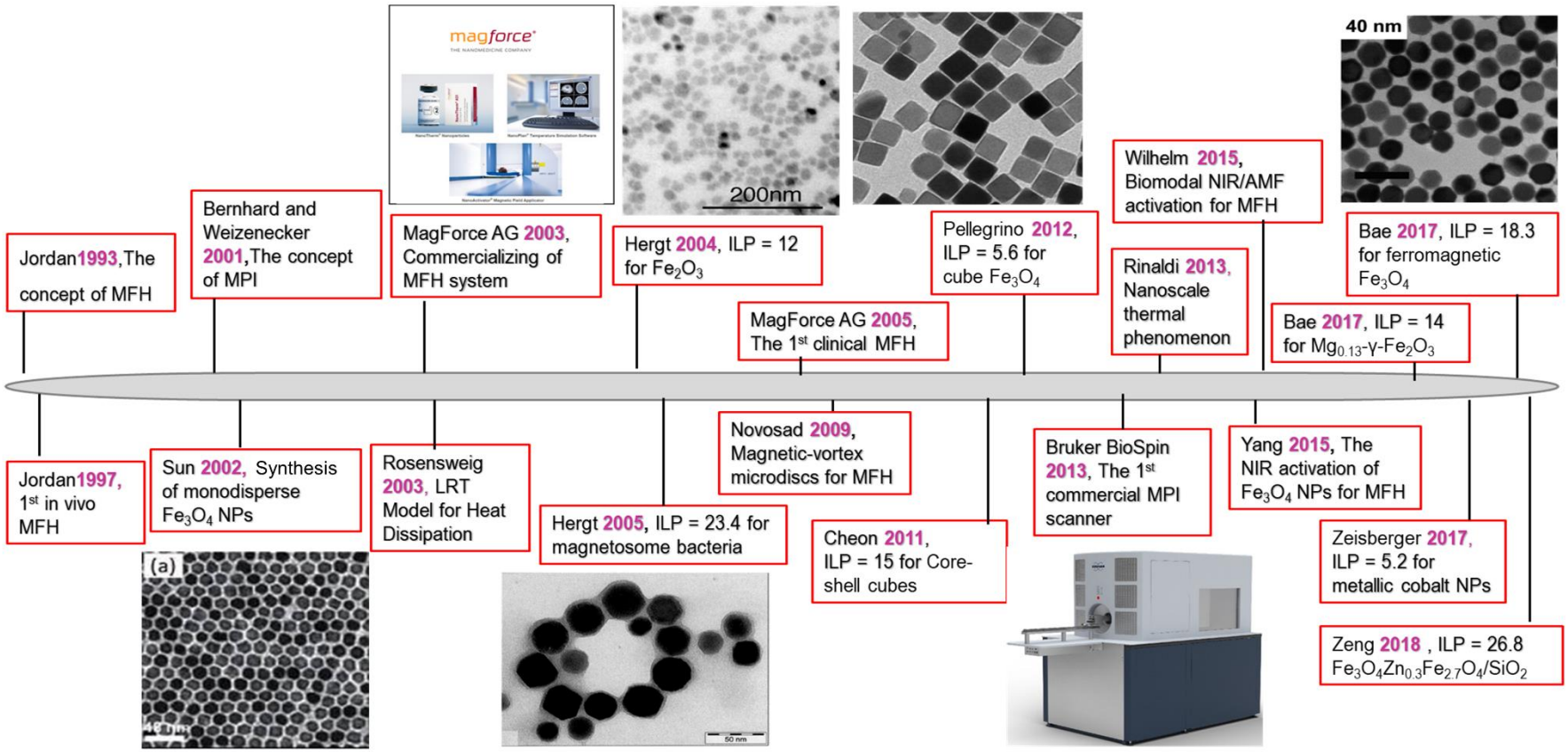

Figure 3.14.A historical perspective of MFH from the initial proposal of the idea to *in vivo* and clinical MFH application. Included are milestones achieved by the MFH community with regards to step - wise improvement in the heating potential of synthesized fluids as indicated by ILP values. MFH (magnetic fluid hyperthermia), MPI (magnetic particle imaging), LRT (linear response theory), ILP (intrinsic loss power), NIR (near-infrared (NIR) light, AMF (alternating magnetic field). The milestones information can be found in the following papers: Jordan 1993[31], Jordan 1997[32b], Bernhard 2001[428b], Sun 2002[120b], Rosensweig 2002[64],Hergt 2004[137],Hergt 2005[121a], Novosad 2009[370], Cheon 2012[250], Pellegrino2012[189], Rinaldi 2013[451], Yang 2015[276], Wilhelm 2015[327], Bae 2107[235], Zeisberger 2107[27a], Bao 2017[144] and Zeng 2018[252].

3.6. Conclusion and outlook

In this review article, we have comprehensively covered the fundamentals of MFH as a promising non-invasive technique for cancer treatment, the technological impediments in clinical settings and massive contributions from different laboratories through a growing body of experimental and theoretical investigations towards the realization of MFH. Relaxation or hysteresis loss mechanisms were initially proposed as the critical pathways to trigger cell death. In addition, magnetically mediated energy delivery (MagMED) also called nanoscale thermal phenomenon has also been proposed as another potential way to destroy cancer cells. Optimizing the intrinsic features of IONPs by modulating their geometry, size, size distribution, crystallinity and compositional tuning has shown promising potential to enhance the heating potency of IONPs. Furthermore, supplementary techniques such as chemotherapy, PTT, PDT and Targeted Nanoscale MFH has led to a much more profound therapeutic index over MFH monotherapy. Though inspirational results have been achieved, there is still much room for further advancement in the field and additional work is needed to promote the possible potential of MFH. The problem with the ongoing research in the field is the inconsistency in experimental set-up in terms of utilized concentration of the fluid and MF parameters (f and H). This variation has made the comparison of the published results infeasible. Accordingly, a standardization is required so that scientific community works on the same experimental conditions under clinically stablished alternating MF conditions. Additionally, advanced instrumentation and high-throughput technologies is needed to maximise the concentration of MNPs in tumor areas and improve the focus of MF precisely on the tumors. Considering the small incremental improvement in SAR/SLP values in the past few decades, it is unlikely that several orders of magnitude improvements in SAR/SLP values are obtainable. Therefore, focus should be given on (i) quantifying the maximum allowable magnetic field for MFH treatment and improvements in obtaining a higher localization of engineered MNPs in cancer tumors via systemic delivery. As such, chemists, physicists, biologists and clinicians need to join forces for a closer interdisciplinary and multidisciplinary collaborative research to fulfill ambitious goals of successful clinical realization of MFH in the foreseeable future.

3.7. Acknowledgement

The authors gratefully acknowledge the New Zealand International Doctoral Research Scholarships (NZIDRS) committee for their financial support. The authors would like to thank Ms Jenna Buchanan for her help with proof reading.

3.8. References:

[1] WHO, Cancer, https://www.who.int/news-room/fact-sheets/detail/cancer, accessed: June, 2020.

[2] W. Fan, B. Yung, P. Huang, X. Chen, *Chem. Rev* **2017**, *117*, 13566.

[3] M. H. Falk, R. D. Issels, *Int J. Hyperthermia* **2001**, *17*, 1.

[4] S. H. Beachy, E. A. Repasky, *Int. J. Hyperthermia* **2011**, *27*, 344.

[5] a) M. P. Calatayud, E. Soler, T. E. Torres, E. Campos-Gonzalez, C. Junquera, M. R. Ibarra, G. F. Goya, *Sci. Rep* **2017**, *7*, 8627; b) C. A. Quinto, P. Mohindra, S. Tong, G. Bao, *Nanoscale* **2015**, *7*, 12728; c) B. Sanz, M. P. Calatayud, T. E. Torres, M. L. Fanarraga, M. R. Ibarra, G. F. Goya, *Biomaterials* **2017**, *114*, 62.

[6] a) B. Hildebrandt, P. Wust, O. Ahlers, A. Dieing, G. Sreenivasa, T. Kerner, R. Felix, H. Riess, *Crit. Rev. Oncol. Hematol.* **2002**, *43*, 33; b) A. Hervault, N. T. K. Thanh, *Nanoscale* **2014**, *6*, 11553.

[7] N. Lee, D. Yoo, D. Ling, M. H. Cho, T. Hyeon, J. Cheon, *Chem. Rev* **2015**, *115*, 10637.

[8] A. J. Giustini, A. A. Petryk, S. M. Cassim, J. A. Tate, I. Baker, P. J. Hoopes, *Nano Life* **2010**, *1*, 17.

[9] a) N. Nizam-Uddin, I. Elshafiey, *BioMed Research International* **2017**, *2017*, 5787484; b) G. Hegyi, G. P. Szigeti, A. Szász, *Evid. Based Complement. Alternat. Med* **2013**, *2013*, 672873; c) Z. Behrouzkia, Z. Joveini, B. Keshavarzi, N. Eyvazzadeh, R. Z. Aghdam, *Oman Med. J* **2016**, *31*, 89.

[10] a) D. Formica, S. Silvestri, *Biomed. Eng. Online* **2004**, *3*, 11; b) S. Laurent, S. Dutz, U. O. Häfeli, M. Mahmoudi, *Adv. Colloid Interface Sci* **2011**, *166*, 8.

[11] S. Laurent, D. Forge, M. Port, A. Roch, C. Robic, L. Vander Elst, R. N. Muller, *Chem. Rev* **2008**, *108*, 2064.

[12] a) J. Xie, G. Liu, H. S. Eden, H. Ai, X. Chen, *Acc. Chem. Res* **2011**, *44*, 883; b) Y. W. Jun, J. W. Seo, J. Cheon, *Acc. Chem. Res* **2008**, *41*, 179; c) Y.-w. Jun, J.-w. Seo, J. Cheon, *Acc. Chem. Res* **2008**, *41*, 179; d) A. H. Latham, M. E. Williams, *Acc. Chem. Res* **2008**, *41*, 411.

[13] V. Zablotskii, T. Polyakova, O. Lunov, A. Dejneka, *Sci. Rep* **2016**, *6*, 37407.

[14] a) A. Farzin, S. A. Etesami, J. Quint, A. Memic, A. Tamayol, *Adv. Healthcare Mater.* **2020**, *9*, 1901058; b) S. Tong, H. Zhu, G. Bao, *Mater. Today* **2019**, *31*, 86; c) G. Barrera, P. Allia, P. Tiberto, *Nanoscale* **2020**, *12*, 6360; d) C. Bárcena, A. K. Sra, J. Gao, in *Nanoscale Magnetic Materials and Applications*, (Eds: J. P. Liu, E. Fullerton, O. Gutfleisch, D. J. Sellmyer), Springer US, Boston, MA **2009**.

[15] M. Jeun, S. Lee, J. Kyeong Kang, A. Tomitaka, K. Wook Kang, Y. Il Kim, Y. Takemura, K.-W. Chung, J. Kwak, S. Bae, *Appl. Phys. Lett* **2012**, *100*, 092406.

[16] a) P. Kaur, M. L. Aliru, A. S. Chadha, A. Asea, S. Krishnan, *Int. J. Hyperthermia* **2016**, *32*, 76; b) M. Bañobre-López, A. Teijeiro, J. Rivas, *Rep. Pract. Oncol. Radiother* **2013**, *18*, 397.

[17] A. Muela, D. Muñoz, R. Martín-Rodríguez, I. Orue, E. Garaio, A. Abad Díaz de Cerio, J. Alonso, J. Á. García, M. L. Fdez-Gubieda, *J. Phys. Chem. C* **2016**, *120*, 24437.

[18] a) J. Jung-tak, L. Jooyoung, S. Jiyun, J. Eric, K. Minkyu, K. Y. Il, K. M. Gyu, T. Yasushi, A. A. Syed, K. K. Wook, P. K. Ho, P. S. Ha, B. Seongtae, *Adv. Mater* **2018**, *30*, 1704362; b) Z. Nemati, S. M. Salili, J. Alonso, A. Ataie, R. Das, M. H. Phan, H. Srikanth, *J. Alloys Compd.* **2017**, *714*, 709; c) M. P. Morales, S. Veintemillas-Verdaguer, M. I. Montero, C. J. Serna, A. Roig, L. Casas, B. Martínez, F. Sandiumenge, *Chem. Mater* **1999**, *11*, 3058; d) A. Sathya, P. Guardia, R. Brescia, N. Silvestri, G. Pugliese, S. Nitti, L. Manna, T. Pellegrino, *Chem. Mater* **2016**, *28*, 1769.

[19] a) Y. Yang, X. Liu, Y. Lv, T. S. Herng, X. Xu, W. Xia, T. Zhang, J. Fang, W. Xiao, J. Ding, *Adv. Funct. Mater* **2015**, *25*, 812; b) A. Walter, C. Billotey, A. Garofalo, C. Ulhaq-Bouillet, C. Lefèvre, J. Taleb, S. Laurent, L. Vander Elst, R. N. Muller, L. Lartigue, F. Gazeau, D. Felder-Flesch, S. Begin-Colin, *Chem. Mater* **2014**, *26*, 5252; c) D. Niculaes, A. Lak, G. C. Anyfantis, S. Marras, O. Laslett, S. K. Avugadda, M. Cassani, D. Serantes, O. Hovorka, R. Chantrell, T. Pellegrino, *ACS Nano* **2017**, *11*, 12121; d) L. Lartigue, D. Alloyeau, J. Kolosnjaj-Tabi, Y. Javed, P. Guardia, A. Riedinger, C. Péchoux, T. Pellegrino, C. Wilhelm, F. Gazeau, *ACS Nano* **2013**, *7*, 3939; e) M. Levy, A. Quarta, A. Espinosa, A. Figuerola, C. Wilhelm, M. García-Hernández, A.

Genovese, A. Falqui, D. Alloyeau, R. Buonsanti, P. D. Cozzoli, M. A. García, F. Gazeau, T. Pellegrino, *Chem. Mater* **2011**, *23*, 4170; f) P. Bender, J. Fock, C. Frandsen, M. F. Hansen, C. Balceris, F. Ludwig, O. Posth, E. Wetterskog, L. K. Bogart, P. Southern, W. Szczerba, L. Zeng, K. Witte, C. Grüttner, F. Westphal, D. Honecker, D. González-Alonso, L. Fernández Barquín, C. Johansson, *J. Phys. Chem. C* **2018**, *122*, 3068.

[20] a) B. Luigjes, S. M. C. Woudenberg, R. de Groot, J. D. Meeldijk, H. M. Torres Galvis, K. P. de Jong, A. P. Philipse, B. H. Erné, *J. Phys. Chem. C* **2011**, *115*, 14598; b) R. Hergt, S. Dutz, M. Röder, *J. Phys.: Condens. Matter* **2008**, *20*, 385214.

[21] a) Y. V. Kolen'ko, M. Bañobre-López, C. Rodríguez-Abreu, E. Carbó-Argibay, A. Sailsman, Y. Piñeiro-Redondo, M. F. Cerqueira, D. Y. Petrovykh, K. Kovnir, O. I. Lebedev, J. Rivas, *J. Phys. Chem. C* **2014**, *118*, 8691; b) Y. Eom, M. Abbas, H. Noh, C. Kim, *RSC Adv* **2016**, *6*, 15861.

[22] X. Liu, Y. Zhang, Y. Wang, W. Zhu, G. Li, X. Ma, Y. Zhang, S. Chen, S. Tiwari, K. Shi, S. Zhang, H. M. Fan, Y. X. Zhao, X.-J. Liang, *Theranostics* **2020**, *10*, 3793.

[23] a) L. León Félix, B. Sanz, V. Sebastián, T. E. Torres, M. H. Sousa, J. A. H. Coaquira, M. R. Ibarra, G. F. Goya, *Sci. Rep* **2019**, *9*, 4185; b) J. B. Vines, J.-H. Yoon, N.-E. Ryu, D.-J. Lim, H. Park, *Front. Chem* **2019**, *7*, 167.

[24] a) S. Vasseur, E. Duguet, J. Portier, G. Goglio, S. Mornet, E. Hadová, K. Knížek, M. Maryško, P. Veverka, E. Pollert, *J. Magn. Magn. Mater* **2006**, *302*, 315; b) L. Bubnovskaya, A. Belous, S. Solopan, A. Kovelskaya, L. Bovkun, A. Podoltsev, I. Kondtratenko, S. Osinsky, *J. Nanoparticles* **2014**, *2014*, 278761.

[25] a) E. Mazario, N. Menéndez, P. Herrasti, M. Cañete, V. Connord, J. Carrey, *J. Phys. Chem. C* **2013**, *117*, 11405; b) C. Iacovita, A. Florea, L. Scorus, E. Pall, R. Dudric, A. I. Moldovan, R. Stiufiuc, R. Tetean, C. M. Lucaciu, *Nanomaterials* **2019**, *9*, 1489; c) R. G. D. Andrade, S. R. S. Veloso, E. M. S. Castanheira, *Int. J. Mol. Sci* **2020**, *21*, 2455.

[26] a) T.-I. Yang, S.-H. Chang, *Nanotechnology* **2016**, *28*, 055601; b) C. G. Hadjipanayis, M. J. Bonder, S. Balakrishnan, X. Wang, H. Mao, G. C. Hadjipanayis, *Small* **2008**, *4*, 1925; c) G. Song, M. Kenney, Y.-S. Chen, X. Zheng, Y. Deng, Z. Chen, S. X. Wang, S. S. Gambhir, H. Dai, J. Rao, *Nat. Biomed. Eng* **2020**, *4*, 325.

[27] a) M. Zeisberger, S. Dutz, R. Müller, R. Hergt, N. Matoussevitch, H. Bönnemann, *J. Magn. Magn. Mater* **2007**, *311*, 224; b) Y. Xu, M. Mahmood, Z. Li, E. Dervishi, S. Trigwell, V. P. Zharov, N. Ali, V. Saini, A. R. Biris, D. Lupu, D. Boldor, A. S. Biris, *Nanotechnology* **2008**, *19*, 435102.

[28] a) V. Sagar, V. S. R. Atluri, A. Tomitaka, P. Shah, A. Nagasetti, S. Pilakka-Kanthikeel, N. El-Hage, A. McGoron, Y. Takemura, M. Nair, *Sci. Rep* **2016**, *6*, 29792; b) X. Xu, H. Lu, R. Lee, *Fronti. Bioeng. Biotech* **2020**, *8*; c) C. Koo, H. Hong, P. W. Im, H. Kim, C. Lee, X. Jin, B. Yan, W. Lee, H.-J. Im, S. H. Paek, Y. Piao, *Nano Converg* **2020**, *7*, 20.

[29] R. K. Gilchrist, R. Medal, W. D. Shorey, R. C. Hanselman, J. C. Parrott, C. B. Taylor, *Ann. Surg* **1957**, *146*, 596.

[30] R. T. Gordon, J. R. Hines, D. Gordon, *Med. Hypotheses* **1979**, *5*, 83.

[31] A. Jordan, P. Wust, H. Fähling, W. John, A. Hinz, R. Felix, *Int J. Hyperthermia* **1993**, *9*, 51.

[32] a) A. Jordan, R. Scholz, P. Wust, H. Schirra, S. Thomas, H. Schmidt, R. Felix, *J. Magn. Magn. Mater* **1999**, *194*, 185; b) A. Jordan, R. Scholz, P. Wust, H. Fähling, J. Krause, W. Wlodarczyk, B. Sander, T. Vogl, R. Felix, *Int J. Hyperthermia* **1997**, *13*, 587.

[33] A. Jordan, R. Scholz, K. Maier-Hauff, F. K. H. van Landeghem, N. Waldoefner, U. Teichgraeber, J. Pinkernelle, H. Bruhn, F. Neumann, B. Thiesen, A. von Deimling, R. Felix, *J. Neurooncol* **2006**, *78*, 7.

[34] a) M. Johannsen, A. Jordan, R. Scholz, M. Koch, M. Lein, S. Deger, J. Roigas, K. Jung, S. Loening, *J. Endourol* **2004**, *18*, 495; b) M. Johannsen, B. Thiesen, U. Gneveckow, K. Taymoorian, N. Waldöfner, R. Scholz, S. Deger, K. Jung, S. A. Loening, A. Jordan, *The Prostate* **2005**, *66*, 97; c) M. Johannsen, B. Thiesen, A. Jordan, K. Taymoorian, U. Gneveckow, N. Waldöfner, R. Scholz, M. Koch, M. Lein, K. Jung, S. A. Loening, *The Prostate* **2005**, *64*, 283.

[35] A. Jordan, R. Scholz, K. Maier-Hauff, M. Johannsen, P. Wust, J. Nadobny, H. Schirra, H. Schmidt, S. Deger, S. Loening, W. Lanksch, R. Felix, *J. Magn. Magn. Mater* **2001**, *225*, 118.

[36] a) Wust, gt, Peter, U. Gneveckow, Wust, gt, Peter, U. Gneveckow, M. Johannsen, D. Böhmer, T. Henkel, F. Kahmann, J. Sehouli, R. Felix, J. Ricke, A. Jordan, *Int J. Hyperthermia* **2006**, *22*, 673; b) K. Maier-Hauff, F. Ulrich, D. Nestler, H. Niehoff, P. Wust, B. Thiesen, H. Orawa, V. Budach, A. Jordan, *J. Neurooncol* **2011**, *103*, 317; c) K. Maier-Hauff, R. Rothe, R.

Scholz, U. Gneveckow, P. Wust, B. Thiesen, A. Feussner, A. von Deimling, N. Waldoefner, R. Felix, A. Jordan, *J. Neurooncol* **2007**, *81*, 53; d) F. K. H. van Landeghem, K. Maier-Hauff, A. Jordan, K.-T. Hoffmann, U. Gneveckow, R. Scholz, B. Thiesen, W. Brück, A. von Deimling, *Biomaterials* **2009**, *30*, 52; e) M. Johannsen, U. Gneveckow, L. Eckelt, A. Feussner, N. WaldÖFner, R. Scholz, S. Deger, P. Wust, S. A. Loening, A. Jordan, *Int J. Hyperthermia* **2005**, *21*, 637; f) M. Johannsen, U. Gneveckow, K. Taymoorian, B. Thiesen, N. Waldöfner, R. Scholz, K. Jung, A. Jordan, P. Wust, S. A. Loening, *Int J. Hyperthermia* **2007**, *23*, 315.

[37] M. Johannsen, U. Gneveckow, B. Thiesen, K. Taymoorian, C. H. Cho, N. Waldöfner, R. Scholz, A. Jordan, S. A. Loening, P. Wust, *Eur. Urol* **2007**, *52*, 1653.

[38] a) S. V. Spirou, M. Basini, A. Lascialfari, C. Sangregorio, C. Innocenti, *Nanomaterials (Basel)* **2018**, *8*, 401; b) T. N. C. MagForce AG, The NanoTherm® therapy, https://www.magforce.com/en/home/our_therapy/, accessed: June, 2020.

[39] S. Mørup, M. F. Hansen, C. Frandsen, in *Comprehensive Nanoscience and Nanotechnology (Second Edition)*, (Eds: D. L. Andrews, R. H. Lipson, T. Nann), Academic Press, Oxford **2019**.

[40] a) Z. Nedelkoski, D. Kepaptsoglou, L. Lari, T. Wen, R. A. Booth, S. D. Oberdick, P. L. Galindo, Q. M. Ramasse, R. F. L. Evans, S. Majetich, V. K. Lazarov, *Sci. Rep* **2017**, *7*, 45997; b) H. Song, H. Lee, J. Lee, J. K. Choe, S. Lee, J. Y. Yi, S. Park, J.-W. Yoo, M. S. Kwon, J. Kim, *Nano Lett* **2020**.

[41] a) J. Mohapatra, J. P. Liu, in *Handbook of Magnetic Materials*, Vol. 27 (Ed: E. Brück), Elsevier, Amsterdam, Netherlands **2018**; b) Z. Shaterabadi, G. Nabiyouni, M. Soleymani, *Prog. Biophys. Mol. Biol* **2018**, *133*, 9.

[42] F. Heider, D. J. Dunlop, N. Sugiura, *Science* **1987**, *236*, 1287.

[43] C. L. Dennis, R. Ivkov, *Int J. Hyperthermia* **2013**, *29*, 715.

[44] a) A. P. Roberts, T. P. Almeida, N. S. Church, R. J. Harrison, D. Heslop, Y. Li, J. Li, A. R. Muxworthy, W. Williams, X. Zhao, *J. Geophys. Res.: Solid Earth* **2017**, *122*, 9534; b) S. Levi, R. T. Merrill, *J. Geophys. Res.: Solid Earth* **1978**, *83*, 309.

[45] a) H. Kirchmayr, in *Encyclopedia of Materials: Science and Technology*, (Eds: K. H. J. Buschow, R. W. Cahn, M. C. Flemings, B. Ilschner, E. J. Kramer, S. Mahajan, P. Veyssière),

Elsevier, Oxford, UK **2001**; b) M. S. S. Brooks, M. Richter, L. M. Sandratskii, in *Encyclopedia of Materials: Science and Technology*, (Eds: K. H. J. Buschow, R. W. Cahn, M. C. Flemings, B. Ilschner, E. J. Kramer, S. Mahajan, P. Veyssière), Elsevier, Oxford, UK **2001**.

[46] G. Cheng, D. Romero, G. T. Fraser, A. R. Hight Walker, *Langmuir* **2005**, *21*, 12055.

[47] S. Dutz, R. Hergt, *Nanotechnology* **2014**, *25*, 452001.

[48] a) E. C. Stoner, E. P. Wohlfarth, *IEEE Trans. Magn* **1991**, *27*, 3475; b) M. H. Mahmoud, A. M. Elshahawy, S. A. Makhlouf, H. H. Hamdeh, *J. Magn. Magn. Mater* **2013**, *343*, 21.

[49] B. D. Cullity, C. D. Graham, *Introduction to Magnetic Materials*, John Wiley & Sons, Inc., Hoboken, NJ, USA **2008**.

[50] a) G. Kandasamy, D. Maity, *Int. J. Pharm* **2015**, *496*, 191; b) M. Mikhaylova, D. K. Kim, N. Bobrysheva, M. Osmolowsky, V. Semenov, T. Tsakalakos, M. Muhammed, *Langmuir* **2004**, *20*, 2472.

[51] I. J. Bruvera, P. Mendoza Zélis, M. Pilar Calatayud, G. F. Goya, F. H. Sánchez, *J. Appl. Phys* **2015**, *118*, 184304.

[52] a) D. Ramimoghadam, S. Bagheri, S. B. A. Hamid, *J. Magn. Magn. Mater* **2014**, *368*, 207; b) I. Belyanina, O. Kolovskaya, S. Zamay, A. Gargaun, T. Zamay, A. Kichkailo, *Mol. Cells* **2017**, *22*, 975.

[53] A. E. Deatsch, B. A. Evans, *J. Magn. Magn. Mater* **2014**, *354*, 163.

[54] a) A. G. Kolhatkar, A. C. Jamison, D. Litvinov, R. C. Willson, T. R. Lee, *Int. J. Mol. Sci* **2013**, *14*, 15977; b) R. Hergt, S. Dutz, M. Röder, *J Phys Condens Matter* **2008**, *20*, 385214; c) G. Podaru, V. Chikan, in *Magnetic Nanomaterials: Applications in Catalysis and Life Sciences*, Vol. 26 (Eds: S. H. Bossman, H. Wang), The Royal Society of Chemistry, Croydon, UK **2017**; d) M. Montazer, T. Harifi, in *Nanofinishing of Textile Materials*, (Eds: M. Montazer, T. Harifi), Woodhead Publishing, **2018**.

[55] a) R. F. Butler, S. K. Banerjee, *J. Geophys. Res* **1975**, *80*, 4049; b) C. Justin, S. A. Philip, A. V. Samrot, *Appl. Nanosci* **2017**, *7*, 463.

[56] a) J. Baumgartner, L. Bertinetti, M. Widdrat, A. M. Hirt, D. Faivre, *PLoS One* **2013**, *8*, e57070; b) J. A. Fuentes-García, A. I. Diaz-Cano, A. Guillen-Cervantes, J. Santoyo-Salazar, *Sci. Rep* **2018**, *8*, 5096; c) G. Kandasamy, D. Maity, *Int. J. Pharm* **2015**, *496*, 191; d) Y.-w. Jun, Y.-

M. Huh, J.-s. Choi, J.-H. Lee, H.-T. Song, KimKim, S. Yoon, K.-S. Kim, J.-S. Shin, J.-S. Suh, J. Cheon, *J. Am. Chem. Soc* **2005**, *127*, 5732; e) D. L. Huber, *Small* **2005**, *1*, 482.

[57] a) S. Dutz, R. Hergt, J. Mürbe, R. Müller, M. Zeisberger, W. Andrä, J. Töpfer, M. E. Bellemann, *J. Magn. Magn. Mater* **2007**, *308*, 305; b) V. Reichel, A. Kovács, M. Kumari, É. Bereczk-Tompa, E. Schneck, P. Diehle, M. Pósfai, A. M. Hirt, M. Duchamp, R. E. Dunin-Borkowski, D. Faivre, *Sci. Rep* **2017**, *7*, 45484.

[58] D. L. Leslie-Pelecky, R. D. Rieke, *Chem. Mater* **1996**, *8*, 1770.

[59] a) M. Ma, Y. Wu, J. Zhou, Y. Sun, Y. Zhang, N. Gu, *J. Magn. Magn. Mater* **2004**, *268*, 33; b) H. Iida, K. Takayanagi, T. Nakanishi, T. Osaka, *J. Colloid Interface Sci* **2007**, *314*, 274; c) J. Santoyo Salazar, L. Perez, O. de Abril, L. Truong Phuoc, D. Ihiawakrim, M. Vazquez, J.-M. Greneche, S. Begin-Colin, G. Pourroy, *Chem. Mater* **2011**, *23*, 1379.

[60] Q. Li, C. W. Kartikowati, S. Horie, T. Ogi, T. Iwaki, K. Okuyama, *Sci. Rep* **2017**, *7*, 9894.

[61] a) Y. Xiao, J. Du, *J. Mater. Chem. B* **2020**, *8*, 354; b) F.-Y. Cheng, C.-H. Su, Y.-S. Yang, C.-S. Yeh, C.-Y. Tsai, C.-L. Wu, M.-T. Wu, D.-B. Shieh, *Biomaterials* **2005**, *26*, 729.

[62] a) P. Tartaj, M. a. d. P. Morales, S. Veintemillas-Verdaguer, T. Gonz lez-Carre o, C. J. Serna, *J. Phys. D: Appl. Phys* **2003**, *36*, R182; b) A. K. Gupta, R. R. Naregalkar, V. D. Vaidya, M. Gupta, *Nanomedicine* **2007**, *2*, 23.

[63] D. Kim, N. Lee, M. Park, B. H. Kim, K. An, T. Hyeon, *J. Am. Chem. Soc* **2009**, *131*, 454.

[64] R. E. Rosensweig, *J. Magn. Magn. Mater* **2002**, *252*, 370.

[65] E. A. Périgo, G. Hemery, O. Sandre, D. Ortega, E. Garaio, F. Plazaola, F. J. Teran, *Appl. Phys. Rev* **2015**, *2*, 041302.

[66] a) N. A. Usov, Y. B. Grebenshchikov, *J. Appl. Phys* **2009**, *106*, 023917; b) Ö. Çelik, T. Fırat, *J. Magn. Magn. Mater* **2018**, *456*, 11.

[67] S. Ota, Y. Takemura, *J. Phys. Chem. C* **2019**, *123*, 28859.

[68] R. Hergt, S. Dutz, R. Müller, M. Zeisberger, *J. Phys.: Condens. Matter* **2006**, *18*, S2919.

[69] a) R. Hergt, S. Dutz, M. Zeisberger, *Nanotechnology* **2009**, *21*, 015706; b) R. Hergt, W. Andra, C. G. d'Ambly, I. Hilger, W. A. Kaiser, U. Richter, H. Schmidt, *IEEE Trans. Magn* **1998**, *34*, 3745.

[70] H. Delavari H, H. R. Madaah Hosseini, M. Wolff, *J. Magn. Magn. Mater* **2013**, *335*, 59.

[71] B. Jeyadevan, *J. Ceram. Soc. Jpn* **2010**, *118*, 391.

[72] M. Kallumadil, M. Tada, T. Nakagawa, M. Abe, P. Southern, Q. A. Pankhurst, *J. Magn. Magn. Mater* **2009**, *321*, 1509.

[73] R. Hergt, S. Dutz, *J. Magn. Magn. Mater* **2007**, *311*, 187.

[74] J. Carrey, B. Mehdaoui, M. Respaud, *J. Appl. Phys* **2011**, *109*, 083921.

[75] a) F. Shubitidze, K. Kekalo, R. Stigliano, I. Baker, *J. Appl. Phys* **2015**, *117*, 094302; b) G. Glöckl, R. Hergt, M. Zeisberger, S. Dutz, S. Nagel, W. Weitschies, *J. Phys.: Condens. Matter* **2006**, *18*, S2935; c) R. Müller, S. Dutz, A. Neeb, A. C. B. Cato, M. Zeisberger, *J. Magn. Magn. Mater* **2013**, *328*, 80.

[76] a) B. Mehdaoui, A. Meffre, L. M. Lacroix, J. Carrey, S. Lachaize, M. Gougeon, M. Respaud, B. Chaudret, *J. Magn. Magn. Mater.* **2010**, *322*, L49; b) P. Pradhan, J. Giri, G. Samanta, H. D. Sarma, K. P. Mishra, J. Bellare, R. Banerjee, D. Bahadur, *J. Biomed. Mater. Res., Part B* **2007**, *81B*, 12.

[77] M. T. Thompson, *IEEE Trans. Magn* **1998**, *34*, 3755.

[78] a) W. J. Atkinson, I. A. Brezovich, D. P. Chakraborty, *IEEE Trans. Biomed. Eng* **1984**, *31*, 70; b) E. Kita, T. Oda, T. Kayano, S. Sato, M. Minagawa, H. Yanagihara, M. Kishimoto, C. Mitsumata, S. Hashimoto, K. Yamada, N. Ohkohchi, *J. Phys. D: Appl. Phys* **2010**, *43*, 474011.

[79] R. Ivkov, S. J. DeNardo, W. Daum, A. R. Foreman, R. C. Goldstein, V. S. Nemkov, G. L. DeNardo, *Clin. Cancer Res* **2005**, *11*, 7093s.

[80] I. Andreu, E. Natividad, *Int J. Hyperthermia* **2013**, *29*, 739.

[81] K. Hynynen, D. DeYoung, M. Kundrat, E. Moros, *Int J. Hyperthermia* **1989**, *5*, 485.

[82] H. H. Pennes, *J. Appl. Physiol* **1948**, *1*, 93.

[83] B. Kozissnik, A. C. Bohorquez, J. Dobson, C. Rinaldi, *Int J. Hyperthermia* **2013**, *29*, 706.

[84] a) E. Garaio, J. M. Collantes, J. A. Garcia, F. Plazaola, S. Mornet, F. Couillaud, O. Sandre, *J. Magn. Magn. Mater* **2014**, *368*, 432; b) J. Mohapatra, F. Zeng, K. Elkins, M. Xing, M. Ghimire, S. Yoon, S. R. Mishra, J. P. Liu, *PCCP* **2018**, *20*, 12879; c) S. A. Gudoshnikov, B. Y.

Liubimov, Y. S. Sitnov, V. S. Skomarovsky, N. A. Usov, *J*. Supercond. Nov. Magn **2013**, *26*, 857.

[85] a) M. Coïsson, G. Barrera, F. Celegato, L. Martino, S. N. Kane, S. Raghuvanshi, F. Vinai, P. Tiberto, *Biochim. Biophys. Acta, Gen. Subj* **2017**, *1861*, 1545; b) S. A. Gudoshnikov, B. Y. Liubimov, N. A. Usov, *AIP Advances* **2012**, *2*, 012143; c) D. W. Wong, W. L. Gan, Y. K. Teo, W. S. Lew, *Nanoscale Res. Lett* **2019**, *14*, 376.

[86] a) I. Hilger, K. Frühauf, W. Andrä, R. Hiergeist, R. Hergt, W. A. Kaiser, *Acad. Radiol* **2002**, *9*, 198; b) S. K. Jones, J. G. Winter, *Phys. Med. Biol* **2001**, *46*, 385.

[87] a) S. K. Venkatasubramaniam, H. Bumsoo, E. H. Bruce, W. S. Thomas, C. B. John, *Nanotechnology* **2005**, *16*, 1221; b) Z. Dong-Lin, Z. Hai-Long, Z. Xian-Wei, X. Qi-Sheng, T. Jin-Tian, *Biomed. Mater* **2006**, *1*, 198.

[88] F. R. Harley, C. Gustavo, M. M. Francyelli, Z. Nicholas, S.-L. Elisângela, F. B. Andris, *Phys. Med. Biol* **2017**, *62*, 4062.

[89] C. A. Monnier, F. Crippa, C. Geers, E. Knapp, B. Rothen-Rutishauser, M. Bonmarin, M. Lattuada, A. Petri-Fink, *J. Phys. Chem. C* **2017**, *121*, 27164.

[90] K. Maier-Hauff, F. Ulrich, D. Nestler, H. Niehoff, P. Wust, B. Thiesen, H. Orawa, V. Budach, A. Jordan, *J. Neurooncol* **2011**, *103*, 317.

[91] a) I. Gresits, G. Thuróczy, O. Sági, B. Gyüre-Garami, B. G. Márkus, F. Simon, *Sci. Rep.* **2018**, *8*, 12667; b) A. Miaskowski, M. Subramanian, *Int. J. Mol. Sci* **2019**, *20*, 4644.

[92] P. Lemal, C. Geers, B. Rothen-Rutishauser, M. Lattuada, A. Petri-Fink, *Mater. Today: Proc.* **2017**, *4*, S107.

[93] I. Andreu, E. Natividad, *Int J. Hyperthermia* **2013**, *29*, 739.

[94] M. Domenech, I. Marrero-Berrios, M. Torres-Lugo, C. Rinaldi, *ACS Nano* **2013**, *7*, 5091.

[95] Y. Rabin, *Int J. Hyperthermia* **2002**, *18*, 194.

[96] P. Keblinski, D. G. Cahill, A. Bodapati, C. R. Sullivan, T. A. Taton, *J. Appl. Phys* **2006**, *100*, 054305.

[97] A. Gupta, R. S. Kane, D.-A. Borca-Tasciuc, *J. Appl. Phys* **2010**, *108*, 064901.

[98] H. Huang, S. Delikanli, H. Zeng, D. M. Ferkey, A. Pralle, *Nat Nanotechnol* **2010**, *5*, 602.

[99] a) M. Creixell, A. C. Bohórquez, M. Torres-Lugo, C. Rinaldi, *ACS Nano* **2011**, *5*, 7124; b) C. Sanchez, D. El Hajj Diab, V. Connord, P. Clerc, E. Meunier, B. Pipy, B. Payré, R. P. Tan, M. Gougeon, J. Carrey, V. Gigoux, D. Fourmy, *ACS Nano* **2014**, *8*, 1350; c) V. Connord, P. Clerc, N. Hallali, D. El Hajj Diab, D. Fourmy, V. Gigoux, J. Carrey, *Small* **2015**, *11*, 2437; d) E. Zhang, M. F. Kircher, M. Koch, L. Eliasson, S. N. Goldberg, E. Renström, *ACS Nano* **2014**, *8*, 3192.

[100] D. Cheng, X. Li, G. Zhang, H. Shi, *Nanoscale Res. Lett* **2014**, *9*, 195.

[101] R. J. Mannix, S. Kumar, F. Cassiola, M. Montoya-Zavala, E. Feinstein, M. Prentiss, D. E. Ingber, *Nat Nanotechnol* **2007**, *3*, 36.

[102] A. M. Master, P. N. Williams, N. Pothayee, N. Pothayee, R. Zhang, H. M. Vishwasrao, Y. I. Golovin, J. S. Riffle, M. Sokolsky, A. V. Kabanov, *Sci. Rep* **2016**, *6*, 33560.

[103] a) M. E. de Sousa, A. Carrea, P. Mendoza Zélis, D. Muraca, O. Mykhaylyk, Y. E. Sosa, R. G. Goya, F. H. Sánchez, R. A. Dewey, M. B. Fernández van Raap, *J. Phys. Chem. C* **2016**, *120*, 7339; b) O. Sandre, C. Genevois, E. Garaio, L. Adumeau, S. Mornet, F. Couillaud, *Genes* **2017**, *8*, 61.

[104] H. Huang, S. Delikanli, H. Zeng, D. M. Ferkey, A. Pralle, *Nat. Nanotechnol* **2010**, *5*, 602.

[105] A. Chiu-Lam, C. Rinaldi, *Adv. Funct. Mater* **2016**, *26*, 3933.

[106] a) R. Di Corato, G. Béalle, J. Kolosnjaj-Tabi, A. Espinosa, O. Clément, A. K. A. Silva, C. Ménager, C. Wilhelm, *ACS Nano* **2015**, *9*, 2904; b) D. Yoo, H. Jeong, C. Preihs, J.-s. Choi, T.-H. Shin, J. L. Sessler, J. Cheon, *Angew. Chem. Int. Ed* **2012**, *51*, 12482.

[107] L. Kafrouni, O. Savadogo, *Prog. Biomater* **2016**, *5*, 147.

[108] S. Dutz, J. H. Clement, D. Eberbeck, T. Gelbrich, R. Hergt, R. Müller, J. Wotschadlo, M. Zeisberger, *J. Magn. Magn. Mater* **2009**, *321*, 1501.

[109] A. A. Golneshan, M. Lahonian, *Mech. Res. Commun* **2011**, *38*, 425.

[110] a) Z. W. Tay, P. Chandrasekharan, A. Chiu-Lam, D. W. Hensley, R. Dhavalikar, X. Y. Zhou, E. Y. Yu, P. W. Goodwill, B. Zheng, C. Rinaldi, S. M. Conolly, *ACS Nano* **2018**, *12*, 3699; b) A. Attaluri, S. K. Kandala, M. Wabler, H. Zhou, C. Cornejo, M. Armour, M. Hedayati, Y. Zhang, T. L. DeWeese, C. Herman, R. Ivkov, *Int J. Hyperthermia* **2015**, *31*, 359.

[111] a) I. Apostolova, J. M. Wesselinowa, *Solid State Commun* **2009**, *149*, 986; b) W. Zhang, C. Wu, S. R. P. Silva, *Expert Rev. Anticancer Ther* **2018**, *18*, 723.

[112] E. Natividad, M. Castro, G. Goglio, I. Andreu, R. Epherre, E. Duguet, A. Mediano, *Nanoscale* **2012**, *4*, 3954.

[113] N. A. Usov, J. **Appl**. Phys **2010**, *107*, 123909.

[114] G. Salas, J. Camarero, D. Cabrera, H. Takacs, M. Varela, R. Ludwig, H. Dähring, I. Hilger, R. Miranda, M. d. P. Morales, F. J. Teran, *J. Phys. Chem. C* **2014**, *118*, 19985.

[115] H. Rudolf, D. Silvio, R. Michael, *J. Phys.: Condens. Matter* **2008**, *20*, 385214.

[116] W. Baaziz, B. P. Pichon, S. Fleutot, Y. Liu, C. Lefevre, J.-M. Greneche, M. Toumi, T. Mhiri, S. Begin-Colin, *J. Phys. Chem. C* **2014**, *118*, 3795.

[117] F. Gazeau, M. Lévy, C. Wilhelm, *Nanomedicine* **2008**, *3*, 831.

[118] Q. A. Pankhurst, J. Connolly, S. K. Jones, J. Dobson, *J. Phys. D: Appl. Phys* **2003**, *36*, R167.

[119] a) J. Park, K. An, Y. Hwang, J.-G. Park, H.-J. Noh, J.-Y. Kim, J.-H. Park, N.-M. Hwang, T. Hyeon, *Nat. Mater* **2004**, *3*, 891; b) T. Hyeon, S. S. Lee, J. Park, Y. Chung, H. B. Na, *J. Am. Chem. Soc* **2001**, *123*, 12798; c) J. Park, E. Lee, N.-M. Hwang, M. Kang, S. C. Kim, Y. Hwang, J.-G. Park, H.-J. Noh, J.-Y. Kim, J.-H. Park, T. Hyeon, *Angew. Chem. Int. Ed* **2005**, *44*, 2872; d) S.-J. Park, S. Kim, S. Lee, Z. G. Khim, K. Char, T. Hyeon, *J. Am. Chem. Soc* **2000**, *122*, 8581; e) B. H. Kim, N. Lee, H. Kim, K. An, Y. I. Park, Y. Choi, K. Shin, Y. Lee, S. G. Kwon, H. B. Na, J.-G. Park, T.-Y. Ahn, Y.-W. Kim, W. K. Moon, S. H. Choi, T. Hyeon, *J. Am. Chem. Soc* **2011**, *133*, 12624; f) Y. Lee, J. Lee, C. J. Bae, J.-G. Park, H.-J. Noh, J.-H. Park, T. Hyeon, *Adv. Funct. Mater* **2005**, *15*, 503.

[120] a) S. Sun, H. Zeng, D. B. Robinson, S. Raoux, P. M. Rice, S. X. Wang, G. Li, *J. Am. Chem. Soc* **2004**, *126*, 273; b) S. Sun, H. Zeng, *J. Am. Chem. Soc* **2002**, *124*, 8204; c) Z. Xu, C. Shen, Y. Hou, H. Gao, S. Sun, *Chem. Mater* **2009**, *21*, 1778; d) S. Peng, S. Sun, *Angew. Chem. Int. Ed.* **2007**, *46*, 4155; e) H. Zhu, S. Zhang, Y.-X. Huang, L. Wu, S. Sun, *Nano Lett* **2013**, *13*, 2947.

[121] a) R. Hergt, R. Hiergeist, M. Zeisberger, D. Schüler, U. Heyen, I. Hilger, W. A. Kaiser, *J. Magn. Magn. Mater* **2005**, *293*, 80; b) E. Céspedes, J. M. Byrne, N. Farrow, S. Moise, V. S. Coker, M. Bencsik, J. R. Lloyd, N. D. Telling, *Nanoscale* **2014**, *6*, 12958; c) R. Le Fèvre, M.

Durand-Dubief, I. Chebbi, C. Mandawala, F. Lagroix, J.-P. Valet, A. Idbaih, C. Adam, J.-Y. Delattre, C. Schmitt, C. Maake, F. Guyot, E. Alphandéry, *Theranostics* **2017**, *7*, 4618; d) J. Xie, K. Chen, X. Chen, *Nano Res* **2009**, *2*, 261.

[122] a) M. Jeun, S. Park, G. H. Jang, K. H. Lee, *ACS Appl. Mater. Interfaces* **2014**, *6*, 16487; b) V. M. Khot, A. B. Salunkhe, N. D. Thorat, R. S. Ningthoujam, S. H. Pawar, *Dalton Trans* **2013**, *42*, 1249; c) M. Jeun, J. W. Jeoung, S. Moon, Y. J. Kim, S. Lee, S. H. Paek, K.-W. Chung, K. H. Park, S. Bae, *Biomaterials* **2011**, *32*, 387; d) G. S. Ningombam, R. S. Ningthoujam, S. N. Kalkura, N. R. Singh, *J. Phys. Chem. B* **2018**, *122*, 6862.

[123] a) H. Zeng, J. Li, J. P. Liu, Z. L. Wang, S. Sun, *Nature* **2002**, *420*, 395; b) V. Nandwana, R. Zhou, J. Mohapatra, S. Kim, P. V. Prasad, J. P. Liu, V. P. Dravid, *ACS Appl. Mater. Interfaces* **2018**, *10*, 27233; c) V. Pilati, R. Cabreira Gomes, G. Gomide, P. Coppola, F. G. Silva, F. L. O. Paula, R. Perzynski, G. F. Goya, R. Aquino, J. Depeyrot, *J. Phys. Chem. C* **2018**, *122*, 3028.

[124] a) A. Tomitaka, H. Arami, A. Raymond, A. Yndart, A. Kaushik, R. D. Jayant, Y. Takemura, Y. Cai, M. Toborek, M. Nair, *Nanoscale* **2017**, *9*, 764; b) F. Mohammad, G. Balaji, A. Weber, R. M. Uppu, C. S. S. R. Kumar, *J. Phys. Chem. C* **2010**, *114*, 19194; c) M. Ravichandran, G. Oza, S. Velumani, J. T. Ramirez, F. Garcia-Sierra, N. B. Andrade, A. Vera, L. Leija, M. A. Garza-Navarro, *Sci. Rep* **2016**, *6*, 34874; d) I. Urries, C. Muñoz, L. Gomez, C. Marquina, V. Sebastian, M. Arruebo, J. Santamaria, *Nanoscale* **2014**, *6*, 9230; e) C. Bao, J. Conde, F. Pan, C. Li, C. Zhang, F. Tian, S. Liang, J. M. de la Fuente, D. Cui, *Nano Res* **2016**, *9*, 1043; f) P. Wang, J. Sun, Z. Lou, F. Fan, K. Hu, Y. Sun, N. Gu, *Adv. Mater* **2016**, *28*, 10801.

[125] a) A. Ereath Beeran, F. B. Fernandez, P. R. H. Varma, *ACS Biomater. Sci. Eng* **2018**; b) M. Yoonessi, B. A. Lerch, J. A. Peck, R. B. Rogers, F. J. Solá-Lopez, M. A. Meador, *ACS Appl. Mater. Interfaces* **2015**, *7*, 16932.

[126] a) K. Hayashi, M. Moriya, W. Sakamoto, T. Yogo, *Chem. Mater* **2009**, *21*, 1318; b) A. Hervault, A. E. Dunn, M. Lim, C. Boyer, D. Mott, S. Maenosono, N. T. K. Thanh, *Nanoscale* **2016**, *8*, 12152; c) S. Patra, E. Roy, P. Karfa, S. Kumar, R. Madhuri, P. K. Sharma, *ACS Appl. Mater. Interfaces* **2015**, *7*, 9235; d) H. Kakwere, M. P. Leal, M. E. Materia, A. Curcio, P. Guardia, D. Niculaes, R. Marotta, A. Falqui, T. Pellegrino, *ACS Appl. Mater. Interfaces* **2015**, *7*, 10132; e) A. Cervadoro, M. Cho, J. Key, C. Cooper, C. Stigliano, S. Aryal, A. Brazdeikis, J. F. Leary, P. Decuzzi, *ACS Appl. Mater. Interfaces* **2014**, *6*, 12939; f) T. T. T. N'Guyen, H. T. T.

Duong, J. Basuki, V. Montembault, S. Pascual, C. Guibert, J. Fresnais, C. Boyer, M. R. Whittaker, T. P. Davis, L. Fontaine, *Angew. Chem. Int. Ed* **2013**, *52*, 14152; g) I. Andreu, E. Natividad, L. Solozábal, O. Roubeau, *ACS Nano* **2015**, *9*, 1408.

[127] M. Gonzales-Weimuller, M. Zeisberger, K. M. Krishnan, *J. Magn. Magn. Mater* **2009**, *321*, 1947.

[128] a) M. Mahmoudi, S. Sant, B. Wang, S. Laurent, T. Sen, *Adv Drug Deliv Rev* **2011**, *63*, 24; b) W. Wu, Z. Wu, T. Yu, C. Jiang, W.-S. Kim, *Sci. Technol. Adv. Mater* **2015**, *16*, 023501; c) S. Gul, S. B. Khan, I. U. Rehman, M. A. Khan, M. I. Khan, *Front. Mater* **2019**, *6*.

[129] a) M. Mahmoudi, S. Sant, B. Wang, S. Laurent, T. Sen, *Adv. Drug Delivery Rev* **2011**, *63*, 24; b) R. Hao, R. Xing, Z. Xu, Y. Hou, S. Gao, S. Sun, *Adv. Mater* **2010**, *22*, 2729; c) N. A. Frey, S. Peng, K. Cheng, S. Sun, *Chem. Soc. Rev* **2009**, *38*, 2532; d) L. Wu, A. Mendoza-Garcia, Q. Li, S. Sun, *Chem. Rev* **2016**, *116*, 10473.

[130] S. Xuan, Y.-X. J. Wang, J. C. Yu, K. Cham-Fai Leung, *Chem. Mater* **2009**, *21*, 5079.

[131] A. Demortière, P. Panissod, B. P. Pichon, G. Pourroy, D. Guillon, B. Donnio, S. Bégin-Colin, *Nanoscale* **2011**, *3*, 225.

[132] R. Y. Hong, B. Feng, L. L. Chen, G. H. Liu, H. Z. Li, Y. Zheng, D. G. Wei, *Biochem. Eng. J* **2008**, *42*, 290.

[133] J. Ge, Y. Hu, M. Biasini, W. P. Beyermann, Y. Yin, *Angew. Chem. Int. Ed* **2007**, *46*, 4342.

[134] S. D. Oberdick, A. Abdelgawad, C. Moya, S. Mesbahi-Vasey, D. Kepaptsoglou, V. K. Lazarov, R. F. L. Evans, D. Meilak, E. Skoropata, J. van Lierop, I. Hunt-Isaak, H. Pan, Y. Ijiri, K. L. Krycka, J. A. Borchers, S. A. Majetich, *Sci. Rep* **2018**, *8*, 3425.

[135] a) C. Cao, S.-J. Liu, S.-L. Yao, T.-F. Zheng, Y.-Q. Chen, J.-L. Chen, H.-R. Wen, *Cryst. Growth Des* **2017**, *17*, 4757; b) D. Peddis, M. V. Mansilla, S. Mørup, C. Cannas, A. Musinu, G. Piccaluga, F. D'Orazio, F. Lucari, D. Fiorani, *J. Phys. Chem. B* **2008**, *112*, 8507.

[136] J.-P. Fortin, C. Wilhelm, J. Servais, C. Ménager, J.-C. Bacri, F. Gazeau, *J. Am. Chem. Soc* **2007**, *129*, 2628.

[137] R. Hergt, R. Hiergeist, I. Hilger, W. A. Kaiser, Y. Lapatnikov, S. Margel, U. Richter, *J. Magn. Magn. Mater* **2004**, *270*, 345.

[138] B. Mehdaoui, A. Meffre, J. Carrey, S. Lachaize, L.-M. Lacroix, M. Gougeon, B. Chaudret, M. Respaud, *Adv. Funct. Mater* **2011**, *21*, 4573.

[139] L. Michael, W. Claire, S. Jean-Michel, H. Olivier, B. Jean-Claude, G. Florence, *J. Phys.: Condens. Matter* **2008**, *20*, 204133.

[140] S. Mornet, S. Vasseur, F. Grasset, E. Duguet, *J. Mater. Chem* **2004**, *14*, 2161.

[141] Z. Nemati, J. Alonso, L. M. Martinez, H. Khurshid, E. Garaio, J. A. Garcia, M. H. Phan, H. Srikanth, *J. Phys. Chem. C* **2016**, *120*, 8370.

[142] C. L. Dennis, A. J. Jackson, J. A. Borchers, R. Ivkov, A. R. Foreman, J. W. Lau, E. Goernitz, C. Gruettner, *J. Appl. Phys* **2008**, *103*, 07A319.

[143] H. Rudolf, D. Silvio, Z. Matthias, *Nanotechnology* **2010**, *21*, 015706.

[144] S. Tong, C. A. Quinto, L. Zhang, P. Mohindra, G. Bao, *ACS Nano* **2017**, *11*, 6808.

[145] a) V. Patsula, M. Moskvin, S. Dutz, D. Horák, *J. Phys. Chem. Solids* **2016**, *88*, 24; b) S. Dutz, M. E. Bellemann, U. Leder, J. Haueisen, *Phys. Med. Biol* **2006**, *51*, 145.

[146] Suriyanto, E. Y. K. Ng, S. D. Kumar, *Biomed. Eng. Online* **2017**, *16*, 36.

[147] S. Dutz, *IEEE Trans. Magn* **2016**, *52*, 1.

[148] a) A. G. Roca, S. Veintemillas-Verdaguer, M. Port, C. Robic, C. J. Serna, M. P. Morales, *J. Phys. Chem. B* **2009**, *113*, 7033; b) D. F. Coral, P. Mendoza Zélis, M. Marciello, M. d. P. Morales, A. Craievich, F. H. Sánchez, M. B. Fernández van Raap, *Langmuir* **2016**, *32*, 1201.

[149] G. Klughertz, L. Friedland, P.-A. Hervieux, G. Manfredi, *Phys. Rev. B* **2015**, *91*, 104433.

[150] a) Y. Lalatonne, J. Richardi, M. P. Pileni, *Nat. Mater* **2004**, *3*, 121; b) S. Singamaneni, V. N. Bliznyuk, C. Binek, E. Y. Tsymbal, *J. Mater. Chem* **2011**, *21*, 16819; c) L. Gutiérrez, L. de la Cueva, M. Moros, E. Mazarío, S. de Bernardo, J. M. de la Fuente, M. P. Morales, G. Salas, *Nanotechnology* **2019**, *30*, 112001.

[151] L. L. Castro, M. F. da Silva, A. F. Bakuzis, R. Miotto, *J. Magn. Magn. Mater* **2005**, *293*, 553.

[152] B. Sanz, M. P. Calatayud, E. De Biasi, E. Lima Jr, M. V. Mansilla, R. D. Zysler, M. R. Ibarra, G. F. Goya, *Sci. Rep* **2016**, *6*, 38733.

[153] A. Urtizberea, E. Natividad, A. Arizaga, M. Castro, A. Mediano, *J. Phys. Chem. C* **2010**, *114*, 4916.

[154] C. Guibert, V. Dupuis, V. Peyre, J. Fresnais, *J. Phys. Chem. C* **2015**, *119*, 28148.

[155] a) C. Haase, U. Nowak, *Phys. Rev. B* **2012**, *85*, 045435; b) R. Fu, Y. Yan, C. Roberts, Z. Liu, Y. Chen, *Sci. Rep* **2018**, *8*, 4704.

[156] a) A. J. Giustini, R. Ivkov, P. J. Hoopes, *Nanotechnology* **2011**, *22*, 345101; b) M. Hedayati, O. Thomas, B. Abubaker-Sharif, H. Zhou, C. Cornejo, Y. Zhang, M. Wabler, J. Mihalic, C. Gruettner, F. Westphal, A. Geyh, T. L. Deweese, R. Ivkov, *Nanomedicine (London, U. K.)* **2013**, *8*, 29; c) M. L. Etheridge, K. R. Hurley, J. Zhang, S. Jeon, H. L. Ring, C. Hogan, C. L. Haynes, M. Garwood, J. C. Bischof, *Technology* **2014**, *2*, 214.

[157] S. Jeon, K. R. Hurley, J. C. Bischof, C. L. Haynes, C. J. Hogan, *Nanoscale* **2016**, *8*, 16053.

[158] a) U. Sakulkhu, M. Mahmoudi, L. Maurizi, J. Salaklang, H. Hofmann, *Sci. Rep* **2014**, *4*, 5020; b) G. Stepien, M. Moros, M. Pérez-Hernández, M. Monge, L. Gutiérrez, R. M. Fratila, M. d. las Heras, S. Menao Guillén, J. J. Puente Lanzarote, C. Solans, J. Pardo, J. M. de la Fuente, *ACS Appl. Mater. Interfaces* **2018**, *10*, 4548; c) M. Mahmoudi, S. E. Lohse, C. J. Murphy, A. Fathizadeh, A. Montazeri, K. S. Suslick, *Nano Lett* **2014**, *14*, 6.

[159] J. G. Ovejero, D. Cabrera, J. Carrey, T. Valdivielso, G. Salas, F. J. Teran, *PCCP* **2016**, *18*, 10954.

[160] K. L. Chen, S. E. Mylon, M. Elimelech, *Langmuir* **2007**, *23*, 5920.

[161] C. L. Dennis, A. J. Jackson, J. A. Borchers, P. J. Hoopes, R. Strawbridge, A. R. Foreman, J. van Lierop, C. Grüttner, R. Ivkov, *Nanotechnology* **2009**, *20*, 395103.

[162] D. Serantes, K. Simeonidis, M. Angelakeris, O. Chubykalo-Fesenko, M. Marciello, M. d. P. Morales, D. Baldomir, C. Martinez-Boubeta, *J. Phys. Chem. C* **2014**, *118*, 5927.

[163] B. Mehdaoui, R. P. Tan, A. Meffre, J. Carrey, S. Lachaize, B. Chaudret, M. Respaud, *Phys. Rev. B* **2013**, *87*, 174419.

[164] S. Dutz, M. Kettering, I. Hilger, R. Müller, M. Zeisberger, *Nanotechnology* **2011**, *22*, 265102.

[165] L. Lartigue, P. Hugounenq, D. Alloyeau, S. P. Clarke, M. Lévy, J. C. Bacri, R. Bazzi, D. F. Brougham, C. Wilhelm, F. Gazeau, *ACS Nano* **2012**, *6*, 10935.

[166] C. Blanco-Andujar, D. Ortega, P. Southern, Q. A. Pankhurst, N. T. K. Thanh, *Nanoscale* **2015**, *7*, 1768.

[167] a) M. Jeun, S. Bae, A. Tomitaka, Y. Takemura, K. H. Park, S. H. Paek, K.-W. Chung, *Appl. Phys. Lett* **2009**, *95*, 082501; b) P. de la Presa, Y. Luengo, V. Velasco, M. P. Morales, M. Iglesias, S. Veintemillas-Verdaguer, P. Crespo, A. Hernando, *J. Phys. Chem. C* **2015**, *119*, 11022.

[168] a) R. Moreno, S. Poyser, D. Meilak, A. Meo, S. Jenkins, V. K. Lazarov, G. Vallejo-Fernandez, S. Majetich, R. F. L. Evans, *Sci. Rep* **2020**, *10*, 2722; b) S. Geng, H. Yang, X. Ren, Y. Liu, S. He, J. Zhou, N. Su, Y. Li, C. Xu, X. Zhang, Z. Cheng, *Chem. Asian J.* **2016**, *11*, 2996.

[169] E. Josten, E. Wetterskog, A. Glavic, P. Boesecke, A. Feoktystov, E. Brauweiler-Reuters, U. Rücker, G. Salazar-Alvarez, T. Brückel, L. Bergström, *Sci. Rep* **2017**, *7*, 2802.

[170] M. V. Kovalenko, M. I. Bodnarchuk, R. T. Lechner, G. Hesser, F. Schäffler, W. Heiss, *J. Am. Chem. Soc* **2007**, *129*, 6352.

[171] J.-H. Lim, S.-G. Min, L. Malkinski, J. B. Wiley, *Nanoscale* **2014**, *6*, 5289.

[172] a) R. A. Bennett, H. A. Etman, H. Hicks, L. Richards, C. Wu, M. R. Castell, S. S. Dhesi, F. Maccherozzi, *Nano Lett* **2018**, *18*, 2365; b) O. Lupan, V. Postica, N. Wolff, O. Polonskyi, V. Duppel, V. Kaidas, E. Lazari, N. Ababii, F. Faupel, L. Kienle, R. Adelung, *Small* **2017**, *13*, 1602868.

[173] R. Das, J. Alonso, Z. Nemati Porshokouh, V. Kalappattil, D. Torres, M.-H. Phan, E. Garaio, J. Á. García, J. L. Sanchez Llamazares, H. Srikanth, *J. Phys. Chem. C* **2016**, *120*, 10086.

[174] F. Ooi, J. S. DuChene, J. Qiu, J. O. Graham, M. H. Engelhard, G. Cao, Z. Gai, W. D. Wei, *Small* **2015**, *11*, 2649.

[175] Z. Zhou, X. Zhu, D. Wu, Q. Chen, D. Huang, C. Sun, J. Xin, K. Ni, J. Gao, *Chem. Mater* **2015**, *27*, 3505.

[176] H. Wang, T. B. Shrestha, M. T. Basel, M. Pyle, Y. Toledo, A. Konecny, P. Thapa, M. Ikenberry, K. L. Hohn, V. Chikan, D. L. Troyer, S. H. Bossmann, *J. Mater. Chem. B* **2015**, *3*, 4647.

[177] C. Li, R. Wei, Y. Xu, A. Sun, L. Wei, *Nano Res* **2014**, *7*, 536.

[178] Z. Zhao, Z. Zhou, J. Bao, Z. Wang, J. Hu, X. Chi, K. Ni, R. Wang, X. Chen, Z. Chen, J. Gao, *Nat. Commun* **2013**, *4*, 2266.

[179] Z. Zhou, C. Wu, H. Liu, X. Zhu, Z. Zhao, L. Wang, Y. Xu, H. Ai, J. Gao, *ACS Nano* **2015**, *9*, 3012.

[180] C. S. B. Dias, T. D. M. Hanchuk, H. Wender, W. T. Shigeyosi, J. Kobarg, A. L. Rossi, M. N. Tanaka, M. B. Cardoso, F. Garcia, *Sci. Rep* **2017**, *7*, 14843.

[181] H. Khurshid, J. Alonso, Z. Nemati, M. H. Phan, P. Mukherjee, M. L. Fdez-Gubieda, J. M. Barandiarán, H. Srikanth, *J. Appl. Phys* **2015**, *117*, 17A337.

[182] a) T. Tanigaki, Y. Takahashi, T. Shimakura, T. Akashi, R. Tsuneta, A. Sugawara, D. Shindo, *Nano Lett* **2015**, *15*, 1309; b) X.-L. Liu, Y. Yang, J.-P. Wu, Y.-F. Zhang, H.-M. Fan, J. Ding, *Chin. Phys. B* **2015**, *24*, 127505.

[183] M. Ma, Y. Zhang, Z. Guo, N. Gu, *Nanoscale Res. Lett* **2013**, *8*, 16.

[184] J.-W. Yoo, N. Doshi, S. Mitragotri, *Macromol. Rapid Commun* **2010**, *31*, 142.

[185] W. Zhang, S. Haas, *Phys. Rev. B* **2010**, *81*, 064433.

[186] G. Zhen, B. W. Muir, B. A. Moffat, P. Harbour, K. S. Murray, B. Moubaraki, K. Suzuki, I. Madsen, N. Agron-Olshina, L. Waddington, P. Mulvaney, P. G. Hartley, *J. Phys. Chem. C* **2011**, *115*, 327.

[187] C. Martinez-Boubeta, K. Simeonidis, A. Makridis, M. Angelakeris, O. Iglesias, P. Guardia, A. Cabot, L. Yedra, S. Estradé, F. Peiró, Z. Saghi, P. A. Midgley, I. Conde-Leborán, D. Serantes, D. Baldomir, *Sci. Rep* **2013**, *3*, 1652.

[188] L. M. Bauer, S. F. Situ, M. A. Griswold, A. C. S. Samia, *Nanoscale* **2016**, *8*, 12162.

[189] P. Guardia, R. Di Corato, L. Lartigue, C. Wilhelm, A. Espinosa, M. Garcia-Hernandez, F. Gazeau, L. Manna, T. Pellegrino, *ACS Nano* **2012**, *6*, 3080.

[190] Z. Nemati, J. Alonso, I. Rodrigo, R. Das, E. Garaio, J. Á. García, I. Orue, M.-H. Phan, H. Srikanth, *J. Phys. Chem. C* **2018**, *122*, 2367.

[191] M. E. Materia, P. Guardia, A. Sathya, M. Pernia Leal, R. Marotta, R. Di Corato, T. Pellegrino, *Langmuir* **2015**, *31*, 808.

[192] L. Lartigue, C. Innocenti, T. Kalaivani, A. Awwad, M. d. M. Sanchez Duque, Y. Guari, J. Larionova, C. Guérin, J.-L. G. Montero, V. Barragan-Montero, P. Arosio, A. Lascialfari, D. Gatteschi, C. Sangregorio, *J. Am. Chem. Soc* **2011**, *133*, 10459.

[193] P. Hugounenq, M. Levy, D. Alloyeau, L. Lartigue, E. Dubois, V. Cabuil, C. Ricolleau, S. Roux, C. Wilhelm, F. Gazeau, R. Bazzi, *J. Phys. Chem. C* **2012**, *116*, 15702.

[194] E. C. Abenojar, S. Wickramasinghe, J. Bas-Concepcion, A. C. S. Samia, *Prog. Nat. Sci.: Mater. Int* **2016**, *26*, 440.

[195] X. L. Liu, Y. Yang, C. T. Ng, L. Y. Zhao, Y. Zhang, B. H. Bay, H. M. Fan, J. Ding, *Adv. Mater* **2015**, *27*, 1939.

[196] H.-M. Fan, M. Olivo, B. Shuter, J.-B. Yi, R. Bhuvaneswari, H.-R. Tan, G.-C. Xing, C.-T. Ng, L. Liu, S. S. Lucky, B.-H. Bay, J. Ding, *J. Am. Chem. Soc* **2010**, *132*, 14803.

[197] R. Di Corato, A. Espinosa, L. Lartigue, M. Tharaud, S. Chat, T. Pellegrino, C. Ménager, F. Gazeau, C. Wilhelm, *Biomaterials* **2014**, *35*, 6400.

[198] J. Kolosnjaj-Tabi, R. Di Corato, L. Lartigue, I. Marangon, P. Guardia, A. K. A. Silva, N. Luciani, O. Clément, P. Flaud, J. V. Singh, P. Decuzzi, T. Pellegrino, C. Wilhelm, F. Gazeau, *ACS Nano* **2014**, *8*, 4268.

[199] Q. Ding, D. Liu, D. Guo, F. Yang, X. Pang, R. Che, N. Zhou, J. Xie, J. Sun, Z. Huang, N. Gu, *Biomaterials* **2017**, *124*, 35.

[200] D. Faivre, D. Schüler, *Chem. Rev* **2008**, *108*, 4875.

[201] S. Bellini, Su di un particolare comportamento di batteri d'acqua dolce (On a unique behavior of freshwater bacteria), Institute of Microbiology, University of Pavia, Italy **1963**.

[202] R. P. Blakemore, *Annu. Rev. Microbiol* **1982**, *36*, 217.

[203] a) C. Chen, L. Chen, Y. Yi, C. Chen, L.-F. Wu, T. Song, *Appl. Environ. Microbiol* **2016**, *82*, 2219; b) C. Chen, L. Chen, P. Wang, L.-F. Wu, T. Song, *Nanomedicine* **2017**, *13*, 363.

[204] A. Plan Sangnier, S. Preveral, A. Curcio, A. K. A. Silva, C. T. Lefèvre, D. Pignol, Y. Lalatonne, C. Wilhelm, *J. Controlled Release* **2018**, *279*, 271.

[205] E. Alphandéry, S. Faure, L. Raison, E. Duguet, P. A. Howse, D. A. Bazylinski, *J. Phys. Chem. C* **2011**, *115*, 18.

[206] E. Alphandéry, C. Carvallo, N. Menguy, I. Chebbi, *J. Phys. Chem. C* **2011**, *115*, 11920.

[207] E. Alphandéry, M. Amor, F. Guyot, I. Chebbi, *Appl. Microbiol. Biotechnol* **2012**, *96*, 663.

[208] E. Alphandéry, S. Faure, O. Seksek, F. Guyot, I. Chebbi, *ACS Nano* **2011**, *5*, 6279.

[209] S. Mannucci, S. Tambalo, G. Conti, L. Ghin, A. Milanese, A. Carboncino, E. Nicolato, M. R. Marinozzi, D. Benati, R. Bassi, P. Marzola, A. Sbarbati, *Contrast Media Mol. Imaging* **2018**, *2018*, 12.

[210] a) E. Alphandéry, A. Idbaih, C. Adam, J.-Y. Delattre, C. Schmitt, F. Guyot, I. Chebbi, *J. Controlled Release* **2017**, *262*, 259; b) C. Mandawala, I. Chebbi, M. Durand-Dubief, R. Le Fèvre, Y. Hamdous, F. Guyot, E. Alphandéry, *J. Mater. Chem. B* **2017**, *5*, 7644; c) E. Alphandéry, F. Guyot, I. Chebbi, *Int. J. Pharm* **2012**, *434*, 444; d) E. Alphandéry, D. Abi Haidar, O. Seksek, F. Guyot, I. Chebbi, *Nanoscale* **2018**, *10*, 10918.

[211] T. Kumeria, S. Maher, Y. Wang, G. Kaur, L. Wang, M. Erkelens, P. Forward, M. F. Lambert, A. Evdokiou, D. Losic, *Biomacromolecules* **2016**, *17*, 2726.

[212] S. K. Alsaiari, A. H. Ezzedine, A. M. Abdallah, R. Sougrat, N. M. Khashab, *OpenNano* **2016**, *1*, 36.

[213] Y. Hamdous, I. Chebbi, C. Mandawala, R. Le Fèvre, F. Guyot, O. Seksek, E. Alphandéry, *J. Nanobiotechnol* **2017**, *15*, 74.

[214] S. Mannucci, S. Tambalo, G. Conti, L. Ghin, A. Milanese, A. Carboncino, E. Nicolato, M. R. Marinozzi, D. Benati, R. Bassi, P. Marzola, A. Sbarbati, *Contrast Media Mol. Imaging* **2018**, *2018*, 2198703.

[215] R.-t. Liu, J. Liu, J.-q. Tong, T. Tang, W.-C. Kong, X.-w. Wang, Y. Li, J.-t. Tang, *Prog. Nat. Sci.: Mater. Int* **2012**, *22*, 31.

[216] E. Alphandéry, A. Idbaih, C. Adam, J.-Y. Delattre, C. Schmitt, F. Guyot, I. Chebbi, *Biomaterials* **2017**, *141*, 210.

[217] S. Mannucci, L. Ghin, G. Conti, S. Tambalo, A. Lascialfari, T. Orlando, D. Benati, P. Bernardi, N. Betterle, R. Bassi, P. Marzola, A. Sbarbati, *PLoS One* **2014**, *9*, e108959.

[218] a) G. Vargas, J. Cypriano, T. Correa, P. Leão, D. A. Bazylinski, F. Abreu, *Mol. Cells* **2018**, *23*, 2438; b) Y. Liu, G. R. Li, F. F. Guo, W. Jiang, Y. Li, L. J. Li, *Microbial cell factories* **2010**, *9*, 99.

[219] a) L. Yang, L. Ma, J. Xin, A. Li, C. Sun, R. Wei, B. W. Ren, Z. Chen, H. Lin, J. Gao, *Chem. Mater* **2017**, *29*, 3038; b) X. Lasheras, M. Insausti, I. Gil de Muro, E. Garaio, F. Plazaola, M. Moros, L. De Matteis, J. M. de la Fuente, L. Lezama, *J. Phys. Chem. C* **2016**, *120*, 3492.

[220] a) J.-H. Lee, Y.-M. Huh, Y.-w. Jun, J.-w. Seo, J.-t. Jang, H.-T. Song, S. Kim, E.-J. Cho, H.-G. Yoon, J.-S. Suh, J. Cheon, *Nat. Med.* **2006**, *13*, 95; b) C. Liu, B. Zou, A. J. Rondinone, Z. J. Zhang, *J. Am. Chem. Soc.* **2000**, *122*, 6263.

[221] G. V. M. Jacintho, A. G. Brolo, P. Corio, P. A. Z. Suarez, J. C. Rubim, *J. Phys. Chem. C* **2009**, *113*, 7684.

[222] H. Deng, X. Li, Q. Peng, X. Wang, J. Chen, Y. Li, *Angew. Chem. Int. Ed* **2005**, *44*, 2782.

[223] J.-H. Lee, Y.-M. Huh, Y.-w. Jun, J.-w. Seo, J.-t. Jang, H.-T. Song, S. Kim, E.-J. Cho, H.-G. Yoon, J.-S. Suh, J. Cheon, *Nat. Med* **2007**, *13*, 95.

[224] S. K. Shaw, S. K. Alla, S. S. Meena, R. K. Mandal, N. K. Prasad, *J. Magn. Magn. Mater* **2017**, *434*, 181.

[225] L. Hu, C. de Montferrand, Y. Lalatonne, L. Motte, A. Brioude, *J. Phys. Chem. C* **2012**, *116*, 4349.

[226] M. F. Casula, E. Conca, I. Bakaimi, A. Sathya, M. E. Materia, A. Casu, A. Falqui, E. Sogne, T. Pellegrino, A. G. Kanaras, *PCCP* **2016**, *18*, 16848.

[227] V. Nandwana, S.-R. Ryoo, S. Kanthala, M. De, S. S. Chou, P. V. Prasad, V. P. Dravid, *ACS Appl. Mater. Interfaces* **2016**, *8*, 6953.

[228] Y. Yang, X. Liu, Y. Yang, W. Xiao, Z. Li, D. Xue, F. Li, J. Ding, *J. Mater. Chem. C* **2013**, *1*, 2875.

[229] Y. Qu, J. Li, J. Ren, J. Leng, C. Lin, D. Shi, *ACS Appl. Mater. Interfaces* **2014**, *6*, 16867.

[230] J. Jung-tak, N. Hyunsoo, L. Jae-Hyun, M. S. Ho, K. M. Gyu, C. Jinwoo, *Angew Chem. Int. Ed* **2009**, *48*, 1234.

[231] N. D. Thorat, R. A. Bohara, S. A. M. Tofail, Z. A. Alothman, M. J. A. Shiddiky, M. S. A Hossain, Y. Yamauchi, K. C. W. Wu*, *Eur. J. Inorg. Chem* **2016**, *2016*, 4586.

[232] N. D. Thorat, R. A. Bohara, H. M. Yadav, S. A. M. Tofail, *RSC Adv* **2016**, *6*, 94967.

[233] S. Matsuda, T. Nakanishi, K. Kaneko, T. Osaka, *Electrochim. Acta* **2015**, *183*, 153.

[234] K. Eiji, O. Tatsuya, K. Takeru, S. Suguru, M. Makoto, Y. Hideto, K. Mikio, M. Chiharu, H. Shinji, Y. Keiichi, O. Nobuhiro, *J. Phys. D: Appl. Phys* **2010**, *43*, 474011.

[235] J.-t. Jang, J. Lee, J. Seon, E. Ju, M. Kim, Y. I. Kim, M. G. Kim, Y. Takemura, A. S. Arbab, K. W. Kang, K. H. Park, S. H. Paek, S. Bae, *Adv. Mater* **2018**, *30*, 1704362.

[236] N. K. Prasad, K. Rathinasamy, D. Panda, D. Bahadur, *J. Mater. Chem* **2007**, *17*, 5042.

[237] A. Makridis, I. Chatzitheodorou, K. Topouridou, M. P. Yavropoulou, M. Angelakeris, C. Dendrinou-Samara, *Mater. Sci. Eng. C* **2016**, *63*, 663.

[238] S. Munjal, N. Khare, B. Sivakumar, D. Nair Sakthikumar, *J. Magn. Magn. Mater* **2018**.

[239] E. Fantechi, C. Innocenti, M. Zanardelli, M. Fittipaldi, E. Falvo, M. Carbo, V. Shullani, L. Di Cesare Mannelli, C. Ghelardini, A. M. Ferretti, A. Ponti, C. Sangregorio, P. Ceci, *ACS Nano* **2014**, *8*, 4705.

[240] M. Ma, Y. Zhang, X. Shen, J. Xie, Y. Li, N. Gu, *Nano Res* **2015**, *8*, 600.

[241] E. Roy, S. Patra, R. Madhuri, P. K. Sharma, *Colloids Surf. B* **2016**, *142*, 248.

[242] J. Xie, C. Yan, Y. Yan, L. Chen, L. Song, F. Zang, Y. An, G. Teng, N. Gu, Y. Zhang, *Nanoscale* **2016**, *8*, 16902.

[243] P. Drake, H.-J. Cho, P.-S. Shih, C.-H. Kao, K.-F. Lee, C.-H. Kuo, X.-Z. Lin, Y.-J. Lin, *J. Mater. Chem* **2007**, *17*, 4914.

[244] M. Lin, J. Huang, J. Zhang, L. Wang, W. Xiao, H. Yu, Y. Li, H. Li, C. Yuan, X. Hou, H. Zhang, D. Zhang, *Nanoscale* **2013**, *5*, 991.

[245] D. Yoo, H. Jeong, S.-H. Noh, J.-H. Lee, J. Cheon, *Angew. Chem. Int. Ed* **2013**, *52*, 13047.

[246] P. T. Yin, B. P. Shah, K.-B. Lee, *Small* **2014**, *10*, 4106.

[247] R. Coehoorn, D. B. de Mooij, C. de Waard, *J. Magn. Magn. Mater* **1989**, *80*, 101.

[248] a) V. Skumryev, S. Stoyanov, Y. Zhang, G. Hadjipanayis, D. Givord, J. Nogués, *Nature* **2003**, 423, 850; b) Q. Song, Z. J. Zhang, *J. Am. Chem. Soc* **2012**, *134*, 10182.

[249] a) M. Estrader, A. López-Ortega, S. Estradé, I. V. Golosovsky, G. Salazar-Alvarez, M. Vasilakaki, K. N. Trohidou, M. Varela, D. C. Stanley, M. Sinko, M. J. Pechan, D. J. Keavney, F. Peiró, S. Suriñach, M. D. Baró, J. Nogués, *Nat. Commun* **2013**, *4*, 2960; b) M. Casavola, A. Falqui, M. A. García, M. García-Hernández, C. Giannini, R. Cingolani, P. D. Cozzoli, *Nano Lett* **2009**, *9*, 366.

[250] S.-h. Noh, W. Na, J.-t. Jang, J.-H. Lee, E. J. Lee, S. H. Moon, Y. Lim, J.-S. Shin, J. Cheon, *Nano Lett* **2012**, *12*, 3716.

[251] Q. Zhang, I. Castellanos-Rubio, R. Munshi, I. Orue, B. Pelaz, K. I. Gries, W. J. Parak, P. del Pino, A. Pralle, *Chem. Mater* **2015**, *27*, 7380.

[252] S. He, H. Zhang, Y. Liu, F. Sun, X. Yu, X. Li, L. Zhang, L. Wang, K. Mao, G. Wang, Y. Lin, Z. Han, R. Sabirianov, H. Zeng, *Small* **2018**, *14*, 1800135.

[253] M. Angelakeris, Z.-A. Li, M. Hilgendorff, K. Simeonidis, D. Sakellari, M. Filippousi, H. Tian, G. Van Tendeloo, M. Spasova, M. Acet, M. Farle, *J. Magn. Magn. Mater* **2015**, *381*, 179.

[254] M. S. Carrião, A. F. Bakuzis, *Nanoscale* **2016**, *8*, 8363.

[255] S. Liébana-Viñas, K. Simeonidis, U. Wiedwald, Z. A. Li, Z. Ma, E. Myrovali, A. Makridis, D. Sakellari, G. Vourlias, M. Spasova, M. Farle, M. Angelakeris, *RSC Adv* **2016**, *6*, 72918.

[256] S. Famiani, A. P. LaGrow, M. O. Besenhard, S. Maenosono, N. T. K. Thanh, *Chem. Mater* **2018**, *30*, 8897.

[257] J.-H. Lee, J.-t. Jang, J.-s. Choi, S. H. Moon, S.-h. Noh, J.-w. Kim, J.-G. Kim, I.-S. Kim, K. I. Park, J. Cheon, *Nat. Nanotechnol* **2011**, *6*, 418.

[258] I. Betancourt, H. A. Davies, *Mater. Sci. Technol* **2010**, *26*, 5.

[259] F. Liu, Y. Hou, S. Gao, *Chem. Soc. Rev* **2014**, *43*, 8098.

[260] A. López-Ortega, M. Estrader, G. Salazar-Alvarez, A. G. Roca, J. Nogués, *Phys. Rep* **2015**, *553*, 1.

[261] R. Tong, D. S. Kohane, Wiley Interdiscip. Rev.: Nanomed. Nanobiotechnol **2012**, 4, 638.

[262] E. S. Shibu, M. Hamada, N. Murase, V. Biju, *J. Photochem. Photobiol C* **2013**, *15*, 53.

[263] X. Huang, P. K. Jain, I. H. El-Sayed, M. A. El-Sayed, *Lasers Med. Sci* **2007**, *23*, 217.

[264] a) A. P. Castano, T. N. Demidova, M. R. Hamblin, *Photodiagnosis Photodyn. Ther* **2004**, *1*, 279; b) C. A. Robertson, D. H. Evans, H. Abrahamse, *J. Photochem. Photobiol., B* **2009**, *96*, 1.

[265] A. M. Gobin, E. M. Watkins, E. Quevedo, V. L. Colvin, J. L. West, *Small* **2010**, *6*, 745.

[266] R. Singh, S. V. Torti, *Adv. Drug Delivery Rev* **2013**, *65*, 2045.

[267] K. Yang, S. Zhang, G. Zhang, X. Sun, S.-T. Lee, Z. Liu, *Nano Lett* **2010**, *10*, 3318.

[268] J. T. Robinson, S. M. Tabakman, Y. Liang, H. Wang, H. Sanchez Casalongue, D. Vinh, H. Dai, *J. Am. Chem. Soc* **2011**, *133*, 6825.

[269] T. N. Lambert, N. L. Andrews, H. Gerung, T. J. Boyle, J. M. Oliver, B. S. Wilson, S. M. Han, *Small* **2007**, *3*, 691.

[270] C. M. Hessel, V. P. Pattani, M. Rasch, M. G. Panthani, B. Koo, J. W. Tunnell, B. A. Korgel, *Nano Lett.* **2011**, *11*, 2560.

[271] Q. Tian, M. Tang, Y. Sun, R. Zou, Z. Chen, M. Zhu, S. Yang, J. Wang, J. Wang, J. Hu, *Adv. Mater* **2011**, *23*, 3542.

[272] a) Q. Fan, K. Cheng, X. Hu, X. Ma, R. Zhang, M. Yang, X. Lu, L. Xing, W. Huang, S. S. Gambhir, Z. Cheng, *J. Am. Chem. Soc* **2014**, *136*, 15185; b) Y. Sun, S. Hong, X. Ma, K. Cheng, J. Wang, Z. Zhang, M. Yang, Y. Jiang, X. Hong, Z. Cheng, *Chem. Sci* **2016**, *7*, 5888.

[273] P. Kalluru, R. Vankayala, C.-S. Chiang, K. C. Hwang, *Angew. Chem. Int. Ed* **2013**, *52*, 12332.

[274] A. Nel, T. Xia, H. Meng, X. Wang, S. Lin, Z. Ji, H. Zhang, *Acc. Chem. Res* **2013**, *46*, 607.

[275] J. Wang, K. Pantopoulos, *Biochem. J* **2011**, *434*, 365.

[276] S. Shen, S. Wang, R. Zheng, X. Zhu, X. Jiang, D. Fu, W. Yang, *Biomaterials* **2015**, *39*, 67.

[277] J. Yu, W. Yin, X. Zheng, G. Tian, X. Zhang, T. Bao, X. Dong, Z. Wang, Z. Gu, X. Ma, Y. Zhao, *Theranostics* **2015**, *5*, 931.

[278] H. Zhou, X. Hou, Y. Liu, T. Zhao, Q. Shang, J. Tang, J. Liu, Y. Wang, Q. Wu, Z. Luo, H. Wang, C. Chen, *ACS Appl. Mater. Interfaces* **2016**, *8*, 4424.

[279] V. Sagar, V. S. R. Atluri, A. Tomitaka, P. Shah, A. Nagasetti, S. Pilakka-Kanthikeel, N. El-Hage, A. McGoron, Y. Takemura, M. Nair, *Sci. Rep* **2016**, *6*, 29792.

[280] C.-H. L. a. Y.-C. C. Ching-Yi Wu, *J. Nanomed. Nanotechnol* **2015**, *6:1*.

[281] X. Han, Z. Deng, Z. Yang, Y. Wang, H. Zhu, B. Chen, Z. Cui, R. C. Ewing, D. Shi, *Nanoscale* **2017**, *9*, 1457.

[282] Y. Deng, E. Li, X. Cheng, J. Zhu, S. Lu, C. Ge, H. Gu, Y. Pan, *Nanoscale* **2016**, *8*, 3895.

[283] X. Jing, Z. Zhi, D. Wang, J. Liu, Y. Shao, L. Meng, *Bioconjugate Chem* **2018**, *29*, 559.

[284] Q. Tian, J. Hu, Y. Zhu, R. Zou, Z. Chen, S. Yang, R. Li, Q. Su, Y. Han, X. Liu, *J. Am. Chem. Soc* **2013**, *135*, 8571.

[285] J.-C. Yang, Y. Chen, Y.-H. Li, X.-B. Yin, *ACS Appl. Mater. Interfaces* **2017**, *9*, 22278.

[286] C. Chen, S. Wang, L. Li, P. Wang, C. Chen, Z. Sun, T. Song, *Biomaterials* **2016**, *104*, 352.

[287] M. Wang, K. Deng, W. Lü, X. Deng, K. Li, Y. Shi, B. Ding, Z. Cheng, B. Xing, G. Han, Z. Hou, J. Lin, *Adv. Mater* **2018**, *30*, 1706747.

[288] M.-Y. Liao, P.-S. Lai, H.-P. Yu, H.-P. Lin, C.-C. Huang, *Chem. Commun* **2012**, *48*, 5319.

[289] L. Cheng, K. Yang, Y. Li, X. Zeng, M. Shao, S.-T. Lee, Z. Liu, *Biomaterials* **2012**, *33*, 2215.

[290] X. Fu, X. Wang, S. Zhou, Y. Zhang, *Int. J. Nanomed* **2017**, *12*, 3751.

[291] R. Guo, H. Peng, Y. Tian, S. Shen, W. Yang, *Small* **2016**, *12*, 4541.

[292] M.-F. Tsai, C. Hsu, C.-S. Yeh, Y.-J. Hsiao, C.-H. Su, L.-F. Wang, *ACS Appl. Mater. Interfaces* **2018**, *10*, 1508.

[293] S. Shen, B. Ding, S. Zhang, X. Qi, K. Wang, J. Tian, Y. Yan, Y. Ge, L. Wu, *Nanomedicine* **2017**, *13*, 1607.

[294] Y. Zhao, W. Song, D. Wang, H. Ran, R. Wang, Y. Yao, Z. Wang, Y. Zheng, P. Li, *ACS Appl. Mater. Interfaces* **2015**, *7*, 14231.

[295] J. Wang, H. Zhao, Z. Zhou, P. Zhou, Y. Yan, M. Wang, H. Yang, Y. Zhang, S. Yang, *ACS Appl. Mater. Interfaces* **2016**, *8*, 19872.

[296] S. Lee, R. George Thomas, M. Ju Moon, H. Ju Park, I.-K. Park, B.-I. Lee, Y. Yeon Jeong, *Sci. Rep* **2017**, *7*, 2108.

[297] S. Shen, F. Kong, X. Guo, L. Wu, H. Shen, M. Xie, X. Wang, Y. Jin, Y. Ge, *Nanoscale* **2013**, *5*, 8056.

[298] M. Chu, Y. Shao, J. Peng, X. Dai, H. Li, Q. Wu, D. Shi, *Biomaterials* **2013**, *34*, 4078.

[299] S. Song, H. Shen, T. Yang, L. Wang, H. Fu, H. Chen, Z. Zhang, *ACS Appl. Mater. Interfaces* **2017**, *9*, 9484.

[300] R. Zheng, S. Wang, Y. Tian, X. Jiang, D. Fu, S. Shen, W. Yang, *ACS Appl. Mater. Interfaces* **2015**, *7*, 15876.

[301] B. Liu, X. Zhang, C. Li, F. He, Y. Chen, S. Huang, D. Jin, P. Yang, Z. Cheng, J. Lin, *Nanoscale* **2016**, *8*, 12560.

[302] M. Zhang, Y. Cao, L. Wang, Y. Ma, X. Tu, Z. Zhang, *ACS Appl. Mater. Interfaces* **2015**, *7*, 4650.

[303] Z.-C. Wu, W.-P. Li, C.-H. Luo, C.-H. Su, C.-S. Yeh, *Adv. Funct. Mater* **2015**, *25*, 6527.

[304] Q. Tian, Q. Wang, K. X. Yao, B. Teng, J. Zhang, S. Yang, Y. Han, *Small* **2014**, *10*, 1063.

[305] Y. Yang, L. Jing, X. Li, L. Lin, X. Yue, Z. Dai, *Theranostics* **2017**, *7*, 466.

[306] E. Cazares-Cortes, S. Cabana, C. Boitard, E. Nehlig, N. Griffete, J. Fresnais, C. Wilhelm, A. Abou-Hassan, C. Ménager, *Adv. Drug Delivery Rev* **2019**, *138*, 233.

[307] L. C. Kennedy, L. R. Bickford, N. A. Lewinski, A. J. Coughlin, Y. Hu, E. S. Day, J. L. West, R. A. Drezek, *Small* **2011**, *7*, 169.

[308] L. R. Hirsch, R. J. Stafford, J. A. Bankson, S. R. Sershen, B. Rivera, R. E. Price, J. D. Hazle, N. J. Halas, J. L. West, *Proc. Natl. Acad. Sci. U. S. A* **2003**, *100*, 13549.

[309] L. Zhou, J. Yuan, Y. Wei, *J. Mater. Chem* **2011**, *21*, 2823.

[310] Y. Li, W. Lu, Q. Huang, C. Li, W. Chen, *Nanomedicine* **2010**, *5*, 1161.

[311] S. Bhana, G. Lin, L. Wang, H. Starring, S. R. Mishra, G. Liu, X. Huang, *ACS Appl. Mater. Interfaces* **2015**, *7*, 11637.

[312] N. Eyvazzadeh, A. Shakeri-Zadeh, R. Fekrazad, E. Amini, H. Ghaznavi, S. Kamran Kamrava, *Lasers Med. Sci* **2017**, *32*, 1469.

[313] J. Zhao, K. Tu, Y. Liu, Y. Qin, X. Wang, L. Qi, D. Shi, *Mater. Sci. Eng., C* **2017**, *80*, 88.

[314] W. Feng, X. Zhou, W. Nie, L. Chen, K. Qiu, Y. Zhang, C. He, *ACS Appl. Mater. Interfaces* **2015**, *7*, 4354.

[315] Y. Hu, L. Meng, L. Niu, Q. Lu, *ACS Appl. Mater. Interfaces* **2013**, *5*, 4586.

[316] X. Wang, H. Liu, D. Chen, X. Meng, T. Liu, C. Fu, N. Hao, Y. Zhang, X. Wu, J. Ren, F. Tang, *ACS Appl. Mater. Interfaces* **2013**, *5*, 4966.

[317] G. A. Sotiriou, F. Starsich, A. Dasargyri, M. C. Wurnig, F. Krumeich, A. Boss, J.-C. Leroux, S. E. Pratsinis, *Adv. Funct. Mater* **2014**, *24*, 2818.

[318] J. Peng, T. Qi, J. Liao, B. Chu, Q. Yang, Y. Qu, W. Li, H. Li, F. Luo, Z. Qian, *Theranostics* **2014**, *4*, 678.

[319] J. Huang, M. Guo, H. Ke, C. Zong, B. Ren, G. Liu, H. Shen, Y. Ma, X. Wang, H. Zhang, Z. Deng, H. Chen, Z. Zhang, *Adv. Mater* **2015**, *27*, 5049.

[320] J. Li, Y. Hu, J. Yang, P. Wei, W. Sun, M. Shen, G. Zhang, X. Shi, *Biomaterials* **2015**, *38*, 10.

[321] C.-W. Chen, W.-J. Syu, T.-C. Huang, Y.-C. Lee, J.-K. Hsiao, K.-Y. Huang, H.-P. Yu, M.-Y. Liao, P.-S. Lai, *J. Mater. Chem. B* **2017**, *5*, 5774.

[322] L. Huang, L. Ao, D. Hu, W. Wang, Z. Sheng, W. Su, *Chem. Mater* **2016**, *28*, 5896.

[323] W.-P. Li, P.-Y. Liao, C.-H. Su, C.-S. Yeh, *J. Am. Chem. Soc* **2014**, *136*, 10062.

[324] Y.-K. Huang, C.-H. Su, J.-J. Chen, C.-T. Chang, Y.-H. Tsai, S.-F. Syu, T.-T. Tseng, C.-S. Yeh, *ACS Appl. Mater. Interfaces* **2016**, *8*, 14470.

[325] S. J. Soenen, W. J. Parak, J. Rejman, B. Manshian, *Chem. Rev* **2015**, *115*, 2109.

[326] a) A. Espinosa, M. Bugnet, G. Radtke, S. Neveu, G. A. Botton, C. Wilhelm, A. Abou-Hassan, *Nanoscale* **2015**, *7*, 18872; b) S. Brulé, M. Levy, C. Wilhelm, D. Letourneur, F. Gazeau, C. Ménager, C. Le Visage, *Adv. Mater* **2011**, *23*, 787.

[327] A. Espinosa, R. Di Corato, J. Kolosnjaj-Tabi, P. Flaud, T. Pellegrino, C. Wilhelm, *ACS Nano* **2016**, *10*, 2436.

[328] H. Yan, W. Shang, X. Sun, L. Zhao, J. Wang, Z. Xiong, J. Yuan, R. Zhang, Q. Huang, K. Wang, B. Li, J. Tian, F. Kang, S.-S. Feng, *Adv. Funct. Mater* **2018**, *28*, 1705710.

[329] G. C. Bolfarini, M. P. Siqueira-Moura, G. J. F. Demets, P. C. Morais, A. C. Tedesco, *J. Photochem. Photobiol., B* **2012**, *115*, 1.

[330] F. Wo, R. Xu, Y. Shao, Z. Zhang, M. Chu, D. Shi, S. Liu, *Theranostics* **2016**, *6*, 485.

[331] Y. Guo, Y. Zhang, J. Ma, Q. Li, Y. Li, X. Zhou, D. Zhao, H. Song, Q. Chen, X. Zhu, *J. Controlled Release* **2018**, *272*, 145.

[332] Q. Lu, X. Dai, P. Zhang, X. Tan, Y. Zhong, C. Yao, M. Song, G. Song, Z. Zhang, G. Peng, Z. Guo, Y. Ge, K. Zhang, Y. Li, *Int. J. Nanomed* **2018**, *13*, 2491.

[333] L. Deng, Q. Li, S. a. Al-Rehili, H. Omar, A. Almalik, A. Alshamsan, J. Zhang, N. M. Khashab, *ACS Appl. Mater. Interfaces* **2016**, *8*, 6859.

[334] F. K. van Landeghem, K. Maier-Hauff, A. Jordan, K. T. Hoffmann, U. Gneveckow, R. Scholz, B. Thiesen, W. Brück, A. von Deimling, *Biomaterials* **2009**, *30*, 52.

[335] a) R. Singh, J. W. Lillard, *Exp. Mol. Pathol* **2009**, *86*, 215; b) A. Babu, A. K. Templeton, A. Munshi, R. Ramesh, *AAPS PharmSciTech* **2014**, *15*, 709.

[336] I. Hilger, R. Hergt, W. A. Kaiser, *Invest. Radiol* **2000**, *35*, 170.

[337] S. Kossatz, R. Ludwig, H. Dähring, V. Ettelt, G. Rimkus, M. Marciello, G. Salas, V. Patel, F. J. Teran, I. Hilger, *Pharm. Res* **2014**, *31*, 3274.

[338] M. Johannsen, U. Gneveckow, B. Thiesen, K. Taymoorian, C. H. Cho, N. Waldöfner, R. Scholz, A. Jordan, S. A. Loening, P. Wust, *Eur. Urol* **2007**, *52*, 1653.

[339] D. Fourmy, J. Carrey, V. Gigoux, *Nanomedicine* **2015**, *10*, 893.

[340] a) H. Maeda, J. Wu, T. Sawa, Y. Matsumura, K. Hori, *J. Controlled Release* **2000**, *65*, 271; b) M. F. Attia, N. Anton, J. Wallyn, Z. Omran, T. F. Vandamme, *J. Pharm. Pharmacol* **2019**, *71*, 1185.

[341] a) J. Yoo, C. Park, G. Yi, D. Lee, H. Koo, *Cancers (Basel)* **2019**, *11*, 640; b) S. A. Costa, D. Mozhdehi, M. J. Dzuricky, F. J. Isaacs, E. M. Brustad, A. Chilkoti, *Nano Lett* **2019**, *19*, 247.

[342] a) P. M. Price, W. E. Mahmoud, A. A. Al-Ghamdi, L. M. Bronstein, *Front. Chem* **2018**, *6*; b) Y.-L. Liu, D. Chen, P. Shang, D.-C. Yin, *J. Controlled Release* **2019**, *302*, 90.

[343] F. Danhier, O. Feron, V. Préat, *J. Controlled Release* **2010**, *148*, 135.

[344] a) S. Barua, S. Mitragotri, *Nano Today* **2014**, *9*, 223; b) Y. Li, Y. Lian, L. T. Zhang, S. M. Aldousari, H. S. Hedia, S. A. Asiri, W. K. Liu, *Interface Focus* **2016**, *6*, 20150086.

[345] N. Hoshyar, S. Gray, H. Han, G. Bao, *Nanomedicine (London, U. K.)* **2016**, *11*, 673.

[346] J. K. Tee, L. X. Yip, E. S. Tan, S. Santitewagun, A. Prasath, P. C. Ke, H. K. Ho, D. T. Leong, *Chem. Soc. Rev* **2019**, *48*, 5381.

[347] B. Li, L. A. Lane, Wiley Interdiscip. Rev.: Nanomed. Nanobiotechnol **2019**, 11, e1542.

[348] a) B. Chen, W. Le, Y. Wang, Z. Li, D. Wang, L. Ren, L. Lin, S. Cui, J. J. Hu, Y. Hu, P. Yang, R. C. Ewing, D. Shi, Z. Cui, *Theranostics* **2016**, *6*, 1887; b) V. Muraleetharan, J. Mantaj, M. Swedrowska, D. Vllasaliu, *RSC Adv* **2019**, *9*, 40487.

[349] T. L. Moore, L. Rodriguez-Lorenzo, V. Hirsch, S. Balog, D. Urban, C. Jud, B. Rothen-Rutishauser, M. Lattuada, A. Petri-Fink, *Chem. Soc. Rev* **2015**, *44*, 6287.

[350] a) P. Aggarwal, J. B. Hall, C. B. McLeland, M. A. Dobrovolskaia, S. E. McNeil, *Adv. Drug Delivery Rev* **2009**, *61*, 428; b) H. Gao, Q. He, *Expert Opin. Drug Delivery* **2014**, *11*, 409.

[351] a) N. Graf, D. R. Bielenberg, N. Kolishetti, C. Muus, J. Banyard, O. C. Farokhzad, S. J. Lippard, *ACS Nano* **2012**, *6*, 4530; b) J. Xie, C. Xu, N. Kohler, Y. Hou, S. Sun, *Adv. Mater* **2007**, *19*, 3163; c) P. Mishra, B. Nayak, R. K. Dey, *Asian J. Pharm. Sci* **2016**, *11*, 337.

[352] Y. Xu, H. Wu, J. Huang, W. Qian, D. E. Martinson, B. Ji, Y. Li, Y. A. Wang, L. Yang, H. Mao, *Theranostics* **2020**, *10*, 2479.

[353] G. L. Zwicke, G. Ali Mansoori, C. J. Jeffery, *Nano Rev* **2012**, *3*, 18496.

[354] M. M. Yallapu, S. F. Othman, E. T. Curtis, B. K. Gupta, M. Jaggi, S. C. Chauhan, *Biomaterials* **2011**, *32*, 1890.

[355] Y. Sheng, S. Li, Z. Duan, R. Zhang, J. Xue, *Mater. Chem. Phys* **2018**, *204*, 388.

[356] I. Almstätter, O. Mykhaylyk, M. Settles, J. Altomonte, M. Aichler, A. Walch, E. J. Rummeny, O. Ebert, C. Plank, R. Braren, *Theranostics* **2015**, *5*, 667.

[357] K. T. Al-Jamal, *Int. J. Pharm* **2013**, *454*, 525.

[358] a) G. R. Mahdavinia, H. Etemadi, F. Soleymani, *Carbohydr. Polym* **2015**, *128*, 112; b) G. R. Mahdavinia, H. Etemadi, *Mater. Sci. Eng., C* **2014**, *45*, 250.

[359] a) B. Polyak, G. Friedman, *Expert Opin. Drug Delivery* **2009**, *6*, 53; b) B. Shapiro, S. Kulkarni, A. Nacev, S. Muro, P. Y. Stepanov, I. N. Weinberg, *Wiley Interdiscip. Rev.: Nanomed. Nanobiotechnol* **2015**, *7*, 446.

[360] a) F. Sonvico, S. Mornet, S. Vasseur, C. Dubernet, D. Jaillard, J. Degrouard, J. Hoebeke, E. Duguet, P. Colombo, P. Couvreur, *Bioconjugate Chem* **2005**, *16*, 1181; b) V. Kalidasan, X. L. Liu, T. S. Herng, Y. Yang, J. Ding, *Nano-Micro Letters* **2016**, *8*, 80; c) J. Key, D. Dhawan, C. L. Cooper, D. W. Knapp, K. Kim, I. C. Kwon, K. Choi, K. Park, P. Decuzzi, J. F. Leary, *Int. J. Nanomed* **2016**, *11*, 4141.

[361] K. Hayashi, M. Nakamura, H. Miki, S. Ozaki, M. Abe, T. Matsumoto, W. Sakamoto, T. Yogo, K. Ishimura, *Theranostics* **2014**, *4*, 834.

[362] a) D.-H. Kim, E. A. Rozhkova, I. V. Ulasov, S. D. Bader, T. Rajh, M. S. Lesniak, V. Novosad, *Nat. Mater* **2010**, *9*, 165; b) C. Sanchez, D. El Hajj Diab, V. Connord, P. Clerc, E. Meunier, B. Pipy, B. Payré, R. P. Tan, M. Gougeon, J. Carrey, V. Gigoux, D. Fourmy, *ACS Nano* **2014**, *8*, 1350.

[363] Y. Cheng, M. E. Muroski, D. Petit, R. Mansell, T. Vemulkar, R. A. Morshed, Y. Han, I. V. Balyasnikova, C. M. Horbinski, X. Huang, L. Zhang, R. P. Cowburn, M. S. Lesniak, *J. Controlled Release* **2016**, *223*, 75.

[364] a) M. E. Muroski, R. A. Morshed, Y. Cheng, T. Vemulkar, R. Mansell, Y. Han, L. Zhang, K. S. Aboody, R. P. Cowburn, M. S. Lesniak, *PLoS One* **2016**, *11*, e0145129; b) M. F. Contreras, R. Sougrat, A. Zaher, T. Ravasi, J. Kosel, *Int J. Hyperthermia* **2015**, *10*, 2141.

[365] a) S. Leulmi, X. Chauchet, M. Morcrette, G. Ortiz, H. Joisten, P. Sabon, T. Livache, Y. Hou, M. Carrière, S. Lequien, B. Dieny, *Nanoscale* **2015**, *7*, 15904; b) M. Goiriena-Goikoetxea, A. García-Arribas, M. Rouco, A. V. Svalov, J. M. Barandiaran, *Nanotechnology* **2016**, *27*, 175302.

[366] T. Vemulkar, E. N. Welbourne, R. Mansell, D. C. M. C. Petit, R. P. Cowburn, *Appl. Phys. Lett* **2017**, *110*, 042402.

[367] H. Chiriac, E. Radu, M. Țibu, G. Stoian, G. Ababei, L. Lăbușcă, D. D. Herea, N. Lupu, *Sci. Rep* **2018**, *8*, 11538.

[368] a) M. F. Contreras, R. Sougrat, A. Zaher, T. Ravasi, J. Kosel, *Int. J. Nanomed* **2015**, *10*, 2141; b) A. I. Martínez-Banderas, A. Aires, F. J. Teran, J. E. Perez, J. F. Cadenas, N. Alsharif, T. Ravasi, A. L. Cortajarena, J. Kosel, *Sci. Rep* **2016**, *6*, 35786.

[369] a) T. Vemulkar, R. Mansell, D. C. Petit, R. P. Cowburn, M. S. Lesniak, *Appl. Phys. Lett.* **2015**, *107*, 012403; b) R. Mansell, T. Vemulkar, D. C. M. C. Petit, Y. Cheng, J. Murphy, M. S. Lesniak, R. P. Cowburn, *Sci. Rep* **2017**, *7*, 4257.

[370] D. H. Kim, E. A. Rozhkova, I. V. Ulasov, S. D. Bader, T. Rajh, M. S. Lesniak, V. Novosad, *Nat. Mater* **2010**, *9*, 165.

[371] E. Cazares-Cortes, A. Espinosa, J.-M. Guigner, A. Michel, N. Griffete, C. Wilhelm, C. Ménager, *ACS Appl. Mater. Interfaces* **2017**, *9*, 25775.

[372] G. Kandasamy, A. Sudame, T. Luthra, K. Saini, D. Maity, *ACS Omega* **2018**, *3*, 3991.

[373] P. Chandrasekharan, D. Maity, C. X. Yong, K.-H. Chuang, J. Ding, S.-S. Feng, *Biomaterials* **2011**, *32*, 5663.

[374] Y.-J. Kim, M. Ebara, T. Aoyagi, *Adv. Funct. Mater* **2013**, *23*, 5753.

[375] S. Balasubramanian, A. R. Girija, Y. Nagaoka, S. Iwai, M. Suzuki, V. Kizhikkilot, Y. Yoshida, T. Maekawa, S. D. Nair, *Int. J. Nanomed* **2014**, *9*, 437.

[376] Y. Qu, J. Li, J. Ren, J. Leng, C. Lin, D. Shi, *Nanoscale* **2014**, *6*, 12408.

[377] L. Lartigue, P. Hugounenq, D. Alloyeau, S. P. Clarke, M. Lévy, J.-C. Bacri, R. Bazzi, D. F. Brougham, C. Wilhelm, F. Gazeau, *ACS Nano* **2012**, *6*, 10935.

[378] G. Kandasamy, A. Sudame, P. Bhati, A. Chakrabarty, S. N. Kale, D. Maity, *J. Colloid Interface Sci* **2018**, *514*, 534.

[379] B. Sivakumar, R. G. Aswathy, Y. Nagaoka, M. Suzuki, T. Fukuda, Y. Yoshida, T. Maekawa, D. N. Sakthikumar, *Langmuir* **2013**, *29*, 3453.

[380] S. Kumar, A. Daverey, V. Khalilzad-Sharghi, N. K. Sahu, S. Kidambi, S. F. Othman, D. Bahadur, *RSC Adv* **2015**, *5*, 53180.

[381] K. H. Bae, M. Park, M. J. Do, N. Lee, J. H. Ryu, G. W. Kim, C. Kim, T. G. Park, T. Hyeon, *ACS Nano* **2012**, *6*, 5266.

[382] R. Kumar, A. Chauhan, S. K. Jha, B. K. Kuanr, *J. Mater. Chem. B* **2018**, *6*, 5385.

[383] L. P. Singh, N. V. Jadhav, S. Sharma, B. N. Pandey, S. K. Srivastava, R. S. Ningthoujam, *J. Mater. Chem. C* **2015**, *3*, 1965.

[384] B. P. Shah, N. Pasquale, G. De, T. Tan, J. Ma, K.-B. Lee, *ACS Nano* **2014**, *8*, 9379.

[385] K. Hayashi, M. Nakamura, W. Sakamoto, T. Yogo, H. Miki, S. Ozaki, M. Abe, T. Matsumoto, K. Ishimura, *Theranostics* **2013**, *3*, 366.

[386] Z.-Q. Zhang, S.-C. Song, *Biomaterials* **2016**, *106*, 13.

[387] E. Guisasola, L. Asín, L. Beola, J. M. de la Fuente, A. Baeza, M. Vallet-Regí, *ACS Appl. Mater. Interfaces* **2018**, *10*, 12518.

[388] S. Kossatz, J. Grandke, P. Couleaud, A. Latorre, A. Aires, K. Crosbie-Staunton, R. Ludwig, H. Dähring, V. Ettelt, A. Lazaro-Carrillo, M. Calero, M. Sader, J. Courty, Y. Volkov, A. Prina-Mello, A. Villanueva, Á. Somoza, A. L. Cortajarena, R. Miranda, I. Hilger, *Breast Cancer Res* **2015**, *17*, 66.

[389] C.-H. Hou, S.-M. Hou, Y.-S. Hsueh, J. Lin, H.-C. Wu, F.-H. Lin, *Biomaterials* **2009**, *30*, 3956.

[390] Q. Zhao, L. Wang, R. Cheng, L. Mao, R. D. Arnold, E. W. Howerth, Z. G. Chen, S. Platt, *Theranostics* **2012**, *2*, 113.

[391] T. Sadhukha, T. S. Wiedmann, J. Panyam, *Biomaterials* **2013**, *34*, 5163.

[392] A. R. K. Sasikala, A. GhavamiNejad, A. R. Unnithan, R. G. Thomas, M. Moon, Y. Y. Jeong, C. H. Park, C. S. Kim, *Nanoscale* **2015**, *7*, 18119.

[393] J. Li, Y. Hu, Y. Hou, X. Shen, G. Xu, L. Dai, J. Zhou, Y. Liu, K. Cai, *Nanoscale* **2015**, *7*, 9004.

[394] W. Xie, Q. Gao, Z. Guo, D. Wang, F. Gao, X. Wang, Y. Wei, L. Zhao, *ACS Appl. Mater. Interfaces* **2017**, *9*, 33660.

[395] L. Pradhan, B. Thakur, R. Srivastava, P. Ray, D. Bahadur, *Theranostics* **2016**, *6*, 1557.

[396] M. Yamaguchi, A. Ito, A. Ono, Y. Kawabe, M. Kamihira, *ACS Synth. Biol* **2014**, *3*, 273.

[397] Y. Chen, L. Jiang, R. Wang, M. Lu, Q. Zhang, Y. Zhou, Z. Wang, G. Lu, P. Liang, H. Ran, H. Chen, Y. Zheng, *Adv. Mater* **2014**, *26*, 7468.

[398] F. Wang, Y. Yang, Y. Ling, J. Liu, X. Cai, X. Zhou, X. Tang, B. Liang, Y. Chen, H. Chen, D. Chen, C. Li, Z. Wang, B. Hu, Y. Zheng, *Biomaterials* **2017**, *128*, 84.

[399] I. V. Belyanina, T. N. Zamay, G. S. Zamay, S. S. Zamay, O. S. Kolovskaya, T. I. Ivanchenko, V. V. Denisenko, A. K. Kirichenko, Y. E. Glazyrin, I. V. Garanzha, V. V. Grigorieva, A. V. Shabanov, D. V. Veprintsev, A. E. Sokolov, V. M. Sadovskii, A. Gargaun, M. V. Berezovski, A. S. Kichkailo, *Theranostics* **2017**, *7*, 3326.

[400] W. Gao, Y. Zheng, R. Wang, H. Chen, X. Cai, G. Lu, L. Chu, C. Xu, N. Zhang, Z. Wang, H. Ran, P. Li, C. Yang, Z. Mei, J. Song, *Acta Biomater* **2016**, *29*, 298.

[401] K. Hayashi, W. Sakamoto, T. Yogo, *Adv. Funct. Mater* **2016**, *26*, 1708.

[402] G. K. Thirunavukkarasu, K. Cherukula, H. Lee, Y. Y. Jeong, I.-K. Park, J. Y. Lee, *Biomaterials* **2018**, *180*, 240.

[403] R. Yang, L. Y. An, Q. F. Miao, F. M. Li, Y. Han, H. X. Wang, D. P. Liu, R. Chen, S. Q. Tang, *Oncotarget* **2016**, *7*, 35894.

[404] P. Zhou, H. Zhao, Q. Wang, Z. Zhou, J. Wang, G. Deng, X. Wang, Q. Liu, H. Yang, S. Yang, *Adv. Healthcare Mater* **2018**, *7*, 1701201.

[405] K. Fang, L. Song, Z. Gu, F. Yang, Y. Zhang, N. Gu, *Colloids Surf., B* **2015**, *136*, 712.

[406] J. Hamzehalipour Almaki, R. Nasiri, A. Idris, M. Nasiri, F. A. Abdul Majid, D. Losic, *J. Mater. Chem. B* **2017**, *5*, 7369.

[407] S. Shirvalilou, S. Khoei, S. Khoee, N. J. Raoufi, M. R. Karimi, A. Shakeri-Zadeh, *Chem. Biol. Interact* **2018**, *295*, 97.

[408] M. Soleymani, M. Edrissi, A. M. Alizadeh, *J. Mater. Chem. B* **2017**, *5*, 4705.

[409] T. N. Brusentsova, N. A. Brusentsov, V. D. Kuznetsov, V. N. Nikiforov, *J. Magn. Magn. Mater* **2005**, *293*, 298.

[410] H. Hejase, S. S. Hayek, S. Qadri, Y. Haik, *J. Magn. Magn. Mater* **2012**, *324*, 3620.

[411] L. Jianbo, Q. Yang, R. Jie, Y. Weizhong, S. Donglu, *Nanotechnology* **2012**, *23*, 505706.

[412] A. T. Apostolov, I. N. Apostolova, J. M. Wesselinowa, *Eur. Phys. J. B* **2013**, *86*, 483.

[413] T. Shimizu, M. Matsui, *Sci. Technol. Adv. Mater* **2003**, *4*, 469.

[414] A. Hanini, L. Lartigue, J. Gavard, K. Kacem, C. Wilhelm, F. Gazeau, F. Chau, S. Ammar, *J. Magn. Magn. Mater* **2016**, *416*, 315.

[415] W. Zhang, X. Zuo, Y. Niu, C. Wu, S. Wang, S. Guan, S. R. P. Silva, *Nanoscale* **2017**, *9*, 13929.

[416] Y. Akin, I. M. Obaidat, B. Issa, Y. Haik, *Cryst. Res. Technol* **2009**, *44*, 386.

[417] A. Yao, F. Ai, D. Wang, W. Huang, X. Zhang, *Mater. Sci. Eng., C* **2009**, *29*, 2525.

[418] N. K. Prasad, M. Srivastava, S. K. Alla, J. R. Danda, D. Aditya, R. K. Mandal, *RSC Adv.* **2016**, *6*, 41268.

[419] J. Makni, K. Riahi, F. Ayadi, V. Nachbaur, W. Cheikhrouhou-Koubaa, M. Koubaa, M. A. Hamayun, E. K. Hlil, A. Cheikhrouhou, *J. Alloys Compd* **2018**, *746*, 626.

[420] H. Das, A. Inukai, N. Debnath, T. Kawaguchi, N. Sakamoto, S. M. Hoque, H. Aono, K. Shinozaki, H. Suzuki, N. Wakiya, *J. Phys. Chem. Solids* **2018**, *112*, 179.

[421] Z. Beji, A. Hanini, L. S. Smiri, J. Gavard, K. Kacem, F. Villain, J. M. Grenèche, F. Chau, S. Ammar, *Chem. Mater* **2010**, *22*, 5420.

[422] M. Veverka, P. Veverka, Z. Jirák, O. Kaman, K. Knížek, M. Maryško, E. Pollert, K. Závěta, *J. Magn. Magn. Mater* **2010**, *322*, 2386.

[423] A. u. Rashid, A. Ahmed, S. N. Ahmad, S. A. Shaheen, S. Manzoor, *J. Magn. Magn. Mater.* **2013**, *347*, 39.

[424] B. Pimentel, R. J. Caraballo-Vivas, N. R. Checca, V. I. Zverev, R. T. Salakhova, L. A. Makarova, A. P. Pyatakov, N. S. Perov, A. M. Tishin, A. A. Shtil, A. L. Rossi, M. S. Reis, *J. Solid State Chem* **2018**, *260*, 34.

[425] J.-t. Jang, S. Bae, *Appl. Phys. Lett* **2017**, *111*, 183703.

[426] a) E. Y. Yu, M. Bishop, B. Zheng, R. M. Ferguson, A. P. Khandhar, S. J. Kemp, K. M. Krishnan, P. W. Goodwill, S. M. Conolly, *Nano Lett* **2017**, *17*, 1648; b) G. K. Michael, S. Johannes, K. Tobias, I. Harald, A. Gerhard, W. Horst, J. Caroline, *Phys. Med. Biol* **2018**, *63*, 064001.

[427] G. Song, M. Chen, Y. Zhang, L. Cui, H. Qu, X. Zheng, M. Wintermark, Z. Liu, J. Rao, *Nano Lett* **2018**, *18*, 182.

[428] a) B. Gleich, J. Weizenecker, *Nature* **2005**, *435*, 1214; b) B. Gleich, J. Weizenecker, *Nature* **2005**, *435*, 1214.

[429] a) E. U. Saritas, P. W. Goodwill, L. R. Croft, J. J. Konkle, K. Lu, B. Zheng, S. M. Conolly, *J. Magn. Reson* **2013**, *229*, 116; b) N. Panagiotopoulos, R. L. Duschka, M. Ahlborg, G. Bringout, C. Debbeler, M. Graeser, C. Kaethner, K. Lüdtke-Buzug, H. Medimagh, J. Stelzner, T. M. Buzug, J. Barkhausen, F. M. Vogt, J. Haegele, *Int. J. Nanomed* **2015**, *10*, 3097.

[430] Y. Takeuchi, H. Suzuki, H. Sasahara, J. Ueda, I. Yabata, K. Itagaki, S. Saito, K. Murase, *Adv. Biomed. Eng* **2014**, *3*, 37.

[431] P. Ludewig, N. Gdaniec, J. Sedlacik, N. D. Forkert, P. Szwargulski, M. Graeser, G. Adam, M. G. Kaul, K. M. Krishnan, R. M. Ferguson, A. P. Khandhar, P. Walczak, J. Fiehler, G. Thomalla, C. Gerloff, T. Knopp, T. Magnus, *ACS Nano* **2017**, *11*, 10480.

[432] E. Y. Yu, P. Chandrasekharan, R. Berzon, Z. W. Tay, X. Y. Zhou, A. P. Khandhar, R. M. Ferguson, S. J. Kemp, B. Zheng, P. W. Goodwill, M. F. Wendland, K. M. Krishnan, S. Behr, J. Carter, S. M. Conolly, *ACS Nano* **2017**, *11*, 12067.

[433] B. Zheng, T. Vazin, W. Yang, P. W. Goodwill, E. U. Saritas, L. R. Croft, D. V. Schaffer, S. M. Conolly, "Quantitative stem cell imaging with magnetic particle imaging", presented at *2013 International Workshop on Magnetic Particle Imaging (IWMPI)*, 23-24 March 2013, 2013.

[434] J. Haegele, S. Biederer, H. Wojtczyk, M. Gräser, T. Knopp, T. M. Buzug, J. Barkhausen, F. M. Vogt, *Magn. Reson. Med* **2013**, *69*, 1761.

[435] T. O. Tasci, I. Vargel, A. Arat, E. Guzel, P. Korkusuz, E. Atalar, *Med. Phys* **2009**, *36*, 1906.

[436] a) H. Daniel, T. Zhi Wei, D. Rohan, Z. Bo, G. Patrick, R. Carlos, C. Steven, *Phys. Med. Biol* **2017**, *62*, 3483; b) W. Franz, F. Thomas, P. Nikolaos, V. Sarah, P. G. Jan, M. V. Florian, A. K. Martin, M. B. Thorsten, B. Joerg, H. Julian, *Phys. Med. Biol* **2018**, *63*, 045005.

[437] N. Banura, A. Mimura, K. Nishimoto, K. Murase, in *arXiv e-prints*, 2016.

[438] a) L. S. Arias, J. P. Pessan, A. P. M. Vieira, T. M. T. d. Lima, A. C. B. Delbem, D. R. Monteiro, *Antibiotics (Basel, Switz.)* **2018**, *7*, 46; b) N. V. S. Vallabani, S. Singh, *3 Biotech* **2018**, *8*, 279.

[439] Z. Hedayatnasab, F. Abnisa, W. M. A. W. Daud, *Mater. Design* **2017**, *123*, 174.

[440] a) X. M. Lin, C. M. Sorensen, K. J. Klabunde, G. C. Hajipanayis, *J. Mater. Res* **1999**, *14*, 1542; b) A. A. El-Gendy, E. M. M. Ibrahim, V. O. Khavrus, Y. Krupskaya, S. Hampel, A. Leonhardt, B. Büchner, R. Klingeler, *Carbon* **2009**, *47*, 2821; c) S. Azzaza, S. Alleg, H. Moumeni, A. R. Nemamcha, J. L. Rehspringer, J. M. Greneche, *J. Phys.: Condens. Matter* **2006**, *18*, 7257.

[441] a) J. Zhang, M. Post, T. Veres, Z. J. Jakubek, J. Guan, D. Wang, F. Normandin, Y. Deslandes, B. Simard, *J. Phys. Chem. B* **2006**, *110*, 7122; b) I. Hilger, W. A. Kaiser, *Nanomedicine* **2012**, *7*, 1443.

[442] R. Hergt, S. Dutz, R. Müller, M. Zeisberger, *Journal of Physics Condensed Matter* **2006**, *18*, S2919.

[443] J. A. Mary, A. Manikandan, L. J. Kennedy, M. Bououdina, R. Sundaram, J. J. Vijaya, *Trans. Nonferrous Met. Soc. China* **2014**, *24*, 1467.

[444] A. Wu, X. Yang, H. Yang, *Dalton Trans* **2013**, *42*, 4978.

[445] T. L. Kline, Y.-H. Xu, Y. Jing, J.-P. Wang, *J. Magn. Magn. Mater* **2009**, *321*, 1525.

[446] I. Astefanoaei, A. Stancu, H. Chiriac, *AIP Conference Proceedings* **2017**, *1796*, 040006.

[447] S. Behrens, H. Bönnemann, N. Matoussevitch, A. Gorschinski, E. Dinjus, W. Habicht, J. Bolle, S. Zinoveva, N. Palina, J. Hormes, H. Modrow, S. Bahr, V. Kempter, *J. Phys.: Condens. Matter* **2006**, *18*, S2543.

[448] D. Carta, G. Mountjoy, M. Gass, G. Navarra, M. F. Casula, A. Corrias, *The Journal of Chemical Physics* **2007**, *127*, 204705.

[449] K. Hamad-Schifferli, J. J. Schwartz, A. T. Santos, S. Zhang, J. M. Jacobson, *Nature* **2002**, *415*, 152.

[450] a) R. S. McCoy, S. Choi, G. Collins, B. J. Ackerson, C. J. Ackerson, *ACS Nano* **2013**, *7*, 2610; b) J. S. Garitaonandia, M. Insausti, E. Goikolea, M. Suzuki, J. D. Cashion, N. Kawamura, H. Ohsawa, I. Gil de Muro, K. Suzuki, F. Plazaola, T. Rojo, *Nano Lett* **2008**, *8*, 661; c) P. Crespo, R. Litrán, T. C. Rojas, M. Multigner, J. M. de la Fuente, J. C. Sánchez-López, M. A. García, A. Hernando, S. Penadés, A. Fernández, *Phys. Rev. Lett* **2004**, *93*, 087204.

[451] M. Creixell, A. C. Bohórquez, M. Torres-Lugo, C. Rinaldi, *ACS Nano* **2011**, *5*, 7124.

MASSEY UNIVERSITY
GRADUATE RESEARCH SCHOOL

STATEMENT OF CONTRIBUTION
DOCTORATE WITH PUBLICATIONS/MANUSCRIPTS

We, the candidate and the candidate's Primary Supervisor, certify that all co-authors have consented to their work being included in the thesis and they have accepted the candidate's contribution as indicated below in the *Statement of Originality*.

Name of candidate:	Hossein Etemadi
Name/title of Primary Supervisor:	Paul G. Plieger
Name of Research Output and full reference:	
Improvements in the Organic Phase Hydrothermal Synthesis of Monodisperse MxFe3-xO4 (M = Fe, Mg, Zn) Spinel Nanoferrites for Magnetic Fluid Hyperthermia Application	
In which Chapter is the Manuscript /Published work:	4
Please indicate:	
• The percentage of the manuscript/Published Work that was contributed by the candidate:	90%
and	
• Describe the contribution that the candidate has made to the Manuscript/Published Work:	
Hossein Etermadi did the experimental design and trials, data analysis and draft of the manuscript. The draft was then proof read by Jenna Buchanan and Paul Plieger. Final edits were then completed by Hossein Etemadi	
For manuscripts intended for publication please indicate target journal:	
ACS omega, 5 (29), 18091-18104, 2020. https://doi.org/10.1021/acsomega.0c01641	
Candidate's Signature:	Hossein Digitally signed by Hossein Date: 2021.02.11 14:10:14 +13'00'
Date:	11/02/2021
Primary Supervisor's Signature:	Paul Plieger Digitally signed by Paul Plieger DN: cn=Paul Plieger, c=NZ, o=Massey University, ou=School of Fundamental Sciences, email=p.g.plieger@massey.ac.nz Date: 2021.02.26 12:10:07 +13'00'
Date:	26/02/2021

(This form should appear at the end of each thesis chapter/section/appendix submitted as a manuscript/ publication or collected as an appendix at the end of the thesis)

Chapter 4. Improvements in the organic phase hydrothermal synthesis of monodisperse $M_xFe_{3-x}O_4$ (M = Fe, Mg, Zn) spinel nanoferrites for magnetic fluid hyperthermia application

Hossein Etemadi[1] and Paul G. Plieger*[1]

School of Fundamental Sciences, Massey University, Private Bag 11 222, Palmerston North, New Zealand

E-mail: p.g.plieger@massey.ac.nz

Fax: +64 6 350 5682; Tel: +64 6 9517647

Abstract

In the quest for optimal heat dissipaters for magnetic fluid hyperthermia (MFH) applications, monodisperse $M_xFe_{3-x}O_4$ (M = Fe, Mg, Zn) spinel nanoferrites were successfully synthesized through a modified organic phase hydrothermal route. The chemical composition effect on the size, crystallinity, saturation magnetization, magnetic anisotropy, and heating potential of prepared nanoferrites were assessed using TEM, DLS, XRD, TGA, EDS, AAS, XPS and VSM techniques. TEM revealed that particle diameter between 6 and 14 nm could be controlled by varying the surfactant ratio and doping ions. EDS, AAS, XRD and XPS confirmed the inclusion of Zn and Mg ions in the Fe_3O_4 structure. Magnetization studies via VSM, revealed both the superparamagnetic nature of the nanoferrites and the dependence on substitution of the doped ions to the final magnetization. The broader ZFC curve of Zn-doped Fe_3O_4 were related to their large size distribution. Finally, a maximum rising temperature (T_{max}) of 66 °C was achieved for an aqueous ferrofluid of non-doped Fe_3O_4 NPs after magnetic field activation for 12 min.

Keywords

Hydrothermal, Nanoferrites, Magnetization, Hyperthermia

4.1. Introduction

Magnetic fluid hyperthermia (MFH) utilising iron oxide nanoparticles (IONPs, Fe_3O_4) is a quickly evolving technology in medical oncology as clinically it is a minimally invasive cancer

therapy. In this scenario, activation of an externally applied alternating magnetic field (AMF) switches the magnetic moments of Fe_3O_4 nanoparticles (NPs) rapidly. This results in heat dissipation in the tumour zone and subsequent necrosis of the tumor.[1] The heat dissipation potency of a clinical Fe_3O_4 fluid is defined by the absorption rate (SAR) or specific loss power (SLP). The heating potential of commercial fluid at quantitates of (~ 112 mg Fe/mL) within a physiologically safe range of AC magnetic field (f =100 kHz, and H ~ 2-18 KA/m), is insufficient for complete elimination of tumor.[2] This low heating potential is hypothesized to be due to the intrinsic low saturation magnetization (*Ms*) value of nanosized Fe_3O_4 particles (~ 50-60 emu/g lower than that of bulk Fe_3O_4 ~ 85-100 emu/g) and a large surface spin disorder of spherical-shaped Fe_3O_4 NPs currently used for MRI and MFH applications.[3] It has been proposed that compositional tuning through a metal dopant substitution of Fe^{2+} with a (M^{2+} cation) in the tetrahedral (T_d) or octahedral (O_h) interstitial sites of an Fe_3O_4 crystal lattice is a viable and potential nanoscale engineering strategy to synthesis metal-doped spinel $M_xFe_{3-x}O_4$ (M = Fe, Mg, Zn) nanoferrites with enhanced heating potential.[4, 5] Of all the proposed classical synthetic protocols thus far, thermal decomposition of metal acetylacetonate precursors $M(acac)_3$ in the presence of surfactants and capping/reducing agents at elevated temperature (~ > 300°C) has manifested itself as an efficient route to ensure synthesis of an arsenal of high-quality and monodisperse hydrophobic single domain Fe_3O_4 and metal-doped spinel $M_xFe_{3-x}O_4$ nanoferrites.[6] This method provides excellent control over the nucleation and growth steps as well as the mean size, shape, and composition. Consequently, various $M_xFe_{3-x}O_4$ nanoferrites have been routinely prepared for potential technological applications.[7, 8] In spite of these advantages, the thermal decomposition method does face with some impediments. These include the high toxicity and cost of the iron precursors and reagents, the utilisation of flammable organic solvents at high temperatures (320 °C), a requirement to use an inert atmosphere (N_2) during the reaction and additional steps to transfer the resulting nanocrystals to the aqueous phase.[9, 10] Hence, there is a need for the community to explore more simple and economical robust protocols to synthesize highly monodisperse water-soluble nanocrystals in mass quantities. As a cost effective and environmentally friendly synthetic approach under mild conditions, the hydrothermal route shows promise as it encourages the growth of single crystals with definite sizes, shapes and narrow polydispersity in an autoclave at temperatures (in the range from 130 to 250 °C) and vapour pressure (ranging from 0.3 to 4 MPa) through a one-

step simple facile reaction scheme.[11] Metal nanoferrites of various sizes and configurations have been synthesized by the hydrothermal synthesis route via either aqueous phase or organic phase reactions of metal precursors with or without surfactants for potential technological applications.[12] Typically, the decomposition of iron precursors in an aqueous solution along with/or without surfactants results in aggregated clusters of larger size distribution. For example, a polyethylene glycol (PEG)-Fe_3O_4 nanodisc [13], ethylene glycol (EG)-Fe_3O_4 nanoflowers [9] ,dodecyltrimethylammonium bromide (DTAB)-Fe_3O_4 nanoparticles [14], Fe_3O_4/C core−shell nanorings with EG/PEG[15] and PEG-$Mn_{0.2}Ni_{0.8}Fe_2O_4$[16] have all been synthesized utilising this method. In contrast to hydrolytic synthesis of nanoferrites, only a limited number of reports have highlighted the organic-phase hydrothermal synthesize of nanocrystals. For example, Tian *et al* fabricated ultrasmall (4-6 nm) monodispersed Fe_3O_4 via the hydrothermal method, with $Fe(acac)_3$ as the iron source, n-octanol as the solvent and n-octylamine as the reductant. [17] In another example, Dendrinou-Samara *et al* have synthesized nanoferrites $NiFe_2O_4$ [18], $CoFe_2O_4$ [19] and $MnFe_2O_4$ [20] with the surfactant oleylamine acting as a stabilizing agent and solvent simultaneously. They observed that the prepared nanocrystals still presented some degree of aggregation. In this contribution, we examine the extent to which a hybrid approach can be applied where the desired properties of thermal decomposition method can be achieved using the more convenient mild hydrothermal route. We demonstrate this by the successful synthesis of highly monodispersed $M_xFe_{3-x}O_4$ (M = Fe, Mg, Zn) nanocrystals of mixed morphologies for use in MFH applications. In addition, the effect of transition metal doping into the crystal lattice was tested with the objective of improving crystallinity and magnetization of bare Fe_3O_4 NPs.

4.2. Results and Discussion

4.2.1. Structural and Compositional Studies

$M_xFe_{3-x}O_4$ (M = Fe, Mg, Zn) spinel nanoferrites were synthesized by decomposition of the metal precursors in a high boiling point solvent, (ODC) under hydrothermal conditions. In a systematic fashion, the molar ratio of OA to OAm, amount of TOPO and reaction time were investigated. Feedback based on size and shape of the particles was obtained using transmission electron microscopy. In terms of the molar ratios of OA to OAm, individual utilization of each surfactant with 0.5 mmol of TOPO at 240 ℃ for 120 min resulted in

aggregated clusters therefore a strategy utilising both surfactants was adopted and it was found that an equal amount of OA to OAm of 1:1, minimized the aggregation to some extent. Eventually, the OA to OAm of 1:4 and 1:5 resulted in particles of great uniformity and size distribution. (Figure 4.10 in Supporting Information). Keeping the other conditions constant, the influence of TOPO variation (0.1, 0.3 and 0.5 mmol) was monitored on the monodispersity and size of the Fe_3O_4 NPs. TOPO typically functions as a particle stabilizer where the phosphine oxide periodically binds to the Fe_3O_4 NPs (Fe atom) controlling the growth rate of particles under the synthetic conditions employed [21]. Eventually, NPs with appropriate uniformity and shape were obtained utilising an optimised TOPO concentration of 0.5 mmol. (Figure 4.11). The effect of time on the morphological evolution of the formation of Fe_3O_4 NPs was also recorded at different reaction times of 30, 60, 90 and 120 min with a molar ratio of OA to OAm of 1:4 and TOPO concentration of 0.5 mmol at 240 ^{0}C for 120 min. An aliquot was withdrawn from the reaction medium after the above indicated time periods of the reaction had elapsed and was imaged by TEM. Depicted in (Figure 4.12), the particles start growing and forming final well-shaped particles as the time is extended. It is postulated that the particles are generated by the coalescence and reshaping of small particles where two or more particles merge during the reaction to form single daughter shaped NP. In summary, a molar ratio of OA to OAm of (1:4) and (1:5), a concentration of 0.5 mmol TOPO and a reaction time of 120 min at 240 °C was found to be the optimal conditions to synthesize a library of monodisperse NPs with narrow size distributions. The Fe1 NPs with an OA to OAm ratio of (1:4) clearly show great uniformity and size distribution with an average size of 10.3 ± 2.8 nm (Figure 4.1 a, b,e). The TEM image reveals the assembly of NPs into a close-packed arrangement without any interfacial contact and aggregation. Chemisorption of surfactants can potentially control the nucleation growth and negate the aggregation, nevertheless, the hydrophobic interaction between the tail groups of surfactants adsorbed on the NPs, encourage the interdigitating of NPs near to each other.[22] Interestingly, a further increase of OA to OAm to a 1:5 ratio, resulted in smaller sized NPs (Fe2) with an average size of 6.1 ± 1.1 nm (Figure 4.1 c,d,f). It has been shown previously that increasing the relative amount of the oleylamine surfactant results in smaller non-uniform particles, no doubt caused by the extra amount of oleylamine, which adsorbs on to the surface of nuclei, preventing crystal growth, which favours the generation of small units. [23]

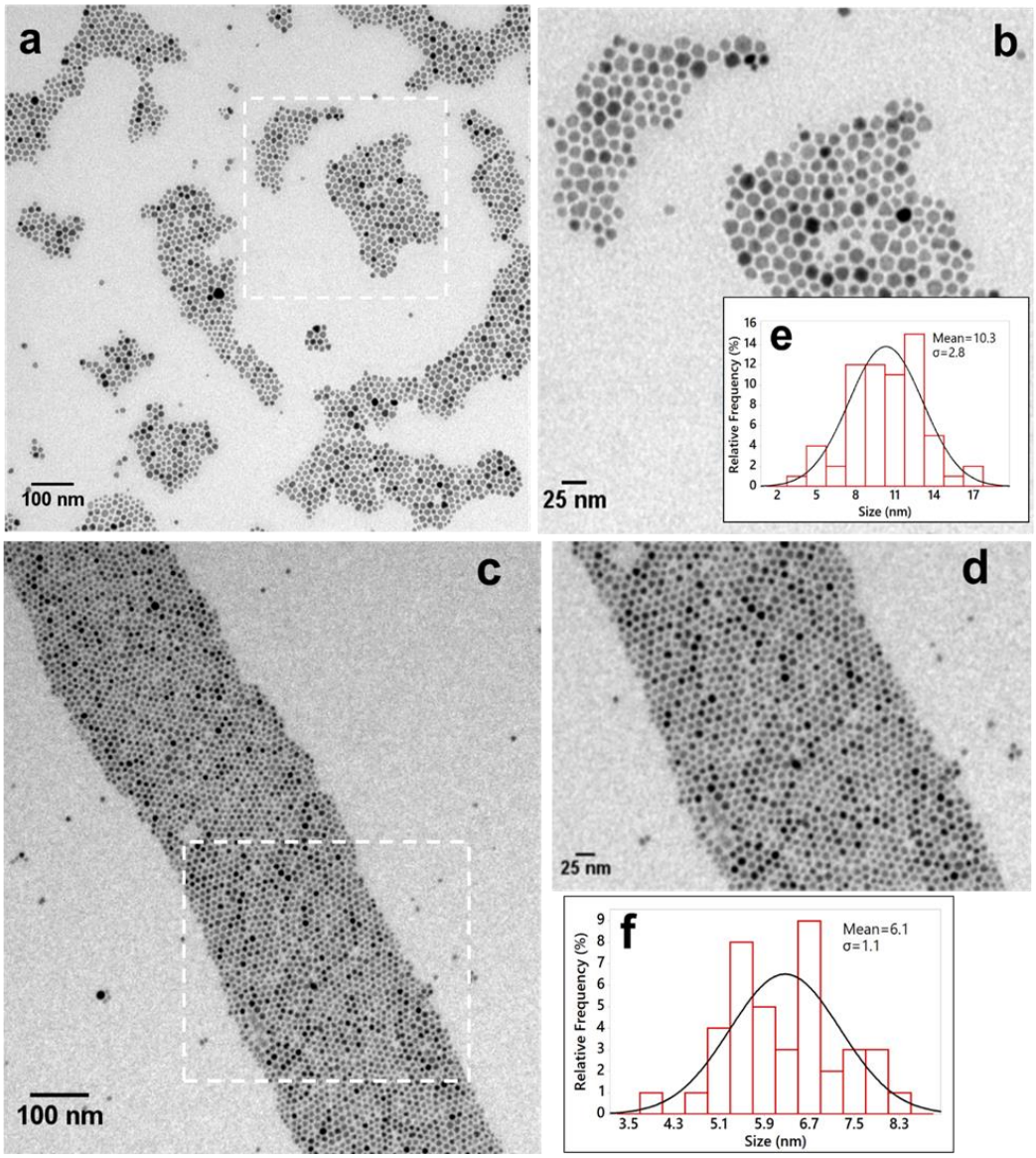

Figure 4.1. TEM images of the synthesized Fe1 (a,b) and Fe2 (c,d) NPs at different magnifications of 100 nm and 25 nm. (TOPO 0.5 mmol, time 120 min at 240 ^{0}C). Inserts: Size distribution of Fe1 (e) and (f) Fe2 with mean size and standard deviation value (σ).

Encouraged by the initial results, we extended this methodology to synthesize cation-substituted magnetite doped $M_xFe_{3-x}O_4$ (M = Zn, Mg) NPs.

Firstly, Zinc was introduced into the Fe_3O_4 lattice in order to obtain uniform monodispersed NPs with increased magnetization. It has been shown by Cheon *et al* [24] that $(Zn_xFe_{1-X})Fe_2O_4$ (x = 0, 0.1, 0.2, 0.3, 0.4, and 0.8) NPs with a single crystallinity phase and size monodispersity could be synthesized from the thermal decomposition of iron and zinc precursors in the presence of surfactants. Their prepared NPs exhibited high and tunable

nanomagnetism with a maximum Ms value of 161 emu/g for the formulation ($Zn_{0.4}$ $Fe_{0.6}$) Fe_2O_4 nano-particle.[24] Our initial attempt began with a dopant of 0.4 mmol zinc utilising a convenient hydrothermal method. As evidenced by the subsequent TEM images, we were able to synthesize high quality particles comparable to that of the prepared particles by Cheon *et al*.

It can be seen from the corresponding TEM images, ZnFe1 NPs (OA to OAm of 1:4; (Figure 4.2 a,b,e) and ZnFe2 NPs (OA to OAm of 1:5; (Figure 4.2 c,d,f) that a variety of morphologies are present including spherical, triangular, cubic and octahedral shapes with an average particle size of 14.1 ± 4.1 nm and 12 ± 7 nm for ZnFe1 and ZnFe2 respectively. The shape evolution process has been delineated in terms of surface free energy. The small particles are unstable due to their high surface free energy therefore, in the process of growth, unconsolidated primary small particles reconstitute into different geometries with more stable structures and less surface free energy [25]. In the case of ZnFe2 NPs, an interesting bimodal distribution of small predominatly spherical NPs and larger particles from the growth of the small NPs can be seen which confirms the growth prohibiting effect of OAm as discussed for Fe1. Notably, the average size of Zn-doped NPs are higher than that of bare Fe_3O_4 NPs which could be due to the substitution of larger radius Zn atoms instead of Fe atoms in the iron oxide structure.[26]

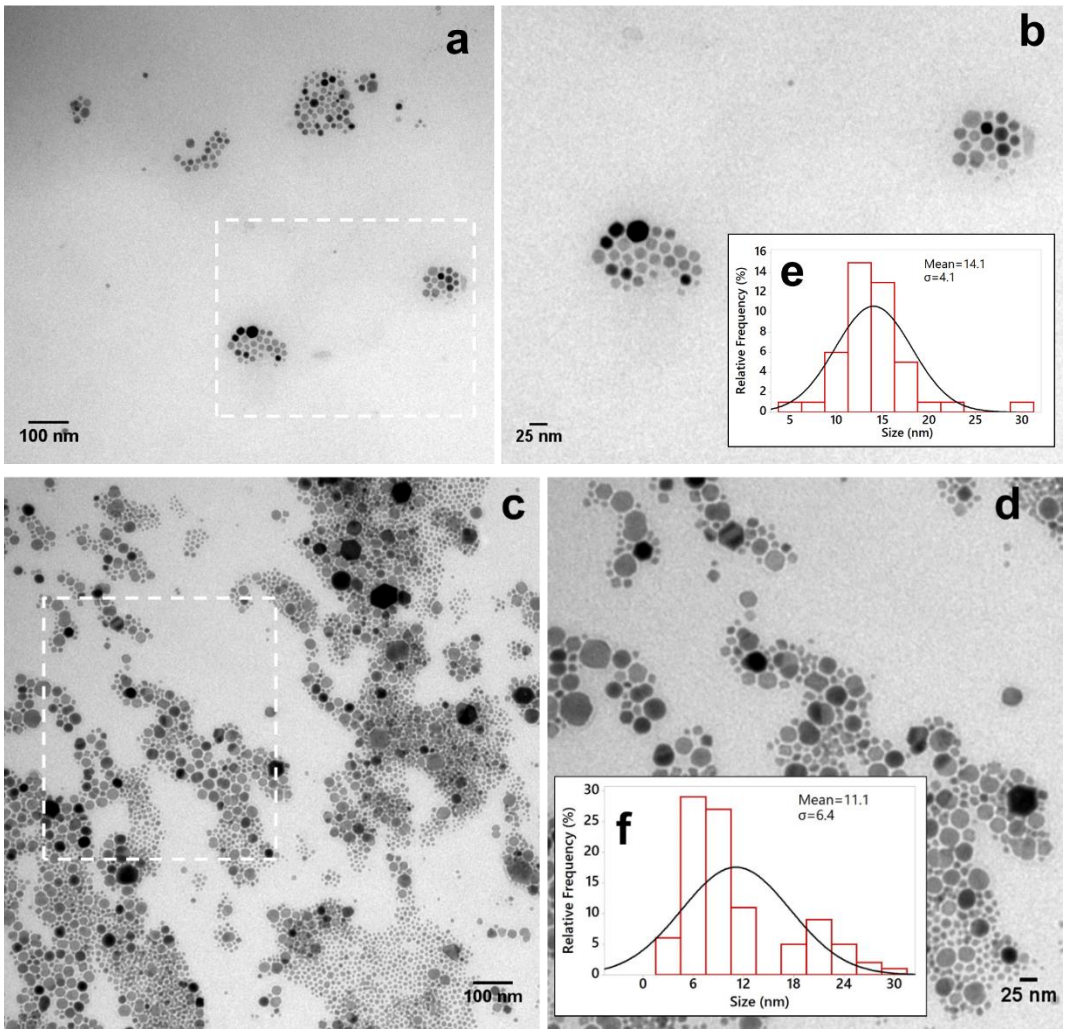

Figure 4.2. TEM images of the synthesized ZnFe1 (a,b) and ZnFe2 (c,d) NPs at different magnifications of 100 nm and 25 nm. (TOPO 0.5 mmol, time 120 min at 240 ^{0}C). Inserts: Size distribution of ZnFe1 (e) and (f) ZnFe2 with mean size and standard deviation value (σ).

Bae et al [2] synthesized magnesium-doped iron oxide NPs with different Mg^{2+} ion concentrations using the thermal decomposition method. The resulting particle achieved a high temperature value of 180 ^{0}C at a biologically safe magnetic induction field with a Mg concentration of 0.13 mmol ($Mg_{0.13}$-Fe_3O_4) using a MFH protocol. We therefore doped 0.13 mmol Mg into Fe_3O_4 NPs with our developed hydrothermal route in order to achieve monodisperse NPs with higher magnetization and heating efficiency. The resulting particles show uniform distribution with low inter-particle distance without aggregation. From their corresponding TEM images, MgFe1 NPs (OA to OAm of 1:4; (Figure 4.3 a,b,e) and MgFe2

NPs (OA to OAm of 1:5; (Figure 4.3 c,d,f) present excellent monodispersity with average particle size of 6.8 ± 1.9 nm and 6.3 ± 1.5 nm respectively.

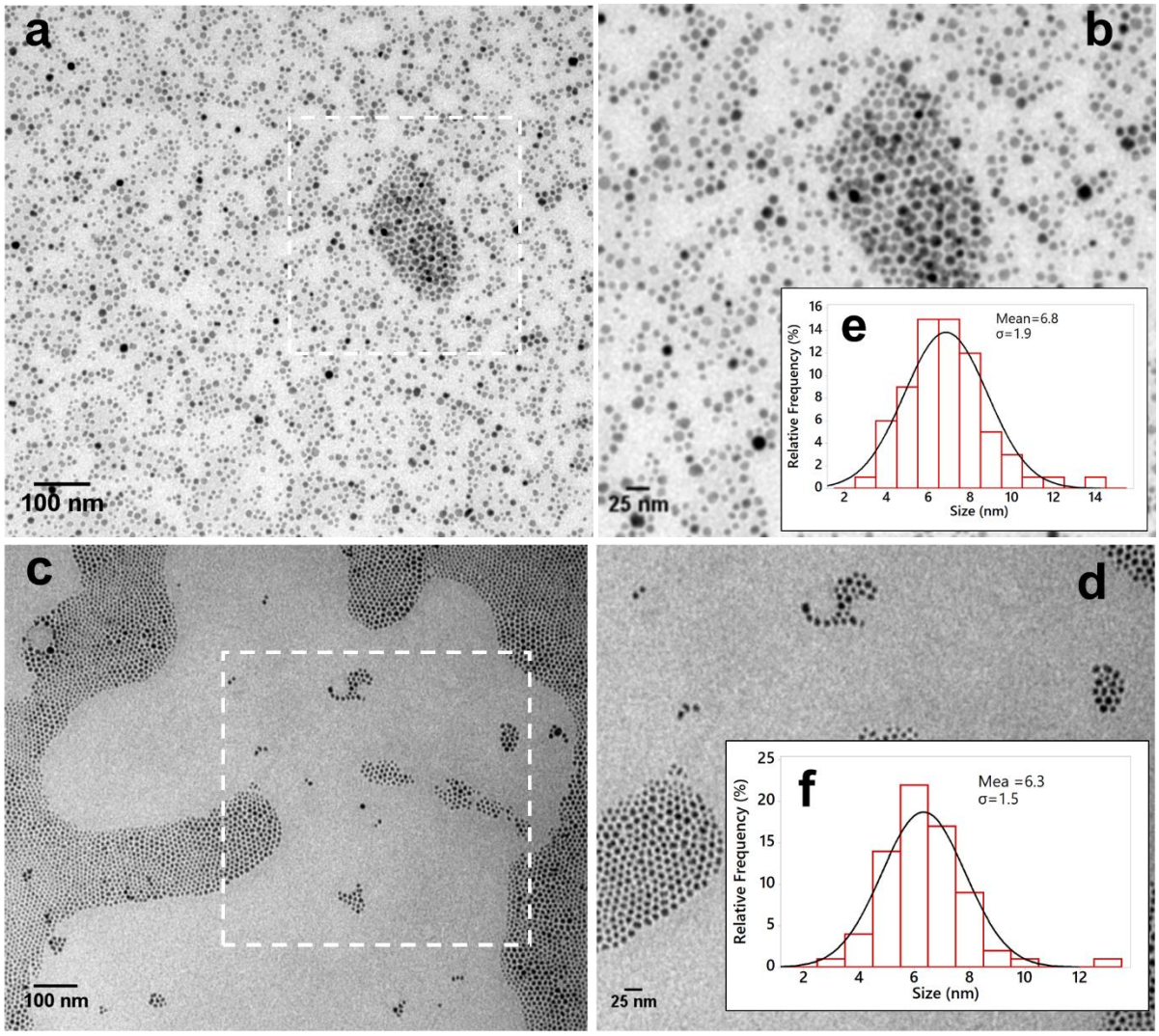

Figure 4.3. TEM images of the synthesized MgFe1 (a,b) and MgFe2 (c,d) NPs at different magnifications of 100 nm and 25 nm. (TOPO 0.5 mmol, time 120 min at 240 ^{0}C). Inserts: Size distribution of MgFe1 (e) and (f) MgFe2 with mean size and standard deviation value (σ).

The size distribution of nanoferrites were also measured using DLS. All the nanoferrites physically clumped together to form bigger size nanocrystals of up to a hundred nanometers, due to van der Waals and magnetic dipole-dipole attractions.[27] The Volume particle size distribution and polydispersity index (PdI) values of the $M_xFe_{3-x}O_4$ (M = Fe, Mg, Zn) nanoferrites are presented in (Figures 4.13-18). Fe1 exhibited the narrowest relative size distribution (d_h ~ 125 nm and PdI = 0.16) which could lead to a high magnetic and heating

response.[28] Overall, the Mg and Zn doped Fe_3O_4 NPs form larger aggregates than that of the undoped variants ($d_h \sim 214.7$ nm and 189.9 for ZnFe2 and MgFe2 respectively). This is an undesirable characteristic for their biomedical utilization, as the large clusters are believed to be removed from the bloodstream more easily and can also cause embolism.[27, 29]

The XRD patterns, average crystallite size and unit cell parameters (d-spacing of lattice planes (*hkl*), and lattice constant (*a*) values) of nanoferrites extracted utilizing Debye−Scherrer and Bragg equations are shown in (Figure 4.4 and Table 4.1).

The XRD patterns of the Fe_3O_4 NPs present the crystallographic planes of (111), (220), (311), (400), (422), (511), and (440) corresponding to the diffraction peaks at 2θ of 18.50°, 30.1°, 35.6°, 43.1°, 53.2°, 57.2°, and 63° respectively (Figure 4.4a). The positions and relative intensities of all diffraction peaks indexed well to the standard cubic spinel structure (JCPDS No. 71- 1232).[30] Lattice parameters were calculated for all $M_xFe_{3-x}O_4$ (M = Fe, Mg, Zn) nanoferrites by consideration of the strong Bragg reflection peak (Miller index 3 1 1). (Table 1). The average crystallite size estimated from Debye−Scherrer equation was 4.8 ± 0.89 and 3.2 ± 1.5 for Fe1 and Fe2 respectively. The achieved lattice parameter for Fe1 and Fe2 NPs were 8.34 Å and 8.35 Å respectively matching well with a = 8.35 Å for nanosized Fe_3O_4 NPs.

The $Mg_{0.13}Fe_3O_4$ nanoferrites, presented with similar values for the diffraction peaks (2θ) corresponding to the (111), (220), (311), (400), (422), (511), and (440) crystal planes which confirms the formation of a pure $MgFe_2O_4$ phase with JCPDS (card No. 36-0398). [31] It is assumed that the replacement of Fe^{2+} ion (atomic radius = 0.64 Å) with Mg^{2+} of similar atomic radius (0.65 Å) may not induce any peak shifts.[32] For instance the lattice parameter for MgFe2 was 2.5184 Å, similar to that of 2.5184 Å for Fe2. (Figure 4b). The average crystallite size estimated from the Debye−Scherrer equation was 4.6 ± 1.1 and 3.1 ± 1.2 for MgFe1 and MgFe2 respectively.[33] Similar to the above $Mg_{0.13}Fe_3O_4$ nanoferrites, diffraction peaks (2θ) corresponding to the (111), (220), (311), (400), (422), (511), and (440) crystal planes were also observed in the XRD pattern of $Zn_{0.4}Fe_3O_4$, confirming the formation of a pure zinc nanoferrite (JCPDS card np. 89-1397).[33]

The introduction of Zn into the Fe_3O_4 structure resulted in sharper peaks indicating an improvement in crystallinity. This was accompanied by the (311) crystal plane of the Zn-

doped Fe_3O_4 shifting to slightly smaller angles, (from 2θ = 35.64° for Fe1 to 35.52° for ZnFe1). (Figure 4.4b). The average crystallite size estimated from the Debye−Scherrer equation was 7.4 ± 0.87 and 6.2 ± 1.3 for ZnFe1 and ZnFe2 respectively. Furthermore, the corresponding lattice constant (*a*) and d-spacing of lattice planes (*d*) increased from 8.3481 to 8.3754 Å and 2.5170 to 2.5253 Å respectively. Substitution of larger Zn ions (atomic radius of 0.74 Å) with a Fe ion ((Fe^{2+} ion (atomic radius = 0.64 Å) and Fe^{3+} ion (atomic radius = 0.49 Å)) in an Fe_3O_4 crystal is thought to cause the expansion in length of the *a*-axis of the crystals unit cell. This has been observed previously.[34] Overall, there is a discrepancy in size measurements from XRD, TEM and DLS techniques. The hydrodynamic size (d_h) obtained from DLS, and mean size (D_h) obtained from TEM are larger than that of the crystallite size (*D*) measured by XRD. This could be ascribed to the different medium in which NPs were measured. In the case of DLS, solution aggregation may be responsible for the enhanced sizes,[35] while nanocrystal stacking may account for the source of error in TEM imaging.

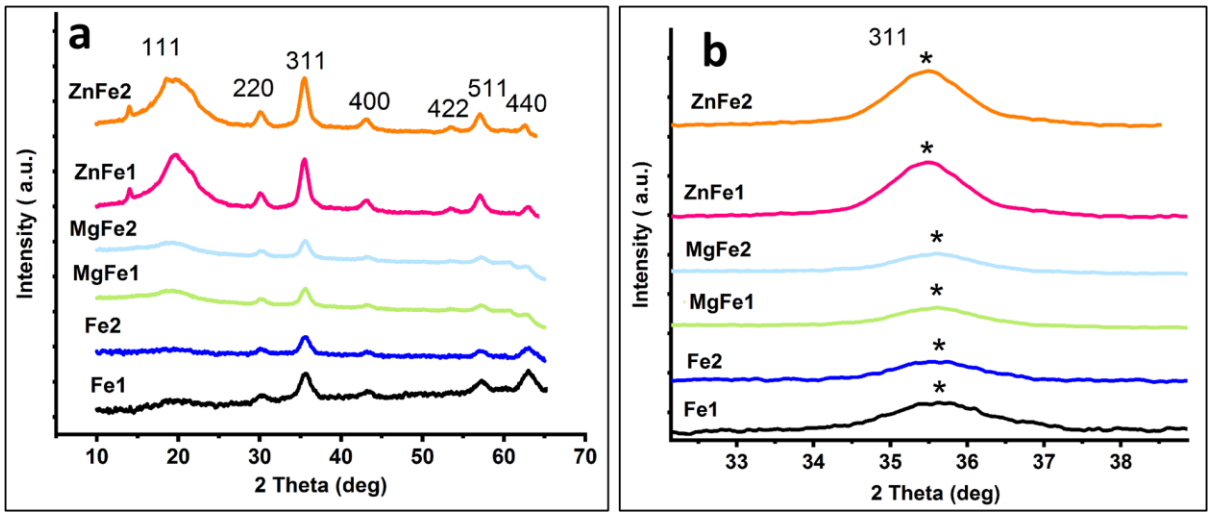

Figure 4.4. (a) Powder X-ray diffraction patterns and (b) the highlighted (311) diffraction peak of $M_xFe_{3-x}O_4$ (M = Fe, Mg, Zn) nanoferrites.

In order to determine the thermal stability and organic fraction of the nanoferrites, thermogravimetric analysis (TGA) was acquired under an N_2 flow with a heating rate of 10 °C/min from room temperature up to 800 °C. The mass percentage of the residue reflects the fraction of inorganic cores inside the nanoferrites. As can be seen from the thermograms, Fe1, Fe2, MgFe1 and MgFe2 nanoferrites exhibit similar profiles with four stages of mass loss (Figure 4.5). The mass loss includes: below 200 °C (evaporation of water

or organic solvents),[36] 200 °C -300 °C (decomposition of free surfactants/ capping molecules adsorbed on the surface),[37] 300 - 450 °C (decomposition of directly attached surfactants)[38] and 650-700 °C corresponding to the reduction of the inorganic core under an inert atmosphere.[39] For the Zn-doped Fe_3O_4 NPs, the mass loss for inorganic core reduction was a two-stage plateau between 600-650 °C and 700-750 °C. Similar results have also been observed for oleic acid-capped zinc nanoferrites.[40] Importantly, the content of organic molecules on the nanoferrite surface decreases with increased magnetic core size. (Table 4.1). This can be ascribed to the smaller surface to volume ratio and subsequent lower active binding sites on the surface of bigger cores, which discourage the adsorption of surfactants.[41]

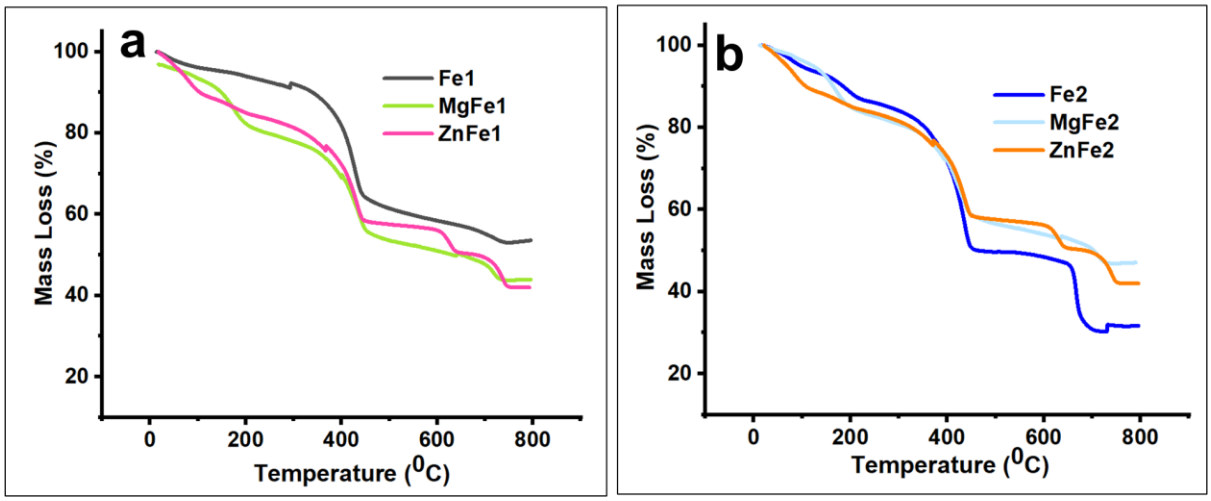

Figure 4.5. (a, b) TGA curves of $M_xFe_{3-x}O_4$ (M = Fe, Mg, Zn) nanoferrites.

Table 4.1. Calculated values of size and lattice parameters for $M_xFe_{3-x}O_4$ (M = Fe, Mg, Zn) spinel nanoferrites

Sample	Size (nm) TEM	Crystallite Size (nm) XRD	Position of 311 peak in degree (θ)	*d*, Lattice spacing (Å)	*a*, Lattice constant (Å)	Organic content from TGA (%)
Fe1	10.3 ± 2.8	4.8 ± 0.89	35.64	2.5170	8.3481	46.39
Fe2	6.1 ± 1.1	3.2 ± 1.5	35.62	2.5184	8.3527	68.29
MgFe1	6.8 ± 1.9	4.6 ± 1.1	35.64	2.5170	8.3481	56.04
MgFe2	6.3 ± 1.5	3.1 ± 1.2	35.62	2.5184	8.3527	52.93
ZnFe1	14.1 ± 4.1	7.4 ± 0.87	35.52	2.5253	8.3754	58.02
ZnFe2	11.1 ± 6.4	6.2 ± 1.3	35.4	2.5336	8.4029	61.35

The elemental composition and atomic percentage (At %) of monodispersed $M_xFe_{3-x}O_4$ (M= Fe, Mg, Zn) nanoferrites were qualitatively evaluated with energy dispersive X-ray spectroscopy (EDS) analysis. The EDS spectra were visualized through a line scan of several randomly selected areas under different magnifications for each nanoferrite. All nanoferrite NPs presented very strong signals corresponding to C atoms which were ascribed to the carbon chains of the surfactants/capping agents on the nanoparticle surface and the coated carbon to increase the conductivity of samples before imaging.[42] The characteristic peaks for Fe and O were detected in the EDS spectra of Fe1 and Fe2 NPs. The EDS spectra of MgFe1 and MgFe2 exhibit the signals for Fe, Mg, and O atoms. In the same fashion, the representative signals for Fe, Zn and O atoms were detected in the EDS spectra of ZnFe1 and ZnFe2. It should be noted that two EDS spectra of similar NPs exhibit very similar atomic percentages (A %). For instance, the A % of the Mg atoms were 0.50 and 0.48 % for MgFe1 and MgFe2 respectively. A similar trend was obtained for Fe and Zn (Figure 4.19-21). This confirms the chemical uniformity and homogeneity of the composition of the nanoferrites. The intensity of Fe signal decreases in the case of Zn and Mg doped NPs. This decrement in intensity is more pounced for Zn which is in good agreement with the initial molar ratio of metal precursors undertaken for the synthesize of nanoferrites with 1/0.4 mmol for Fe/Zn in contrast to 1/0.13 mmol for Fe/Mg doped Fe_3O_4 NPs. These results are an indication of

utility of the substitutional feature of the hydrothermal method for the doped Fe_3O_4 NPs. Kolen'ko *et al* observed the same trend by doping Zn in the Fe_3O_4 NPs.[43] The elemental atomic ratios of Mg, Zn and Fe and actual chemical composition of $M_xFe_{3-x}O_4$ nanoferrites were quantified by AAS following the procedure as reported by Pellegrino *et al*.[3] (Table 2). Taking into account the AAS results, the elemental atomic ratios and the chemical composition from theoretical assumptions deviates from experimental values so that all doped nanoferrites except ZnFe1 present compositional deficiency. This deviation from theoretical stoichiometry has also been observed in Co and Mn doped Fe_3O_4 nanoparticles.[44, 45] Different thermal stability of ions (Fe^{3+}, Co^{2+}, Mn^{2+}) is supposed to be an influential contributor. Additionally, the excessive portion of surfactant might decrease decomposition temperature of the metal complex and affect the growth mechanism. In addition, the reductive nature of the reaction medium may encourage the partial reduction of iron (III) to iron (II) which would compete with the doped ions in the growth process.[45]

Table 4.2. Molar ratios and chemical formula for $M_xFe_{3-x}O_4$ (M = Mg, Zn) nanoferrites found by AAS.

Nanoferrites	**Molar ratio**		**Chemical formula**	
	Theoretical	**Experimental**	**Theoretical**	**Experimental**
MgFe1	0.13:1 Mg/Fe	0.13:1.8 Mg/Fe	$Mg_{0.35}Fe_{2.65}O_4$	$Mg_{0.2}Fe_{2.8}O_4$
MgFe2	0.13:1 Mg/Fe	0.06:1.7 Mg/Fe	$Mg_{0.35}Fe_{2.65}O_4$	$Mg_{0.1}Fe_{2.9}O_4$
ZnFe1	0.4:1 Zn/Fe	0.48:1.2 Zn/Fe	$Zn_{0.85}Fe_{2.15}O_4$	$Zn_{0.85}Fe_{2.15}O_4$
ZnFe2	0.4:1 Zn/Fe	0.45:0.82 Zn/Fe	$Zn_{0.85}Fe_{2.15}O_4$	$Zn_{0.77}Fe_{2.23}O_4$

X-ray photoelectron spectroscopy (XPS) was conducted to gain insight into the chemical compositions and metal (M^{2+}, Fe^{3+}) valance states of $M_xFe_{3-x}O_4$ (M = Fe, Mg, Zn) nanoferrites. Wide-scan survey spectra of the nanoferrites revealed photoelectron lines related to C*1s*, O*1s*, Fe*2p*, Zn*2p*, Mn*2p* and Mg *1s* as illustrated in (Figure 4.6 and Figure 4.22-26). The binding energy scale was calibrated utilizing the C*1s* signal (originating from adventitious hydrocarbon) at 285 eV as an energy reference. For each nanoferrites, the high-resolution narrow-scan XPS spectra of the related elements were also recorded.

The C*1s* XPS spectra of all nanoferrites revealed a single peak centred at 285 eV arising from C-C bonds from organic molecules adsorbed on the surface.[46] and adventitious carbon from exposure of the samples to the air[42] The O 1s core level spectra of all nanoferrites exhibit a main peak at ~ 532 eV corresponding to −COO−carboxylate groups[42] and a second signal centred at ~ 530 eV corresponding to the lattice oxygen of metal–oxygen bonds (M-O) of $M_xFe_{3-x}O_4$.[47]-[48]

Typically, Fe^{3+} ions at the O_h site of Fe_3O_4, exhibit the spin−orbit split doublet of Fe $2p_{1/2}$ and Fe$2p_{3/2}$ at 724 and 711 eV [42] while, the Fe$2p_{3/2}$ peak at ~ 707 and ~ 709 eV verify the existence of Fe in either 0 and +2 oxidation states .[49] Additionally, γ-Fe_2O_3 will exhibit a small satellite peak at 718-719 eV between the $2p_{1/2}$ and $2p_{3/2}$ peaks which is ascribed to Fe*2p* XPS spectrum of Fe^{3+} ions.[50] Taking into account the electronic state of Fe^{3+} and Fe^{2+} ions, the high-resolution regional XPS spectra of Fe*2p* were recorded for all nanonferrites as shown in (Figure 4.6 and Figure 4.22-26). Each Fe*2p* peak reflects additional satellite peaks at higher binding energies due to the possible excitation of an unpaired electron (from a 3d orbital) to a higher bound energy level (4s orbital line). The fine scan of the Fe*2p* region in the spectra for the non-doped Fe_3O_4 nanoparticles (Fe1 and Fe2), reveals two peaks centered at 711.1 eV corresponding to the Fe $2p_{3/2}$ peak of Fe^{3+} ions at the O_h site and 724.5 eV corresponding to the Fe $2p_{1/2}$ peak of Fe^{3+} ions at the T_d site. The observed binding energies match well with literature values for magnetite formation. Notably, the Fe*2p* spectra of the Fe2 and MgFe1 NPs do not exhibit any diagnostic peaks indicating the absence of Fe on their surface. In the case of Mg doped Fe_3O_4, (MgFe1 and MgFe2), the absence of peaks in the high-resolution Mg*1s* photoelectron spectra, indicates the absence of magnesium on the surface. Additionally, the Fe*2p* peaks identifies an oxidation state of 3+ for iron which is in line with the XRD results, confirming the formation of magnesium ferrite ($MgFe_2O_4$)[51]

For the Zn-doped Fe_3O_4 nanoferrites (ZnFe1), the presence of two major peaks at 711 and 724 eV corresponding to Fe$2p_{3/2}$ and Fe$2p_{1/2}$ respectively rules out the possibility of a 3 + oxidation state for Fe. The Zn*2p* core-level XPS spectrum reveals two typical peaks at binding energies of 1021 and 1045 eV corresponding to Zn$2p_{3/2}$ and Zn$2p_{1/2}$ photolines respectively. The values match well with the reported literature values for a 2 + oxidation state for the Zn ions verifying the formation of zinc ferrite $ZnFe_2O_4$[52]

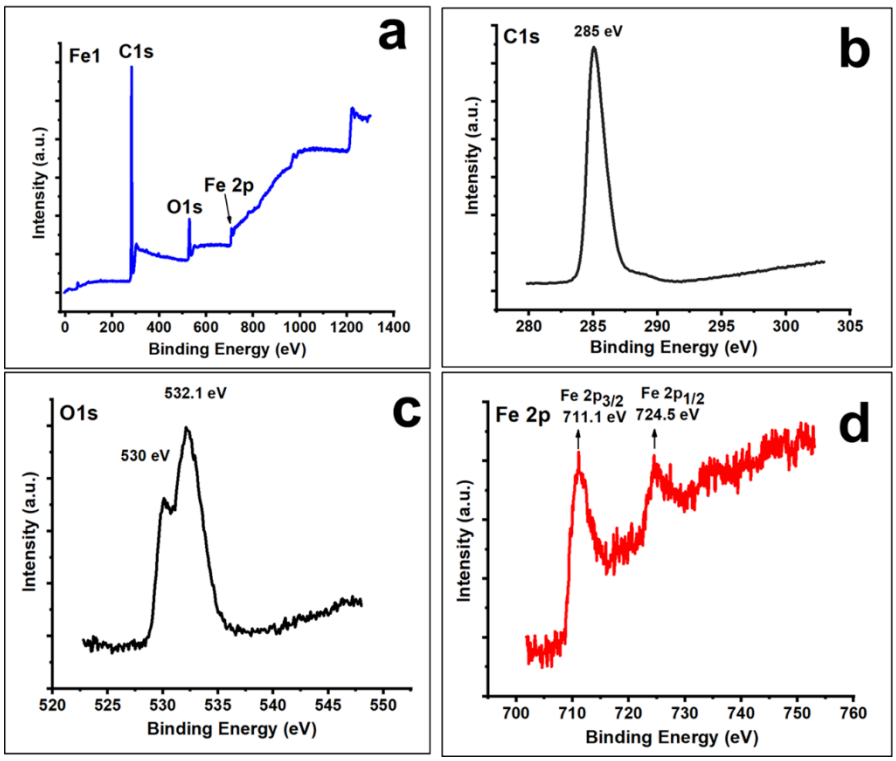

Figure 4.6. XPS spectra of the Fe1 nanoferrite (a) survey scan (b) C1s (c) O 1s and (d) Fe 2p regional scans.

4.2.2. Magnetization Studies

To identify the magnetic nature of the synthesized nanoferrites, magnetization measurements were recorded as a function of magnetic field (M−H) and temperature (M−T) with a vibrating sample magnetometer (VSM). Magnetization curves as a function of the applied magnetic field (M−H loops) were collected from −20 to 20 kOe magnetic field strength at room temperature (~ 300 K) (Figure 7). From these scans the related parameters such as M_r, H_c and normalized remanence (M_r/M_S) values were calculated (Table 4.3). The prepared NPs exhibit a Langevin-like approach to magnetization saturation, with negligible coercivity and remanence as observed in the hysteresis loops shown in Figure 4.7 and Table 4.3. This negligible remanence and coercivity can be ascribed to the particle size distributions.[53] The inclusion of Mg^{2+} and Zn^{2+} ions in the spinel structure of Fe_3O_4, does not alter its superparamagnetic characteristic which is advantageous for biomedical applications.[54] Looking into the magnetization values, a reduction in magnitude was observed when the ration of surfactants (OA: OAm) increased from 1:4 to 1:5. Oleic acid (OA) and oleylamine (OAm) were used as surfactants to stabilize the particles and reduce the aggregation through steric repulsion. It has been shown that coating a nonmagnetic

layer on their surface can significantly reduce the magnetic moment as a fraction of total mass.[55]

The saturation magnetization of nanoparticles can be influenced by their particle size and composition. For the iron oxide nanoparticles, (Fe1 and Fe2) there is a correlation between size (TEM) and magnetization values where the magnetization decrease with a decrease in particle size. This trend has been observed in some other ferrites and is ascribed to the surface spin canting effect.[56] Another influential contributor is the control distribution of dopant ions into the Fe_3O_4 unit cell for maximal magnetization.[57] The magnetization value for Fe1 was 31.6 emu/g (Figure 4.7, black line). Doping Zn ions (0.4 mmol) into Fe_3O_4 reduces the magnetization to 10.7 emu/g (Figure 4.7, pink line). Similarly, doping Mg ions (0.13 mmol) resulted in reduction in magnetization to 7.5 emu/g (Figure 4.7, green line). The magnetization value for Fe2 was measured to be 18.6 emu/g (Figure 4.7, dark blue line). In a similar fashion, doping Zn ions (0.4 mmol) and Mg ions (0.13 mmol) into Fe_3O_4, reduced the magnetization to 16.2 emu/g (Figure 4.7, orange line) and 10.6 emu/g (Figure 4.7, light blue line) respectively. The utilized concentration of 0.4 mmol and 0.13 mmol for Zn and Mg resulted in reduction in magnetic moment values which were different to those reported in the literature.[58] These results can be explained by consideration of the Fe_3O_4 nanoparticle atomic structure. Fe_3O_4 also represented as Fe^{3+}. Fe_3O_4 /$Fe^{2+}O_4$ is an inverse spinel ferrite (AB_2O_4 type) where Fe^{3+} is in tetrahedral site (T_d) and Fe^{3+}/Fe^{2+} ions have occupied octahedral interstices (O_h) in a ratio of 1:1.[4, 59] The magnetic moments of the Fe^{3+} ions at the T_d and O_h sites are aligned in opposite directions and cancel each other. Accordingly, the magnetic moment of Fe^{2+} ions (4 μB) in the O_h sites determine the net magnetization of the Fe_3O_4 nanoparticle. Both, Zn^{2+} and Mg^{2+} ions are diamagnetic with zero magnetic moment (0 μB). Considering the reduced magnetization, we can safely assume that both Zn^{2+} and Mg^{2+} ions have occupied the T_d sites with the Fe^{3+} ions occupying the O_h sites, leading to antiferromagnetic coupling interactions of Fe^{3+} atoms between these sites which decrease the magnetization moment.[60]

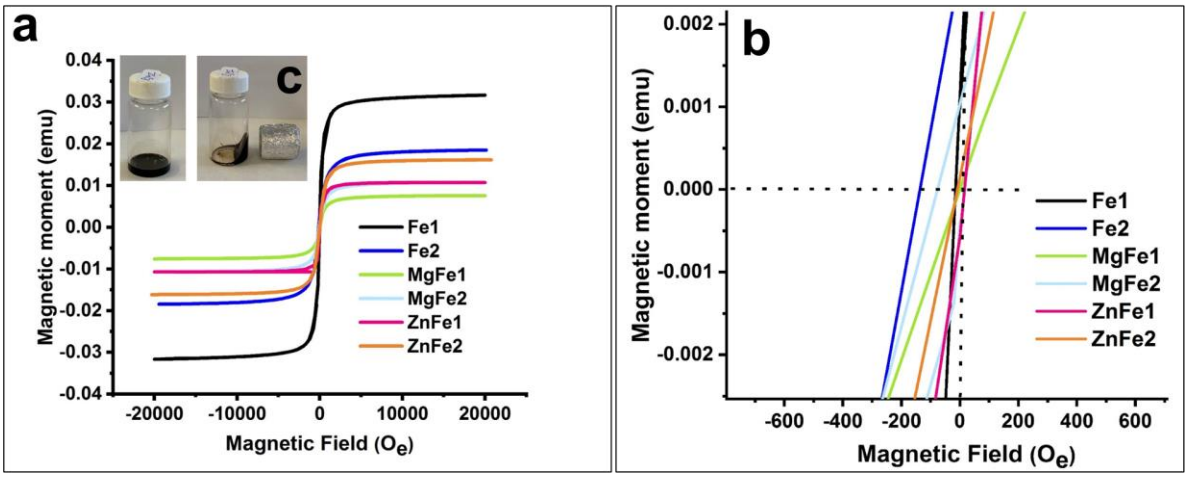

Figure 4.7. (a) Magnetic hysteresis loops of $M_xFe_{3-x}O_4$ (M = Fe, Mg, Zn) nanoferrites at room temperature (b) Magnified view of hysteresis loop of nanoferrites in low magnetic field, as indicated by red bracket in (a). (c) The inset shows the magnetic response of ZnFe2 to an external magnetic field.

The temperature dependence of magnetization (M-T curves) were plotted following the field cooling (FC) and zero field cooling (ZFC) protocols between 10 and 350 K under a constant magnetic field of 10 Oe. The M-T curves and extracted blocking temperature, T_B and magnetic crystalline anisotropy energy (K_{eff}) of all nanoferrites are shown in Figure 4.8 and Table 4.3.

Utilizing Néel law, $K_{eff} = 25k_BT_B/V_m$, the magnetic anisotropy constant (K_{eff}) were calculated for all nanoferrites where k_B is Boltzmann's constant (1.3807 x 10^{-23} J/K) and V_m is the volume of a single nanocrystal assuming sphere as $V_m = \pi D_m^3/6$ (D_m is the magnetic core diameter from TEM) .[7, 61] For all nanoferrites, there is a peak in the ZFC measurements, indicating a blocking behaviour, with the blocking temperature T_B well below room temperature (300 K). FC/ZFC curves are converged at temperatures higher than the blocking temperatures ($T > T_B$). These are signs of superparamagnetic-like behaviour. ZFC measurements typically exhibit a qualitative indication of the size distribution of the particles and T_B refers to the maximum of the ZFC magnetization plot. For an ideal system of non-interacting monodispersed particles, T_B would be one single temperature. For a collection of particles with narrow size distribution, the ZFC curve would present a sharp peak. However, for a collection of particles with a large size distribution, there would be a distribution of the T_B so that the ZFC curve maxima would be broad.[62] In our case the Zn-

doped nanoferrites present with a broader ZFC curve. This is consistent with the TEM images where the standard deviation (σ) values of particle size are larger due to the large size distribution.[63]

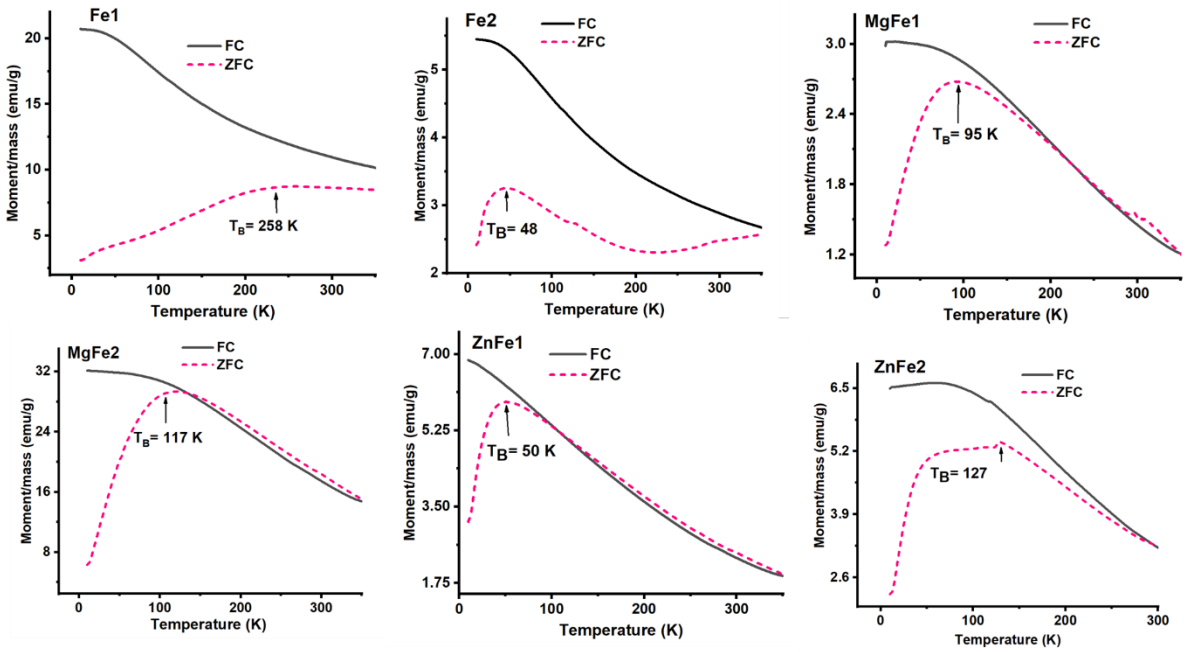

Figure 4.8. FC/ZFC curves of the MxFe3−xO4 (M = Fe, Mg, Zn) nanoferrites recorded at a constant magnetic field of 10 Oe.

Table 4.3. Parameters of ZFC/FC and M-H hysteresis loops for $M_xFe_{3-x}O_4$ (M = Fe, Mg, Zn) nanoferrites

Nanoferrites	M_s (emu/g)	M_r (emu/g)	H_c (O_e)	M_s/M_r	T_B	k_{eff} (j.m^{-3}) × 10^4
Fe1	31.6	13	48	2.4	260	15.6
MgFe1	7.5	2.1	37	3.5	95	28.7
ZnFe1	10.7	4.5	14	2.3	50	1.2
Fe2	18.6	6.3	168	2.9	48	13.9
MgFe2	10.7	1.3	109	8.2	120	31.6
ZnFe2	16.1	7.2	43	2.2	128	6.2

4.2.3. Magnetic hyperthermia studies:

The heating potential of prepared nanoferrites were determined in water through a calorimetric non-adiabatic set up. With consideration towards clinical applications, the product of H and f should be below the threshold limit of $H \times f = 5 \times 10^9$ A m^{-1} s^{-1}. In our experiments the field configuration was one order of magnitude higher than the required

safety limit (1.7×10^{10} A m^{-1} s^{-1}), however other research groups have also considered the same order of magnitude as the threshold limit for their applications.[64]

The heating profile of samples is presented in Figure 4.9a. As can be seen from the curve, the temperature increases monotonically and saturates after a certain time. This rapid rise is correlated to Néel relaxation and Brownian rotation of particles under a switching magnetic field.[53] The temperature saturation is due to temperature loss from the magnetic fluid to the environment.[65] The nanoferrites differ both in the initial speed of the temperature rise and the time taken to reach the hyperthermic threshold temperature (43 °C). For instance, Fe1 NPs reach the temperature (45 °C) within 3 min, before all other nanoferrites. Additionally, the maximum rising temperature (T_{max}) was 66 °C for Fe1 NPs after activation of the magnetic field for 12 min compared to 50 °C for ZnFe1.

It should be noted that the concentration of nanoferrites in our study (5 mg/mL) is lower than other published accounts and significantly lower than the recognized clinical concentration of ferrofluid at 112 mgFe/mL by Jordan et al. Accordingly, an increased temperature in a shorter time might be feasible with a higher concentration.[66] The heat dissipation rate of the ferrofluids (termed as specific absorption rate (SAR)) was quantified by the initial slope method from heating curves for all nanoferrites and is summarized in Table 4.4. The maximum SAR value was 87 W/g for Fe1 NPs (Figure 4.9b). Since, SAR values are usually obtained under different extrinsic magnetic field parameters (*H* and *f*), it is not feasible to directly compare the heating potential of similar ferrofluids in terms of size and chemical composition. Accordingly, SAR values were normalized to the intrinsic loss power (ILP) as an AC field-independent parameter to allow the direct comparison of the heating efficiency of prepared nanoferrites in our work with the available literature data for similar ferrofluids (Figure 4.9c). The ILP values of the aqueous dispersions of the prepared nanoferrites listed In Table 4, span from 0.02 - 0.05 nH m^2 kg^{-1} which are smaller than reported values in the literature for nanoferrites with a similar average core size and composition. For instance, ILP values of 3.8 nH m^2 kg^{-1} and 1.75 nH m^2 kg^{-1} have been reported for Fe_3O_4 nanoparticles.[67] Kusigerski et al. achieved an ILP value of 0.57 nH m^2 kg^{-1} for $Mg_{0.1}Fe_{2.9}O_4$ NPs which is slightly higher than that of the $Mg_{0.13}Fe_{2.87}O_4$ nanoferrites prepared by our group. Kallumadil et al investigated the heating potentials of commercially available iron oxide ferrofluids supplied by different companies with different iron content,

nanocrystallinity and hydrodynamic diameter (d_h). Calorimetric measurements recorded at 900 kHz with a field amplitude of 5.66 kA/m, revealed ILP values ranging from 0.15 to 3.1 nH m^2 kg^{-1}. (Resovist, ILP ≈ 3.1, d_h: 60 nm, carboxy dextran-Fe_3O_4). Later studies have reported ILP values higher than that of commercial ones. These include ILP of 4.1 nH m^2 kg^{-1} by Thanh *et al* [68] (citric acid -Fe_3O_4, d_h: 141 nm), ILP of 5.6 nH m^2 kg^{-1} by Pellegrino *et al* [69] (Fe_3O_4 nanocubes, d_h: 19 nm) and ILP of 6.1 nH m^2 kg^{-1} by Parkin *et al* [70] (Tiopronin -Fe_3O_4, d_h : 135 nm). Several intrinsic features such as particle size and size distribution,[71] geometry,[72] chemical composition, magnetocrystalline anisotropy,[73] saturation magnetization, concentration, agglomeration state[74] and dipole–dipole interactions[75] affect the heating performance of the ferrofluids. In case of our nanoferrites, Fe1 has the highest heating potency due to lower aggregation (DLS), lower surfactant fraction on the surface (TGA) and a higher magnetization value (VSM). Considering the simultaneous contribution of these factors to the final heating outputs, it is however rather complex to interpret the heating outputs of Mg and Zn-doped nanoferrites. ZnFe2 has the higher heating efficiency than MgFe2 cause of higher magnetization and lower surfactant fraction on the surface. On the other hand, MgFe1 has the higher heating efficiency than ZnFe1 due to lower surfactant fraction on the surface however the magnetization is lower. It is worth noting that there is no full consensus on the influence of the aggregation state (dipolar interactions) on heating efficiency of fluids due to controversial results reported in the literature.[76] It has been shown that the dipolar interactions significantly impair the heat dissipation process because of the disturbed magnetisation relaxation time.[77] Conversely, superior heating performance (5 orders of magnitude) has been reported for Fe_3O_4 clusters compared to randomly distributed NPs.[78] In the present study, the potential aggregation for Mg and Zn-doped nanoferrites is larger than non-doped Fe_3O_4 nanoparticles (DLS). This has translated to the lower magnetization (VSM) and heating performance of the doped versus undoped nanoferrites. The mechanism by which the heat can be created was explored further. Upon exposure of the nanoparticles to an alternating magnetic field, heat is dissipated into the medium through a variety of different pathways depending on their magnetic profile and size. Either by relaxation loss (Néel or Brown spin relaxations for a superparamagnetic regime size < 30 nm) or hysteresis loss (for a ferromagnetic regime size > 30 nm).[79] In our case, hysteresis loss does not dominate due to the superparamagnetic behaviour of our nanoferrites with negligible hysteresis.[80] (Figure 4.7). Therefore, it appears that magnetic

relaxation loss is the greatest contributor to the heat generation. For a single domain non-interacting magnetic particle, the particle can generate heat through two related mechanisms, either Néel or Brown relaxations. Néelian relaxation is the energy loss in the form of heat by an internal rotation of individual magnetic moments within the particle. Brownian relaxation pertains to the energy loss in the form of heat by the physical rotation of the particle itself under AMF.[81] The Brownian (τ_B) and Néel (τ_N) relaxation times of a single particle assuming as sphere can be calculated utilising the following formulas:

$$\tau_N = \tau_0 \exp\left[\frac{K\pi D_m^3}{6k_B T}\right] \quad (1)$$

$$\tau_B = \left[\frac{\pi \eta D_h^3}{2k_B T}\right] \quad (2)$$

Where τ_N = Néel relaxation time, τ_0 = effective relaxation time (~ 10^{-9} s), K = effective anisotropy constant, D_m is the magnetic core diameter from TEM, , k_B =Boltzmann constant (1.38×10^{-23}J/K), T = the absolute temperature in Kelvin, τ_B = Brownian relaxation time, η = dynamic viscosity of the surrounding medium ($\eta = 0.7978 \times 10^{-3}$ Pa·s for water) and D_h is the hydrodynamic diameter of the particle from DLS measurements.[82] Considering that these two mechanisms take place in parallel but independently, the effective relaxation time τ_{eff} is given by

$$\tau_{eff} = \frac{\tau_N \tau_B}{\tau_N + \tau_B} (3)$$

When $\tau_N \gg \tau_B$ or $\tau_N \ll \tau_B$, τ_{eff} is minimised. Utilising the corresponding equations (1-3), τ_N, τ_B and τ_{eff} were calculated for all nanoferrites. (Table 4.4). An examination of the data reveals that $\tau_N \ll \tau_B$ for all nanoferrites except for Fe1 which results in $\tau_{eff} \approx \tau_N$. This implies that the Néel relaxation is the dominant mechanism whereby rotation of the magnetic moments inside the particles contribute to the heat generation. However, for Fe1, $\tau_B \ll \tau_N$ which suggests that Brownian relaxation is the dominant pathway. This coexistence behaviour has been observed before.[83]

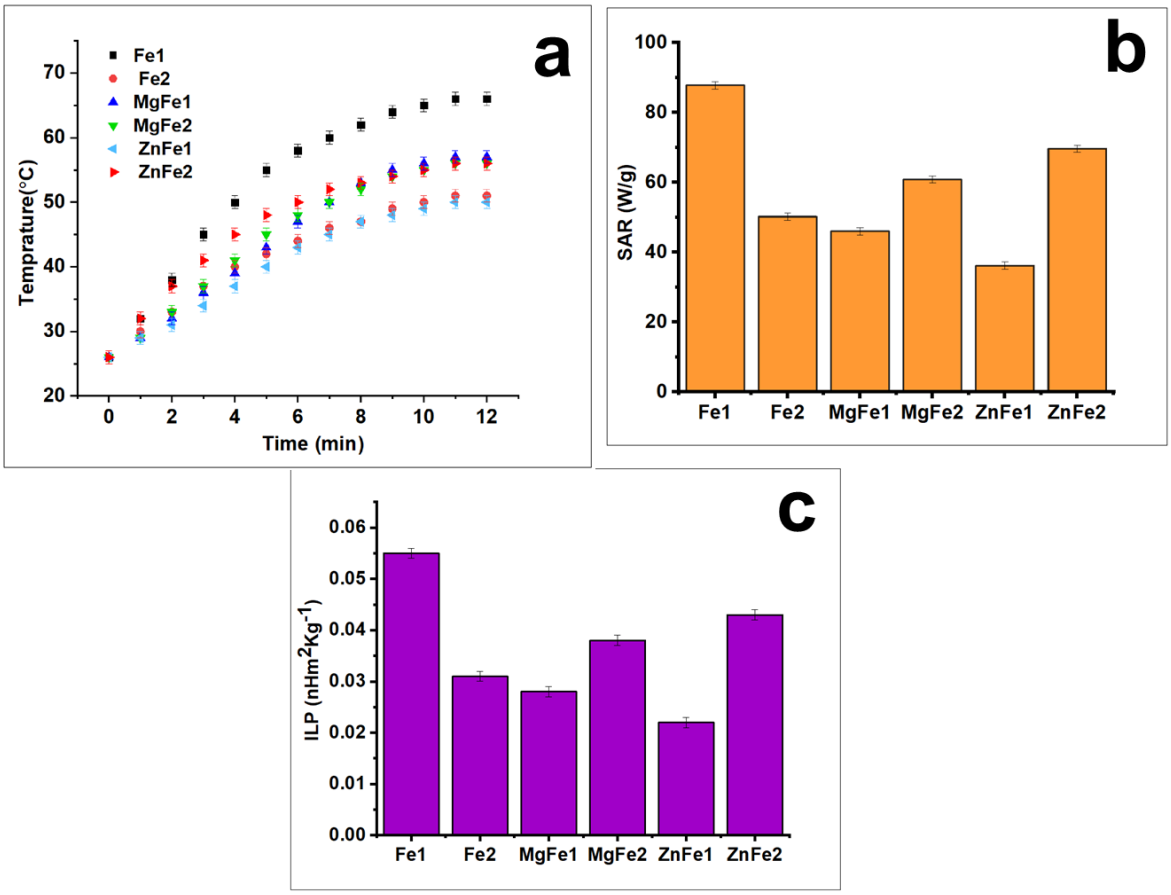

Figure 4.9. (a) Heating curves of water-dispersed MxFe3−xO4 (M = Fe, Mg, Zn) nanoferrites at field amplitude 114.01 mT. (b) SAR and (c) ILP values obtained from these curves.

Table 4.4. Relaxation times and heating parameters for $M_xFe_{3-x}O_4$ (M = Fe, Mg, Zn) nanoferrites

Nanoferrites	τ_B	τ_N	T_{eff}	SAR (W/g)	ILP (nHm^2Kg^{-1})
Fe1	2.3×10^{-4}	2.6×10^{1}	2.3×10^{-4}	87.8	0.055
MgFe1	2.1×10^{-2}	9.6×10^{-5}	9.6×10^{-5}	46.0	0.028
ZnFe1	3.3×10^{-3}	6.4×10^{-8}	6.4×10^{-8}	36.2	0.022
Fe2	1.2×10^{-5}	5.3×10^{-8}	5.3×10^{-8}	50.2	0.031
MgFe2	9.1×10^{-3}	2.3×10^{-5}	2.3×10^{-5}	60.8	0.038
ZnFe2	6.2×10^{-2}	4.1×10^{-5}	4.1×10^{-5}	69.7	0.043

4.3. Conclusion

A series of monodispersed $M_xFe_{3-x}O_4$ (M = Fe, Mg, Zn) spinel nanoferrites were successfully synthesized using the hydrothermal method. By monitoring the resulting NPs utilizing TEM, a molar ratio of surfactants (OA: OAm of 1:4), a reaction time of 120 min and temperature of 240 °C were found to be the optimum conditions to create high quality nanoferrites of different shapes and sizes. The corresponding unit cell parameters were constant after Mg^{2+} ion doping but the inclusion of Zn^{2+} ions resulted in the expansion of the crystal unit of the pure Fe_3O_4. TGA and XPS results confirmed a high concentration of carbon atoms present on the surface of the nanoferrites. The composition experimental values, as determined from AAS results, are consistent with the EDS elemental results, but these both differ from the chemical compositions obtained from theoretical assumptions such that all doped nanoferrites except for ZnFe1 are compositionally deficient. The magnetization values and heating potential of naked Fe_3O_4 were decreased by the inclusion of Mg^{2+} and Zn^{2+} ions. The content of organic molecules on the nanoferrite surface decreased with increased magnetic core size as evidenced by TGA results. Néel spin relaxation was found to be the dominant mechanism for heat production.

4.4. Experimental Section

4.4.1. Materials

Iron (III) acetylacetonate ($Fe(acac)_3$ ≥ 99.9 % trace metals basis), oleylamine (OAm ≥ 70 %), oleic acid (OA 90 %), *tri-n*-octylphosphine oxide (TOPO 99 %), octadecene (ODC 90 %), tetramethylammoniumhydroxide (20 % w/w) and magnesium acetate ($Mg(CH_3COO)_2$) were purchased from Sigma-Aldrich and used without further purification. Zinc chloride ($ZnCl_2$) was purchased from Ajax Finechem. Milli-Q water was used after first being filtered through a 0.22 µm pore size hydrophilic filter with a resistivity of 18.2 MΩ cm from Millipore. All other chemicals were of analytical grade and used as received from commercial sources without further purification.

4.4.2. Synthesis of Monodisperse $M_xFe_{3-x}O_4$ (M = Fe, Mg, Zn) Spinel Nanoferrites

Monodispersed Fe_3O_4 NPs at various set surfactant ratios and reaction times were developed by a simple one-step hydrothermal route. In a typical procedure, $Fe(acac)_3$ (1 mmol), TOPO (0.5 mmol), oleic acid (0.64 mL) and oleylamine (2.56 mL) were mixed in

octadecene (20 mL) under stirring (500 rpm) at 100 ˚C for 60 min. Afterwards, Ar (g) was bubbled into the solution for 2 min to remove the air and the mixture was then transferred into a 100 mL polytetra-fluoroethylene (PTFE)-lined autoclave. The autoclave was sealed and maintained at 200 ˚C for 30 min then heated to 240 ˚C for 120 min. After this time the reaction was deemed complete and the autoclave was left on the bench to cool naturally slowly to RT over 3 hours. Upon addition of ethanol (10 mL), black NPs were precipitated from the solution and isolated by centrifugation. Consecutively NPs were dispersed in hexane for further use. Using the methodology of Cheon et al *and* Dang et al*,* a series of monodisperse $M_xFe_{3-x}O_4$ (M = Fe, Mg, Zn) nanoferrites were synthesized. A summary of the experimental ratios employed is given in Table 5.

Table 4.5. Synthesis conditions of $M_xFe_{3-x}O_4$ (M = Fe, Mg, Zn) spinel nanoferrites

Nanoferrite	**OA: OAm**	**OA (mL)**	**OAm (mL)**	**$Fe(acac)_3$ mmol)**	**$ZnCl_2$ (mmol)**	**Mg $(CH_3COO)_2$ (mmol)**	**TOPO (mmol)**
Fe_3O_4 (Fe1)	1:4	0.64	2.56	1	0.0	0.0	0.5
Fe_3O_4 (Fe2)	1:5	0.64	3.2	1	0.0	0.0	0.5
$Mg_{0.13}$ Fe_3O_4 (MgFe1)	1:4	0.64	2.56	1	0.0	0.13	0.5
$Mg_{0.13}$ Fe_3O_4 (MgFe2)	1:5	0.64	3.2	1	0.0	0.13	0.5
$Zn_{0.4}$ Fe_3O_4 (ZnFe1)	1:4	0.64	2.56	1	0.4	0.0	0.5
$Zn_{0.4}Fe_3O_4$ (ZnFe2)	1:5	0.64	3.2	1	0.4	0.0	0.5

4.4.3. Instrumentation and Measurements

Structural characterization, chemical composition and magnetic features of the newly synthesized nanoferrites were probed with transmission electron microscopy (TEM, Tecnai G2 Spirit Bio-TWIN*)*, powder X-ray diffraction (XRD) (Rigaku Spider X-ray diffractometer), dynamic light scattering (DLS) (Zetasizer; Nano ZS, Malvern),energy-dispersive X-ray connected scanning electron microscopy (SEM−EDX) (FE-SEM FEI Quanta), atomic absorption spectroscopy (AAS) (AAS-9000 spectrometer, Shimadzu), Thermogravimetric Analyzer (TA Instruments Q500) X-ray photoelectron spectroscopy (Kratos Axis Ultra^{DLD}) and vibrating sample magnetometer (VSM) (Quantum Design P935A USA, physical property measurement system (PPMS)). The heating potential of nanoferrites was assessed with a

commercialized magnetic alternating generator (Ambrell EASYHEAT, 2.4 kW, 196 - 197 kHz). More details regarding characterization are described in the Supporting Information.

Acknowledgments

The authors gratefully acknowledge the New Zealand International Doctoral Research Scholarships (NZIDRS) committee for their financial support.

Supporting Information

More details regarding structural characterization and magnetic hyperthermia measurements of the synthesized $M_xFe_{3-x}O_4$ (M = Fe, Mg, Zn) nanoferrites, (Figures 4.10-4.12) TEM images of the synthesised Fe_3O_4 NPs at different reaction parameters, (Figures 4.13-18) The volume particle size distribution of $M_xFe_{3-x}O_4$ (M = Fe, Mg, Zn) nanoferrites, (Figures 4.19-21) EDX patterns of Fe1, Fe2, MgFe1, MgFe2, ZnFe1 and ZnFe2 nanoferrites, (Figures 4.22-4.26) XPS spectra of the Fe2, MgFe1, MgFe2, ZnFe1 and ZnFe2 nanoferrites.

4.5. References

[1] J.-H. Lee, J.-t. Jang, J.-s. Choi, S. H. Moon, S.-h. Noh, J.-w. Kim, J.-G. Kim, I.-S. Kim, K. I. Park, J. Cheon, Nat. Nanotechnol. 2011, 6, 418.

[2] J. Jung-tak, L. Jooyoung, S. Jiyun, J. Eric, K. Minkyu, K. Y. Il, K. M. Gyu, T. Yasushi, A. A. Syed, K. K. Wook, P. K. Ho, P. S. Ha, B. Seongtae, Adv. Mater. 2018, 30, 1704362.

[3] A. Sathya, P. Guardia, R. Brescia, N. Silvestri, G. Pugliese, S. Nitti, L. Manna, T. Pellegrino, Chem. Mater. 2016, 28, 1769.

[4] L. Yang, L. Ma, J. Xin, A. Li, C. Sun, R. Wei, B. W. Ren, Z. Chen, H. Lin, J. Gao, Chem. Mater. 2017, 29, 3038.

[5] J.-H. Lee, Y.-M. Huh, Y.-w. Jun, J.-w. Seo, J.-t. Jang, H.-T. Song, S. Kim, E.-J. Cho, H.-G. Yoon, J.-S. Suh, J. Cheon, Nat. Med. 2006, 13, 95.

[6] J. Park, E. Lee, N.-M. Hwang, M. Kang, S. C. Kim, Y. Hwang, J.-G. Park, H.-J. Noh, J.-Y. Kim, J.-H. Park, T. Hyeon, Angew. Chem. Int. Ed. 2005, 44, 2872; S. Sun, H. Zeng, D. B. Robinson, S. Raoux, P. M. Rice, S. X. Wang, G. Li, J. Am. Chem. Soc. 2004, 126, 273.

[7] J. Park, K. An, Y. Hwang, J.-G. Park, H.-J. Noh, J.-Y. Kim, J.-H. Park, N.-M. Hwang, T. Hyeon, Nat. Mater 2004, 3, 891.

[8] S. Sun, H. Zeng, J. Am. Chem. Soc. 2002, 124, 8204.

[9] R. Ramesh, M. Rajalakshmi, C. Muthamizhchelvan, S. Ponnusamy, Mater. Lett. 2012, 70, 73.

[10] S. Ge, X. Shi, K. Sun, C. Li, C. Uher, J. R. Baker, M. M. Banaszak Holl, B. G. Orr, J. Phys. Chem. C. 2009, 113, 13593.

[11] J. A. Darr, J. Zhang, N. M. Makwana, X. Weng, Chem. Rev. 2017, 117, 11125; W. Shi, S. Song, H. Zhang, Chem. Soc. Rev. 2013, 42, 5714.

[12] S. M. Ansari, B. B. Sinha, D. Phase, D. Sen, P. U. Sastry, Y. D. Kolekar, C. V. Ramana, ACS Appl. Nano Mater 2019, 2, 1828.

[13] G. Zou, K. Xiong, C. Jiang, H. Li, Y. Wang, S. Zhang, Y. Qian, Nanotechnology. 2005, 16, 1584.

[14] R. Rajendran, R. Muralidharan, R. Santhana Gopalakrishnan, M. Chellamuthu, S. U. Ponnusamy, E. Manikandan, Eur. J. Inorg. Chem. 2011, 2011, 5384.

[15] T. Wu, Y. Liu, X. Zeng, T. Cui, Y. Zhao, Y. Li, G. Tong, ACS Appl. Mater. Interfaces 2016, 8, 7370.

[16] T. J. Daou, G. Pourroy, S. Bégin-Colin, J. M. Grenèche, C. Ulhaq-Bouillet, P. Legaré, P. Bernhardt, C. Leuvrey, G. Rogez, Chem. Mater. 2006, 18, 4399.

[17] Y. Tian, B. Yu, X. Li, K. Li, J. Mater. Chem. 2011, 21, 2476.

[18] M. Menelaou, K. Georgoula, K. Simeonidis, C. Dendrinou-Samara, Dalton Trans. 2014, 43, 3626.

[19] V. Georgiadou, C. Kokotidou, B. Le Droumaguet, B. Carbonnier, T. Choli-Papadopoulou, C. Dendrinou-Samara, Dalton Trans. 2014, 43, 6377.

[20] K. Vamvakidis, M. Katsikini, D. Sakellari, E. C. Paloura, O. Kalogirou, C. Dendrinou-Samara, Dalton Trans. 2014, 43, 12754.

[21] N. T. K. Thanh, L. A. W. Green, Nano Today 2010, 5, 213.

[22] A. P. LaGrow, B. Ingham, M. F. Toney, R. D. Tilley, J. Phys. Chem. C. 2013, 117, 16709.

[23] W. Bu, Z. Chen, F. Chen, J. Shi, J. Phys. Chem. C. 2009, 113, 12176.

[24] J. Jung-tak, N. Hyunsoo, L. Jae-Hyun, M. S. Ho, K. M. Gyu, C. Jinwoo, Angew. Chem. Int. Ed. 2009, 48, 1234.

[25] J. Liu, Z. Wu, Q. Tian, W. Wu, X. Xiao, CrystEngComm 2016, 18, 6303.

[26] M. Albino, E. Fantechi, C. Innocenti, A. López-Ortega, V. Bonanni, G. Campo, F. Pineider, M. Gurioli, P. Arosio, T. Orlando, G. Bertoni, C. de Julián Fernández, A. Lascialfari, C. Sangregorio, J. Phys. Chem. C. 2019, 123, 6148; S. Yang, Y. Xu, Y. Cao, G. Zhang, Y. Sun, D. Gao, RSC Adv. 2013, 3, 21994.
[27] Z. Nemati, J. Alonso, I. Rodrigo, R. Das, E. Garaio, J. Á. García, I. Orue, M.-H. Phan, H. Srikanth, J. Phys.. Chem. C 2018, 122, 2367.
[28] M. Gonzales-Weimuller, M. Zeisberger, K. M. Krishnan, J. Magn. Magn. Mater. 2009, 321, 1947; R. Hergt, S. Dutz, M. Röder, J. Phys.: Condens. Matter 2008, 20, 385214.
[29] X. Liu, Y. Chen, H. Li, N. Huang, Q. Jin, K. Ren, J. Ji, ACS Nano 2013, 7, 6244.
[30] X. M. Guo, B. Guo, Q. Zhang, X. Sun, Dalton Trans. 2011, 40, 3039.
[31] K. Kirchberg, A. Becker, A. Bloesser, T. Weller, J. Timm, C. Suchomski, R. Marschall, J. Phys. Chem. C. 2017, 121, 27126.
[32] K. K. Bamzai, G. Kour, B. Kaur, M. Arora, R. P. Pant, J. Magn. Magn. Mater. 2013, 345, 255.
[33] P. Saha, R. Rakshit, K. Mandal, J. Magn. Magn. Mater. 2019, 475, 130.
[34] J. Perrière, C. Hebert, M. Nistor, E. Millon, J. J. Ganem, N. Jedrecy, J. Mater. Chem C. 2015, 3, 11239; X. Li, E. Liu, Z. Zhang, Z. Xu, F. Xu, J. Mater. Sci.: Mater. Electron 2019, 30, 3177.
[35] J. Mohapatra, F. Zeng, K. Elkins, M. Xing, M. Ghimire, S. Yoon, S. R. Mishra, J. P. Liu, PCCP 2018, 20, 12879.
[36] J. Cai, Y. Q. Miao, B. Z. Yu, P. Ma, L. Li, H. M. Fan, Langmuir 2017, 33, 1662.
[37] A. L. Willis, N. J. Turro, S. O'Brien, Chem. Mater. 2005, 17, 5970.
[38] A. G. Roca, M. P. Morales, K. O'Grady, C. J. Serna, Nanotechnology 2006, 17, 2783.
[39] C. Moya, X. Batlle, A. Labarta, PCCP 2015, 17, 27373.
[40] S. Ayyappan, S. Mahadevan, P. Chandramohan, M. P. Srinivasan, J. Philip, B. Raj, J. Phys. Chem. C. 2010, 114, 6334.
[41] L. Li, A. Ruotolo, C. W. Leung, C. P. Jiang, P. W. T. Pong, Microelectron. Eng. 2015, 144, 61.
[42] S. M. Ansari, B. B. Sinha, D. Phase, D. Sen, P. U. Sastry, Y. D. Kolekar, C. V. Ramana, ACS Appl. Nano Mater. 2019, 2, 1828.
[43] F. L. Deepak, M. Bañobre-López, E. Carbó-Argibay, M. F. Cerqueira, Y. Piñeiro-Redondo, J. Rivas, C. M. Thompson, S. Kamali, C. Rodríguez-Abreu, K. Kovnir, Y. V. Kolen'ko, J. Phys. Chem. C. 2015, 119, 11947.
[44] S. D. Oberdick, A. Abdelgawad, C. Moya, S. Mesbahi-Vasey, D. Kepaptsoglou, V. K. Lazarov, R. F. L. Evans, D. Meilak, E. Skoropata, J. van Lierop, I. Hunt-Isaak, H. Pan, Y. Ijiri, K. L. Krycka, J. A. Borchers, S. A. Majetich, Sci. Rep. 2018, 8, 3425.
[45] L. Hu, C. de Montferrand, Y. Lalatonne, L. Motte, A. Brioude, J. Phys. Chem. C. 2012, 116, 4349.
[46] W. Wang, B. Tang, B. Ju, Z. Gao, J. Xiu, S. Zhang, J. Mater. Chem. A 2017, 5, 958.
[47] C. Iacovita, R. Stiufiuc, T. Radu, A. Florea, G. Stiufiuc, A. Dutu, S. Mican, R. Tetean, C. M. Lucaciu, Nanoscale Res. Lett. 2015, 10, 391.
[48] M. Li, Y. Xiong, X. Liu, X. Bo, Y. Zhang, C. Han, L. Guo, Nanoscale 2015, 7, 8920.
[49] J. Zhu, S. Tang, H. Xie, Y. Dai, X. Meng, ACS Appl. Mater. Interfaces 2014, 6, 17637.
[50] H.-J. Cui, J.-W. Shi, B. Yuan, M.-L. Fu, J. Mater. Chem. A 2013, 1, 5902.
[51] A. Manikandan, J. Judith Vijaya, M. Sundararajan, C. Meganathan, L. J. Kennedy, M. Bououdina, Superlattices Microstruct. 2013, 64, 118; V. K. Mittal, S. Bera, R. Nithya, M. P. Srinivasan, S. Velmurugan, S. V. Narasimhan, J. Nucl. Mater. 2004, 335, 302.

[52] X. Guo, H. Zhu, M. Si, C. Jiang, D. Xue, Z. Zhang, Q. Li, J. Phys. Chem. C. 2014, 118, 30145; N. Baird, Y. Losovyj, E. Y. Yuzik-Klimova, N. V. Kuchkina, Z. B. Shifrina, M. Pink, B. D. Stein, D. G. Morgan, T. Wang, M. A. Rubin, A. I. Sidorov, E. M. Sulman, L. M. Bronstein, ACS Appl. Mater. Interfaces 2016, 8, 891.
[53] Ç. E. Demirci Dönmez, P. K. Manna, R. Nickel, S. Aktürk, J. van Lierop, ACS Appl. Mater. Interfaces 2019, 11, 6858.
[54] T. Neuberger, B. Schöpf, H. Hofmann, M. Hofmann, B. von Rechenberg, J. Magn. Magn. Mater. 2005, 293, 483.
[55] E. D. Smolensky, H.-Y. E. Park, T. S. Berquó, V. C. Pierre, Contrast Media Mol. Imaging 2011, 6, 189.
[56] M. P. Morales, S. Veintemillas-Verdaguer, M. I. Montero, C. J. Serna, A. Roig, L. Casas, B. Martínez, F. Sandiumenge, Chem. Mater. 1999, 11, 3058; R. Mondal, S. Dey, S. Majumder, A. Poddar, P. Dasgupta, S. Kumar, J. Magn. Magn. Mater. 2018, 448, 135.
[57] W. Szczerba, J. Żukrowski, M. Przybylski, M. Sikora, O. Safonova, A. Shmeliov, V. Nicolosi, M. Schneider, T. Granath, M. Oppmann, M. Straßer, K. Mandel, PCCP 2016, 18, 25221.
[58] J. Jung-tak, N. Hyunsoo, L. Jae-Hyun, M. S. Ho, K. M. Gyu, C. Jinwoo, Angew Chem. Int. Ed. 2009, 48, 1234; J. Jung-tak, L. Jooyoung, S. Jiyun, J. Eric, K. Minkyu, K. Y. Il, K. M. Gyu, T. Yasushi, A. A. Syed, K. K. Wook, P. K. Ho, P. S. Ha, B. Seongtae, Adv. Mater. 2018, 30, 1704362.
[59] X. Lasheras, M. Insausti, I. Gil de Muro, E. Garaio, F. Plazaola, M. Moros, L. De Matteis, J. M. de la Fuente, L. Lezama, J. Phys. Chem. C. 2016, 120, 3492.
[60] J. Appl. Phys. 2013, 113, 033912.
[61] M. da Costa Borges Soares, F. F. Barbosa, M. A. M. Torres, A. Valentini, A. dos Reis Albuquerque, J. R. Sambrano, S. B. C. Pergher, N. Essayem, T. P. Braga, Catalysis Science & Technology 2019, 9, 2469.
[62] I. Galarreta, M. Insausti, I. Gil de Muro, I. Ruiz de Larramendi, L. Lezama, Nanomaterials (Basel) 2018, 8, 63.
[63] S. Gyergyek, D. Makovec, M. Jagodič, M. Drofenik, K. Schenk, O. Jordan, J. Kovač, G. Dražič, H. Hofmann, J. Alloys Compd. 2017, 694, 261.
[64] E. Wetterskog, M. Agthe, A. Mayence, J. Grins, D. Wang, S. Rana, A. Ahniyaz, G. Salazar-Alvarez, L. Bergström, Sci Technol Adv Mat 2014, 15, 055010; Z. Nemati, J. Alonso, I. Rodrigo, R. Das, E. Garaio, J. Á. García, I. Orue, M.-H. Phan, H. Srikanth, J. Phys. Chem. C. 2018, 122, 2367.
[65] B. B. Lahiri, S. Ranoo, J. Philip, Infrared Phys. Technol. 2017, 80, 71.
[66] A. Hervault, A. E. Dunn, M. Lim, C. Boyer, D. Mott, S. Maenosono, N. T. K. Thanh, Nanoscale 2016, 8, 12152.
[67] J.-P. Fortin, C. Wilhelm, J. Servais, C. Ménager, J.-C. Bacri, F. Gazeau, J. Am. Chem. Soc. 2007, 129, 2628.
[68] C. Blanco-Andujar, D. Ortega, P. Southern, Q. A. Pankhurst, N. T. K. Thanh, Nanoscale 2015, 7, 1768.
[69] P. Guardia, R. Di Corato, L. Lartigue, C. Wilhelm, A. Espinosa, M. Garcia-Hernandez, F. Gazeau, L. Manna, T. Pellegrino, ACS Nano 2012, 6, 3080.
[70] L. A. Thomas, L. Dekker, M. Kallumadil, P. Southern, M. Wilson, S. P. Nair, Q. A. Pankhurst, I. P. Parkin, J. Mater. Chem. 2009, 19, 6529.
[71] P. de la Presa, Y. Luengo, M. Multigner, R. Costo, M. P. Morales, G. Rivero, A. Hernando, J. Phys. Chem. C 2012, 116, 25602.

[72] C. Martinez-Boubeta, K. Simeonidis, A. Makridis, M. Angelakeris, O. Iglesias, P. Guardia, A. Cabot, L. Yedra, S. Estradé, F. Peiró, Z. Saghi, P. A. Midgley, I. Conde-Leborán, D. Serantes, D. Baldomir, Sci. Rep. 2013, 3, 1652.
[73] E. Lima, E. De Biasi, R. D. Zysler, M. Vasquez Mansilla, M. L. Mojica-Pisciotti, T. E. Torres, M. P. Calatayud, C. Marquina, M. Ricardo Ibarra, G. F. Goya, J. Nanopart. Res. 2014, 16, 2791.
[74] S. L. Saville, B. Qi, J. Baker, R. Stone, R. E. Camley, K. L. Livesey, L. Ye, T. M. Crawford, O. Thompson Mefford, J. Colloid Interface Sci. 2014, 424, 141.
[75] D. F. Coral, P. Mendoza Zélis, M. Marciello, M. d. P. Morales, A. Craievich, F. H. Sánchez, M. B. Fernández van Raap, Langmuir 2016, 32, 1201; D. Serantes, D. Baldomir, C. Martinez-Boubeta, K. Simeonidis, M. Angelakeris, E. Natividad, M. Castro, A. Mediano, D. X. Chen, A. Sanchez, L. I. Balcells, B. Martínez, J. Appl. Phys. 2010, 108, 073918.
[76] M. Jeun, S. Bae, A. Tomitaka, Y. Takemura, K. H. Park, S. H. Paek, K.-W. Chung, Appl. Phys. Lett. 2009, 95, 082501; A. Urtizberea, E. Natividad, A. Arizaga, M. Castro, A. Mediano, J. Phys. Chem. C 2010, 114, 4916; P. de la Presa, Y. Luengo, V. Velasco, M. P. Morales, M. Iglesias, S. Veintemillas-Verdaguer, P. Crespo, A. Hernando, J. Phys. Chem. C 2015, 119, 11022.
[77] B. Sanz, M. P. Calatayud, E. De Biasi, E. Lima Jr, M. V. Mansilla, R. D. Zysler, M. R. Ibarra, G. F. Goya, Sci. Rep. 2016, 6, 38733.
[78] D. Serantes, K. Simeonidis, M. Angelakeris, O. Chubykalo-Fesenko, M. Marciello, M. d. P. Morales, D. Baldomir, C. Martinez-Boubeta, J. Phys. Chem. C 2014, 118, 5927.
[79] M. Filippousi, M. Angelakeris, M. Katsikini, E. Paloura, I. Efthimiopoulos, Y. Wang, D. Zamboulis, G. Van Tendeloo, J. Phys. Chem. C 2014, 118, 16209.
[80] A. Ahmad, H. Bae, I. Rhee, S. Hong, J. Magn. Magn. Mater. 2018, 447, 42.
[81] S. Ota, Y. Takemura, J. Phys. Chem. C 2019, 123, 28859.
[82] P. Bender, J. Fock, C. Frandsen, M. F. Hansen, C. Balceris, F. Ludwig, O. Posth, E. Wetterskog, L. K. Bogart, P. Southern, W. Szczerba, L. Zeng, K. Witte, C. Grüttner, F. Westphal, D. Honecker, D. González-Alonso, L. Fernández Barquín, C. Johansson, J. Phys. Chem. C 2018, 122, 3068.
[83] G. Salas, J. Camarero, D. Cabrera, H. Takacs, M. Varela, R. Ludwig, H. Dähring, I. Hilger, R. Miranda, M. d. P. Morales, F. J. Teran, J. Phys. Chem. C 2014, 118, 19985; V. Singh, V. Banerjee, M. Sharma, J. Phys. D: Appl. Phys. 2009, 42, 245006.

4.6. Supporting Information

Improvements in the Organic Phase Hydrothermal Synthesis of Monodisperse $M_xFe_{3-x}O_4$ (M = Fe, Mg, Zn) Spinel Nanoferrites for Magnetic Fluid Hyperthermia Application

Hossein Etemadi and Paul G. Plieger*

School of Fundamental Sciences, Massey University, Private Bag 11 222, Palmerston North, New Zealand

E-mail: p.g.plieger@massey.ac.nz

Fax: 0064 6 350 5682; Tel: 0064 6 356 9099, extension 7825

Instrumentation and Measurements

Structural Characterization

Powder X-ray diffraction (XRD) patterns were recorded on a Rigaku Spider X-ray diffractometer with Cu K_α radiation (λ = 1.5406 Å), at 40 kV and 50 mA from 10° to 80° in the Bragg configuration. Indexing the XRD patterns, *d*-spacing of lattice planes (*hkl*), lattice constant (*a*) and crystallite size (*D*) were determined for all $M_xFe_{3-x}O_4$ (M = Fe, Mg, Zn) nanoferrites. The β values of the most intense X-ray peaks corresponding to (220), (311), (400), (422), (511) and (440) was calculated through Origin software with Gaussian function.

Applying Debye−Scherrer equation to the diffraction peaks together with achieved β values, the crystallite size was calculated. Eq.1:

$$D = \frac{K\lambda}{\beta Cos\theta} \quad (1)$$

Where *D* is the crystallite size, *K* is Scherrer shape factor (0.9), λ is the wavelength of Cu-K_α radiation (λ = 1.5406 Å), β is the full-width-half-maximum (FWHM) value of the peak in radians and θ is the Bragg diffraction angle of the (*hkl*) reflection.

Additionally, *d*-spacing of lattice planes (*hkl*), and lattice constant (*a*) values were calculated by the Bragg equation, Eq.2 and 3:

$$\lambda = 2dSin\theta \qquad (2)$$

$$a = d(h^2 + k^2 + l^2)^{1/2} \qquad (3)$$

The monodispersity and diameter of the nanoferrites was probed using transmission electron microscopy (TEM, Tecnai *G2 Spirit Bio-TWIN,* Oregon, USA) at an acceleration voltage of 200 kV. For TEM imaging, drops of a diluted solution (× 100) of the sample was cast onto a Cu grid and dried for several minutes before imaging. ImageJ software was utilized for post-processing and particle size analysis. Outlines of 70-80 particles were traced manually, and the corresponding diameters with their standard deviation were given. The hydrodynamic size (d_h) and polydispersity index (PDI) of the particles dispersed in hexane were measured by dynamic light scattering (DLS) instrument (Zetasizer; Nano ZS, Malvern, UK) utlizing a red laser (633 nm) in backscatter mode, with an angle detection of 173 °. The samples were diluted (100x), filtered through a pre-rinsed 0.2-µm filter, equilibrated at 25 ° C for 1 min then measured three times. The mean values were reported.

Chemical Composition

The elemental atomic ratios of monodisperse nanoferrites were probed by atomic absorption spectroscopy (AAS) (GBC Scientific) and an energy dispersive spectrometer (EDS) connected to field-emission scanning electron microscopy (FE-SEM FEI Quanta 200). For EDS studies, small amount of as-made nanoferrites dispersed in hexane, was sonicated for 30 min and directly mounted onto an aluminium stub using double sided tape, carbon coated (Baltec SCD 050 sputter coater) and viewed in the FEI Quanta 200 Environmental Scanning Electron Microscope (FE-SEM FEI Quanta 200). To ensure a good accuracy, several areas from different regions of each sample were scanned and spectral data was collected with a silicon EDAX unit (NJ, USA) running Genesis Spectrum software (version 5.21). For AAS analysis, 125 µL of the as-made nanoferrites dispersed in hexane were sonicated for 30 min and completely digested in concentrated HNO_3 70 %: H_2O_2 32 %: HCl 37 % with a ratio of 1:1:0.5 mL at 100 °C overnight. The solutions were finally diluted to 10 mL with Milli-Q

water for quantification. The metal calibration standards (10−100 ppm) were prepared by diluting aliquots from a 1000 ppm stock metal solution. Standard solutions of 10, 20, 30, 40, 60, 80 and 100 ppm were used to plot a regression curve for intensity vs. concentration. The concentrations of Fe, Zn and Mg were measured using an AAS spectrometer (GBC Scientific) with a Fe hollow cathode lamp (252.3 nm), Zn hollow cathode lamp (279.8 nm) or Mg hollow cathode lamp (285.2 nm) respectively.

The proportion of inorganic cores and organic surfactants/capping agents in the sample was obtained through the heating of samples on a TA Instruments Q50 instrument. Samples were mounted to a silica sample pan and heated from room temperature up to 800 °C under an N_2 flow with a heating rate of 10 °C /min. To keep the consistency for reliable information the same nanoferrites solutions were utilized for (TEM, DLS) and (EDS, AAS) measurements respectively.

The metal (M, Fe) and oxygen valence states of $M_xFe_{3-x}O_4$ (M = Fe, Mg, Zn) nanoferrites were probed with Kratos Axis Ultra^{DLD} X-ray Photoelectron Spectrometer (Kratos Analytical, Manchester, UK) equipped with a hemispherical electron energy analyser. Spectra were excited using monochromatic Al K_α X-rays (1486.69 eV) with the X-ray source operating at 150 W. The analysis area was a 300 by 700 micron spot obtained using the hybrid magnetic and electrostatic lens and the slot aperture. Powder samples were mounted on a stainless steel holder with double sided carbon tape. A sufficient amount was used to cover the tape. The measurements were carried out in a normal emission geometry. A charge neutralization system was used to alleviate surface charge build-up, resulting in a shift of approximately 3 eV to lower binding energy. During curve fitting of the binding energy of *C 1s*, the adventitious hydrocarbon on the surface was used to correct for this shift, with the saturated hydrocarbon peak set to 285 eV. Survey scans were collected with a 160 eV pass energy, whilst core level scans were collected with a pass energy of 20 eV. The analysis chamber was at pressures in the 10^{-9} torr range throughout the data collection. Data analysis was performed using CasaXPS (www.casaXPS.com).

Magnetic Measurements

Magnetic characterization was recorded in a vibrating sample magnetometer (VSM) (Quantum Design P935A USA, physical property measurement system (PPMS). Magnetization curves as a function of the applied magnetic field (M−H loops) were collected

from −2.00 to 2.00 T magnetic field at room temperature (300 K) to estimate saturation magnetic moment (emu), remnant magnetizations (M_r), and coercivities (H_c) values. Magnetization curves as a function of the temperature (M -T) also termed as zero field cooling/field cooling (ZFC/FC) curves, were recorded between 10 and 350 K to assess the blocking temperature and effective anisotropy constant (K_{eff}) of nanoferrites. During the Zero-field-cooling (ZFC), the samples were cooled down to 10 K (from room temperature ~ 300 K) under a zero magnetic field. Then under an applied magnetic field of 0.02 T, magnetization was recorded as the temperature was increased from 10 K to 350 K. During FC, samples were cooled from 350 K to 10 K and the magnetization was recorded under the applied magnetic field of the same magnitude. For the XRD, TGA, VSM and XPS measurements, the nanoferrites were dispersed in hexane, precipitated with ethanol and dried under vacuum overnight prior to measurement.

Measurement of magnetically induced hyperthermic effect

The heating potential of synthesized nanoferrites was considered through a calorimetric non-adiabatic set up with a commercialized magnetic alternating generator (Ambrell EASYHEAT, 2.4 kW, 196 - 197 kHz). Hexane-soluble nanoferrites were put in the aqueous phase through vigorously agitation with tetramethylammonium hydroxide. The aqueous solution of nanoferrites (5 mg/mL) were sonicated for 60 min in order to negate the potential aggregation. Thereafter, aqueous dispersions in plastic micro centrifuge tube were placed inside a water-cooled induction coil (8-turn coil, i.d.= 25 mm, L = 35 mm). When the coil was thermalized at ≈ 26 °C, a measurement was initiated by heating samples for 12 min with a generator operating at a frequency of f = 194.5 kHz and field amplitude of H = 114.01 mT at the desired current (385.6 A). The temperature elevation of the solutions was recorded in real time with a fiber optic probe (Lumasense m3300) placed in the center of the centrifuge tube. The heat dissipation rate of ferrofluids donated as specific absorption rate (SAR) was quantified by assessing the initial rate of temperature rise under a non-adiabatic approximation, Eq.4

$$SAR\ ({}^{W}/_{g}) = Cp\frac{m_s}{m_n}\frac{dT}{dt} \quad (4)$$

Where C_p *is* the specific heat of the solution (C_p water = 4186 W.s/lit.K), m_s is the sample volume (L), m_n is the mass of nanoferrite (g), and *dT/dt* is the initial slope of the heating curve by applying a linear fit to the change in temperature over the first 180 s (K/s). Each sample was analysed in triplicate and an average T_{max} and SAR values were recorded. To exclude the dependence of the SAR value on the amplitude of the applied AMF and allow a direct comparison of the heating potential of our nanoferrites with the available literature data of similar ferrofluids, we utilized the intrinsic loss power (ILP)[60] defined as Eq.5:

$$ILP\ (nHm^2\ kg^{-1}) = \frac{SLP\ (\ Wkg^{-1}\ )}{f\ (kHz)\ H^2(kA\ m^{-1})} \quad (5)$$

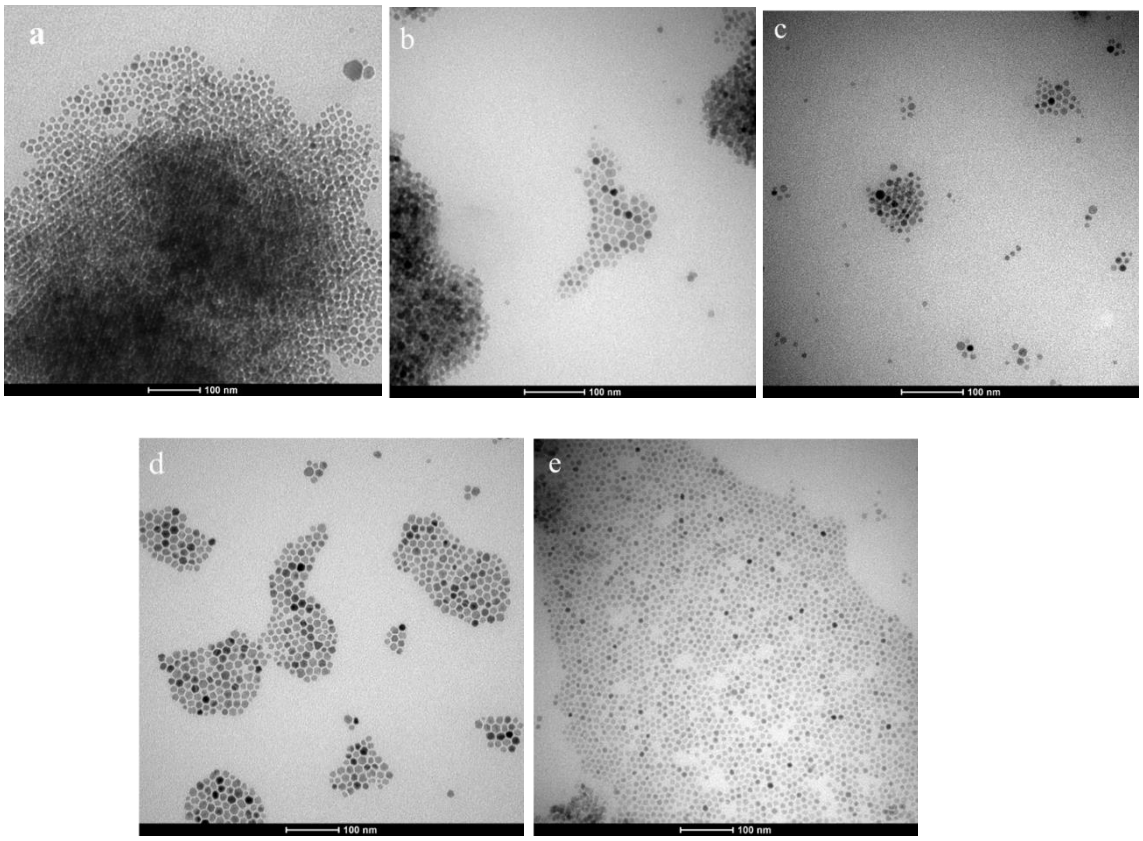

Figure 4.10. TEM images of the synthesised Fe3O4 NPs with molar ratio of OA to OAm (a) 1:0 (b) 0:1 (c) 1:1; (d) 1:4 and (e) 1:5 mmol; 0.5 mmol of TOPO at 240 °C for 120 min.

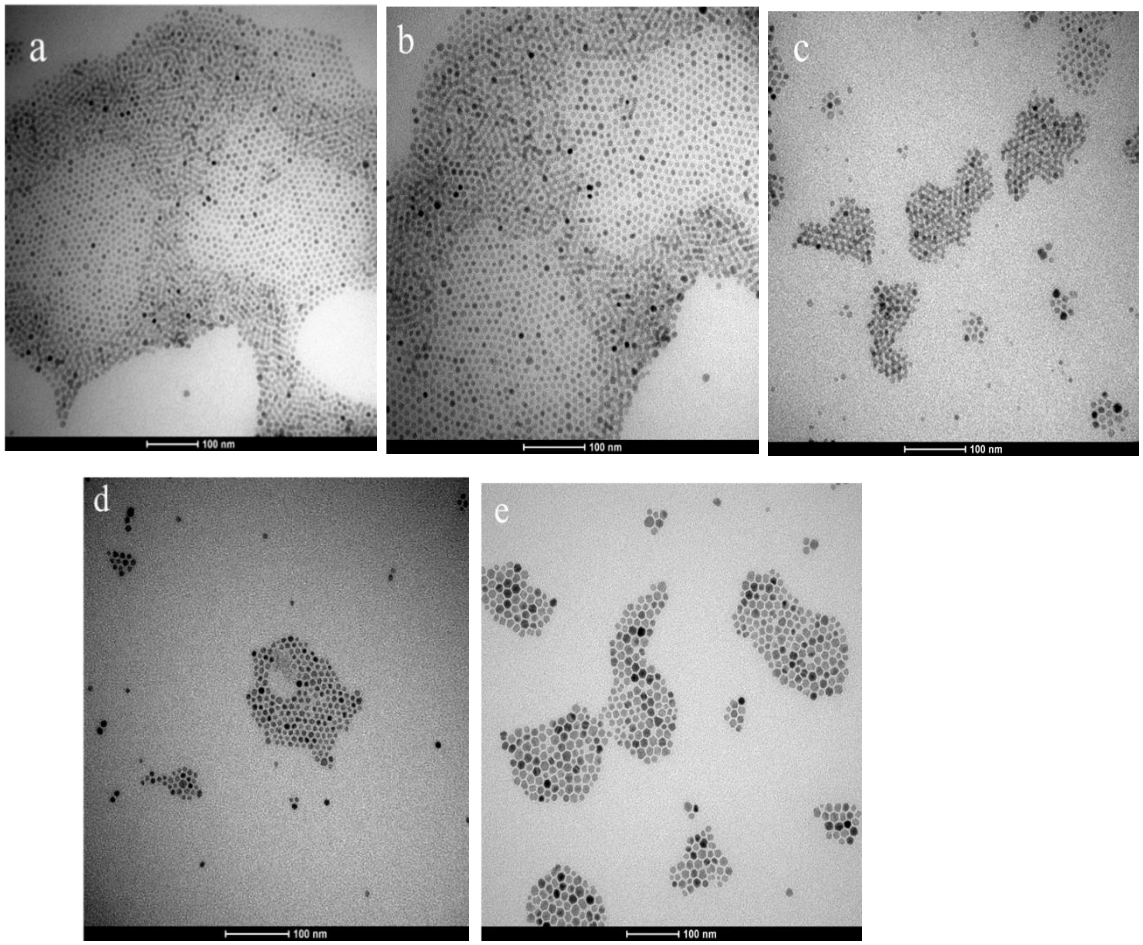

Figure 4.11. TEM images of the synthesized Fe3O4 NPs with a 1:4 molar ratio of OA to OAm by different amounts of TOPO: (a) without TOPO; (b) 0.1 mmol; (c) 0.3 mmol; (d) 0.4 mmol; (e) 0.5 mmol of TOPO at 240 °C for 120 min.

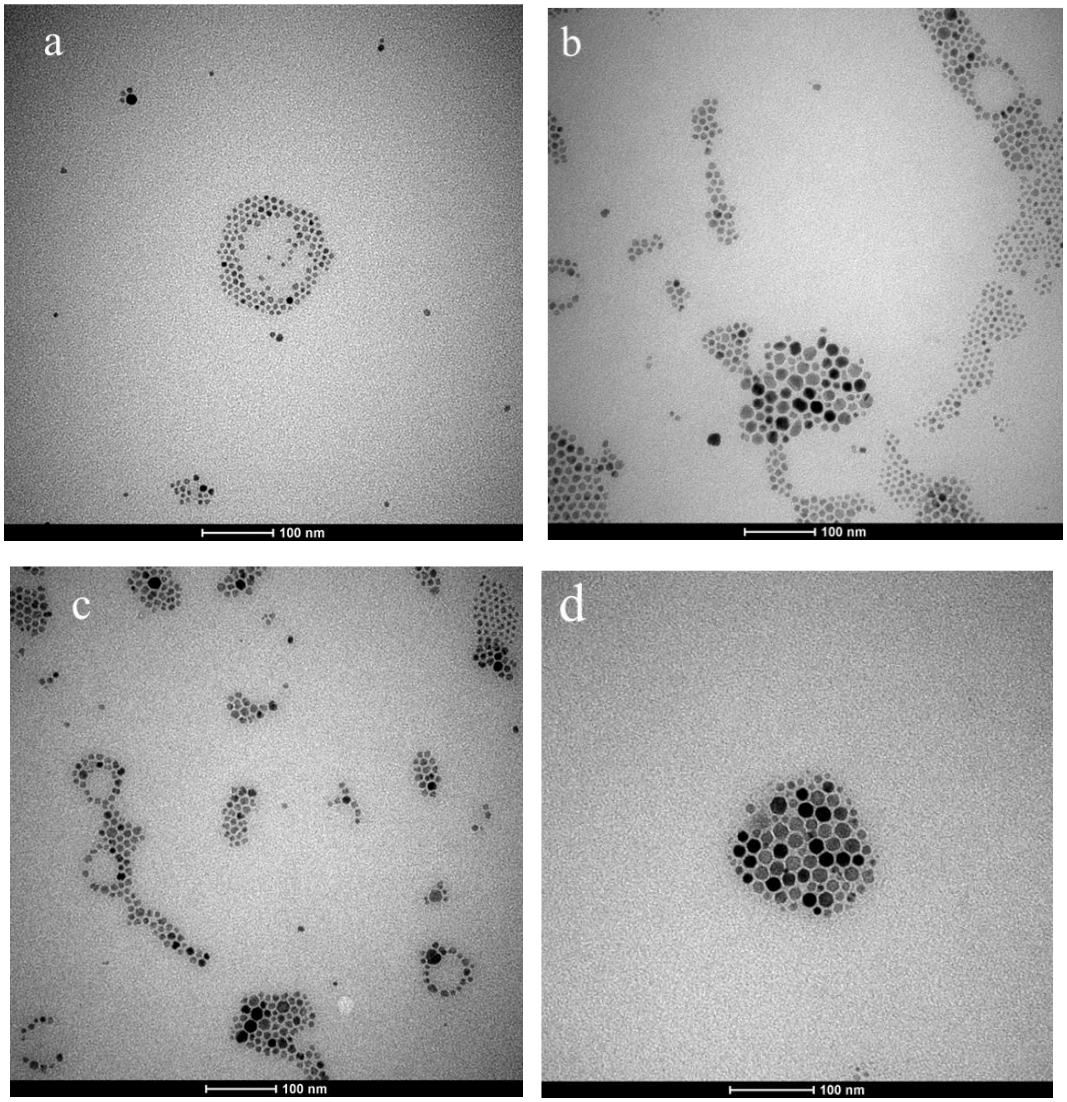

Figure 4.12. TEM images of the synthesised Fe3O4 NPs with a 1:4 molar ratio of OA to OAm; TOPO 0.5 mmol at different reaction times of (a) 30 min; (b) 60 min (c) 90 min and (d) 120 min.

		Size (d.nm):	% Intensity:	St Dev (d.nm):
Z-Average (d.nm): 125.5	Peak 1:	146.9	100.0	63.17
PdI: 0.166	Peak 2:	0.000	0.0	0.000
Intercept: 0.919	Peak 3:	0.000	0.0	0.000
Result quality : Good				

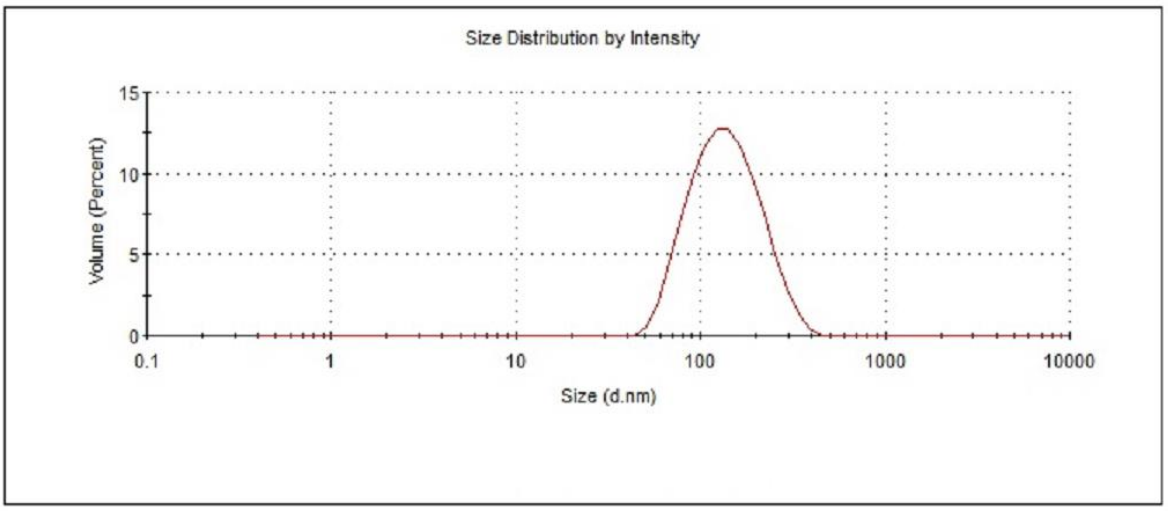

Figure 4.13. Volume particle size distribution (based on DLS data) of Fe1. PdI referrers to polydispersity index.

		Size (d.nm):	% Intensity:	St Dev (d.nm):
Z-Average (d.nm): 170.3	Peak 1:	161.0	100.0	46.93
PdI: 0.267	Peak 2:	0.000	0.0	0.000
Intercept: 0.896	Peak 3:	0.000	0.0	0.000
Result quality : Good				

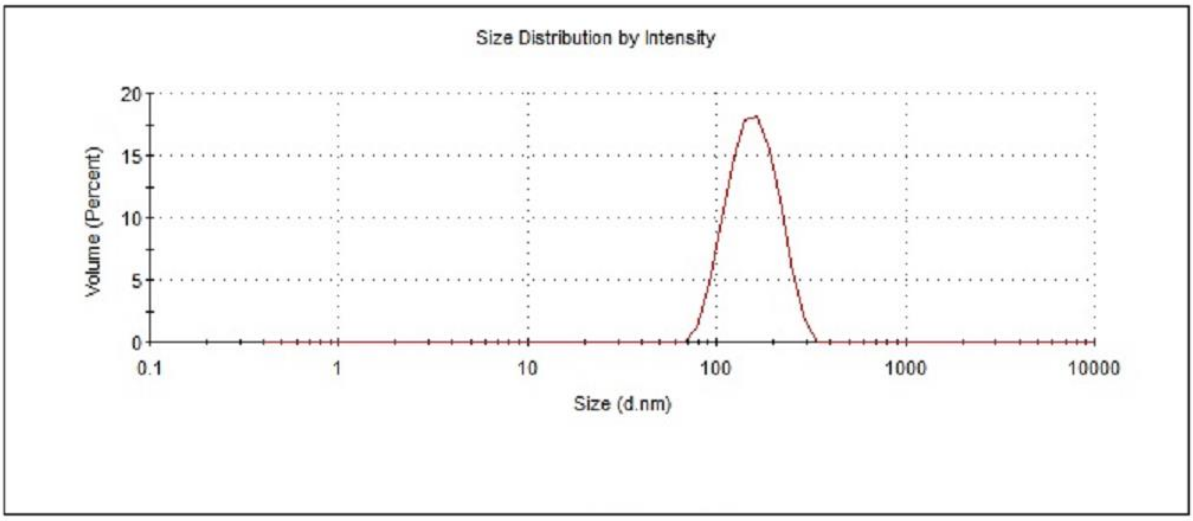

Figure 4.14. Volume particle size distribution of Fe2.

		Size (d.nm):	% Intensity:	St Dev (d.nm):
Z-Average (d.nm): 178.9	Peak 1:	178.2	100.0	62.61
PdI: 0.318	Peak 2:	0.000	0.0	0.000
Intercept: 0.911	Peak 3:	0.000	0.0	0.000

Result quality : Good

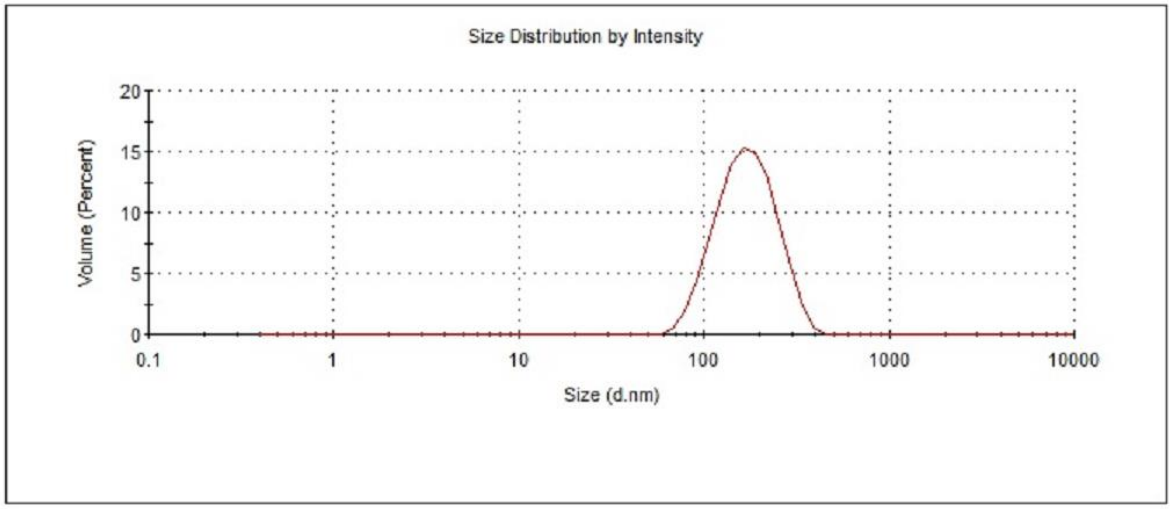

Figure 4.15. Volume particle size distribution of MgFe1.

		Size (d.nm):	% Intensity:	St Dev (d.nm):
Z-Average (d.nm): 189.5	Peak 1:	163.3	100.0	40.21
PdI: 0.247	Peak 2:	0.000	0.0	0.000
Intercept: 0.813	Peak 3:	0.000	0.0	0.000

Result quality : Refer to quality report

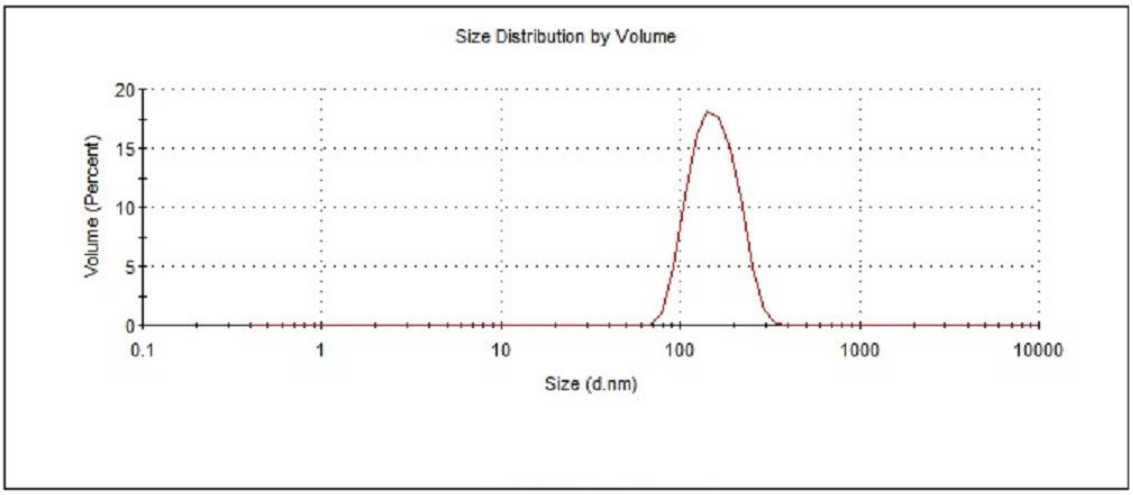

Figure 4.16. Volume particle size distribution of ZnFe1.

		Size (d.nm):	% Intensity:	St Dev (d.nm):
Z-Average (d.nm): 189.9	Peak 1:	175.2	100.0	34.12
PdI: 0.224	Peak 2:	0.000	0.0	0.000
Intercept: 0.511	Peak 3:	0.000	0.0	0.000

Result quality : Refer to quality report

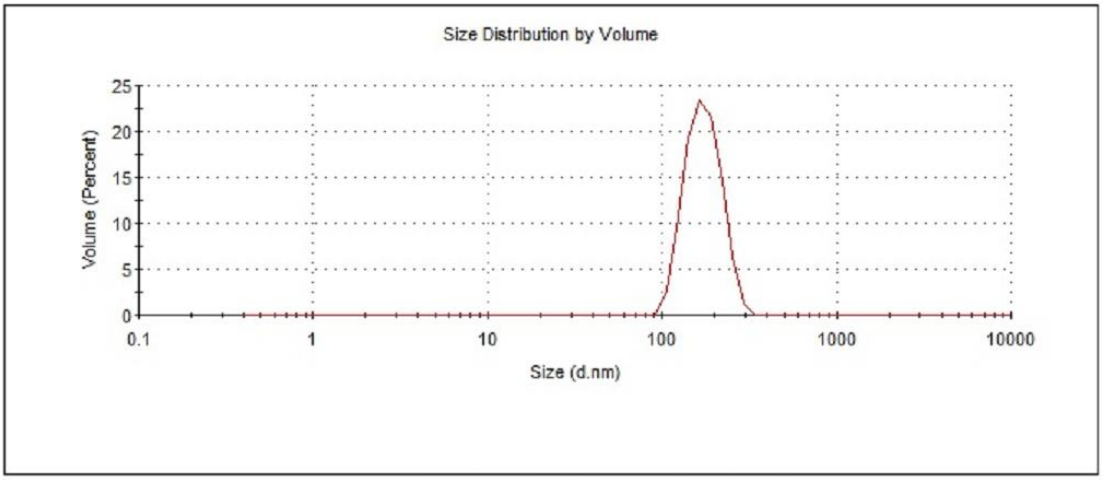

Figure 4.17. Volume particle size distribution of MgFe2.

		Size (d.nm):	% Intensity:	St Dev (d.nm):
Z-Average (d.nm): 214.7	Peak 1:	185.8	100.0	48.33
PdI: 0.259	Peak 2:	0.000	0.0	0.000
Intercept: 0.842	Peak 3:	0.000	0.0	0.000

Result quality : Refer to quality report

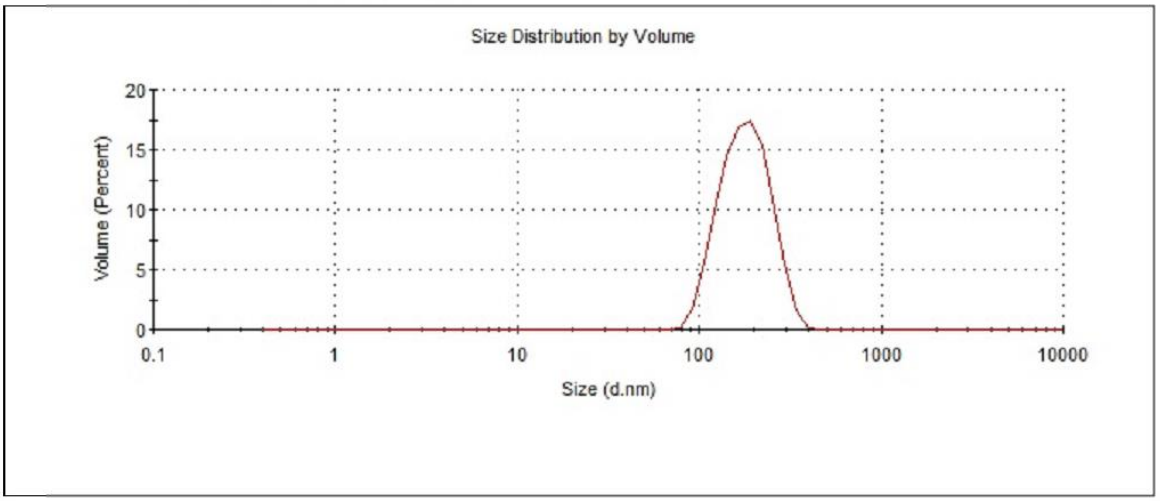

Figure 4.18. Volume particle size distribution of ZnFe2

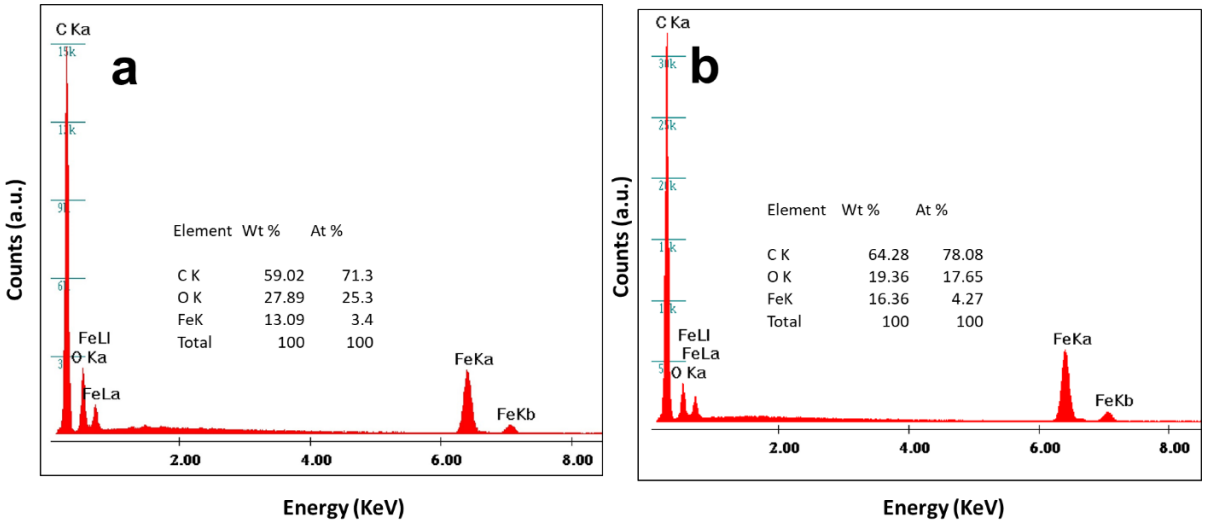

Figure 4.19. EDX pattern of (a) the Fe1 and (b) the Fe2 NPs.

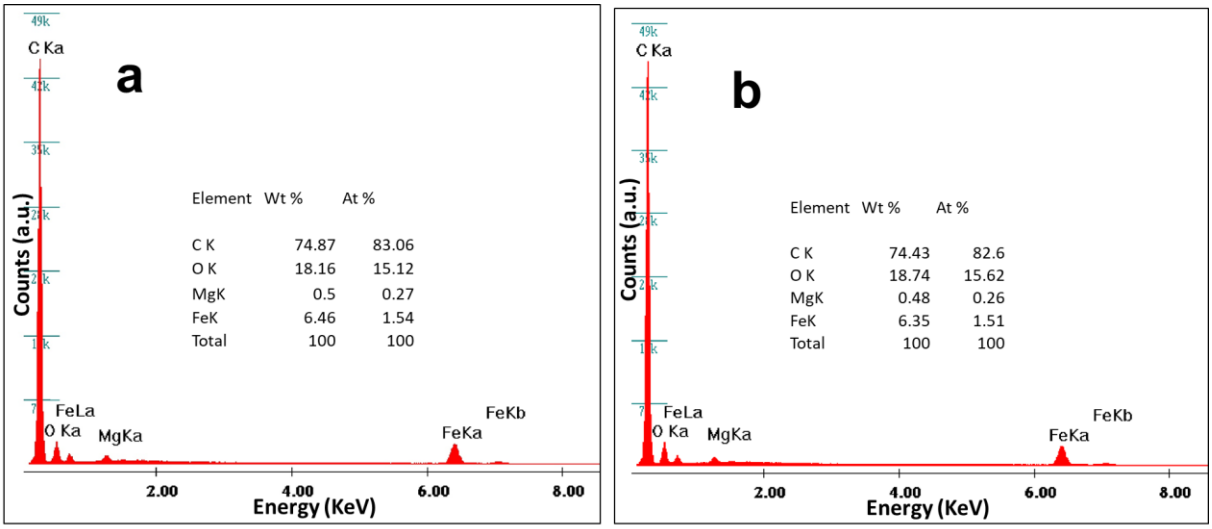

Figure 4.20. EDX pattern of (a) the MgFe1 and (b) the MgFe2 NPs.

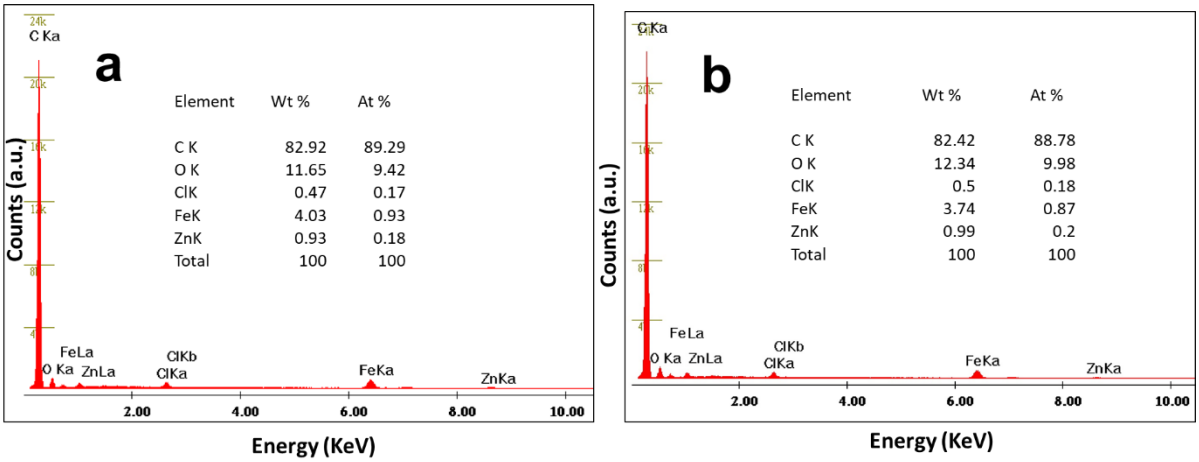

Figure 4.21. EDX pattern of (a) the ZnFe1 and (b) the ZnFe2 NPs.

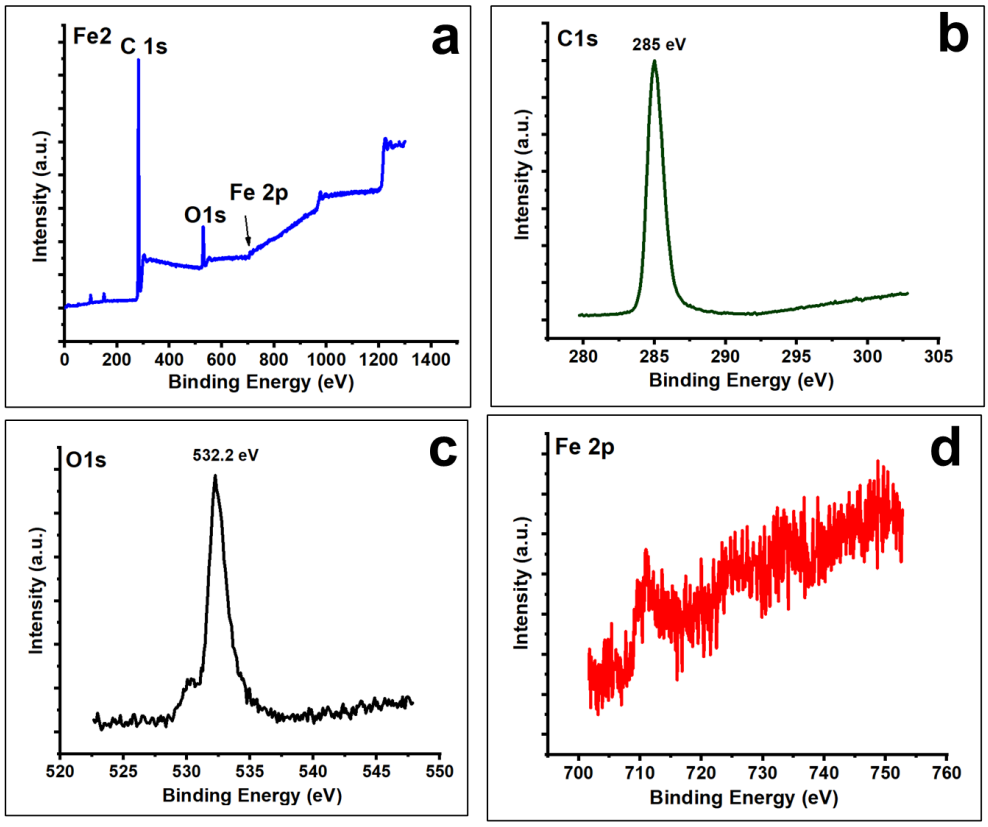

Figure 4.22. nanoferrite (a) survey scan (b) C1s (c) O1s and (d) Fe2p regional scans.

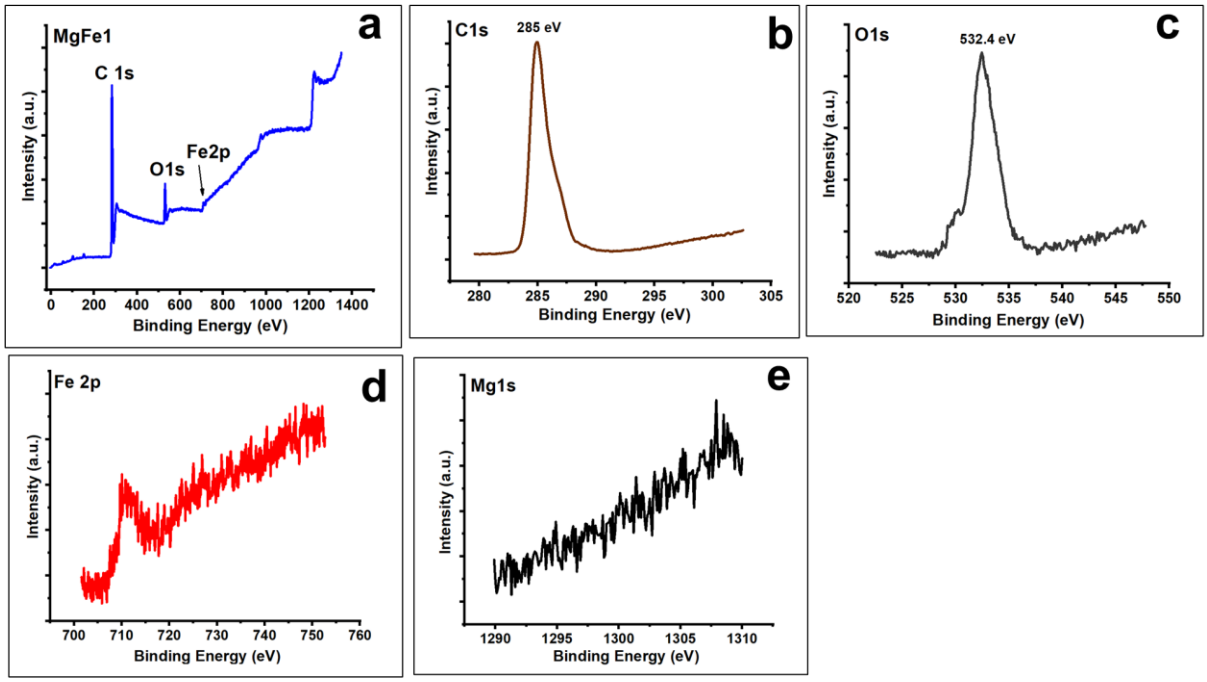

Figure 4.23. XPS spectra of the MgFe1 nanoferrite (a) survey scan (b) C1s (c) O1s (d) Fe2p and (e) Mg1s regional scans

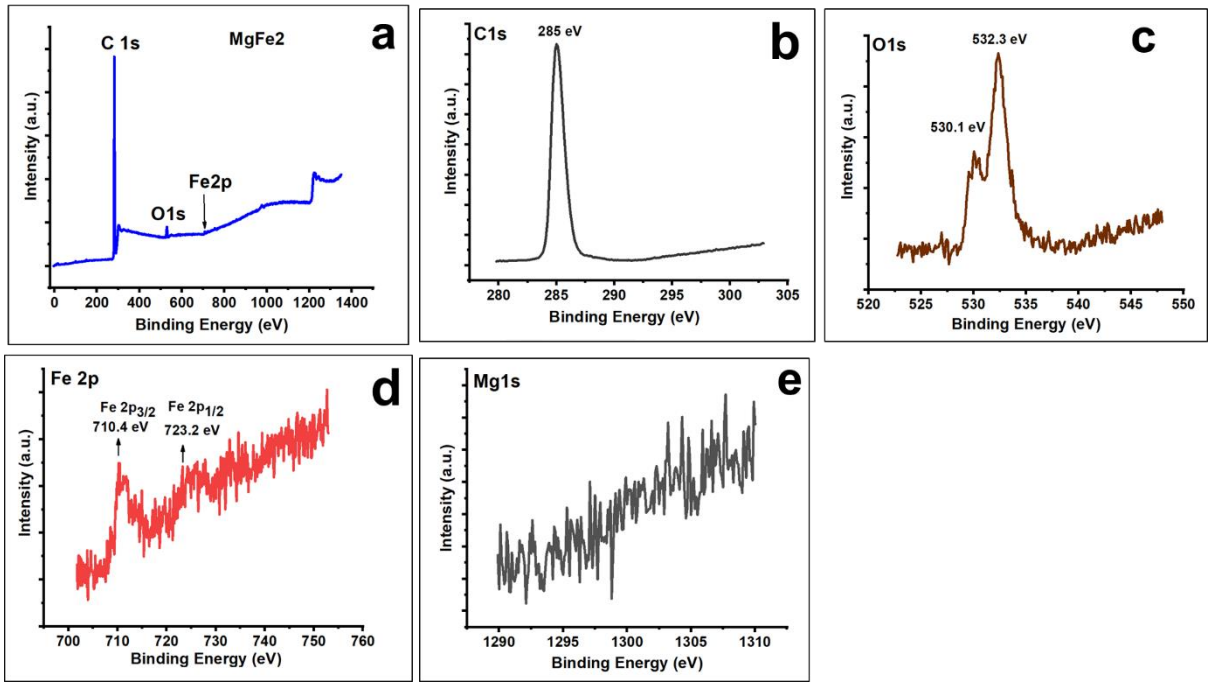

Figure 4.24. XPS spectra of the MgFe2 nanoferrite (a) survey scan (b) C1s (c) O1s (d) Fe2p and (e) Mg1s regional scans.

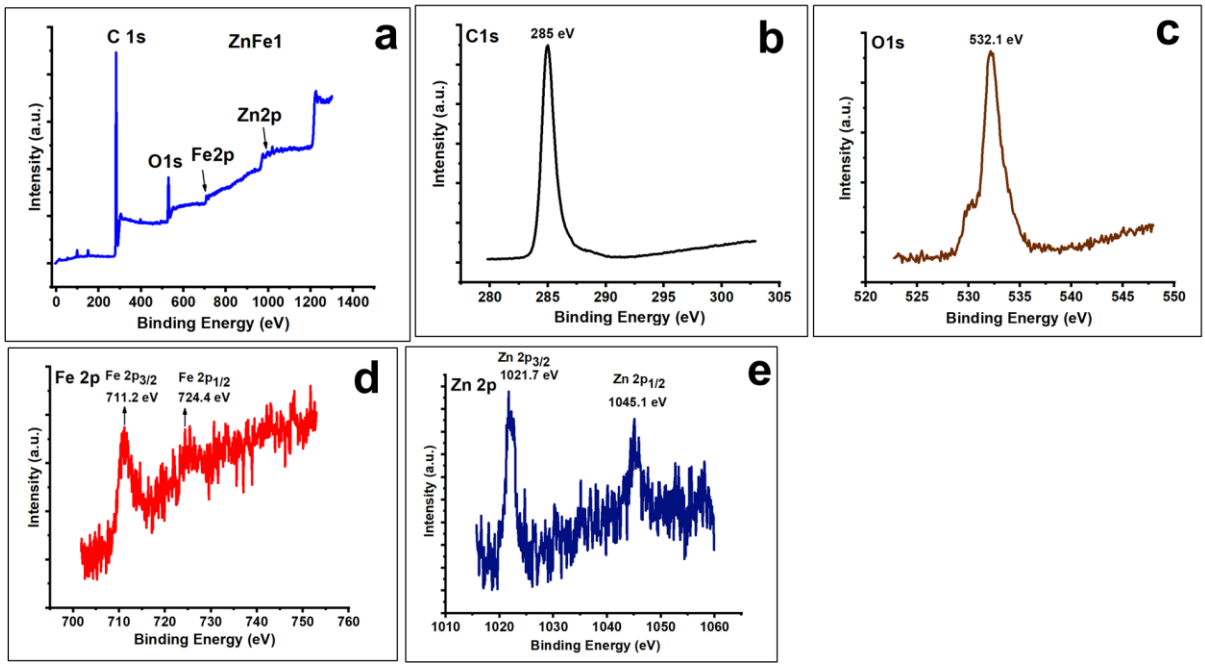

Figure 4.25. XPS spectra of the ZnFe1 nanoferrite (a) survey scan (b) C1s (c) O1s (d) Fe2p and (e) Zn2p regional scans.

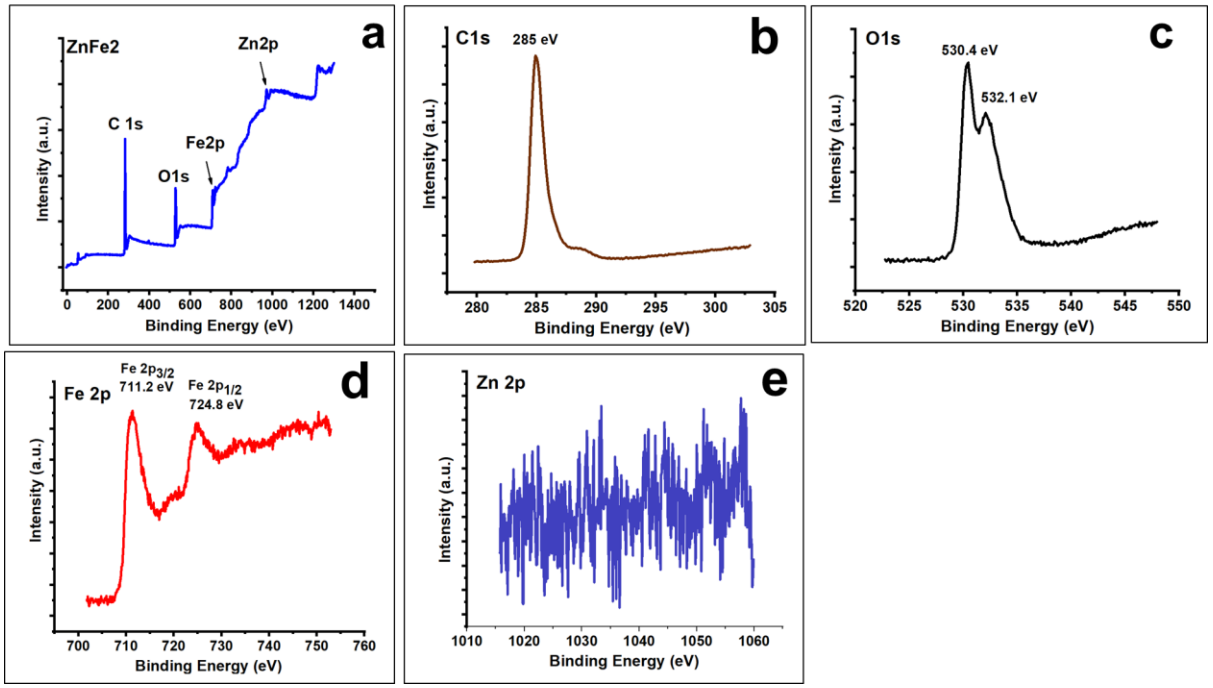

Figure 4.26. XPS spectra of the ZnFe2 nanoferrite (a) survey scan (b) C1s (c) O1s (d) Fe2p and (e) Zn2p regional scans.

MASSEY UNIVERSITY
GRADUATE RESEARCH SCHOOL

STATEMENT OF CONTRIBUTION
DOCTORATE WITH PUBLICATIONS/MANUSCRIPTS

We, the candidate and the candidate's Primary Supervisor, certify that all co-authors have consented to their work being included in the thesis and they have accepted the candidate's contribution as indicated below in the *Statement of Originality*.

Name of candidate:	Hossein Etemadi
Name/title of Primary Supervisor:	Paul. G. Plieger
Name of Research Output and full reference:	
Synthesis and Characterisation of MxFe3−xO4 (M = Fe, Mn, Zn) Spinel Nanoferrites through a Solvothermal Route	
In which Chapter is the Manuscript /Published work:	5
Please indicate:	
• The percentage of the manuscript/Published Work that was contributed by the candidate:	90
and	
• Describe the contribution that the candidate has made to the Manuscript/Published Work:	
Hossein Etermadi did the experimental design and trials, data analysis and draft of the manuscript. The draft was then proofread by Jenna Buchanan and Paul Plieger. Final edits were then completed by Hossein Etemadi and Paul Plieger	
For manuscripts intended for publication please indicate target journal:	
Accepted for publication at Journal of Material Science	
Candidate's Signature:	Hossein Digitally signed by Hossein Date: 2021.08.28 11:49:47 +12'00'
Date:	28/08/21
Primary Supervisor's Signature:	Paul Plieger Digitally signed by Paul Plieger DN: cn=Paul Plieger, c=NZ, o=Massey University, ou=School of Fundamental Sciences, email=p.g.plieger@massey.ac.nz Date: 2021.08.30 15:07:00 +12'00'
Date:	30/08/21

(This form should appear at the end of each thesis chapter/section/appendix submitted as a manuscript/ publication or collected as an appendix at the end of the thesis)

Chapter 5. Synthesis and characterisation of $M_xFe_{3-x}O_4$ (M = Fe, Mn, Zn) spinel nanoferrites through a solvothermal route

Hossein Etemadi and Paul G. Plieger*

School of Fundamental Sciences, Massey University, Private Bag 11 222, Palmerston North, New Zealand

E-mail: p.g.plieger@massey.ac.nz
ORCID iD: 0000-0003-4886-7677

Abstract:

Given the technical hurdles associated with the thermal decomposition method for the synthesis of monodisperse nanocrystals, metal spinel nanoferrites $M_xFe_{3-x}O_4$ (M = Fe, Mn, Zn) were prepared by the solvothermal method. Structural, morphological and magnetic characterisations were completed using powder X-ray diffraction (XRD), transmission electron microscopy (TEM), thermogravimetric analysis (TGA), energy dispersive spectroscopy (EDS), atomic absorption spectroscopy (AAS), vibrating sample magnetometry (VSM) and X-ray photoelectron spectroscopy (XPS) techniques. The size of the synthesised nanoferrites spanned from 7 to 16 nm based on TEM results. EDS, AAS and XPS evidenced successful doping of Zn^{2+} and Mn^{2+} into the Fe_3O_4 structure. XRD revealed the expansion of the cell unit of Fe_3O_4 with the substitution of the larger Zn^{2+} and Mn^{2+} ions. All prepared nanoferrites presented with superparamagnetism at room temperature (300 K) with a blocking temperature less than room temperature ($T_B < T$).

Keywords: Nanoferrites, ions, magnetic properties, transmission electron microscopy, solvothermal

Declarations:

Funding
The authors gratefully acknowledge the New Zealand International Doctoral Research Scholarships (NZIDRS) committee for their financial support.

Conflicts of interest/Competing interests
The authors declare that they have no conflicts of interest.

Availability of data and material

The datasets analysed during the current study are available from the corresponding author on request.

Code availability
Not applicable

Authors' contributions
Research conducted by HE under the guidance of PP. Initial paper draft by HE, editing, suggestions and final checks organised and conducted by PP.

5.1. Introduction

The synthesis of small (diameter < 30 nm) iron oxide (Fe_3O_4 or γ-Fe_2O_3) nanoparticles (NPs) with narrow size distributions (< 5 %) and pronounced saturation magnetisation (M_s), is an important prerequisite for their potential technological applications.[1, 2] Magnetite (Fe_3O_4) crystallizes in a cubic inverse spinel configuration where Fe^{3+} ions are evenly distributed among the tetrahedral (A) and octahedral (B) sites and Fe^{2+} ions occupy the remaining octahedral sites, yielding the empirical formula $[Fe^{3+}]_A[Fe^{3+}Fe^{2+}]_BO_4$.[3, 4] Typically, Fe_3O_4 NPs exhibit lower saturation magnetisation values (50 – 60 emu/g) than bulk Fe_3O_4 (85 – 100 emu/g) at 300 K, induced by a large spin disorder on their surface.[5] In recent years, several strategies have been considered to improve their M_s by tuning their geometry, size, size distribution and composition. One potential strategy to enhance the M_s value of magnetite is to substitute Fe^{2+} with M^{2+} cations (M = Mn, Co, Ni).[3, 6] This has been achieved through several synthetic protocols such as sol–gel pyrolysis,[7] reverse micelle emulsion,[8] polyol,[9] solvothermal,[10] and co-precipitation[11] techniques. Nevertheless, technological success in the synthesis of single-domain crystalline nanoferrites of low dispersity has been limited.

The thermal decomposition method has been proposed for the synthesis of monodisperse nanoferrites with high crystallinity. This method involves the decomposition of metal precursors, such as metal carbonyls $M(CO)_5$,[12] metal acetylacetonates $M(acac)_3$,[13] and iron oleate,[2] in high-boiling point organic solvents at very high temperatures (~ 320 °C) and in the presence of surfactants. It encourages the synthesis of monodisperse Fe_3O_4 and analogous $M_xFe_{3-x}O_4$ nanocrystals of great size uniformity, crystallinity, and well-shaped configurations. Consequently, various nanoferrites such as Fe_3O_4,[14] $Li_{0.3}Zn_{0.3}Co_{0.1}Fe_{2.3}O_4$,[15] $Zn_xFe_{3-x}O_4$,[16] $Mg_xMn_{1-x}Fe_2O_4$,[17] $Mn_{0.5}Zn_{0.5}Fe_2O_4$,[18] $MgFe_2O_4$,[19] $Co_{0.03}Mn_{0.28}Fe_{2.7}O_4$,[20] $Mn_xZn_{1-x}Fe_2O_4$,[21] and $Co_xFe_{3-x}O_4$ nanoferrites[22] have been synthesised through this

method for various applications. Despite the progress in the synthesis of monodisperse crystalline nanoferrites with high precision using this method, there are still some obstacles for its practical realisation. These include the complexity of the chemical synthesis, the need for an inert (N_2) atmosphere during the reaction, the use of flammable organic solvents at higher temperatures (320 °C), and the difficult separation of solvents from the product. Another disadvantage is that the synthesised nanocrystals are dispersible in organic solvents, which requires additional steps to transfer them to the aqueous phase specially for biomedical applications. To address this, exchange agents such as PEG-phospholipid (DSPE-PEG2000),[23] methoxy-polyethyleneglycol-silane-500 Da (PEG),[24] 2,3-dimercaptosuccinic acid (DMSA),[25] Acrypol 934,[26] citric acid,[27] and PVP[28] have been utilized to help with this. Solvothermal methods (or hydrothermal methods when water is used as the solvent) are alternative synthetic methods which encourage the synthesis of nanocrystals with definite sizes, geometries and narrow size distributions. Generally these are conducted using an autoclave under mild conditions.[29] For example, MFe_2O_4 nanoferrites (M = Co, Mn, Ni, Zn),[30] MFe_2O_4 (M = Cu, Ni),[31] MFe_2O_4 (M = Mn, Fe, Co, Ni),[32] $CoFe_2O_4$[33], $Mg_{1-x}Zn_xFe_2O_4$ (x = 0.4 – 0.7),[34] $MnFe_2O_4$ and MFe_2O_4-Ag_2O (M = Zn, Co, & Ni)[35] have all been synthesised using hydrothermal decomposition of metal precursors, however the prepared nanocrystals were aggregated even in the presence of surfactants. To synthesis nanoferrites with high monodispersity, organic phase (solvothermal) decomposition of metal precursors have been examined. For example, Tian *et al.* synthesised ultrasmall monodispersed magnetite NPs of 4 – 6 nm as potential MRI contrast agents by the decomposition of $Fe(acac)_3$ in *n*-octanol. Additionally, Dendrinou-Samara *et al.* have utilised oleylamine (OAm) as both the solvent and surface-functionalising agent to synthesise $NiFe_2O_4$ NPs (9 – 11.7 nm) with M_s values of 32.0 – 53.5 emu/g, $CoFe_2O_4$ NPs (9 – 11 nm) with M_s values of 84.7 – 87.5 emu/g and 9 nm sized $MnFe_2O_4$ with M_s values of 65.7 emu/g for biomedical applications. However, some aggregation was observed in the prepared nanocrystals.[36] In our previous work, we addressed this aggregation issue by the careful control of reaction parameters leading to highly uniform $M_xFe_{3-x}O_4$ (M = Fe, Mg, Zn) nanoferrites using a mild solvothermal route. However we found that our particles exhibited decreased magnetisation after substituting Fe_3O_4 with diamagnetic Mg^{2+} ions.[37] Additionally, they were only dispersible in an organic solvent (hexane). In the present work, we have attempted to increase the magnetisation by the substitution of paramagnetic Mn^{2+} ions into the Fe_3O_4 structure and subsequently

explored the effect of this substitution on the crystallinity and magnetisation values of bare Fe_3O_4 NPs. In addition, considering that polyvinylpyrrolidone (PVP) is a water-soluble stabilising agent, we replaced oleic acid (OA) with PVP in an attempt to directly synthesise water-dispersible nanoferrites without additional phase exchange treatments.

5.2. Experimental Section

5.2.1. Materials

Iron (III) acetylacetonate ($Fe(acac)_3$ ≥ 99.9 % trace metals basis), oleylamine (≥70 %), polyvinylpyrrolidone (Mw ≈ 25,000), tri-n-octylphosphine oxide (TOPO, 99 %), octadecene (ODC, 90 %), AR grade 1,5-pentanediol, tetramethylammoniumhydroxide (20 % w/w) and manganese (II) chloride ($MnCl_2$) were purchased from Sigma-Aldrich. Zinc chloride ($ZnCl_2$) was purchased from Ajax Finechem. All other chemicals were of analytical grade and used as received from commercial sources without further purification.

5.2.2. Synthesis of $M_xFe_{3-x}O_4$ (M = Fe, Mn, Zn) Spinel Nanoferrites

Similar to our previous work, [42] we used a solvothermal route with some modifications to develop monodisperse $M_xFe_{3-x}O_4$ (M = Fe, Mn, Zn) spinel nanoferrites. For a typical synthesis of spinel $M_xFe_{3-x}O_4$ (M = Fe, Mn, Zn) NPs, the defined amounts of metal, (the Zn, Fe and Mn precursors), OAm and TOPO (Table 5.1) were mixed in octadecene (20 mL) under stirring (500 rpm) at 100 °C for 60 min. Polyvinylpyrrolidone (0.20 g) was dissolved in 1,5-pentanediol (5 mL) and heated to 150°C for 60 min. The reason for using 1,5-pentanediol is to improve the solubility of PVP in octadecene. The two solutions were then mixed and deoxygenated with Ar (2 min), then transferred into a 100 mL polytetra-fluoroethylene (PTFE)-lined autoclave. The autoclave was sealed and maintained at 200 °C for 30 min, then heated to 240 °C for 2 h. After this time the autoclave was left to cool to RT naturally. The $M_xFe_{3-x}O_4$ (M = Fe, Mn, Zn) nanoferrites were precipitated upon the addition of ethanol (10 mL), washed with an ethanol/hexane (1:2) solution mixture several times and then dispersed in hexane for further use.

Nanoferrite	OAm (mL)	PVP (mg)	$Fe(acac)_3$ (mmol)	$ZnCl_2$ (mmol)	$MnCl_2.4H_2O$ (mmol)	TOPO (mmol)
Fe1	2.56	200	1	0	0	0.5
Fe2	3.2	200	1	0	0	0.5
MnFe1	2.56	200	0.8	0	0.2	0.5
MnFe2	3.2	200	0.8	0	0.2	0.5
ZnFe1	2.56	200	0.6	0.4	0	0.5
ZnFe2	3.2	200	0.6	0.4	0	0.5

Table 5.1 Synthesis conditions for $M_xFe_{3-x}O_4$ (M = Fe, Mn, Zn) nanoferrites.

5.2.3. Characterisation.

The structure, chemical composition and magnetic features of the synthesised nanoferrites were probed with transmission electron microscopy (TEM; Tecnai G2 Spirit Bio-TWIN), powder X-ray diffraction (XRD; Rigaku Spider X-ray diffractometer), energy-dispersive X-ray connected scanning electron microscopy (SEM−EDX; FE-SEM FEI Quanta), atomic absorption spectroscopy (AAS; AAS-9000 spectrometer, Shimadzu), thermogravimetric analysis (TGA; TA Instruments Q500), X-ray photoelectron spectroscopy (XPS; Kratos Axis Ultra^{DLD}) and vibrating sample magnetometry (VSM; Quantum Design P935A USA, physical property measurement system (PPMS)). Further details regarding characterisation are described in the Supporting Information.

5.3. Results And Discussion

5.3.1. Structural and Compositional Studies

In our previous research, we investigated the effect of various experimental conditions and reaction parameters to successfully synthesise monodisperse $M_xFe_{3-x}O_4$ (M = Fe, Mg, Zn) spinel nanoferrites.[37] The optimal conditions for the synthesis of a range of monodisperse NPs with high uniformity were found to be a 1:4 OA to OAm molar ratio, 0.5 mmol TOPO, 120 min reaction time and a temperature of 240 °C.[37] The resulting nanoparticles were not dispersible in water. Therefore, phase exchange treatment was performed using tetramethylammonium hydroxide to transfer hexane-dispersible nanoferrites to the aqueous phase. In an attempt to directly synthesise water-dispersible nanoferrites without

an additional ligand exchange process, we replaced OA with PVP. The rational is that polyvinylpyrrolidone (PVP) is a non-charged amphiphilic polymer which can be dissolved in either water or organic solvents.[38] Huang *et al* synthesized water-dispersible stable colloidal Fe_3O_4 nanocrystals through thermal decomposition of $Fe(Co)_5$ in the presence of PVP as the sole stabilizer for MRI applications.[23] It was expected that PVP molecules adsorbed on the particle surface, would help to improve the dispersibility of the resultant nanocrystals in water. However, the obtained nanoferrites were not water-dispersible due to the presence of OAm and TOPO in the reaction medium. The TEM images of Fe1 and Fe2 (Figure 5.1a, b) show the arrangement of NPs in a close-packed assembly. The Fe1 and Fe2 NPs exhibit predominantly spherical shapes with mean particle sizes of 7.9 ± 1.2 nm and 8.5 ± 2.2 nm respectively (Figure 5.1c, d). Substitution of Mn^{2+} ions into Fe_3O_4 results in deformed NPs with larger sizes than that of Fe1–2 as shown in the corresponding TEM micrographs of MnFe1 (Figure 5.2a) and MnFe2 (Figure 5.2b). The average particle sizes were determined to be 8.9 ± 1.9 nm (Figure 5.2c) and 10.6 ± 2.9 nm (Figure 5.2d) for MnFe1 and MnFe2 respectively. The TEM images of ZnFe1 (Figure 5.3a) and ZnFe2 (Figure 5.3b) show some well-separated spherical particles of good size uniformity. The ZnFe1 and ZnFe2 NPs have average particle sizes of 9.4 ± 2.5 nm (Figure 5.3c) and 10.3 ± 2.1 nm (Figure 5.3d) respectively. Increasing the concentration of OAm has resulted in both increased and decreased size effects in the past. In terms of size and morphology, an increase in the OAm amount in the present study does not appear to have had an influence (within experimental error).

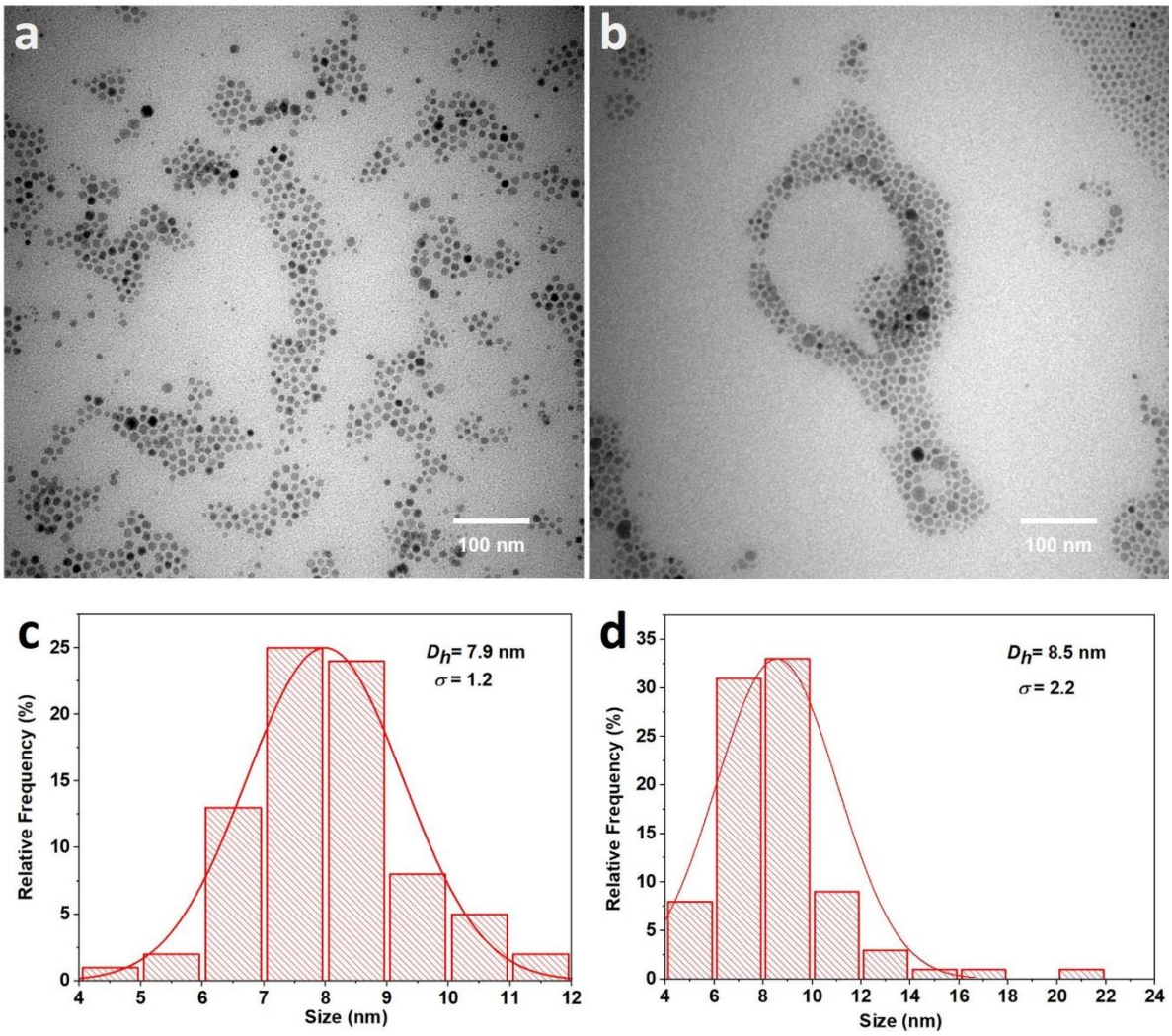

Figure 5.1 TEM images of the synthesised Fe1 (a, b) and Fe2 (c, d) NPs at different magnifications. Inserts: Size distribution of Fe1 (e) and Fe2 (f) with mean size (Dh)and standard deviation (σ).

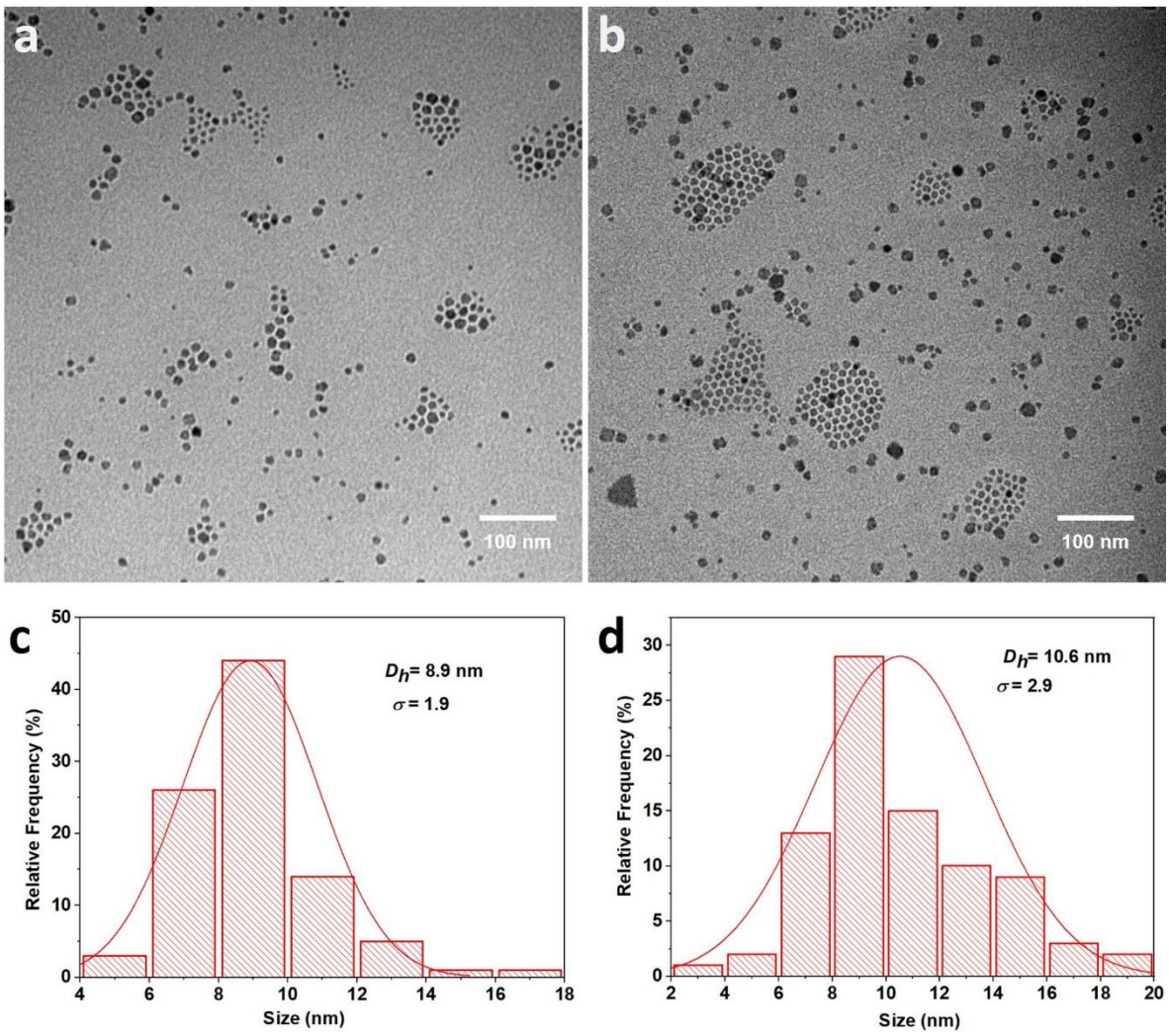

Figure 5.2 TEM images of the synthesised MnFe1 (a, b) and MnFe2 (c, d) NPs at different magnifications Inserts: Size distribution of MnFe1 (e) and MnFe2 (f) with mean size (Dh) and standard deviation (σ).

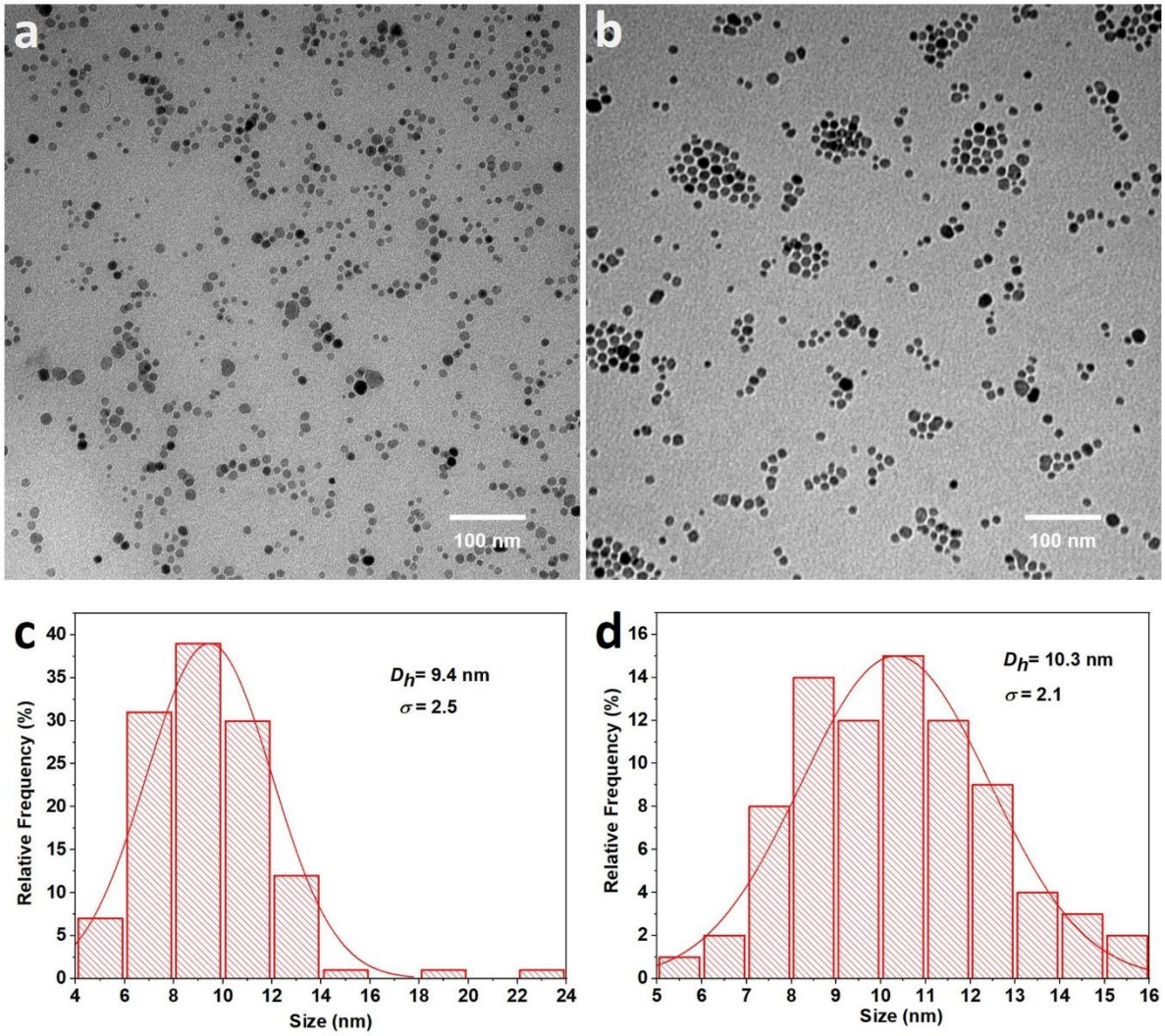

Figure 5.3 TEM images of the synthesised ZnFe1 (a, b) and ZnFe2 (c, d) NPs at different magnifications. Inserts: Size distribution of ZnFe1 (e) and ZnFe2 (f) with mean size (Dh) and standard deviation (σ).

The crystalline phase and purity of $M_xFe_{3-x}O_4$ (M = Fe, Mg, Zn) nanoferrites were studied by powder X-ray diffraction (PXRD) (Figures 5.4 and 5.9). The XRD patterns of Fe_3O_4 NPs (Fe1 and Fe2) at 2θ = 18.50°, 30.1°, 35.6°, 43.1°, 53.2°, 57.2° and 63° can be indexed to the crystallographic planes of (111), (220), (311), (400), (422), (511), and (440).[39] Importantly, no other impurities corresponding to other iron oxide crystal phases such as γ-Fe_2O_3 (additional peaks at 2θ = 23.77° (210) and 26.10° (211) (JCPDS no. 39-1346)),[40] α-Fe_2O_3 (2θ = 24.1° (012), 33.1° (104), 40.8° (113), 49.4° (024), 53.9° (116), 57.4° (018), 62.3° (214) and 63.9° (300) (JCPDS no. 24-0072)),[41] or FeO (2θ = 36.0° (113), 41.8° (200), and 60.7° (220) (JCPDS no. 06-0615))[42] were detected in the XRD patterns, confirming the purity of

the synthesised Fe_3O_4 crystals. The average crystallite sizes of Fe1 and Fe2 calculated from the Debye−Scherrer equation were 7.2 ± 0.89 nm and 6.9 ± 0.38 nm respectively. Considering the strong Bragg reflection peak (Miller index 3 1 1), the lattice spacing (*d*) and lattice constant (*a*) were determined for all $M_xFe_{3-x}O_4$ (M = Fe, Mn, Zn) nanoferrites (Table 5.2). The lattice constants were both 8.3481 Å for Fe1 and Fe2 NPs, consistent with *a* = 8.35 Å reported for Fe_3O_4 NPs.[43]

Table 5.2 Calculated values of size and lattice parameters for MxFe3−xO4 (M = Fe, Mn, Zn) nanoferrites

Nanoferrites	**Crystallite Size (nm) XRD**	**Size (nm) TEM**	**Position of 311 peak in degree (*ϑ*)**	***d*, Lattice spacing (Å)**	***a*, Lattice constant (Å)**	**Organic content (%)**
Fe1	7.2 ± 0.89	7.9 ± 1.2	35.64	2.5170	8.3481	72.3
Fe2	6.7 ± 0.38	8.5 ± 2.2	35.64	2.5170	8.3481	74.84
MnFe1	8.8 ± 1.4	8.9 ± 1.9	35.5	2.5266	8.3800	66.41
MnFe2	9.4 ± 0.89	10.6 ± 2.9	35.54	2.5239	8.3709	56.03
ZnFe1	5.3 ± 1.46	9.4 ± 2.5	35.4	2.5336	8.4029	81.70
ZnFe2	5.7 ± 1.35	10.3 ± 2.1	35.5	2.5266	8.3800	76.11

The XRD patterns of Mn-doped Fe_3O_4 are well matched with the single-phase spinel cell geometry. The Bragg diffraction peaks at 2θ values of 18.5°, 30.1°, 35.5°, 42.80°, 52.8°, 57.1°, and 62.5° corresponded to the crystal reflection planes of (111), (220), (311), (400), (422), (511), and (440), respectively (JCPDS no. 74-2403).[44] There is no evidence of impurities related to manganese oxide secondary phases such as α-MnO_2 (2θ = 12.7° (110), 18.1° (200), 28.8° (310), 37.5° (211), 42.1° (301), 49.9° (411), 56.2° (600) and 60.3° (521) (JCPDS no. 44-0141))[45] or MnO_2 (2θ = 37.12° (100) and 66.75° (110) (JCPDS No. 30-0820)).[46] This confirms that Mn^{2+} ions substituted Fe^{2+}/Fe^{3+} in the Fe_3O_4 crystal unit rather

than being distributed on the surface of Fe_3O_4 as a manganese oxide. The (311) crystal plane of Mn-doped Fe_3O_4 shifted from 2θ = 35.6° for Fe1 to 35.56° for MnFe1. Moreover, *a* increased from 8.3481 Å to 8.3800 Å and *d* increased from 2.5170 Å to 2.5266 Å.[47] The diffraction peaks of $ZnFe_2O_4$ representing the (111), (220), (311), (400), (422), (511), and (440) crystal planes agree well with the standard cubic spinel $ZnFe_2O_4$.[47] Importantly, sharper peaks were observed in the XRD patterns of Zn-doped Fe_3O_4, which suggested greater crystallinity compared to undoped Fe_3O_4. No secondary phases of zinc oxides (2θ = 31.7° (100), 34.4° (002), 36.2° (101), 47.5° (105) and 56.5° (110)) (JCPDS 36-1451) were detected, indicating the purity of the crystals.[48] Nevertheless, in line with Mn-doped Fe_3O_4, the (311) crystal plane of Zn doped Fe_3O_4 slightly shifted from 2θ = 35.64° for Fe1 to 35.52° for ZnFe1 (Figure 5.4b, labelled with a #). Furthermore, the corresponding lattice constant and lattice spacing increased from 8.3481 to 8.3754 Å and 2.5170 to 2.5253 Å respectively. The increase in lattice parameters (expansion of the unit cell volume) of Fe_3O_4 after doping is due to the replacement of Fe^{3+} (r_{ionic} = 0.64 Å)[49] and/or Fe^{2+} ions (r_{ionic} = 0.76 Å)[50] with larger Mn^{2+} (r_{ionic} = 0.80 Å)[51] or Zn^{2+} ions (r_{ionic} = 0.74 Å).[52] Lattice expansion of Fe_3O_4 by Zn^{2+} [50, 53] or Mn^{2+} [54] has been previous reported.

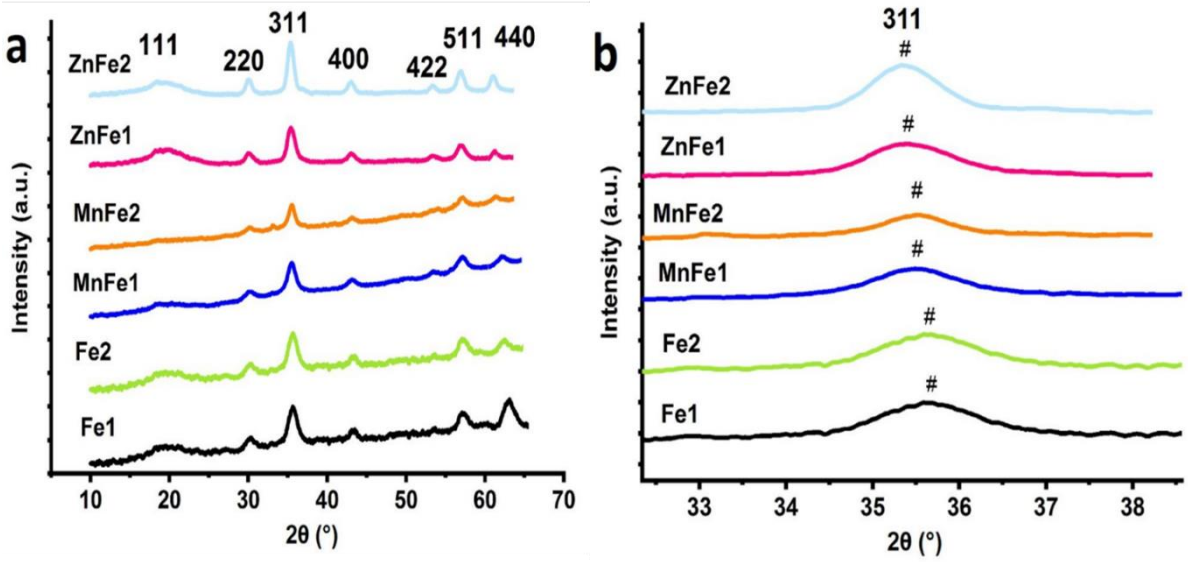

Figure 5.4(a) Powder X-ray diffraction patterns and (b) the highlighted (311) diffraction peaks of MxFe3−xO4 (M = Fe, Mg, Zn) nanoferrites.

The physical sizes obtained from TEM are larger for the ZnFe nanoferrites than that of the crystallite sizes measured by XRD, with the remaining nanoferrites all within experimental

error. This increase in size for the ZnFe nanoferrites could be ascribed to the fact that the reaction performance does not always lead to single crystal particles. Thermogravimetric analysis (TGA) under an N_2 flow with a heating rate of 10 °C/min from room temperature to 800 °C was used to quantitatively determine the organic fraction of nanoferrites (Figure 5.5). The fraction of inorganic cores inside the nanoferrites is represented by the mass percentage of the residue hence the weight fraction of the surfactants in the nanoferrites can be established. The first loss of mass below 200 °C in all samples refers to the removal of water or organic solvents from the nanoferrite surface.[55] The mass loss between 250 – 350 °C in the thermograms of all samples can be attributed to the decomposition of the free surfactants adsorbed on the surface of the NPs.[56] The mass loss between 450 – 620 °C corresponds to the decomposition of directly attached surfactants.[57] The final loss of weight was observed between 600 – 750 °C for all nanoferrites can be assigned to the reduction of the inorganic metal core under a N_2 atmosphere. For Fe1, the loss of weight was a two-stage process between 600 – 700 °C and 700 – 750 °C. Ayyappan *et al.* and Mameli *et al.* have reported the same behaviour for $CoFe_2O_4$ [58] and $Zn_xCo_{1-x}Fe_2O_4$ ($0 < x < 0.6$) nanoferrites.[16] Notably, there are discontinuities in the thermograms of MnFe2 (just above 400 °C and at approximately 500 °C), Fe1 (just past 600 °C) and MnFe1 (at approximately 300 and 500 °C). This may be the result of the instrument being slightly bumped during the measurements.

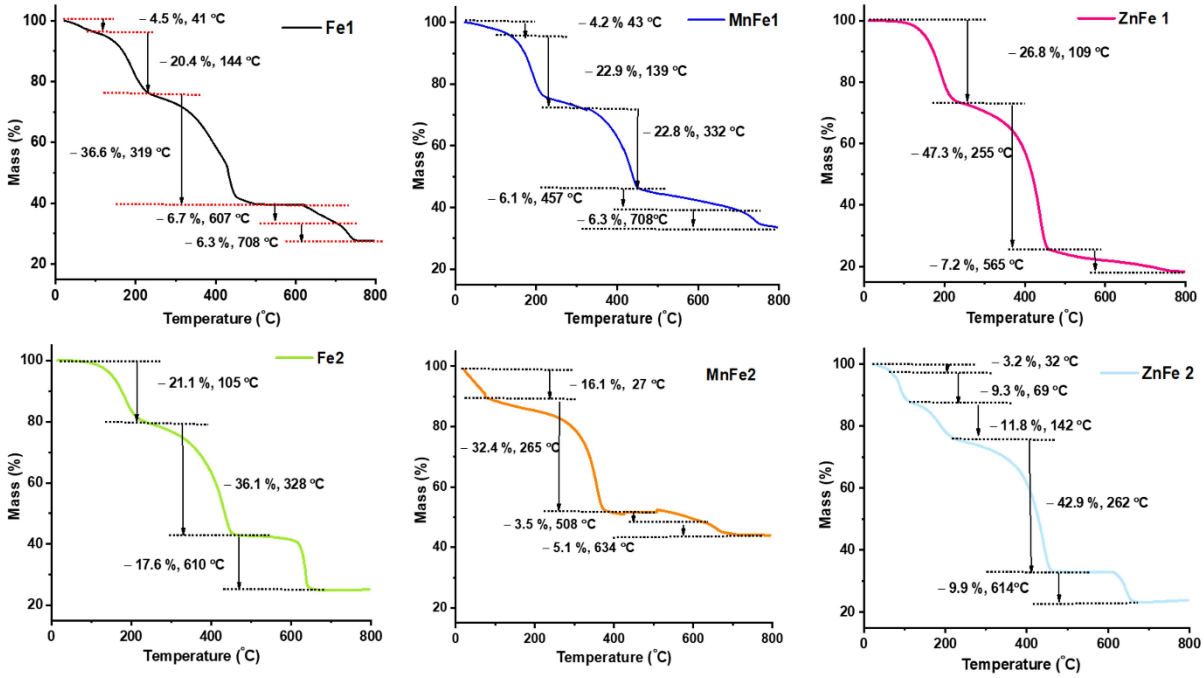

Figure 5.5 TGA curves of $M_xFe_{3-x}O_4$ (M = Fe, Mn, Zn) nanoferrites.

The fraction of stabilising surfactants around the nanoferrites tends to reduce with increased magnetic core size (Table 5.2). Larger nanocores possess lower surface to volume ratios which results in less active sites available for binding surfactants.[59, 60] EDS spectra of nanoferrites were obtained through line scans of selected sites at various magnifications to analyse the chemical compositions in a semi-quantitative manner. The EDS results for all nanoferrites collected from different positions exhibited similar atomic percentages (At %), indicating the composition homogeneity of the nanoferrites.[61] For instance, the At % of Mn atoms were 4.81 % and 4.03 % for MnFe1 and MnFe2 NPs respectively. A similar trend could also be seen in EDS results of Fe1–2 and Zn1–2 as depicted in Figures 5.10–5.12. Peaks corresponding to C atoms, due to surfactants and the carbon coating prior to analysis, were observed in the EDS spectra of all nanoferrites. The characteristic peaks for Fe and O were observed in the EDS spectra of Fe1–2 (Figure 5.10). The EDS spectra of MnFe1–2 contained Fe, Mn and O peaks (Figure 5.11) and the EDS spectra of ZnFe1–2 featured Fe, Zn and O peaks (Figure 5.12). Notably, in the case of Mn-doped Fe_3O_4 NPs, the signals of Mn and Fe overlap at 6.5 keV. This has also been observed for other Fe−Mn nanoferrites,[46, 62] and is due to the close energy levels of Mn K_β and Fe K_α, which makes it difficult to distinguish them on EDS spectra. Based on EDS analysis, the Fe:O, Mn:Fe:O and Zn:Fe:O atomic ratios

differed from the expected stoichiometries. Atomic absorption spectroscopy (AAS) was used to determine the experimental chemical formula of M_xFe_3-xO_4 nanoferrites (Table 5.3). The calibration curve equations and R^2 for each analyte along with the experimental absorption values are presented in Figure 5.13-15 for the nanoferrites Consistent with the EDS results, the molar ratios and chemical formula derived from AAS results were not in agreement with the corresponding theoretical values. Our group , Hu *et al.* and Oberdick *et al.* have also reported this deviation from theoretical stoichiometry in $M_xFe_{3-x}O_4$ $Co_xFe_{3-x}O_4$ and core/shell $Fe_3O_4/Mn_xFe_{3-x}O_4$ NPs.[63, 64] This might be due to the different decomposition temperatures of $Fe(acac)_3$, $MnCl_2$ and $ZnCl_2$ salts.[65] In addition, the large magnitude of surfactants used in the synthetic process may alter the decomposition temperatures of $Fe(acac)_3$, $MnCl_2$ and $ZnCl_2$ salts and influence the growth mechanism.[63, 66]

Table 5.3 Theoretical and experimental (AAS) molar ratios and chemical formula of $M_xFe_{3-x}O_4$ (M = Mn, Zn) nanoferrites.

Nanoferrite	Molar ratio			Chemical formula	
	Theoretical		Experimental	Theoretical	Experimental
MnFe1	0.2:0.8	Mn/Fe	0.054/0.225 Mn/Fe	$Mn_{0.6}Fe_{2.4}O_4$	$Mn_{0.58}Fe_{2.42}O_4$
MnFe2	0.2:0.8	Mn/Fe	0.107/0.6 Mn/Fe	$Mn_{0.6}Fe_{2.4}O_4$	$Mn_{0.45}Fe_{2.55}O_4$
ZnFe1	0.4:0.6	Zn/Fe	0.06/0.135 Zn/Fe	$Zn_{1.2}Fe_{1.8}O_4$	$Zn_{0.93}Fe_{2.07}O_4$
ZnFe2	0.4:0.6	Zn/Fe	0.104/0.174 Zn/Fe	$Zn_{1.2}Fe_{1.8}O_4$	$Zn_{1.12}Fe_{1.87}O_4$

The chemical compositions and oxidation states of $M_xFe_{3-x}O_4$ (M = Fe, Mn, Zn) nanoferrites were investigated via X-ray photoelectron spectroscopy (XPS). The C *1s* signal at 284.6 eV (adventitious carbon) was utilised as an energy reference in order to calibrate the binding energy (B.E) scale ranging from 0 – 1300 eV. Wide-scan surveys confirmed the peaks of carbon (C 1s), oxygen (O 1*s*), iron (Fe 2*p*), zinc (Zn 2*p*) and manganese (Mn 2*p*) photoelectron lines recorded at B.E values of 280 – 300 eV, 520 – 550 eV, 702 – 750 eV, 630 – 665 eV and 1015 – 1055 eV respectively (Figures 5.6 and 5.16 – 20). A sharp peak at 285 eV was observed in the high-resolution C *1s* XPS spectra of all nanoferrites, which corresponded to the C–C bond of surfactants and adventitious carbon.[67, 68] For all

nanoferrites, the O *1s* core level spectrum showed a low intensity signal centred at lower B.E value of ~ 530 eV, attributed to the metal–oxygen bonds of $M_xFe_{3-x}O_4$,[69],[70] and a larger peak at ~ 532 eV assigned to carboxylate groups.[68] For the Fe1 NPs, the Fe *2p* core level spectrum indicates the absence of Fe ions on the surface (Figure 5.6) For the Fe2 NPs, the doublet peaks centred at B.E values of 710.6 and 723.8 eV are ascribed to Fe $2p_{3/2}$ and Fe $2p_{1/2}$ of Fe^{3+} in Fe_3O_4 (Figure 5.16).[71] The spin-orbit splitting energy difference was 13.2 eV which is in accordance with earlier reports for Fe_3O_4.[72] Furthermore, the presence of both the +2 and +3 oxidation states of Fe and the formation of Fe_3O_4 rather than γ-Fe_2O_3 are thought to cause the broadness of the Fe *2p* peaks.[73] In the case of Mn-doped Fe_3O_4 (MnFe1 and MnFe2), the presence of Mn $2p_{3/2}$ and Mn $2p_{1/2}$ spin-orbit peaks at B.E values of ~ 641.5 and 653.5 eV (MnFe1) and 641.7 and 653.8 eV (MnFe2) indicate the oxidation state of Mn^{2+} (Figures 5.17-18).[3, 74] For the Zn-doped Fe_3O_4 nanoferrites, the presence of Fe in the +3 oxidation state is indicated by two major peaks, located at 711.8 and 724.8 eV for ZnFe1 and at 711 and 724.2 eV for ZnFe2, consistent with Fe $2p_{3/2}$ and Fe $2p_{1/2}$ respectively. Furthermore, two peaks in the Zn *2p* core-level XPS spectrum indicate Zn in the +2-oxidation state, with B.E values of 1021.6 and 1044.8 eV (ZnFe1) and 1022.2 and 1045.4 eV (ZnFe2) and attributed to Zn $2p_{3/2}$ and Zn $2p_{1/2}$ (Figures 5.19-20). The obtained values are in accordance with values reported in the literature for Zn in the +2 oxidation state, which confirms the formation of zinc ferrite $ZnFe_2O_4$.[75]

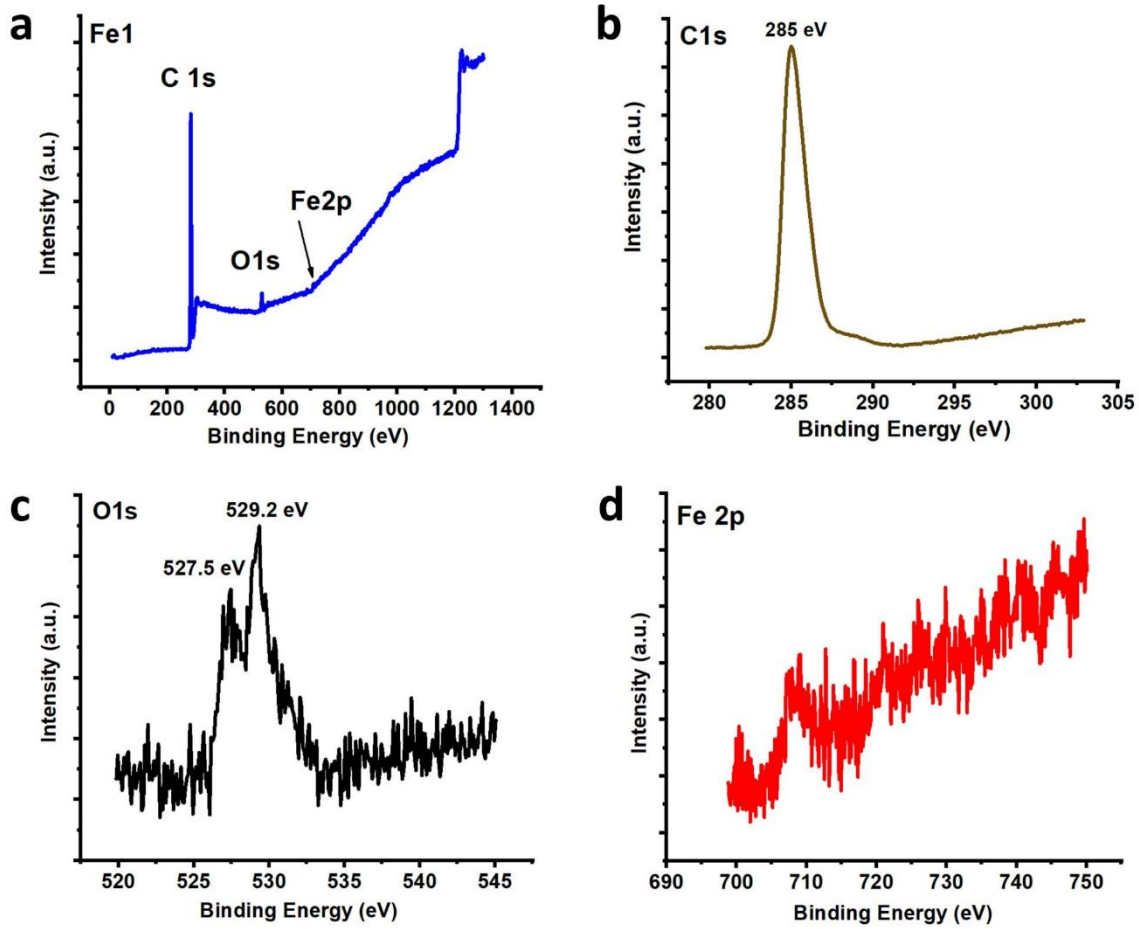

Figure 5.6 XPS spectra of the Fe1 nanoferrite (a) survey scan (b) C*1s* (c) O*1s* and (d) Fe*2p* regional scans.

5.3.2. Magnetometry

Magnetisation (emu/g) as a function of the applied magnetic field (Oe) (M−H loops) were recorded using VSM at room temperature (~ 300 K) for all nanoferrites to obtain M_s, remnant magnetisation (M_r), coercivity (H_c) and normalised remanence (M_r/M_s) values (Figure 5.7 and Table 5.3). Individual VSM plots and sample masses of nanoferrites are provided in Figure 5.21. The H_c and M_r values at low fields were almost negligible for all nanoferrites, indicating their superparamagnetic characteristics. This reveals that the superparamagnetic behaviour of Fe_3O_4 (Fe1 and Fe2) does not change after doping Zn^{2+} and Mn^{2+} ions into its spinel structure.[76] The relationship between particle size and the magnetic properties of Fe_3O_4 NPs has been examined. If the particle sizes measured with XRD and TEM are between 10 – 80 nm, particles are in single-domain state, however

particles with diameters > 80 nm present multi-domain structure. Additionally, if the measured size is < 30 nm, particles present superparamagnetic behaviour. [77] The sizes of our particles measured with TEM and XRD are < 30 nm which indicates they are single-domain superparamagnetic feature as evidenced by VSM measurements. Magnetisation values decreased with increased OAm content, so that M_s (Fe1) > M_s (Fe2), and M_s (MnFe1) > M_s (MnFe2). Since M_s is described on a per gram basis (emu/g), a non-magnetic coating OAm layer will diminish its value which equates to a decrease in the magnetisability.[78] However, in the case of ZnFe nanoferrites, the M_s value of ZnFe2 > ZnFe1. The magnetisation difference between these particles is very small and so is most likely related to the size effect.[79] The concentration and occupation sites of doped ions are also important factors. In the crystal structure of Fe_3O_4, all Fe^{2+} ions (magnetic moment = 4 μB) occupy B sites while the Fe^{3+} ions (magnetic moment = 5 μB) are distributed equally between A and B sites. Therefore, the net magnetisation of Fe_3O_4 is decided by Fe^{2+} ions at B sites, as Fe^{3+} ions at A and B sites align opposite to each other and their magnetic moments cancel. When doped with Mn^{2+} or Zn^{2+} ions, the A and B sites of Fe_3O_4 can be occupied by these ions and the ferromagnetic and/or antiferromagnetic coupling interactions between Fe^{2+} and Fe^{3+} ions are modulated by their concentrations and distribution of the doped ions at the A and B sites.

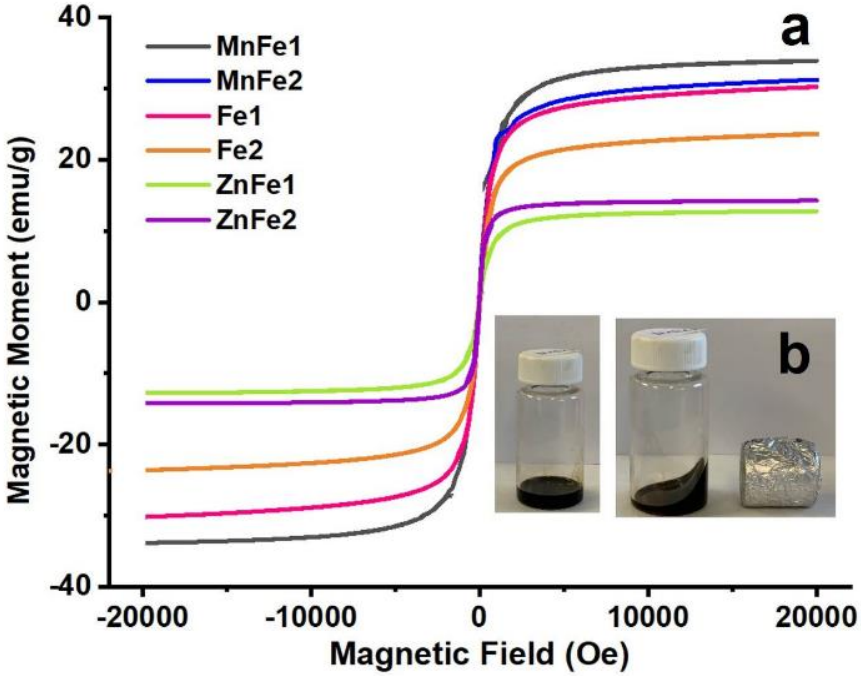

Figure 5.7(a) Magnetic hysteresis loops of MxFe3−xO4 (M = Fe, Mn, Zn) nanoferrites at room temperature and (b) the magnetic response of MnFe2 to an external magnetic field.

For Mn-doped Fe_3O_4, the substitution of Fe^{3+} ions (5 μB) by Mn^{2+} ions (5 μB) does not change the net magnetisation of the Fe_3O_4 unit. However, if the Mn^{2+} ions (5 μB) substitute the octahedral Fe^{2+} ions (4 μB), the saturation magnetisation is expected to increase. Doping Mn^{2+} ions (0.2 mmol) into Fe_3O_4 increased the M_s from 30.2 to 33.9 emu/g for MnFe1 and from 24.8 to 31.2 emu/g for MnFe2, suggesting that Mn^{2+} substituted Fe^{2+} ions. Additionally, MnFe1 and MnFe2 nanoferrites exhibit larger sizes compared to Fe1 and Fe2, resulting in a smaller spin canting effect and higher magnetisation.[59] Doping Zn^{2+} ions (0.4 mmol) results in a reduced M_s of 14.2 emu/g for ZnFe1 and 12.7 emu/g for ZnFe2. For Zn-doped Fe_3O_4, the decrease in magnetisation is ascribed to the substitution of diamagnetic Zn^{2+} ions (0 μB) in the tetrahedral site with the Fe^{3+} ions occupying the octahedral sites, decreasing the strength of antiferromagnetic coupling interactions (the A−B superexchange interaction) of Fe^{3+} atoms and subsequent reduced magnetisability .[34, 80] Magnetisation of nanoferrites as a function of the temperature (T) (M-T curves) were investigated in the field-cooled (FC) and zero-field-cooled (ZFC) regimes under a constant magnetic field of 10 Oe to extract magnetic crystalline anisotropy energy (K_{eff}) and blocking temperature (T_B) values (Figure 5.8 and Table 5.3). The magnetic anisotropy constant (K) was calculated for all nanoferrites using

the equation, $K = 25k_BT_B/V$, where T_B is the blocking temperature, k_B is Boltzmann's constant (1.3807×10^{-23} J K^{-1}) and V is the volume of a single nanocrystal (m^3).[2]

Table 5.4 Parameters of ZFC/FC and M-H hysteresis loops for $M_xFe_{3-x}O_4$ (M = Fe, Mg, Zn) nanoferrites

Nanoferrite	*Ms* (emu/g)	M_r (emu/g)	H_c (O_e)	M_r/M_s	T_B	$K \times 10^5$ (J/m^3)
Fe1	30.2	4.8	111	0.15	40	3.2
MnFe1	33.9	3.6	1.7	0.10	133	3.3
ZnFe1	14.2	2.2	60.6	0.15	45	19.9
Fe2	24.8	2.3	90.2	0.02	56	4
MnFe2	31.2	5.8	4.8	0.18	146	20.9
ZnFe2	12.7	1.18	52.4	0.09	97	12.3

A marked increase in T_B was observed for Zn and Mn-doped Fe_3O_4 NPs. This shift towards higher temperatures could be attributed to increased magneto-crystalline anisotropy of the system (Table 5.4). The strong coupling strength between orbital angular momentum and electron spin (L-S) can also contribute to higher blocking temperatures.[81] The Mn-doped nanoferrites presented with broader ZFC curves. This is ascribed to the larger size distribution of NPs and increased interparticle interactions as shown by TEM results.[82]

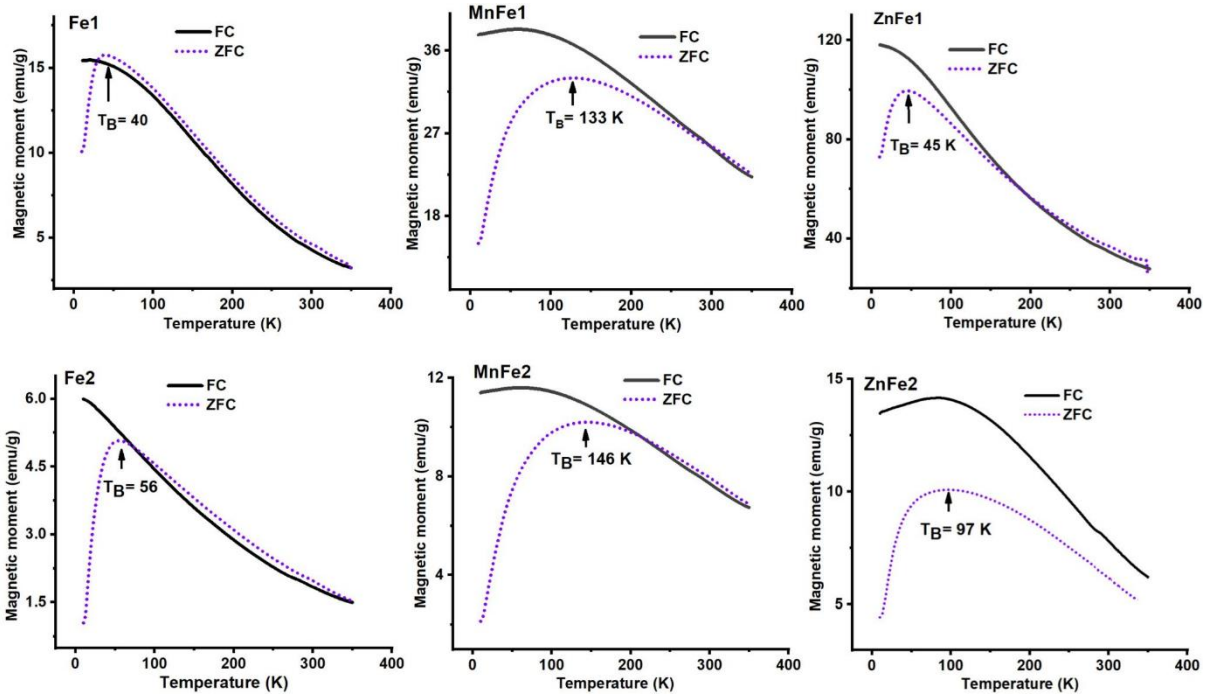

Figure 5.8 FC/ZFC curves of the MxFe3−xO4 (M = Fe, Mn, Zn) nanoferrites recorded at a constant magnetic field of 10 Oe.

5.4. Conclusion

The synthesis of a series of low dispersity $M_xFe_{3-x}O_4$ (M = Fe, Mn, Zn) spinel nanoferrites was achieved through the solvothermal route. The substitution of Fe^{2+} ions with paramagnetic Mn^{2+} ions resulted in improved magnetisation compared to the previous study which incorporated Mg^{2+} ions. [42] Zn^{2+} doping was effective for the formation of well-shaped nanoferrites of improved crystallinity, however this substitution decreased the magnetisation. XPS provided evidence for the formation of $M_xFe_{3-x}O_4$ (M = Fe, Mn, Zn) spinel nanoferrites, but revealed a high organic content on the surface of the NPs. Considering the AAS results, all doped nanoferrites exhibited compositional deficiency. Our rationale to directly synthesise water-dispersible nanoferrites without subsequent treatments proved to be unsuccessful utilising PVP, however in the future we aim to study the ratio between PVP, OAm and TOPO through which the possibility of synthesis of direct in situ water dispersible low dispersity particles might be achieved.

5.5. References

[1] J. Jung-tak, N. Hyunsoo, L. Jae-Hyun, M. S. Ho, K. M. Gyu, C. Jinwoo, Angew Chem. Int. Ed. 2009, 48, 1234.

[2] J. Park, K. An, Y. Hwang, J.-G. Park, H.-J. Noh, J.-Y. Kim, J.-H. Park, N.-M. Hwang, T. Hyeon, Nat. Mater 2004, 3, 891.

[3] L. Yang, L. Ma, J. Xin, A. Li, C. Sun, R. Wei, B. W. Ren, Z. Chen, H. Lin, J. Gao, Chem. Mater. 2017, 29, 3038.

[4] X. Lasheras, M. Insausti, I. Gil de Muro, E. Garaio, F. Plazaola, M. Moros, L. De Matteis, J. M. de la Fuente, L. Lezama, J. Phys. Chem. C. 2016, 120, 3492.

[5] J. Jung-tak, L. Jooyoung, S. Jiyun, J. Eric, K. Minkyu, K. Y. Il, K. M. Gyu, T. Yasushi, A. A. Syed, K. K. Wook, P. K. Ho, P. S. Ha, B. Seongtae, Adv. Mater. 2018, 30, 1704362.

[6] J.-H. Lee, Y.-M. Huh, Y.-w. Jun, J.-w. Seo, J.-t. Jang, H.-T. Song, S. Kim, E.-J. Cho, H.-G. Yoon, J.-S. Suh, J. Cheon, Nat. Med. 2006, 13, 95; H. Etemadi, P. G. Plieger, Advanced Therapeutics, n/a, 2000061.

[7] F. Li, J. Liu, D. G. Evans, X. Duan, Chem. Mater. 2004, 16, 1597.

[8] Y. Lee, J. Lee, C. J. Bae, J. G. Park, H. J. Noh, J. H. Park, T. Hyeon, Adv. Funct. Mater. 2005, 15, 2036.

[9] D. V. Wagle, A. J. Rondinone, J. D. Woodward, G. A. Baker, Cryst. Growth Des. 2017, 17, 1558.

[10] F. L. Deepak, M. Bañobre-López, E. Carbó-Argibay, M. F. Cerqueira, Y. Piñeiro-Redondo, J. Rivas, C. M. Thompson, S. Kamali, C. Rodríguez-Abreu, K. Kovnir, Y. V. Kolen'ko, J. Phys. Chem. C. 2015, 119, 11947.

[11] C. Pereira, A. M. Pereira, C. Fernandes, M. Rocha, R. Mendes, M. P. Fernández-García, A. Guedes, P. B. Tavares, J.-M. Grenèche, J. P. Araújo, C. Freire, Chem. Mater. 2012, 24, 1496.

[12] T. Hyeon, S. S. Lee, J. Park, Y. Chung, H. B. Na, J. Am. Chem. Soc. 2001, 123, 12798.

[13] S. Sun, H. Zeng, J. Am. Chem. Soc. 2002, 124, 8204.

[14] K. Yoo, B.-G. Jeon, S. H. Chun, D. R. Patil, Y.-j. Lim, S.-h. Noh, J. Gil, J. Cheon, K. H. Kim, Nano Lett. 2016, 16, 7408; S. Tong, C. A. Quinto, L. Zhang, P. Mohindra, G. Bao, ACS Nano 2017, 11, 6808.

[15] M. Dalal, J.-M. Greneche, B. Satpati, T. B. Ghzaiel, F. Mazaleyrat, R. S. Ningthoujam, P. K. Chakrabarti, ACS Appl. Mater. Interfaces 2017, 9, 40831.

[16] V. Mameli, A. Musinu, A. Ardu, G. Ennas, D. Peddis, D. Niznansky, C. Sangregorio, C. Innocenti, N. T. K. Thanh, C. Cannas, Nanoscale 2016, 8, 10124.

[17] M. Jeun, S. Park, G. H. Jang, K. H. Lee, ACS Appl. Mater. Interfaces 2014, 6, 16487.

[18] M. Jeun, J. W. Jeoung, S. Moon, Y. J. Kim, S. Lee, S. H. Paek, K.-W. Chung, K. H. Park, S. Bae, Biomaterials 2011, 32, 387.

[19] V. M. Khot, A. B. Salunkhe, N. D. Thorat, R. S. Ningthoujam, S. H. Pawar, Dalton Trans. 2013, 42, 1249.

[20] S. He, H. Zhang, Y. Liu, F. Sun, X. Yu, X. Li, L. Zhang, L. Wang, K. Mao, G. Wang, Y. Lin, Z. Han, R. Sabirianov, H. Zeng, Small 2018, 14, 1800135.

[21] Y. Qu, J. Li, J. Ren, J. Leng, C. Lin, D. Shi, ACS Appl. Mater. Interfaces 2014, 6, 16867.

[22] A. Sathya, P. Guardia, R. Brescia, N. Silvestri, G. Pugliese, S. Nitti, L. Manna, T. Pellegrino, Chem. Mater. 2016, 28, 1769.

[23] J. Huang, L. Bu, J. Xie, K. Chen, Z. Cheng, X. Li, X. Chen, ACS Nano 2010, 4, 7151.

[24] J.-t. Jang, J. Lee, J. Seon, E. Ju, M. Kim, Y. I. Kim, M. G. Kim, Y. Takemura, A. S. Arbab, K. W. Kang, K. H. Park, S. H. Paek, S. Bae, Adv. Mater. 2018, 30, 1704362.

[25] P. T. Yin, B. P. Shah, K. B. Lee, Small 2014, 10, 4106.

[26] N. K. Prasad, K. Rathinasamy, D. Panda, D. Bahadur, J. Mater. Chem. 2007, 17, 5042.

[27] S. Munjal, N. Khare, B. Sivakumar, D. Nair Sakthikumar, J. Magn. Magn. Mater. 2019, 477, 388.

[28] X. Hu, Y. Ji, M. Wang, F. Miao, H. Ma, H. Shen, N. Jia, J. Biomed. Nanotechnol. 2013, 9, 976.

[29] J. A. Darr, J. Zhang, N. M. Makwana, X. Weng, Chem. Rev. 2017, 117, 11125; W. Shi, S. Song, H. Zhang, Chem. Soc. Rev. 2013, 42, 5714.

[30] P. Dolcet, S. Diodati, F. Zorzi, P. Voepel, C. Seitz, B. M. Smarsly, S. Mascotto, F. Nestola, S. Gross, Green Chem. 2018, 20, 2257.

[31] A. Soto-Arreola, A. M. Huerta-Flores, J. M. Mora-Hernández, L. M. Torres-Martínez, J. Photochem. Photobiol. A. 2018, 357, 20.

[32] A. Chattopadhyay, S. Samanta, R. Srivastava, R. Mondal, P. Dhar, J. Magn. Magn. Mater. 2019, 491, 165622.

[33] M. Bastianello, S. Gross, M. T. Elm, RSC Adv. 2019, 9, 33282.

[34] C.-Y. Tsay, Y.-C. Chiu, Y.-K. Tseng, Physica B: Condensed Matter 2019, 570, 29.

[35] F. Sun, Q. Zeng, W. Tian, Y. Zhu, W. Jiang, J. Environ. Chem. Eng. 2019, 7, 103011.

[36] V. Georgiadou, C. Kokotidou, B. Le Droumaguet, B. Carbonnier, T. Choli-Papadopoulou, C. Dendrinou-Samara, Dalton Trans. 2014, 43, 6377; K. Vamvakidis, M. Katsikini, D. Sakellari, E. C. Paloura, O. Kalogirou, C. Dendrinou-Samara, Dalton Trans. 2014, 43, 12754; M. Menelaou, K. Georgoula, K. Simeonidis, C. Dendrinou-Samara, Dalton Trans. 2014, 43, 3626.

[37] H. Etemadi, P. G. Plieger, ACS Omega 2020, 5, 18091.

[38] X. Lu, M. Niu, R. Qiao, M. Gao, The Journal of Physical Chemistry B 2008, 112, 14390.

[39] G. R. Mahdavinia, H. Etemadi, F. Soleymani, Carbohydr. Polym. 2015, 128, 112; G. R. Mahdavinia, H. Etemadi, Materials Science and Engineering: C 2014, 45, 250.

[40] A. Ruiz -Baltazar, R. Esparza, G. Rosas, R. perez J. Nanomater. 2015, 2015, 8; W. Kim, C.-Y. Suh, S.-W. Cho, K.-M. Roh, H. Kwon, K. Song, I.-J. Shon, Talanta 2012, 94, 348.

[41] Y. Huang, D. Ding, M. Zhu, W. Meng, Y. Huang, F. Geng, J. Li, J. Lin, C. Tang, Z. Lei, Z. Zhang, C. Zhi, Sci. Technol. Adv. Mater. 2015, 16, 014801.

[42] Y. Yin, M. Zeng, J. Liu, W. Tang, H. Dong, R. Xia, R. Yu, Sci. Rep. 2016, 6, 25075.

[43] Y. V. Kolen'ko, M. Bañobre-López, C. Rodríguez-Abreu, E. Carbó-Argibay, A. Sailsman, Y. Piñeiro-Redondo, M. F. Cerqueira, D. Y. Petrovykh, K. Kovnir, O. I. Lebedev, J. Rivas, J. Phys. Chem. C. 2014, 118, 8691.

[44] P. Kollu, P. R. Kumar, C. Santosh, D. K. Kim, A. N. Grace, RSC Adv. 2015, 5, 63304.

[45] L. Feng, Z. Xuan, H. Zhao, Y. Bai, J. Guo, C.-W. Su, X. Chen, Nanoscale Res. Lett. 2014, 9, 290.

[46] J. Zhu, S. Tang, H. Xie, Y. Dai, X. Meng, ACS Appl. Mater. Interfaces 2014, 6, 17637.

[47] P. Saha, R. Rakshit, K. Mandal, J. Magn. Magn. Mater. 2019, 475, 130.

[48] S. D. Kulkarni, S. Kumbar, S. G. Menon, K. S. Choudhari, S. C, Mater. Res. Bull. 2016, 77, 70; T. Sun, H. Hao, W.-t. Hao, S.-m. Yi, X.-p. Li, J.-r. Li, Nanoscale Res. Lett. 2014, 9, 98.

[49] J. Perrière, C. Hebert, M. Nistor, E. Millon, J. J. Ganem, N. Jedrecy, J. Mater. Chem C. 2015, 3, 11239.

[50] J. Perrière, C. Hebert, M. Nistor, E. Millon, J. J. Ganem, N. Jedrecy, J. Mater. Chem C. 2015, 3, 11239.

[51] S. O. Hwang, C. H. Kim, Y. Myung, S.-H. Park, J. Park, J. Kim, C.-S. Han, J.-Y. Kim, J. Phys.. Chem. C 2008, 112, 13911.

[52] J. Liu, Y. Bin, M. Matsuo, J. Phys. Chem. C 2012, 116, 134.

[53] X. Li, E. Liu, Z. Zhang, Z. Xu, F. Xu, J. Mater. Sci.: Mater. Electron 2019, 30, 3177.

[54] M. A. Ahmed, K. E.-S. Rady, K. M. El-Shokrofy, A. A. Arais, M. S. Shams, MSA. 2014, Vol. 05 No. 13, 11.

[55] J. Cai, Y. Q. Miao, B. Z. Yu, P. Ma, L. Li, H. M. Fan, Langmuir 2017, 33, 1662.

[56] A. L. Willis, N. J. Turro, S. O'Brien, Chem. Mater. 2005, 17, 5970; T. R. Bastami, M. H. Entezari, Q. H. Hu, S. B. Hartono, S. Z. Qiao, Chem. Eng. J. 2012, 210, 157.

[57] A. G. Roca, M. P. Morales, K. O'Grady, C. J. Serna, Nanotechnology 2006, 17, 2783.

[58] S. Ayyappan, S. Mahadevan, P. Chandramohan, M. P. Srinivasan, J. Philip, B. Raj, J. Phys. Chem. C. 2010, 114, 6334.

[59] L. Del Bianco, F. Spizzo, G. Barucca, M. R. Ruggiero, S. Geninatti Crich, M. Forzan, E. Sieni, P. Sgarbossa, Nanoscale 2019, 11, 10896.

[60] L. Li, A. Ruotolo, C. W. Leung, C. P. Jiang, P. W. T. Pong, Microelectron. Eng. 2015, 144, 61.

[61] B. Y. Yu, S.-Y. Kwak, Dalton Trans. 2011, 40, 9989.

[62] D. P. Dubal, W. B. Kim, C. D. Lokhande, J. Phys. Chem. Solids 2012, 73, 18.

[63] L. Hu, C. de Montferrand, Y. Lalatonne, L. Motte, A. Brioude, J. Phys. Chem. C. 2012, 116, 4349.

[64] S. D. Oberdick, A. Abdelgawad, C. Moya, S. Mesbahi-Vasey, D. Kepaptsoglou, V. K. Lazarov, R. F. L. Evans, D. Meilak, E. Skoropata, J. van Lierop, I. Hunt-Isaak, H. Pan, Y. Ijiri, K. L. Krycka, J. A. Borchers, S. A. Majetich, Sci. Rep. 2018, 8, 3425.

[65] R. Otero-Lorenzo, E. Fantechi, C. Sangregorio, V. Salgueiriño, Chem. Eur. J. 2016, 22, 6666.

[66] Q. Song, Y. Ding, Z. L. Wang, Z. J. Zhang, Chem. Mater. 2007, 19, 4633.

[67] W. Wang, B. Tang, B. Ju, Z. Gao, J. Xiu, S. Zhang, J. Mater. Chem. A 2017, 5, 958.

[68] S. M. Ansari, B. B. Sinha, D. Phase, D. Sen, P. U. Sastry, Y. D. Kolekar, C. V. Ramana, ACS Appl. Nano Mater. 2019, 2, 1828.

[69] C. Iacovita, R. Stiufiuc, T. Radu, A. Florea, G. Stiufiuc, A. Dutu, S. Mican, R. Tetean, C. M. Lucaciu, Nanoscale Res. Lett. 2015, 10, 391.

[70] M. Li, Y. Xiong, X. Liu, X. Bo, Y. Zhang, C. Han, L. Guo, Nanoscale 2015, 7, 8920.

[71] G. Sathishkumar, V. Logeshwaran, S. Sarathbabu, P. K. Jha, M. Jeyaraj, C. Rajkuberan, N. Senthilkumar, S. Sivaramakrishnan, Artif Cells Nanomed Biotechnol 2018, 46, 589.

[72] M. Zhang, F. Zhao, Y. Yang, H. Li, H. Gao, E. Yao, J. Zhang, T. An, Z. Jiang, J. Therm. Anal. Calorim. 2020, 141, 1413.

[73] F. Han, L. Ma, Q. Sun, C. Lei, A. Lu, Nano Research 2014, 7, 1706.

[74] Y. Liu, N. Zhang, C. Yu, L. Jiao, J. Chen, Nano Lett. 2016, 16, 3321; X.-Y. Long, J.-Y. Li, D. Sheng, H.-Z. Lian, Talanta 2017, 166, 36.

[75] X. Guo, H. Zhu, M. Si, C. Jiang, D. Xue, Z. Zhang, Q. Li, J. Phys. Chem. C. 2014, 118, 30145; N. Baird, Y. Losovyj, E. Y. Yuzik-Klimova, N. V. Kuchkina, Z. B. Shifrina, M. Pink, B. D. Stein, D. G. Morgan, T. Wang, M. A. Rubin, A. I. Sidorov, E. M. Sulman, L. M. Bronstein, ACS Appl. Mater. Interfaces 2016, 8, 891.

[76] T. Neuberger, B. Schöpf, H. Hofmann, M. Hofmann, B. von Rechenberg, J. Magn. Magn. Mater. 2005, 293, 483.

[77] Q. Li, C. W. Kartikowati, S. Horie, T. Ogi, T. Iwaki, K. Okuyama, Sci. Rep. 2017, 7, 9894.

[78] A. G. Kolhatkar, A. C. Jamison, D. Litvinov, R. C. Willson, T. R. Lee, Int. J. Mol. Sci. 2013, 14, 15977.

[79] M. Darbandi, F. Stromberg, J. Landers, N. Reckers, B. Sanyal, W. Keune, H. Wende, J. Phys. D: Appl. Phys. 2012, 45, 195001.

[80] I. Ibrahim, I. O. Ali, T. M. Salama, A. A. Bahgat, M. M. Mohamed, Appl. Catal. B. 2016, 181, 389.

[81] V. Nandwana, S.-R. Ryoo, S. Kanthala, M. De, S. S. Chou, P. V. Prasad, V. P. Dravid, ACS Appl. Mater. Interfaces 2016, 8, 6953; Q. Song, Z. J. Zhang, J. Phys. Chem. B. 2006, 110, 11205.

[82] M. F. Casula, E. Conca, I. Bakaimi, A. Sathya, M. E. Materia, A. Casu, A. Falqui, E. Sogne, T. Pellegrino, A. G. Kanaras, PCCP 2016, 18, 16848.

5.6. Supporting Information for

Synthesis and Characterisation of $M_xFe_{3-x}O_4$ (M = Fe, Mn, Zn) Spinel Nanoferrites through a Solvothermal Route

Hossein Etemadi and Paul G. Plieger*

School of Fundamental Sciences, Massey University, Private Bag 11 222, Palmerston North, New Zealand

E-mail: p.g.plieger@massey.ac.nz

Phone: +64 (06) 356 9099 ext. 84647

Synthesis of Nanoparticles – specific example

For the nanoferrite MnFe1: Both $Fe(acac)_3$ (0.8 mmol, 0.283 g) and $MnCl_2{\cdot}4H_2O$ (0.2 mmol, 0.040 g) were mixed in octadecene (20 mL). To this was added tri-n-octylphosphine oxide (0.5 mmol, 0.193 g) and oleylamine (70 %, 2.56 mL). The combined mixture was heated to 100 °C and left to stir (500 rpm) for 60 min. Polyvinylpyrrolidone (0.20 g) was dissolved in 1,5-pentanediol (5 mL) and heated to 150°C for 60 min. The two solutions were then mixed and deoxygenated with Ar (2 min), then transferred into a 100 mL polytetra-fluoroethylene (PTFE)-lined autoclave. The autoclave was sealed and maintained at 200 °C for 30 min, then heated to 240 °C for 2 h. After this time the autoclave was left to cool to RT naturally. MnFe1 nanoferrites were precipitated upon the addition of ethanol (10 mL), washed with an ethanol/hexane (1: 2) solution mixture several times and then dispersed in hexane for further use.

Instrumentation and Measurements

For the XRD, TGA, VSM and XPS measurements, the nanoferrites were dispersed in hexane, precipitated with ethanol and dried under vacuum overnight prior to measurement.

Structural Characterisation

Powder X-ray diffraction (XRD) patterns were recorded on a Rigaku Spider X-ray diffractometer with Cu-K_α radiation (λ = 1.5406 Å), at 40 kV and 50 mA from 10° to 80° in the Bragg configuration. Indexing the XRD patterns, *d*-spacing (*d*) of lattice planes (*hkl*), lattice constant (*a*) and crystallite size (*D*) were determined for all $M_xFe_{3-x}O_4$ (M = Fe, Mg, Zn) nanoferrites. The θ values of the most intense X-ray peaks corresponding to (220), (311),

(400), (422), (511) and (440) were calculated through Origin software with the Gaussian function. The crystallite size was calculated using the Debye−Scherrer equation:

$$D = \frac{K\lambda}{\beta Cos\theta} \quad (1)$$

Where *D* is the crystallite size, *K* is the Scherrer shape factor (0.9), λ is the wavelength of Cu-K_α radiation (λ = 1.5406 Å), β is the full-width-half-maximum (FWHM) value of the peak in radians and θ is the Bragg diffraction angle of the (*hkl*) reflection.

Lattice *d*-spacing and lattice constant values were calculated using the Bragg equation

(Equation 2 and 3):

$$n\lambda = 2d \sin\theta \quad (2)$$

$$a = d(h^2 + k^2 + l^2)^{1/2} \quad (3)$$

The monodispersity and diameter of the nanoferrites was probed using transmission electron microscopy (TEM; Tecnai G2 Spirit Bio-TWIN, Oregon, USA) at an acceleration voltage of 200 kV. For TEM imaging, drops of a diluted solution (× 100) of the sample were cast onto a Cu grid and dried for several minutes before imaging. Image J software was utilised for post-processing and particle size analysis. Outlines of 300-400 particles were traced manually, and the corresponding diameters with their standard deviation were determined.

Chemical Composition

The elemental atomic ratios of monodisperse nanoferrites were probed by atomic absorption spectroscopy (AAS; GBC Scientific) and an energy dispersive spectrometer (EDS) connected to field-emission scanning electron microscopy (FE-SEM; FEI Quanta 200). For EDS studies, a small amount of nanoferrites dispersed in hexane were sonicated for 30 min and directly mounted onto an aluminium stub using double sided tape, carbon coated (Baltec SCD 050 sputter coater) and viewed in the FEI Quanta 200 Environmental Scanning

Electron Microscope (FE-SEM FEI Quanta 200). To ensure good accuracy, several areas from different regions of each sample were scanned and spectral data was collected with a silicon EDAX unit (NJ, USA) running Genesis Spectrum software (version 5.21). For AAS analysis, 125 µL of the nanoferrites dispersed in hexane were sonicated for 30 min and completely digested in concentrated HNO_3 70 %: H_2O_2 32 %: HCl 37 % with a ratio of 1:1:0.5 mL at 100 °C overnight. The solutions were then diluted to 10 mL with Milli-Q water for quantification. Standard solutions of 10, 20, 30, 40, 60, 80 and 100 ppm were used to plot a calibration curve for absorbance versus concentration. The concentrations of Fe, Zn and Mg were measured using an AAS spectrometer (GBC Scientific) with an Fe hollow cathode lamp (252.3 nm), Zn hollow cathode lamp (279.8 nm) or Mg hollow cathode lamp (285.2 nm) respectively. The proportion of inorganic cores and organic surfactants/capping agents in the sample was obtained through the heating of samples on a TA Instruments Q50 thermogravimetric analyser instrument. Samples were mounted to a silica sample pan and heated from room temperature to 800 °C under an N_2 flow with a heating rate of 10 °C /min. For consistency, the same nanoferrites solutions were utilised for all TEM, DLS, EDS and AAS measurements respectively. The metal (M, Fe) and oxygen valence states of $M_xFe_{3-x}O_4$ (M = Fe, Mg, Zn) nanoferrites were probed with Kratos Axis Ultra^{DLD} X-ray Photoelectron Spectrometer (Kratos Analytical, Manchester, UK) equipped with a hemispherical electron energy analyser. Samples were excited using monochromatic Al-K_α X-rays (1486.69 eV) with the X-ray source operating at 150 W. The analysis area was a 300 by 700 micron spot obtained using the hybrid magnetic and electrostatic lens and the slot aperture. Powder samples were mounted on a stainless steel holder covering the double sided carbon tape. The measurements were carried out in a normal emission geometry. A charge neutralisation system was used to alleviate surface charge build-up, resulting in a shift of approximately 3 eV to lower binding energy. During curve fitting of the binding energy of *C 1s*, the adventitious hydrocarbon on the surface was used to correct for this shift, with the saturated hydrocarbon peak set to 285 eV. Survey scans were collected with a 160 eV pass energy, whilst core level scans were collected with a pass energy of 20 eV. The analysis chamber was at pressures in the 10^{-9} torr range throughout the data collection. Data analysis was performed using CasaXPS processing software version 2.3.15 (Casa 22 Software Ltd., Teignmouth, UK)

Magnetic Measurements

Magnetic characterisation was recorded in a vibrating sample magnetometer (VSM; Quantum Design P935A USA, physical property measurement system (PPMS). Sample holders were weighed and the powder samples were then transferred into the holders. The holders were loaded into the brass VSM holder half-tube, and the brass holder was attached to the VSM rod for magnetization measurements. Magnetisation curves as a function of the applied magnetic field (M−H loops) were collected from −2.00 to 2.00 T magnetic field at room temperature (300 K) to estimate saturation magnetic moment (emu), remnant magnetizations (M_r), and coercivities (H_c) values. Magnetisation curves as a function of the temperature (M−T), also called zero field cooling/field cooling (ZFC/FC) curves, were recorded between 10 and 350 K to assess the blocking temperature and effective anisotropy constant (K_{eff}) of nanoferrites. During the zero-field-cooling, the samples were cooled from room temperature (~ 300 K) to 10 K under zero magnetic field. Then under an applied magnetic field of 0.02 T, magnetisation was recorded as the temperature was increased from 10 K to 350 K. During field cooling, samples were cooled from 350 K to 10 K and the magnetisation was recorded under the applied magnetic field of the same magnitude.

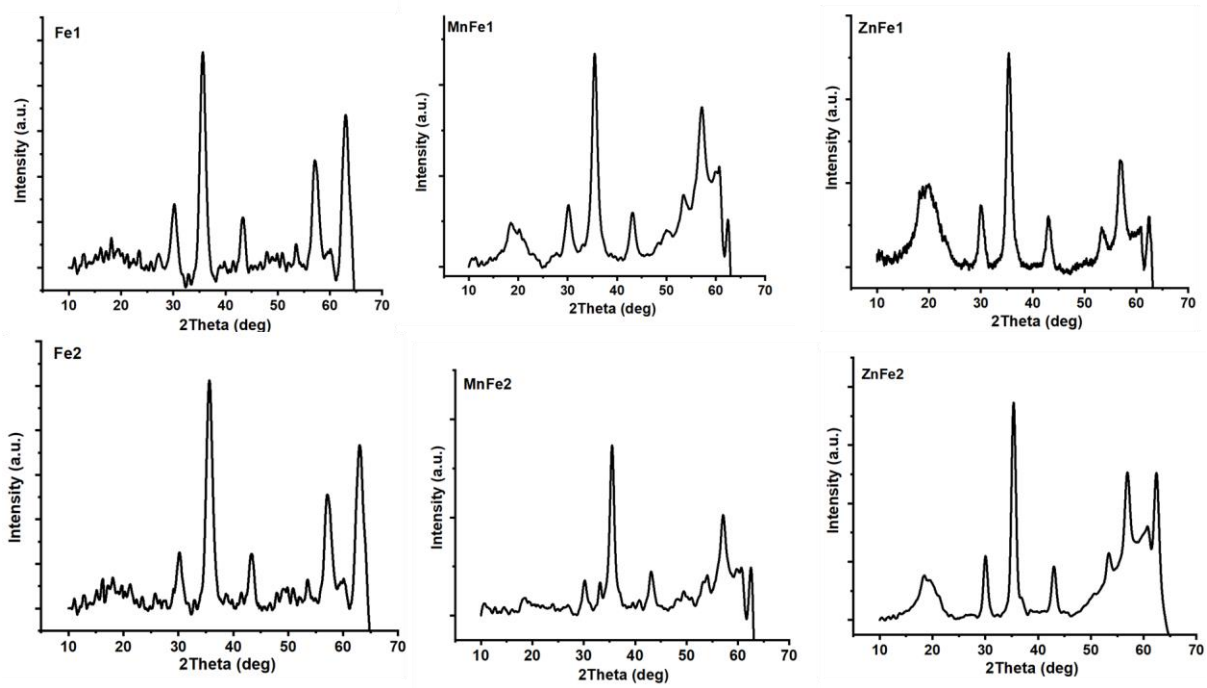

Figure 5.9 Powder X-ray diffraction (XRD) patterns of $M_xFe_{3-x}O_4$ (M = Fe, Mg, Zn) nanoferrites.

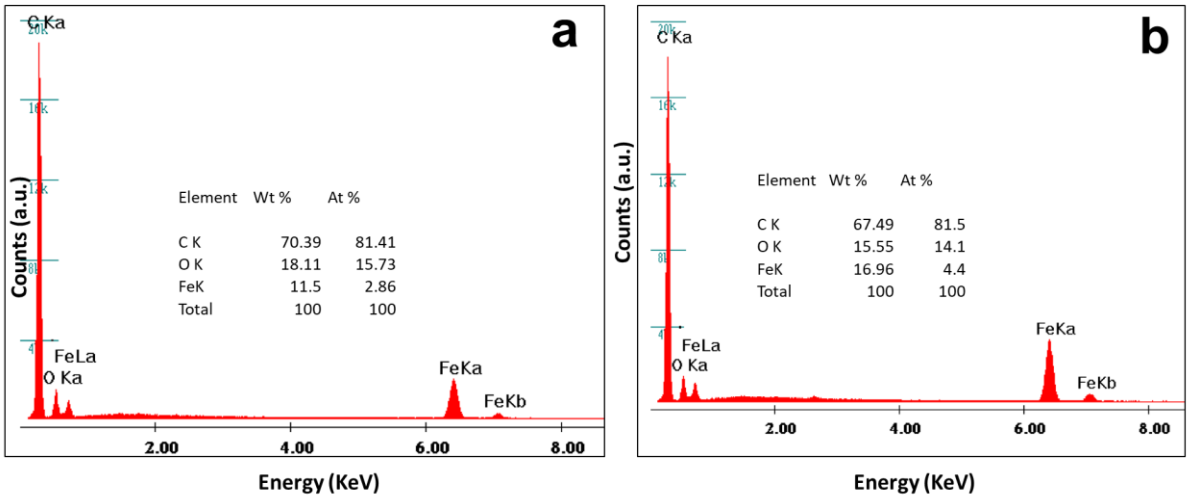

Figure 5.10 EDS pattern of (a) the Fe1 and (b) the Fe2 NPs.

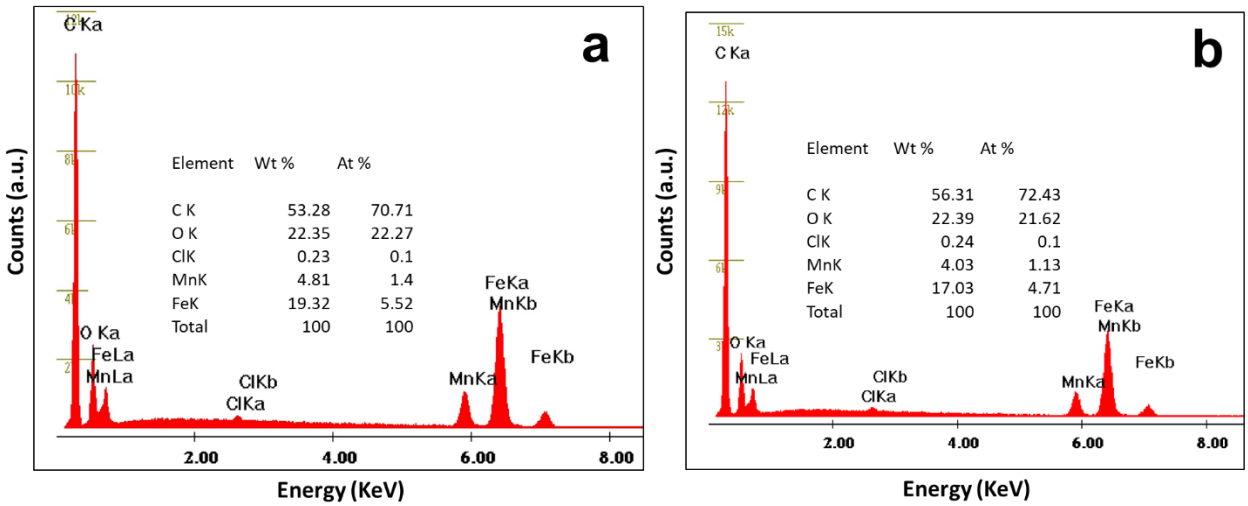

Figure 5.11 EDS pattern of (a) the MnFe1 and (b) the MnFe2 NPs.

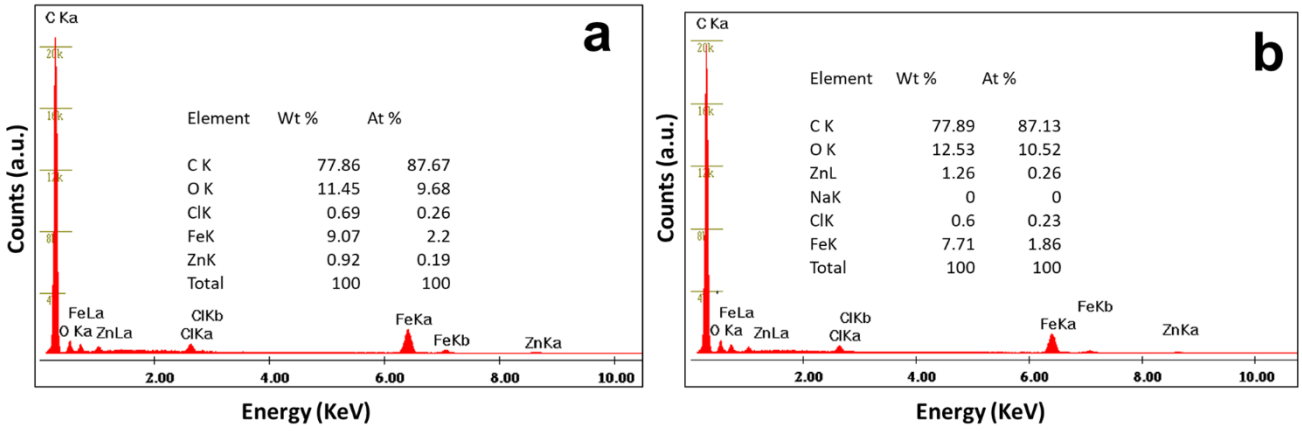

Figure 5.12 EDS pattern of (a) the ZnFe1 and (b) the ZnFe2 NPs.

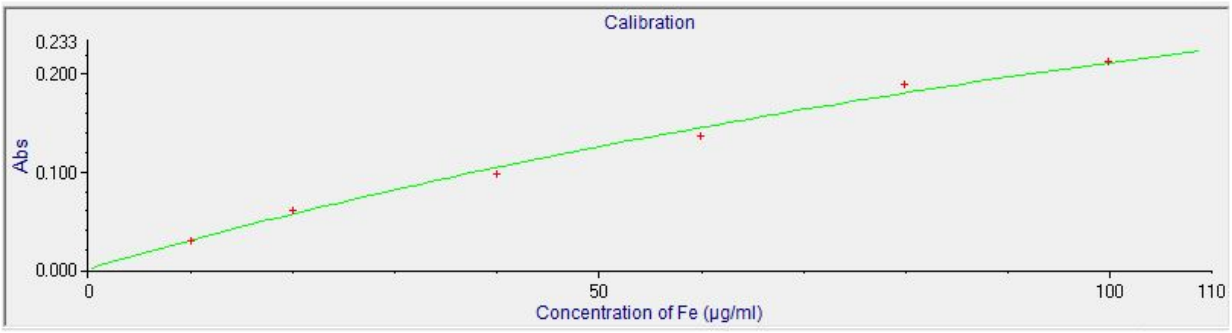

Cal Blank	——	-0.001	HIGH	Full Calibration
10 ppm	10.00	0.093	1.96	Wed Dec 19 12:02:26 2018
20 ppm	20.00	0.197	0.29	Calibration Mode : Conc Least Squares
30 ppm	30.00	0.249	0.52	Max Error : 5.1033 R² : 0.9922 R : 0.9961
40 ppm	40.00	0.310	1.87	Conc = Abs / (0.0031 + -0.0045 * Abs)
60 ppm	60.00	0.383	2.46	
80 ppm	80.00	0.484	1.18	
100 ppm	100.00	0.551	1.99	
Fe3O4 1	66.00	0.431	1.71	
Fe3O4 2	64.87	0.427	2.01	

Figure 5.13 Calibration results obtained for the determination of Fe by atomic absorption spectrometry.

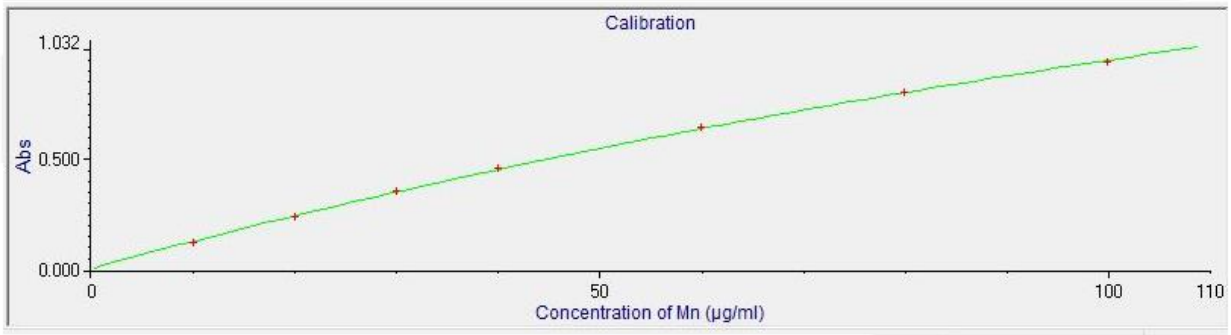

Cal Blank	——	-0.002	7.92
10 ppm	10.00	0.124	1.11
20 ppm	20.00	0.238	0.91
30 ppm	30.00	0.354	0.67
40 ppm	40.00	0.457	1.35
60 ppm	60.00	0.640	1.02
80 ppm	80.00	0.799	1.59
100 ppm	100.00	0.938	0.82
MnFe2O4 1	36.78	0.419	2.56
MnFe2O4 2	18.71	0.226	0.83

Full Calibration
Mon Feb 11 15:06:46 2019
Calibration Mode : Conc Least Squares
Max Error : 1.2631 R² : 0.9997 R : 0.9998
Conc = Abs / (0.0129 + -0.0036 * Abs)

Figure 5.14 Calibration results obtained for the determination of Mn by atomic absorption spectrometry.

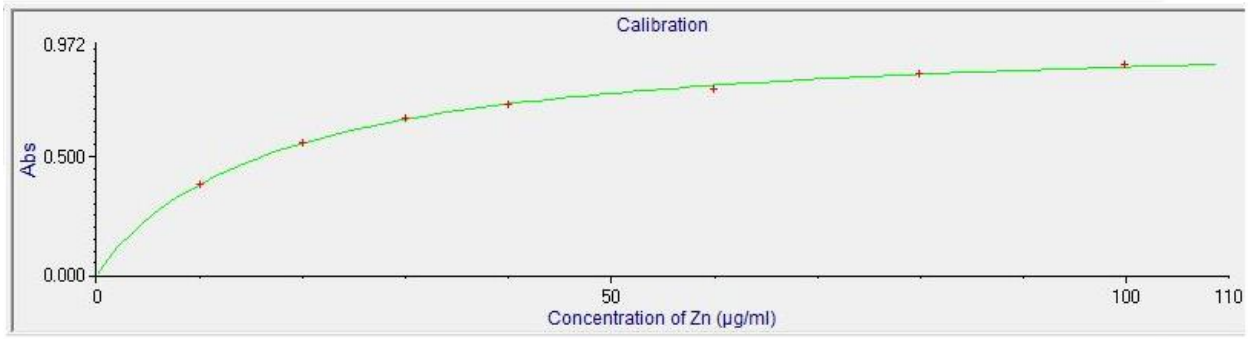

Cal Blank	——	-0.001	HIGH
10 ppm	10.00	0.379	0.81
20 ppm	20.00	0.552	0.09
30 ppm	30.00	0.656	0.23
40 ppm	40.00	0.714	0.35
60 ppm	60.00	0.782	0.26
80 ppm	80.00	0.844	0.17
100 ppm	100.00	0.884	0.06
ZnFe2O4 1	19.94	0.551	0.48
ZnFe2O4 2	18.41	0.531	0.69

Full Calibration
Mon Feb 11 14:47:17 2019
Calibration Mode : Conc Least Squares
Max Error : 8.6486 R^2 : 0.9982 R : 0.9991
Conc = Abs / (0.0599 + -0.0586 * Abs)

Figure 5.15 Calibration results obtained for the determination of Zn by atomic absorption spectrometry.

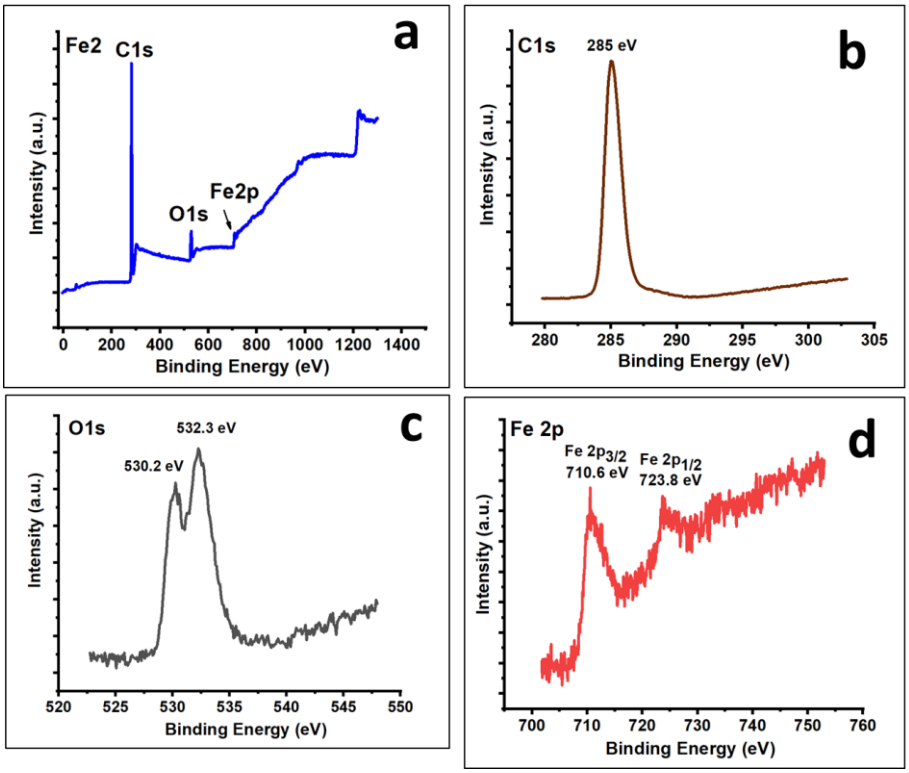

Figure 5.16 XPS spectra of the Fe2 nanoferrite (a) survey scan (b) C *1s* (c) O *1s* and (d) Fe *2p* regional scans.

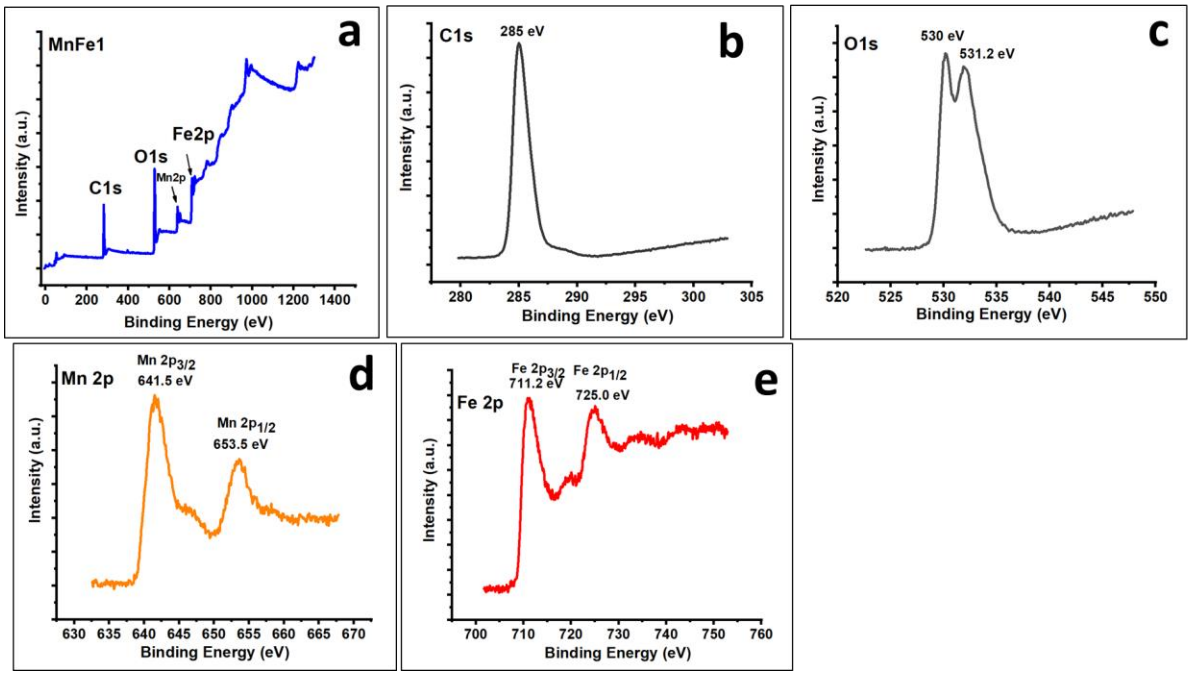

Figure 5.17 XPS spectra of the MnFe1 nanoferrite (a) survey scan (b) C *1s* (c) O *1s* (d) Mn *2p* and (e) Fe *2p* regional scans.

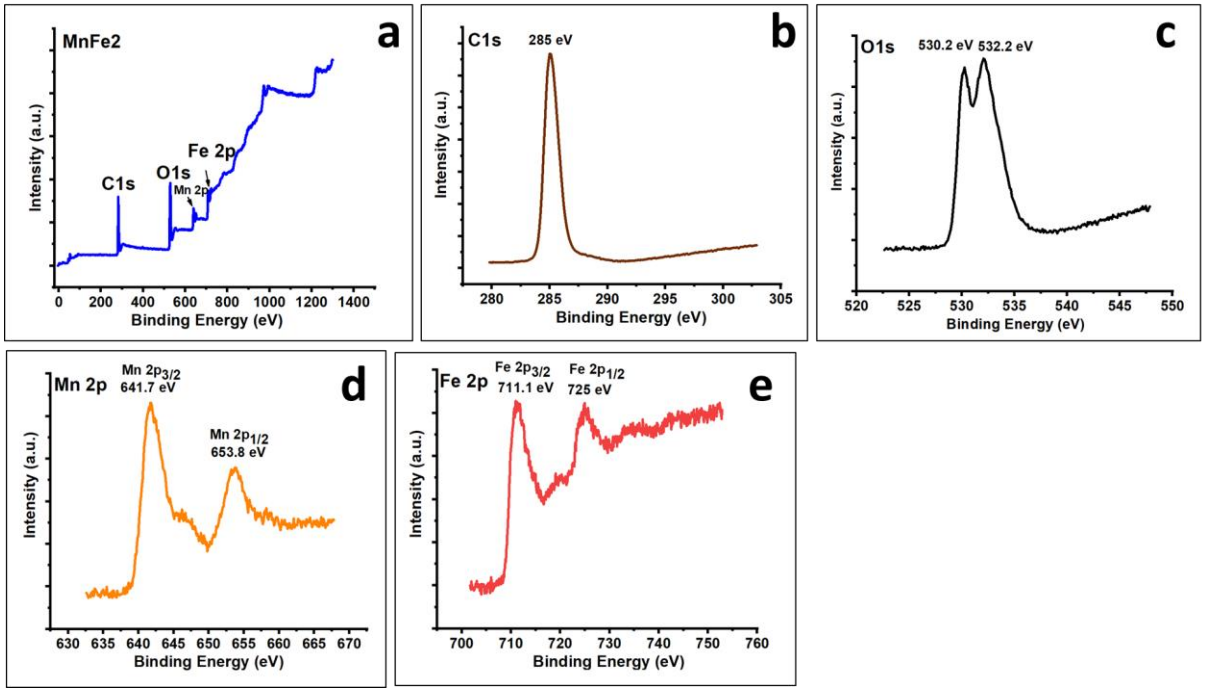

Figure 5.18 XPS spectra of the MnFe2 nanoferrite (a) survey scan (b) C *1s* (c) O *1s* (d) Mn *2p* and (e) Fe *2p* regional scans.

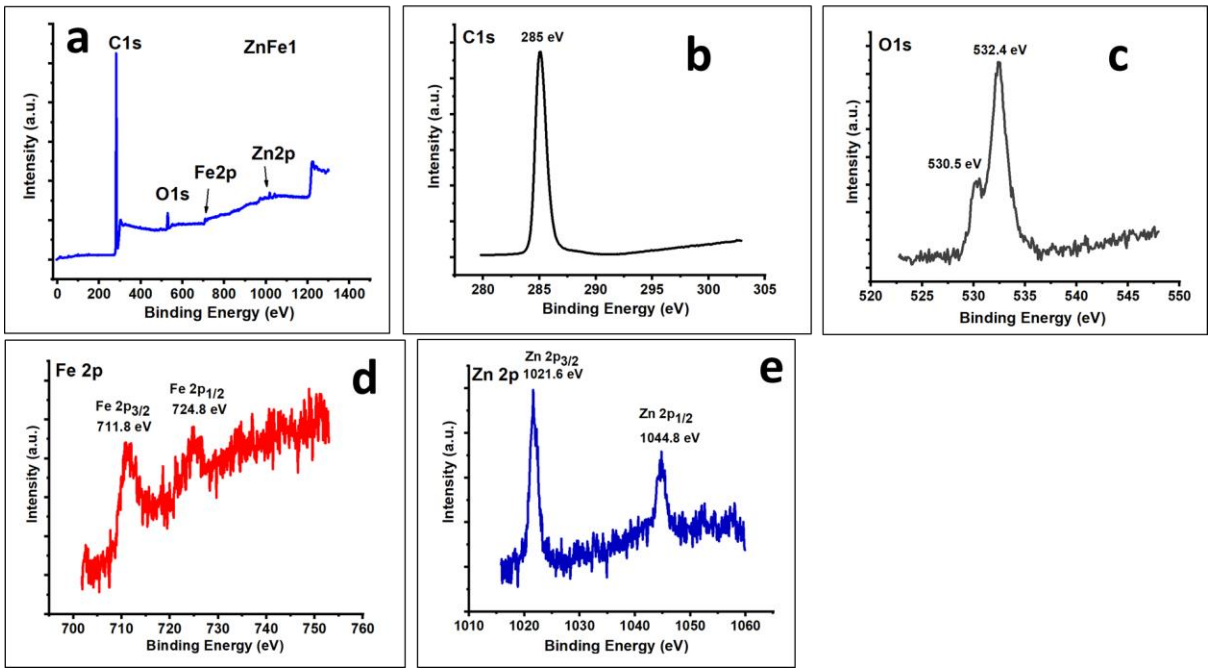

Figure 5.19 XPS spectra of the ZnFe1 nanoferrite (a) survey scan (b) C*1s* (c) O*1s* (d) Fe*2p* and (e) Zn*2p* regional scans.

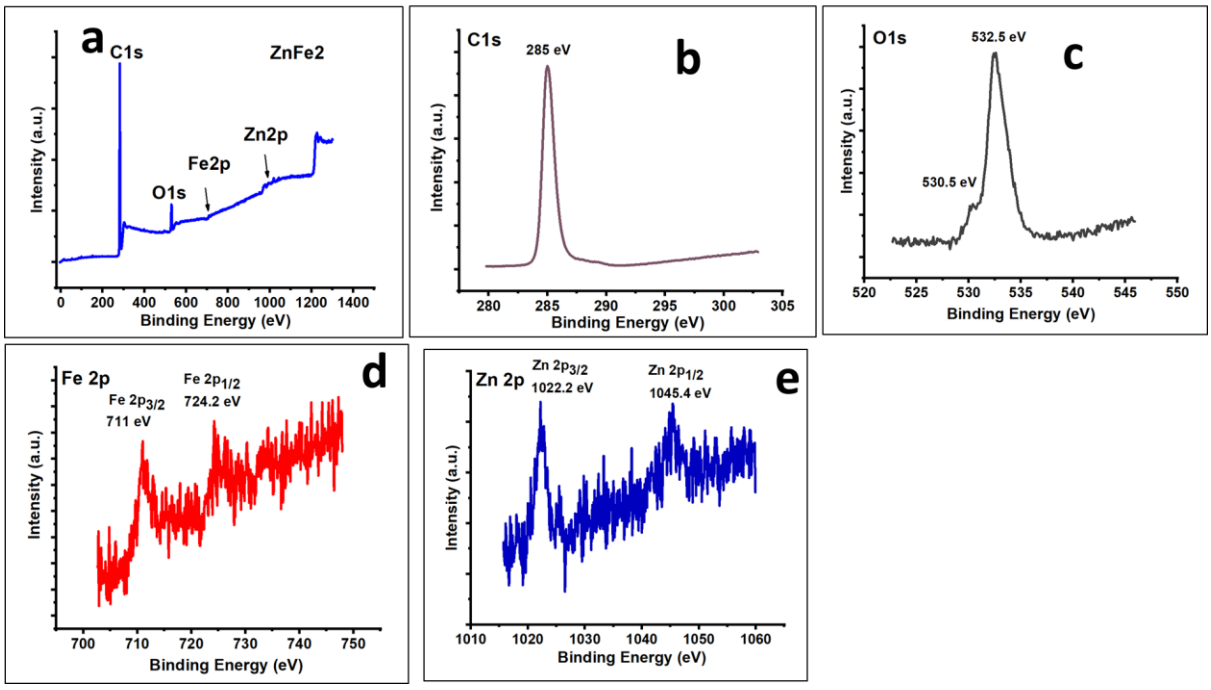

Figure 5.20 XPS spectra of the ZnFe2 nanoferrite (a) survey scan (b) C*1s* (c) O*1s* (d) Fe*2p* and (e) Zn*2p* regional scans.

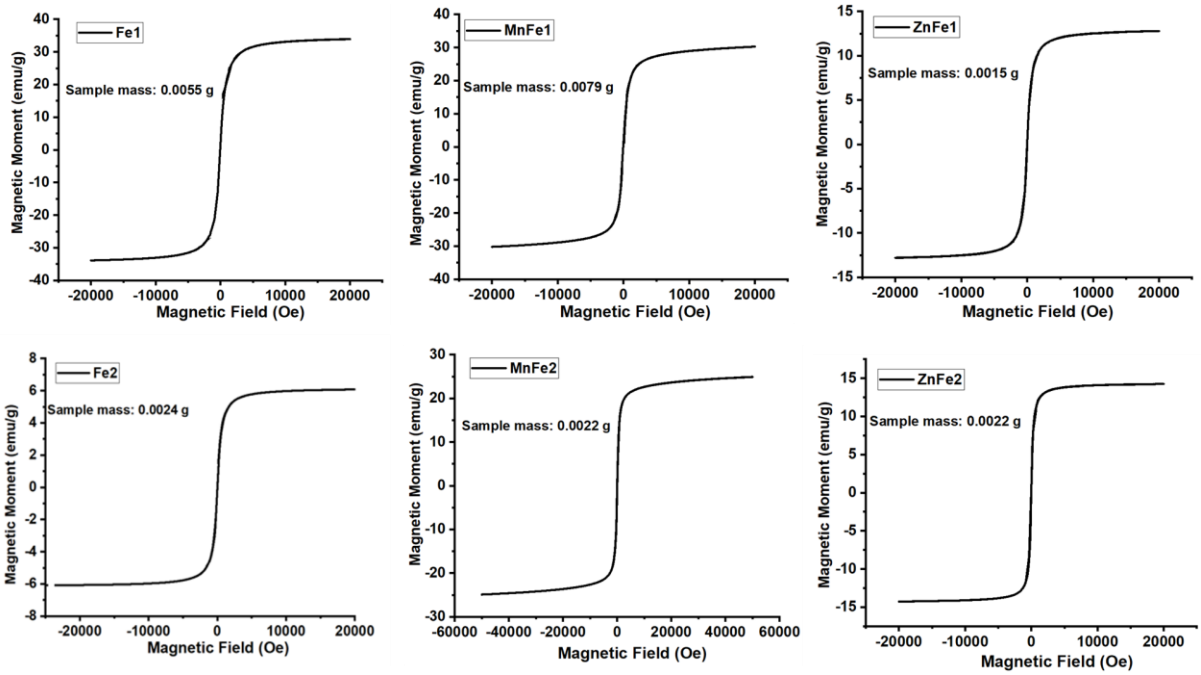

Figure 5.21(a) Magnetic hysteresis loops of $M_xFe_{3-x}O_4$ (M = Fe, Mn, Zn) nanoferrites at room temperature (sample masses used are recorded on each spectra).

Chapter 6. An Introduction to H_2 production from water splitting / ethanol photoreforming

6.1. H_2 production from water splitting

Non-renewable fossil fuels such as coal and oil are still the main sources for meeting the global demand for energy. However, a challenging problem to overcome is the massive emission of CO_2 into the atmosphere upon their combustion which has led to climate change and global warming.[1] Therefore, it is of supreme importance to develop secure, clean and renewable energy sources. Sunlight is a green and inexhaustible source of energy with high abundance which holds great promise for solving the global energy crisis.[1] One way to use sunlight is the splitting of H_2O over the surface of a photocatalyst, generating H_2 and O_2 as clean and environmentally-friendly green energy sources.[2] Overall, the water splitting (WS) reaction involves four main steps (Figure 6.1). The process starts with the absorption of light in the ultraviolet (400 nm > λ > 290 nm) or the visible region (700 nm > λ > 400 nm) by a semiconducting photocatalyst, followed by the excitation of electrons (e^-) from the valence band (VB) to the conduction band (CB) of the semiconductor, leaving vacancies known as holes (h^+) in the VB. The photoexcited electrons are transported to the reduction site to drive the H_2O reduction to H_2 (hydrogen evolution reaction (HER)). The holes are transported to the oxidation site to oxidise the H_2O to O_2 (oxygen evolution reaction (OER)). Therefore, the photocatalytic WS reaction can be written as follows:[3]

$$Light\ absorption\text{: Semiconductor} + hv\ (> E_g) \rightarrow e_{CB}^- + h_{VB}^+ \quad (1)$$

$$Proton\ Reduction\text{:}: 2e^- + 2H^+ \rightarrow H_2 \quad E^0_{H^+/H_2} = 0\ \text{V vs NHE pH} = 0 \quad (2)$$

$$Water\ Oxidation\text{: } 2H_2O + 4h_{VB}^+ \rightarrow O_2 + 4H^+ \quad E^0_{O_2/H_2O} = 1.23\ \text{V vs NHE pH} = 0 \quad (3)$$

$$Overall\ Water\ Spliting\text{: } 2H_2O \rightarrow 2H_2 + O_2 \quad \Delta E = 1.23\ \text{V vs NHE pH} = 0 \quad (4)$$

The WS reaction is endoenergetic, requiring a Gibbs free energy of 237.2 kJ per mole of generated H_2 or an overall redox potential of 1.23 eV per electron. It means a photocatalyst must have a bandgap value ($E_g = E_{CB} - E_{VB}$) greater than 1.23 eV for optimal WS output.[4] Considering the intrinsic kinetic limitations of the HER and OER half reactions, photocatalysts with E_g values in the range of 1.6 – 2.4 eV are reported as optimal for a practical WS reaction.[5]

The potent photocatalyst should also feature high chemical stability, photostability, long carrier lifetime, high carrier mobility, chemical and biological inertness, low cost and non-toxicity.[6] The width of the band gap and levels of the valence and conduction bands are also important. The CB edge potential (E_{CB}) of the semiconductor must be more negative than the redox potential of H^+/H_2 (0 V *vs*. normal hydrogen electrode (NHE at pH =0)), while the VB edge potential (E_{VB}) must be more positive than the redox potential of O_2/H_2O (1.23 V *vs* NHE at pH =0).[1, 7, 8] Figure 6.2 highlights the band edges and E_g values of semiconductors typically explored for the WS reaction.

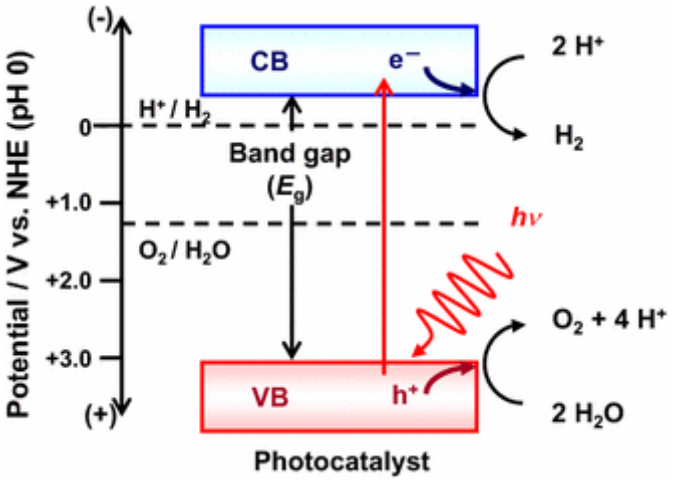

Figure 6.1 Basic principle of overall water splitting on a semiconductor particle. Reprinted with permission from Ref. [8]. Copyright 2007 ACS group.

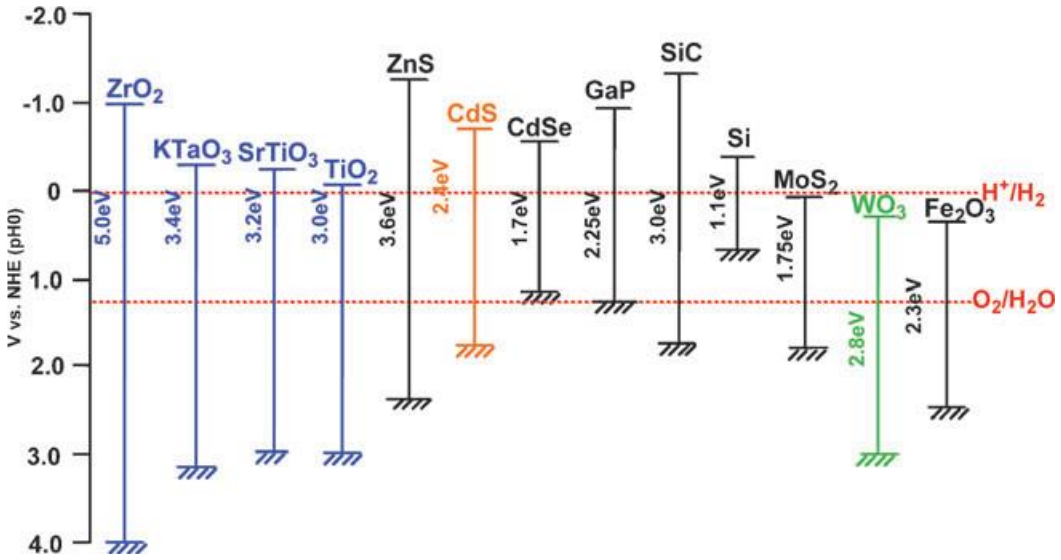

Figure 6.2 Band edge positions of representative semiconductors on the basis of redox potentials. Reprinted with permission from Ref. [7]. Copyright 2015 MPDI group.

6.2. H_2 production from alcohol (ROH) photoreforming

Photocatalytic production of hydrogen has been realized not only by water splitting, but also by reforming of alcohols, ROH (ethanol and methanol). Photocatalytic reforming of R-OH for H_2 production can be conducted at ambient conditions under irradiation. The mechanism of action for alcohol photoreforming is similar to WS in that it leads to H_2 production through photoexcited electrons at the reduction site, nevertheless, the holes in the oxidation site, oxidise the ROH to CO_2 in contrast to WS in which holes oxidize H_2O to O_2. [9]

6.2.1 Photocatalytic Reforming of Methanol

Methanol is the most widely used substrate in photocatalytic reforming.[10] Unlike photocatalytic water splitting, where the products are H_2 and O_2, the products of photocatalytic reforming of methanol are H_2 and CO_2 (Reaction 5).[10]

$$CH_3OH + H_2O + h\nu \rightarrow CO_2 + 3H_2 \qquad \Delta H^0 = 130.897 \text{ kJ/mol} \qquad (5)$$

The reaction pathway for the photocatalytic reforming of methanol on a TiO_2 photocatalyst involves the following processes: (i) Photogeneration of charge carriers (electrons and holes), (ii) The reaction of adsorbed species on the surface with the separated charge

carriers: i.e., adsorbed H_2O and CH_3OH are oxidized by holes to form OH^- and various fragments including CH_3O^-, CH_2O^-, CHO^-, $HCOO^-$ and HCOOH, and (iii) As-formed HCOOH is further oxidized to CO_2, and protons are reduced by the electrons to form H_2. [10]

6.2.2 Photocatalytic Reforming of Ethanol

Kawai *et al*. reported on photocatalytic reforming of ethanol on TiO_2 in 1981.[11] Theoretically, the overall reaction for photocatalytic reforming of ethanol is as follow:

$$CH_3CH_2OH + 3H_2O + h\nu \rightarrow 2CO_2 + 6H_2 \qquad \Delta H^0 = 348.122 \text{ kJ/mol} \quad (6)$$

Different mechanistic schemes for ethanol reforming have been proposed in order to shed light on the real ethanol conversion over the catalyst surface [165–169]. However, there still has no consensus on the detailed reaction pathways due to the complexities in largely varied catalyst's constituents and reaction conditions. The generally acknowledged reaction steps is as follows. Ethanol is first photocatalytically converted to acetylaldehyde with the release of H_2 (Eqn. 7), the as-formed acetaldehyde can either react with water to form CO_2 and H_2 (Eqn. 8), or be further converted to acetic acid (Eqn. 9), which further reacts with water to form CO_2 and H_2 (Eqn. 10). [12]

$$CH_3CH_2OH + h\nu \rightarrow CH_3CHO + H_2 \quad (7)$$

$$CH_3CHO + 3H_2O + h\nu \rightarrow 2CO_2 + 5H_2 \quad (8)$$

$$CH_3CHO + H_2O + h\nu \rightarrow CH_3COOH + H_2 \quad (9)$$

$$CH_3COOH + 2H_2O + h\nu \rightarrow 4CO_2 + 4H_2 \quad (10)$$

6.3. Photocatalysts for H_2 Production

A broad range of semiconductor-based photocatalysts have been exploited for the WS and PR reactions in the past decades. These include a) metal oxides such as TiO_2, CeO, Fe_2O_3, ZnO, CuO, SiO_2, WO_3, $BiVO_4$ and SnO_2,[13] b) metal chalcogenides such as SnS, SnS_2, MoS_2, CdS, SnSe, and Bi_2S_3,[14] c) 2D photocatalysts such as single-layer black phosphorus,[15] d) graphite analogue carbon nitride (g-C_3N_4),[16] e) quantum dot (QD) photocatalysts such as

graphene dots, carbon dots, CdTe QDs and CdSe QDs,[17] and f) plasmonic metals (e.g. Pt, Au, Ag, Pd , Al, and Bi).[18]

6.4. Challenges of a single photocatalyst

In spite of massive efforts undertaken in the field with hundreds of proposed semiconductors, no single practical semiconductor has yet been recognised due to their low solar-to-hydrogen energy conversion efficiency.[1].[19] The challenges are (*i*) fast recombination rate of the photogenerated e^-/h^+ pairs due to the strong Coulombic force, (*ii*) limited light absorption efficiency, (*iii*) low charge transport properties, (*iv*) low charge mobility, (*vi*) photocorrosion and (*vii*) instability in water solutions.[20] Additionally, to achieve high H_2 production potency, a strong redox ability provided by a larger bandgap together with strong light harvesting provided by a smaller bandgap is required. Therefore, a single photocatalyst cannot provide these two features simultaneously.[3] Another challenge is the occurrence of energetically favourable backward hydrogen oxidation reaction (HOR) and oxygen reduction reaction (ORR) beside the OER and HER half reactions.[7]

6.5. Proposed strategies to improve the H_2 evolution efficiency

Various strategies have been proposed in the past decades to conquer the challenges associated with performance of a single photocatalyst. This has been achieved by (*i*) modifying the intrinsic electronic properties of the photocatalyst such as charge mobility, conductivity and bandgap engineering or (*ii*) modifying the surface in order to improve the kinetics of water oxidation.[1] These strategies have been applied individually or synergistically as detailed below.

6.5.1. Elemental doping

One way to improve the photocatalytic performance is by doping metallic elements such as Ru, Nb or Ta,[21] or non-metallic elements such as B, C, N, P and, S,[22] into the crystal lattice of the photocatalyst. The performance can be affected by the chemical state, concentration and location of the dopant. This doping process is aimed to *i*) improve the electrical conductivity and density of the charge carriers (e^-/h^+) in the photocatalyst (usually at low dopant concentrations) or extending the light absorption of UV-active photocatalysts such

as TiO_2 into the visible light range by narrowing E_g through forming electronic intragap states (usually at high dopant concentrations) (Figure 6.3a).[1]

6.5.2. Heterojunction engineering

Upon illumination of a photocatalyst, some of the photogenerated e^-/h^+ pairs recombine within microseconds, while others transfer to the surface of the photocatalyst and take part in redox reactions on a μs – ns scale. This means that there is always a competition between the recombination and transfer of e^-/h^+ pairs.[1] One common strategy to negate the e^-/h^+ recombination is through the creation of a heterojunction.[23] Heterophotocatalysts possess the functionality of the constituent catalysts. In addition to improved charge separation, heterocatalysts can also provide advantages such as chemical stability and appropriate band-edge features. The charge separation is achieved when e^- species flow from the higher to the lower lying CB while h^+ migrates in the opposite direction from the higher to lower lying VB (Figure 6.3b).[23, 24] Heterojunctions can be in different configurations where both constituent photocatalysts absorb light and create e^-/h^+ pairs such as α-Fe_2O_3–TiO_2,[25] TiO_2–WO_3,[26] $SrTiO_3/Ag_2O$,[27] or only one partner is photoactive such as metal oxide/QDs.[28]

6.5.3. Decoration of photocatalyst surface with a cocatalyst

A widely studied approach towards higher photocatalytic performance is the surface decoration of the photocatalyst with hydrogen and oxygen evolution cocatalysts.[29] The loaded cocatalyst is believed to lower the activation energy for OER and HER kinetics.[29] When a photocatalyst loaded with a cocatalyst is illuminated with UV or visible light, the photogenerated e^- in the CB moves to the surface of the photocatalyst. In the absence of the cocatalyst, the excited e^- species will either recombine with h^+ in the VB or are involved in the H_2 production reaction as discussed earlier. However, in the presence of the cocatalyst, some of the excited e^- species can be transferred from the CB of the photocatalyst to the cocatalyst, as the Fermi energy level of cocatalyst is always lower than that of photocatalyst. Meanwhile, the photogenerated h^+ stay at the VB of the photocatalyst and diffuse to its surface. This leads in the efficient separation of the photogenerated e^-/h^+ pairs.[1] In fact, dispersed cocatalysts provide additional reaction sites for the redox reactions. Without cocatalysts, some photocatalysts are very poorly efficient and some do not function at all.[30] Cocatalysts are mainly noble metals such as Pt, Au, Pd, and Rh which favour HER kinetics and transition metal oxides such as NiO, Co_3O_4, MnOx and CuOx which

favour the OER kinetics.[31] The processes of charge transfer between photocatalyst and deposited cocatalyst are described in Figure 6.3c.

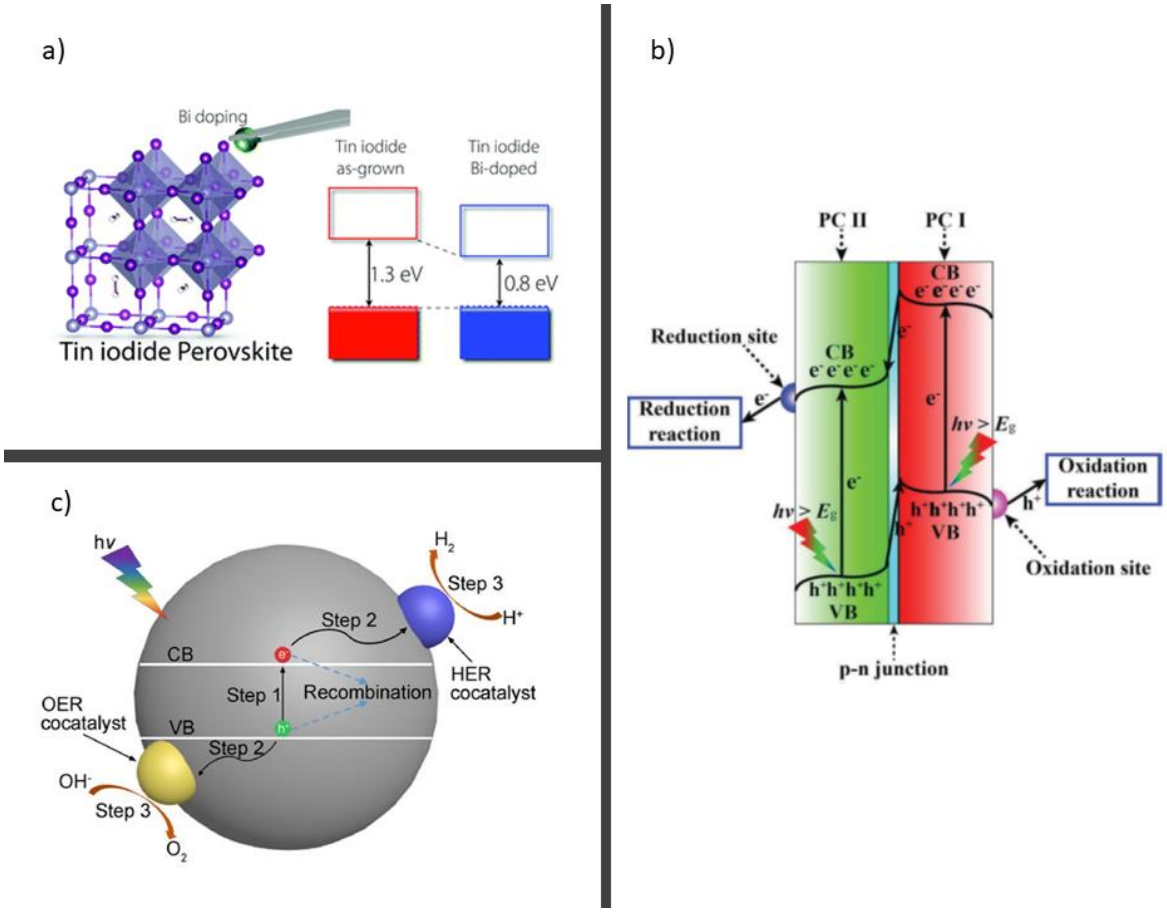

Figure 6.3 a) Proposed band diagram for the as-grown and bismuth-doped crystals. Reprinted with permission from Ref. [17]. Copyright 2017 RSC group. b) Charge transfer in a heterojunction-type photocatalytic system. Reprinted with permission from Ref. [20]. Copyright 2014 Wiley group. c) Schematic of solar-driven WS process in the presence of cocatalysts. Reprinted with permission from Ref. [17]. Copyright 2019 Science Direct group.

6.5.4. Nanostructuring

Developing nanoscale-sized photocatalysts is another viable strategy to achieve high H_2 production performance. This is an efficient approach as when the size of a bulk photocatalyst decreases to the nanoscale, it results in high surface-to-volume ratio and large surface area, which eases the charge transfer process.[1] A larger specific surface area means a short diffusion length for e^-/h^+ charge carriers, more active sites for redox reactions and higher reaction rates.[32] Tuning the shape of a photocatalyst into nanotubes, nanoplatelets, or nanoflowers where the most active crystal facets are exposed, can also improve the efficiency. Additionally, highly crystalline photocatalysts present higher

performance than amorphous structures due to the higher mobility of e^-/h^+ charge carriers within the solid.[33]

6.6. References:

[1] S. Kment, F. Riboni, S. Pausova, L. Wang, L. Wang, H. Han, Z. Hubicka, J. Krysa, P. Schmuki, R. Zboril, Chem. Soc. Rev. 2017, 46, 3716.
[2] A. Fujishima, K. Honda, Nature 1972, 238, 37.
[3] Q. Xu, L. Zhang, J. Yu, S. Wageh, A. A. Al-Ghamdi, M. Jaroniec, Mater. Today 2018, 21, 1042.
[4] J. R. Bolton, S. J. Strickler, J. S. Connolly, Nature 1985, 316, 495.
[5] A. B. Murphy, P. R. F. Barnes, L. K. Randeniya, I. C. Plumb, I. E. Grey, M. D. Horne, J. A. Glasscock, Int. J. Hydrogen Energy 2006, 31, 1999.
[6] S. Zhu, D. Wang, Adv. Energy Mater. 2017, 7, 1700841.
[7] T. Hisatomi, K. Takanabe, K. Domen, Catal. Lett. 2015, 145, 95.
[8] J. Highfield, Molecules 2015, 20, 6739.
[9] S. Cavallaro, V. Chiodo, A. Vita, S. Freni, J. Power Sources 2003, 123, 10; S. Freni, S. Cavallaro, N. Mondello, L. Spadaro, F. Frusteri, Catal. Commun. 2003, 4, 259.
[10] Y. Yao, X. Gao, Z. Li, X. Meng, Catalysts 2020, 10, 335.
[11] T. Sakata, T. Kawai, Chem. Phys. Lett. 1981, 80, 341.
[12] A. C. Sola, N. Homs, P. Ramírez de la Piscina, Int. J. Hydrogen Energy 2016, 41, 19629.
[13] M. M. Khan, S. F. Adil, A. Al-Mayouf, J. Saudi Chem. Soc. 2015, 19, 462.
[14] Q. Lu, Y. Yu, Q. Ma, B. Chen, H. Zhang, Adv. Mater. 2016, 28, 1917.
[15] T. Sakthivel, X. Huang, Y. Wu, S. Rtimi, Chem. Eng. J. 2020, 379, 122297.
[16] G. Dong, Y. Zhang, Q. Pan, J. Qiu, J. Photochem. Photobiol. C. 2014, 20, 33.
[17] A. H. Reshak, PCCP 2017, 19, 24915.
[18] K. Sytwu, M. Vadai, J. A. Dionne, Advances in Physics: X 2019, 4, 1619480.
[19] K. Maeda, J. Photochem. Photobiol. C. 2011, 12, 237.
[20] D. W. Bahnemann, Res. Chem. Intermed. 2000, 26, 207.
[21] H. Hasegawa, K. Kobayashi, Y. Takahashi, J. Harada, T. Inabe, J. Mater. Chem C. 2017, 5, 4048.
[22] C. Di Valentin, G. Pacchioni, Catal. Today. 2013, 206, 12.
[23] J. Low, J. Yu, M. Jaroniec, S. Wageh, A. A. Al-Ghamdi, Adv. Mater. 2017, 29, 1601694.
[24] P. Zhou, J. Yu, M. Jaroniec, Adv. Mater. 2014, 26, 4920.
[25] H. H. Mohamed, N. A. Alomair, S. Akhtar, T. E. Youssef, J. Photochem. Photobiol. A. 2019, 382, 111951.
[26] L. F. Paula, M. Hofer, V. P. B. Lacerda, D. W. Bahnemann, A. O. T. Patrocinio, Photochem. Photobiol. Sci. 2019, 18, 2469.
[27] Y. Cui, H. Sun, P. Guo, Nanotechnology 2020, 31, 245702.
[28] S. M. Sadeghi, R. R. Gutha, W. J. Wing, J. Phys. Chem. C. 2020, 124, 4261.
[29] J. D. Benck, T. R. Hellstern, J. Kibsgaard, P. Chakthranont, T. F. Jaramillo, ACS Catal. 2014, 4, 3957.
[30] H. Yu, J. Tian, F. Chen, P. Wang, X. Wang, Sci. Rep. 2015, 5, 13083.

[31] J. Ran, J. Zhang, J. Yu, M. Jaroniec, S. Z. Qiao, Chem. Soc. Rev. 2014, 43, 7787; Y. Chen, X. Feng, X. Guo, W. Zheng, Current Opinion in Green and Sustainable Chemistry 2019, 17, 21.
[32] D. Huang, S. Chen, G. Zeng, X. Gong, C. Zhou, M. Cheng, W. Xue, X. Yan, J. Li, Coord. Chem. Rev. 2019, 385, 44.
[33] H. Wu, H. L. Tan, C. Y. Toe, J. Scott, L. Wang, R. Amal, Y. H. Ng, Adv. Mater. 2020, 32, 1904717.

MASSEY UNIVERSITY
GRADUATE RESEARCH SCHOOL

STATEMENT OF CONTRIBUTION
DOCTORATE WITH PUBLICATIONS/MANUSCRIPTS

We, the candidate and the candidate's Primary Supervisor, certify that all co-authors have consented to their work being included in the thesis and they have accepted the candidate's contribution as indicated below in the *Statement of Originality*.

Name of candidate:	Hossein Etemadi
Name/title of Primary Supervisor:	Paul. G. Plieger
Name of Research Output and full reference:	
Synergistic Effect of Redox Dual PdOx/MnOx Cocatalysts on Enhanced H2 Production Potential of SnS/α-Fe2O3 heterojunction via Ethanol Photoreforming	
In which Chapter is the Manuscript /Published work:	7
Please indicate:	
• The percentage of the manuscript/Published Work that was contributed by the candidate:	85
and	
• Describe the contribution that the candidate has made to the Manuscript/Published Work:	
Hossein Etemadi did experimental design and trials, data analysis and draft of the manuscript. Jenna Buchanan proofread the manuscript. Shane and Yiming contributed to BET measurements. Tayyebeh and Hisao contributed to	
For manuscripts intended for publication please indicate target journal:	
Nano Research	
Candidate's Signature:	Hossein Digitally signed by Hossein Date: 2021.08.28 19:10:01 +12'00'
Date:	28/08/2021
Primary Supervisor's Signature:	Paul Plieger Digitally signed by Paul Plieger DN: cn=Paul Plieger, c=NZ, o=Massey University, ou=School of Fundamental Sciences, email=p.g.plieger@massey.ac.nz Date: 2021.08.30 15:09:53 +12'00'
Date:	30/08/2021

(This form should appear at the end of each thesis chapter/section/appendix submitted as a manuscript/ publication or collected as an appendix at the end of the thesis)

Chapter 7. Synergistic Effect of Redox Dual PdO_x/MnO_x Cocatalysts on Enhanced H_2 Production Potential of SnS/α-Fe_2O_3 heterojunction via Ethanol Photoreforming

Hossein Etemadi,[a] Tayyebeh Soltani,[b] Hisao Yoshida,[b,c] Yiming Zhang,[d] Shane G. Telfer[d] and Paul G. Plieger*[a]

[a] School of Fundamental Sciences, Massey University, Private Bag 11 222, Palmerston North, New Zealand

[b] Graduate School of Human and Environmental Studies, Kyoto University, Kyoto 606-8501, Japan

[c] Elements Strategy Initiative for Catalysts and Batteries (ESICB), Kyoto University, Kyoto 615-8520, Japan

[d] MacDiarmid Institute for Advanced Materials and Nanotechnology, Massey University, Palmerston North 4442, New Zealand

E-mail: p.g.plieger@massey.ac.nz

Tel: +64 6 9517647

Abstract:

In the quest for optimal H_2 evolution (HE) through ethanol photoreforming, a dual cocatalyst-modified heterocatalyst strategy is utilized. Tin (II) sulfide (SnS) was hybridized with α-Fe_2O_3 to form the heterocatalyst FeOSnS with a p−n heterojunction structure as confirmed by XRD, FT-IR, UV-Vis DRS and Brunauer-Emmett Teller (BET) techniques. PdO_x and PdO_x/MnO_x cocatalysts were loaded onto the FeOSnS heterocatalyst through the impregnation method as verified by HRTEM, XPS and elemental mappings. Photocatalytic ethanol photoreforming resulted in the production of H_2 as the main product with a selectivity of 99 % and some trace amounts of CH_4. Remarkably, FeOSnS2-PdO_x 2 % / MnO_x 1 % achieved the highest HE rate of 1654 μmol/g up to 2 times and 2.3 times as high as that of FeOSnS2- PdO_x 2 % and FeOSnS, respectively.

Keywords: SnS, α-Fe_2O_3, band gap, heterocatalyst, H_2 evolution, photocatalyst

7.1. Introduction

Hydrogen (H_2) is a crucial requirement for many industrial chemical processes such as ammonia synthesis (~ 50 %), oil refining (~ 40 %), methanol synthesis (~ 8 %), and transportation. As of 2020, approximately 87 million tons of H_2 was generated worldwide, 95 % of which is from fossil fuels by steam reforming of methane and other hydrocarbons, as well as coal gasification. Nevertheless, the burning of fossil fuels emit large amounts of greenhouse gasses such as CO_2 into the atmosphere, leading to global warming.[1] Solar energy is considered an ideal alternative for fossil fuels due to its high energy capacity (~ 1.2×10^{14} kJ received at the Earth's surface every second), low cost and abundance.[2] Solar-light assisted splitting of H_2O over a TiO_2 photocatalyst was proposed in 1972 by Honda and Fujishima as a sustainable way of H_2 production. Currently, the best performance has been achieved by TiO_2-based systems using UV light. The advantages of TiO_2 include availability, low cost, chemical stability, high chemical inertness and nontoxicity.[3] Nevertheless, one disadvantage of using TiO_2 is its limited activity in the visible spectrum due to its the large band gap ($E_g \approx 3.2$ eV) and fast recombination of photogenerated electron−hole pairs.[4] In spite of the significant body of research conducted with TiO_2, other UV-active photocatalysts such as ZnO[5] and $BiPO_4$,[6], and even visible- active photocatalysts such as Bi_2WO_6,[7], WO_3,[8] and $BiVO_4$[9] with wide band gaps ($E_g < 3$ eV), the H_2 production efficiency achieved in water photosplitting is still too low for industrial viability. This is due to the occurrence of energetically favourable backward H_2 and O_2 reaction to yield water; fast recombination of photogenerated electron and hole (e^-/h^+) pairs due to the strong Coulombic force, limited light absorption efficiency, low charge transport properties, photocorrosion and instability in water solutions.[10] An alternative strategy is the photoreforming of aqueous solutions containing biomass-derived oxygenates such as ethanol, glycerol, and glucose. Additionally, photoreforming can lead in the production of benzaldehyde, formaldehyde, and cyclohexanone as industrially attractive products.[11] Hematite (α-Fe_2O_3) is an n-type photocatalyst and has been examined for photocatalytic H_2 production through H_2O splitting due to its abundance, non-toxicity, good corrosion resistance, low cost and high photo/thermostability.[12] Importantly, the narrow band gap of 1.9 – 2.2 eV renders it with the ability to absorb about 40 % of the incident visible solar energy.[13] Nevertheless, the performance of α-Fe_2O_3 is still limited by its low electrical conductivity (~ 10 − 14 Ω^{-1} cm^{-1}),

short hole-diffusion distance (2 – 4 nm), poor electron-hole pair lifetime (< 10 ps), poor oxygen evolution reaction (OER) kinetics and weak charge mobility (10^{-2} to 10^{-1} cm^2 V^{-1} s^{-1}).[14] Furthermore, its conduction band (CB) is not negative enough to reduce H^+ ions to H_2.[15] Various strategies have been adopted to address these drawbacks associated with α-Fe_2O_3 , for water slitting. These include the development of α-Fe_2O_3 nanoarchitectures with sizes smaller than its hole diffusion length,[16] surface state passivating,[17] the creation of oxygen vacancies,[18] doping of α-Fe_2O_3 with heteroatoms such as Sc, Ti, Cr, Mn, and Ni [19] and construction of Z-scheme p-n junction heterostructures .[20] In contrast to water splitting, few studies have highlighted the H_2 production through ethanol photoreforming by using α-Fe_2O_3. For example, Carraro *et al* reported that control of the crystal phase of α-Fe_2O_3 can significantly improve the H_2 production potential. The results revealed H_2 production rates of 40, 225 and 125 mmol h^{-1} m^{-2} for α-Fe_2O_3, β-Fe_2O_3 and ε-Fe_2O_3 respectively through photoreforming of ethanol/water solutions under irradiation from a 150 W Xe lamp.[21] Wender *et al* reported an improved H_2 production rate of 546 mmol h^{-1} g^{-1} for an α-Fe_2O_3 nanoring loaded with a 7 % $Co(OH)_2$ cocatalyst versus 350 µmol h^{-1} g^{-1} for pure α -Fe_2O_3.[22] Tin monosulfide (SnS), is a p-type semiconductor with excellent opto-electric characteristics.[23] SnS has an indirect band gap of 1 – 1.2 eV and a direct optical band gap of 1.2 – 1.5 eV, high absorption coefficient (10^4 – 10^5 cm^{-1} in the visible region), high conductivity, low cost and high charge mobility.[24] Cocatalysts such as noble metals (Ni, Pt, Au, Pd, and Rh and Ag or transition metal oxides (NiO, Co_3O_4, MnO_x and CuO_x) have been extensively examined as important charge mediators to boost the photocatalytic performances.[25] In this contribution, we have optimized the conduction band (CB) energy of α-Fe_2O_3 through hybridization with SnS to improve the reduction of H^+ ions to H_2 via ethanol photoreforming. Additionally, FeOSnS heterocatalyst were decorated with PdO_x and MnO_x dual cocatalysts to boost the H_2 production efficiency. This is the first report on tertiary mixture of α-Fe_2O_3/SnS with dual redox cocatalysts for photocatalytic H_2 production.

7.2. Experimental Section

7.2.1. Synthesis of the α-Fe_2O_3 Catalyst

The α-Fe_2O_3 catalyst was synthesized through our previous published hydrothermal route.[26]

7.2.2. Synthesis of the SnS Catalyst

The flower-like SnS catalyst was synthesized by the above hydrothermal method except $SnCl_2$ (0.2 mmol), PVP (0.4 mmol) and sulfur powder (0.1 mmol) precursors were mixed in DMF (20 mL) under stirring (500 rpm) at 70 °C for 120 min followed by hydrothermal reaction at 180 °C for 6 h and eventual washing process as above.

7.2.3. Synthesis of α-Fe_2O_3 - SnS (FeOSnS) Heterocatalysts

The *in situ* chemical precipitation method was utilized to synthesize FeOSnS heterocatalysts using different mass ratios of as-prepared SnS and α-Fe_2O_3 constituents. In a typical experiment, SnS: α-Fe_2O_3 (1:1 w/w), were dispersed by ultrasonication in 50 mL of ETOH/H_2O solution (20:80 v/v) for 30 min and stirred in a fume hood at 80 °C for 24 h. The resultant product was collected by centrifugation, rinsed with distilled water and absolute ethanol three times, and dried at 80 °C for 6 h in an electric oven. The obtained heterocatalyst was denoted as FeOSnS1. Similarly, FeOSnS2 (SnS: α-Fe_2O_3 = 1.5:0.5 w/w) and FeOSnS3 (SnS: α-Fe_2O_3 = 0.5:1.5 w/w) were also prepared following the above procedure. The prepared FeOSnS1-3 heterocatalysts were then placed inside ceramic crucibles and calcined under Ar(g) at 500 °C for 5 h.

7.2.4. Loading of PdO_x/MnO_x Cocatalysts onto FeOSnS2

An impregnation method was utilized to load cocatalysts on the FeOSnS heterocatalyst. To synthesize FeOSnS2-PdO_x 1 %, 0.5 g FeOSnS2 was soaked in a solution (100 mL) containing the Pd precursor (0.008 g $PdCl_2$ and continuously stirred in a water bath at 120 rpm at 80 °C until the evaporation of the water from the suspension. The resulting solid was washed with absolute ethanol and distilled water three times, dried at 70 °C in an electric oven overnight followed by a calcination on a ceramic crucible in air at 350 °C for 2 h. FeOSnS2-PdO_x 2 % and FeOSnS2-PdO_x 2 % / MnO_x 1 % catalysts were prepared using the same procedure with stochiometric amounts of Pd (0.016 g $PdCl_2$) and MnO_x precursors (0.016 g $PdCl_2$ and Mn $(NO_3)_2{\cdot}4H_2O$ (0.027 g).

7.2.5. Photocatalytic Water Splitting and Ethanol Reforming for Hydrogen Production

The photocatalytic water splitting reaction was conducted using a flow system with an inner irradiation photochemical reactor. In a typical experiment, 0.1 g of photocatalyst was added to ion-exchanged water (350 mL) and suspended under magnetic stirring. Then Ar gas was

bubbled into the solution at a flow rate of 30 mL min^{-1} without irradiation for 1 h. The solution temperature was kept at 293 K during the reaction using external cooling water circulation. The photocatalytic H_2 production was commenced by irradiation of the solution using a 100 W high-pressure mercury lamp (4.4 mW cm^{-2} measured at λ = 254 ± 10 nm). The amount of H_2 in the outlet gas was quantified by an on-line gas chromatograph (Shimadzu, GC-8A, TCD, Shincarbon ST column, argon carrier). The experiment was carried out using a 20:80 ethanol-water solution where ethanol was used as the sacrificial reagent to consume the photogenerated holes during the reaction. The selectivity toward H_2 evolution compared with CH_4, S_{H2}, were calculated using the formula (1):

$$S_{H2}(\%) = R_{H2} / (R_{H2} + R_{CH4}) \times 100$$

where R_{H2} and R_{CH4} describe the production rate of H_2 and CH_4 respectively. The amount of CO and CO_2 produced was negligible and not considered in this equation.

7.3. Results and Discussion

The crystalline phase and purity of the as-prepared α-Fe_2O_3, SnS, FeOSnS1-3 and FeOSnS2-PdO_x/MnO_x catalysts were studied by powder X-ray diffraction (PXRD) (Figure 7.1). Pristine α-Fe_2O_3 which was synthesised from the decomposition of $Fe(acac)_3$ in DMF, in the presence of PVP surfactant at 180 °C, presents distinct diffraction peaks at 2θ = 24.1°, 33.1° (main characteristic peak), 35.6°, 40.8° and 49.4°, assigned to the crystal planes of (012), (104), (110), (113) and (024), respectively (Figure 7.1a). [27] For pristine SnS, formed from $SnCl_2$ and sulfur in the presence of PVP in DMF, the characteristic diffraction peaks were observed at 2θ = 21.9°, 25.9°, 27.6°, 31.9 39.2° 42.6°, 45.5° and 48.5° corresponding to the (011), (012), (102), (004) , (113), (021) , (015), and (023) diffraction planes respectively (Figure 7.1a).[28]

In the PXRD pattern of FeOSnS1-3 heterocatalysts (Figure 7.1a), a series of characteristic diffractions peaks from α-Fe_2O_3 (indicated by the symbol #) and SnS (indicated by the symbol *) are observed. In addition, the main diffraction peaks in the heterocatalysts have minor changes compared with pristine, α-Fe_2O_3 and SnS suggesting that the hybridization had negligible influence on the original crystal structure of constituents.[29] This also indicates that any improvement in photocatalytic potential is not caused by the crystal structure alteration of the constituents.[30] It is worth noting that we used an *in situ* chemical precipitation method to synthesis FeOSnS heterocatalysts rather direct physical mixing. The

reason was to improve the charge transfer between the two photocatalysts through the strong chemical bonding formed at the interface.[31] In the case of FeOSnS2-PdO_x/MnO_x catalysts, no obvious characteristic peaks of PdO_x species (metallic Pd or PdO) or MnO_x species (MnO, Mn_2O Mn_2O_3 and Mn_3O_4) were detected (Figure 7.1b). This could be due to *(i)* the low loading amount (1 and 2 %) of the PdO_x and MnO_x cocatalyst being below the detection threshold of XRD, *(ii)* the amorphous nature of loaded cocatalysts or *(iii)* the uniform dispersion of catalyst on the heterostructure.[32]

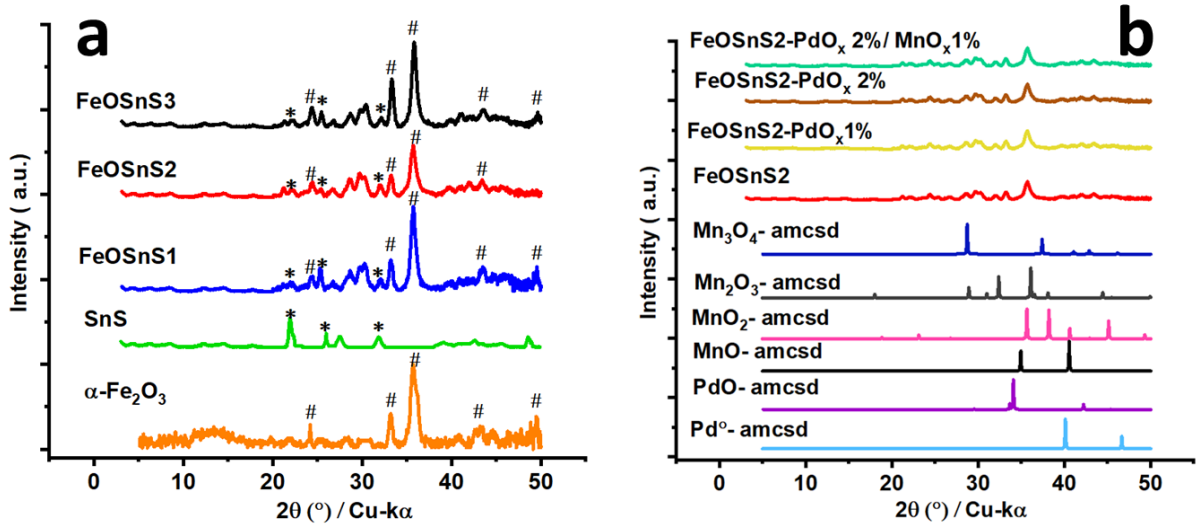

Figure 7.1 PXRD patterns of as-synthesized α-Fe_2O_3 and SnS, FeOSnS1-3 and (c) FeOSnS2- PdO_x/MnO_x catalysts.

TEM images of synthesized α-Fe_2O_3 displays nanometer sized particles with high monodispersity and an average diameter of 120 ± 24 nm (Figure 7.2a, b). The high-resolution TEM (HRTEM) image, reveals lattice spacing of 0.36 nm, and 0.27 nm, referring to (012), and (104) crystal planes, respectively (Figure 7.2c).[33] The observed values match with the PXRD pattern of standard American Mineralogist Crystal Structure Database (AMCSD card no. 0000143) for rhombohedral (hexagonal) α-Fe_2O_3 with lattice constants of a = b = 0.503 nm and c = 1.377 nm. (Figure 7.2d).

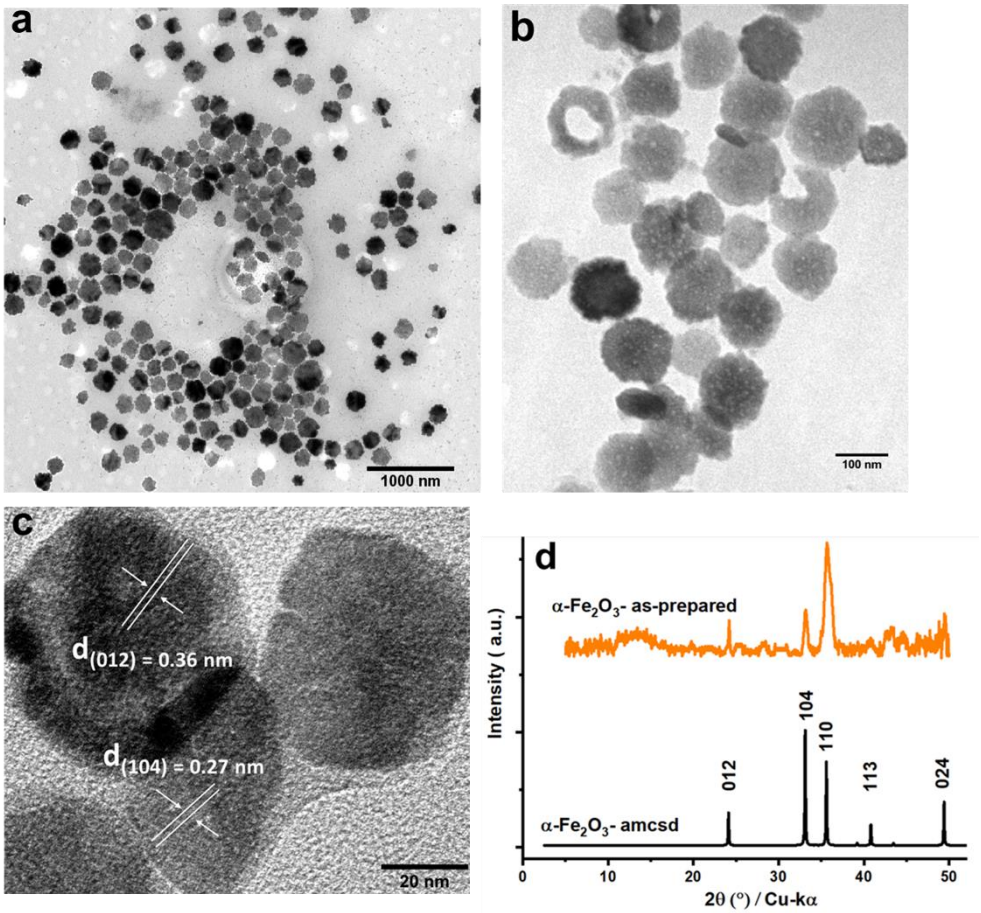

Figure 7.2 TEM images (a, b), HRTEM image (c) and PXRD pattern (d) of α-Fe_2O_3 catalyst. Patterns for α-Fe_2O_3 (AMCSD card no. 0000143) is shown for comparison.

TEM image of SnS reveals the characteristic formation of interconnected flower-like structures (Figure 7.3a). [34] Each nanoflower consists of thin 2D nanosheets with sharp edges growing anisotropically in all directions (Figure 7.3b).[35] The HRTEM image reveals lattice spacing of 0.34 nm ascribed to (012) crystal planes (Figure 7.3c).[36] The observed values match with PXRD pattern of standard American Mineralogist Crystal Structure Database assigned to the orthorhombic phase of SnS with lattice parameters *a* = 0.433, *b* = 1.11 and *c* = 0.398 nm (AMCSD card no 0018115) (Figure 7.3d).

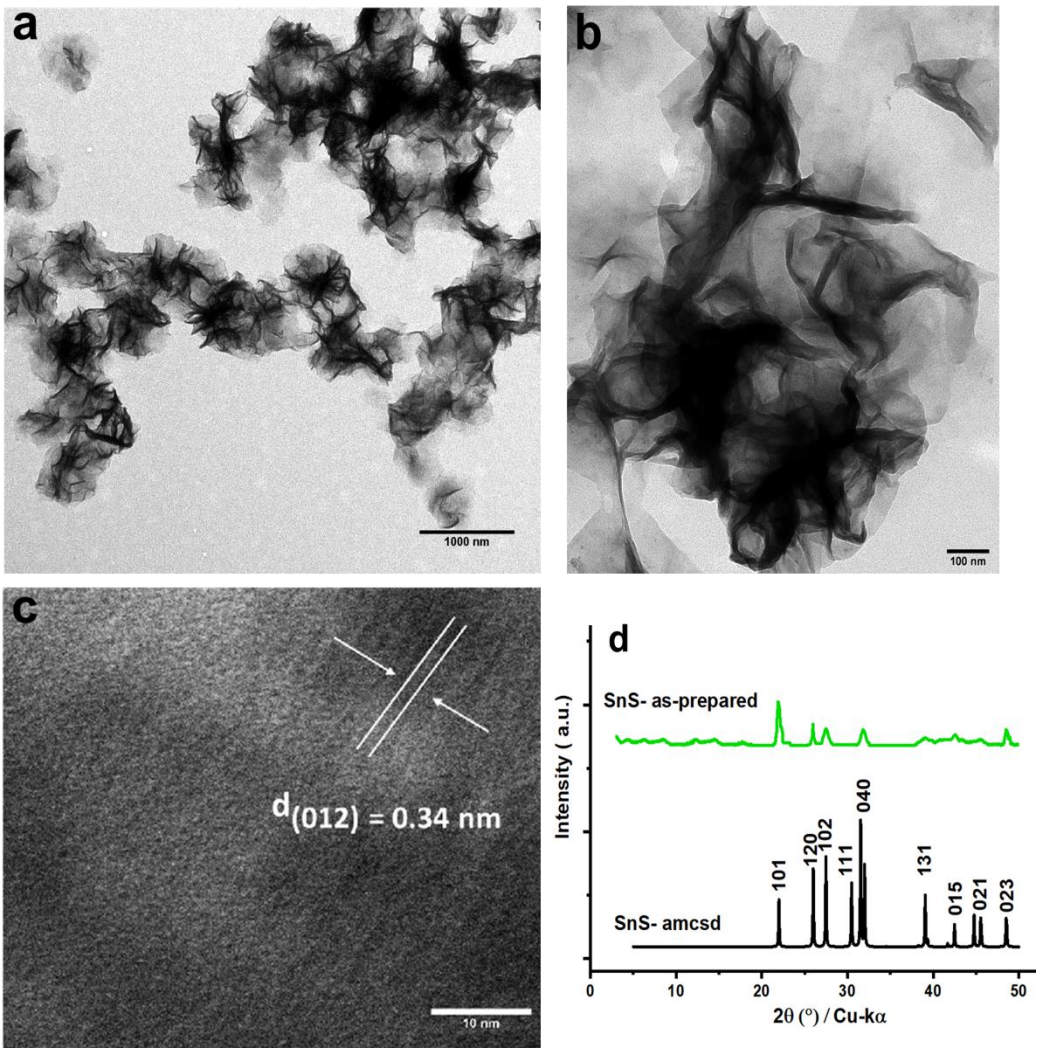

Figure 7.3 TEM images (a, b), HRTEM image (c) and a typical XRD pattern (d) of SnS catalyst. Patterns for SnS (AMCSD 0018115) is shown for comparison

The TEM image of the α-Fe_2O_3 and SnS heterostructure (FeOSnS) shows that α-Fe_2O_3 is dispersed onto the surface of SnS nanoflowers, likely forming a heterostructural interface through interactions between the two as evidenced by TEM images of FeOSnS2 (Figure7. 4a).[37] Ultrasonication prior to TEM imaging did not separate SnS and α-Fe_2O_3, implying that it is not a simple physical mixture of two components. Furthermore, α-Fe_2O_3 and SnS are shown in the TEM images to retain their original shape without morphological changes after hybridization.[38] The TEM image of FeOSnS2-PdO_x 2 % shows the morphology changes after loading PdO_x nanoparticles, in which the PdO_x nanoparticles are observed as black dots, are dispersed on the surface of the heterocatalyst (Figure 7.4b, d). The size distribution profile shows an average size of 3.7 ± 1 nm (Figure 7.4e). The TEM image of FeOSnS2-PdO_x 2 % /

MnO_x 1 % exhibits the same morphology as FeOSnS2-PdO_x 2 % with PdO_x nanoparticles seen as black dots, with an average size of 2.8 ± 0.87 nm (Figure 7.4c, f and g). Notably, the MnO_x cocatalyst is not localized due to the low concentration. STEM imaging using a High Angle Annular Dark Field (HAADF) detector and an Energy Dispersive Spectroscopy (EDS) attachment evidenced the presence of C, O, Fe, Sn, S and Pd elements without any signal for Mn in the FeOSnS2-PdO_x 2 % / MnO_x 1 % catalyst (Figure 7.5).

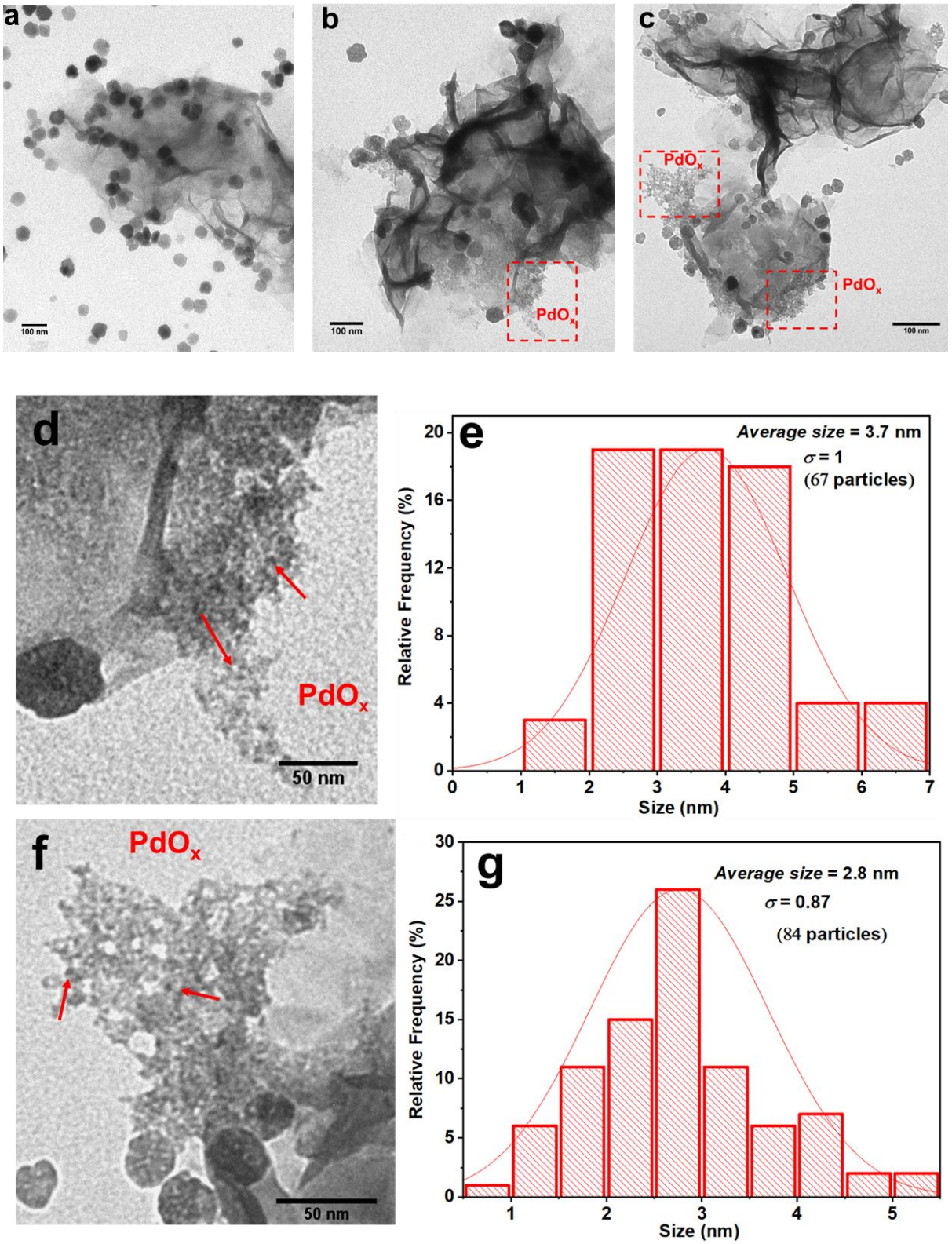

Figure 7.4 TEM images FeOSnS2 (a), FeOSnS2- PdO_x 2 % (b), and FeOSnS2-PdO_x 2 % / MnO_x 1 % (c), catalysts. HRTEM images (d, f) and the corresponding particle size distributions (e, g) of PdO_x in FeOSnS2- PdO_x 2 % (b), and FeOSnS2- PdO_x 2 % / MnO_x 1 % (c), catalysts.

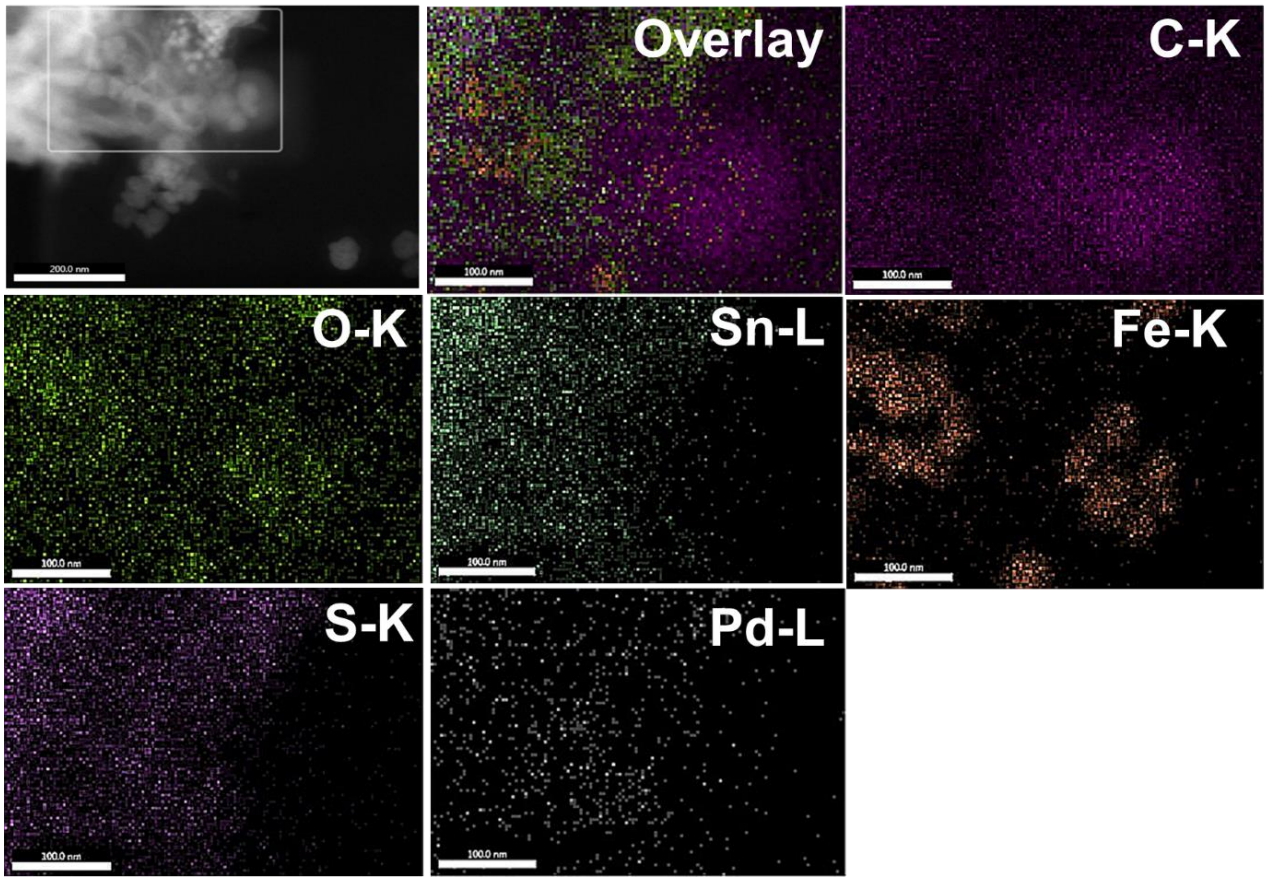

Figure 7.5 HAADF-STEM, and EDX elemental mapping images of FeOSnS2-PdO_x 2 % / MnO_x 1 % catalyst.

The heterostructure formation was further studied using the Brunauer-Emmett Teller (BET) method. We calculated the specific surface area (S_{BET}) and pore volume of the synthesized catalysts from adsorption-desorption isotherms. SnS presented S_{BET} and pore volume values of 60.9 m^2 g^{-1} and 0.063 cc/g which were higher than that of α-Fe_2O_3 with S_{BET} and pore volume values of 24.6 m^2 g^{-1} and 0.031 cc/ g respectively. (Figure 7.6a). The higher surface area of the SnS catalyst is due to its hierarchical porous architecture, whereas in the case of α-Fe_2O_3, a small surface area and low pore volume indicates that the α-Fe_2O_3 primary crystals are densely packed as evidenced by TEM results.[39] Integration of α-Fe_2O_3 with SnS resulted in FeOSnS heterocatalysts (FeOSnS1-3) with reduced specific surface areas and pore volumes (Figure 7.6a and Table 7.2). This is due to the decrease in the pore volume of SnS or blocking of the porous channels of SnS when coupling with α-Fe_2O_3 as reported by Yousatit *et al*.[40] The pore volume and diameter values for FeOSnS1-3 catalysts were not consistent with the initial undertaken ratios (Table 7.2) indicating that α-Fe_2O_3 nanoparticles

are not uniformly distributed on SnS which agrees with the TEM results. Furthermore, loading of the cocatalyst further reduced the surface area and pore volume of the FeOSnS2 heterocatalyst from 24.9 m^2/g and 0.008 cc/g down to 15.6 m^2/g and 0.005 cc/g for FeOSnS2-PdO_x 2 % / MnO_x 1 %. (Figure 7.6b and Table 7.2). This phenomenon is attributed to the partial surface coverage of the heterocatalyst by the deposited cocatalysts.[41]

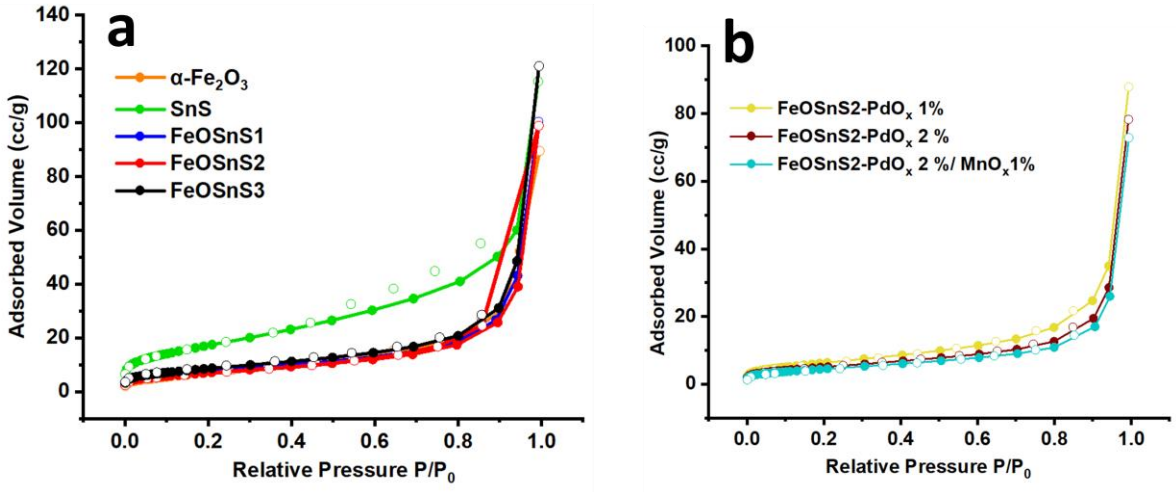

Figure 7.6 N_2 adsorption-desorption isotherm of as-synthesized α-Fe_2O_3, SnS, FeOSnS1-3 (a) and FeOSnS2 / PdO_x / MnO_x catalysts (b) measured at 77 K. Filled circles = adsorption points; empty circles = desorption points.

The heterostructure formation was further confirmed by ATR-FTIR and UV-Vis DRS results. (See supporting information Figures 7.11, 7.12, 7.13 and accompanying explanation). XRD and FT-IR studies did not confirm the presence of the cocatalysts in the FeOSnS heterostructures, however EDS analysis was able to. Unfortunately, as the detection limit of EDS used in this study was < 1 wt %, the technique was not able to give accurate quantitative values (See supporting information Figure 7.14 and accompanying explanation). Atomic absorption spectroscopy (AAS) was therefore utilised to confirm the content of the cocatalyst in the synthesized FeOSnS2 heterocatalyst (See supporting information Table 7.3 and accompanying explanation). To further explore the presence of the cocatalysts and identify the related oxidation states, XPS was performed. Wide-scan survey spectra revealed photoelectron lines at binding energies (BEs) of 23.6 eV (Sn 4d), (153 – 175) eV (S 2p), 278 - 300 eV (C 1s), 328 - 348 eV (Pd 3d), 480 – 505 eV (Sn 3d), 520-545 eV (O 1s), 556 - 630 eV

(Mn 2p) and (697 - 745 eV (Fe 2p), at the surface (≤ 3 nm), as illustrated in Figures 7.7a. This is consistent with the EDS results and revealed the successful impregnation of PdO_x and MnO_x cocatalysts on FeOSnS2. The high resolution XPS window of C1s core level (Figures 7.7b) is deconvoluted into three peaks at BEs of 284.8, 285.7 and 288.3 eV respectively corresponding to C-C sp^2 from PVP molecules and adventitious carbon, C-OH bond, and carbonyl (-OC=O) bond, respectively.[42] – The O 1s core - level spectra (Figures 7.7c) exhibit a high intensity peak at ∼ 530.3 eV corresponding to the lattice oxygen of iron−oxygen bonds (Fe−O) of the α-Fe_2O_3 component in the heterocatalyst. The high intensity of the peak is due to the high number of iron ions (Fe^{3+}) strongly interacting with the lattice oxygen (O^{2-}) in the crystal lattice. The peak centered at 532.2 eV is associated with the surface –OH groups (adsorbed water) and oxygen bonded with the PVP C-atoms (Fe – O – C bond).[43] As can be seen in the wide-scan survey spectra and high-resolution S 2p photoelectron spectra (Figure 7.7d), the peaks at 161-162 and 162-163 eV corresponding to S $2p_{3/2}$ and S $2p_{1/2}$ are absent. This is due to the presence of trace amounts of sulfur which is in accordance with EDS and elemental mapping results.[44] Sn manifests itself with strong peaks centred at 24 eV (Sn 4d), 486.4 eV (Sn $3d_{5/2}$), 494.9 eV (Sn $3d_{3/2}$), 713.6 eV (Sn $3p_{3/2}$) and 755.2 eV (Sn $3p_{1/2}$) (Figures 7.7a). The deconvolution of Sn 3d energy state (Figures 7.7e) revealed spin–orbit doublet peaks at 486.4 eV (Sn $3d_{5/2}$) and 494.9 eV (Sn$3d_{3/2}$) with a separation of 8.5 eV which confirms the oxidation state of +2 and formation of single phase SnS. In addition, two small peaks at slightly higher BEs of 487.8 Sn($3d_{5/2}$) and 496.2 eV (Sn$3d_{3/2}$) are assigned to Sn^{4+}, indicating the partial oxidation of the edges of SnS due to the unstable state of Sn^{2+} at the annealing temperature (500 °C).[45] Overall, XPS analysis indicates SnS as the major phase and SnS_2 as an impurity in the FeOSnS2/ PdO_x/MnO_x catalyst. The high-resolution Fe 2p spectrum in Figure 7.7f exhibits the BEs of Fe$2p_{3/2}$ and Fe$2p_{1/2}$ at 710.9 and 724.5 eV with additional satellite peaks at 734.7 eV which verify the valence of Fe ions as +3 in α-Fe_2O_3. The result indicates that calcination at 500 °C does not change the valence state of Fe^{3+} to the reduced or oxidized valence states (e.g. Fe^{2+} or Fe^{4+}). Notably, as marked in the dotted square in the low resolution survey spectrum (Figure 7.7a), the core-level lines assigned to Sn3p located at BEs of 715.6 eV for Sn$3p_{3/2}$ and 757.7 eV for Sn$3p_{1/2}$ overlap with the Fe2p core-levels.[46] The core–level high-resolution orbital scan of the Pd 3d spectra were deconvoluted into four peaks cantered at BEs of 336.9, 335.4, 342.4, and 343.5 eV respectively (Figure 7.7g). The high intensity peaks at BEs of 336.9 ($3d_{5/2}$) and 342.4 eV

($3d_{3/2}$) are assigned to Pd^{2+} from the palladium precursor, ($PdCl_2$) or PdO which is in agreement with the reported value of BE at 336.8–337.4 eV.[47] The very low intensity peaks at BEs of 337.7, and 343.5 eV are attributed to Pd^{4+} suggesting that a low percentage of Pd^{2+} has been oxidized during the impregnation/calcination process.[48] There was no metallic Pd (Pd^0) detected on the surface of the catalyst with typical BEs at 335.1 and 341.1 eV respectively.[49] The high-resolution spectrum of Mn2p exhibited two main peaks at BEs of 641.8 and 653.3 eV assigned to $Mn2p_{3/2}$ and Mn $2p_{1/2}$, respectively. The spin−orbit splitting energy value of Mn 2p was 11.5 eV, close to 11.6 eV as reported by Yu *et al*.[50] The peaks were deconvoluted to identify the chemical valence of the MnO_x cocatalyst. As can be seen from Figure 7.7h, the Mn $2p_{1/2}$ and Mn 2p3/2 peaks can be resolved into two pairs of triplet peaks, respectively. The Mn 2p3/2 peaks at BEs of 640.6, 641.8 and 642.4 eV correspond to Mn^{2+}(MnO), Mn^{3+} (Mn_2O_3) and Mn^{4+} cations (MnO_2) respectively. Similarly, the Mn $2p_{1/2}$ peaks appeared at BEs of 652.4, 653.3 and 653.8 eV which correspond to $Mn^{2+,}$ Mn^{3+} and Mn^{4+} cations respectively. These results indicate the coexistence of MnO, Mn_2O_3 and MnO_2 species. The loaded manganese oxide is labelled as MnO_x ($1 < x < 2$).[51]

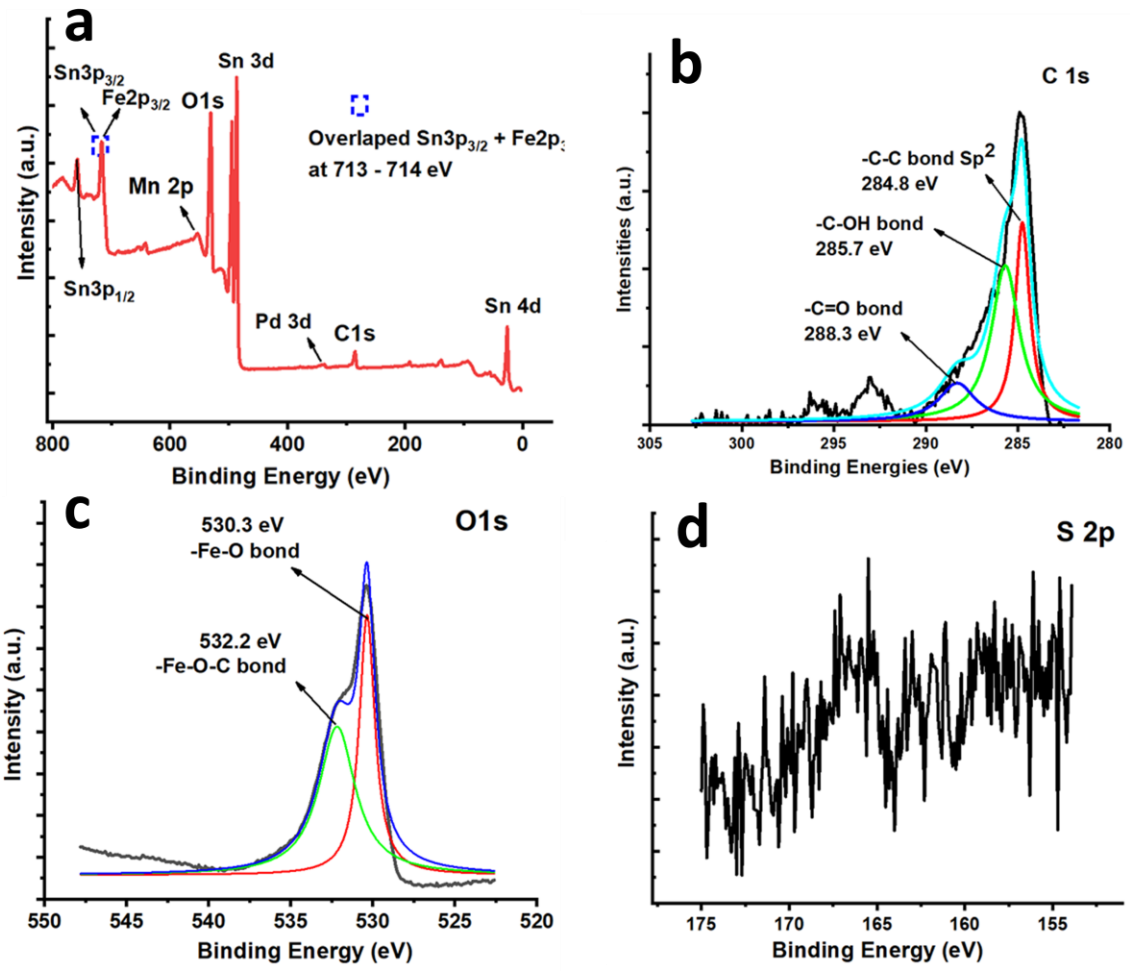
a
Sn3p3/2
Fe2p3/2
O1s
Sn 3d
Overlaped Sn3p3/2 + Fe2p
at 713 - 714 eV
Mn 2p
Sn3p1/2
Pd 3d
C1s
Sn 4d
Intensity (a.u.)
800
600
400
200
0
Binding Energy (eV)
b
C 1s
-C-C bond Sp2
284.8 eV
-C-OH bond
285.7 eV
-C=O bond
288.3 eV
Intensities (a.u.)
305
300
295
290
285
280
Binding Energies (eV)
c
O1s
530.3 eV
-Fe-O bond
532.2 eV
-Fe-O-C bond
Intensity (a.u.)
550
545
540
535
530
525
520
Binding Energy (eV)
d
S 2p
Intensity (a.u.)
175
170
165
160
155
Binding Energy (eV)

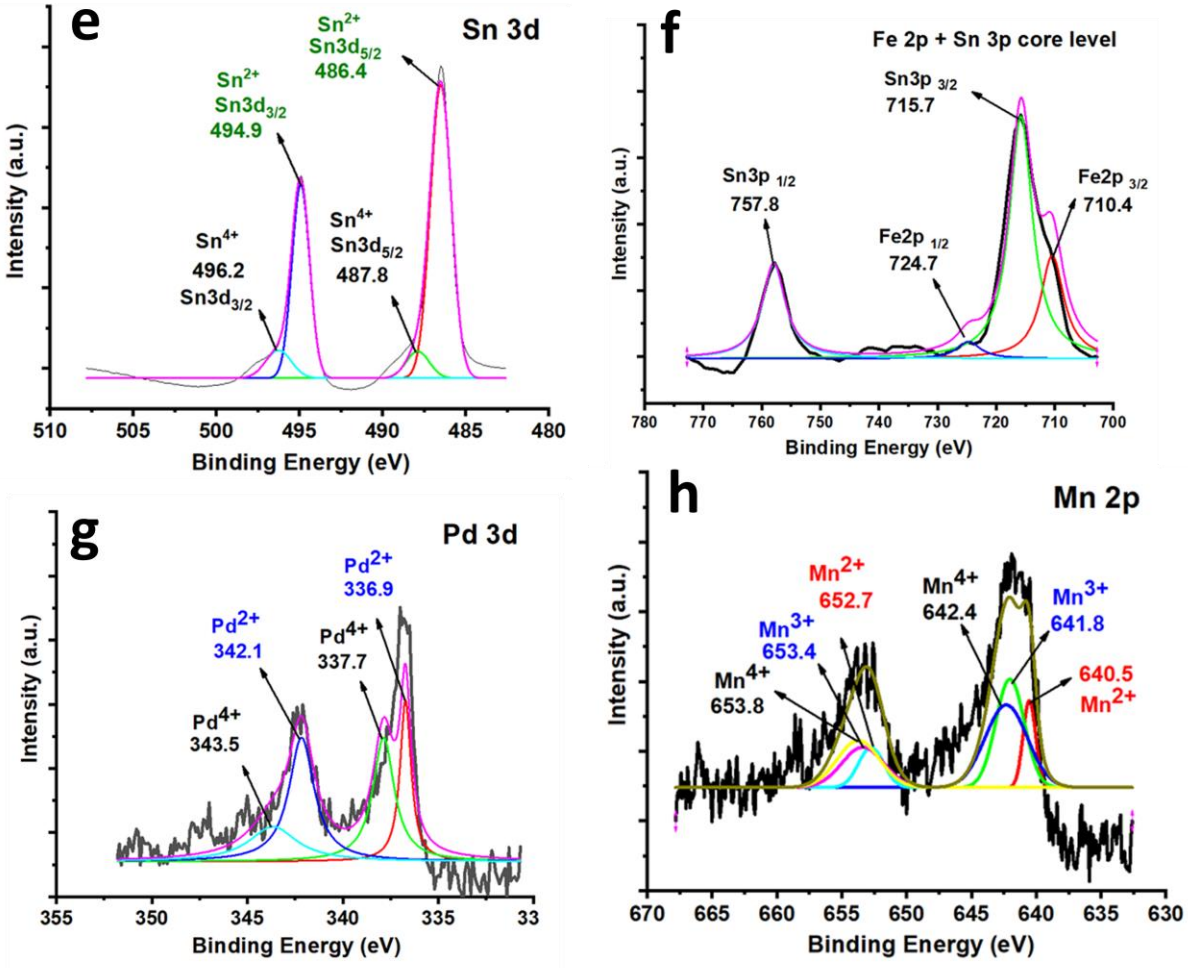

Figure 7.7 XPS survey spectra (a), and high-resolution XPS spectra of (b) C 1s, (c) O 1s, (d) S 2p, (e) Sn 3d, (f) 2p, (g) Pd 3d and (h) Mn 2p for FeOSnS2-PdO_x 2 % / MnO_x 1 % catalyst.

7.3.1. Photocatalytic water splitting

We initially investigated the photocatalytic performance of as synthesized α-Fe_2O_3, SnS and FeOSnS1-3 heterocatalysts toward their ability to perform as water splitting catalysts. The photocatalyst was tested with a photocatalytic water splitting protocol using a Hg lamp under Ar and led to the production of H_2 and O_2 as reductive and oxidative products (Equations 1 and 2), which accumulated in the gas phase:

$$2H^+ + 2e^- \rightarrow H_2 \qquad E^o(H^+/H_2) = 0 \text{ V vs. NHE, pH=0} \qquad (1)$$

$$2H_2O + 4h^+ \rightarrow O_2 \qquad E^o(O_2/H_2O) = 1.23 \text{ V vs. NHE, pH=0} \qquad (2)$$

Low H_2 generation of 12 and 64 µmol/g was observed after 3 h of illumination for pristine

SnS and α-Fe_2O_3, respectively. After the integration of the equal mass % of SnS and α-Fe_2O_3 (FeOSnS1 heterocatalyst), the H_2 formation yield increased to 192 µmol/g, which was much higher than that of pristine SnS and α-Fe_2O_3. The H_2 formation yield, using the FeOnS2 heterocatalyst with a higher α-Fe_2O_3 content, further increased to 218 µmol/g, which was more than 3.5 times higher than pure α-Fe_2O_3 samples (Figure 7.8a). The improved photocatalytic potency of the heterocatalyst FeOSnS2 could be attributed to the improved charge separation and reduced recombination rates and light-harvesting ability due to the successful heterojunction interface formation between SnS and α-Fe_2O_3 as already confirmed by XRD, FT-IR, UV-Vis DRS and Brunauer-Emmett Teller (BET) techniques. Our utilization of the in-situ chemical precipitation method provides the catalysts with a closer interface for a better charge transfer efficiency.[31] It was noted however that the photocatalytic efficiency decreased to 19 µmol/g when the SnS W % was increased (FeOSnS3 heterocatalyst) (Figure 7.8a). This was attributed to the low light harvesting ability and higher e^-/h^+ recombination rate, evidenced by UV-Vis DRS and PL emission studies respectively. (See supporting information Figures 7.12, 7.13, 7.15 and accompanying explanation). In contrast to H_2, no detectable formation of oxygen was observed under the present experimental conditions for all samples tested, a result which is in agreement with many other literature examples.[52] One possible reason for this is the difficulty of water oxidation due to the high overpotential required for O_2 evolution, a phenomenon which probably originates from the formation of deep trapping and stabilization of positive charge by the surface sites. Other possible reasons may be that the produced O_2 is adsorbed on the catalyst surface or some competitive side reactions may be occurring.[53] Considering the achieved H_2 formation yields, FeOSnS2 was found to be the optimal sample. Therefore, PdO_x and MnO_x were coloaded to investigate the potential of the created system for H_2 formation through ethanol photoreforming in the next set of experiments.

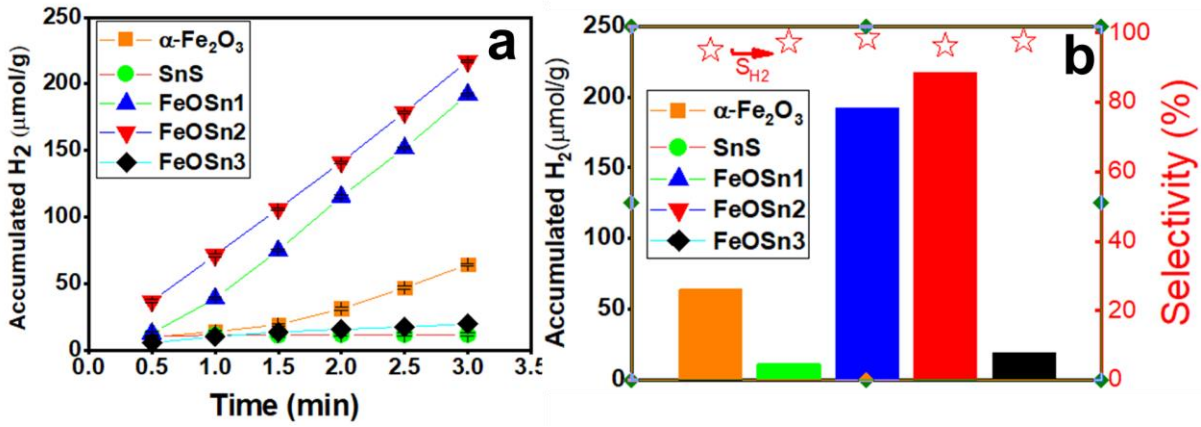

Figure 7.8 a) Time course and b) accumulated H_2 evolution amount from water splitting over 0.2 g α-Fe_2O_3, SnS, and FeOSnS catalysts after a 3 h illumination.

7.3.2. Photocatalytic Reforming of Ethanol

To explore the role of cocatalyst on the photocatalytic activity, single PdO_x and PdO_x/MnO_x dual cocatalyst were loaded on the optimal FeOSnS2, and results for photocatalytic reforming of ethanol in ethanol / water solutions compared with bare FeOSnS2 were performed. The results are shown in Figure 7.9a-b and Table 7.1. Blank tests were carried out, without a photocatalyst in the presence of ethanol (entry 1), or without photoirradiation in the presence of both ethanol and photocatalyst (entry 2), resulting in lower or negligible photocatalytic production rates. This confirms that this reaction does proceed photocatalytically with photoirradiation in the presence of the photocatalyst. The photocatalytic reforming of ethanol using ethanol / water solutions for the whole of single and dual cocatalysts loaded on FeOSnS2 resulted in the production of H_2, with only trace amounts of CH_4 produced. Product selectivity of H_2 among other possible gases reached 99 % (Table 7.1), with formation of other oxygenated organic compounds unable to be detected, therefore this method produces very high levels of pure H_2 gas. Time course data for H_2 formation in the photocatalytic reforming of ethanol over the FeOSnS2, and FeOSnS2/ PdO_x/MnO_x catalyst are shown in Figure 7.9a. An overall increase in H_2 formation yield with time of illumination was observed for all samples (Figure 7.9a) but a low amount of H_2 (42 μmol/g) was produced from the non-catalysed irradiation of ethanol after 3.5 h of illumination (Table 7.1). The FeOSnS2 sample produced a high amount of H_2 (702 μmol/g) after 3.5 h of illumination, indicating the successful trapping of h^+ by ethanol during the reaction.[54] The consumption of the photo-generated holes by ethanol results in the

accumulation of photo-generated electrons on the photocatalyst surface, leading to a higher H_2 formation. [52] Considering the previously reported α-Fe_2O_3 with other metal sulfide-based photocatalysts, our prepared FeOSnS2 heterocatalyst presents better performance. For example, Lu *et al.* reported an HE rate of 6.9 µmol/g/h over Zn-doped α-Fe_2O_3 modified WS2 after 2 h solar light irradiation.[55] Kadam *et al.* reported the highest HE rate of 136 µmol/g/ h for a 10 % Mo doped SnS photocatalyst at 400 nm.[56] When PdO_x species was loaded as cocatalyst on FeOSnS2, H_2 formation yield was increased from 702 µmol/g for FeOSnS2 to 821 µmol/g for FeOSnS2- PdO_x 1% and 1444 µmol/g for FeOSnS2-PdO_x 2 % after 3.5 h of illumination (Figure 7.9b). The high formation yield of H_2 for FeOSnS2-PdO_x 2 % / MnO_x 1 % with a higher loading amount of PdO_x as cocatalyst demonstrates that the photogenerated electrons and holes indeed could be efficiently separated once PdO_x was loaded on the surface of FeOSnS2 by the impregnation method. The loading of the MnOx species as an additional cocatalyst on FeOSnS2-PdO_x 2 % can increase the H_2 formation yield from 1444 µmol/g for FeOSnS2-PdO_x 2 % to 1654 µmol/g for FeOSnS2-PdO_x 2 % / MnO_x 1 % photocatalyst under the same conditions (Figure 7.9b). The formation of PdO_x and MnO_x cocatalysts was evidenced by XPS and UV-Vis DRS analysis, confirming the role of dual cocatalysts of PdO_x/MnO_x in photocatalytic reforming of ethanol, where the PdO_x serves as an electron trap (catalytic sites for H_2 reduction) and MnO_x serves as a hole trap (catalytic sites for oxidation reaction). This vicinal charge separation by dual cocatalysts of PdO_x/MnO_x can also lead to efficient photocatalytic reforming of ethanol. Since reduction and oxidation reactions take place in a pair, any improvements in the oxidation would result in improved reduction and subsequent higher H_2 formation rates.[57] This indicates that the coexistence of reductive and oxidative cocatalysts could synergistically improve the photocatalytic potential. López-Martínez *et al.* observed the same phenomenon where the maximum HE rate of 728 µmol/m^2 was achieved over dual AuPd cocatalysts loaded onto SnS after 3 h irradiation (Xe lamp of 450 W and 100 mW/cm^2).[58]

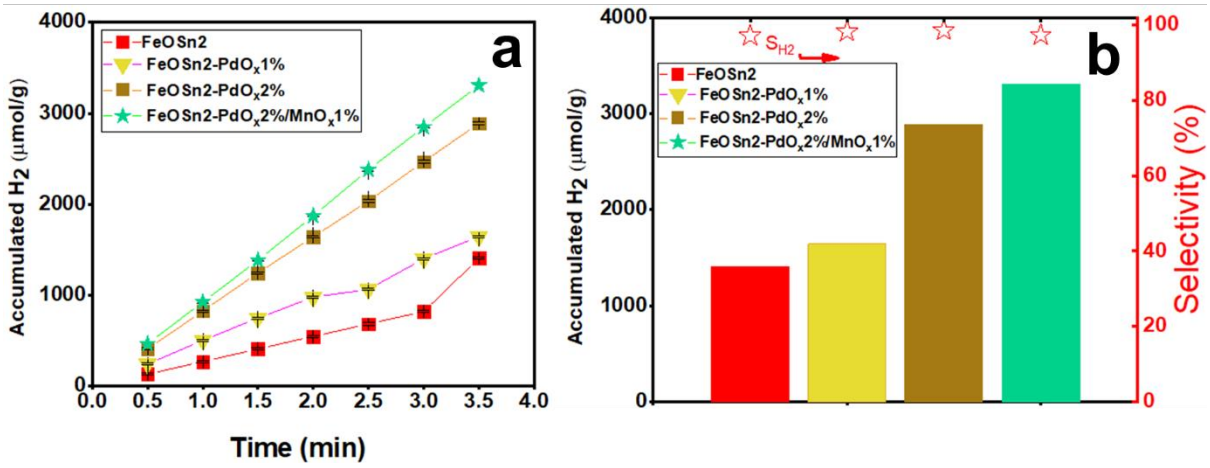

Figure 7.9 a) Time course and b) accumulated H_2 evolution amount from water splitting over 1 g α-Fe_2O_3, SnS and FeOSnS catalysts after a 3 h illumination.

Table 7.1 Products yields for the photocatalytic reforming by photocatalyst.

Entry	Gas	Photocatalyst	Production rate (μmol/g)				S_{H2}
			H_2	CH_4	CO	CO_2	
	Ar	No photocatalyst	21	0.5	-	-	99.36
	Ar	No light	-	-	-	-	-
1	Ar	FeOSnS2	702	1.75	-		99.75
2	Ar	FeOSnS2-PdO_x 1 %	821	4.75	-	-	99.42
3	Ar	FeOSnS2-PdO_x 2 %	1444	5.5	-	-	99.62
4	Ar	FeOSnS2-PdO_x 2 % / MnO_x 1 %	1654	11	-	-	99.33

7.3.3. Proposed Mechanism for H_2 production

The possible charge separation at the interface of PdO_x/MnO_x dual cocatalyst loaded on FeOSnS2 for the photocatalytic reforming of ethanol is depicted in Figure 7.10. Before contact, the conduction band and valence band edge positions (E_{VB} and E_{CB}) of SnS and α-Fe_2O_3 catalysts are independent of each other and were calculated to be 2.89 and 0.96 eV for α-Fe_2O_3 and 1.04 and - 0.40 eV for SnS (Supporting Information). The coupling of p-type SnS and n-type Fe_2O_3 form a p-n junction at the heterostructure interfaces, which leads to the formation of an internal electric field ($E_{internal}$) between the p-type side and the n-type

side and band bending.[59] On going from the p-type side to n-type side tends to separate the electrons and holes and enhances the photogenerated electrons transferring from the CB of p-type SnS to the CB of n-type α-Fe_2O_3 (Scheme 1). Loading PdO_x and MnO_x on the FeOSnS2 surface improves the interface reaction speed because the cocatalysts can reduce the activity energy of the reduction and oxidation reaction for the photocatalytsic reforming of ethanol as shown in Figure 7.10. The TEM images revealed the PdO_x NPs were deposited on the surface of α-Fe_2O_3 and SnS. However, we couldn't distinguish the exact position of MnO_x on the surface of FeOSnS2, and it seems that $MnO_{x\ is}$ randomly distributed on the surface of the FeOSnS2 catalyst. Considering the improved HE rate for dual cocatalyst, one possible explanation may arise from the fact that the loaded cocatalysts are spatially far from each other so that the recombination of electron/hole pairs is minimized. Therefore, PdO_x functions as the reduction site and receives the photoexcited electrons from the CB of Fe_2O_3 to produce H_2 while MnOx functions as the oxidation site and receives the photoexcited holes from the CB of SnS to produce CH_4.

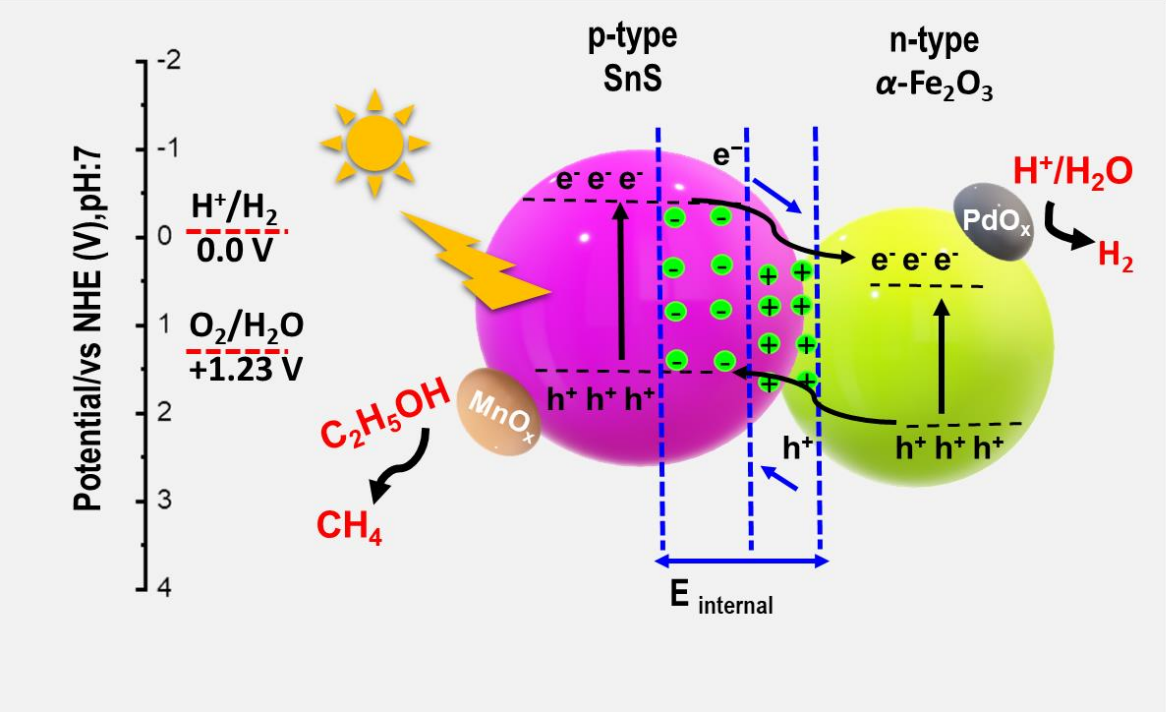

Figure 7.10 Band bending and carrier transport at the surface or interface for FeOSnS2/PdO_x/MnOx catalysts.

7.4. Conclusion

We have successfully synthesized FeOSnS heterocatalysts using a simple *in situ* chemical precipitation method. The prepared FeOSnS2 heterocatalyst exhibits excellent HE performance relative to pristine α-Fe_2O_3 and SnS, due to the new heterostructural interface provided by this technique. Loading of redox PdO_x and MnO_x cocatalysts did not influence the crystal structure of the FeOSnS2 heterocatalyst, but they were partially oxidized during loading. The loaded cocatalysts masked the pores of the FeOSnS2 heterocatalyst, resulting in reduction of the active surface area (S_{BET}). HE results revealed the success of the undertaken strategies, namely the integration of α-Fe_2O_3, SnS and co-loading of redox PdO_x and MnO_x cocatalysts. The highest HE rate was achieved for FeOSnS2-PdO_x 2 % / MnO_x 1 %, ascribed to the synergistic redox contribution of the PdO_x and MnOx species. In order to increase the HE rate further, two strategies will be considered in future work including (i) the loading of cocatalysts using different methods onto the optimal heterocatalyst and (ii) altering the ratios of the loaded PdO_x and MnO_x cocatalysts.

Supporting Information

Further details regarding structural characterization and valence band edge measurements; ATR-FTIR spectra of as-synthesized α-Fe_2O_3, SnS, FeOSnS1-3 and FeOSnS2/PdO_x/MnO_x catalysts (Figure 7.11); Physicochemical properties of as-synthesized α-Fe_2O_3, SnS, FeOSnS1-3 and FeOSnS2/PdO_x/MnO_x catalysts**.** (Table 7.2); UV-VIS diffuse reflectance spectra represented as the Kubelka-Munk function for as-synthesized α-Fe_2O_3, SnS, FeOSnS1-3 and FeOSnS2/PdO_x/MnO_x catalysts (Figure 7.12); Tauc plots for calculation of the direct optical band gaps of as-synthesized α-Fe_2O_3, SnS, FeOSnS1-3 and FeOSnS2/PdO_x/MnO_x catalysts (Figure 7.13); EDS patterns of (a) α-Fe_2O_3 (b) SnS, (c) FeOSnS1, (d) FeOSnS2, (e) FeOSnS3, (f) FeOSnS2-PdO_x 1 % (g) FeOSnS2-PdO_x 2 % and (c) FeOSnS2-PdO_x 2 %/MnO_x 1 % catalysts. (Figure 7.14); Quantification of PdO_x and MnO_x cocatalyst in FeOSnS2 heterocatalysts. (Table 7.3); PL spectra of as-synthesized α-Fe_2O_3, SnS, FeOSnS1-3 (a) and FeOSnS2/PdO_x/MnO_x catalysts (b) under 325 nm excitation. (Figure 7.15); Hysteresis loops of α-Fe_2O_3 and FeOSnS2 catalysts measured at RT. (Figure 7.16).

Acknowledgements

The authors gratefully acknowledge the New Zealand International Doctoral Research Scholarships (NZIDRS) committee for their financial support.

Conflict of interest

The authors declare no competing financial interest.

7.5. References

[1] A. V. Puga, A. Forneli, H. García, A. Corma, Adv. Funct. Mater. 2014, 24, 241; V. Gombac, L. Sordelli, T. Montini, J. J. Delgado, A. Adamski, G. Adami, M. Cargnello, S. Bernal, P. Fornasiero, The Journal of Physical Chemistry A 2010, 114, 3916.

[2] A. Hossain, K. Sakthipandi, A. K. M. Atique Ullah, S. Roy, Nano-Micro Lett. 2019, 11, 103.

[3] S. Filice, R. Fiorenza, R. Reitano, S. Scalese, S. Sciré, G. Fisicaro, I. Deretzis, A. La Magna, C. Bongiorno, G. Compagnini, ACS Appl. Nano Mater 2020, 3, 9127.

[4] D. Barreca, L. Bigiani, M. Monai, G. Carraro, A. Gasparotto, C. Sada, S. Martí-Sanchez, A. Grau-Carbonell, J. Arbiol, C. Maccato, P. Fornasiero, Langmuir 2018, 34, 4568.

[5] K. M. Lee, C. W. Lai, K. S. Ngai, J. C. Juan, Water Res. 2016, 88, 428.

[6] Y. Zhu, Q. Ling, Y. Liu, H. Wang, Y. Zhu, Appl. Catal. B. 2016, 187, 204.

[7] X. Meng, Z. Zhang, J. Photochem. Photobiol. A. 2015, 310, 33.

[8] J. E. Yourey, J. B. Kurtz, B. M. Bartlett, J. Phys. Chem. C. 2012, 116, 3200.

[9] D. Wang, R. Li, J. Zhu, J. Shi, J. Han, X. Zong, C. Li, Phys. Chem. C. 2012, 116, 5082.

[10] D. W. Bahnemann, Res. Chem. Intermed. 2000, 26, 207.

[11] S. L. Kollmannsberger, C. A. Walenta, C. Courtois, M. Tschurl, U. Heiz, ACS Catalysis 2018, 8, 11076.

[12] M. Mishra, D.-M. Chun, Appl Catal A-Gen. 2015, 498, 126.

[13] I. N. Reddy, C. V. Reddy, A. Sreedhar, M. Cho, D. Kim, J. Shim, J. Electroanal. Chem. 2019, 842, 146.

[14] W.-S. Jung, S.-H. Park, A. N. Kadam, H. Kim, S.-W. Lee, Dalton Trans. 2020, 49, 2924; L. Wang, J. Zhu, X. Liu, ACS Appl. Mater. Interfaces. 2019, 11, 22272.

[15] S. Zhu, F. Yao, C. Yin, Y. Li, W. Peng, J. Ma, D. Zhang, Microporous Mesoporous Mater. 2014, 190, 10.

[16] S. Shen, S. A. Lindley, X. Chen, J. Z. Zhang, Energy Environ. Sci. 2016, 9, 2744.

[17] Q. Bu, S. Li, Q. Wu, L. Bi, Y. Lin, D. Wang, X. Zou, T. Xie, ChemSusChem. 2018, 11, 3486.

[18] Y. Ling, G. Wang, H. Wang, Y. Yang, Y. Li, ChemSusChem. 2014, 7, 848.

[19] F. Li, J. Li, J. Zhang, L. Gao, X. Long, Y. Hu, S. Li, J. Jin, J. Ma, ChemSusChem. 2018, 11, 2156.

[20] S.-S. Yi, B.-R. Wulan, J.-M. Yan, Q. Jiang, Adv. Funct. Mater. 2019, 29, 1801902.

[21] G. Carraro, C. Maccato, A. Gasparotto, T. Montini, S. Turner, O. I. Lebedev, V. Gombac, G. Adami, G. Van Tendeloo, D. Barreca, P. Fornasiero, Adv. Funct. Mater. 2014, 24, 372.

[22] H. Wender, R. V. Gonçalves, C. S. B. Dias, M. J. M. Zapata, L. F. Zagonel, E. C. Mendonça, S. R. Teixeira, F. Garcia, Nanoscale 2013, 5, 9310.

[23] J. Kim, J. Kim, S. Yoon, J.-y. Kang, C.-W. Jeon, W. Jo, J. Phys. Chem. C. 2018, 122, 3523.

[24] G. Mohan Kumar, X. Fu, P. Ilanchezhiyan, S. U. Yuldashev, D. J. Lee, H. D. Cho, T. W. Kang, ACS Appl. Mater. Interfaces 2017, 9, 32142.

[25] J. Ran, J. Zhang, J. Yu, M. Jaroniec, S. Z. Qiao, Chem. Soc. Rev. 2014, 43, 7787.

[26] H. Etemadi, P. G. Plieger, ACS Omega 2020, 5, 18091.

[27] A. Lassoued, B. Dkhil, A. Gadri, S. Ammar, Results in Physics 2017, 7, 3007.

[28] C. Rana, S. Saha, J. Mater. Sci.: Mater. Electron 2019, 30, 21160.

[29] R. Shen, L. Zhang, X. Chen, M. Jaroniec, N. Li, X. Li, Applied Catalysis B: Environmental 2020, 266, 118619; S. Han, L. Hu, Z. Liang, S. Wageh, A. A. Al-Ghamdi, Y. Chen, X. Fang, Adv. Funct. Mater. 2014, 24, 5719.
[30] Z. Yang, L. Chen, Y. Yang, J. Wang, Y. Huang, X. Liu, S. Yang, Semicond. Sci. Technol. 2017, 32, 065008.
[31] Y. Zang, L. Li, X. Li, R. Lin, G. Li, Chem. Eng. J. 2014, 246, 277.
[32] K. Qi, Y. Li, Y. Xie, S.-y. Liu, K. Zheng, Z. Chen, R. Wang, Front. Chem. 2019, 7.
[33] M. A. Mohamed, N. A. Rahman, M. F. M. Zain, L. J. Minggu, M. B. Kassim, J. Jaafar, S. Samad, M. S. Mastuli, R. J. Wong, J. Alloys Compd. 2020, 820, 153143.
[34] S. Li, W. Jiang, K. Xu, S. Hu, Y. Liu, Y. Zhou, J. Liu, Front. Chem. 2018, 6.
[35] S. Liang, Z. Zhou, X. Wu, S. Zhu, J. Bi, L. Zhou, M. Liu, L. Wu, Molecules (Basel, Switzerland) 2016, 21, 213.
[36] B. H. Baby, D. Bharathi Mohan, Solar Energy 2018, 174, 373.
[37] K. C. Christoforidis, A. Sengele, V. Keller, N. Keller, ACS Appl. Mater. Interfaces. 2015, 7, 19324.
[38] R. Shen, L. Zhang, X. Chen, M. Jaroniec, N. Li, X. Li, Appl. Catal. B. 2020, 266, 118619.
[39] H.-Y. Si, C.-J. Mao, Y.-M. Xie, X.-G. Sun, J.-J. Zhao, N. Zhou, J.-Q. Wang, W.-J. Feng, Y.-T. Li, Dalton Trans. 2017, 46, 200.
[40] S. Yousatit, H. Pitayachinchot, A. Wijitrat, S. Chaowamalee, S. Nuntang, S. Soontaranon, S. Rugmai, T. Yokoi, C. Ngamcharussrivichai, Sci. Rep. 2020, 10, 12977.
[41] Z. Zhu, Y. Han, C. Chen, Z. Ding, J. Long, Y. Hou, ChemCatChem 2018, 10, 1627.
[42] P. Huang, W. Tao, H. Wu, X. Li, T. Yin, Q. Zhang, W. Qi, G. Gao, D. Cui, Journal of Energy Chemistry 2018, 27, 1453.
[43] N. Thangavel, S. Bellamkonda, A. D. Arulraj, G. Ranga Rao, B. Neppolian, Catalysis Science & Technology 2018, 8, 5081.
[44] Z. He, Y. Wang, X. Dong, N. Zheng, H. Ma, X. Zhang, RSC Adv. 2019, 9, 21646; G. Kogo, B. Xiao, S. Danquah, H. Lee, J. Niyogushima, K. Yarbrough, A. Candadai, A. Marconnet, S. K. Pradhan, M. Bahoura, Sci. Rep. 2020, 10, 1067.
[45] R. M. I. Bandara, K. D. G. I. Jayawardena, S. O. Adeyemo, S. J. Hinder, J. A. Smith, H. M. Thirimanne, N. C. Wong, F. M. Amin, B. G. Freestone, A. J. Parnell, D. G. Lidzey, H. J. Joyce, R. A. Sporea, S. R. P. Silva, J. Mater. Chem C. 2019, 7, 8389.
[46] C. Leostean, O. Pana, M. Stefan, A. Popa, D. Toloman, M. Senila, S. Gutoiu, S. Macavei, Appl. Surf. Sci. 2018, 427, 192.
[47] H. Xu, K. Ni, X. Li, G. Fang, G. Fan, RSC Adv. 2017, 7, 51403.
[48] L. Di, J. Zhang, M. Craven, Y. Wang, H. Wang, X. Zhang, X. Tu, Catalysis Science & Technology 2020, 10, 6129.
[49] A. Kumar, R. Srivastava, ACS Appl. Energy Mater. 2020, 3, 9928.
[50] A. Meng, L. Zhang, B. Cheng, J. Yu, ACS Appl. Mater. Interfaces. 2019, 11, 5581.
[51] H.-b. Li, G.-y. Huang, J. Zhang, S.-h. Fu, T.-g. Wang, H.-w. Liao, Transactions of Nonferrous Metals Society of China 2017, 27, 1127.
[52] T. Soltani, X. Zhu, A. Yamamoto, S. P. Singh, E. Fudo, A. Tanaka, H. Kominami, H. Yoshida, Applied Catalysis B: Environmental 2021, 286, 119899.
[53] T. Soltani, A. Yamamoto, S. P. Singh, A. Anzai, E. Fudo, A. Tanaka, H. Kominami, H. Yoshida, ACS Applied Energy Materials 2021, 4, 6500.
[54] J. T. Schneider, D. S. Firak, R. R. Ribeiro, P. Peralta-Zamora, PCCP 2020, 22, 15723.
[55] D. Chu, K. Li, A. Liu, J. Huang, C. Zhang, P. Yang, Y. Du, C. Lu, Int. J. Hydrog. Energy. 2018, 43, 7307.

[56] S. R. Kadam, S. Ghosh, R. Bar-Ziv, M. Bar-Sadan, Chem. Eur. J. 2020, 26, 6679.
[57] X. Zhu, A. Yamamoto, S. Imai, A. Tanaka, H. Kominami, H. Yoshida, Chem. Commun. 2019, 55, 13514.
[58] S. D. López-Martínez, I. Juárez-Ramírez, L. M. Torres-Martínez, P. Babar, A. Lokhande, J. H. Kim, J. Photochem. Photobiol. A. 2018, 361, 19.
[59] T. Soltani, B.-K. Lee, Sci. Total Environ. 2020, 736, 138640.

Supporting Information for

7.6. Synergistic Effect of Redox Dual PdO_x/MnO_x Cocatalysts on Enhanced H_2 Production Potential of $SnS/\alpha\text{-}Fe_2O_3$ heterojunction via Ethanol Photoreforming

Hossein Etemadi,[a] Tayyebeh Soltani,[b] Hisao Yoshida,[b,c] Yiming Zhang,[d] Shane G. Telfer[d] and Paul G. Plieger*[a]

[a] School of Fundamental Sciences, Massey University, Private Bag 11 222, Palmerston North, New Zealand

[b] Graduate School of Human and Environmental Studies, Kyoto University, Kyoto 606-8501, Japan

[c] Elements Strategy Initiative for Catalysts and Batteries (ESICB), Kyoto University, Kyoto 615-8520, Japan

[d] MacDiarmid Institute for Advanced Materials and Nanotechnology, Massey University, Palmerston North 4442, New Zealand

E-mail: p.g.plieger@massey.ac.nz

Fax: +64 6 350 5682; Tel: +64 6 9517647

Materials. Iron (III) acetylacetonate ($Fe(acac)_3$ ≥ 99.9 % trace metals basis), poly(vinylpyrrolidone) (PVP, average molecular weight 40,000 $gmol^{-1}$), *N,N*-dimethylformamide (DMF), sulfur powder (99.99 %) and tin chloride dihydrate ($SnCl_2{\cdot}2H_2O$, 99 %), were purchased from Sigma-Aldrich. All other chemicals were of the analytical grade and used as received from commercial sources without further purification.

Characterization

Powder X-ray diffraction (PXRD) patterns were recorded on a Rigaku Spider X-ray diffractometer with Cu K_α radiation (λ = 1.5406 Å), at 40 kV and 50 mA from 10° to 80° in the Bragg configuration. The morphology of the catalysts was examined using transmission electron microscopy (TEM, Tecnai *G2 Spirit Bio-TWIN,* acceleration voltage of 200 Kv) and scanning electron microscopy (SEM, FE-SEM FEI Quanta 200). *Image J software* was acquired for post-processing and particle size analysis. The elemental mapping images and

energy-dispersive X-ray spectroscopy (EDX) spectra of catalysts were probed by an energy dispersive spectrometer connected to field-emission scanning electron microscopy (FE-SEM FEI Quanta 200) to verify the chemical composition. The spectral data was collected with a silicon EDAX unit (NJ, USA) running Genesis Spectrum software (version 5.21). The EDS spectra were generated for each catalyst by a line scan of several randomly selected areas under different magnifications. The chemical state of catalysts was probed with X-ray photoelectron spectroscopy (XPS) (Kratos Axis Ultra^{DLD} X-ray Photoelectron Spectrometer) at the pressure of 10^{-9} torr with Al K_α X-rays (1486.69 eV) as the X-ray source. All spectra were calibrated with respect to the C 1s signal from adventitious hydrocarbon set at 285 eV. The high-resolution narrow-scan XPS spectra. Included non-linear (Shirley) background subtraction and peaks deconvolution by using mixed Gaussian-Lorentzian functions. The mass percentages of PdO_x and MnO_x cocatalysts were analyzed by atomic absorption spectroscopy (AAS; GBC Scientific Perkin-Elmer Instrument) with a slit width of 0.2 nm, a lamp current of 5 mA and an air-acetylene flame, with a Pd hollow cathode lamp (340.5 nm) and Mn hollow cathode lamp (403.1 nm) for PdO_x and MnO_x, respectively. For AAS analysis, approximately 5 mg of catalyst was digested in a mixture of concentrated HCl (37 %, 0.5 mL), HNO_3 (70 %, 1.0 mL) and H_2O_2 (32 %, 1.0 mL) at 100 °C overnight followed by dilution to 50 mL with Milli-Q water. Standard 1000 ppm Pd in HCl and Mn in HNO_3 (Sigma-Aldrich) solutions were used to prepare metal calibration standards solutions (10 −100 ppm) from which the intensity vs. concentration plot was acquired for quantification.[1] The N_2 adsorption–desorption isotherms were analysed on a Quantachrome BELSORP Mini Autosorb nitrogen-adsorption apparatus. Samples were evacuated at 120 °C for 20 h prior to Brunauer-Emmett-Teller (BET) measurements with autosorb at liquid nitrogen temperature (77 K). The BET specific surface area (S_{BET}) of the catalysts were investigated by a multipoint BET method utilizing the adsorption data in the relative pressure (P/P_0) range of 0 – 1. The optical characteristics and band gap values of the catalysts were acquired via a UV-Vis diffuse reflectance spectrometer (V-640 (JASCO)) with an integrating sphere attachment in the wavelength range of 200 – 800 nm at RT. High purity barium sulfate ($BaSO_4$) powder was used as a reflectance standard. Photoluminescence (PL) emission spectra were collected at RT using a Horiba Scientific Fluoromax-4 Spectrofluorometer. All samples with concentrations of 0.06 mg/mL in EtOH were excited at 330 nm with a 150 W

ozone-free xenon arc lamp as the excitation source and the emission spectra were recorded from 330 to 620 nm.

ATR-FTIR Results

Attenuate total reflection Fourier transform infrared (ATR-FTIR) spectra were recorded in the range of 400 – 4000 cm^{-1} to verify the presence of functional groups, chemical bonding and heterostructural formation. The IR spectra of pure PVP, pristine α-Fe_2O_3, SnS, FeOSnS1-3 and FeOSnS2/ PdO_x /MnO_x catalysts are presented in Figure 7.11**.** The pure PVP spectrum exhibits peaks located at 1285 cm^{-1} (-C–N bending vibration from the pyrrolidone structure), 1372 cm^{-1} (-CH deformation of the -CH_2 group), 1422 cm^{-1} (-CH_2 scissoring vibrations), 1662 cm^{-1} (stretching vibration of -C=O in the functional pyrrolidone group), the doublet bands at 2950 and 2880 cm^{-1} (asymmetric and symmetric stretching vibrations of the aliphatic -CH_2 unit) and 3473 cm^{-1} (stretching vibration of the hydroxyl group (OH) of PVP).[2] The spectrum of SnS shows a strong peak at 605 cm^{-1} (Sn-S vibration) and a doublet with medium intensity at 1028 cm^{-1} and 1140 cm^{-1}, ascribed to the -SO_3 stretching vibration.[3] For α-Fe_2O_3, two distinct peaks appear below 1000 cm^{-1} corresponding to metal oxygen (Fe–O–Fe) stretching frequencies in the crystalline lattice. The high frequency band located at 548 cm^{-1} is attributed to intrinsic stretching vibrations of Fe–O–Fe bonds at the tetrahedral (T_d) site, while the low frequency band located at 460 cm^{-1} is attributed to stretching vibrations of Fe–O–Fe bonds at octahedral (O_h) sites of α-Fe_2O_3.[4] In addition, the intensity of the absorption peak at 548 cm^{-1} is stronger than that at 460 cm^{-1} emphasizing the formation of α-Fe_2O_3.[4] The stretching vibration peak of -C=O, originally at 1668 cm^{-1} in pure PVP, was blue shifted to lower frequencies in SnS, α-Fe_2O_3 and FeOSnS1-3 catalysts (Figure 7.11 a). These observations confirm the formation of coordination bonds between Fe and Sn atoms with N or O atoms of PVP molecules.[5] FeOSnS1-3 heterocatalysts exhibit the characteristic peaks of α-Fe_2O_3 and SnS constituents which evidence the successful heterocatalyst formation.[6, 7] Additionally, the peak intensities at 1372, 1422, 1662, 2880 and 2950 cm^{-1} decreased dramatically for all catalysts, indicating that the PVP surfactant was decomposed extensively after calcination at 550 °C for 5 h (Figure 7.11 a,b). After loading PdO_x and MnO_x cocatalysts on the surface of FeOSnS2, spectral differences were negligible (Figure 7.11c).[7] No functional groups associated with PdO_x and MnO_x species

were observed, even though their corresponding peaks were detected in the EDS and XPS spectra.[8] This is in line with PXRD results, indicate that the chemical structure of FeOSnS2 was not affected by the modification process and the cocatalysts were distributed rather than covalently coupling with α-Fe_2O_3 and SnS constituents.[9]

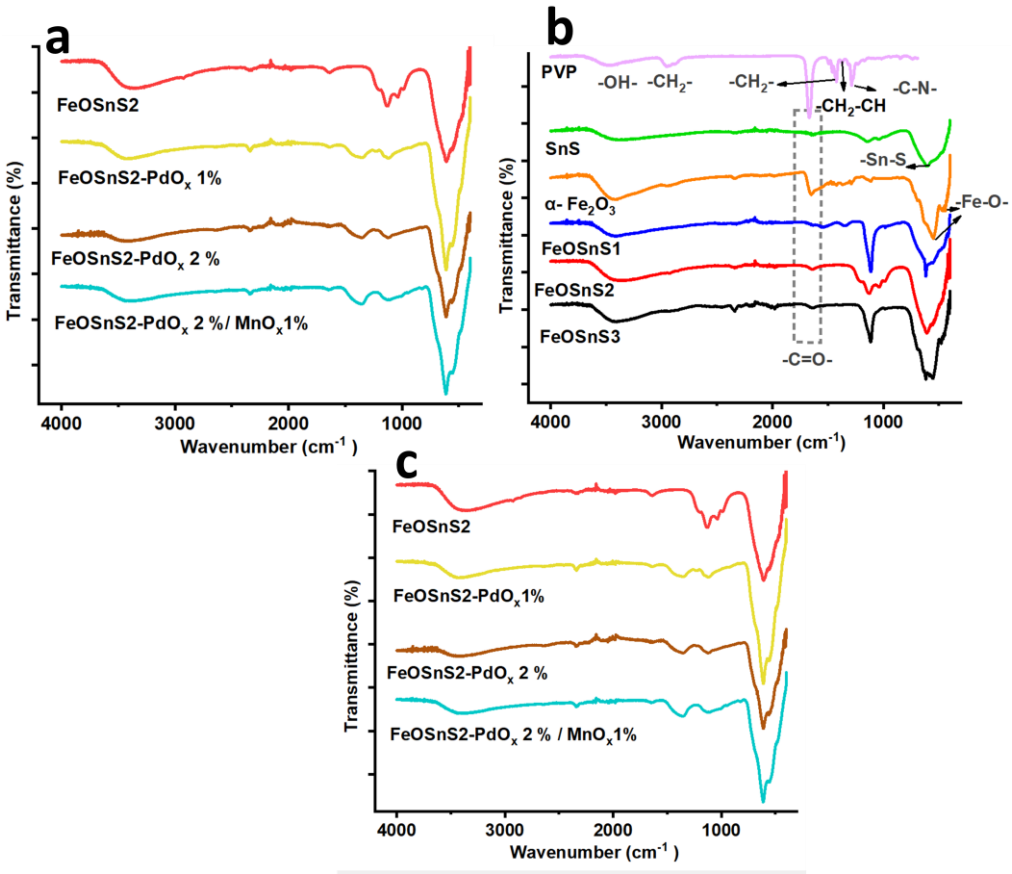

Figure 7.11 (a) ATR-FTIR spectra of as-synthesized α-Fe_2O_3, SnS, and FeOSnS1-3 catalysts, (b) magnified view of the ATR-FTIR spectra showing the chemical shift of -C=O functional group after heterostructure formation, (c) ATR-FTIR spectra of FeOSnS2/ PdO_x/MnO_x catalysts.

Catalyst	Surface area, S_{BET} (m^2/g)	Pore volume (cc/g)
α-Fe_2O_3	24.6	0.031
SnS	60.9	0.063
FeOSnS1	27.1	0.029
FeOSnS2	24.9	0.008
FeOSnS3	30.7	0.011
FeOSnS2-PdO_x 1 %	22.1	0.007
FeOSnS2-PdO_x 2 %	18.5	0.006
FeOSnS2-PdO_x 2 % / MnO_x 1 %	15.6	0.005

Table 7.2 Physicochemical properties of as-synthesized α-Fe_2O_3, SnS, FeOSnS1-3 and FeOSnS2/PdO_x/MnO_x catalysts.

The UV−vis diffuse reflectance revealed absorption edges at 280 nm, 528 nm and 648 nm for pure α-Fe_2O_3 and 667 nm for pure SnS which agress well with literature (Figure 7.12). [10] After heterostructure formation, an increase in the absorption intensity a red-shift towards longer wavelengths with the absorption edges at 693, 704, and 728 nm were obtained for FeOSnS1, FeOSnS2 and FeOSnS3 respectively (Figure 7.12). Furthermore, a slight blue-shift of the absorption from 704 nm for FeOSNS2 to 635, 656 and 665 nm for FeOSNS2- PdO_x 1%, FeOSNS2- PdO_x 2 % and FeOSNS2- PdO_x 2 %/MnO_x1 % respectively was observed, in addition to improved visible light harvesting intensity in the range of 400−550 nm (Figure 7.12).[11] These results imply that the integration of two moieties to form a heterojunction structure and loading of cocatalyst, improves the visible light harvesting efficiency due to the local surface plasmon resonance effect (SPR) of Pd nanoparticles and the *d* − *d* transition between Mn^{3+} and Mn^{4+} in MnO_x.[12] Based on the Tauc Plot, the band gap (E_g) value of α-Fe_2O_3 was 1.93 eV smaller than previously reported by Carmalt *et al*.[13] and Schwaminger *et*

al. [14] an increase in the particle size, as in our case, arising from the aggregation of primary crystals evidenced by TEM results, is believed to contribute to a reduced E_g value.[14] Pristine SnS exhibited E_g values of 1.44 eV comparable to the 1.41 eV reported for SnS nanoflakes reported by Mohan Kumar *et al*.[15]The calculated direct E_g values of the FeOSnS1-3 heterocatalysts were 1.52, 1.75 and 1.68 eV respectively. (Figure 7.13) The calculated direct E_g values of FeOSnS2- PdO_x/MnO_x catalysts show increased compared to FeOSnS2. The obtained values were 2.01, 1.98 and 1.97 eV for for FeOSNS2- PdO_x 1 %, FeOSNS2- PdO_x 2 % and FeOSNS2- PdO_x 2 %/MnO_x1 % respectively.

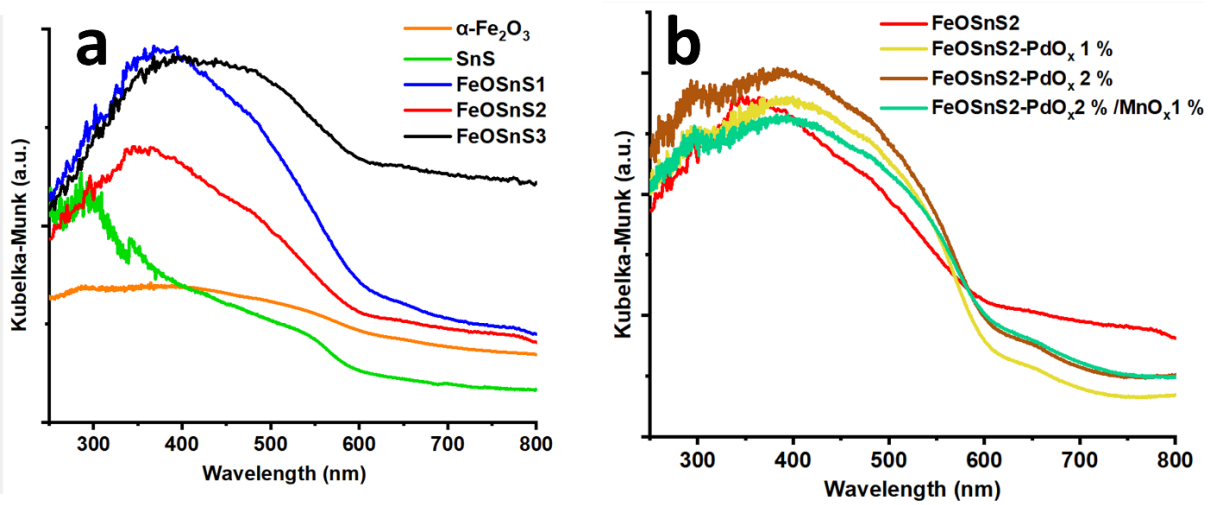

Figure 7.12 UV-VIS diffuse reflectance spectra represented as Kubelka-Munk Function of as-synthesized (a) α-Fe_2O_3, SnS, FeOSnS1-3 and (b) FeOSnS2/ PdO_x/MnO_x catalysts.

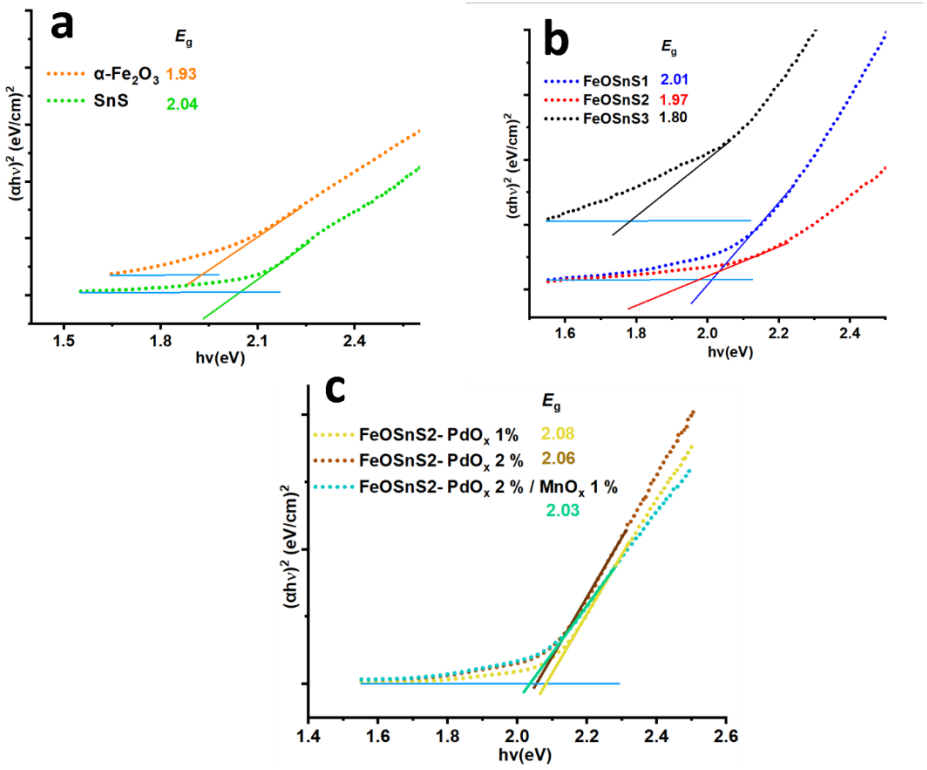

Figure 7.13**.** Tauc plots for calculation of the direct optical band gaps of as-synthesized α-Fe_2O_3, SnS, FeOSnS1-3 and FeOSnS2/PdO_x/MnO_x catalysts.

EDS analysis was acquired to investigate the chemical composition and atomic ratio of the catalysts. The characteristic peaks for iron (Fe), oxygen (O) and carbon (C) were detected in the EDS spectrum of α-Fe_2O_3. (Figure 7.14a). Considering the EDS semi-quantitative data, the atomic percentage (At %) of Fe and O gives the Fe:O atomic ratio of 2:2.7, verifying the formation of stoichiometric α-Fe_2O_3.[16] The EDS spectra of SnS exhibits the signals for C, Sn and S atoms ((Figure 7.14b). The presented data reveal an atomic ratio for Sn:S of 70.3, indicating the synthesized SnS catalyst deviated from stoichiometry. This high sulfur-deficiency is due to post-calcination of SnS which results in significant evaporation of sulfur due to its high volatility.[17] Banu *et al.* reported the atomic ratio of Sn:S = 21.97 after annealing the prepared SnS thin films at 500 °C for 30 min.[18]

The EDS spectra of FeOSnS1, FeOSnS2 and FeOSnS3 (Figures 7.14c, d & e) exhibit the signals for C, O, Fe, Sn and S atoms, confirming the presence of both α-Fe_2O_3 and SnS species and the successful formation of the FeOSnS heterocatalysts.[19] The intensity of Fe and O signals are higher in FeOSnS3 than that of FeOSnS2. Conversely, the intensity of the Sn signal is higher in FeOSnS2 than FeOSnS3, which is consistent with the weight percentage of the

initial α-Fe_2O_3 and SnS catalysts used in the synthesis of the heterocatalysts. This indicates the homogeneity and chemical uniformity of the heterocatalysts. Notably, the Cl and Si signals in the EDS spectrum come from unreacted $SnCl_2$ and $PdCl_2$, and the Si coating onto which the powder sample was mounted in sample preparation. Qualitative measurements using EDS suggested the presence of both Pd and Mn cocatalysts in the FeOSnS2 heterocatalyst (Figures 7.4f, g & h).[20] The detection limit of EDS used in this study was < 1 wt %, hence the technique was not able to give accurate quantitative values.

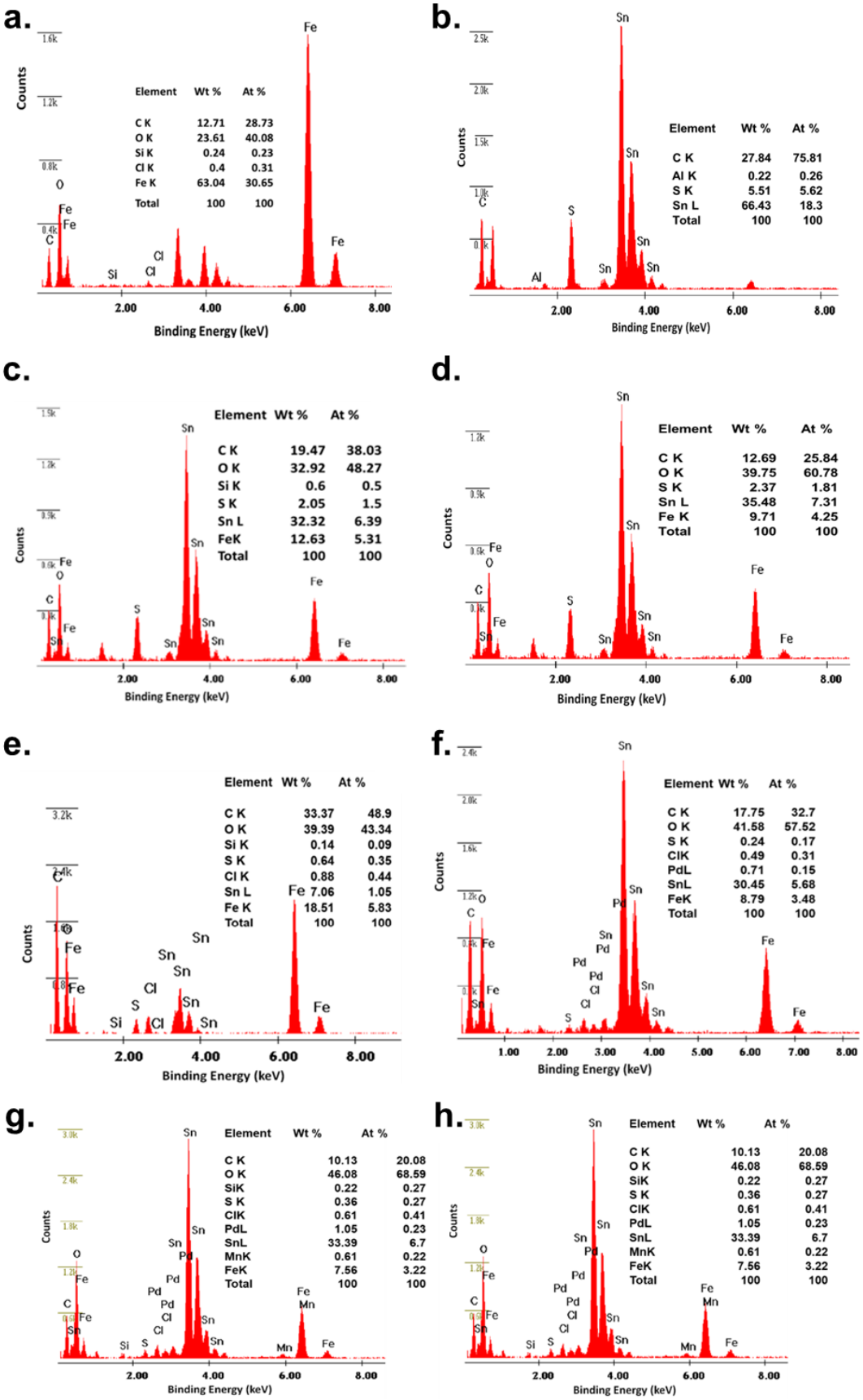

Figure 7.14 EDS patterns of (a) α-Fe_2O_3 (b) SnS, (c) FeOSnS1, (d) FeOSnS2, (e) FeOSnS3, (f) FeOSnS2-PdO_x 1 % (g) FeOSnS2-PdO_x 2 % and (c) FeOSnS2-PdO_x 2 % / MnO_x 1 % catalysts.

The actual content of PdO_x and MnO_x loaded in the FeOSnS2 photocatalyst was measured using atomic absorption spectroscopy (AAS). The quantities were close to the detection limits of the instrument, resulting in large errors. As presented in Table 7.3, the estimated value was 0.90 (± 0.18) % for FeOSnS2- PdO_x 1 %, close to the theoretical value of 1 %. The Wt % was 43% smaller than the theoretical value in the case of FeOSnS2- PdO_x 2 % and 51% for FeOSnS2- PdO_x 2 %/MnO_x 1 %. This could be attributed to the loss of cocatalyst during the loading and washing processes.[21] Moreover, the specific surface areas decrease as the content of PdO_x increases from 1 % to 2 % and also when MnO_x co-loaded on the surface of FeOSnS2 photocatalyst as evidenced by BET results (Table 7.2). Yang *et al.* reported the lowest PdO_x loading on the synthesized Fe_3O_4@SiO_2 catalyst, ascribed to the smaller surface area.[22]

Table 7.3 Quantification of PdO_x and MnO_x cocatalyst in FeOSnS2 heterocatalysts.

Catalyst	PdO_x Wt %			MnO_x Wt %		
	Theoretical	EDS	AAS	Theoretical	EDS	AAS
FeOSnS2- PdO_x 1 %	1	0.71	0.90 ± 0.18	-	-	-
FeOSnS2- PdO_x 2 %	2	1.56	1.1 ± 0.22	-	-	-
FeOSnS2- PdO_x 2 % / MnO_x 1 %	2	1.05	0.98 ± 0.19	1	0.61	0.81 ± 0.16

Room-temperature photoluminescence studies of the synthesized catalysts dissolved in ethanol were carried out to survey the e^-/h^+ separation potential (Figure 7.15). Pristine SnS presents the highest PL emission intensity, whilst α-Fe_2O_3 exhibits the lowest PL emission intensity for 320 nm excitation corresponding to the higher and lower e^-/h^+ recombination rate. After integration of α-Fe_2O_3 and SnS components, the PL emission intensity of the resulting heterocatalysts (FeOSnS1-3) decreases. This suggests that the transfer of e^- species between SnS and α-Fe_2O_3 as a result of heterostructuring may suppress the e^-/h^+ recombination process.[23] Loading PdO_x and MnO_x cocatalysts further reduces the PL

intensity of the FeOSnS2 heterocatalyst, indicating the further suppression of e^-/h^+ recombination, possibly due to the e^- transfer process from FeOSnS2 to PdO_x cocatalysts.[24]

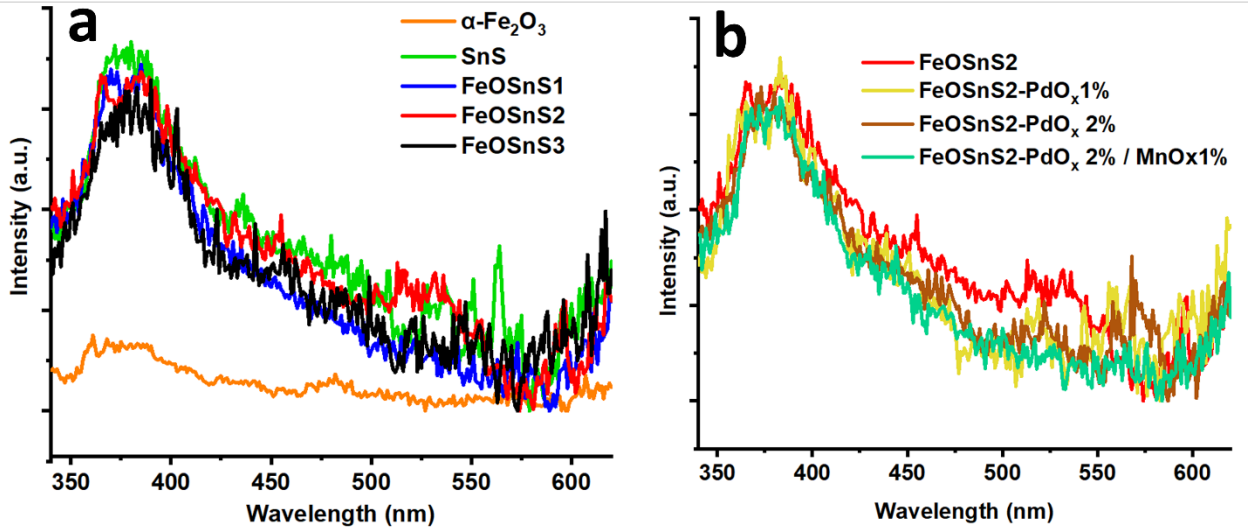

Figure 7.15 PL spectra of as-synthesized α-Fe_2O_3, SnS, FeOSnS1-3 (a) and FeOSnS2/PdO_x/MnO_x catalysts (b) under 325 nm excitation.

Magnetic Properties

The static magnetization measurements as a function of the applied magnetic field (M−H loops) were recorded by VSM for α-Fe_2O_3 and FeOSnS2 catalysts at room temperature (300 K) (Figure 7.16 a,b). Parameters including saturation magnetization (M_s), remanence (M_r), and coercivity (H_c) were extracted from the M – H loops. It is well-known that α-Fe_2O_3 exhibits ferromagnetism,[25] however characteristics of superparamagnetic behaviour were observed for both catalysts based on the M–H curves, with near-zero coercivity and remanence values. Similar superparamagnetic behaviour was reported by Tadic *et al.* for 8 nm α-Fe_2O_3 with an M_S value of 3.98 emu/g, Bødker *et al.* for 5 nm spherical α-Fe_2O_3 with an M_S value of 8.5 emu/g and Manukyan *et al.* for ultrasmall (< 5 nm) α-Fe_2O_3 with an M_S value of 21 emu/g.[26] Additionally, Wang *et al*. reported that the magnetic properties of α-Fe_2O_3 can be tuned by controlling the morphology, where 60 nm spherical α-Fe_2O_3 presented superparamagnetic behaviour (with coercivity almost zero), while hollow microspheres showed strong ferromagnetic behaviour and coercivity of 2528 Oe at RT.[27] Our as-

synthesized pristine α-Fe_2O_3 exhibited the saturation magnetization of 2.22 emu/g at 300 K, with H_c and M_r values of 2.16 Oe and 0.4 emu/g, respectively. The achieved M_s value for our α-Fe_2O_3 is higher than that of bulk α-Fe_2O_3 (M_s = 0.3 emu/g) and values reported for pure α-Fe_2O_3 (normally below 1 emu/g).[28] As confirmed by TEM, the prepared α-Fe_2O_3 catalyst resulted from the aggregation of primarily individual nanocrystals. The net magnetization results from the magnitude and orientations of the magnetic moment of the individual nanocrystals. Magnetic moments of individual nanocrystals add up vectorially resulting in increased magnetization.[29] The saturation magnetization of FeOSnS2 was found to be lower than that of pristine α-Fe_2O_3 with M_s = 0.523 emu/g at 300 K, H_c = 4.86 Oe and M_r = 0.055 emu/g. The lower M_s in the FeOSnS2 heterocatalyst is consistent with the lower iron concentration (the iron cation concentration is 100 % for α-Fe_2O_3 versus 25 % for FeOSnS2, the remaining 75 % wt being diamagnetic SnS, contributing to the overall mass fraction and reduced magnetization).[30] In spite of the reduced magnetization, the FeOSnS2 photocatalyst can still be easily recycled from the solution after photocatalysis through the application of a magnetic field (Figure 7.16c).[31]

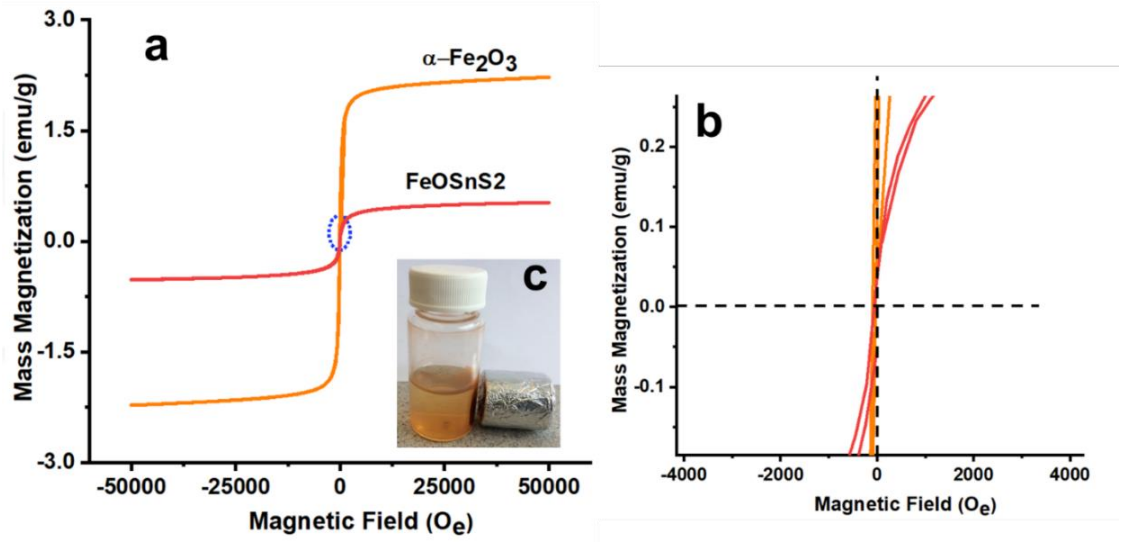

Figure 7.16 (a) Hysteresis loops of α-Fe2O3 and FeOSnS2 catalysts measured at RT. (b) Magnified view of hysteresis loop in low magnetic field, as indicated by blue circle in (a). (c) Inset shows the magnetic response of FeOSnS2 catalysts to an external magnetic field.

To explore the electron flow in the SnS/α-Fe_2O_3 heterocatalyst, the conduction band (CB) and valence band (VB) edge positions of SnS and α-Fe_2O_3 photocatalysts were acquired using the following equations:[19]

$$E_{CB} = \chi - E_C - 0.5E_g \quad (1)$$

$$E_{VB} = E_{CB} + E_g \quad (2)$$

where E_{VB} and E_{CB} are the VB and CB edge potentials of the photocatalyst, χ is the electronegativity of the photocatalyst and was calculated by the following equation:

$$\chi = [x(A)^a x(B)^b]^{1/(a+b)} \quad (3)$$

In which a, b, and c are the number of atoms in the compounds.

χ for α-Fe_2O_3 can be calculated as follows:

For Fe:

EIE = 762.5 kJ/mol ÷ 96.48 = 7.9 eV
EEA = 15.7 kJ/mol ÷ 96.48 = 0.17 eV
χ Fe= 1/2(7.9 + 0.17) = 4.11

For O:

EIE = 1313.9 kJ/mol ÷ 96.48 = 13.5 eV
EEA = 141 kJ/mol ÷ 96.48 = 1.45 eV
χ O= 1/2(13.6 + 1.46) = 7.53

χ α-Fe_2O_3 = $[x(Fe)^2 x(O)^3]^{1/(2+3)}$ = $[7212.2]^{1/5}$ = 5.89

χ for SnS can be calculated as follows:

For Sn:

EIE = 708.6 kJ/mol ÷ 96.48 = 7.34 eV
EEA = 107.3 kJ/mol ÷ 96.48 = 1.11 eV
χ Sn = ½ (7.34 + 1.11) = 4.22

For S:

EIE = 999.6 kJ/mol ÷ 96.48 = 10.36 eV
EEA = 200 kJ/mol ÷ 96.48 = 2.07 eV
χ Sn = ½ (10.36 + 2.07) = 5.69
χ_{SnS} = $[x(Sn)x(S)]^{1/(1+1)}$ = $[4.22*5.69]^{1/2}$ = 4.90

EIE and EEA are the first ionization energy and atomic electron affinity, respectively, E_c is the energy of free electrons (4.5 eV on the hydrogen scale) and E_g the band gap energy of the photocatalysts extracted from the UV−vis DRS spectra.[32]

Applying the obtained χ values of SnS and α-Fe_2O_3 as 4.90 and 5.89 eV and E_g values of SnS and α-Fe_2O_3 extracted from the Tauc and Davis – Mott model as 1.44 and 1.93 eV, E_{VB} and E_{CB} were calculated to be 2.24 and 0.54 eV for α-Fe_2O_3 and –0.56 and 1.36 eV for SnS respectively.

$E_{CB\ \alpha\text{-}Fe2O3}$ = 5.89-4.5-0.85= 0.96 eV

$E_{VB\ \alpha\text{-}Fe2O3}$ = 0.96 +1.93= 2.89 eV

$E_{CB\ SnS}$ = 4.9-4.5-0.72= - 0.40 eV

$E_{VB\ SnS}$ = -0.40 + 1.44= 1.04 Ev

References:

[1] S. Saha, B. Martin, B. Leonard, D. Li, J. Mater. Chem. A 2016, 4, 9253.
[2] I. A. Safo, M. Werheid, C. Dosche, M. Oezaslan, Nanoscale Adv. 2019, 1, 3095.
[3] A. Javed, N. Khan, S. Bashir, M. Ahmad, M. Bashir, Mater. Chem. Phys. 2020, 246, 122831; J. Henry, K. Mohanraj, S. Kannan, S. Barathan, G. Sivakumar, J. Exp. Nanosci. 2015, 10, 78.
[4] G. Wu, X. Tan, G. Li, C. Hu, J. Alloys Compd. 2010, 504, 371.
[5] R. Bryaskova, D. Pencheva, S. Nikolov, T. Kantardjiev, J. Chem. Biol. 2011, 4, 185.
[6] S. Han, L. Hu, Z. Liang, S. Wageh, A. A. Al-Ghamdi, Y. Chen, X. Fang, Adv. Funct. Mater. 2014, 24, 5719.
[7] X. Meng, Z. Zhang, Appl. Catal. B. 2017, 209, 383.
[8] M. Anas, Dong S. Han, K. Mahmoud, H. Park, A. Abdel-Wahab, Mater. Sci. Semicond. Process. 2016, 41, 209.
[9] T. Han, Y. Wei, X. Jin, H. Jiu, L. Zhang, Y. Sun, J. Tian, R. Shang, D. Hang, R. Zhao, Journal of Materials Science 2019, 54, 7119.
[10] L. Yu, Y. Zhang, J. He, H. Zhu, X. Zhou, M. Li, Q. Yang, F. Xu, J. Alloys Compd. 2018, 753, 601; X. Yan, K. Ye, T. Zhang, C. Xue, D. Zhang, C. Ma, J. Wei, G. Yang, New J. Chem. 2017, 41, 8482.
[11] P. J. Mafa, A. T. Kuvarega, B. B. Mamba, B. Ntsendwana, Appl. Surf. Sci. 2019, 483, 506.
[12] X. Meng, Z. Li, N. Yun, Z. Zhang, J. Nanomater. 2018, 2018, 1234506.
[13] A. Jiamprasertboon, A. Kafizas, M. Sachs, M. Ling, A. M. Alotaibi, Y. Lu, T. Siritanon, I. P. Parkin, C. J. Carmalt, Chem. Eur. J. 2019, 25, 11337.
[14] S. P. Schwaminger, R. Surya, S. Filser, A. Wimmer, F. Weigl, P. Fraga-García, S. Berensmeier, Sci. Rep. 2017, 7, 12609.

[15] H. Chauhan, M. K. Singh, S. A. Hashmi, S. Deka, RSC Adv. 2015, 5, 17228; G. Mohan Kumar, X. Fu, P. Ilanchezhiyan, S. U. Yuldashev, D. J. Lee, H. D. Cho, T. W. Kang, ACS Appl. Mater. Interfaces 2017, 9, 32142.
[16] M. Imran, A. B. Yousaf, P. Kasak, A. Zeb, S. J. Zaidi, J. Catal. 2017, 353, 81.
[17] D. Ding, T. Rath, L. Lanzetta, J. Manuel Marin-Beloqui, S. A. Haque, ACS Appl. Energy Mater. 2018, 1, 3042.
[18] S. Banu, S. J. Ahn, Y. J. Eo, J. Gwak, A. Cho, Sol Energy. 2017, 145, 33.
[19] K. C. Christoforidis, A. Sengele, V. Keller, N. Keller, ACS Appl. Mater. Interfaces. 2015, 7, 19324.
[20] K. Qi, Y. Li, Y. Xie, S.-y. Liu, K. Zheng, Z. Chen, R. Wang, Front. Chem. 2019, 7.
[21] W. Liang, X. Du, Y. Zhu, S. Ren, J. Li, Catalysts 2020, 10, 347.
[22] L. Yang, X. Chen, Z. Zhou, R. Zhang, L. Li, Z. Cheng, X. Fang, ChemistrySelect. 2016, 1, 5599.
[23] P. Cai, S.-M. Zhou, D.-K. Ma, S.-N. Liu, W. Chen, S.-M. Huang, Nanomicro Lett. 2015, 7, 183.
[24] H. Enzweiler, P. H. Yassue-Cordeiro, M. Schwaab, E. Barbosa-Coutinho, M. H. N. Olsen Scaliante, N. R. C. Fernandes, Int. J. Hydrog. Energy. 2018, 43, 6515.
[25] H. Yin, Y. Zhao, Q. Hua, J. Zhang, Y. Zhang, X. Xu, Y. Long, J. Tang, F. Wang, Front. Chem. 2019, 7.
[26] M. Tadic, N. Citakovic, M. Panjan, B. Stanojevic, D. Markovic, Đ. Jovanovic, V. Spasojevic, J. Alloys Compd. 2012, 543, 118; F. Bødker, M. F. Hansen, C. B. Koch, Phys. Rev. B Condens. Matter Mater. Phys. 2000, 61, 6826; K. V. Manukyan, Y.-S. Chen, S. Rouvimov, P. Li, X. Li, S. Dong, X. Liu, J. K. Furdyna, A. Orlov, G. H. Bernstein, W. Porod, S. Roslyakov, A. S. Mukasyan, J. Phys. Chem. C. 2014, 118, 16264.
[27] H. Wang, W. Geng, Y. Wang, Res. Chem. Intermed. 2011, 37, 389.
[28] J. Lian, X. Duan, J. Ma, P. Peng, T. Kim, W. Zheng, ACS Nano 2009, 3, 3749; M. Tadic, M. Panjan, V. Damnjanovic, I. Milosevic, Appl. Surf. Sci. 2014, 320, 183.
[29] F. Ahrentorp, A. Astalan, J. Blomgren, C. Jonasson, E. Wetterskog, P. Svedlindh, A. Lak, F. Ludwig, L. J. van Ijzendoorn, F. Westphal, C. Grüttner, N. Gehrke, S. Gustafsson, E. Olsson, C. Johansson, J. Magn. Magn. Mater. 2015, 380, 221.
[30] C. Haw, W. Chiu, S. Abdul Rahman, P. Khiew, S. Radiman, R. Abdul Shukor, M. A. A. Hamid, N. Ghazali, New J Chem. 2016, 40, 1124.
[31] H. Wang, L. Xu, C. Liu, Z. Jiang, Q. Feng, T. Wu, R. Wang, Ceram. Int. 2020, 46, 460.
[32] M. Mousavi, A. Habibi-Yangjeh, M. Abitorabi, J. Colloid Interface Sci. 2016, 480, 218.

Chapter 8. Conclusion and future directions

The objective of this thesis was to synthesise two phases of IONPs, Fe_3O_4 and α-Fe_2O_3, with low polydispersity by a simple hydrothermal method.

In Chapter 1, the crystalline structure, physicochemical and magnetic properties of Fe_3O_4 and α-Fe_2O_3 were compared and discussed.

The thesis was thereafter divided into sections. Section 1, containing Chapters 2 – 5, investigated Fe_3O_4 NPs. In Section 2, α-Fe_2O_3 was considered, and the results were summarised in Chapters 6 and 7.

In Chapter 2, a literature review was completed for Fe_3O_4 NPs, including their properties and potential technological applications, which encompass biomedicine, healthcare, environmental remediation, agriculture, food, energy, defence, and aerospace construction. In terms of biomedical applications, Fe_3O_4 NPs were found to be under research development for enzyme/protein immobilisation, magnetofection, cell labelling, DNA detection and tissue engineering. The focus of the literature review then shifted to the biomedical applications which have been developed, from laboratory-based research to clinical approval and commercialisation. Five applications including MRI, MDT, MFH, IMS and MPI were discussed. Finally, the advancement of Fe_3O_4-based fluids through theranostic applications which have been commercialised or gained FDA or EU approval were examined. Overcoming the physicochemical and biological limitations of Fe_3O_4 NPs, such as potential aggregation and toxicity at higher dose through proper design and functionalisation procedures, should be investigated for the future success of the technologies based on Fe_3O_4 NPs in the biomedical field.

Chapter 3 focuses on MFH due to its importance in cancer treatment, considering the high cancer mortality rate in New Zealand. The literature over the last 27 years (1993 – 2020) was comprehensively examined, including the fundamentals of MFH, its clinical status, the low heating potential associated with commercial Fe_3O_4 fluid, the technical limitations of clinical settings, and proposed solutions to improve the efficiency of MFH. The future directions for improving the efficiency of MFH include a) standardisation of the concentration of Fe_3O_4 fluid and MF parameters (f and H) in the field, b) advances in

instrumentation to maximise the localisation of Fe_3O_4 fluid in tumour areas and c) improvement in the focus of the MF on the tumours.

In Chapter 4, Fe_3O_4 nanoparticles were synthesised through a modified organic phase hydrothermal route by decomposition of iron acetylacetonate in the presence of a set of surfactants and stabilising agents, namely oleic acid, oleylamine and tri-*n*-octylphosphine oxide, in octadecene as the solvent. By controlling reaction parameters such as time, temperature, and surfactant to metal core ratios, a molar ratio of OA to OAm of (1:4), TOPO amount of 0.5 mmol and reaction time of 120 min at 240 °C were found to be the optimal conditions for the synthesis of nanoparticles with low polydispersity. Diamagnetic Zn^{2+} and Mg^{2+} ions were introduced into Fe_3O_4 to develop monodisperse $MFe_{3-x}O_4$ (M = Fe, Mg, Zn) spinel nanoferrites. TEM results showed that the prepared nanoferrites were assembled in a close-packed arrangement, however the interfacial contact between the nanoparticles was very low. DLS studies revealed that nanoferrites clumped together in solution (hexane) and formed larger nanocrystals of up to a hundred nanometres, due to van der Waals and magnetic dipole-dipole attractions. AAS showed a deviation in the chemical compositions from theoretical assumptions for all doped nanoferrites except ZnFe1. This was ascribed to excessive surfactants used in the synthesis, which may decrease the decomposition temperature of the metal precursors and influence the growth mechanism. Strong signals for carbon in EDS, XPS and TGA results confirmed the excess of surfactants. Magnetisation measurements showed negligible coercivity and remanence in the hysteresis loops of $MFe_{3-x}O_4$ (M = Fe, Mg, Zn) nanoferrites. The temperature dependence of magnetisation revealed T_B to be well below room temperature for all nanoferrites. These results suggested a superparamagnetic-like behaviour for all nanoferrites. Magnetic hyperthermia measurements displayed a T_{max} of 66 °C for an aqueous ferrofluid of non-doped Fe_3O_4 NPs under magnetic field operating at a frequency of f = 194.5 kHz and field amplitude of H = 114.01 mT for 12 min.

In Chapter 5, two modifications were made to the method in Chapter 4 for the synthesis of $M_xFe_{3-x}O_4$ (M = Fe, Mn, Zn) nanoferrites. Firstly, OA was replaced with PVP to investigate its effect on the monodispersity and shape of prepared NPs. Secondly, Mn^{2+} paramagnetic ions replaced the Mg^{2+} diamagnetic ions to study their effect on magnetisation. The TEM images revealed a bimodal arrangement of NPs, where some NPs were in a close-packed assembly

with close interfacial contact with adjacent NPs and others were at significant interparticle distances from each other. The nanoferrites exhibited deformed morphologies in comparison to the previous chapter which had OA as the stabiliser. XRD results revealed an increase in the lattice parameters for Fe_3O_4 after doping with Zn^{2+} and Mn^{2+} due to the expansion of the unit cell volume. The organic contents on the surface of $M_xFe_{3-x}O_4$ (M = Fe, Mn, Zn) nanoferrites were generally higher than that of $M_xFe_{3-x}O_4$ (M = Fe, Mg, Zn) nanoferrites as evidenced by TGA results. XPS studies showed that the Mn and Zn ions were in the 2+ the oxidation state and manganese and zinc ferrite had been formed. VSM studies suggested that the inclusion of Mn^{2+} and Zn^{2+} ions did not alter the superparamagnetic feature of the Fe_3O_4 NPs. Additionally, the replacement of Mg^{2+} with Mn^{2+} was successful in terms of increasing the magnetisation of bare Fe_3O_4 NPs, while, similar to Chapter 4, the substitution of diamagnetic Zn^{2+} resulted in reduced magnetisation of bare Fe_3O_4 NPs.

- Future directions for Chapters 4 and 5:

The use of different surfactants such as natural polymers (chitin, chitosan, cellulose or starch) or synthetic polymers (such as polyethylene glycol or polyvinyl alcohol) to investigate their effect on size monodispersity and shape.

- NPs could be prepared with higher magnetic core ratios and less surfactants in order to have monodisperse NPs with less carbon atoms on the surface, higher magnetisation and improved heating performances.
- Different transition *d* block elements such as Ni, Cr, and Co with different concentration could be doped into Fe_3O_4 and the magnetic and MFH properties could be investigated.

MFH measurements could be conducted under different frequencies and field amplitudes, and different concentration of fluids under the safe threshold of $H \times f < 4.8 \times 10^9$ A m^{-1} s^{-1} in order to find the optimal operating conditions which may lead to an improved T_{max} (i.e. higher than the 66 °C achieved in this thesis). *In vitro* and *in vivo* studies should be done in order to gain better insights into the potential of the prepared nanoferrites for MFH studies. The T_{max} achieved in *in vivo* trials is generally lower than T_{max} achieved in *in vitro* studies due to the blood circulation, nevertheless the actual T_{max} achieved in the *in vivo* trials present the true potential of NPs for the effective killing of cancer cells.

- Nanoferrites could be synthesised in different shapes by controlling experiment conditions such as time, temperature and surfactant amount, and the effect of shape on the heating potential of fluids could be then be investigated.

In Chapter 6, after a literature review of the potential industrial and biomedical applications of α-Fe_2O_3, the photocatalytic splitting of water was selected in order to study the potential application of synthesised α-Fe_2O_3. The literature on photocatalytic water splitting and the basic principles of the process that leads to the generation of H_2 and O_2 fuels through H_2O splitting was first reviewed, including a consideration of the challenges associated with single photocatalysts in the field. Proposed strategies to address these challenges were then studied, with a hybrid strategy selected for further investigation in Chapter 7 involving α-Fe_2O_3 with a heterojunction and loaded with cocatalysts.

In Chapter 7, hematite was synthesised using an aqueous-phase hydrothermal method through systematic studies controlling reaction parameters such as time, temperature and PVP amount. After optimisation of reaction parameters, monodisperse α-Fe_2O_3 NPs were synthesised with $Fe(acac)_3$ (0.2 mmol), PVP (0.4 mmol) in DMF (20 mL) at 180 °C after 2 h. The prepared α-Fe_2O_3 was integrated with SnS to form a Fe_2O_3/SnS heterocatalyst.

XRD results showed no changes in the diffraction peak positions for α-Fe_2O_3 and SnS in the prepared FeOSnS heterocatalyst, which suggested successful hybridisation. No obvious characteristic peaks of PdO_x and MnO_x loaded FeOSnS2 heterocatalyst were identified. TEM also revealed the dispersion of α-Fe_2O_3 onto the SnS catalyst without morphological changes after hybridisation. EDS spectra and mapping results confirmed the distribution of Pd and Mn cocatalysts onto the FeOSnS2 heterocatalyst. In support of XRD and TEM results, TGA studies suggested the FeOSnS heterocatalyst had improved thermal stability, corresponding to the successful conjugation of individual catalysts. VSM studies showed a reduction in magnetisation for the FeOSnS heterocatalyst compared to pristine α-Fe_2O_3, due to the presence of the non-magnetic SnS constituent. BET surface analysis revealed a reduction of active surface area for the FeOSnS heterocatalyst compared to pristine α-Fe_2O_3 and SnS due to the blockage of pores as a result of coupling. In addition, co-loading of PdO_x and MnO_x cocatalysts further reduced the specific surface area. The photoluminescent emission intensity of SnS decreased after hybridisation with α-Fe_2O_3, indicating the suppression of e^- /h^+ recombination. The results of photocatalytic water splitting reactions suggested an

improvement in H_2 evolution for the FeOSnS heterocatalyst compared to that of pristine SnS and α-Fe_2O_3. Furthermore, co-loading of PdO_x and MnO_x cocatalysts on the heterocatalyst achieved the highest H_2 evolution through ethanol photoreforming.

- Future directions that can be taken for this work include:
- Calcination of SnS could be completed at lower temperatures in order to minimise the evaporation of sulfur.
- The calcination process could also be conducted at different temperatures to assess the effect on morphology of the SnS catalyst.
- Construction of the α-Fe_2O_3/SnS heterocatalyst could be attempted using other chemical methods such as hydrothermal, deposition-precipitation, pyrolysis, electrodeposition, photo-deposition and thermal decomposition or physical-mixing methods. This will allow the effect of the synthetic method on WS performance to be studied, bearing in mind that the synthetic method can affect the WS efficiency through the creation of different sizes and shapes of NPs. Furthermore, effective interfacial contact between components can also improve WS performance.
- α-Fe_2O_3 could be hybridised with other transition metal dichalcogenides such as SnSe, Bi_2S_3, ZnS, and MoS_2, InSe, and CdS, in order to study the effect of band engineering of synthesised hybridised system on WS potency.
- Reduction cocatalysts such as Pt, Au, Ag, Pd, Rh, Al, and Bi or oxidation cocatalysts such as CuO_x, IrO_x, NiCoP, NiCoPi, CoO_x, FeO_x, NiO_x, $FeCoO_x$, and $FeNiCoO_x$ could also be tested for H_2 production experiments. The effect of the ratio and concentration of redox co-catalysts on the H_2 production efficiency of the heterocatalyst could be investigated.